NASA/CR—1999–209427

Guidelines for Proof Test Analysis

G.G. Chell, R.C. McClung, and C.J. Kuhlman
Southwest Research Institute, San Antonio, Texas

D.A. Russell, K. Garr, and B. Donnelly
Rocketdyne Division, Boeing North American, Canoga Park, California

Prepared for Marshall Space Flight Center
under Contract NAS8–39380

July 1999

The NASA STI Program Office...in Profile

Since its founding, NASA has been dedicated to the advancement of aeronautics and space science. The NASA Scientific and Technical Information (STI) Program Office plays a key part in helping NASA maintain this important role.

The NASA STI Program Office is operated by Langley Research Center, the lead center for NASA's scientific and technical information. The NASA STI Program Office provides access to the NASA STI Database, the largest collection of aeronautical and space science STI in the world. The Program Office is also NASA's institutional mechanism for disseminating the results of its research and development activities. These results are published by NASA in the NASA STI Report Series, which includes the following report types:

- TECHNICAL PUBLICATION. Reports of completed research or a major significant phase of research that present the results of NASA programs and include extensive data or theoretical analysis. Includes compilations of significant scientific and technical data and information deemed to be of continuing reference value. NASA's counterpart of peer-reviewed formal professional papers but has less stringent limitations on manuscript length and extent of graphic presentations.

- TECHNICAL MEMORANDUM. Scientific and technical findings that are preliminary or of specialized interest, e.g., quick release reports, working papers, and bibliographies that contain minimal annotation. Does not contain extensive analysis.

- CONTRACTOR REPORT. Scientific and technical findings by NASA-sponsored contractors and grantees.

- CONFERENCE PUBLICATION. Collected papers from scientific and technical conferences, symposia, seminars, or other meetings sponsored or cosponsored by NASA.

- SPECIAL PUBLICATION. Scientific, technical, or historical information from NASA programs, projects, and mission, often concerned with subjects having substantial public interest.

- TECHNICAL TRANSLATION. English-language translations of foreign scientific and technical material pertinent to NASA's mission.

Specialized services that complement the STI Program Office's diverse offerings include creating custom thesauri, building customized databases, organizing and publishing research results...even providing videos.

For more information about the NASA STI Program Office, see the following:

- Access the NASA STI Program Home Page at ***http://www.sti.nasa.gov***

- E-mail your question via the Internet to help@sti.nasa.gov

- Fax your question to the NASA Access Help Desk at (301) 621-0134

- Telephone the NASA Access Help Desk at (301) 621-0390

- Write to:
  NASA Access Help Desk
  NASA Center for AeroSpace Information
  800 Elkridge Landing Road
  Linthicum Heights, MD 21090-2934

NASA/CR—1999–209427

Guidelines for Proof Test Analysis

G.G. Chell, R.C. McClung, and C.J. Kuhlman
Southwest Research Institute, San Antonio, Texas

D.A. Russell, K. Garr, and B. Donnelly
Rocketdyne Division, Boeing North American, Canoga Park, California

Prepared for Marshall Space Flight Center
under Contract NAS8–39380

National Aeronautics and
Space Administration

Marshall Space Flight Center • MSFC, Alabama 35812

July 1999

Acknowledgments

The continuing encouragement and support of the NASA Marshall Space Flight Center technical staff is gratefully acknowledged. In particular, Charles L. Denniston provided assistance and advice on many occasions which benefited the program, and together with Gwyn C. Faile, Henry M. Lee, and Rod Stallworth, contributed to informative and helpful discussions during program review meetings.

A number of our colleagues at Southwest Research Institute made important contributions to the program. Tom Masden conducted the laboratory fracture testing and measurements; Harry R. Millwater performed the statistical analysis on the finite element *J* results; and Stephen J. Hudak, Jr., provided continuing help and support throughout the program. The patience and perseverance of Patty A. Soriano in helping to prepare the draft report, and Julie A. McCombs in helping to prepare the final version of the report, are also gratefully acknowledged.

Available from:

NASA Center for AeroSpace Information
800 Elkridge Landing Road
Linthicum Heights, MD 21090–2934
(301) 621–0390

National Technical Information Service
5285 Port Royal Road
Springfield, VA 22161
(703) 487–4650

TABLE OF CONTENTS

	Page
LIST OF ILLUSTRATIONS	x
LIST OF TABLES	xvi
DEFINITIONS	xviii
ACRONYMS/ABBREVIATIONS	xxiv
NOMENCLATURE	xxv
SCOPE OF GUIDELINES	xxix
BACKGROUND	xxx
EXECUTIVE SUMMARY	xxxii
1. INTRODUCTION	1
2. OVERVIEW	3
3. PROOF TEST LOGIC	6
3.1 Flaw Screening	6
3.2 Determining a Minimum Proof Load	8
4. PROOF TESTING IMPLEMENTATION ISSUES	10
4.1 Overview	10
4.2 Hardware Definition	10
4.3 Test Environment	10
4.4 Proof Load Factors	12
4.4.1 Minimum Requirements	12
4.4.2 Safe-Life Analysis	13
4.4.3 Proof Load Factors	14
4.4.4 Detrimental Deformations and Load-Induced Damage	15
4.5 Load Application	15
4.5.1 Loading and Unloading Rates and Hold Times	15
4.5.2 Number of Proof Cycles	16
4.6 Role of Non-Destructive Examination (NDE)	17
4.6.1 Pre-Test and Post-Test NDE	18
4.6.2 Flaw Detection and Growth During Testing	21
4.7 General Issues	21
4.7.1 Test Procedures	21
4.7.2 Fixture Design	22
4.7.3 Safety Considerations	22
4.7.4 Post-Mortem Analysis	22

TABLE OF CONTENTS (CONT.)

Page

4.7.5 Costs 23
4.7.6 Practical Difficulties 23

5. STATE-OF-THE-ART TECHNOLOGY FOR PROOF TEST ANALYSIS: FRACTURE MECHANICS AND VALIDATION 24
5.1 Fracture Mechanics 24
5.2 Validation of the Proof Test Methodology 27

6. GUIDELINES FOR PROOF TEST ANALYSIS: FLAW SCREENING AND MINIMUM PROOF LOADS 28
6.1 Road Map for Flaw Screening and Minimum Proof Load Analyses 28
6.2 Example Proof Test Analyses 48
6.3 Sensitivity Analysis 48

7. ASPECTS OF ADVANCED PROOF TEST ANALYSES 49
7.1 Probability Analysis 49
7.2 Multiple Cycling Proof Test Analysis 49
7.2.1 Background 49
7.2.2 MCPT Versus SCPT 50
7.2.3 Use of the Road Map in an MCPT Analysis 54

8. RAMIFICATIONS OF PROOF TESTING ON SERVICE ANALYSIS 55
8.1 Stress Analysis 55
8.2 Fracture Behavior 57
8.2.1 Brittle Materials 57
8.2.2 Ductile Materials 57
8.3 Fatigue Crack Growth Behavior 60
8.4 Flaw Characterization 62

9. SUMMARY AND CONCLUSIONS 66

10. REFERENCES 69

APPENDIX A: GUIDE TO STATE-OF-THE-ART FRACTURE MECHANICS FOR PROOF TEST ANALYSIS

A1. STRESS ANALYSIS A.1
A1.1 Structural and Constitutive Modeling A.1
A1.2 Categorization of Loads and Stresses A.2
A1.3 Residual Stresses A.2
A1.4 Stress Re-distribution A.3
A1.5 Conservative Stress Analyses A.3

TABLE OF CONTENTS (CONT.)

		Page
A2.	LINEAR ELASTIC FRACTURE MECHANICS	A.3
	A2.1 Stress Intensity Factors	A.3
	A2.2 Combined Primary and Secondary Loads	A.4
A3.	NET SECTION YIELD LOADS	A.5
	A3.1 Introduction	A.5
	A3.2 Fundamental Considerations	A.6
	A3.3 Available Solutions	A.6
A4.	ELASTIC-PLASTIC FRACTURE MECHANICS: CRACK TIP DRIVING FORCE, *J*	A.7
	A4.1 Failure Criteria	A.9
	A4.2 *J* Estimation Scheme for Primary Loads	A.9
	A4.3 Treatment of Stress Concentrators (Geometrical Discontinuities)	A.14
	A4.4 Treatment of Combined Primary and Secondary Loads	A.16
	A4.5 Treatment of Combined Primary Loads	A.17
	A4.6 Treatment of Multiaxial Applied Stresses	A.17
	A4.7 Treatment of Flaws with Multiple Degrees of Freedom (DOF)	A.18
	A4.8 Treatment of Welds	A.20
	A4.9 A Simplified Approach: Material Specific *J* Estimation Scheme	A.21
	A4.10 Effects of Plastic Constraint on *J*	A.23
	A4.11 A Summary of Recommended *J* Estimation Schemes	A.23
A5.	ELASTIC-PLASTIC FRACTURE MECHANICS: FAILURE ASSESSMENT DIAGRAMS (FADs)	A.27
	A5.1 Background	A.27
	A5.2 Relationship to *J* and Construction of Failure Assessment Diagrams for Primary Loads	A.29
	A5.3 Failure Curves and Failure Criteria	A.29
	A5.4 Treatment of Stress Concentrators (Geometrical Discontinuities)	A.35
	A5.5 Treatment of Combined Primary and Secondary Loads	A.38
	A5.6 Treatment of Combined Primary Loads	A.38
	A5.7 Treatment of Multiaxial Applied Stresses	A.38
	A5.8 Treatment of Flaws with Multiple Degrees of Freedom	A.38
	A5.9 Treatment of Welds	A.40
	A5.10 A Simplified Approach: Material Dependent FADs	A.40
	A5.11 Effects of Plastic Constraint	A.44
A6.	FAILURE MECHANISMS AND FAILURE CRITERIA	A.44
	A6.1 Brittle Materials	A.44
	A6.2 Ductile Materials	A.46
	A6.3 Sub-critical Crack Growth	A.49
	A6.4 Mixed Mode Failure	A.50

TABLE OF CONTENTS (CONT.)

Page

A7. MATERIAL PROPERTIES A.50
- A7.1 Mechanical Properties A.50
- A7.2 Fracture Toughness A.52
- A7.3 Sub-critical Crack Growth A.55
- A7.4 Conservative Data for use in a Proof Test Analysis A.56

A8. FRACTURE AND FAILURE MODES A.59
- A8.1 Brittle Structural Fracture A.59
- A8.2 Ductile Structural Fracture A.60
- A8.3 Functional Failure A.60
- A8.4 Structural Failure A.60

A9. DETERMINING CRITICAL APPLIED LOADS A.61
- A9.1 Brittle Materials: *J*-Based Analysis A.61
- A9.2 Brittle Materials: FAD-Based Analysis A.62
- A9.3 Ductile Materials: *J*-Based Analysis A.64
- A9.4 Ductile Materials: FAD-Based Analysis A.65

A10. DETERMINING CRITICAL CRACK SIZES A.68
- A10.1 Brittle Materials: *J*-Based Analysis A.68
- A10.2 Brittle Materials: Material Dependent FAD-Based Analysis A.69
- A10.3 Ductile Materials: *J*-Based Analysis A.69
- A10.4 Ductile Materials: Material Dependent FAD-Based Analysis A.72
- A10.5 Special Aspects of Critical Crack Size Calculations A.72

A11. LEAK-BEFORE-BREAK (LBB): (APPLICABLE ONLY TO DUCTILE MATERIALS) A.74
- A11.1 LBB Logic A.74
- A11.2 LBB Diagram A.76
- A11.3 Critical LBB Load A.76

APPENDIX B: VALIDATION

B1. THEORETICAL VALIDATION: *J* ESTIMATION SCHEMES/FAILURE ASSESSMENT DIAGRAMS B.1
- B1.1 Introduction B.1
- B1.2 Primary Loads B.1
  - B1.2.1 Reference Stress Approach B.1
  - B1.2.2 Derivation of an Optimum Reference Stress Solution B.2
  - B1.2.3 Validation of the Reference Stress *J* Estimation Scheme B.5
  - B1.2.4 Statistical Analysis of Calculated Values of *V* B.5
  - B1.2.5 Material Dependent FADs for Primary Loading B.11
  - B1.2.6 Conclusions B.12

TABLE OF CONTENTS (CONT.)

Page

B1.3 Cracks at Stress Concentrators B.12
B1.3.1 Introduction B.12
B1.3.2 J Estimation Scheme B.15
B1.3.3 Validation Using Failure Assessment Diagrams B.16
B1.3.4 Conclusions B.17
B1.4 Combined Primary and Secondary Loads B.17
B1.4.1 Introduction B.17
B1.4.2 Validation: EPRI Elastic-Plastic Handbook Solutions B.24
B1.5 Multiaxial Stresses B.24
B1.5.1 Introduction B.24
B1.5.2 Validation Based on Failure Assessment Diagrams B.25
B1.6 Cracks at Welds B.25
B1.6.1 Introduction B.25
B1.6.2 Validation for Over-Matched Welds B.26
B1.6.3 Validation for Under-Matched Weld B.32
B1.6.4 Conclusions B.32

B2. LABORATORY VALIDATION: J ESTIMATION SCHEMES/FAILURE ASSESSMENT DIAGRAMS B.32
B2.1 Introduction B.32
B2.2 Test Analysis Methods B.34
B2.2.1 Estimating J B.34
B2.2.2 Evaluating η-factors B.36
B2.2.3 Elastic Displacements and Stress Intensity Factors B.38
B2.2.4 Specimen Stiffness for Unloading Compliance B.44
B2.3 Test Results B.45
B2.3.1 J_R-Curves for Nickel-Based Superalloy IN-718 . . . . . B.45
B2.3.2 Failure Assessment Diagrams for Nickel-Based Superalloy IN-718 . . . . . B.52
B2.3.3 Failure Assessment Diagrams for Aluminum Alloy 2024-T3511 . . . . . B.59

B3. LABORATORY VALIDATION: PREDICTING CRITICAL CRACK SIZES AND CRITICAL LOADS FOR IN-718 . . . . . B.62
B3.1 Critical Loads B.62
B3.2 Critical Crack Sizes B.73
B3.3 Analysis Using FADs B.73

B4. HARDWARE VALIDATION: PREDICTING CRITICAL CRACK SIZES AND CRITICAL LOADS FOR IN-718 . . . . . B.86
B4.1 Overview of Hardware Tests B.86
B4.2 Assessment Data for J Estimation and Material Specific Failure Assessment Diagram B.94

TABLE OF CONTENTS (CONT.)

Page

B4.2.1 Tensile Data B.95
B4.2.2 J-R Curves B.95
B4.2.3 Stress Intensity Factor Solutions B.98
B4.2.4 Net Section Yield Pressures B.98
B4.3 Determination of Critical Pressures and Crack Depths B.99
B4.4 Leak-Before-Burst Analyses B.100
B4.5 Discussion and Conclusions B.115

B5. HARDWARE VALIDATION: PREDICTING CRITICAL CRACK SIZES AND CRITICAL LOADS FOR FERRITIC STEELS B.120
B5.1 Ferritic Steel Pressure Vessel: CEGB Test 1 . . . . . B.120
B5.1.1 Overview of Testing B.120
B5.1.2 Assessment Data for *J* Estimation and Material Specific Failure Assessment Diagram B.120
B5.1.3 Determination of Critical Pressures and Crack Depths B.122
B5.1.4 Leak-Before-Burst B.124
B5.2 High Toughness Steel Pressure Vessel with Circumferential Through Crack: NASA Ames Test B.124
B5.2.1 Overview of Testing B.124
B5.2.2 Assessment Data for *J* Estimation and Material Specific Failure Assessment Diagram B.124
B5.2.3 Determination of Critical Pressures and Crack Depths B.126
B5.3 Ferritic Steel Pressure Vessel with Flawed Weld: CEGB Test 3 . . . . . B.128
B5.3.1 Overview of Testing B.128
B5.3.2 Assessment Data for *J* Estimation and Material Specific Failure Assessment Diagram B.128
B5.3.3 Determination of Constant Load Locus B.131

B6. LABORATORY VALIDATION: EFFECT OF PROOF TEST OVERLOAD ON SUBSEQUENT SERVICE FATIGUE AND FRACTURE BEHAVIOR B.133
B6.1 Introduction B.133
B6.2 Scenario 1: Simulated Proof Overload Followed by Service Cycling to Failure B.133
B6.3 Scenario 2: Simulated Service Cycling to Failure Without a Proof Load . . B.137
B6.4 Comparison of Scenario 1 and Scenario 2 Fatigue and Fracture Behaviors B.138
B6.5 Conclusions B.140

APPENDIX C: EXAMPLE PROOF TEST ANALYSES

C1. EXAMPLE 1: SEAM-WELDED PRESSURE VESSEL: FLAW SCREENING . . C.1

C2. EXAMPLE 2: HIGH PRESSURE OXIDIZER DUCT: MINIMUM PROOF PRESSURE C.4

TABLE OF CONTENTS (CONT.)

Page

APPENDIX D: ASPECTS OF ADVANCED PROOF TEST ANALYSIS

D1. PROBABILITY ANALYSIS D.1
D1.1 Limit States and Distribution Functions D.1
D1.2 Data Requirements D.2
D1.3 Application to Proof Test Analysis D.2
D1.4 Enabling Technology D.5

D2. MULTIPLE CYCLE PROOF TEST ANALYSIS: CRACK GROWTH DUE TO STATIC AND CYCLIC LOADING D.6
D2.1 Memory Model D.6
D2.2 Loss of Memory Model D.11

D3. SUBSTANTIATION OF THE TEAR-FATIGUE MODELS D.13

LIST OF ILLUSTRATIONS

Figure	Title	Page
2.1	Overview of Guidelines	4
3.1	Proof test logic: flaw screening for a one degree of freedom flaw	7
3.2	Proof test logic: flaw screening and safe-life analysis for a two degree of freedom flaw	9
4.1	Proof Test Issues	11
4.2	Standard Crack Geometries	20
5.1	Overview and guide to the technical areas addressed in Appendix A	25
5.2	Guide to the validation provided in Appendix B	26
6.1	Road Map for flaw screening and minimum proof loads	29
6.2	Schematic flaw screening diagram showing normalized half crack surface length (c/t) plotted against normalized flaw depth (a/t)	39
6.3	Schematic proof load diagram showing critical pressure against initial flaw size	42
7.1	Example results for a proof factor of 1.3 showing in-service failure probability after different numbers of cycles (N), conditional on proof test success	52
8.1	(a) Example of beneficial effects of shakedown from proof testing that results in a compressive residual stress	56
8.2	Schematic showing the enhancement in fracture toughness of brittle materials that are subjected to warm prestressing	58
8.3	Illustration of tear-fatigue up to incipient instability during proof testing	59
8.4	Schematic showing that overloading, when characterized by $(J_o/J_{max})^{1/2}$, is more significant in the plastic regime for the same ratio of overload (P_o) to maximum cyclic load (P_{max})	61
8.5	Plot of measured and predicted crack growth for tear-fatigue under a rising J_{max} and following a load control mode change to constant J_{max}	63
8.6	Schematic representation of initial and final crack length distributions for proof testing of ductile materials	64
A4.1	The toughness of ductile materials has no unique value but depends on the tear length, Δc_t	A.10
A4.2	In the EPRI J estimation scheme, the expression for J is resolved into elastic, J_e, and plastic, J_p, components	A.12
A4.3	Schematic showing the nomenclature used to describe the dimensions associated with a flaw at a stress concentrator	A.15
A5.1	A Failure Assessment Diagram (FAD) showing a failure curve, the safe and unsafe regions, assessment points (A and B), and the result of varying toughness and yield stress on the position of an assessment point	A.28
A5.2	Determining the critical crack size for a brittle material using the FAD approach	A.31
A5.3	The FAD can be partitioned into three regions	A.32
A5.4	The critical load for a ductile material can be obtained using the FAD approach by determining the applied load that results in a constant load locus that forms a tangent to the failure curve (load P_s in the figure)	A.34

LIST OF ILLUSTRATIONS (CONT.)

Figure	Title	Page
A5.5	The critical crack size for a ductile material can be obtained using the FAD approach by determining the crack length that has a constant load locus that forms a tangent to the failure curve (crack size, c_5, in the figure)	A.36
A5.6	Shallow cracks at geometrical discontinuities can have failure curves that are significantly different from deeper cracks, or cracks that emanate from smooth surfaces	A.37
A5.7	Failure curves for flaws subjected to combined primary and secondary loads can be significantly different from the failure curves for the same flaws subjected to primary loading, as shown in this figure	A.39
A5.8	Failure curves for four hypothetical materials with strain hardening exponents similar to those that may be measured for an aluminum alloy (n=25), a nickel-based superalloy (n=15), a ferritic pressure vessel steel (n=10), and an austenitic steel (n=5)	A.42
A5.9	The failure curves for shallow flaws at stress concentrators may be significantly different from the failure curve for a flaw at a smooth surface	A.43
A5.10	The failure curves for flaws subjected to combined primary and secondary loads may be significantly different from the failure curve for a primary load	A.45
A6.1	Schematic showing how the toughness of brittle materials depends on temperature, loading rate, section thickness, and plastic constraint in the ductile-brittle toughness transition region	A.47
A6.2	Schematic showing how *J-R* curves change with plastic constraint and section thickness	A.48
A6.3	Illustration of the Mode I, II, and III loads and the resulting deformations	A.51
A9.1	Determining the critical load of a flawed brittle material for combined primary and secondary loadings using the FAD	A.63
A9.2	Determining the critical load of a flawed ductile material	A.67
A10.1	Determining the critical crack size (c_4) for a brittle material	A.70
A10.2	Determining the critical crack size (c_5) for a ductile material	A.73
A10.3	Schematic showing how, under some circumstances (such as combined primary and secondary loads), two critical crack sizes, c'_{crit} and c''_{crit}, may be predicted	A.75
A11.1	Leak-before-burst diagram	A.77
B1.1	Comparison of computed plane strain values of the h_1 functions for a single edge cracked plate in tension for n = 2, 3, 5, 7, 10, 13, and 16 with the predictions of the reference stress approach derived using the optimization scheme	B.6
B1.2	Comparison of computed values of the h_1 functions for a surface flaw in a plate subjected to tension for n = 5, 10, and 15 with the predictions of the reference stress approach derived using the optimization scheme	B.7
B1.3	Cumulative distribution function for the engineering parameter, V, for Group (i) data	B.10
B1.4	Effect of uncertainty in the value of V on the material specific failure curve for IN-718	B.13

LIST OF ILLUSTRATIONS (CONT.)

Figure	Title	Page
B1.5	Failure curves derived from finite element J solutions using optimized (a) and conventional (b) net section yield loads, P_o, to calculate L_r	B.14
B1.6	Comparison of failure curves derived from finite element computations with optimized RSM solutions for cracks emanating from double edge notched plates subjected to uniform stressing for K_I=4.2, c/r_n=0.1194, c_{ext}/w=0.315, and n=10 .	B.18
B1.7	Comparison of failure curves derived from finite element computations with optimized RSM solutions for cracks emanating from double edge notched plates subjected to uniform stressing for K_I=4.2, c/r_n=0.6431, c_{ext}/w=0.380, and n=10 .	B.19
B1.8	Comparison of failure curves derived from finite element computations with optimized RSM solutions for cracks emanating from double edge notched plates subjected to uniform stressing for K_I=6.3, c/r_n=0.3063, c_{ext}/w=0.315, and n=10 .	B.20
B1.9	Comparison of failure curves derived from finite element computations with optimized RSM solutions for cracks emanating from double edge notched plates subjected to uniform stressing for K_I=6.3, c/r_n=1.6495, c_{ext}/w=0.380, and n=10 .	B.21
B1.10	Comparison of failure curves derived from finite element computations with optimized RSM solutions for cracks emanating from double edge notched plates subjected to uniform stressing for K_I=8.4, c/r_n=0.1550, c_{ext}/w=0.304, and n=10 .	B.22
B1.11	Comparison of failure curves derived from finite element computations with optimized RSM solutions for cracks emanating from double edge notched plates subjected to uniform stressing for K_I=8.4, c/r_n=3.1008, c_{ext}/w=0.380, and n=10 .	B.23
B1.12	Failure curves for a center cracked plate subjected to uniform biaxial stressing based on the results of Wang, Li, and Ding [44]	B.27
B1.13	Schematic representation of the circumferential cracked weld analyzed by Joch et al. [76]	
B1.14	Comparison of failure curves for an over-matched weld (Case 1) for proof and service applications generated using the recommended procedures and the finite element results of Joch et al. [76]	B.28
B1.15	Comparison of failure curves for an over-matched weld (Case 2) for proof test and service applications generated using the recommended procedures and the finite element results of Joch et al. [76]	B.29
B1.16	Comparison of failure curves for an over-matched weld (Case 3) for proof test and service applications generated using the recommended procedures and the finite element results of Joch et al. [76]	B.30
B1.17	Comparison of failure curves for an over-matched weld (Case 4) for proof test and service applications generated using the recommended procedures and the finite element results of Joch et al. [76]	B.31
	. . . . .	B.33
B2.1	Restrained edge cracked plate (RSECP) test specimen design	B.46
B2.2	Typical load-displacement trace for specimen 3.1.B showing unloading steps used in unloading compliance crack depth measurements	B.49
B2.3	Calculated values of $Y(c/w, s/w)$ as a function of c/w for various S/w for the RSECP specimens	B.51

LIST OF ILLUSTRATIONS (CONT.)

Figure	Title	Page
B2.4	Substantiation of procedure followed to compensate for crack backup effects for specimen 1.1.A	B.53
B2.5	Substantiation of procedure followed to compensate for crack backup effects for specimen 1.1.B	B.54
B2.6	Substantiation of procedure followed to compensate for crack backup effects for specimen 1.1.C	B.55
B2.7	J_R-curves measured on the RSECP specimens showing effects of low constraint compared to compact tension data	B.56
B2.8	Comparison of IN-817 material specific failure curve (full line) with experimentally measured curves derived from the RSECP test results	B.58
B2.9	Comparison of the material specific failure curve (solid line) for the aluminum alloy with the experimentally determined failure curves obtained from tests on center cracked panels (CCPs) containing crack depths varying between 30% and 80% of the thickness	B.60
B2.10	Comparison of normalized maximum limit loads, P_{max}/P_y, for SECPs as a function of normalized crack depth, c/w, where P_y is the load to yield the flaw-free specimen	B.63
B2.11	Comparison of the material specific failure curve (solid line) for the aluminum alloy with the experimentally determined failure curves obtained from tests on single edge cracked panels (SECPs) containing crack depths varying between 30% and 80% of the thickness	B.64
B3.1	Comparison of predicted (solid line) and experimental (open symbols) load versus tear length behaviors of RSECP specimens 1.1A, 1.1B, and 1.1C	B.65
B3.2	Comparison of predicted (solid line) and experimental (open symbols) load versus tear length behaviors of RSECP specimens 1.2.A, 1.2.B, and 1.2.C	B.66
B3.3	Comparison of predicted (solid lines) and experimental (open symbols) load versus tear length behavior of specimen 3.1.B	B.67
B3.4	Comparison of predicted (solid lines) and experimental (open symbols) load versus tear length behavior of specimen 3.2.B	B.68
B3.5	Comparison of measured and predicted critical loads for IN-718 RSECP specimens	B.72
B3.6	Comparison of measured and predicted normalized critical crack depths for IN-718 RSECP specimens	B.76
B3.7	Comparison of derived experimental assessment points at initiation and ductile instability (full symbols) with the theoretical failure curve for specimen 1.1.A	B.77
B3.8	Comparison of derived experimental assessment points at initiation and ductile instability (full symbols) with the theoretical failure curve for specimen 1.1.B	B.78
B3.9	Comparison of derived experimental assessment points at initiation and ductile instability (full symbols) with the theoretical failure curve for specimen 1.1.C	B.79
B3.10	Comparison of derived experimental assessment points at initiation and ductile instability (full symbols) with the theoretical failure curve for specimen 1.2.A	B.80

LIST OF ILLUSTRATIONS (CONT.)

Figure	Title	Page
B3.11	Comparison of derived experimental assessment points at initiation and ductile instability (full symbols) with the theoretical failure curve for specimen 1.2.B . .	B.81
B3.12	Comparison of derived experimental assessment points at initiation and ductile instability (full symbols) with the theoretical failure curve for specimen 1.2.C . .	B.82
B3.13	Comparison of derived experimental assessment points at initiation and ductile instability (full symbols) with the theoretical failure curve for specimen 3.1.B . .	B.83
B3.14	Comparison of derived experimental assessment points at initiation and ductile instability (full symbols) with the theoretical failure curve for specimen 3.2.B . .	B.84
B3.15	Summary of predicted values of assessment points for all the tested IN-718 RSECP specimens at ductile crack initiation and instability compared to the theoretical material specific failure curve for IN-178	B.85
B4.1	Photograph of one of the tested ducts	B.87
B4.2	Schematic of part of the first SSME duct tested at Rocketdyne showing the straight section where the EDM notches were machined	B.88
B4.3	Photograph of one of the EDM notches	B.89
B4.4	All three ducts failed in a burst mode similar to the example shown here	B.90
B4.5	Photograph of one of the fractured halves of the crack at location R which resulted in failure showing the EDM notch, the fatigue crack, and the region of fast ductile failure	B.92
B4.6	Micrograph of the crack at location R showing the stretch zone beyond the fatigue crack, and the ductile failure region beyond the stretch zone	B.93
B4.7	Measured J_R-curves for IN-718 showing the lower and upper J_R-curves used in the fracture analyses	B.97
B4.8	The measured internal pressures at instability plotted against the predicted values for the three flawed SSME HP oxidizer ducts	B.107
B4.9	The normalized measured critical crack depths plotted against the predicted values for the three flawed SSME HP oxidizer ducts	B.108
B4.10	Failure assessment diagram showing the failure loci for the four flaws in Duct 1 calculated assuming lower toughness behavior	B.109
B4.11	Failure assessment diagram showing the failure loci for the four flaws in Duct 1 calculated assuming upper toughness behavior	B.110
B4.12	Failure assessment diagram showing the failure loci for the four flaws in Duct 2 calculated assuming lower toughness behavior	B.111
B4.13	Failure assessment diagram showing the failure loci for the four flaws in Duct 2 calculated assuming upper toughness behavior	B.112
B4.14	Failure assessment diagram showing the failure loci for the four flaws in Duct 3 calculated assuming lower toughness behavior	B.113
B4.15	Failure assessment diagram showing the failure loci for the four flaws in Duct 3 calculated assuming upper toughness behavior	B.114
B4.16	Failure assessment diagram showing failure loci for an axial through-wall flaw located at position R in Duct 1 calculated assuming upper and lower toughness behavior	B.116
B4.17	Failure assessment diagram showing failure loci for an axial through-wall flaw located at position R in Duct 2 calculated assuming upper and lower toughnessbehavior	B.117

LIST OF ILLUSTRATIONS (CONT.)

Figure	Title	Page
B4.18	Failure assessment diagram showing failure loci for an axial through-wall flaw located at position R in Duct 3 calculated assuming upper and lower toughness behaviors	B.118
B5.1	Geometry of CEGB test vessel	B.121
B5.2	Constant load locus evaluated for the measured instability pressure in CEGB Test 1 compared to the material specific failure curve for the ferritic pressure vessel steel	B.123
B5.3	Constant load locus evaluated at the measured instability pressure in CEGB Test 1 for a through crack compared to the material specific failure curve for the pressure vessel steel	B.125
B5.4	Constant load locus evaluated at the measured instability pressure for the NASA Ames pressure vessel compared to the material specific failure curve for the ferritic steel	B.127
B5.5	Location of the flaw in the CEGB Test 3 pressure vessel with respect to the weld repair	B.129
B5.6	Typical profile of residual stress across crack plane in CEGB pressure vessel Test 3	B.130
B5.7	Constant load locus evaluated at the measured instability pressure for CEGB Test 3 compared to material specific failure curves for use in proof test and service analyses	B.132
B6.1	Load displacement trace for specimen 3.1.B illustrating a simulated proof test overload followed by continuous simulated service cycling to failure	B.134
B6.2	Load displacement trace for specimen 2.1.B subjected to simulated service cycles under load control	B.135
C1.1	Example 1: Applied J as a function of crack depth	C.5
C1.2	Example 1: Critical crack depth determined from the FAD	C.6
C1.3	Example 1: Flaw screening diagram	C.7
C2.1	Example 2: Applied J values as a function of pressure for various tear lengths.	C.12
C2.2	Example 2: Pressure as a function of tear length	C.13
C2.3	Example 2: Determining the minimum proof pressure using the FAD	C.14
D1.1	Distribution of crack depths and corresponding exponential distribution	D.3
D1.2	Schematic representation of interacting reliability issues associated with proof testing and subsequent service	D.4
D2.1	Example of the enhanced crack growth rate due to tear-fatigue compared to fatigue crack growth rates	D.7
D2.2	Schematic representation of tear-fatigue Memory Model	D.10
D2.3	Schematic representation of tear-fatigue Loss of Memory Model	D.12
D2.4	Predicted tear-fatigue crack growth rates versus measured values for a mild steel (after Nixet et al. [37])	D.14
D2.5	Example of the suppression of tearing during a tear-fatigue test when a control mode change reduced dJ_{max}/dN from 22.6 kN/m to 0 kN/m (after Nixet et al. [37])	D.15

LIST OF TABLES

Table	Title	Page
4.1	Typical minimum proof load factors for pressurized hardware	13
4.2	Minimum initial flaw sizes for safe-lifing testing based on NDE	19
7.1	Summary of five-cycle proof test (pre-1979) for cases in which pre-existing defect was identified	51
A2.1	Available technology for determining stress intensity factors	A.5
A4.1	Summary of EPRI J estimation scheme solutions	A.8
A4.2	Recommended value of V for use in fracture mechanics applications; $V^*=\mu V$, where $\mu=1$ for plane stress and $\mu=(1-\nu_p^2)/(1-\nu_e^2)$ for plane strain	A.14
A4.3	Approximate combined elastic-plastic stress for evaluating $J_e(c_e, P+S)$	A.17
A4.4	Recommended tensile properties to be used in the evaluation of J for cracks in over-matched and under-matched welds	A.21
A4.5	J estimation formulae	A.24
A7.1	Approximate Ramberg-Osgood parameters	A.59
B1.1	Type 1 EVD parameter values derived from the sample V values in groups (i)-(iii)	B.9
B1.2	Summary of the over-matched cases used in the validation	B.26
B1.3	Summary of the under-matched case used in the validation	B.31
B2.1	η_p values corresponding to n=10 for use in experimentally measuring J_p from the Plastic work under the load/load pin displacement curve	B.39
B2.2	η_p values corresponding to n=16 for use in experimentally measuring J_p from the plastic work under the load/load pin displacement curve	B.39
B2.3	η_p^* values corresponding to n=10 for use in experimentally measuring J_p from the plastic work under the load/mouth opening displacement curve	B.40
B2.4	η_p^* values corresponding to n=16 for use in experimentally measuring J_p from the plastic work under the load/mouth opening displacement curve	B.40
B2.5	Specimen and crack dimensions for the RSECP specimens	B.47
B2.6	Calculated effective spans over which ends of RSECP specimens were restrained	B.50
B3.1	Toughness parameters related to the quadratic fit to the measured J_R-curves of the IN-718 RSECP specimens	B.70
B3.2	Predicted and measured critical and instability crack depths corresponding to the maximum load (ductile failure)	B.71
B3.3	Predicted and measured critical crack depths corresponding to the load at initiation (or brittle failure)	B.74
B3.4	Predicted and measured loads at initiation (or brittle failure) and ductile instability (maximum load)	B.75
B4.1	Local wall thicknesses and dimensions of cracks after pre-fatigue cracking in units of inches	B.91
B4.2	Characterization of the structurally relevant toughness of IN-718	B.96
B4.3	Predicted initiation and instability pressures for Duct 1	B.101
B4.4	Predicted initiation and instability pressures for Duct 2	B.102
B4.5	Predicted initiation and instability pressures for Duct 3	B.103

LIST OF TABLES (CONT.)

Table	Title	Page
B4.6	Predicted critical and instability crack sizes for Duct 1	B.104
B4.7	Predicted critical and instability crack sizes for Duct 2	B.105
B4.8	Predicted critical and instability crack sizes for Duct 3	B.106
B5.1	Characterization of the structurally relevant toughness of A533B steel	B.122
B5.2	Comparison of the measured and predicted critical pressure and flaw depth for CEGB Test 1	B.122
B5.3	Characterization of the structurally relevant toughness of A106B steel	B.126
B5.4	Comparison of the measured and predicted critical pressures for the NASA Ames hydrostatic test	B.128
B5.5	Characterization of the structurally relevant toughness of A533B steel	B.131
B6.1	Data measured in the tests to investigate the effect of simulated proof test overload on subsequent service lifetime	B.136
B6.2	Measured and predicted cycles to failure	B.137
B6.3	Calculated critical conditions at the start of service cycling in the absence of the proof test overload	B.140
C1.1	Base and weld metal tensile properties	C.2
C2.1	Tensile properties for IN-718	C.8
C2.2	J_R-curve parameters	C.10
C2.3	J_R-curve parameters for through-wall cracks	C.16

DEFINITIONS

ACCEPTANCE TESTS — Acceptance tests are the required formal tests conducted on hardware to ascertain that the materials, manufacturing processes, and workmanship meet specifications and that the hardware is acceptable for delivery. A proof test may form part of the acceptance testing.

APPLIED LOAD (STRESS) — The actual applied load (stress) on a structure is the load (stress) imposed on the structure in the design or service environment.

BRITTLE FAILURE MECHANISM — Brittle failure mechanisms operate local to a loaded crack tip and control the events on the microstructural scale that lead to rapid crack extension. Fracture is usually transgranular and has a crystalline appearance, typical of cleaved grains. The fracture surface is normally flat and failure occurs at average stress levels below those of general yielding. The fracture toughness of brittle materials can be characterized by a single value.

BRITTLE STRUCTURAL FRACTURE — Brittle structural fracture is a type of catastrophic failure in structural materials that usually occurs without significant prior plastic deformation and at extremely high speed.

CONSERVATIVE PROOF TEST ANALYSIS DATA — These are data which, when used in a fracture mechanics analysis, will result in a conservative proof test analysis, such as a conservative proof load factor or a conservative estimate of the flaw screening capability. The values of the parameters which comprise the data may have lower or upper bound values depending on how they influence the outcome of the assessment, where "upper" and "lower" imply statistically significant quantities.

CONSERVATIVE SERVICE ANALYSIS DATA — These are data which, when used in a fracture mechanics analysis will result in a conservative assessment of the integrity of a part under service loading conditions. The values of the parameters which comprise the data may have lower or upper bound values depending on how they influence the outcome of the assessment, where "upper" and "lower" imply statistically significant quantities.

CRACK TIP DRIVING FORCE — A fracture mechanics quantity that provides a single parameter characterization of the magnitude of the fields at a loaded crack tip and/or the potential energy release rate associated with an incremental crack extension.

CRITICAL CRACK OR FLAW — The critical crack or flaw in a brittle material is one of sufficient size and shape that unstable growth will occur under the specific operating load and environment. The critical crack or flaw in a ductile material is one of sufficient size and shape that ductile tearing will initiate leading to crack instability under the specific operating load and environment.

CRITICAL INITIAL SERVICE CRACK OR FLAW SIZE — The maximum preexisting flaw size for which the part, by analysis or test, would survive exactly the service life times the service life factor, typically a factor of four.

CRITICAL PROOF LOAD (PRESSURE) — The load (pressure) determined by analysis which would result in structural fracture of the part during proof testing.

CRITICAL SERVICE CRACK OR FLAW SIZE — The minimum flaw size determined by analysis which would result in structural fracture of the part under the maximum expected operating loads.

CRITICAL SERVICE LOAD — The minimum load (e.g. pressure, rotational speed, acceleration) determined by analysis which would result in fracture of the part under peak operating loads (including residual stresses, thermal stresses, etc.).

DAMAGE TOLERANCE — The damage tolerance of a structure is its ability to resist failure due to the presence of flaws, cracks, or other damage for a specified period of unrepaired usage.

DEGREE OF FREEDOM (DOF) — This describes the number of crack tip driving force values needed to adequately characterize directionally dependent flaw growth rates and shape changes during crack extension. A one degree of freedom (DOF) flaw is characterized for analysis purposes by a single value for the crack tip driving force. A two DOF flaw is characterized by two values of the crack tip driving force which may, for example, correspond to the values at the deepest and surface points on a semi-elliptical surface flaw.

DETRIMENTAL DEFORMATION — Detrimental deformations include all structural deformations, deflections, or displacements that prevent any portion of the structure from performing its intended function.

DUCTILE FAILURE MECHANISM — Ductile failure mechanisms operate local to a loaded crack tip and control crack extension on the microstructural scale. The fracture surface usually has a dimpled appearance, characteristic of the growth and coalescence of voids. The fracture toughness of ductile materials is not usually characterized by a single value, as they display an increase in toughness with crack extension under a rising load. Fracture generally occurs at high average stress levels and is normally (but not always) preceded by significant amounts of plastic deformation characteristic of ductile structural fracture.

DUCTILE STRUCTURAL FRACTURE — Ductile structural fracture is a type of failure in structural materials generally preceded by significant amounts of plastic deformation.

ELASTIC-PLASTIC FRACTURE MECHANICS (EPFM) — The application of fracture mechanics to non-linear elastic materials which deform according to a non-linear relationship between stress and strain. EPFM should be applied to assessing cracks which develop significant crack tip plasticity prior to fracture.

FAILURE ASSESSMENT DIAGRAM (FAD) — This is a diagrammatic means of representing the results of a J analysis. The FAD consists of two axes, the abscissa measures the nearness of the structure to net section yielding, and hence plastic collapse, the ordinate measures the nearness to failure under linear elastic conditions.

FATIGUE CRACK GROWTH — Fatigue crack growth occurs in a defected material subjected to repeated, cyclic, or fluctuating loads. The rate of crack propagation is related to the cyclic change in the crack driving force, e.g., stress intensity factor range under linear elastic conditions, resulting from load fluctuations. Fatigue crack extension may culminate in fracture after a sufficient number of fluctuations.

FLAW — A flaw is a local discontinuity in a structural material, such as a scratch, notch, crack or void.

FRACTURE CONTROL — The rigorous application of those branches of engineering, assurance management, manufacturing, and operations dealing with the analysis and prevention of crack propagation leading to catastrophic failure.

FRACTURE CRITICAL REGIONS — These are areas of the fracture critical hardware determined to be the most life limiting based on the amplitude of operational stresses and strains in the region and on the detection capability of applicable flaw screening procedures.

FRACTURE CRITICAL HARDWARE — Hardware, whose failure consequence would be catastrophic, resulting in loss of mission, vehicle, or human life.

FRACTURE MECHANICS — Fracture mechanics is an engineering discipline used to predict flaw-growth and fracture behavior of materials and structures under load containing cracks or crack-like flaws.

FRACTURE TOUGHNESS — Fracture toughness is a material characteristic which reflects flaw tolerance and resistance to fracture. Fracture toughness is generally dependent on the temperature, loading rate, and plastic constraint.

FUNCTIONAL FAILURE — Functional failure prevents a part from performing its design function, but does not result in catastrophic failure of the part. An example of functional failure is non-hazardous leak-before-burst in a pressure vessel.

ELASTIC STRAIN ENERGY RELEASE RATE, G — The elastic strain energy release rate due to crack extension. This linear elastic crack tip driving force parameter is related to the square of the stress intensity factor.

G-R CURVE — A measure of a material's resistance to crack growth under monotonic loading expressed in terms of the elastic strain energy release rate, G.

HAZARDOUS FLUID — Any liquid or gas which, if released, could result in personnel injury or loss of hardware.

HYDROGEN EMBRITTLEMENT — Hydrogen embrittlement is a mechanical-environmental failure process that results from the initial presence or absorption of excessive amounts of hydrogen in metals, usually in combination with residual or applied tensile stresses.

INITIAL CRACK OR FLAW SIZE — The maximum size flaw, as defined by proof test or non-destructive examination (NDE), which could exist in parts without failure during the proof test or without reliable detection by NDE, given a prescribed level of detection probability and confidence (typically 90/95). The initial crack is that size which is calculated to be on the point of incipient instability at the start of the final unloading from maximum proof load (assuming a sufficiently rapid unloading rate in stress-corrosive environments). For ductile materials it is equal to the critical crack size determined under maximum proof test load conditions plus the amount of tearing that is calculated to occur under that load up to the point of incipient instability.

J-INTEGRAL — An elastic-plastic fracture mechanics parameter that describes the stress and strain fields at the tip of a loaded crack undergoing plastic (nonlinear elastic) deformation. It is a natural extension of G to cracks undergoing elastic-plastic deformations, and represents the potential energy release rate due to crack extension. Normally, $J \geq G$, and becomes equal to G when crack tip plasticity is negligible.

J-R CURVE — A measure of a material's resistance to crack growth under monotonic loading expressed in terms of the J-Integral.

K-R CURVE — A measure of a material's resistance to crack growth under monotonic loading expressed in terms of the stress intensity factor, K.

LARGE SCALE YIELDING — This describes a situation where the crack tip plastic zone size is comparable to or larger than the crack size or structural dimensions typical of the cracked section (e.g. the uncracked ligament).

LEAK-BEFORE-BURST (LBB) — A fracture mechanics design concept in which it is shown that an initial flaw will grow through the wall of a pressure vessel and cause leakage rather than burst (catastrophic failure). (To be effective, the leak must be detectable prior to rupture as a through crack for instances where the pressure source is not a static head and/or leakage reactions can cause a shift in metal temperature.)

LINEAR ELASTIC FRACTURE MECHANICS (LEFM) — The application of fracture mechanics to linear elastic materials which deform according to a linear relationship between stress and strain. LEFM can be applied to assessing cracks which undergo small scale yielding prior to fracture.

LOWER BOUND VALUE — A lower bound value of a parameter is a statistically meaningful quantity derived from the lower statistical values of the parameter's scatter band. It can be expressed in the form of a factor to be applied to the mean value of the parameter, or directly as a value corresponding to a defined cumulative probability and confidence level.

MAXIMUM (EXPECTED) OPERATING PRESSURE (MOP) (MEOP) — The maximum pressure at which the system or component actually operates in a particular application. MOP is synonymous with MEOP (Maximum Expected Operating Pressure) or maximum working pressure. MOP includes the effects of temperature, transient peaks, vehicle acceleration, and relief valve tolerance.

MINIMUM PROOF LOAD (PRESSURE) — This can be calculated from fracture mechanics as the load (pressure) required to ensure that a proof tested component will not enter service with a flaw greater than a specified size.

NET SECTION YIELD — This occurs when plastic deformation has spread from the crack tip across the load-bearing section containing the flaw so that the stresses in this region are everywhere at yield point magnitude.

NET SECTION YIELD LOAD — The applied load at which plastic deformation spreads from the crack tip across the load bearing section containing the flaw so that the stresses in this region are everywhere at yield point magnitude (net section yield). Its value depends on the flaws present in the structure, and the yield stress. The yield load is equal to the plastic collapse load for materials that have no strain hardening capability (elastic-perfectly plastic behavior).

NON-DESTRUCTIVE EVALUATION (NDE) — Inspection techniques that do not cause physical or chemical changes to the part being inspected, or otherwise impair its adequacy for operational service, and that are applied to materials and structures to verify required integrity and detect characteristic flaws.

PEAK OPERATING LOAD (POL) — This is the combination of operating loads which at any time during the service life results in peak loading in a fracture critical area. In general, each fracture critical region will have different POLs and they will occur at different times. The POLs may not necessarily occur at the same time as the MEOP.

PLASTIC COLLAPSE — This is a mode of failure undergone by materials which have very high ductilities and are very tough. It is an extreme form of ductile structural fracture where failure occurs because the uncracked load-bearing section can no longer carry load and undergoes large deformations at constant load. It is analogous to the phenomenon of necking exhibited by ductile materials in uniaxial stress-strain tests.

PLASTIC COLLAPSE LOAD — The applied load at which plastic collapse occurs in a structure. Its value depends on the flaws present in the structure, and the yield stress (or flow stress).

PLASTIC CONSTRAINT — High plastic constraint is synonymous with plane strain conditions at a crack tip. Loss of plastic constraint at a crack tip is promoted by the proximity of free surfaces (reduced structural thickness and shallow cracks), large scale plastic deformation, tensile and pressure loading as opposed to bending, and reduction in hydrostatic stresses.

PRESSURE VESSEL — Any component designed for the storage of pressurized gases or liquid.

PRIMARY LOAD (STRESS) — A load (stress) that contributes to plastic collapse. Primary stresses are produced by externally applied loads, such as tensile forces and moments, and internal pressure and must satisfy static equilibrium.

PROOF LOAD — The proof load is the test load that components shall sustain without detrimental deformation. Survival of the proof load is used to give evidence of satisfactory workmanship and material quality, and/or establish maximum initial flaw sizes in hardware for operational service. It is equal to the product of the maximum expected operating load and the proof factor. Alternatively, it can be calculated from fracture mechanics.

PROOF LOAD FACTOR — The proof load factor is a multiplying factor applied to the MEOP to obtain proof load or proof pressure, for use in demonstration of component acceptance by proof testing. Values of proof factors for various types of hardware are listed in NASA fracture control documents. The proof factor can also be calculated using fracture mechanics concepts and the results of a safe life analysis.

PROOF TEST — The test which a part must sustain to give evidence of satisfactory workmanship, material quality, and to verify structural integrity or to screen initial flaws.

PROOF TEST LOAD — The product of maximum operating load times the proof factor.

RESIDUAL STRESS — Residual stress is a stress which remains in a structural detail as a result of manufacturing processing, testing and operation.

ROTATING MACHINERY — Any rotating part whose fracture could result in a catastrophic event.

SAFE-LIFE — The service life established by analysis, or testing, and NDE which ensures that no flaws (cracks) exist which will grow to critical size in less than the service life times the service life factor, typically four, when subjected to the expected cyclic and sustained loads and environments likely to be encountered during operation.

SECONDARY LOAD (STRESS) — A load (stress) that does not contribute to plastic collapse. Secondary stresses are self-equilibrated and are induced in a structure by prescribed strains and displacements. Thermal and residual stresses are examples of secondary stresses.

SERVICE LIFE — The service life of a component or space vehicle is the total life expectancy of the item.

SERVICE LIFE FACTOR — A factor, typically four, times the total life expectancy of the item. This factor accounts for the uncertainties in the observed measured material crack growth properties and fracture mechanics analysis.

SMALL SCALE YIELDING — This describes a situation where the crack tip plastic zone size is small compared with the crack size or structural dimensions typical of the cracked section so that the elastic fields immediately outside of the zone can still be characterized in terms of a stress intensity factor. Typically, the small scale yielding regime applies for loads less than 60% of the net section yield load.

STRESS-CORROSION CRACKING — Stress-corrosion cracking is a mechanical-environmental induced failure process in which sustained tensile stress and chemical attack combine to initiate and propagate a flaw in a metal part.

STRESS INTENSITY FACTOR (K) — The stress intensity factor is a parameter that describes the elastic stress field in the vicinity of a crack tip.

STRUCTURAL FAILURE — Structural failure is synonymous with catastrophic fracture.

THERMAL STRESS — Thermal stress is a structural stress arising from temperature gradients and/or differential thermal deformation in or between structural components, assemblies, or systems.

THRESHOLD STRESS INTENSITY FACTOR (K_{TH}) — The threshold stress intensity factor is the maximum value of the stress intensity factor below which environmentally induced flaw-growth, under sustained static tensile stress, does not occur for a given material in a specified environment.

UPPER BOUND VALUE — An upper bound value of a parameter is a statistically meaningful quantity derived from the upper statistical values of the parameter's scatter band. It can be expressed in the form of a factor to be applied to the mean value of the parameter, or directly as a value corresponding to a defined cumulative probability and confidence level.

VERIFICATION/RE-CERTIFICATION TESTS — Verification/re-certification tests are tests conducted to verify/recertify the integrity of structures after some specific period of operation or storage or after exposure to some adverse conditions.

ACRONYMS/ABBREVIATIONS

ABAQUS	a computer program for performing stress analysis based on the finite element method
AE	acoustic emission
ANSYS	a computer program for performing stress analysis based on the finite element method
ASTM	American Society for Testing and Materials
CEGB	Central Electricity Generating Board
CIFS	critical initial flaw size
DOF	degree(s) of freedom
EPFM	elastic-plastic fracture mechanics
EPRI	Electric Power Research Institute
FAD	Failure Assessment Diagram
FCR	Fracture Control Requirements
FPI	Fast Probability Integration
LBB	leak-before-burst
LEFM	linear elastic fracture mechanics
LSY	large scale yielding
MCPT	multiple cycle proof test
MEOP	maximum expected operating pressure
MOP	maximum operating pressure
MSFC	Marshall Space Flight Center
NASA	National Aeronautics and Space Administration
NASGRO	a fatigue crack growth computer program developed by NASA
NDE	non-destructive examination
NDI	non-destructive inspection
NESSUS	Numerical Evaluation of Stochastic Structures Under Stress
POL	peak operating load
PSAM	Probabilistic Structural Analysis Methods
PTC	part-through crack
RSECP	restrained edge cracked plate
RSM	Reference Stress Method
SCC	stress corrosion cracking
SCPT	single cycle proof test
SIF	stress intensity factor
SSME	space shuttle main engine
SSY	small scale yielding
SwRI	Southwest Research Institute
WPS	warm prestressing

NOMENCLATURE

a	crack depth
a_{crit}	critical crack depth
a_{NDE}	characterized crack size for use in fracture mechanics analysis based on measured NDE indicated size
$a_{min\ NDE}$	minimum detectable flaw size defined by NASA
$a_{min\ NDE}^*$	minimum detectable flaw size defined by NASA plus sub-critical crack growth during the proof test
a_{NDE}^*	crack size, a_{NDE}, plus sub-critical crack growth calculated to occur during the proof test
a_e	first order plastically corrected crack depth
a_{ci}	critical initial service flaw size or depth
a_{cs}	critical service flaw size or depth
$a_{i,1}, a_{i,2}\ etc$	initial defect depths that could just survive the proof test
a_i	initial flaw size that could just survive the proof test
A	constant in Paris fatigue crack growth law
A_k	constant in NASGRO toughness relation between K_c and K_{Ic}
A_1	constant in power law expression for J_R
A_2	exponent in power law expression for J_R
B_k	constant in NASGRO toughness relation between K_c and K_{Ic}
c	half the crack surface length for embedded flaws, crack length for surface through-cracks
C_k	constant in NASGRO toughness relation between K_{Ie} and K_{Ic}
$CIFS$	critical initial flaw size: a flaw size that is predicted to survive the service lifetime times a multiplying factor which is typically 4
c	through crack length
c_{crit}	critical crack length
c_{instab}	crack length at ductile instability
c_e	first order plastically corrected crack length
c_{ext}	$= D_n + c$, extended through-crack length
c_i	half surface length of surface flaw that could just survive the proof test or initial flaw length
c_0	crack length at the start of the proof testing
c_{cs}	half surface length of critical service flaw
D	typical dimension associated with the cracked structure
D_n	depth of edge notch
e	aspect ratio of ellipse
E	Young's modulus
E'	$=E$, in plane stress, $=E/(1-\nu^2)$, in plane strain
$f_X(x)$	probability density function for random variable X
F	influence function appearing in expression for K
F_{sl}	service life factor, typically 4

F_{sl}	service life factor, typically 4
g	limit state used in probability analysis
G	elastic strain energy release rate, linear elastic crack tip driving force
h_1	a plastic "influence" function appearing in the EPRI expression for J_p that is dependent on the strain hardening exponent, n
h_1*	a plastic "influence" function appearing in the RSM expression for J_p
J	J-Integral, crack tip driving force in elastic-plastic fracture mechanics
J_e	elastic component of J-Integral
J_p	plastic component of J-Integral
J_{mat}	a measure of fracture toughness expressed in terms of J
J_{max}	the applied value of J at the maximum load in a proof test or service cycle
J_o	value of J due to proof test overload
$J_R(\Delta c_t)$	toughness corresponding to ductile tear length Δc_t expressed in terms of J
J_0, J_1, J_2	coefficients in quadratic fit to J_R-curve
K	stress intensity factor
K_c	thickness dependent fracture toughness expressed in terms of K
K_{Ic}	plane strain fracture toughness expressed in terms of K
K_{IC}^P, K_{IC}^S	fracture toughness under proof and service conditions, respectively
K_{Ie}	surface crack fracture toughness expressed in terms of K
K_{ISCC}	stress corrosion cracking threshold value of K
K_{mat}	a measure of fracture toughness expressed in terms of K
K_r	FAD parameter equal to ratio of K to fracture toughness
K_r^o	coordinate of assessment origin
K_r^*	$=(J_e/J)^{1/2}$, FAD parameter, related to the failure curve
$K_R(\Delta c_t)$	toughness corresponding to ductile tear length Δc_t expressed in terms of K
K_t	stress concentration factor equal to local stress divided by nominal or gross stress
l_{crit}	critical through-wall crack length in an LBB analysis
l_{LBB}	assumed through-wall crack length for an LBB analysis
L	structural dimension; e.g. radius of cylinder or notch root radius
L_r	FAD parameter equal to the ratio of applied load to net section yield load
L_r^o	coordinate of assessment origin
L_r^*	$=P/P_y^*$, FAD parameter related to the failure curve
m	exponent in Paris fatigue crack growth law
M_1, M_2	symbols signifying base or weld metal
n	exponent in Ramberg-Osgood law
N	number of fatigue or proof test cycles
P	primary load
P_1, P_2	primary loads
P_{crit}	critical fracture load
P_f	probability of failure
P_{LBB}	critical load to cause fracture of a through-wall crack in an LBB analysis

P_{MEOP}	maximum expected operating pressure
$P_{min,p}$	minimum proof load to screen for a critical initial service flaw
P_o	characterizing yield load used in EPRI J estimation scheme
P_o^*	net section yield load, or yield load obtained from applying the optimized reference stress approach, estimated using the characterizing yield stress, σ_o
P_p	proof test load
P_{POL}	peak operating load
P_y^*	net section yield load, or yield load obtained from applying the optimized reference stress approach, estimated using the 0.2% yield stress, σ_y
Q	a stress based parameter used to characterize constraint
R_m	mean radius
r_y	half small scale yielding estimate of plastic zone size, used in EPRI J estimation scheme
r_y^a, r_y^a	half plastic zone sizes at θ=90° (deepest point) and θ=0° (surface point) on a surface flaw
S	secondary load
t	section thickness
$t_{mission}$	mission life
$t_{service}$	calculated service life
t_o	$=2.5(K_{Ic}/\sigma_y)^2$
t_1, t_2 *etc*	times to service failure
V	a dimensionless structural parameter appearing in the reference stress J estimation scheme
V^*	$=\mu V$
w	half section width for embedded through cracks, section width for surface through cracks
x	position coordinate
X_{mean}	mean value of the random variable X
α	constant in Ramberg-Osgood law
α^*	$=\alpha\sigma_o^{n-1}/E$, constant in modified Ramberg-Osgood law
α_p, α_s	proof load factors under proof test and service conditions, respectively, equal to the proof load or pressure divided by the MEOP
β	=2, for plane stress, =6 for plane strain: constraint factor appearing in EPRI J estimation scheme
β^a	=6, constant determining plane strain plastic zone size
β^c	=2, constant determining plane stress plastic zone size
$\Delta a_{f,n}$	total fatigue crack extension after N cycles
Δa_t	tear length in the depth direction
$\Delta a_{t,n}$	total ductile tearing after N cycles
Δc	fatigue crack extension after N cycles
Δc_b	crack tip blunting
Δc_{max}	upper validity range of quadratic fitted to J_R-curve
Δc_{min}	$(=\Delta c_b)$ lower validity range of quadratic fit to J_R-curve

ϵ	total strain
ϵ_{eng}	engineering strain
ϵ_f	strain at maximum uniform elongation
ϵ_o	$=\sigma_o/E$, characterizing yield strain in Ramberg-Osgood stress-strain law
ϵ_{ref}	reference strain corresponding to σ_{ref}
ϵ_{ref}^p	plastic component of the reference strain
Γ	dimensional parameter, a measure of structural brittleness
λ	$=P_2/P_1$, load ratio for combined primary loading, $=\sigma_2/\sigma_1$ for biaxial stressing
λ^*	$=1/X_{mean}$, constant in exponential distribution function
μ	$=(1-\nu_p^2)/(1-\nu_e^2)$ for plane strain, =1 for plane stress
ν	Poisson's ratio
ν_e	elastic value of Poisson's ratio
ν_p	plastic value of Poisson's ratio
ϕ	plastic zone size multiplier in EPRI J estimation scheme
ρ	$=c/\sqrt{R_m t}$
σ	applied stress
σ_{eng}	engineering stress
σ_1, σ_2	multiaxial components of stress
$\sigma(x)$	local variation of stress at position x
σ_{nom}	nominal or gross stress
σ_o	characterizing yield stress in Ramberg-Osgood law
σ_y	0.2% yield stress
σ_u	ultimate stress
σ_{ref}	reference stress, $=(P/P_o^*)\sigma_o$
σ_X	standard deviation of the random variable X
θ	angle that locates a crack tip position on an elliptical flaw

SCOPE OF GUIDELINES

These Guidelines address proof test issues and describe procedures, in the form of a Road Map, for implementing state-of-the-art fracture mechanics technology into the design and analysis of a proof test. The main sections of the Guidelines are supported by four appendices that review and recommend state-of-the-art fracture mechanics methods (Appendix A), provide validation to substantiate the recommendations (Appendix B), present examples of how the Guidelines can be applied to analyzing proof tested hardware (Appendix C), and discuss advanced analyses involving reliability concepts and multiple cycle proof testing (Appendix D).

The Guidelines will assist engineers in maximizing the utility of the proof test for flaw screening and in increasing the reliability of proof tested hardware entering service or being re-certified for service. To facilitate these tasks, the Guidelines provide procedures for calculating maximum flaw sizes that could be present in hardware that survives proof testing (flaw screening analysis), and for determining proof load factors (minimum proof load analysis). Key issues associated with implementing a proof test are also discussed.

These Guidelines are applicable to metallic structures, such as pressure vessels, that fracture in either a brittle or a ductile mode. They can be used to assess the critical conditions for failure in hardware containing part-penetrating and fully-penetrating crack-like flaws. These Guidelines are appropriate for determining the effects on fracture behavior of combined primary (e.g. applied forces, moments, internal pressure and rotation) and secondary (e.g. residual and thermal) loads; plastic deformation at a crack tip; and the enhanced resistance to crack extension displayed by ductile materials. In addition, the Guidelines outline the procedures to be followed when analyzing a multiple cycle proof test; indicate the steps to be followed when performing a probability based analysis to estimate the reliability of hardware entering service after being proof tested; and discuss some of the ramifications of proof test overloading on subsequent fracture behavior under service conditions.

These Guidelines do not explicitly address fatigue and other sub-critical crack growth mechanisms, service life evaluations, and, among other things, composite materials, detailed design and selection of proof test apparatus and equipment, and detailed cost benefit analyses related to proof testing.

BACKGROUND

The practice of proof testing is one of the most utilized methods in the aerospace industry for assuring product integrity. Because proof testing plays such an important role in acceptance testing of hardware, it is highly desirable from economic and safety standpoints to be able to design a proof test so as to minimize failures during the test while still preventing in-service failures. Over the years it has become apparent that NASA's proof test philosophy requires up-dating to take into account current state-of-the-art technology. There have been major advances in fracture mechanics over the last two decades which have highlighted the fact that a proof test analysis involves numerous parameters which interact in complex ways. Although many of these parameters and the interactions between them are now understood, there are areas of uncertainty which are still being addressed by the technical community.

The objective of this program was to develop and document in a guidelines handbook a test verified state-of-the-art methodology for proof test analysis which addresses the key issues believed to be factors impacting the effectiveness of a proof test. To accomplish this objective, the program was divided into six separate but interrelated tasks as follows:

Task 1: Review and Evaluate Current Methods
Task 2: Define Proof Test Parameters
Task 3: Develop Test Verification Plan
Task 4: Select Methods and Philosophy
Task 5: Test Verification of the Selected Methods
Task 6: Proof Test Requirements / Guidelines Handbook

The results of Tasks 1 and 2 have been reported in NASA Contractor Report 4628: "Significant Issues in Proof Testing: A Critical Appraisal," September, 1994. This report addressed the roles and status of the following in proof test analysis:

- proof test load factor
- proof loading and unloading rates, hold times and time dependent crack growth
- selection of test fluid and temperature
- number of proof test cycles and the effect of consequential fatigue crack extension
- pre- and post-test and real time non-destructive evaluation
- effects of complex geometries
- flaw characterization
- aspects of structural stress analysis
- limitations of linear elastic fracture mechanics
- elastic-plastic fracture mechanics
- elastic-plastic crack tip driving forces and their evaluation
- J_R-curve approach and ductile crack instability analysis
- synergistic interactions between fatigue and ductile tearing
- effects of residual stresses on fracture behavior
- effect of wall thickness and plastic constraint on fracture toughness
- material variability and inhomogeneity (welds)
- damage accumulation
- probability analysis to establish service reliability
- the influence of proof test overload on subsequent fatigue crack growth (retardation)
- the influence of the overload on subsequent fracture behavior.

The major conclusions of that review (Task 4) are that elastic-plastic fracture mechanics and ductile crack instability analyses are essential for accurate prediction of the flaw screening capabilities offered by proof testing. It is imperative in ductile materials that allowance be made for stable ductile crack extension during the test, otherwise the flaw screening capability of the proof test could be significantly over-estimated. In addition, the review clearly showed that the elastic-plastic fracture mechanics parameter, J, should be used to evaluate fracture behavior in preference to the linear elastic stress intensity factor, K, when crack-tip plasticity is judged to be important. The review also highlighted a fundamental problem associated with proof test analyses: a conservative analysis requires the use of conservative data, but the meaning of conservative data in the context of a proof test analysis is opposite to the meaning of conservative data used in the context of service analysis. As a consequence, there are presently no standards governing the measurement and generation of data which are directly suitable for proof test analysis.

Both theoretical and experimental test programs were planned in Task 3 for substantiating the use of J as the fracture parameter of choice in proof test analysis. The programs were designed to validate the use of J, assess the accuracy of simplified approaches to the evaluation of J, and to verify its use under elastic-plastic conditions and in ductile crack instability analyses.

The theoretical validation program performed under Task 5 was predominantly aimed at assessing the accuracy of approximate J estimation schemes for use in evaluating J under proof test and service conditions. Use of Failure Assessment Diagrams (FADs) as a diagrammatic interpretation of a J analysis was also investigated. As a consequence of this work, an approach based on the so-called reference stress method was recommended for estimating J in situations where more rigorously derived solutions were not available. The reference stress method was employed to determine applied J values for use in the analysis of the experimental test results generated in Task 5. The results of these J analyses were presented diagrammatically using the Failure Assessment Diagram.

The experimental verification program performed under Task 5 was divided into laboratory and hardware testing. Laboratory-based experimental test programs were performed at Southwest Research Institute (SwRI) on specimens designed to simulate proof test loading and plastic constraint typically found in reusable aerospace propulsion systems, such as the Space Shuttle Main Engine (SSME). Tests were performed on the nickel-based superalloy IN-718, and the aluminum alloy, 2024-T3511. Laboratory tests were supplemented by simulated proof tests performed by Rocketdyne under sub-contract to SwRI using actual hardware containing machined flaws. The hardware consisted of three SSME high pressure oxidizer ducts made of IN-718 which were pressurized to failure in Rocketdyne's proof test facilities at Canoga Park, California. In every case, failure of the ducts was by ductile crack instability. The laboratory and hardware test verification programs were both successful, and fully substantiated the choice of J as the most appropriate fracture parameter for use in proof test analysis. Additional hardware analyses were performed by SwRI on three ferritic pressure vessels that had been pressurized to failure in test programs carried out by the Central Electricity Generating Board in the U. K. and NASA Ames Research Center. Results of these analyses also validated the use of J.

The conclusions drawn from the work performed under Tasks 1 to 5 have been incorporated into this proof test guidelines handbook. The Guidelines consist of a main section and four Appendices that have been prepared and delivered under Task 6 of the program.

EXECUTIVE SUMMARY

Fracture Control Documents issued by the National Aeronautical and Space Administration (NASA) require state-of-the-art fracture mechanics to be employed in support of proof test analyses of fracture critical components. The current NASA guidelines on performing a proof test analysis are detailed in the document NASA SP-8040, "Fracture Control of Metallic Pressure Vessels," which is now over twenty years old. This document is based on linear elastic fracture mechanics (LEFM) and provided state-of-the art fracture technology at the time it was issued. However, over the intervening years since the release of NASA SP-8040 there have been profound advances in fracture mechanics with the development and maturation of elastic-plastic fracture mechanics (EPFM) and its application to predicting crack instability in brittle and ductile materials. EPFM extends the concepts of LEFM to address issues concerned with the treatment of crack tip plasticity; stable tearing before fracture; cracks at geometrical discontinuities where local yielding occurs; crack-tip stress states (multiaxial stressing and plastic constraint); net section yielding; interaction effects between primary (mechanical) and secondary (residual and thermal) loads; cracks in inhomogeneous materials (welds); leak-before-burst; and fracture criteria, material properties and crack-tip driving force parameters that determine the critical crack sizes and critical applied loads for fracture. All of these aspects need to be included in a proof test analysis if the flaw screening capability conferred by the test, and a minimum proof load factor, are to be accurately determined.

This document addresses these fracture issues together with related proof test implementation issues concerned with the logic underpinning proof testing, definition of conservative data for use in proof test analysis, test environment, loading media, loading and unloading rates, number of test cycles, pre- and post non-destructive examination (NDE) and stress analysis, in order to provide guidelines for the design of an efficacious proof test for flaw screening of fracture critical components.

In these Guidelines, the many elements of a proof test analysis are integrated into a comprehensive procedure which is represented in the form of a Road Map. The Road Map guides the proof test analyst through the various stages of the procedure to identify the types of data and fracture mechanics based parameters and calculations needed to perform flaw screening and minimum proof load analyses. At each stage in the Road Map, the user is directed to sections in the Guidelines where further details are provided. Worked examples are presented to illustrate the application of the Road Map to proof test analysis.

The state-of-the-art fracture technology employed in these Guidelines is based on the EPFM parameter, J, and a pictorial representation of the results of a J fracture analysis, called the Failure Assessment Diagram (FAD) approach. Relatively simple procedures are recommended and described for evaluating J and FADs and applying them in conjunction with brittle and ductile fracture criteria to determine the critical crack sizes and critical loads of defected hardware. The recommended fracture technology is validated using theoretical and experimental data. The theoretical data is based on finite element results derived from elastic-plastic computations of J, and the conversion of these results into FADs. The finite element results verify the use of the recommended J/FAD estimation schemes and provide data which are used to specify conservative factors for use in proof test and service analyses. The experimental validation is based on the results of laboratory and hardware tests on pre-cracked components. The laboratory tests specifically verify the use of the recommended EPFM concepts for the nickel-based superalloy, IN-718, and the aluminum alloy 2024-T3511, through fracture tests conducted on restrained single edge cracked plates, and single edge and center cracked plates, containing through-wall cracks. The hardware tests verify the recommended J/FAD estimation schemes for axial surface flaws in thin-walled ductile components (specifically, retired space shuttle main engine high pressure

oxidizer ducts), axial surface flaws in the base and weld metals of thick-walled ferritic steel pressure vessels, and a through-wall circumferential crack in thin-walled ferritic steel pressure vessel. In all cases the laboratory specimens and hardware failed by ductile mechanisms.

The role of probability analysis and multiple cycle proof testing (MCPT) are discussed. The former can be used to design a proof test to meet a specified service reliability, but there are still outstanding technical issues that limit its application, as well as a dearth of statistical data to support its implementation. MCPT has been shown in theory and practice to improve fleet reliability for ductile materials under some circumstances. However, a probability analysis is needed to theoretically establish its benefits compared to single cycle proof testing as these cannot be made using deterministic analyses. Procedures are described for estimating the crack extension that can occur due to combined ductile tearing and fatigue crack growth during MCPT. Finally, the effects of the proof test overload on subsequent service fatigue and fracture behaviors are discussed and recommendations are provided as to how to account for these in a safe-life analysis.

1. INTRODUCTION

Proof or overstress testing a component consists of applying a load greater than it would experience during service. This practice is well established as a means of assuring fabrication quality; detecting (possibly, but not intentionally, by loading to destruction) gross manufacturing and material defects before the product is delivered; ensuring structural reliability; providing an enhancement of non-destructive examination (NDE); defect sizing and flaw screening through analysis in situations where NDE is not useable; mechanical stress relieving; and verifying stress analysis.

In general, the decision to proof test hardware rests on the perceived benefits relative to other in-process and final non-destructive examination (NDE) inspection techniques. However, there are situations in the aerospace industry where Fracture Control Requirements (FCR) mandate the use of proof testing as part of the acceptance testing of hardware. This mandate applies to all fracture critical components, such as pressure vessels and rotating machinery, which should be given special attention because of the potential for catastrophic failure. For example, the Marshall Space Flight Center (MSFC) FCR states that pressure vessels and rotating machinery shall be proof tested (MSFC-HDBK-1453, [1]), and the NASA FCR for Payloads Using the National Space Transportation System (NHB 8071.1, [2]) and the Johnson Space Center flight hardware fracture control plan (JSC 25863, [3]) specify that all fracture critical components shall be subjected to NDE inspection or proof testing to screen flaws. These requirements are reinforced by MSFC's Structural Strength Program Requirements which states that proof testing, supplemented by NDE, shall be the preferred method for establishing the maximum flaw or crack-like defect to be used in the service life analysis (MSFC-DHBK-505, Revision A, [4]), and the Military Standard MIL-STD-1522A [5], that has played an influential role in the development of NASA fracture control documents. The latter document states that acceptance tests shall be conducted on every pressure vessel before commitment to flight, and, as a minimum, every pressure vessel shall be proof-pressure tested to verify that the materials, manufacturing processes, and workmanship meet design specifications and that the hardware is suitable for flight.

The usefulness of proof testing in the fracture control of fracture critical and other components is greatly enhanced by the availability of analysis techniques which can utilize the proof test conditions to infer important information about the state of the proof tested hardware as it enters service. Prior to 1959, proof testing was a qualitative measure performed to expose material and/or manufacturing deficiencies, but there was no quantitative interpretation as to what a successful proof test meant in terms of subsequent operational usage. A quantitative interpretation based on linear elastic fracture mechanics was first introduced in that year and reported some years later by Tiffany and Masters [6] along with other applications of fracture mechanics to pressure vessels. Later, Tiffany [7] developed a fracture mechanics-based proof test analysis methodology for application in the fracture control of metallic pressure vessels in the aerospace industry. This methodology addresses such components as high pressure gas bottles, solid propellant motor cases and storable and cryogenic liquid propellant tanks. Soon afterwards, the review of fracture control methods for space vehicles performed by Ehret [8] further established the importance of fracture mechanics in the assessment and proof test analysis of space shuttle hardware. As a consequence of these and other developments, fracture mechanics analysis is considered an integral part of Fracture Control and is mandated, for example, in MSFC FCR document MSFC-HDBK-1453 [1], which states that pressure vessels and rotating machinery shall have a complete fracture mechanics analysis or damage tolerant test program.

Over the past 20 odd years since the early pioneering work of Tiffany [7] and Ehret [8] there have been major developments in fracture mechanics which have important ramifications on the way a proof test is analyzed. For example, there have been significant developments in elastic-plastic fracture mechanics technology and in the assessment of crack instability in ductile materials. These developments have been reviewed for NASA by Besuner et al. [9], and more recently, as part of the current program of work, by Chell et al. [10]. However, these advances have not been formalized in guidelines for use by NASA engineers in the same way that Tiffany's fracture mechanics approach to the fracture control of metallic pressure vessels was in 1970. This is the case even though, for example, MSFC-HDBK-1453 [1] and NASA-STD-5003 [11] state that current state-of-the-art fracture mechanics analytical techniques shall be used in establishing proof test requirements. The present Guidelines are intended to rectify that situation.

The purpose of these Guidelines is to provide sufficient information for NASA engineers to perform state-of-the-art proof test analyses based on fracture mechanics and to inform them about the interactions and roles played by the various parameters that influence the outcome and significance of a proof test, such as environment, loading and unloading rates, hold time, failure mechanism, crack tip plasticity, residual stress, welds, proof load level, and the material's resistance to subcritical growth and fracture. In particular, detailed guidelines are provided on the use of fracture mechanics technology for assessing the flaw screening capability of a proof test, and for determining the minimum proof load (and hence the proof load factor) to support a safe-life analysis in the absence of viable alternative NDE techniques. The Guidelines also identify aspects of fracture mechanics technology which are pertinent to proof test analysis but which have not been sufficiently established for general usage by practicing engineers. Recommendations are provided whenever possible on how to implement these.

An overview of the contents and layout of the Guidelines is provided in Section 2.

2. OVERVIEW

An overview of the Guidelines contents and layout is shown in Figure 2.1. The Guidelines consist of a main section and four supporting appendices. The main section addresses proof test issues and provides guidance, in the form of a Road Map, on performing proof test analyses. State-of-the-art fracture mechanics is reviewed in Appendix A and covers the theoretical background to the analysis approach and the technology that is available for implementing it. The validation data that substantiates the recommended fracture technology are presented in Appendix B. Finally, Appendix C provides worked examples on how to apply the proof test analysis Road Map and Appendix D describes some advanced analysis concepts.

These Guidelines are divided into four topic areas in Figure 2.1: Topic 1 addresses proof test logic, implementation issues and analysis procedures (Sections 3 and 4); Topic 2 addresses the technologies needed to perform a proof test analysis (Sections 5, 6, 7, and Appendices A, C, and D); Topic 3 addresses the possible effects of the proof overload on subsequent service (Section 8); and Topic 4 addresses validation (Section 5 and Appendix B).

Topic 1: Proof Test Logic and Issues (Sections 3 and 4)

The logic behind a proof analysis is outlined in Section 3. This section addresses the two major questions which the proof analyst has to answer, namely, "What is the flaw screening capability of the proof test for a specified proof load?" and "What is the minimum proof load to ensure a specified safe-life?" To answer the first question requires the application of fracture mechanics to determine the maximum flaw sizes that could be present in the tested hardware for it to just survive the proof load. To answer the second question requires the application of fracture mechanics to determine the critical proof load for the tested hardware assuming it contains flaws of specified sizes.

Section 4 on proof test implementation includes discussions on the roles played in proof testing by test environment, such as temperature and test fluid; proof load factors and how their selection is influenced by NASA Fracture Control Requirements, safe-life analysis, and the need to avoid detrimental deformations; the way the proof load is applied in terms of loading and unloading rates, hold times, and the number of proof cycles; the need for and advantages of pre- and post-test, and real-time, non-destructive examinations; and other more general issues, such as test procedures, fixture design, safety considerations, post-mortem analysis (in the event of a proof test failure), costs and potential practical difficulties.

Topic 2: Techniques for Proof Test Analysis (Sections 5, 6, 7, Appendix A, Appendix C and Appendix D)

Section 5 and Appendix A present a review of those aspects of state-of-the-art fracture mechanics which are applicable to a proof test analysis. In particular, Appendix A covers a wide range of technical areas which includes ductile and brittle failure mechanisms and their corresponding failure criteria; the material properties needed to perform an analysis, such as stress-strain data, fracture toughness and J-R curves, and sub-critical crack growth data; brittle and ductile structural fracture modes and their relationship to functional and structural failures; aspects of stress analysis including

Topic 1: Proof Test Logic and Issues

Proof Test Logic
(Section 3)
- flaw screening
- minimum proof load

Issues Related to Proof Testing
(Section 4)
- hardware definition
- test environment
- proof load
- load application
- non-destructive examinations
- general issues

Topic 2: Technologies for Proof Test Analysis

Fracture Mechanics Analysis
(Section 5 and Appendix A)
- stress analysis
- linear elastic fracture mechanics
- failure criteria
- elastic-plastic fracture mechanics
- failure assessment diagram
- failure mechanisms
- material properties
- fracture and failure modes
- critical applied loads
- critical crack sizes
- leak-before-burst

Proof Test Analysis: Flaw Screening and Minimum Proof Loads
(Section 6 and Appendix C)
- analysis road map
- example applications
- analysis of brittle materials
- analysis of ductile materials
- leak-before-burst
- sensitivity analysis

Advanced Analysis
(Section 7 and Appendix D)
- multiple cycles
- reliability analysis

Topic 3: Service Implications

Ramifications for Service Analysis
(Section 8)
- stress analysis
- fracture
- fatigue
- flaw characterization

Topic 4: Validation of the Proof Test Methodology
(Section 5 and Appendix B)
- theoretical validation
- laboratory validation
- hardware validation

Figure 2.1. Overview of Guidelines.

structural modeling, the categorization of loads into primary and secondary, residual stresses and stress re-distribution; the elastic-plastic fracture mechanics crack tip driving force, J; how J can be estimated for cracks at stress concentrators and in the presence of combined primary and secondary loading; the treatment of flaws with multiple degrees of freedom and flaws located at welds; how J is influenced by plastic constraint; and how a J analysis can be diagrammatically represented in the form of a Failure Assessment Diagram which provides a concise and easily understood summary of the results; the steps to be followed in determining critical applied loads for brittle and ductile materials; the steps to be followed in determining critical flaw sizes for brittle and ductile materials; and, the logic underpinning leak-before-burst (LBB), and the calculation of critical through-crack lengths which are essential to formulating an LBB case.

A detailed description on how to perform a proof test analysis to determine critical flaw sizes and critical proof loads is given in Section 6 in the form of a Road Map. Example applications of this Road Map are presented in Appendix C.

Some aspects of advanced analyses are discussed in Section 7 and Appendix D. These cover the role that multiple cycle proof tests and reliability analyses can play in proof testing. The former includes a discussion on crack propagation under combined static and cyclic loading and how it can be calculated; the latter provides information related to the probability of failure during single and multiple cycle proof testing, and the reliability conferred on hardware in service following proof testing.

Topic 3: Service Implications (Section 8)

This consists of a single section (Section 8) which highlights the ways the proof overload can influence subsequent fracture behavior and the ramifications this can have on service analysis. The effects of the overload on subsequent fracture, fatigue and flaw characterization are briefly discussed.

Topic 4: Validation of the Proof Test Methodology (Section 5 and Appendix B)

The validation that supports the fracture technology described in Topic 2 is presented in Section 5 and Appendix B, and covers verification based on theoretical considerations, and laboratory and hardware testing results. This validation substantiates the use of J as an elastic-plastic fracture mechanics parameter, its estimation by the described J estimation schemes, and the use of Failure Assessment Diagrams.

3. PROOF TEST LOGIC

A successful proof test supported by fracture mechanics analysis enables hardware to enter service with a high degree of confidence that no flaw is present in fracture critical regions greater than a size that is determined from fracture mechanics principles. The significance of this is threefold: first, confidence is gained in utilizing the component during subsequent service since uncertainty related to the existence of large defects and poor material is reduced (flaw screening analysis); second, an initial safety margin may be identified based on the ratio of the largest flaw size surviving the proof test (the initial flaw size) to the critical flaw size calculated under operating conditions (the critical service flaw size); third, it enables the minimum proof load to be determined that will screen the hardware for all flaws greater than a critical initial size.

3.1 Flaw Screening

The logic behind the use of proof testing as a flaw screening method is illustrated in Figure 3.1 for the case of a single cycle proof load application to a material which fractures by a brittle failure mechanism. In Figure 3.1, the one degree of freedom (DOF) initial flaw size, a_i, that could just survive the proof test load, P_p, is calculated using fracture mechanics principles. Limited knowledge of the defect size distribution remaining in the component is obtained if the test is successful; it can be argued that no defect of size greater than a_i exists in the component after the test.

The proof test logic assumes the worst case scenario that an initial defect of size a_i is present in the component, and this is used as the initial crack size in a service life estimation. By adjusting the value of P_p it is hoped to arrive at a calculated value of a_i so that the required service life can be realized without incurring an unacceptable risk of failure during the proof loading. The service life is determined by calculating the amount of sub-critical crack growth incurred during service, due to mechanisms such as fatigue, environmental attack and creep, up to a critical service flaw size, a_{cr}, that is determined from fracture mechanics principles for the peak operating loads (POLs), P_{POL}. The calculated service life should equal or exceed the safe-life, equal to the complete mission lifetime multiplied by an appropriate service life factor, F_{sl}, which is typically 4.

In practice, to facilitate fracture mechanics analyses, naturally occurring surface and embedded flaws are idealized as semi-elliptical and elliptical in shape, respectively. This means that they cannot be characterized by a single crack-size parameter, a. A range of defect depths and lengths have to be assessed, and proper account taken for the potential change in defect shape during proof loading and subsequent service, if specific information on typical crack shapes is not available.

NASA has specified maximum initial flaw sizes that should be assumed present in the hardware for safe-life analysis based on experience gained from flaw sizes that could evade non-destructive examination (NDE). These sizes are based on minimum initial flaw size detectable assumptions given in NASA-STD-1249 [12]. The NDE based maximum initial flaw sizes are the minimum flaw sizes that should be introduced into the hardware for safe-life testing to demonstrate a prescribed life. Table 4.2, which is copied from NASA-STD-5003 [11], shows minimum initial flaw sizes for safe-life testing, and, absent explicit flaw size measurements by NDE during the proof test, these should be assumed to be the flaws that are being screened by the proof test. Typical minimum initial flaws have aspect ratios a/c in the range of 0.2 to 1, where a is the crack depth, and c half the surface length. (More information on these initial flaw sizes is given in Section 4.6.1.)

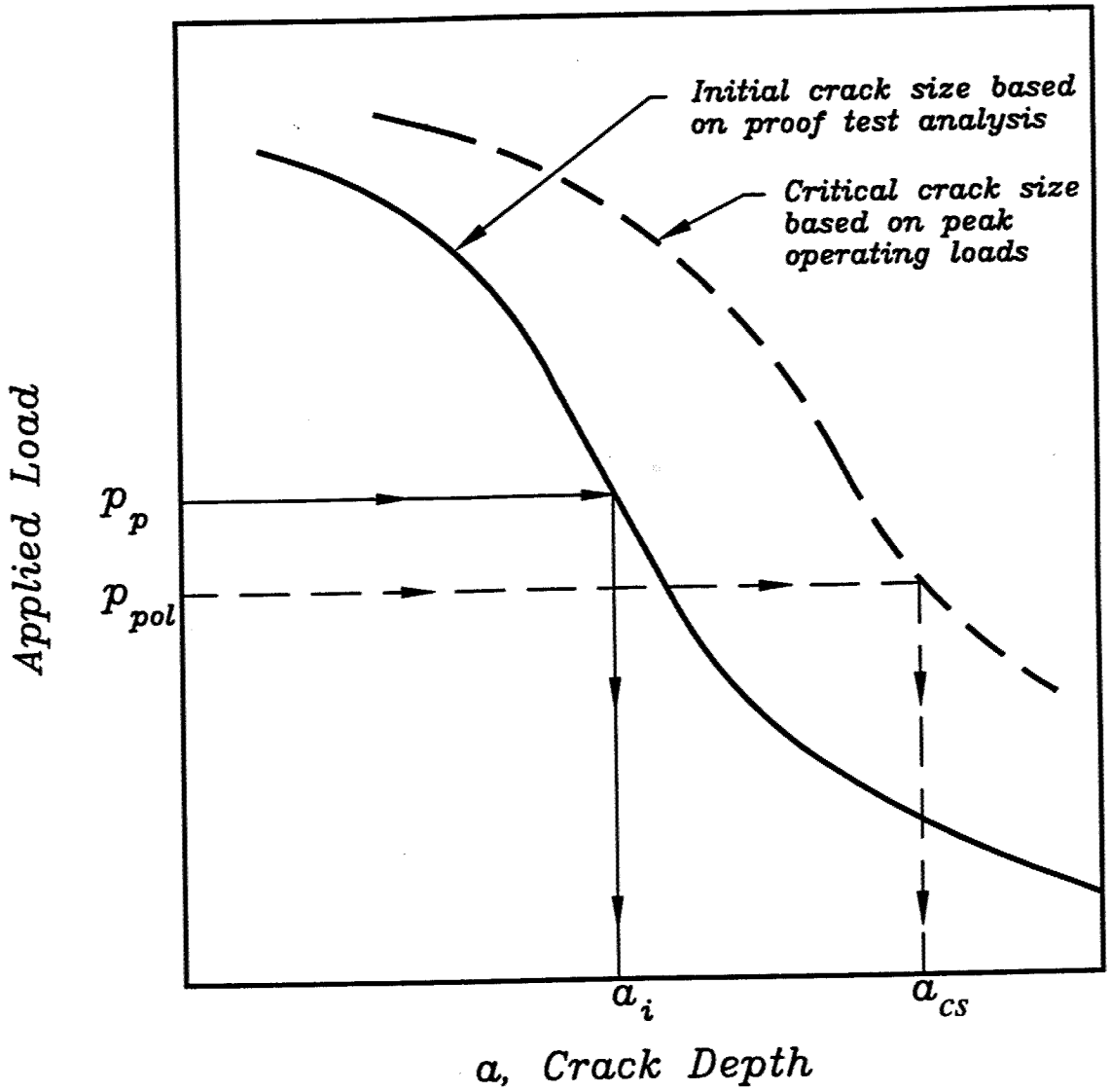

Figure 3.1. Proof test logic: flaw screening for a one degree of freedom flaw.

Figure 3.2 illustrates the application of the flaw screening analysis to determine the service life of an assumed defected component when the flaws are surface breaking. A locus of initial crack depths, a_i, and surface lengths, $2c_i$, of defects which could just survive the proof loading is determined using fracture mechanics principles. This locus represents the flaw screening capability of the proof test for the specified proof load. A similar exercise is then performed using the peak operating loads to obtain a locus of critical service crack depths, a_{cs}, and surface lengths, $2c_{cs}$, that would cause failure under these conditions. The flaw screening results from the proof test analysis are used to define a set of initial defect depths ($a_{i,1}$, $a_{i,2}$, $a_{i,3}$, etc., in Figure 3.2) and the growth of these flaws is assessed under service conditions, taking full account of the change in crack shape, to obtain the corresponding times (t_1, t_2, t_3, etc.), or cycles to failure. The minimum of these times or cycles represents the analytical service life of the component.

3.2 Determining a Minimum Proof Load

The logic behind the determination of a minimum proof load, or proof load factor, to ensure a specified safe-life, is straightforward for a one DOF flaw in a brittle material. The minimum proof load, $P_{min,p}$, is the calculated load that will result in incipient fracture of the hardware under proof test conditions assuming a flaw is present equal to the critical initial service flaw size a_{ci}. The critical initial service flaw size is equal to the crack size that would survive exactly the specified safe-life, equal to the mission life times the service life factor, typically a factor of four. If the proof load is of the same type as the service load (e.g. internal pressure) then a proof load factor, α_p, can be defined as

$$\alpha_p = \frac{P_{min,p}}{P_{MEOP}} \tag{3.1}$$

where P_{MEOP} is the maximum expected value of the load during service. In order to maintain generality, the minimum proof load is mainly used in these guidelines in preference to the proof load factor.

The calculation of the minimum proof loads for hardware containing surface flaws in a brittle material with two DOF is also straightforward. In these cases, critical initial flaw sizes are characterized by their depths and half surface lengths. Given these dimensions, fracture mechanics principles can be applied to determining the minimum proof load in a similar way to the procedures for a one DOF flaw.

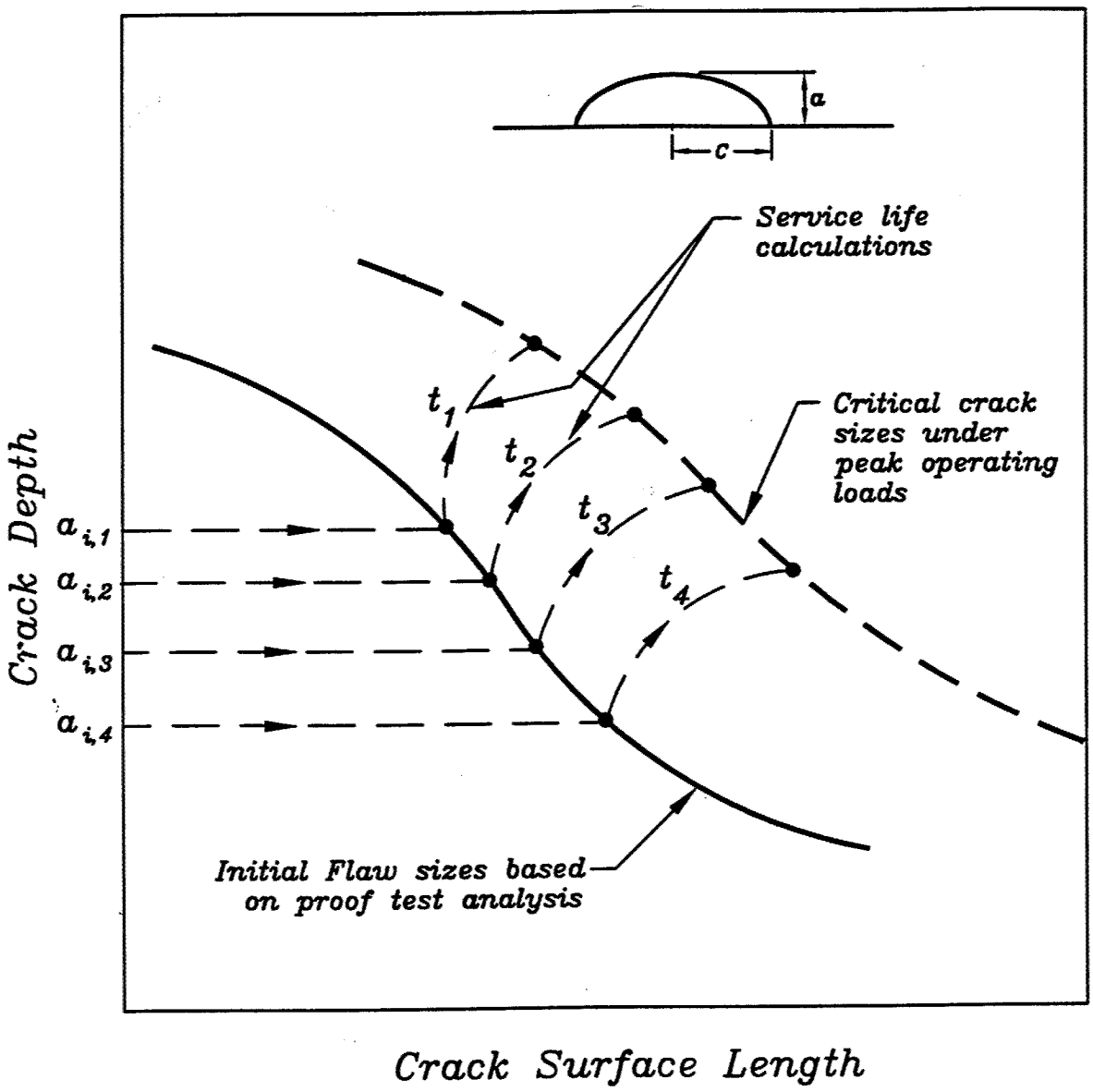

Figure 3.2. Proof test logic: flaw screening and safe-life analysis for a two degree of freedom flaw.

4. PROOF TEST IMPLEMENTATION ISSUES

4.1 Overview

Figure 4.1 shows six major tasks which are involved in planning and implementing a proof test. The figure identifies the sub-sections below which contain guidance on each task. These sub-sections do not contain specific information on how to perform each task; rather, they describe the key issues related to them and how these issues influence the choice of proof test parameters, such as test environment, loading rates and proof load factors. A list of the key issues is shown under each task heading in Figure 4.1.

4.2 Hardware Definition

The hardware to be proof tested should be well understood in terms of its service function (pressure vessel, rotating machinery), its structural geometry and dimensions (from drawings, confirmed by measurements if possible), the presence of structural details that may need special consideration in a proof test analysis (such as geometrical discontinuities and welds), and the material(s) of construction (chemical composition confirmed by analysis, heat treatments and minimum material property requirements).

4.3 Test Environment

The choice of specific environmental conditions for the proof test, (i.e., temperature and media), are dependent upon numerous considerations. These include safety considerations, demands to conform to FCRs and standard structural guidelines, and the need to directly demonstrate component survival in the operating environment through structural testing. If safety considerations are paramount, hydrostatic pressurization is generally preferred over pneumatic due to the significant reduction in stored potential energy. If the primary purpose of the proof test is intended to demonstrate that the component can survive service conditions, then it is generally accepted that the test should be carried out in an environment which simulates operational circumstances. For example, Section 15.4 of MSFC-HDBK-1453 [1] states that proof testing shall be performed in the actual expected environment (temperature and media) when feasible, but when this is not feasible, environmental correction factors shall be used to adjust the proof load factor.

Alternatively, if the proof test is used as a flaw screening method (assumed to be the main purpose of the proof test in these guidelines), then any complications which make this objective difficult to accomplish should be avoided. In particular, sub-critical flaw growth which is difficult to quantify can occur in chemically aggressive environments with the result that needless uncertainties may be introduced into determining flaw screening capability. The conditions affording the most confidence toward accurately interpreting the impact of the proof test (e.g. an inert medium with moderate loading rates applied at temperatures where time dependent phenomena are not significant) avoid these complications.

Task 1: Hardware Definition

(Sections 4.2)

- function
- structure
- material

Task 2: Specify Test Environment

(Sections 4.3)

- temperature
- media

Task 3: Assess Proof Load Factors

(Sections 4.4)

- minimum requirements
- safe-life analysis
- detrimental deformations

Task 4: Specify Proof Loading

(Sections 4.5)

- loading rates and hold times
- number of proof cycles

Task 5: Define Role of NDE

(Sections 4.6)

- pre-test
- post-test
- flaw detection and growth

Task 6: Consider General Issues

(Sections 4.7)

- test procedures
- fixture design
- safety considerations
- post-mortem analysis
- costs
- practical difficulties

Figure 4.1. Proof test issues.

Whether severe complications exist due to environmental conditions or not, it is essential that the full implications of testing in a specific environment are fully understood if a proof test is to be successful. As an example, proof testing at temperatures below operation can afford better flaw screening potential because the yield stress is typically raised by lowering the temperature. This increase in yield stress allows the hardware to continue to undergo elastic deformations to higher load levels. Furthermore, in materials that fail by brittle mechanisms, the toughness is generally lowered as the yield stress increases. Both of these factors contribute towards increasing the efficacy of the proof test as a flaw screening measure. However, this increase in flaw screening potential may be countered by an increase in proof test mortalities due to the increased brittleness of the material. In addition, the phenomenon of warm prestressing[1] could complicate the interpretation of a successful proof test used as part of a component re-certification procedure if the service temperature exceeds the test temperature and the proof load is below the maximum load experienced in service prior to testing.

In addition, unnecessary damage can be introduced into a component during proof testing when the sizes of existing defects increase by subcritical flaw growth occurring by monotonic, cyclic and time dependent mechanisms. This damage can weaken surviving components relative to the pre-test condition. Flaw growth can be particularly onerous if it occurs during unloading or subsequent storage prior to operational usage. The possibility of causing unnecessary component damage due to proof testing in an aggressive or embrittling environment, or at severe temperatures, needs to be avoided if at all possible. Examples of conditions that can contribute to component damage are temperatures where strain or strain age embrittlement may occur; environments that cause accelerated rates of crack growth (true corrosion and stress corrosion fatigue and high oxidation rates); embrittlement due to ductile-brittle transition temperature and/or material-environment incompatibility; and proof testing at high temperatures where creep deformation during the time of the test may become significant.

4.4 Proof Load Factors

4.4.1 Minimum Requirements

The selection of a specific proof load level is perhaps the central decision in proof test design. The larger the factor, the smaller are the defects screened by the proof test. It follows that a high proof load will generally increase confidence that the tested hardware will have good reliability during subsequent service exposure. A high proof load may also have other beneficial effects, such as enhancing shakedown, creating compressive residual stresses, and blunting sharp crack tips.

---

[1]Warm prestressing is a special case of overstressing where a structure is initially loaded at a temperature above the ductile-brittle toughness transition temperature, unloaded , cooled to below the transition temperature, and then reloaded (for more details concerning this phenomenon, see Chell and Curry [13]). This sequence of events is very similar to those which would occur if proof testing was performed at a temperature below the transition temperature following service loading (warm prestressing) at a temperature above the transition temperature. In brittle materials which fail by stress controlled mechanisms below the transition temperature (such as ferritic steels) the warm prestressing changes the effective fracture toughness at the lower temperatures in a complex manner. Hence, post-test flaw sizes that are inferred from a proof test flaw screening analysis based on measured toughness values at the proof test temperature may be in error.

NASA Fracture Control documents require that the proof load factor shall be the larger of the values determined by fracture mechanics analysis[2] and proof test requirements designed to meet a specified safe-life, or those values specified in the factor of safety requirements. Typical factors of safety extracted from the MSFC Structural Strength Program requirements documents MSFC-HDBK-505A [4] and NASA-STD-5001 [22] are shown in Table 4.1. The former document states that in no case shall the adjusted proof test factor be less than 1.05 without MSFC approval.

Table 4.1 Typical minimum proof load factors for pressurized hardware

Hardware Description	Proof Factor (Proof Pressure/MEOP)
propellant tanks	1.05
solid motor casings	1.05
engine structures	1.20
hydraulic and pneumatic actuating cylinders	1.50
personnel compartments	1.50

Although it is advantageous to apply similar types of loading during the proof test as are applied during service, in reality it is normally only practicable to apply relatively simple types of loads during proof testing, such as internal pressure, tensile forces and rotational loading. More complicated loads, especially those that do not have a mechanical source (such as thermal stresses), will generally be either too difficult or too expensive to apply, or both, unless there is suitable justification for doing so.

The detailed determination of the proof load level needed to meet flaw screening criteria is described in Section 6.1. The procedures take advantage of state-of-the-art elastic-plastic fracture mechanics to update and elaborate on the approach used by Tiffany [7]. In general, the flaw screening capability of the proof test cannot be simply characterized as a proof load factor (see Section 4.4.3). Instead, the procedures in Section 6.1 describe how to estimate the minimum proof load level which is necessary to assure a specified safe-life. The procedures also describe how to calculate the maximum flaw sizes that could just survive a specified proof load level. All sizes greater than this will be screened out by the proof test.

4.4.2 Safe-Life Analysis

A safe-life analysis is performed to ensure that no flaws exist which will grow to critical size in less than the service life times a factor, typically four. The proof load should be high enough to interrogate those life limiting and fracture critical regions identified in the safe-life analysis. A safe-life analysis will provide information on the initial flaw sizes that have to be screened against. The proof load should be high enough to accomplish these requirements without unduly threatening the integrity of the tested hardware.

---

[2]This is not always possible nor practical if very large factors are required based on fracture mechanics requirements. In these cases, alternatives to the proof test should be investigated.

Selection of a proof load level is complicated by differences between proof test and actual service conditions, such as load types, local stress profiles, temperatures, and environments which are allowed for in a safe-life analysis. Also, proof test fixturing may not exactly simulate boundary conditions experienced in service. While typical proof loading of pressurized systems involves only an applied internal pressure, service loads may also include thermal stressing, tensile forces and bending moments. In addition, there is a potential during the proof loading for redistribution of stresses to occur in those regions of the hardware where the local stress is at or near yield point magnitude. These regions are normally associated with geometric discontinuities (such as sharp corners and holes) and residual welding stresses. If the component is being recertified after being subjected to service loadings, then there is the further possibility that additional non-welding related residual stresses are present, which are the consequence of local plasticity generated by severe thermal loading during operation, or local geometric discontinuities.

It is clear that in complex geometrical components there will always be the likelihood that local stresses occurring during service will exceed the maximum level which can safely be generated in the proof test using simple loading devices. Thus it should be conceded that there may be parts of a component that can experience local stressing during service that is more onerous than that which can be applied at the proof test stage. In these cases complementary flaw screening methods, such as non-destructive examination (NDE), must be performed.

4.4.3 Proof Load Factors

Situations may arise where the proof test is conducted in an environment different to the service environment. This situation was addressed by Tiffany [7] using LEFM for the case where the proof test and service conditions pertained to different temperatures, and the hardware was subjected to the same loading type (e.g. internal pressure). In these cases Tiffany showed that it is possible to define the proof load factor given by equation (3.1) in the form

$$\alpha_p = \alpha_s \frac{K_{Ic}^p}{K_{Ic}^s} \tag{4.1}$$

where α_s is the proof factor corresponding to a proof test conducted at the service temperature, and K_{Ic}^p and K_{Ic}^s are the fracture toughness at the proof and service temperatures, respectively. However, this approach cannot be readily generalized to include instances where:

- the proof test and service load types are different;
- thermal stresses are present during service but not during the proof test;
- the screened flaws are located at non-stress relieved welds where residual stresses are present;
- crack tip plasticity necessitates the use of EPFM;
- there is a change in failure mechanism in going from the service to the proof test temperature (e.g. brittle and ductile failure in ferritic steels);
- ductile failure accompanied by tearing occurs at both service and proof test temperatures.

Under these conditions, a proof load factor can only be specified by calculating $P_{min,p}$ and employing equation (3.1).

The fracture mechanics approach adopted in the present Guidelines is not based on determining proof load factors but on ensuring that the proof test conditions provide the flaw screening capability necessary to guarantee a desired service life. Hence, when viewed in this light, the major impact of service environmental conditions is dictated by the perceived need to perform the proof test under similar conditions to the service conditions as a quality assurance measure in order to demonstrate the integrity of the hardware under these conditions. This use of the proof test to ensure product integrity is qualitative. The use of the proof test in these Guidelines as a flaw screening measure, which depends on a quantitative fracture mechanics-based analysis, provides additional important information that complements the quality assurance approach. If considered necessary, a proof load factor can be derived from the calculated minimum proof load using equation (3.1), but the value of this factor (whether it is greater or less than one) is not of itself relevant as to whether the proof test will adequately screen against undesirable flaws, and, in general, it does not characterize this flaw screening capability.

4.4.4 Detrimental Deformations and Load-Induced Damage

There is clearly a limit to the size of the proof load beyond which unacceptable deleterious effects begin to occur. Some of these limits are specified in order to avoid detrimental yielding and plastic failure in uncracked regions of the component. For example, NASA Fracture Control documents specify that proof load factors must be chosen so that proof testing will not subject the flight article to detrimental deformations beyond the elastic limit. Most importantly, high proof loads increase the chance of expensive hardware failures during the proof test from defects which would have been innocuous under the subsequent service history. The potential for subcritical growth of existing defects under high proof loads also cannot be ruled out. The possibility of these unwanted events occurring can be reduced by the application of fracture mechanics analysis to determine the critical flaw sizes in tested hardware as a function of the proof load.

In addition, potential degradation of future component performance or material capability after proof testing can occur due to a reduction in ductility by prestraining, as well as the creation of local tensile residual stresses at regions of stress concentration.

4.5 Load Application

4.5.1 Loading and Unloading Rates and Hold Times

The selected time during which the maximum pressure or maximum load is held constant is influenced by both operational and fracture mechanics concerns. The hold time should be at least long enough to ensure that the maximum load is actually attained and can be maintained stably. Additional time may be required to adequately monitor the component for leaks or other irregularities. However, the length of the hold time has to take into account the potential for material degradation due to strain ageing as well as time-dependent flaw growth at a constant load. This latter phenomenon can result from two major causes: sub-critical growth due to environmental attack or creep deformation at the crack tip, and, in ductile materials, stable tearing.

The influence of subcritical growth during the proof test on component reliability in service is not always easily deduced a priori. This is because relatively small and innocuous defects may be extended in size by sub-critical crack growth mechanisms to give a greater population of larger defects at the end of the proof test than existed before it, which increases the probability of service failure. In contrast, subcritical growth could promote failure of service life threatening defects during proof loading by

propagating them to a critical size. This scenario would beneficially screen out damaging defects and could increase service reliability. Since both of these effects could occur concurrently, it is not clear without performing a detailed probability analysis whether the end result would be deleterious or advantageous.

The situation is complicated if the proof test is performed in an aggressive environment which accelerates the time-dependent growth. The environment could do this by reducing the toughness of the material (in a hydrogen environment, hydrogen may diffuse into the highly stressed material around the crack tip and cause embrittlement) or by a synergistic interaction whereby the crack extension due to the environment (i.e., subcritical crack growth) increases the crack driving force, which in turn promotes more tearing. Although this scenario would manifest itself as enhanced time-dependent tearing, the possibility that the environment degrades the fracture toughness could have serious implications with regard to structural reliability during subsequent service operation.

The choice of loading and unloading rates are closely related to the factors affecting the choice of hold times. Some concerns are operational: practical limits exist on how fast a complex engineering component can be pressurized or depressurized while maintaining adequate control on total pressure and adequate monitoring of component response. Slow loading or unloading rates also raise the possibility of time-dependent crack growth due to environmental attack or creep deformation (if the test temperature is high enough). Tiffany [7] makes the pertinent point that the damage resulting from subcritical growth during sustained loading could be dangerously enhanced by a slow unloading rate which still permitted subcritical growth to occur while suppressing the possibility of the larger defects initiating failure. A reasonable engineering solution is not to proof test in an aggressive environment, or, if this is unavoidable, to minimize the time spent during the load increasing or load decreasing portions of the proof test. This is especially true for the unloading half of the cycle.

Although extremely fast loading rates may induce changes in the material properties of rate sensitive materials (the values of yield stress and fracture toughness could significantly differ from the values measured in a conventional static test if strain rates are high enough), typical maximum attainable loading rates during proof testing will generally be too low for these effects to be of any significance in aerospace materials.

Real-time acoustic emission (AE) monitoring during the proof test may be employed to detect time-dependent subcritical crack growth, and the availability of this capability will influence hold time selection. The use of AE or other real-time NDE techniques may also require additional time at maximum load to permit complete interrogation of the component.

4.5.2 Number of Proof Cycles

It has been argued that there is nothing to be gained from multiple cycle proof testing (MCPT) and, indeed, multiple cycling could do some needless damage to the component because of cyclic crack growth [7]. This position is generally accepted for brittle materials, and there are good reasons for taking this view if the proof test is performed in an aggressive environment. However, the experiences of Rocketdyne in successfully using MCPT methods on ductile materials provides practical evidence that there are exceptions to this view [14]. In addition, recent probabilistic-based investigations performed at SwRI under sponsorship from NASA have quantified extra benefits that MCPT can confer on service reliability compared to a single cycle proof test [15].

Irrespective of whether multiple cycling is planned as part of the proof test procedure, some components may be subjected to cyclic loadings which inadvertently simulate a planned MCPT. These situations can arise when additional proof testing is performed on components which have been repaired or modified following the initial proof test; in complex component systems which must be proof tested at different times during their assembly; and in repeat proof testing for component recertification.

As stated, the present justification for a planned multiple cycle test is based on the practical experience of Rocketdyne and the theoretical analysis results of McClung et al. [15]. MCPT of components fabricated from ductile materials has been performed at Rocketdyne for many years, and was originally motivated by failures of components which had survived an initial single-cycle test and were subsequently retested. Later Rocketdyne experience with MCPT has shown that component failures can occur on the second, third, fourth, or fifth cycles at significantly lower pressures than applied on the first cycle [16]. These failures generally initiated from undetected flaws in the component, typically in thin sections where the defects were large compared to the thickness. In several cases these hardware deficiencies, revealed only after the hardware had passed the first proof pressure cycle, were judged to have presented a significant risk of component failure or malfunction in service.

The successful record of performance of Rocketdyne engines whenever MCPT has been implemented, along with occasional failures of defective hardware during MCPT, have served as engineering justification for the practice at Rocketdyne, at least on components and under conditions where verification has been obtained.

The choice of number of proof test cycles based on purely analytical considerations is a complicated process, and some of the stages of the analysis are still not fully developed. The optimum design of a MCPT will depend, at least in part, on the specific geometry, material properties, and probable pre-existing flaw distributions for each component. Recent research performed at SwRI under NASA sponsorship to investigate the effectiveness of MCPT indicates that the calculated service reliability of a fleet of hardware may be increased by performing more than a single proof test cycle, but that this increase is small compared with the increase conferred by survival after the first cycle [15].

At the present time, no definitive recommendations can be given based on analysis regarding the optimum number of proof cycles that will maximize the effectiveness of the proof test. It is re-emphasized that MCPT is an option which should be considered only for materials which fail by ductile mechanisms.

4.6 Role of Non-Destructive Examination (NDE)

According to NASA FCRs, all fracture critical parts shall be subjected to NDE to screen for flaws and crack-like defects, and, with approval, the proof test may be used as an NDE enhancement. If a primary motivation for the proof test is to facilitate improved NDE inspections, then it should be possible to decrease the proof load factor and hence reduce the potential for unnecessary damage to the component.

NDE is not an essential part of proof testing, but it can greatly increase its effectiveness. Although flaw screening by proof testing is sometimes conducted as an alternative to NDE, particularly when the effectiveness of NDE is compromised by geometric complexities of the component, more frequently proof testing is conducted in coordination with NDE inspections. Special attention should be given to the types of defects which are most or least likely to be detected by NDE or by proof testing, with a view towards maximizing the total probability of detection by coordinating the two inspection protocols. Coordination between NDE and the proof test can be especially important for components fabricated from tough, ductile materials, where stable growth of pre-existing flaws, crack-tip blunting and LBB are more likely before instability.

NDE also interacts with other technical proof testing issues which are discussed elsewhere in this report. These include incorporating the influence of NDE on a probabilistic treatment of structural reliability (see Appendix D).

Although NDE is most often conducted before and/or after the proof test, useful NDE techniques for real-time proof test monitoring are also available.

4.6.1 Pre-Test and Post-Test NDE

It is prudent to require pre- and post-test NDE of fracture critical welds for pressurized components in space flight structures displaying brittle structural fracture or hazardous LBB [17].

The techniques available for pre- and post-test NDE are long established and the principles behind them are well understood. The main techniques—ultrasonics, eddy current, radiography, magnetic particle and dye penetrant—have established protocols for use by certified technicians. Some of these methods, such as dye penetrant and magnetic particle inspections are only applicable to surface flaws, while ultrasonics can also detect subsurface defects. The eddy current method is used to detect surface and near subsurface defects. The minimum initial flaw size detectability assumptions for the various NDE methods are detailed in NASA-STD-1249 [12]. An indication of the minimum sizes of assumed undetected flaws is shown in Table 4.2, extracted from NASA-STD-5003 [11]. This table serves to identify the minimum initial flaw sizes that are required to be present in structures that are tested to verify safe-lives. These sizes correspond to a 90% probability/95% confidence level of inspection reliability. A schematic illustration of the crack geometries referred to in this table is shown in Figure 4.2 which is copied from NASA-STD-5003 [11].

Post-proof NDE is especially useful for two reasons: deformation caused by the proof loading may increase the detectability of pre-existing flaws, and the proof loading may also cause additional damage in the form of subcritical crack growth which needs to be detected. Enhanced flaw detectability due to proof loading is a well-documented phenomenon. Local plastic deformation can permanently "open up" cracks such as tight weld fissures in compressive residual stress fields, so that standard post-test NDE inspection can find flaws which might have been missed by pre-test NDE. For example, following the application of multiple proof test cycles to engine combustor cases for the C-5 aircraft in 1969, conventional dye penetrant inspections found cracks in 6 cases which were undetectable prior to proof testing [18]. Similar experiences were reported by Martin Marietta during ultrasonic inspections of 2219 aluminum weldments for the Space Shuttle External Tank [19].

Table 4.2 Minimum initial flaw sizes for safe-life testing based on NDE
(Extracted from NASA-STD-5003)

NDI Method	Crack Location	Part Thickness	Crack Type	Crack Size	
		t, in.		a, in.	c, in.
Dye Penetrant	Open Surface	t≤0.050	Through	t	0.100
		0.050<t≤0.075	Through	t	0.15-t
		t>0.075	PTC	0.025	0.125
				0.075	0.075
	Edge or Hole	t≤0.100	Through	t	0.100
		t>0.100	Corner	0.100	0.100
Magnetic Particle	Open Surface	t≤0.075	Through	t	0.125
		t>0.075	PTC	0.038	0.188
				0.075	0.125
	Edge or Hole	t≤0.075	Through	t	0.250
		t<0.075	Corner	0.075	0.250
Eddy Current	Open Surface	t≤0.050	Through	t	0.050
		t>0.050	PTC	0.020	0.100
				0.050	0.050
	Edge or Hole	t≤0.075	Through	t	0.100
		t>0.075	Corner	0.075	0.075
Radiographic	Open Surface	0.025≤t≤0.107	PTC	0.7t	0.075
		t>0.107		0.7t	0.7t
Ultrasound	Open Surface	t≥0.100	PTC	0.030	0.15
				0.065	0.065

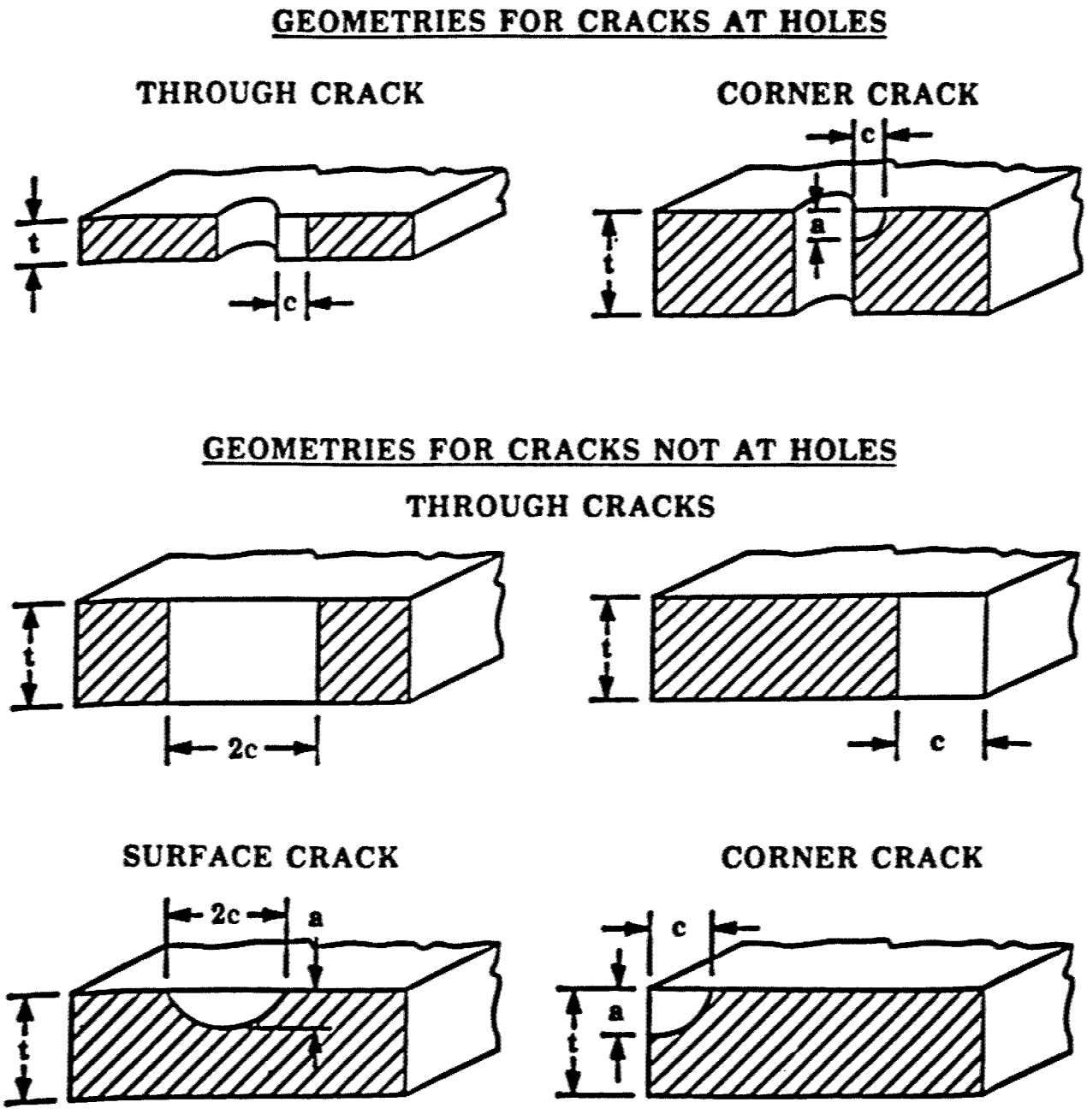

Figure 4.2 Standard crack geometries. (Extracted from NASA-STD-5003.)

The requirement for post-test NDE is increased if the proof loading causes a significant increase in damage (e.g., crack size) during the test. In these cases valuable information may be obtained by comparing NDE results from different inspections. For example, by employing post-test NDE to focus on regions where there were indications from pre-test monitoring, or comparing pre-test with post-test signals to note significant differences.

4.6.2 Flaw Detection and Growth During Testing

Several NDE techniques can be employed to detect the real-time response of a crack or flaw during proof test loading. The most mature NDE technology for real-time monitoring is acoustic emission (AE), which detects the elastic energy spontaneously released by nearly all materials when they undergo deformation. AE was first employed to monitor proof testing around 1965, and AE applications to proof testing and related structural reliability problems are now common in many different industries [20].

The primary target of AE monitoring during proof testing is the emissions from localized deformation associated with flaws and flaw growth. Acoustic emissions can be generated from cracks by several different mechanisms, including plastic deformation at the tip of stationary or growing cracks, creation of new surfaces during crack growth, and the contact and rubbing of opposing crack faces during loading or unloading. The relative amplitude of emissions from these different sources may vary from application to application, and this may have implications for the optimum selection of hold times or loading/unloading rates. Emissions activated by crack propagation may be predominant only during periods of appreciable growth, such as near failure, when an increasing AE event rate is a likely predictor of flaw criticality [21]. AE methods cannot be used by themselves with sufficient accuracy for measuring flaw size, orientation, or depth, although they can locate the region of the structure from which the emissions are coming. Hence, a follow-up inspection with another NDE method is often required at the located AE source for further verification.

4.7 General Issues

4.7.1 Test Procedures

Test procedures are a critical element of the proof test since they contain the necessary system setup information and the test parameters needed for successful test completion.

A good pressure test procedure, for example, should contain the following elements to insure safety, test data quality, and overall high efficiency:

- test system mechanical and electrical/ instrumentation schematics, including detailed component description lists;
- all test parameters such as final absolute and/or differential pressure(s), test item temperature, number of pressure cycles, dwell times at various pressure levels, and pressurization/depressurization rates;
- reference to resident facility operating procedures describing facility setup, operation, and troubleshooting and contingency plans needed in the event the test item and/or facility experiences an anomalous condition;
- data collection instrumentation and critical system component redundancy;
- test item/facility cleanliness control.

In addition, each procedure must receive a hazard analysis to assure that all scenarios involving adverse pressure and/or external load conditions have been addressed by the test procedure and compensated for in the test system.

4.7.2 Fixture Design

Test fixturing is an integral part of any proof test for creating the load conditions necessary for component evaluation. Some of the more important fixture design features that should be considered are compartmentalization of a test item based on various pressure zones present during test; simulation of internal pressure loads; application of external mechanical loads; structural simulation of the components or assemblies attached to the test item during service; incorporation of pressure and/or volume control devices to allow control of adverse absolute and/or differential pressures, internal and/or external mechanical restraints to limit test item and/or fixture displacement; high strength material availability for very large fixtures and fasteners; and systems for controlling and monitoring concentrations of hazardous substances that are part of simulating adverse environments.

4.7.3 Safety Considerations

The type of "fluid" used in the proof test and whether pneumatic or hydrostatic pressurization is used has ramifications regarding safety considerations, proof failure and the possibility of performing post mortem failure analysis. Due to the incompressible nature of liquids, hydrotesting will usually result in a leak-before-burst situation for ductile materials. In contrast, the compressibility of gases enables them to store large quantities of energy which can be released suddenly, giving rise to a potentially catastrophic rupture. This possibility requires special precautions to be implemented in the test facility design and operating procedures, as well as additional leak detection equipment and analytical support to assess the likelihood for leak-before-burst. Special precautions are also required when rotational loading is used in the proof test.

Determining the cause of proof failure is much easier when the failure is contained and the fracture region is readily accessible. There have been numerous instances where brittle failures have occurred during a proof test and produced so much destruction in the component and surrounding structure that diagnostic failure analysis was greatly hampered.

4.7.4 Post-Mortem Analysis

The value of the proof test is based on avoiding failure during operation by ensuring failure will occur during proof testing if minimum structural integrity requirements are not met by the hardware under the proof test conditions. The intent is not to have a high proof test mortality rate, but to minimize this through pre-test fracture analysis while still maintaining a high reliability for successfully tested hardware during subsequent service. However, inevitably, some hardware will fail during the proof test. When this occurs, a post-mortem analysis is desirable.

Post mortem hardware assessment can provide valuable feedback information identifying actual material capability and quality, evaluating the accuracies of structural and fracture mechanics analyses and/or revealing failure and fracture mode characteristics. These are all items that can be used to increase understanding and knowledge of a particular design and potentially serve as verification of the assumptions in the analysis or the analysis methodology itself. Corrective actions resulting from the knowledge gained from the proof failure can proceed along the lines of modifying and improving the

design, enforcing tighter inspection or process control standards, improving traceability in ensuring that all critical process or fabrication steps have been completed satisfactorily or imposing more restrictive hardware usage limits.

4.7.5 Costs

The costs associated with proof testing include the expense of performing the test and the risk of component failure. The latter expenses include possible damage to the tooling and test facilities, as well as the component replacement cost. However, these costs have to be weighed against the ramifications of service failure which oftentimes can be extremely severe. An obvious criterion for choosing a flaw screening procedure is that it minimizes the total expected cost while meeting a particular structural reliability level during operation. Although increasing the severity and/or number of proof tests can lead to greater structural reliability in service, it may needlessly increase the number of component failures during proof testing which arise from flaw sizes that are smaller than the size that would have grown during subsequent service to have caused failure. In addition, if the primary quality assurance measure is through nondestructive inspection procedures, unnecessary risk of proof failure can occur if the flaw size screened by the proof test is smaller than that which is readily detectable by NDE.

Besides the cost of the proof test per se, there will be additional expenses that arise from planning and setup (e.g. the need for stress analysis information and the acquisition of material property data that pertains to the test conditions, both of which are needed for a proof test analysis.)

4.7.6 Practical Difficulties

The feasibility of performing proof tests is intimately related to practical issues concerning difficulties in performing the test. For example, difficulties in full-scale proof testing of large structural systems may preclude any possibility of doing these; cryogenic proof testing may be desirable, but impractical due to effective sealing concerns; simulation of operational stresses is very desirable, but may not be possible due to the existence of thermal stresses or external loading during operation. Proof testing in potentially explosive media such as high pressure hydrogen, may be impractical due to safety concerns.

The conditions under which a key component is proof tested may be qualified by the incidental effects that these have on other components which are intimately associated with the testing. For example, the maximum proof load which can be applied may be limited in order to avoid the consequences of inadvertent failure of sub-assembled items.

Irrespective of the difficulties outlined, a proof test must be performed for critical hardware if there is not a reliable alternative NDE method available, if in-service failures cannot be tolerated or if the hardware is subject to a specific mandate to do so in a NASA FCR document.

5. STATE-OF-THE-ART TECHNOLOGY FOR PROOF TEST ANALYSIS: FRACTURE MECHANICS AND VALIDATION

5.1 Fracture Mechanics

State-of-the-art fracture mechanics should be used in proof test analyses according to NASA Marshall FCRs (NASA-STD-5003, [11]). The purpose of this section is to provide the proof test analyst with a guide to the more detailed aspects of modern fracture technology that are described in Appendix A and are needed to implement the state-of-the-art fracture mechanics requirement. Appendix A concentrates on summarizing the data that are needed to apply fracture mechanics principles, on providing a description of some of the methods that are available for determining fracture mechanics parameters, with emphasis on simplicity and useability, and on how the data and principles are combined in assessing the critical conditions for fracture in defected structures. Some of the fracture mechanics aspects described are well established, while others are still in the developmental stage. In the latter case, pragmatic recommendations are given as to how the available knowledge can be used, with the proviso that these recommendations may need modification at a later time as the level of knowledge increases and more accurate approaches are developed.

Appendix A is divided into eleven separate but interrelated technical areas. These areas are shown schematically in Figure 5.1, together with the appropriate section where they are discussed in Appendix A. The key points that are addressed under each technical area are listed in the figure. The main theme of the section is elastic-plastic fracture mechanics (EPFM) based on the parameter, J, and its pictorial equivalent, Failure Assessment Diagrams (FADs), although some aspects of stress analysis are also discussed. Relatively simple estimation schemes are provided for evaluating J under conditions that could be encountered in a proof test. The concept of the FAD is introduced as this provides a powerful pictorial tool for representing the results of an EPFM analysis based on J. The material properties needed to perform an EPFM analysis are detailed, and the way the fracture properties are used in conjunction with J to determine critical applied loads and crack sizes are described. Finally, the prediction of LBB in the proof test is addressed.

Detailed theoretical and experimental validation of the EPFM approach described in Section 5.1 is provided in Appendix B. Figure 5.2 represents a guide to the topics that are validated and references the sections were the appropriate verification can be found. The theoretical validation in Section B1 is focussed on comparing the results of elastic-plastic finite element computations of J with the estimation schemes and equivalent FAD approaches detailed in Sections A4 and A5 in Appendix A. Verification is provided for using the recommended J estimation schemes and FADs for primary loads, cracks at stress concentrators, combined primary and secondary loads, biaxial stressing, and cracks at welds.

The experimental validation is divided into laboratory and hardware tests. The laboratory test results reported in Section B2 substantiate the use of material specific J/FAD estimation schemes for the nickel-based superalloy IN-718 and an aluminum alloy when assessing fracture under primary loading. In addition, when used in conjunction with Sections A9 and A10 of Appendix A, the J estimation schemes successfully predicted the fracture behavior of the cracked IN-718 specimens.

Stress Analysis
(Section A1)
- structural and constitutive modeling
- categorization of loads and stresses
- residual stresses
- stress redistribution
- conservative analyses

Linear Elastic Fracture Mechanics
(Section A2)
- stress intensity factors
- combined primary and secondary loads

Net Section Yield Loads
(Section A3)
- fundamental considerations
- availability of solutions

Elastic-Plastic Crack Tip Driving Force, J
(Section A4)
- failure criteria
- J estimation (primary loads)
- J estimation (stress concentrators)
- J estimation (combined primary and secondary loads)
- J estimation (combined primary loads)
- J estimation (multiaxial applied stresses)
- J estimation (flaws with multiple degrees of freedom)
- J estimation (cracks at welds)
- plastic constraint effects
- summary of J estimations

Failure Assessment Diagrams (FADs)
(Section A5)
- construction of FADs (background)
- treatment of primary loads
- failure curves and failure criteria
- treatment of stress concentrators
- treatment of combined primary and secondary loads
- treatment of combined primary loads
- treatment of multiaxial stresses
- treatment of flaws with multiple degrees of freedom
- treatment of welds
- plastic constraint effects
- simplified approach

Failure Mechanisms and Failure Criteria
(Section A6)
- brittle materials
- ductile materials
- sub-critical crack growth
- mixed mode failure

Material Properties
(Section A7)
- mechanical properties
- fracture toughness
- sub-critical crack growth
- conservative data

Fracture and Failure Modes
(Section A8)
- brittle structural fracture
- ductile structural fracture
- functional failure
- structural failure

Critical Applied Loads
(Section A9)
- brittle materials: J-based analysis
- brittle materials: FAD analysis
- ductile materials: J-based analysis
- ductile materials: FAD analysis

Critical Crack Sizes
(Section A10)
- brittle materials: J-based analysis
- brittle materials: FAD analysis
- ductile materials: J-based analysis
- ductile materials: FAD analysis
- special considerations

Leak-Before-Burst (LBB)
(Section A11)
- LBB logic
- LBB diagram
- critical LBB load

Figure 5.1 Overview and guide to the technical areas addressed in Appendix A.

Theoretical Validation: J/FAD Estimation Schemes
(Section B1)
* analytical basis
* primary loads
* cracks at stress concentrators
* combined primary and secondary loading
* multiaxial stressing
* cracks at welds

Laboratory Validation: J/FAD Estimation Schemes
(Section B2)
* nickel-based superalloy, IN-718
* aluminum alloy 2024-T3511

Laboratory Validation: Predicting Critical Crack Sizes and Critical Loads for IN-718
(Section B3)
* critical loads
* critical crack sizes

Hardware Validation: Predicting Fracture Conditions for IN-718 High Pressure Ducts
(Section B4)
* critical pressures
* critical crack sizes
* leak-before-burst

Hardware Validation: Predicting Fracture Conditions for Ferritic Steel Pressure Vessels
(Section B5)
* critical pressures
* critical crack sizes
* crack in a weld
* leak-before-burst

Laboratory Validation: Effects of Proof Test Overload on Subsequent Service Failure Behavior
(Section B6)
* fatigue crack growth following the proof overload
* ductile fracture behavior following the proof overload

Figure 5.2 Guide to the validation provided in Appendix B.

5.2 Validation of the Proof Test Methodology

The hardware test results presented in Sections B3 and B4 verify that the methods described in Sections A9 and A10 in Appendix A can also be successfully employed to predict the fracture conditions in defected pressurized components, such as thin-walled space shuttle main engine high pressure oxidizer ducts, and thick-walled ferritic steel pressure vessels. In all, the fracture analyses of three ducts and three pressure vessels is presented. Every test failure was by ductile mechanisms involving stable tearing prior to instability. The leak-before-burst analyses presented in Section A11 of Appendix A were also verified for the IN-718 ducts and shown to be conservative when applied to one of the ferritic steel pressure vessels (Section B5).

Finally, Section B6 reports on a series of laboratory tests performed to investigate the effects of the proof overload on subsequent service fatigue and fracture behavior. The conclusion drawn from these tests substantiates some of the recommendations made in Sections 8.2 and 8.3.

6. GUIDELINES FOR PROOF TEST ANALYSES: FLAW SCREENING AND MINIMUM PROOF LOADS

6.1 Road Map for Flaw Screening and Minimum Proof Load Analyses

A Road Map for performing deterministic flaw screening and minimum proof load analyses for a single cycle proof test (SCPT) is shown in Figure 6.1. This Road Map can also be used in more advanced proof test analyses involving probabilistic analyses and/or MCPT. Probabilistic-based service reliability analyses which include proof testing offer significant advantages over deterministic analyses. However, probabilistic proof test analyses still require a deterministic fracture model for the calculation of critical flaw sizes and minimum proof loads; the Road Map provides a state-of-the-art basis for this fracture model. Aspects of probabilistic-based proof test analyses are discussed further in Sections 7.1 and D1.

Under some conditions, MCPT can improve service reliability compared to SCPT (see Sections 4.5.2 and 7.2). A summary of the major factors which may influence the decision as to whether to perform MCPT or SCPT are given in Section 7.2.2. The use of the Road Map in an MCPT analysis is discussed in Section 7.2.3, and details regarding the additional calculations needed to assess flaw growth under MCPT conditions are provided in Section D2.2.

In a flaw screening analysis the type and magnitude of the proof load is known, and the maximum sizes of flaws that could just survive the specified proof load are determined. In a minimum proof load analysis the locations, types, and sizes of flaws in the hardware are known or assumed, and the minimum proof load that can be applied for the hardware to just survive the proof test are determined.

The Road Map identifies the data needed at the various stages in the two types of analyses, and the calculations and decisions that need to be made. The intent of the Map is primarily to direct the proof test analyst to those sections in these Guidelines and the accompanying appendices that provide additional and more detailed information concerning each of the stages. A brief discussion on the key issues raised at each stage of the Road Map is given below. Each stage is numbered, and the numbers reference the appropriate stages listed in the Road Map. The following text contains general information describing each stage. Other sections of this document, including appendices, that are referenced within each stage provide further guidelines and information that are vital for properly executing a proof test analysis.

Stage 1: Hardware Definition

The proof test analyst should understand the hardware being tested. Section 4.2 describes the key aspects that serve to define the hardware's function and structure, and the material(s) used in its manufacture. These data help verify that the hardware is what it is supposed to be, and will help in the structural and constitutive modeling of the hardware for the purpose of stress analysis. Important hardware dimensions, such as wall thickness, should be directly measured as the use of minimum dimensions from drawings can lead to overestimating the flaw screening capability of proof testing (i.e., underestimating the flaw sizes that could just survive a proof test).

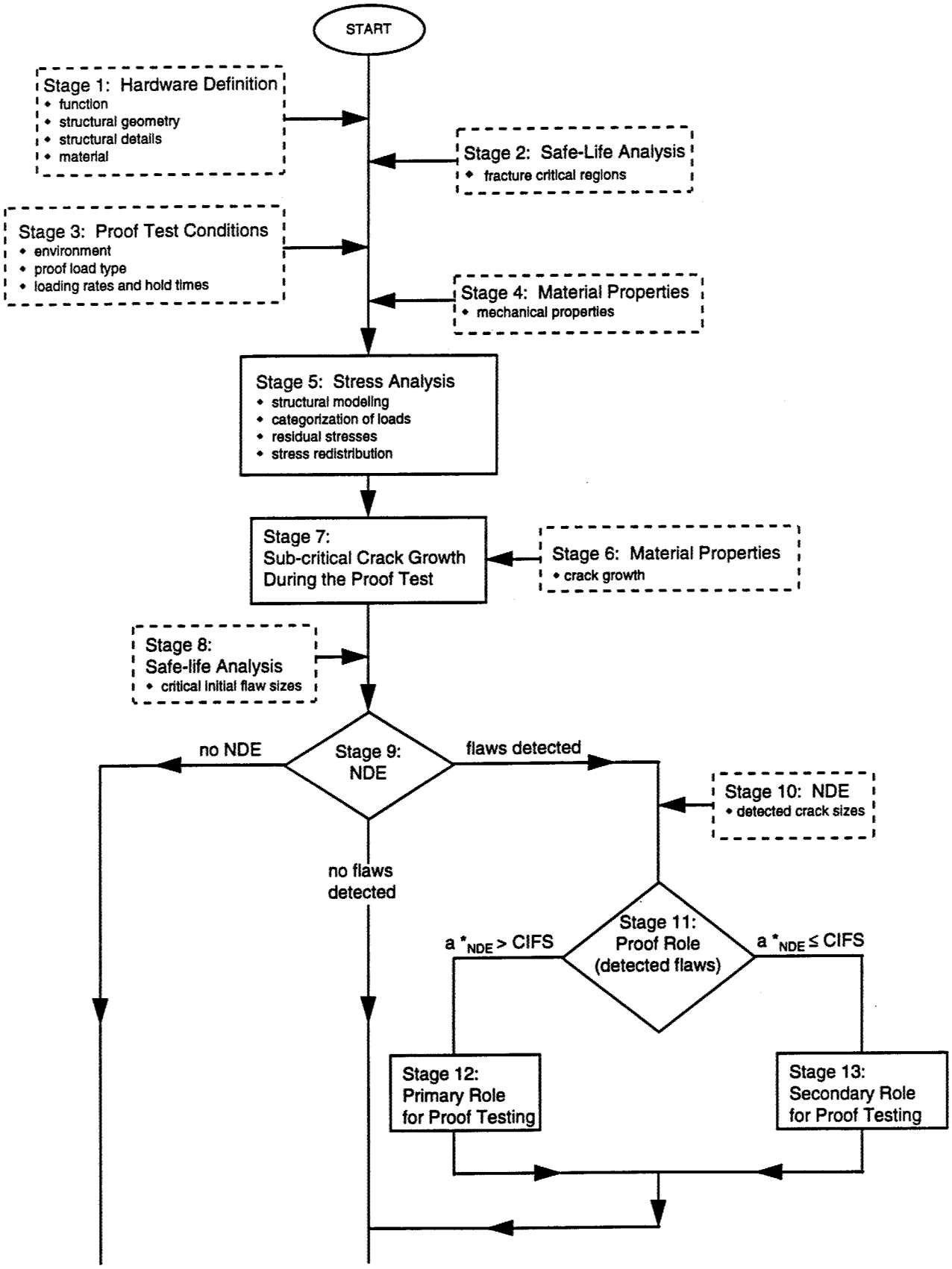

Figure 6.1 Road Map for flaw screening and minimum proof loads.

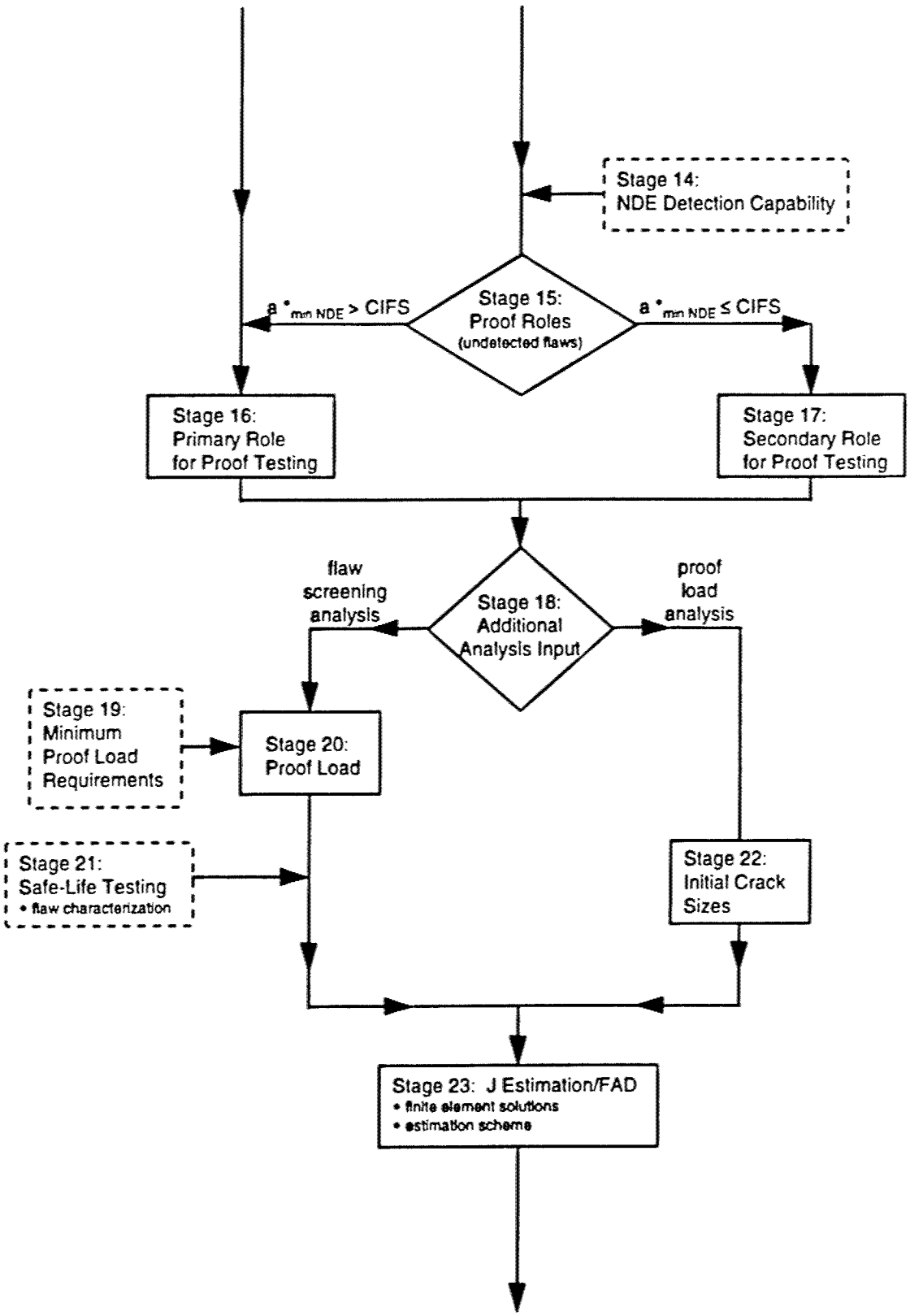

Figure 6.1 (continued) Road Map for flaw screening and minimum proof loads.

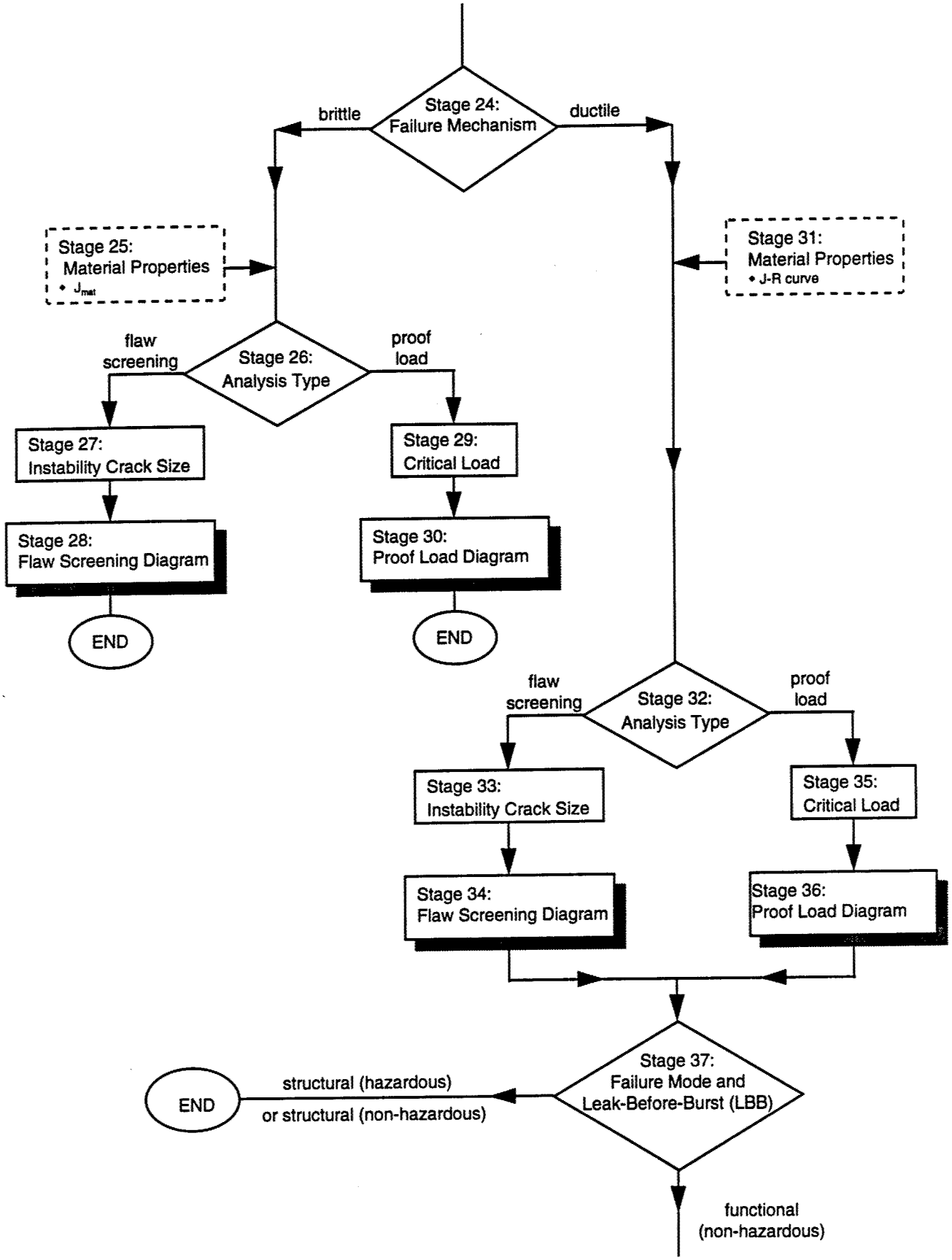

Figure 6.1 (continued) Road Map for flaw screening and minimum proof loads.

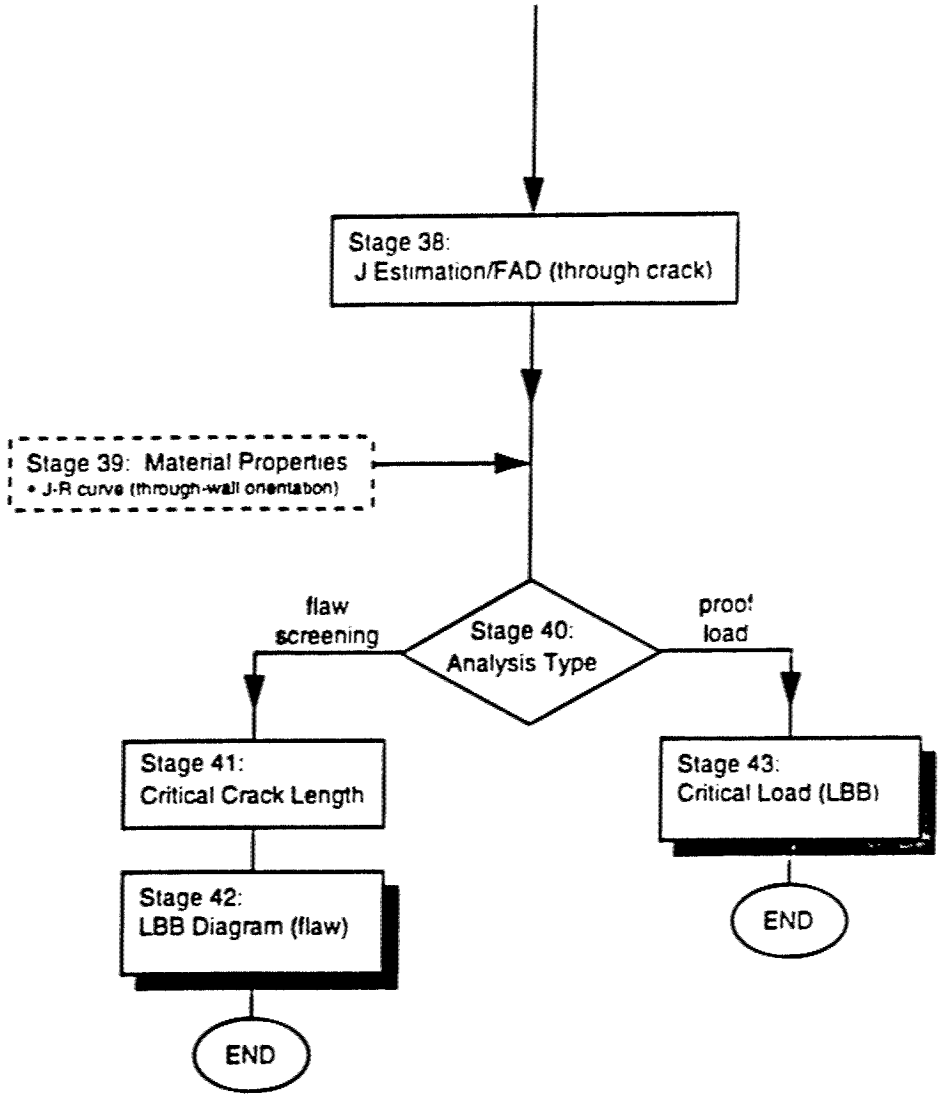

Figure 6.1 (continued) Road Map for flaw screening and minimum proof loads.

Stage 2: Safe-Life Analysis (Fracture Critical Regions)

The safe-life analysis is not part of a proof test analysis, but it can provide valuable data for the successful design and analysis of a proof test. In particular, it is essential that the proof test analyst be aware of fracture critical regions that limit the service lifetime of the hardware. These regions should be the major locations in the hardware that are investigated through stress analysis under proof test conditions. Section 4.4.2 provides more information on how a safe-life analysis impacts the design of a proof test.

Stage 3: Proof Test Conditions

The proof load type, loading and unloading rates, hold times and the proof test temperature are needed for analysis purposes and for assessing the potential for sub-critical crack growth during the test. The possible influences test environment can have on a proof test analysis are described in Section 4.3. The effects of loading and unloading rates, and hold times are intimately related to the test environment, and are identified in Section 4.5.1.

Stage 4: Material Properties (Mechanical)

The modulus and the stress-strain curve of the material are needed for stress analysis and to determine the EPFM parameter, J (for example, see Table A4.5). These properties are discussed in Section A7.1. The stress-strain data can either be in the form of a Ramberg-Osgood equation (see equation (A4.4)), or in arbitrary form expressed as a table of strains corresponding to specified stress values. The choice of values for a proof test analysis is addressed in Section A7.4.

Stage 5: Stress Analysis

Accurate stress analysis of the hardware under proof test conditions is essential for an accurate fracture mechanics analysis. Care should be taken in the modeling of the hardware based on the data obtained in Stage 1, particularly in fracture critical regions. Further aspects of hardware modeling are addressed in Section A1.1. In addition, a proof test analysis requires that the loads present during the proof test be characterized as primary and secondary (Section A1.2). Residual stresses associated with welds are secondary stresses (Section A1.3). An assessment should be made, particularly for recertifiable hardware, on the potential ramifications of localized stresses due to shakedown and stress re-distribution (Section A1.4). Conservative data for use in the stress analysis is discussed in Section A1.5.

Stage 6: Material Properties (Crack Growth)

The two most likely mechanisms that could produce sub-critical crack growth from pre-existing flaws during a single cycle proof test are stress corrosion cracking and so-called low temperature creep, see Section A6.3. The material data needed to characterize these forms of cracking are outlined in Section A7.3. Typical data consists of values for material constants that appear in crack growth rate laws that are expressed in terms of fracture mechanics parameters.

Stage 7: Sub-Critical Crack Growth During the Proof Test

Consideration should be given to the possibility of crack extension due to sub-critical crack growth, particularly if the proof test is performed in an aggressive chemical environment. The damage induced in the hardware by sub-critical crack growth will be related to load level, loading and unloading rates, and the hold time. The potential deleterious effects of these parameters in a badly planned proof test are outlined in Section 4.5.1. Slow unloading rates should be avoided if at all possible, especially if the hardware is subjected to an aggressive environment. Under the latter conditions, crack growth is possible even after the proof test is completed if parts of the hardware remain under load (for example, from tensile residual stresses) while in normal storage. A conservative assessment should be made using crack growth data (Stage 6) of the likely amount of sub-critical crack growth from testing and storage prior to entering service (see Section A7.3). This amount should be added to calculated instability crack sizes when inferring flaw screening capability. The assessment of flaw growth during testing and afterward will be greatly facilitated by performing real time NDE during the test (see Section 4.6.2) and post-test inspection (see Section 4.6.1).

Stage 8: Safe-Life Analysis (Critical Initial Flaw Sizes)

The safe-life analysis will result in calculated critical initial flaw sizes (CIFS) that, if present in the hardware under service conditions, will survive the service lifetime times a service life factor which is typically four. In the absence of NDE inspection results to justify otherwise, these crack sizes are the maximum sized flaws that should be assumed to be present in the hardware surviving proof testing, and it is against these crack sizes that the minimum proof loads should be determined (see Section 4.4.2). Alternatively, if NDE is performed, then it should be able to reveal flaws that are smaller than or equal to the CIFS if it is to be an effective flaw screening measure.

Stage 9: Non-Destructive Examination (NDE)

The Road Map has a signpost at this point indicating the three directions to be followed depending on whether a pre-test NDE inspection is carried out, or, if it is, depending on the result obtained. One direction corresponds to the decision not to perform a pre-test NDE, either because the proof test is considered adequate as a flaw screening measure, or because of the practical difficulties in carrying out an inspection. The other two directions indicate the branches to be followed if NDE is performed but no indications are recorded, and if NDE does reveal flaw indications.

SIGNPOST: No NDE (left branch), NDE performed but no flaws detected (center branch), and NDE performed and flaws detected (right branch)

<u>No NDE Branch</u>
Go to Stage 16.

<u>No Flaws Detected Branch</u>
Go to Stage 14.

<u>Flaws Detected Branch</u>

Stage 10: Non-Destructive Evaluation (NDE)

A pre-test NDE will provide an indication of the actual flaws that are present in the hardware during proof testing (see Section 4.6.1). All fracture critical regions should be inspected and any indications recorded. These indications should be characterized by a flaw size a_{NDE} for use in a fracture mechanics analysis. The sizing accuracy of the selected NDE method(s) should be considered when determining a_{NDE}.

Proof testing in addition to NDE will be necessary if some fracture critical regions are not inspectable by NDE methods.

Stage 11: Proof Role (detected flaws)

The Road Map has a signpost here indicating the routes to be followed if proof testing is the primary flaw screening measure or if NDE is to play a primary flaw screening role with proof testing playing a secondary role. To make this decision the user should first determine a conservative estimate of the flaw sizes likely to be present at the end of proof testing by adding the amount of sub-critical crack growth determined at Stage 7 to the fracture mechanics characterized sizes, a_{NDE}, of the NDE indications measured during the inspection at Stage 9, to obtain the final flaw sizes, a_{NDE}^*, calculated to be present at the end of the proof test. If $a_{NDE}^* >$ CIFS, then proof testing is required in addition to NDE inspection if repair or replacement of the hardware is to be avoided. If $a_{NDE}^* \leq$ CIFS, then NDE will be sufficient as a flaw screening measure for the detected defects.

SIGNPOST: $a_{NDE}^* >$ CIFS (left branch) and $a_{NDE}^* \leq$ CIFS (right branch)

<u>$a_{NDE}^* >$ CIFS Branch</u>

Stage 12: Primary Role

An NDE indication should be conservatively characterized and sized as a crack-like flaw for use in fracture mechanics analysis. Because of the conservatisms that are included in the characterization, sizing and assumed orientation of a_{NDE}, and in calculating the amount of sub-critical crack growth that could occur during the test, then a_{NDE}^* may exceed CIFS without actually impairing the safe-life of the hardware. Hence, the condition $a_{NDE}^* >$ CIFS is, of itself, not necessarily sufficient to justify a replacement or repair decision. Costly replacement or repair actions may be avoided by proof testing the hardware at a proof load which would result in failure if flaws more severe than the CIFS were present in the hardware. If the observed indications survived this proof load then the analyst may be able to make a case for avoiding the need to replace or repair based on proof test logic.

<u>$a_{NDE}^* \leq$ CIFS Branch</u>

Stage 13: Secondary Role

At this stage in the Road Map, NDE will likely be the primary means of flaw screening for detected flaws as NDE is capable of sizing detected flaws so that the specified safe-life can be assured. This means that a detailed fracture mechanics based proof test analysis may not be necessary.

Stage 14: NDE Detection Capability

An indication of the minimum flaw sizes that can be detected in structures by various NDE techniques has been drawn-up by NASA. These minimum flaw sizes ($a_{min\ NDE}$) are displayed in Table 4.2 in Section 4.6.1 and correspond to a 90% probability/95% confidence level of inspection reliability. Even if flaws have been detected at Stage 10, it is still necessary to determine the NDE detection capability in order to avoid the possibility of undetected flaws entering service that are life threatening.

Stage 15: Proof Role (undetected flaws)

The Road Map has a signpost here indicating the routes to be followed depending on whether proof testing is the primary flaw screening measure or whether NDE is to play a primary flaw screening role with proof testing playing a secondary role. To make this decision the user should first determine a conservative estimate of the flaw sizes likely to be present at the end of proof testing by adding the amount of sub-critical crack growth determined at Stage 7 to the minimum initial flaw sizes, $a_{min\ NDE}$, specified at Stage 14, to obtain the final flaw sizes, $a_{min\ NDE}^{*}$, predicted to be present at the end of the proof test. If $a_{min\ NDE}^{*} >$ CIFS, then proof testing is required in addition to NDE inspection. If $a_{min\ NDE}^{*} \leq$ CIFS, then NDE will be sufficient as a flaw screening measure.

SIGNPOST: $a_{min\ NDE}^{*} >$ CIFS (left branch) and $a_{min\ NDE}^{*} \leq$ CIFS (right branch)

<u>$a_{min\ NDE}^{*} >$ CIFS Branch</u>

Stage 16: Primary Role

At this stage in the Road Map limits on NDE capability indicate that proof testing should be the primary means of flaw screening as NDE is unable to ensure that undetected flaws will be of sufficiently small size that the specified safe-life can be assured. This means that a fracture mechanics based proof test analysis will be necessary to establish initial flaw sizes or to determine the proof load.

<u>$a_{min\ NDE}^{*} \leq$ CIFS Branch</u>

Stage 17: Secondary Role

At this stage in the Road Map it is confirmed that NDE should be the primary means of flaw screening as it is capable of detecting flaws of sufficiently small size that the specified safe-life can be assured. This means that a detailed fracture mechanics based proof test analysis may not be necessary.

Stage 18: Additional Analysis Input

The Road Map has a signpost at this crossroads indicating the directions for performing a flaw screening analysis and a minimum proof load calculation. Although the determination of the flaw screening capability does not require crack sizes as input, the analyst has to be aware of the types of flaw that are to be screened against. In contrast, explicit flaw sizes have to be postulated as existing in the hardware for the purposes of calculating the minimum proof load. These data can be obtained as hypothetical flaw sizes based on the results of a safe-life analysis, or from NDE inspections. Sections 3.1 and 3.2 provide descriptions of the logic underpinning the determination of flaw screening capability and minimum proof loads, respectively.

SIGNPOST: Flaw Screening (Left Branch) and Proof Load (Right Branch)

Flaw Screening Branch

Stage 19: Minimum Proof Load Requirements

The proof load level is needed for analysis purposes. The NASA minimum requirements concerning the value of the proof load are detailed in Section 4.4.1 and typical values are displayed in Table 4.1. Essentially, the larger of the proof loads calculated from fracture mechanics and the minimum requirements should be used in the test.

Stage 20: Proof Load

In addition to NASA minimum proof test load requirements, the analyst should ensure that fracture critical regions are screened (Section 4.4.2) while avoiding detrimental deformations and excessive load induced damage (Section 4.4.4). The analyst should be aware that proof load factors may not adequately characterize the flaw screening capability of the proof test (Section 4.4.3).

Stage 21: Safe-Life Testing

In order to determine the proof load the types of flaws likely to be present in the hardware should be characterized in terms of shape and size. An indication of the types of flaws to be screened by proof testing is provided by NASA requirements for minimum initial flaw sizes for safe-life testing. The role of these flaws in proof test analysis is discussed in Section 3.1, and Table 4.2 gives actual minimum initial flaw dimensions for safe-life testing of defected structures.

Proof Load Branch

Stage 22: Initial Crack Sizes

The information obtained from a safe-life analysis (Stages 2 and 8) and NDE (Stages 10 and 14) should be used to define the locations, shapes and sizes of flaws for which minimum proof loads are to be determined.

Stage 23: J Estimation and Failure Assessment Diagrams (FADs)

The elastic-plastic crack tip driving force, *J*, has to be evaluated to enable the critical conditions for fracture to be calculated for the tested hardware. *J* solutions will be needed for various crack geometries (for example, see Figure 4.2), and possibly at different locations in the hardware corresponding to the fracture critical regions, and other locations where cracking is considered a threat. Existing handbook solutions for *J* are summarized in Section A4.2. Unfortunately, these solutions are limited in terms of the range of structural geometries, crack shapes and sizes, and applied load types that they cover. In many cases the analyst will have to revert to using approximate estimation schemes to evaluate *J*, or the equivalent pictorially based FAD approach. In this respect it is useful to know the likely fracture mode of the tested hardware as this indicates whether crack-tip plasticity will be important and EPFM is needed, or whether LEFM is sufficient in providing an accurate estimate for *J*. Simple methods of estimating whether the structural failure mode will be brittle (generally synonymous with small scale yielding) or ductile (generally synonymous with large scale yielding) are provided in Section A8.1 and A8.2, respectively.

A significant part of these Guidelines is directed at providing the analyst with recommended expressions for *J* (and for failure curves, the FAD equivalent to *J* solutions) that cover a wide range of situations which are of major practical interest. The *J* estimation schemes are presented in Sections A4.2 to A4.9, and are summarized in Table A4.5 of Section A4.11. The solutions include relatively simple analytical *J* expressions for:

- primary (mechanical) loading (Sections A4.2 and A4.9)
- flaws at stress concentrating features (Section A4.3)
- combined primary and secondary (residual, thermal) loads (Section A4.4)
- two combined primary loads (Section A4.5)
- multiaxial stressing (Section A4.6)
- flaws with multiple degrees of freedom (surface flaws) (Section A4.7)
- flaws in welds (Section A4.8)
- assessing the effects of plastic constraint (Section A4.10)

The following data are necessary to implement the *J* and FAD estimation schemes:

- the applied proof load(s) (e.g. pressure, tensile force)
- the through-wall stress distribution normal to the plane containing the assessed crack corresponding to the proof load(s)
- the through-wall stress distribution normal to the plane containing the assessed crack corresponding to any secondary load (such as residual stresses)
- postulated or observed flaw shapes and sizes
- stress intensity factor solutions corresponding to the proof and secondary loads (see Section A2 and its sub-sections A2.1 and A2.2)
- net section yield loads corresponding to the proof load(s) (see Section A3 and its sub-sections A3.1 to A3.3. Note particularly the warning in Section A3.3 that many theoretically derived net section yield loads are lower bound solutions that, if used in a proof test analysis, can result in an over-estimate of the flaw screening capability.)
- uniaxial stress-strain data
- stresses parallel to the flaw for biaxial stressing situations

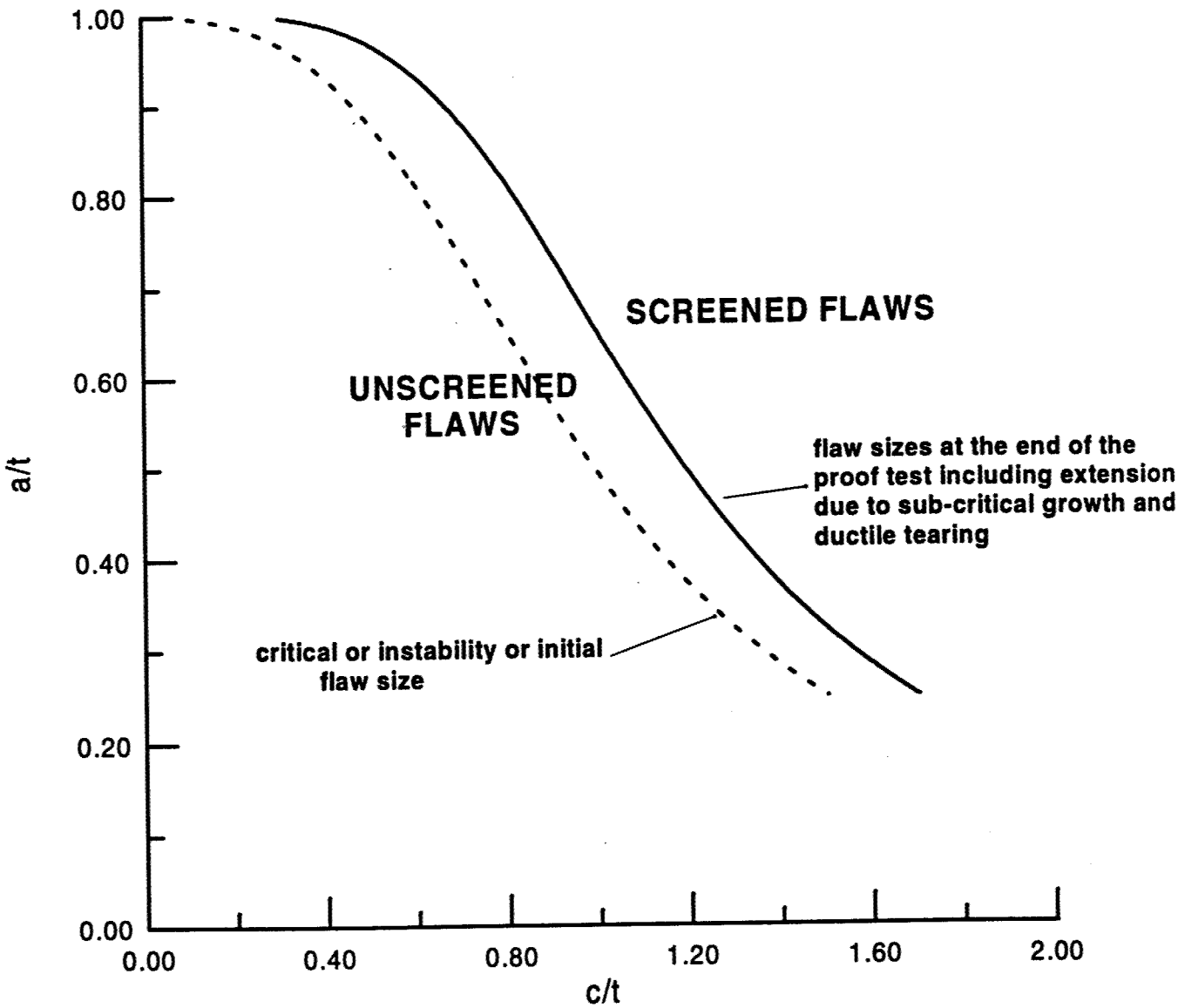

Figure 6.2 Schematic flaw screening diagram showing normalized half crack surface length (c/t) plotted against normalized flaw depth (a/t).

Procedures for deriving failure curves from J for use in a FAD analysis are detailed in Section A5.2 and Sections A5.4 to A5.9. A simplified FAD approach that enables a failure curve to be derived from only uniaxial stress-strain data is described in Section A5.10. Background information to the FAD approach is provided in Section A5.1, and Section A5.11 includes a brief discussion on the effects of plastic constraint on failure curves.

Stage 24: Failure Mechanism

At this stage in the Road Map, a signpost indicates the directions for analyzing materials that fail by brittle and ductile mechanisms. It is imperative for a proof test analysis that the mechanism of failure be known under proof test conditions, since different types of analyses and material fracture properties are needed to address materials that fail by brittle and ductile mechanisms. A brittle failure mechanism implies structural failure, with the potential for high energy fragment projectiles that could result in severe secondary damage. A leak-before-burst argument cannot be made for materials that fail by this mechanism. A ductile failure mechanism implies that stable tearing will probably occur before instability, but secondary damage from fragment projectiles is less likely than for brittle materials. This failure mechanism could result in either a structural or functional failure. More information related to brittle and ductile failure mechanisms is provided in Sections A6.1 and A6.2, respectively. Although mixed mode loading is discussed in Section A6.4, these Guidelines do not explicitly address mixed mode failure.

SIGNPOST: Brittle (Left Branch) and Ductile (Right Branch)

<u>Brittle Branch</u>

Stage 25: Material Properties (J_{mat})

The fracture toughness as characterized by the parameter J_{mat} is needed to assess the critical conditions for fracture in the hardware. Values of J_{mat} can be derived from conventional measures of fracture toughness (e.g. K_{Ic}, K_c, K_{Ie}) by using the relationship $J=K^2/E'$. Brittle fracture toughness values can be very sensitive to temperature and plastic constraint under some circumstances, and care should be exercised in using conventional toughness data obtained on standard test specimens in a proof test analysis. These aspects are discussed in more detail in Sections A7.2 and A7.4.

Stage 26: Analysis Type (Brittle)

This signpost indicates directions to be followed in order to calculate instability crack sizes (needed for a flaw screening analysis) and to evaluate critical loads (needed for a minimum proof load analysis).

SIGNPOST: Flaw Screening (Left Branch) and Proof Load (Right Branch)

<u>Flaw Branch</u>

Stage 27: Instability Crack Size (Brittle)

The instability crack size can be determined following the procedures detailed in Sections A10.1 (*J* analysis) and A10.2 (FAD approach) based on the brittle failure criterion described in Sections A4.1 and A5.3, respectively. In general, it will be necessary to perform a number of instability calculations to cover the different fracture critical regions of the hardware, and the types of flaws that could exist in each of these regions. The analyst should be aware of the special aspects of critical crack size calculations detailed in Section A10.5.

Stage 28: Flaw Screening Diagram (Brittle)

The critical crack size is not unique for a specified proof load unless a flaw with one degree of freedom (DOF) is being assessed and even for this case it may not be unique (see Figure A10.3). In general, the proof test will screen for a range of flaw sizes consisting of (in the case of surface flaws) combinations of crack depths and surface lengths. These sizes can be represented by flaw screening diagrams representing each fracture critical region. In the absence of sub-critical crack growth (see Stage 7), the diagrams consist of curves composed of the critical values of the flaw depth plotted against the corresponding critical surface lengths (see Figure 6.2). If sub-critical crack growth is predicted as a result of a Stage 7 evaluation, then this should be added to the calculated critical crack sizes and the enlarged flaws used in the construction of the flaw screening diagrams. All flaws with combinations of depths and surface lengths that produce points on the flaw screening diagram that fall outside of the critical curve are predicted to be screened during proof testing. Flaws with sizes that fall within the curve will have survived the proof test and should be assumed to be present in the hardware as it enters service, or should be specified as initial crack or flaw sizes for the purposes of a safe-life analysis.

The analysis ends at this point.

<u>Proof Load Branch</u>

Stage 29: Critical Load (Brittle)

The critical load can be determined following the procedures detailed in Sections A9.1 (*J* analysis) and A9.2 (FAD approach) based on the brittle failure criterion described in Sections A4.1 and A5.3, respectively. In general, it will be necessary to perform a number of critical load calculations to cover the fracture critical regions of the hardware, and the types of initial service crack sizes that could exist in each of these regions.

Stage 30: Proof Load Diagram (Brittle)

The minimum proof load is the calculated critical load that has to be applied to cause fracture from a flaw that is postulated to be present in the tested hardware. The critical load is not unique but will be different for different assumed initial flaw shapes and sizes, and for different fracture critical regions. The calculated critical loads can be displayed in proof load diagrams representing each fracture critical region and consisting of a curve composed of the critical loads plotted against the corresponding initial flaw sizes (see Figure 6.3). In evaluating minimum proof loads

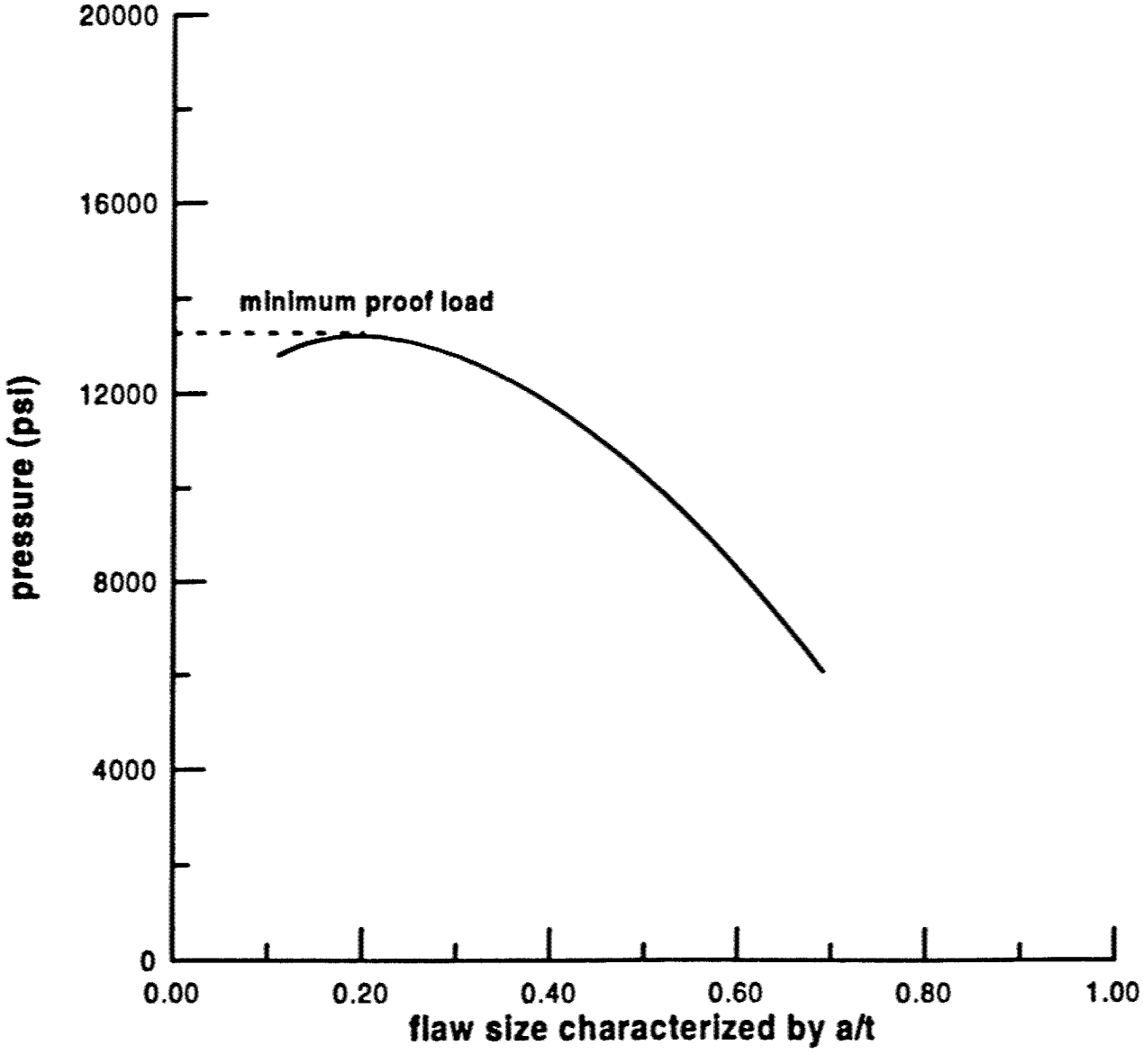

Figure 6.3 Schematic proof load diagram showing critical pressure against initial flaw size.

it is conservative to ignore the potential increase in initial flaw sizes due to sub-critical crack growth (see Stage 7). Flaws with multiple DOF can be represented by a single crack size parameter (say the flaw depth in the case of surface flaws) for the purposes of constructing the proof load diagram provided some way of cross referencing the flaw size parameter with the actual flaw shape and size is provided in support of the diagram. The minimum proof load is the maximum critical load obtained for the analyzed initial flaws. Proof loads less than this maximum load will not screen out some of the postulated initial flaws.

It is important to note that some flaws may undergo sub-critical crack extension during the proof test and increase their size (see Stage 7). If the initial flaw sizes assumed in the proof load analysis were based on crack sizes derived from a safe-life analysis, then the ramifications of the increased flaw sizes caused by the proof test on the safe-life calculations should be assessed. If the service life needed for a safe-life can still be established with the new enlarged population of flaws, then no further action is necessary. However, if sub-critical crack extension seriously erodes safe-life margins, then the assumed initial flaw size population at the start of the proof test should be reduced in size and the minimum proof load calculations repeated. Further reductions in the assumed initial flaw sizes and/or changes to the test environment to reduce sub-critical crack growth should be made if necessary until the needed safe-life is assured. The change in flaw size distribution as a result of the proof test is likely only to have a significant influence on the service life if the sub-critical crack growth resulting from proof loading is comparable in size to the initial flaw size, or to the size of the remaining uncracked ligament. **The minimum proof load used in the proof test should be the maximum critical load determined from an assumed initial flaw size population in the hardware that results in a calculated flaw size distribution at the end of the test consistent with ensuring the needed safe-life.**

The actual proof load specified for the test should preferably exceed the calculated minimum value, subject to the need to avoid detrimental deformations in the hardware (see Section 4.4.3). The actual specified load should also equal or exceed the minimum proof loads specified in NASA fracture control requirements (see Section 4.4.1).

It is prudent to identify how the flaw size distribution changes as a result of proof testing. This can be done by plotting, for a given fracture critical region, the initial flaw distribution in a form similar to the flaw screening diagram (see Figure 6.2); namely initial crack depth versus the corresponding initial surface length, and on the same diagram plotting the flaw depths and corresponding surface lengths at the end of the proof test.

The analysis ends at this point.

Ductile Branch

Stage 31: Material Properties (J-R Curve)

The fracture toughness of ductile materials is not characterized by a unique value but by a *J-R* curve because the toughness increases as ductile crack extension occurs under a rising load. A *J-R* curve can be derived from a *K-R* curve developed through toughness testing in the small scale yielding regime by using the relationship $J_R(\Delta a_t)=K_R^2(\Delta a_t)/E'$. Measured *J-R* curves can be sensitive to plastic constraint under some circumstances, and prudence should be exercised in a proof test

analysis before using conventional toughness data obtained from standard test specimens. These aspects are discussed in more detail in Sections A7.2 and A7.4.

Stage 32: Analysis Type (Ductile)

The signpost at this crossroads points the direction for calculating ductile instability crack sizes (needed for a flaw screening analysis) and for evaluating critical loads (needed for a minimum proof load analysis).

SIGNPOST: Flaw Screening (Left Branch) and Proof Load (Right Branch)

Flaw Screening Branch

Stage 33: Instability Crack Size (Ductile)

The ductile instability crack size can be determined following the procedures detailed in Sections A10.3 (*J* analysis) and A10.4 (FAD approach) based on the ductile failure criterion described in Sections A4.1 and A5.3, respectively. The instability crack size is the size of the initial flaw plus any ductile tearing that occurs up to incipient fracture in the proof test. In general, it will be necessary to perform a number of instability calculations to cover the fracture critical regions of the hardware, and the types of flaws that could exist in each of these regions. The analyst should be aware of the special aspects of critical crack size calculations detailed in Section A10.5.

Stage 34: Flaw Screening Diagram (Ductile)

The instability crack size is not unique for a specified proof load unless a flaw with one degree of freedom (DOF) is being assessed and even in this case it may not be unique (see Figure A10.3). In general, the proof test will screen for a range of flaw sizes consisting of (in the case of surface flaws) combinations of crack depths and surface lengths. These sizes can be displayed in flaw screening diagrams representing each fracture critical region. In the absence of sub-critical crack growth (see Stage 7), these consist of a curve composed of the instability values of the flaw depth plotted against the corresponding instability surface lengths (see Figure 6.2). If sub-critical crack growth is predicted as a result of a Stage 7 evaluation, then this should be added to the calculated critical crack sizes and the enlarged flaws used in the construction of the flaw screening diagrams. All flaws with combinations of flaw depths and surface lengths that produce points on the flaw screening diagram that fall outside of the critical curve are predicted to be screened during proof testing. Flaws with sizes that fall within the curve will have survived the proof test and should be assumed to be present in the hardware as it enters service, or should be specified as initial crack or flaw sizes for the purposes of a safe-life analysis. Some flaws that are just less than the instability length will grow by tearing during the proof test but will not attain their instability sizes. The instability curve bounds the enlarged sizes of these flaws.

Proof Load Branch

Stage 35: Critical Load (Ductile)

The critical load can be determined following the procedures detailed in Sections A9.3 (*J* analysis) and A9.4 (FAD approach) based on the ductile instability failure criterion described in Section A4.1 and A5.3, respectively. When performing these calculations, allowance has to be made for ductile crack growth and *J-R* curve behavior during the proof loading. In general, it will be necessary to perform a number of critical load calculations to cover the fracture critical regions of the hardware, and the types of initial service crack sizes that could exist in each of these regions.

Stage 36: Proof Load Diagram (Ductile)

The minimum proof load is the calculated critical load that has to be applied to screen against a given initial flaw that is postulated or observed to be present in the hardware. In evaluating minimum proof loads it is conservative to ignore the potential increase in initial flaw sizes due to sub-critical crack growth (see Stage 7). The critical load is not unique but will be different for different assumed initial flaw shapes and sizes, and for different fracture critical regions. The critical loads can be represented by proof load diagrams representing each fracture critical region that consists of a curve composed of the calculated critical loads plotted against the corresponding initial flaw sizes (see Figure 6.3). Flaws with multiple DOF can be represented by a single crack size parameter (say the flaw depth in the case of surface flaws) for the purposes of constructing the proof load diagram provided some way of cross referencing the flaw size parameter with the actual flaw shape and size is provided in support of the diagram. The minimum proof load is the maximum critical load derived from the analysis of all of the initial flaws. Proof loads less than this will not screen out some of the postulated initial flaws.

It is important to note that some flaws will grow by ductile tearing during the proof test and increase their size. In addition, their size may also increase due to sub-critical crack growth (see Stage 7). If the initial flaw sizes assumed in the proof load analysis were based on crack sizes derived from a safe-life analysis, then the ramifications of the increased flaw sizes on the safe-life calculations should be assessed. If the service life needed for a safe-life can still be established with the new enlarged population of flaws, then no further action is necessary. However, if crack extension due to ductile tearing and/or sub-critical crack growth seriously erodes safe-life margins, then the assumed initial flaw size population at the start of the proof test should be reduced in size and the minimum proof load calculations repeated. Further reductions in initial flaw sizes and/or changes to the test environment should be made if necessary until the needed safe-life is assured. The change in flaw size distribution as a result of the proof test is likely to have a significant influence on the service life only if the tear length and/or sub-critical crack growth resulting from proof loading is comparable in size to the initial flaw size, or to the size of the remaining uncracked ligament. **The minimum proof load used in the proof test should be the maximum critical load determined from an assumed initial flaw size population in the hardware that results in a calculated flaw size distribution at the end of the test consistent with ensuring the needed safe-life.**

The actual proof load specified for the test should preferably exceed the calculated minimum value, subject to the need to avoid detrimental deformations in the hardware (see Section A3.3). The actual specified load should also equal or exceed the minimum proof loads specified in NASA fracture control requirements (see Section A3.1).

It is prudent to identify how the flaw size distribution changes as a result of proof testing. This can be done by plotting, for a given fracture critical region, the initial flaw distribution in a form similar to the flaw screening diagram (compare Figure 6.2); namely initial crack depth versus the corresponding initial surface length, and on the same diagram plotting the flaw depths and corresponding surface lengths at the end of the proof test.

Stage 37: Failure Mode and Leak-Before-Burst (LBB)

It is useful for safety considerations when designing the proof test to establish whether the failure mode will be structural (e.g. burst) or functional (e.g. LBB) (see Sections A8.3 and A8.4). Brittle materials are automatically classified as failing in a structural mode. Ductile materials can fail in two possible failure modes, structural or functional. If the hardware contains hazardous materials during the proof testing then the failure mode should be classified as structural. Otherwise, if no hazardous materials are present, then a preliminary leak-before-burst assessment should be considered to determine whether the likely failure mode will be structural (non-hazardous, i.e., would not result in personnel injury or loss of hardware) or functional (LBB). The logic underpinning an LBB analysis is outlined in Section A11.1. However, a decision may be made not to perform an LBB analysis even though the failure is non-hazardous. In this case it is prudent, unless justification is available through other arguments, to assume that the failure mode will be structural (non-hazardous).

SIGNPOST: Structural (Left Branch) and Functional (Non-hazardous) (Right Branch)

Structural Branch

The analysis ends at this point.

Non-hazardous Branch

Stage 38: *J* Estimation/FAD (through-crack)

At this stage in the Road Map it is necessary to establish the *J* solutions and/or FAD for through-wall cracks to enable the critical crack lengths and loads to be calculated for the tested hardware. An outline as to how this can be done is described in Stage 23.

Stage 39: Material Properties (J-R Curve, through-crack)

A *J-R* curve for the material in the orientation of the through-wall crack is needed for an LBB analysis. This curve can be derived from a *K-R* curve developed through toughness testing in the small scale yielding regime by using the relationship $J_R(\Delta c_t)=K_R^2(\Delta c_t)/E'$. *J-R* curves can be sensitive to wall thickness, particularly in thin sections (see Section A7.2), and prudence should be exercised before using conventional toughness data obtained on standard test specimens where the thickness differs from that of the component. Lower bound *J-R* curves should be used in an LBB analysis (Section A11.1), in contrast to a flaw screening analysis where upper bound toughness data are generally recommended unless the use of alternative data can be justified.

Stage 40: Analysis Type (LBB)

The signpost at this crossroads indicates the directions for calculating critical crack lengths and critical loads.

SIGNPOST: Flaw Screening (Left Branch) and Proof Load (Right Branch)

Flaw Screening Branch

Stage 41: Critical Crack Length (LBB)

The critical length of a through-crack subjected to the specified proof load can be determined following the procedures in Sections A10.3 (*J* analysis) and A10.4 (FAD approach) based on the ductile instability failure criteria described in Sections A4.1 and A4.3, respectively. For an LBB analysis it is necessary to determine the critical crack length, as a flaw of this length will tear under the proof load until it reaches the instability crack length, when burst will occur. Critical crack lengths should be calculated for all the fracture critical regions.

Stage 42: LBB Diagram (Flaw)

As described in Section A11.2, an LBB diagram (flaw) can be constructed based on the flaw screening results determined in Stage 34 and the critical crack lengths calculated in Stage 41. This diagram (see **Figure A11.1**) enables the identification of those surface flaws that will result in burst (structural failure) and those that will result in LBB (functional failure).

The analysis ends at this point.

Proof Load Branch

Stage 43: Critical Load (LBB)

The critical load can be determined following the procedures detailed in Sections A9.3 (*J* analysis) and A9.4 (FAD approach) based on the ductile instability failure criteria described in Sections A4.1 and A5.3, respectively. When performing these calculations, allowance can be made for ductile crack growth and *J-R* curve behavior during the proof loading. In general, it will be necessary to perform a number of critical load calculations to cover all of the fracture critical regions of the hardware.

It is necessary to assume a through-wall crack length in order to determine the critical load for burst, P_{LBB} (see Section A11.3). This length should be derived by adding the wall thickness (t) to the longest surface length ($2c$) of the flaws calculated in Stage 36 to be unstable under the actual proof load.

Proof loads that equal or exceed P_{LBB} will result in burst (structural failure) and those that are less than P_{LBB} will result in LBB (functional failure) for the specified initial flaw sizes.

The analysis ends at this point.

6.2 Example Proof Test Analyses

Two example proof test analyses based on the Road Map detailed in Section 6.1 are presented in Appendix C. Although the examples are intended to simulate real analyses, it is emphasized that they are hypothetical and have been chosen and designed to illustrate important aspects of proof test analyses. The first example describes the determination of the flaw screening capability of a proof test (see Section C1). This example is based on an axial flaw in an over-matched longitudinal seam-weld of a ferritic pressure vessel that is tested below its ductile-brittle toughness transition temperature and fails by a brittle mechanism. The second example describes the calculation of the minimum proof pressure needed to screen against an axial flaw whose size is based on the results of a safe-life analysis (see Section C2). The hardware analyzed is a thin-walled high pressure duct that is internally pressurized. The duct is made of the nickel-based superalloy, IN-718, which fails by a ductile mechanism.

6.3 Sensitivity Analysis

A sensitivity analysis is made by systematically changing the value of a variable and assessing the effect these changes have on the outcome. It is useful to perform a sensitivity analysis to identify the variables that most contribute to uncertainties in the flaw screening and minimum proof load calculations. Sensitivity analyses are particularly important when insufficient data are available to specify the statistical significance of upper and lower bound values of the variables. In these cases, a sensitivity analysis may advantageously demonstrate that uncertainties in the value of a variable do not seriously influence the results. Alternatively, it is also beneficial to know those situations in which small changes in a variable have a major effect on the results. Thus, the advantage of a sensitivity analysis is that it enables available resources to be concentrated on refining those data that have the maximum impact on the outcome of the calculations.

The variables that should be considered for a sensitivity study are:

- proof load (especially in a flaw screening analysis)
- structural modeling
- residual stresses
- proof test temperature (especially for brittle materials at temperatures around the ductile-brittle toughness transition temperature)
- initial flaw size distribution (for a minimum proof load analysis)
- toughness properties
- tensile properties
- stress intensity factor solutions
- net section yield solutions (especially important for ductile materials)
- modeling of multiple DOF flaws

The FAD provides a convenient way of investigating sensitivities to some of these variables, as indicated in Section A5.3.

7. ASPECTS OF ADVANCED PROOF TEST ANALYSES

7.1 Probability Analysis

In a deterministic proof test analysis it is necessary to use specific data in the fracture mechanics calculations and to ensure safety by employing conservative assessment data. Although this approach appears to be a simple and scientific way of assuring component safety during operation, it provides no quantitative information concerning the desired increase in reliability of a fleet of hardware during its service life as a consequence of proof testing. In addition, the compounding effects of using conservative assessment data can seriously erode the efficacy of the proof test as concluded from a proof test analysis.

The survival of proof tested hardware does not, in general, guarantee a zero probability of subsequent failure in service. To quantify the effect on component reliability (defined as 1– probability of failure) requires a probability analysis. A probability analysis provides unique opportunities to optimize the initial design of the proof test, and to optimize the intervals between proof tests for re-certifiable components, in order to ensure an acceptable service reliability. The benefits of performing a comprehensive probability analysis involving combined proof test and service analyses were recognized in the early days of proof testing analysis. For example, Shinozuka and Yang [23] addressed the problem of optimum structural design based on cost constraints, and Yang [24,25] has presented reliability analyses for fatigue critical structures in aircraft based on periodic proof testing. The combined effects of proof testing and NDE on the reliability of cyclically loaded structures has been explored by Harris [26].

In addition to reliability analysis, the results of a probabilistic analysis are useful in helping to rank the relative importance of proof test parameters and in determining the sensitivity of the results to specific input items. It is useful to know, for example, that the results of a proof test analysis may be insensitive to how flaws are characterized in terms of shape, or the nature of the test media. This kind of information may not be readily extracted from a deterministic approach, even though a deterministically based sensitivity analysis is performed (see Section 6.3).

The probability of detecting flaws is an important consideration in proof test applications where a pre-test NDE is carried out. The effect of the NDE will beneficially change the assumed initial flaw shape and size distributions relative to the assumed distributions in the absence of the inspection as it will provide hardware specific data which will help remove conservative assumptions made in the formulation of the latter distributions.

Additional technical details related to probabilistic analysis are given in Section D1 of Appendix D. These details cover limit states and distribution functions, data requirements, application to proof test analysis, and available enabling technology.

7.2 Multiple Cycle Proof Test Analysis

7.2.1 Background

Some aspects of multiple cycle proof testing (MCPT) have already been discussed in Section 4.5.2. The potential advantage of MCPT is that a life threatening flaw that is just short of being large enough to cause failure during the first proof cycle may reveal its presence due to growth during subsequent cycles. The potential disadvantage is that existing flaws may be enlarged by fatigue and ductile tearing

without causing failure during multiple cycling, so that the service life is reduced by the increased damage resulting from MCPT. This competition between beneficial and deleterious effects can only be resolved either through reference to historical data, or through a probability analysis to establish the increase or decrease in service reliability from performing MCPT. An investigation into these aspects based on probability analysis has recently been completed by McClung et al. [15] under sponsorship of NASA Marshall Space Flight Center.

The historical basis for implementing MCPT rests mainly on the experience of Rocketdyne. MCPT of pressurized components has been implemented by Rocketdyne since 1952 and originated as a result of failures on the NALAR program at pressures below the initial hydrostatic test pressures [14]. At that time it was recommended that five-cycle proof testing with 10-second hold times be employed in order to avoid service failures following proof testing. This recommendation has since been refined, and it is now recommended that MCPT be performed using five-cycles at a minimum proof pressure of 1.2 times the maximum expected operating pressure with each cycle having a hold time of 30 seconds. Application of these kinds of procedures have demonstrated that proof tested hardware can fail from undetected flaws on the second, third, fourth or fifth cycle at pressures below those applied on the first cycle. Table 7.1 is reproduced from Hudak et al. [14] and gives pre-1979 examples where failure occurred during MCPT after the first cycle due to a pre-existing defect. The extension of MCPT by Rocketdyne to most production programs as a supplement to other primary NDE measures has virtually eliminated service failures of pressurized components due to undetected flaws.

7.2.2 MCPT Versus SCPT

Given the clear benefits on subsequent fleet reliability of MCPT for ductile materials, as demonstrated by the Rocketdyne experience, it is surprising that the benefits of MCPT cannot be established from a deterministic proof test analysis, a fact that led Tiffany [7] to recommend that MCPT not be performed. To demonstrate the benefits of MCPT it is necessary to perform probability analyses, as illustrated by the analytical investigations into quantifying MCPT benefits carried out in another NASA sponsored program of work performed at SwRI. This work has recently been completed and the methods used and results obtained are detailed in the final report (McClung et al., [15], hereafter referred to as the MCPT Report), which describes the application of probability analysis to investigate the relative advantages and disadvantages of MCPT compared to single cycle proof testing (SCPT). The results of that work provide guidance on when MCPT should be performed in preference to single cycle proof testing (SCPT). This guidance is based on the results of calculations performed to determine how changes in the assumed initial distribution of crack sizes (compare Figure D1.1) due to MCPT impacts the distribution of component life after the component is put into service. The latter is quantified in terms of the probability of failure in service after a specified number of service cycles. A proof test protocol that decreases the service failure probability is desirable. Hence, from a fracture mechanics perspective, the in-service reliability calculations provide a rational basis on which to compare and ultimately optimize different proof test protocols. To illustrate this, an example result which is taken from the MCPT Report is shown in Figure 7.1. This figure shows how the probability of failure is predicted to vary with service cycles as the number of proof test load cycles is changed from zero to 20 for an assumed proof factor of 1.3. The benefits

Table 7.1 Summary of five-cycle proof test (pre-1979) for cases in which pre-existing defect was identified (Note: does not include those instances where failure occurred on the first proof cycle)

Program	Component	Material	Failure Cycle	% Proof Pres. at Failure	Component Thickness, in.	Defect Information (dimensions in inches)
SSME	LPOTP Housing	Tens-50	4	80%	—	Casting Defect
SSME	Nozzle Mixer Bowl	Inconel 718	2,3	Leak	—	Casting Porosity
SSME	Turbine Disch. Duct Bellows Assy	Inconel 718	2	56%	~.030	Weld Porosity
SSME	High Press. Fuel Duct	Ti 5-2.5	4 (Cryo)	100% @ 5 Sec	.133	I. D. Axial (HAZ)
SSME	Fuel Turb. Drive Duct	Inconel 718	2	75%	—	Cracks at Lugs
SSME	Powerhead Preburner Fuel Supply Duct	Incoloy 903	5	100%	.145	.08 × 1.1 Non-Metallic Inclusion
SSME	Flight Nozzle Tubes	A-286	2, 3, 4, 5 3 Examples	Various 72% 80% 100% (12 sec hold)	~.010 .010 .0105 .010	 .007 × .070 .006 × .180 .007 × .060
F-1 F-1	Thrust Chamber Tubes MK-10 Fuel Volute Casting	Inco X-750 Tens-50	3 5	61% 100% (Depressurization) from	.018 .600	.0057 × Long Lap .09 × .31 Inclusion (1% Permanent Deformation at Splitter Leading Edge)
RS-27	Turbopump fuel Inlet Elbow	6061 Al	2 (4 incidents)	100%	—	Vane Fillet Cracks

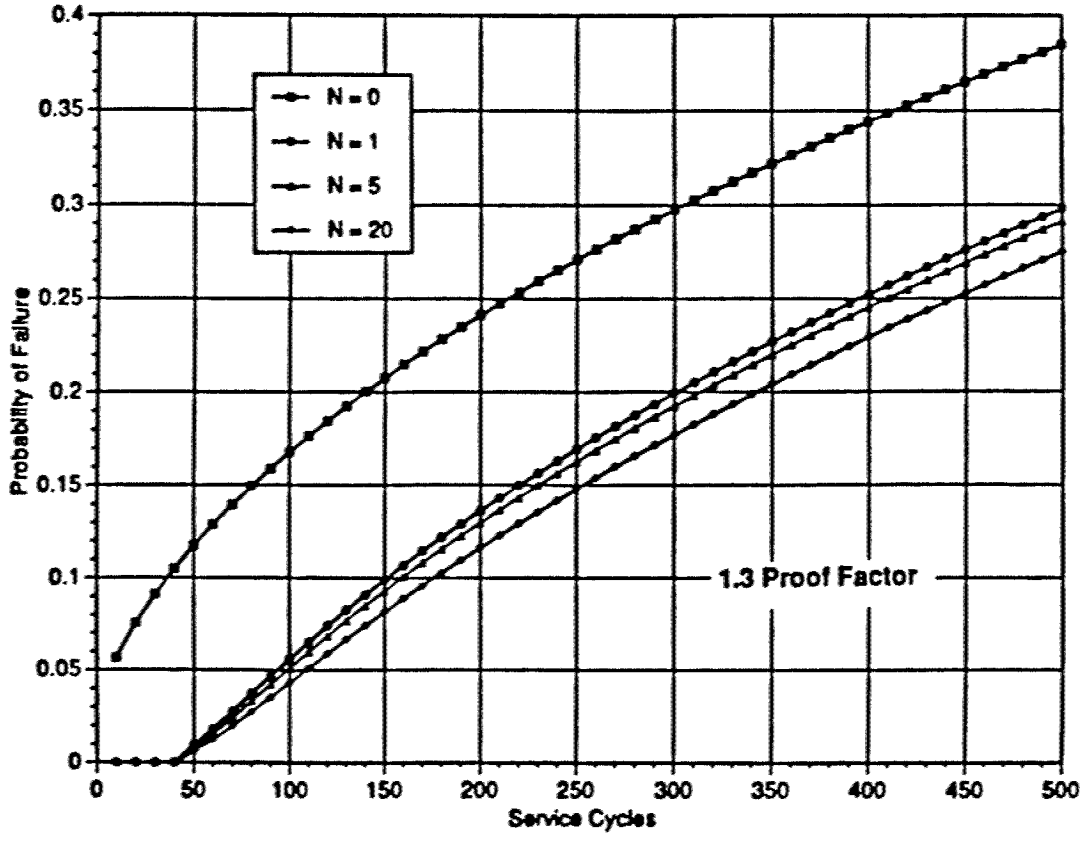

Figure 7.1 Example results for a proof factor of 1.3 showing in-service failure probability after different numbers of cycles (N), conditional on proof test success. N=0 corresponds to the hardware entering service without a proof test.

of an SCPT (N=1) compared to no proof test (N=0) are readily apparent in the significant reduction in service failure probabilities produced by SCPT. Additional proof cycles are seen to improve service reliability even more, but by incremental amounts which are less significant compared with the benefits of SCPT.

Results, such as those presented in Figure 7.1, were used in the MCPT Report to draw up guidelines on when MCPT should be employed in preference to SCPT. These guidelines are not reproduced here since the decision making process depends on a number of interacting circumstances. The reader is referred to Section 7 of the MCPT Report for details. However, there are some clear cut cases when MCPT is not recommended, and others when it would be preferable to perform MCPT in preference to SCPT.

The situations where MCPT should be avoided if at all possible are when

(1) The material is known to fracture by a brittle mechanism under the proof test environment. MCPT is not recommended in this case since it is expected that only negligible crack extension will occur as a result of applying multiple cycles. Note that this recommendation is not applicable to materials (such as some ferritic steels at temperatures just above the ductile-brittle toughness transition temperature) that can undergo significant tearing prior to failure by a brittle mechanism.

(2) The test is performed in a chemically aggressive environment that could result in sub-critical crack growth due to SCC during the proof loading. The risk in this case is that enlargement of relatively innocuous small flaws could occur from SCC which seriously reduces service reliability without significantly increasing the probability of failure during proof testing from larger flaws.

(3) The proof loading is likely to produce conditions in fracture critical regions where the crack tip driving force decreases, or is insensitive, to increases in crack size. Under these conditions, large cracks could extend during MCPT without the possibility of failure occurring during the test. Situations where these conditions could arise are where there exists local displacement or strain controlled loading, or severe stress gradients (for example, resulting from geometrical discontinuities or residual stresses).

Given that the foregoing three conditions are excluded, then the situations where MCPT was analytically demonstrated to provide clear additional benefits to SCPT are when:

(1) The material displays a pronounced increase in toughness with increasing ductile tear length. This material attribute improves the efficacy of the proof test flaw screening capability since it allows significant ductile tearing to occur due to proof load cycling prior to failure.

(2) There is the possibility that large "rogue" flaws are present in the hardware. This observation is consistent with Rocketdyne experience since most Rocketdyne MCPT failures have occurred in the early stages of the hardware development process where there is increased likelihood of a rogue flaw. No additional failures have been observed after the development process was matured.

7.2.3 Use of the Road Map in a MCPT Analysis

If an MCPT is performed, then it is necessary to assess the impact of multiple cycling on the flaw screening capability of the test, and the calculated minimum proof loads required to screen specified flaw sizes. These assessments can be done within the framework of the Road Map outlined in Section 6.1 and shown schematically in Figure 6.1.

The calculated flaw screening capability of a proof test is the same for an MCPT and an SCPT provided that the procedures described in Stage 34 of the Road Map are followed. This is because the flaw screening diagram is derived from calculated instability flaw sizes and these provide upper bounds to the crack extensions that can occur from stable tearing during the proof test. Hence, flaws that are below their critical size at the start of the proof test can grow during the test from combined fatigue and ductile tearing, but they cannot exceed their instability size without causing the hardware to fail during the test.

MCPT can impact calculated minimum proof loads through the additional crack extension that can occur during the test from combined fatigue and ductile tearing. It is emphasized in Stage 36 of the Road Map that the analyst should determine the increase in flaw sizes that result from the proof test to confirm that the flaw size distribution at the end of the test is consistent with ensuring the needed safe-life. In the case of MCPT these calculations should be performed using the procedures detailed in Section D2.

8. RAMIFICATIONS OF PROOF TESTING ON SERVICE ANALYSIS

The overload resulting from proof testing can have significant effects on the way in which a service life assessment is performed. Some of the effects may be beneficial, while others may be detrimental. The proof test analyst should ensure that the service analyst is aware of these effects so that they can be included in the determination of the service lifetime. Proof test overload effects can influence the residual stress distribution in the hardware through shakedown, the fracture and fatigue behavior of the material, and the flaw size distribution assumed present in the hardware at the start of service.

8.1 Stress Analysis

There is a potential during the proof loading for redistribution of stresses to occur in those regions of the component where the local stress is at or near yield point magnitude. These regions are normally associated with geometric discontinuities, such as sharp corners and holes, and residual welding stresses.

The effect of additional stresses from proof loading in local regions of existing high stress may be either beneficial or detrimental. Benefits may arise from shakedown when the stresses are tensile. This is illustrated in Figure 8.1(a), where yielding produces a non-linear relationship between the local stress and the applied load, so that the change in the local stress as the load is increased is far less than if the material behaved linear elastically. The benefits of shakedown arise because when the applied load is reduced the material unloads linear elastically so that the stress after unloading is less than it was before the proof load (Figure 8.1(a)).

The detrimental aspects arise from the inverse behavior to this, as shown in Figure 8.1(b). Here the proof loading results in a local compressive stress which reinforces an existing compressive stress to produce yielding. When the proof load is removed, a tensile stress remains which could reinforce any tensile loading experienced by the region during service. One of the authors is aware of one instance where a notched bar loaded by a compressive force fractured in a brittle mode during unloading due to the generation of tensile residual stresses at the root of the notch resulting from the compressive yielding that had occurred during loading.

In general, it is conservative and prudent to ignore compressive residual stresses resulting from proof test shakedown in post-proof test service assessments. It is recommended that justification be provided by the analyst before taking potential benefits from predicted compressive shakedown stresses. However, the detrimental effects of generating tensile residual stresses by proof testing in regions where there were previously compressive stresses needs to be addressed. Regions where this is likely to occur should be identified and appropriate stress analysis performed to establish whether the region is fracture sensitive.

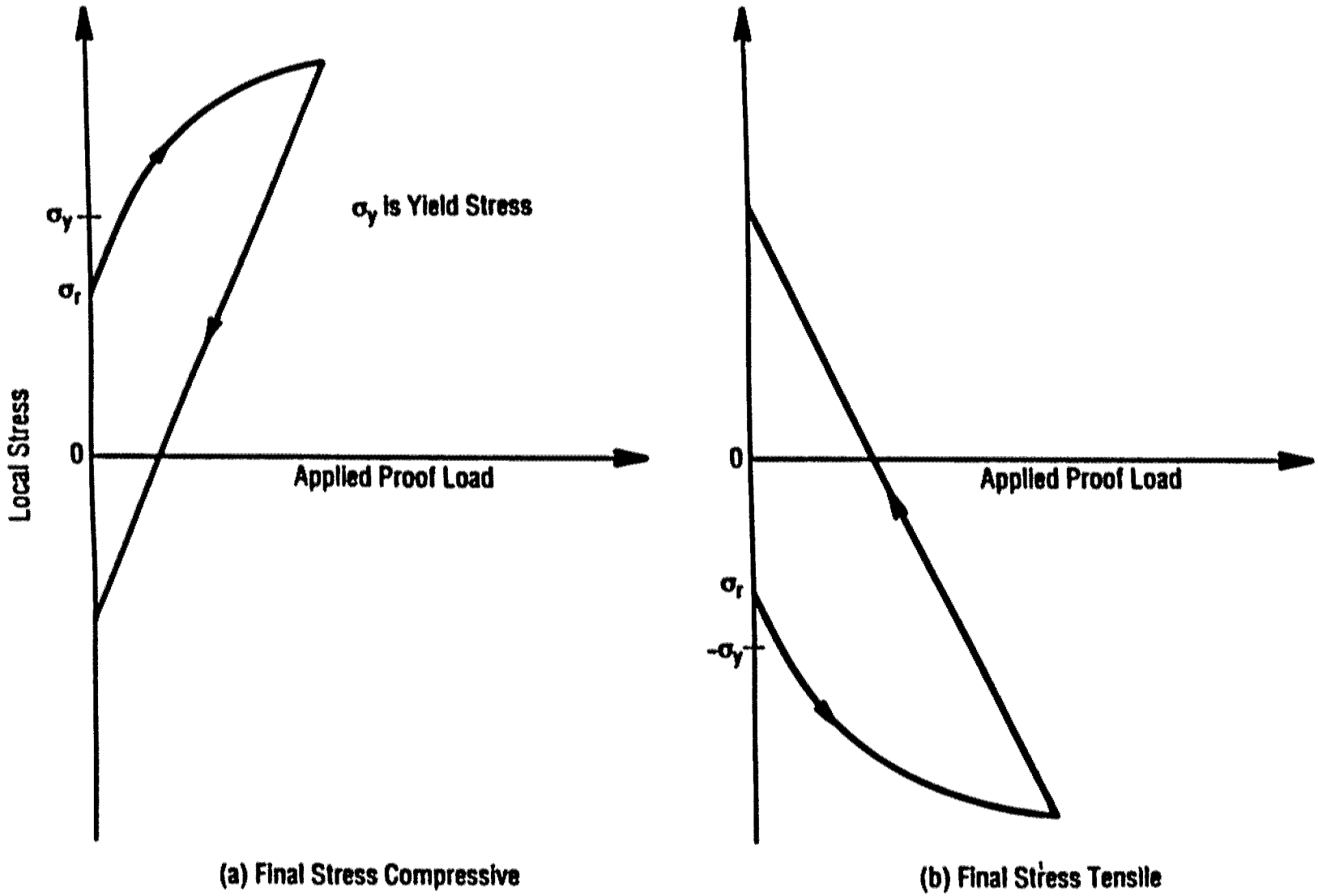

Figure 8.1 (a) Example of beneficial effects of shakedown from proof testing that results in a compressive residual stress. (b) Example of deleterious effects from proof test shakedown that results in a residual tensile stress.

8.2 Fracture Behavior

The application of a proof test load which exceeds the normal service loading can have important implications on the fracture behavior of the material during subsequent operation. The effects of proof overloading on toughness is dependent on whether the material is brittle or ductile.

8.2.1 Brittle Materials

It is now widely recognized that (proof) loading a material at a temperature above the service temperature to a load which exceeds its maximum expected operating load (MEOL) changes the fracture toughness at the service temperature if the failure mechanism at that temperature is brittle (i.e., stress controlled cleavage) [27-29]. This effect is called warm prestressing (WPS) and is illustrated in Figure 8.2. It has been widely observed in ferritic steels where final fracture occurred at temperatures below the ductile-brittle toughness transition temperature. The reasons the WPS effects occur are understood and theoretical models based on the mechanisms of cleavage, and the mechanics of plastic flow have been successfully proposed to explain WPS [13]. The enhancement in toughness is observed even if ductile tearing occurs during the proof loading [30]. Toughness enhancement is not predicted to occur if the proof loading occurs at the same temperature as the service temperature, or at a temperature below it. The WPS phenomenon appears to be dependent on the failure mechanisms being stress controlled: there is no evidence that WPS will affect the toughness of materials failing by ductile mechanisms.

It is prudent not to invoke the benefits from warm prestressing due to a proof test overload because of the possibility of sub-critical crack growth during service. Although there is some theoretical evidence that the WPS effect persists even after some sub-critical crack extension, the amount of crack growth required before the effects are removed is small, and, under some circumstances, the threat of catastrophic failure occurring at an apparent enhanced toughness level during growth cannot be ruled out [31].

Under some conditions material embrittlement could occur during the proof test from strain ageing, dynamic ageing, environmental exposure (e.g. hydrogen), or other causes. The time over which the proof load is sustained, and the temperature of the test and the environment, will be important parameters in determining the degree of embrittlement, if any is anticipated to occur. It is important to quantify the reduction in toughness due to embrittling mechanisms and to use the degraded toughness value in the service analysis.

8.2.2 Ductile Materials

The effect of ductile tearing due to proof loading on the ductile toughness under service conditions is little understood, particularly if the two loadings occur at different temperatures. This observation applies whether the proof test consists of a single cycle or multiple cycles. The deterministic methodology of proof testing requires that a postulated defect remains on the point of incipient instability after the last proof test load cycle. This implies that the defect grew by tear or tear-fatigue during the proof testing, as shown schematically in Figure 8.3. Models of tear-fatigue have now advanced to the stage where the instability point and the amount of tear-fatigue preceding it can be predicted (see Section D2.2). These models enable the effect of the proof overload on subsequent crack growth at a lower cyclic load (service load) to be qualitatively predicted. However, the models do not provide predictions regarding the influence of the proof loading on the subsequent fracture toughness under service conditions. The problem is illustrated schematically in Figure 8.3, which shows the situation under service loading after the proof loading. It is essential for assessing the integrity of the component under

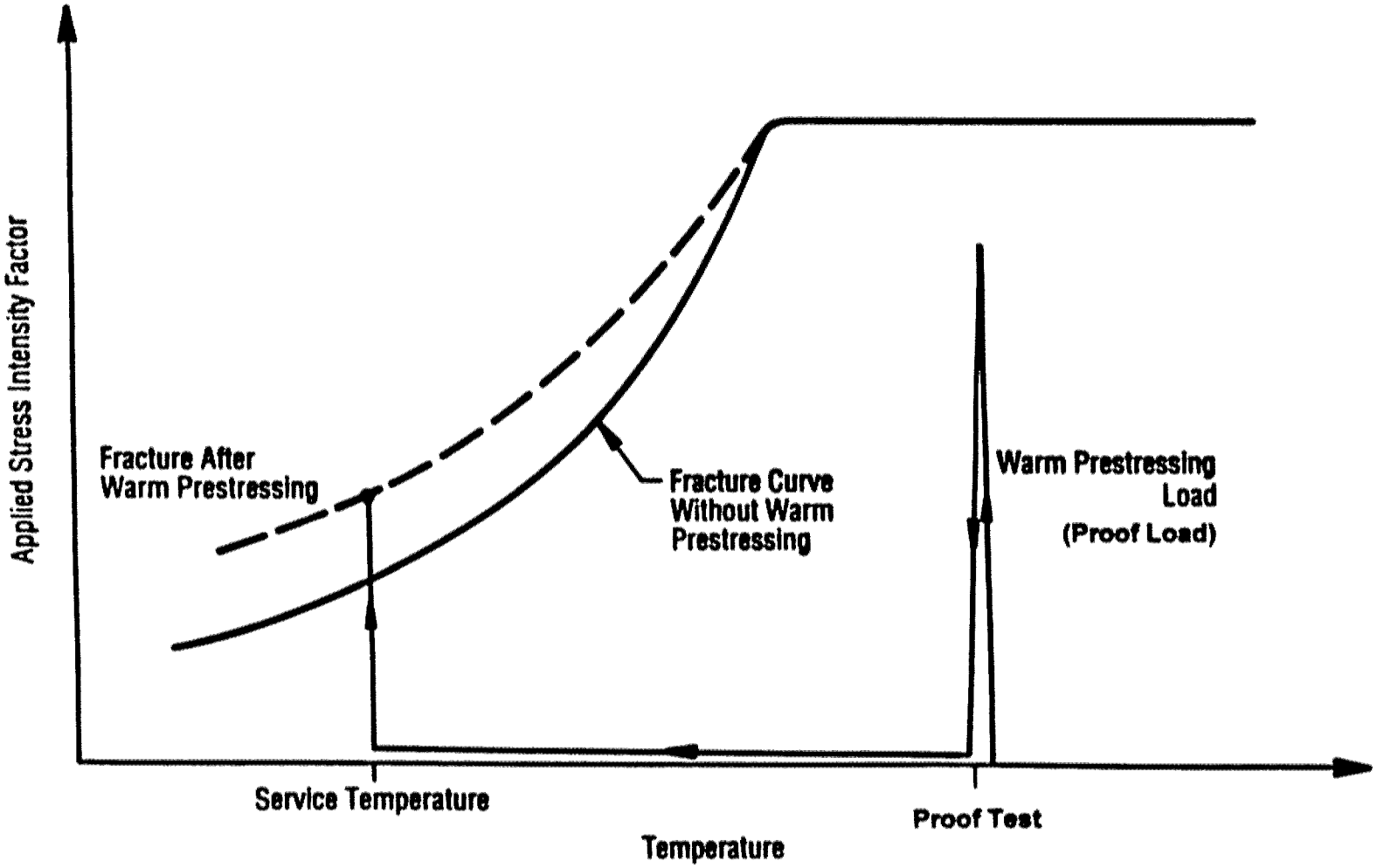

Figure 8.2 Schematic showing the enhancement in fracture toughness of brittle materials that are subjected to warm prestressing.

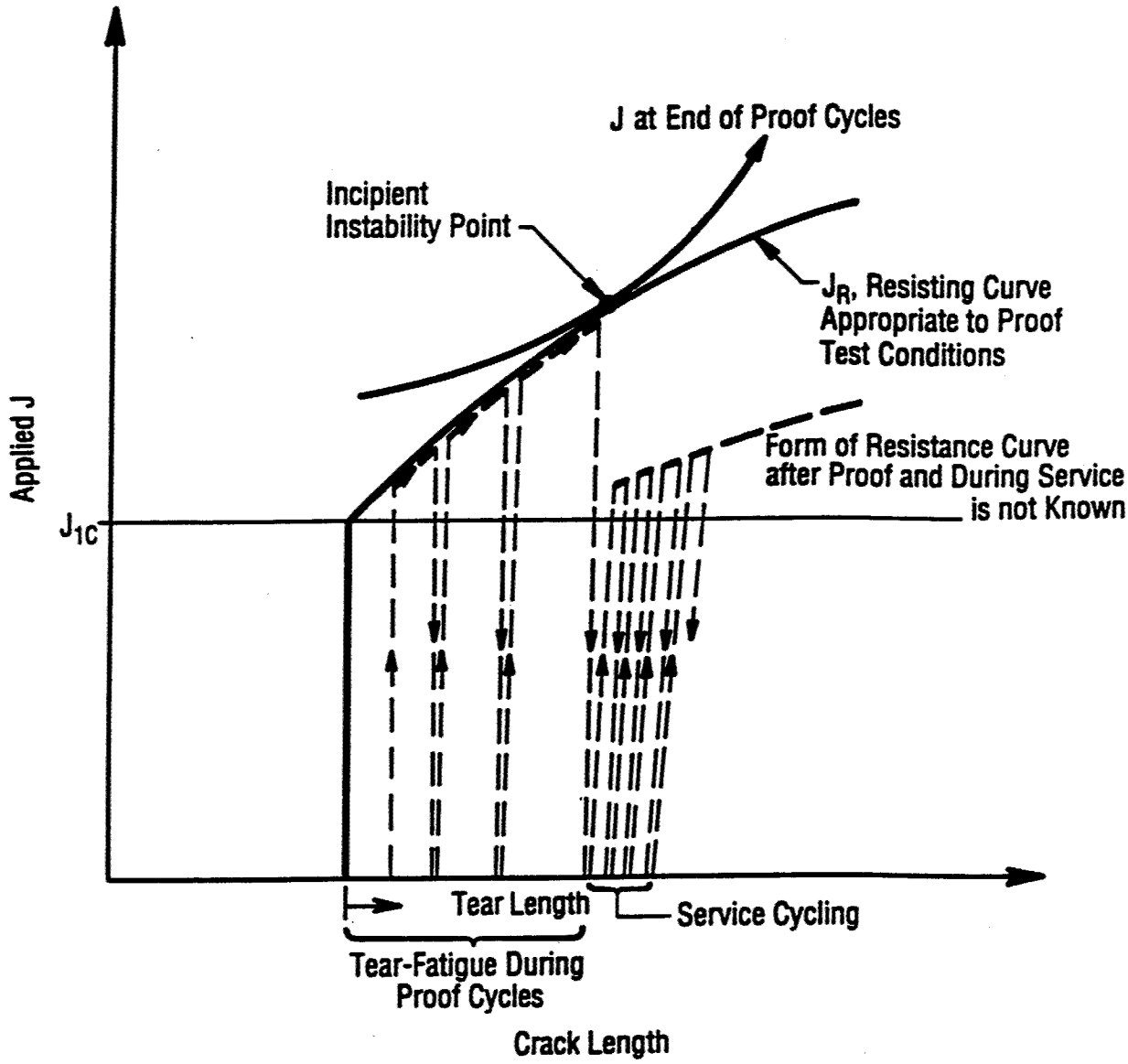

Figure 8.3 Illustration of tear-fatigue up to incipient instability during proof testing. The effects of the corresponding overload on subsequent fracture behavior in service is not known.

service conditions immediately following the proof test that at least a lower bound initiation toughness is known. At the current time there is no simple way of quantifying the damage introduced by the proof test without resorting to experimental measurement. Theoretical predictions of the effects of the damage, based upon the local damage approach [32], are not practical at the present time and are not sufficiently validated to be used with confidence on aerospace components.

In the absence of quantitative evidence to demonstrate otherwise, it is recommended that the service analysis be made using a lower bound J_R-curve derived from toughness measurements performed according to ASTM test standards and ignoring the influence of the proof overload. Limited experimental validation in support of this recommendation is provided in Section B6 of Appendix B.

8.3 Fatigue Crack Growth Behavior

The proof test overload could result in retardation of fatigue crack growth during service conditions [33]. However, although this effect can be pronounced for through cracks in thin sections, it is likely to be significant for part-through-wall defects only if the proof load cycles are substantially higher than the service cycles [34]. Large overloads can arise for very tough materials if the overload is characterized in terms of applied J values rather than applied loads. In these cases the calculated value of J for assumed hardware flaws due to the proof overload, J_o, may be very large and incipient ductile instability may be very near to the plastic collapse load of the component. In this regime, the applied value of J is very sensitive to the value of the load and the proof loading could constitute a large overload with respect to service conditions when characterized by the ratio $(J_o/J_{max})^{1/2}$ (see Figure 8.4).

It is conservative in service analyses to ignore the potential for crack growth retardation because the effect will be to increase the calculated remaining life of the component with respect to the life determined with no retardation. It is recommended that justification be provided by the analyst before taking potential benefits from crack growth retardation.

A more important consideration is the possibility of an enhancement in the growth rate during service due to combined static and fatigue crack growth mechanisms (see Section D2.2). In a normal remaining life assessment the reduction in the total fatigue life due to the interaction of static brittle and fatigue crack growth mechanisms is probably not significant, since the predominant part of the life is spent in propagating small defects with low applied values of J_{max}. However, the predicted value of the largest defect a_o that could just survive the proof test loading may be large enough to produce a significant interaction between static and cyclic failure modes during subsequent service at lower load levels.

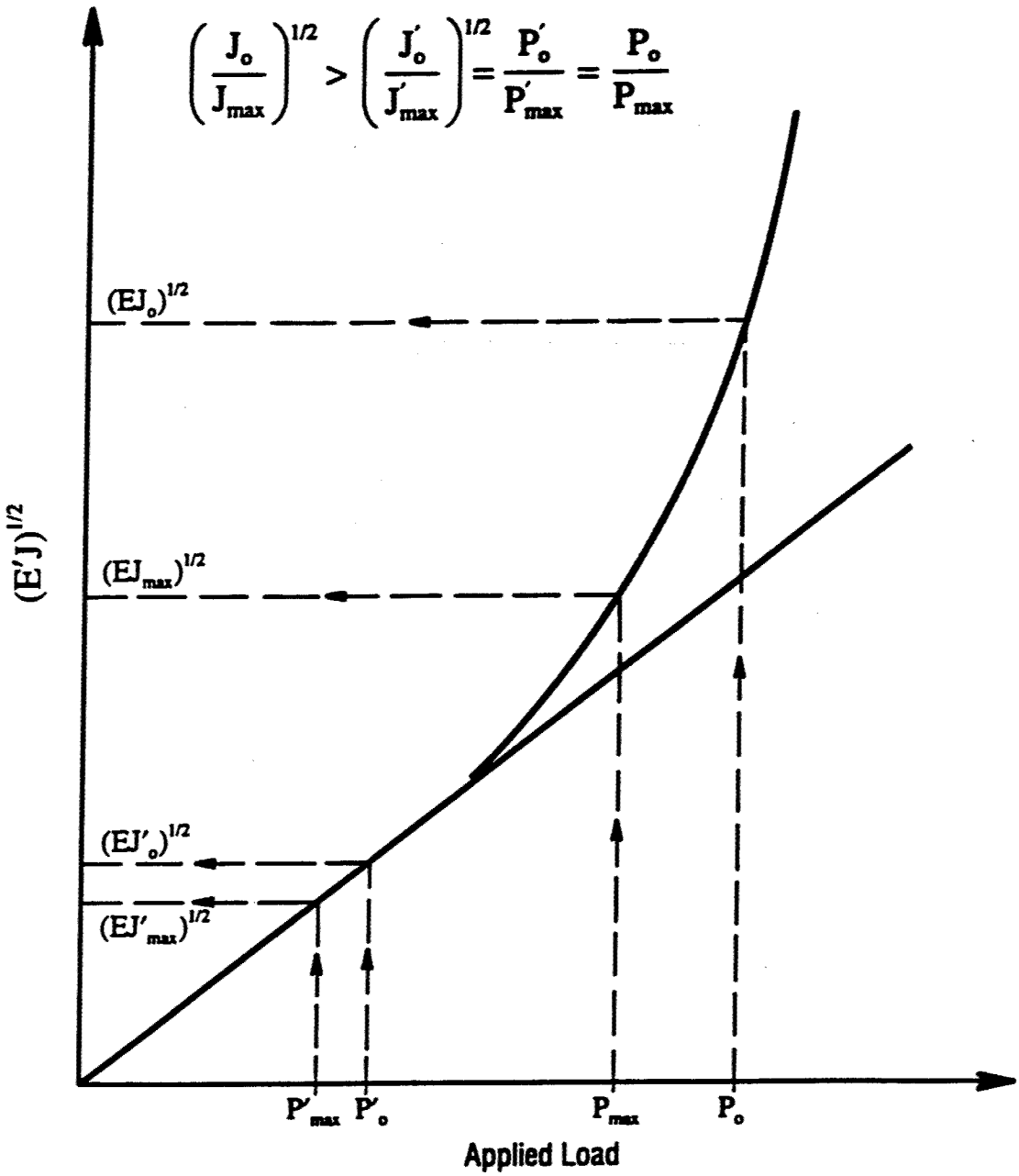

Figure 8.4 Schematic showing that overloading, when characterized by $(J_o/J_{max})^{1/2}$, is more significant in the plastic regime for the same ratio of overload (P_o) to maximum cyclic load (P_{max}).

It is known from work on ferritic steels that brittle as well as ductile materials show an acceleration in the crack propagation rate as the load at the maximum part of the cycle approaches the load required to cause fracture under monotonic loading conditions. For brittle materials that do not display any significant resistance to stable crack extension under a rising load, and where fracture is coincident with crack growth initiation, this effect becomes significant when J_{max} exceeds about 0.6 J_{mat}. Theoretical modelling of this acceleration indicates that the enhancement in the growth rate is inversely proportional to the term J_{mat}-J_{max} [35,36].

For ductile materials, there is evidence from tear-fatigue tests on ductile ferritic steels and the nickel-based superalloy IN-718 that, provided J_{max} is less than J_o, then although $J_{max} > J_{mat}$, the growth rate will return immediately after the overload to its calculated value in the absence of tearing (see Nix et al. [37], and Section B6 of Appendix B). This effect is illustrated in Figure 8.5. However, as service cycling propagates the crack through the ductile fracture process zone corresponding to J_o, the influence of the overload will be wiped out as a new process zone is established corresponding to the instantaneous value of J_{max}. After this event, tear-fatigue and an acceleration in the cyclic growth rate can again occur when $J_{max} > J_{mat}$ (see Section B6).

It is recommended that the potential benefits of the proof overload in suppressing tear-fatigue crack growth during service be ignored in service analyses as it is presently not possible to quantify these effects. In the event that these benefits are sort, then justification should be provided by the analyst to substantiate using them in a post-proof test assessment.

8.4 Flaw Characterization

The most fundamental effect of proof testing on the subsequent component reliability in service– in fact, the direct effect most often intended by the proof test – is increased knowledge regarding the distribution of flaw sizes in the component. Fracture mechanics assessments of remaining service life are based on some presumption about the size and shape of the crack-like defects already present in the component. A properly designed proof test will eliminate the possibility of large flaws being part of the defect population that enters service by failing hardware which contains these flaws. However, the change in defect distribution due to the possibility that some flaws have grown in size during the proof test should also be considered when evaluating the effects of proof on in-service reliability.

For brittle materials, the largest calculated flaw that could just survive the proof test can be used in a deterministic analysis of the remaining service life. In a probabilistic analysis the flaw distribution can be truncated at the largest survivable defect size, and the distribution renormalized with respect to the remaining population.

However, determining the post-proof flaw size distribution for ductile materials is more complicated. The pre-proof distribution can be changed by the proof test in three ways, as shown in schematically in Figure 8.6. Some flaws are sufficiently small (Region 1) that ductile crack growth is not initiated, and so they do not change in size. More accurately, flaws in this region can be treated as having experienced a single cycle of fatigue crack growth, although in many cases the amount of crack growth so calculated will be negligible. At the other extreme (Region 3), some flaws are sufficiently large that they cause component failure during the proof test, and so they are removed from the population. In the intermediate case (Region 2), the flaws experience some stable growth

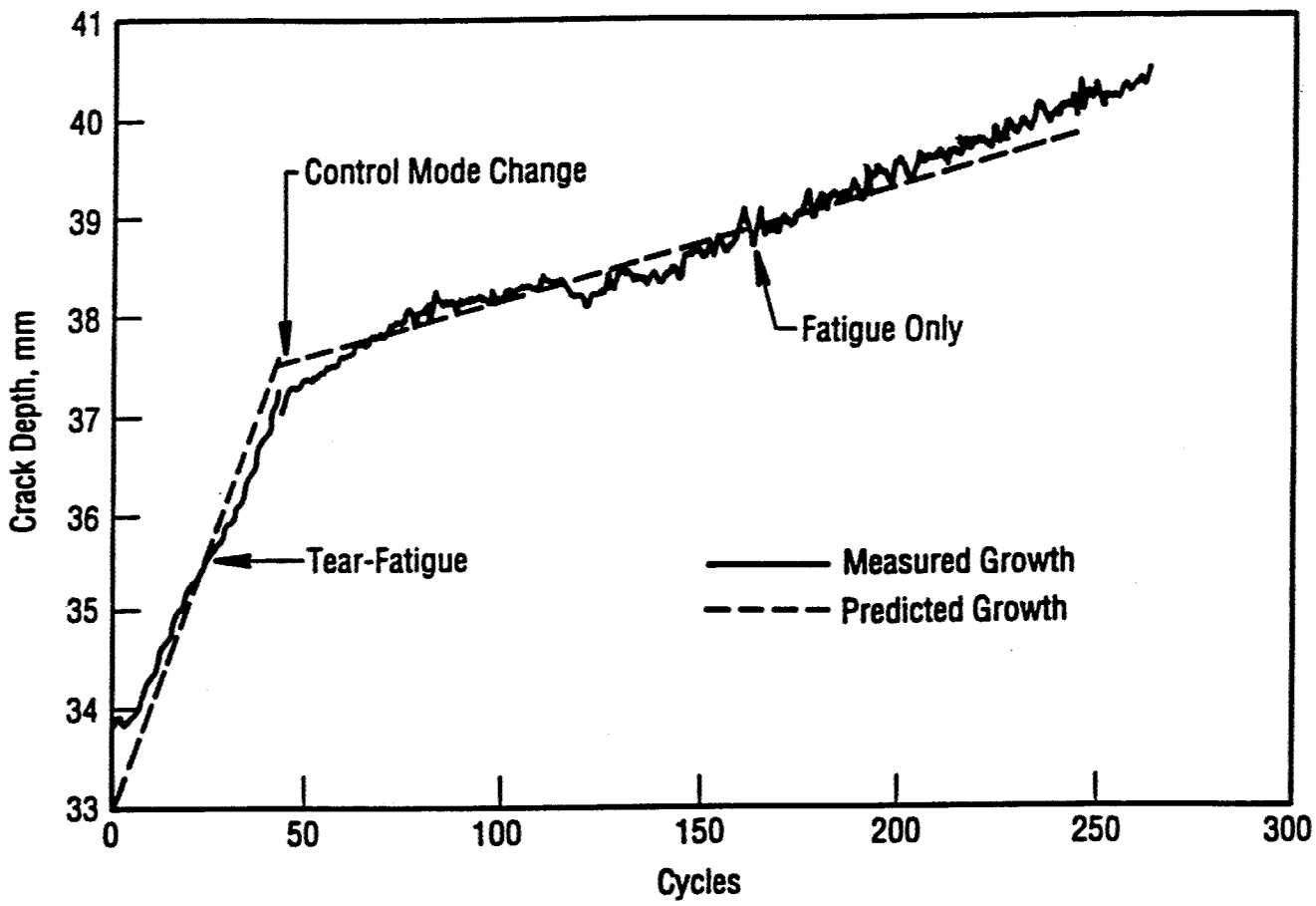

Figure 8.5 Plot of measured and predicted crack growth for tear-fatigue under a rising J_{max} and following a load control mode change to constant J_{max}.

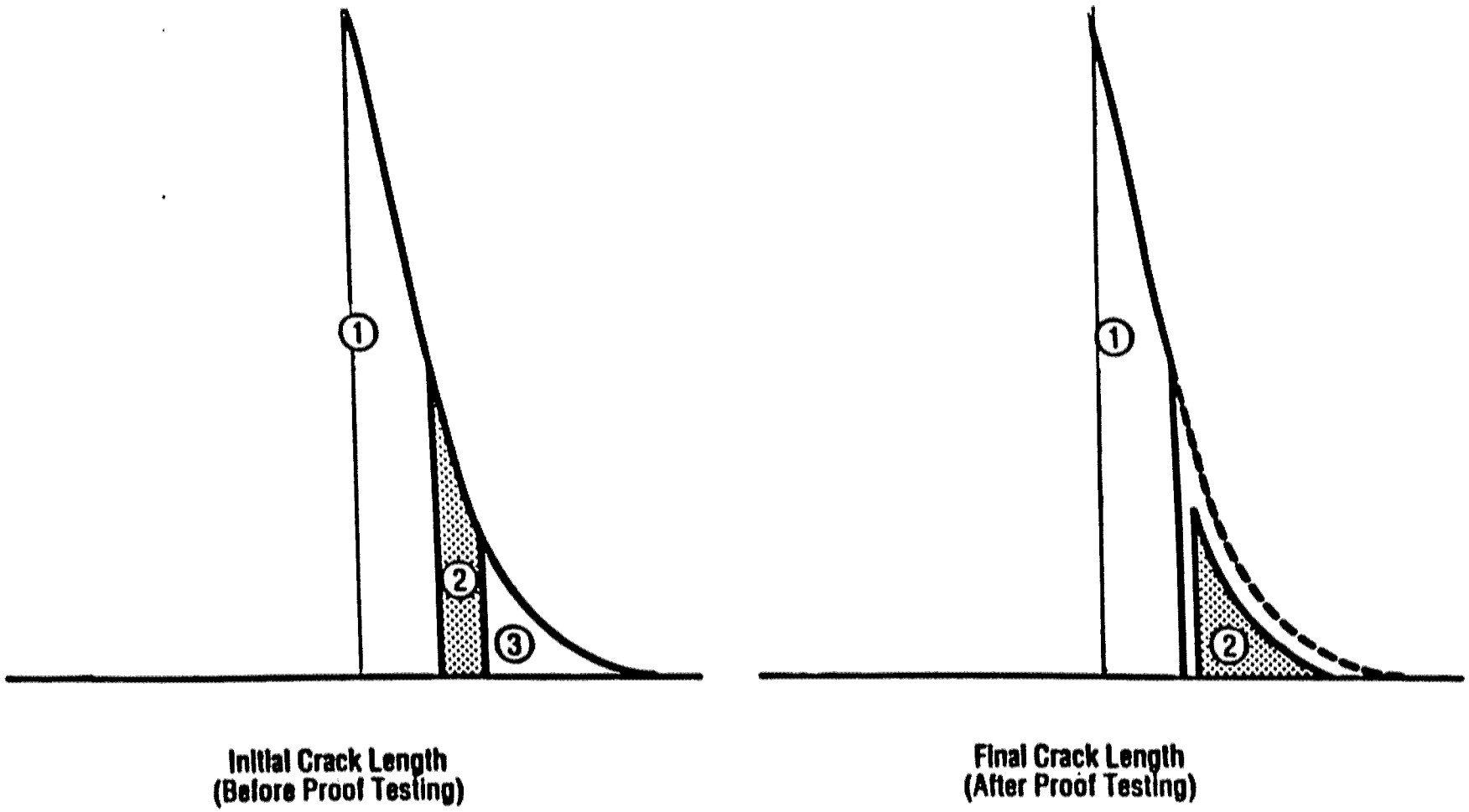

Figure 8.6 Schematic representation of initial and final crack length distributions for proof testing of ductile materials.

but do not cause failure. Computation of the boundaries between these three regions and the extent of crack growth in region 2 requires application of ductile fracture mechanics. Depending on the nature of the proof test history, these computations may include elements of *J*-resistance curve, SCC, fatigue crack growth, and time-dependent crack growth analyses.

Many naturally occurring flaws will be highly irregular in shape, rather than mathematically straight or semi-elliptical as frequently assumed in fracture mechanics analyses. Proof loading of these defects can cause a variety of other changes in flaw geometry besides self-similar growth. The flaw can extend or change shape locally by separation of small ligaments or "fingers" along the crack front, and closely adjacent defects can link up to form a single larger flaw. These effects are essentially impossible to quantify or to predict from a formal fracture mechanics standpoint. Instead, appropriately conservative assumptions should be made about the simplified initial and final shapes and sizes of the crack-like defects.

Proof loading can also cause the formation of sharp, crack-like flaws from previously blunt or non-planar defects, especially in weldments and perhaps near stress concentrations. This phenomenon may be more likely when proof loading is especially severe or when multiple cycles are applied. Multiple cycles can potentially cause localized low cycle fatigue deformation which can enhance flaw initiation or sharpening in locally susceptible regions. Again, characterizing or predicting these effects is not practical in an engineering methodology, but it should be recognized that they introduce a possible nonconservatism into service analyses.

9. SUMMARY AND CONCLUSIONS

Guidelines are presented showing how state-of-the-art fracture mechanics can be used in the design and analysis of a proof test. Fracture mechanics enables the proof test analyst to determine the flaw screening capability of a test for a specified proof load, and, conversely, the minimum proof load necessary to screen against a specified flaw size. It is necessary to employ elastic-plastic fracture mechanics, particularly for ductile materials, in order to perform an accurate proof test analysis and to avoid eroding the efficacy of the proof test. In addition, it is essential that the fracture mechanics technology includes the effects of ductile tearing in materials that fail by ductile mechanisms otherwise a non-conservative proof test analysis will result.

The elastic-plastic fracture mechanics approach described in these Guidelines is based on the *J*-Integral. Relatively simple *J* estimations schemes are described based on a modified version of the EPRI scheme together with the reference stress approach. An equivalent approach is also presented based on the Failure Assessment Diagram (FAD) which provides a pictorial representation of a *J* analysis. Recommended and validated expressions are provided for evaluating *J* and deriving FADs for flaws in proof tested hardware subjected to primary and secondary loads and multiaxial stressing; for defects located at stress concentration features and welds; and for flaws with multiple degrees of freedom. The use of these solutions together with brittle and ductile failure criteria to determine the critical conditions for fracture in proof tested hardware is described and the procedures verified against laboratory and hardware fracture results.

A Road Map is provided to guide the engineer through the many stages involved in a proof test analysis. This Road Map provides an overview of the proof test process and shows how the many different aspects covered in the Guidelines are integrated into a proof test analysis. These aspects include safe-life analysis, implementation issues, fracture analysis, leak-before-burst, and the role of proof testing compared to alternative non-destructive examination methods. Worked examples are provided to illustrate how the Road Map can be applied to help design an effective proof test. The EPFM analysis needed to implement the Road Map would be greatly facilitated by the availability of suitable tools (e.g. computer programs) for performing the appropriate calculations of *J* and for determining critical loads and crack sizes.

Outlines of advanced proof test analyses pertaining to reliability estimations and multiple cycle proof testing are presented. Probability analysis enables a proof test to be designed to guarantee a needed service reliability taking into account uncertainties in materials data, NDE detection, and operating conditions. Such an approach could significantly increase the efficacy of a proof test by removing the conservatisms which are systematically built in to a deterministic analysis. Under specific conditions, MCPT has been shown in practice, and analytically, to increase the service reliability of a fleet of tested hardware.

Some possible effects that the proof overload can have on structural integrity during subsequent service have been highlighted. Specific effects addressed concern stress re-distribution, fatigue crack propagation behavior, fracture behavior, and flaw characterization. Engineers who perform safe-life analyses should be aware of these effects and make appropriate allowance for them.

Finally, although these Guidelines provide comprehensive recommendations and procedures for implementing state-of-the-art fracture mechanics into proof test analyses, inevitably there are still outstanding technical issues that remain unresolved at the present time. In these cases, the recommended

procedures provided in the Guidelines should be considered as provisional. The most important of these issues are:

- The absence of testing standards and/or guidelines for measuring material properties needed in proof test analyses. For example, ASTM fracture toughness testing standards E813 and E1152 for measuring J_{Ic} and J_R-curve data specify validity limits on the cracked test specimen size in order to guarantee high plastic crack-tip constraint conditions are maintained during the testing. To be conservative, a proof test analysis should employ toughness data that is measured under conditions that either simulate the constraint in defected hardware, or produces conditions of less constraint. In general, toughness data obtained under high constraint conditions will produce lower toughness values than toughness data obtained under low constraint conditions. This means that the flaw screening capability of a proof test will be over-estimated, and the proof load factor needed to screen a specific flaw size will be under-estimated, if toughness data that is obtained under high constraint conditions is applied in the proof test analysis of a structure with lower constraint, resulting in a non-conservative analysis result. Although guidelines are provided to address this problem in the current document, there is a need to refine and standardize the testing requirements for materials data to be used in proof test analyses.

- The treatment of combined primary and secondary (residual) loads has been validated for combined stress distributions that do not exceed the yield stress. Although a simple, approximate method for allowing for stress relaxation and re-distribution due to plastic deformation in estimating J has been described, this approach has not been substantiated and requires further investigation and refinement.

- Although a method of estimating J for cracks in over-matched and under-matched welds has been recommended for use in proof test and service applications, the validation provided in support of the method is limited. Since welds are structural details that are prone to cracking, it would be prudent to provide further verification for the recommended approach.

- To facilitate analyses, the current Guidelines recommend that flaws with multiple degrees of freedom (such as surface flaws) be reduced using various approximations to one degree of freedom. Recommended ways of performing this reduction are suggested, and the results of verification testing on hardware appears to substantiate these approaches. However, these approximate procedures may need refinement and eventually procedures that address multiple degrees of freedom should be developed.

- Although a J estimation scheme for evaluating cracks subjected to multiaxial stressing has been recommended, this procedure is substantiated by only a single set of finite element results for cracks subjected to varying levels of uniform biaxial stressing. Additional validation should be sought to address this situation and provide more extensive verification, especially for the case of non-uniform multiaxial stressing arising from stress gradients.

- The recommended J estimation schemes have been validated for materials whose stress-strain behavior has been approximated by a Ramberg-Osgood power law. Some material tensile behavior cannot be adequately represented by this kind of law. For example, materials that display discontinuous yielding, or a yield drop. Additional validation is needed to demonstrate that the current estimation scheme is applicable to these kinds of materials.

- The net section yield load for a defected structure plays an important role in the J estimation scheme. Plastic limit theory provides a way of estimating these loads, but frequently these estimations rely on a lower bound theorem that under-predicts the actual net section yield load. This was found to be the case for the pressurized ducts and pressure vessels analyzed as part of the hardware validation performed in the present work (see Sections B4 and B5 of Appendix B). The use of lower bound values of the net section yield load will result in a non-conservative proof test analysis. Simple procedures should be investigated for deriving net section yield loads which are suitable for use in proof test analyses.

- The influence of mixed mode loading (combined tensile, shear and torsion) on fracture behavior has not been addressed in these Guidelines. There are situations where mixed mode loading may be important. Further investigations into defining mixed mode failure criteria for brittle and ductile materials should be considered.

10. REFERENCES

1. NASA MSFC-HDBK-1453, *Fracture Control Program Requirements*, October 1987.

2. NASA NHB 8071.1, *Fracture Control Requirements for Payloads Using the National Space Transportation System (NSTS)*, September 1988.

3. JSC-25863, "Fracture Control Plan for JSC Flight Hardware," Lyndon B. Johnson Space Center.

4. NASA MSFC-HDBK-505, Structural Strength Program Requirements, Revision A, January 1981.

5. MIL-STD-1522A (USAF), "Military Standard: Standard General Requirements fro Safe Design and Operation of Pressure Missile and Space Systems," May, 1984.

6. Tiffany, C. F., and Masters, J. N., "Applied Fracture Mechanics," *Fracture Toughness Testing, ASTM STP 381*, 1965, pp. 249-277.

7. Tiffany, C. F., "Fracture Control of Metallic Pressure Vessels", NASA Report SP-8040, May 1970.

8. Ehret, R. M. "Fracture Control Methods for Space Vehicles," NASA Report CR-134597, NASA Lewis Research Center, August, 1974.

9. Besuner, P. M., Harris, D. O., and Thomas, J. M., "A Review of Fracture Mechanics Life Technology," NASA CR-3957, February 1986.

10. Chell, G. G., McClung, R. C., Russell, D. A., Chang, K. J., and Donnelly, B., "Significant Issues in Proof Testing: A Critical Appraisal," NASA Contractor Report 4628, Marshall Space Flight Center, September 1994.

11. NASA-STD-5003, "Fracture Control Requirements for Payloads Using the Space Shuttle," October 7, 1996.

12. NASA MSFC-STD-1249, "Standard NDE Guidelines and Requirements for Fracture Control Programs," September, 1985.

13. Chell, G. G., and Curry, D. A., "Mechanics and Mechanisms of Cleavage Fracture", in 'Developments in Fracture Mechanics-2,' Ed. G. G. Chell, Applied Science Publishers, 1981, pp. 101-192.

14. Hudak, Jr., S. J., McClung, R. C., Bartlett, M. L., FitzGerald, J. H., and Russell, D. A., "A Comparison of Single-Cycle Versus Multiple-Cycle Proof Testing Strategies," NASA Contractor Report 4318, August 1990.

15. McClung, R. C., Chell, G. G., Millwater, H. R., Russell, D. A., and Orient, G. E., "A Comparison of Single-Cycle Versus Multiple-Cycle Proof Testing Strategies: Final Report," NASA Contractor Report, Contract NAS8-37451, Marshall Space Flight Center, December 1996.

16. Hallden, A. L., Rockwell International Internal Letter 9114-8062, 28 September 1979.

17. Chang, J. B., "On Test Verification of Space Flight Structures and Pressure Systems," 36th AIAA/ASME/ASCE/AHS/ASC Structures, Structural Dynamics and Materials Conference, New Orleans, April 10-12, 1995.

18. Cowie, B., Aeronautical Systems Division, Wright-Patterson AFB, private communication, May 1990.

19. Schwartzberg, F. R., King, R. G., and Todd, Jr., P. H., "Definition of Mutually Optimum NDI and Proof Test Criteria for 2219 Aluminum Pressure Vessels, Volume 1: Methods," NASA CR-135445, 1979.

20. American Society for Nondestructive Testing, *Nondestructive Testing Handbook, Second Edition, Volume 5: Acoustic Emission Testing*, R. K. Miller, Editor, 1987 (several sections discuss proof testing applications).

21. Harris, D. O., and Dunegan, H. L., "Verification of Structural Integrity of Pressure Vessels by Acoustic Emission and Periodic Proof Testing," *Testing for Prediction of Material Performance in Structures and Components, ASTM STP 515*, 1972, pp. 158-170.

22. NASA-STD-5001, "Structural Design and Test Factors of Safety for Spaceflight Hardware," June 21, 1996.

23. Shinozuka, M., and Yang, J.-N., "Optimum Structural Design Based on Reliability and Proof-Load Test," Proc. 8th Reliability and Maintainability Conference, July 1969, pp. 375-391.

24. Yang, J.-N.,"Reliability Analysis of Structures under Periodic Proof Tests in Service," *AIAA Journal*, Vol. 14, No. 9, September 1976, pp. 1225-1234.

25. Yang, J.-N., "Optimal Periodic Proof Test Based on Cost-Effective and Reliability Criteria," *AIAA Journal*, Vol. 15, No. 3, March 1977, pp. 402-409.

26. Harris, D. O., "A Means of Assessing the Effects of Periodic Proof Testing and NDE on the Reliability of Cyclically Loaded Structures," *Journal of Pressure Vessel Technology*, Vol. 100, ASME, May 1978, pp. 150-157.

27. Nichols, R. W., "The Use of Overstressing Techniques to Reduce the Risk of Subsequent Brittle Fracture Part 1," *British Welding Journal*, Vol. 15, January 1968, pp. 21-42 and "Part 2," *British Welding Journal*, Vol. 15, February 1968, pp. 75-84.

28. Chell, G. G., Haigh, J. R., and Vitek, V., "A Theory of Warm Prestressing: Experimental Validation and the Implications for Elastic Plastic Failure Criteria," *International Journal of Fracture*, Vol. 17, No. 1, February 1981, pp. 61-81.

29. Chell, G. G., and Haigh, J. R., "The Effect of Warm Prestressing on Proof Tested Pressure Vessels," *Int. J. Press. Ves. & Piping*, Vol. 23, 1986, pp. 121-132.

30. Haigh, J. R., "Effects of Combined Warm Prestressing, Strain Ageing and Ductile Crack Growth on the Toughness and Load-bearing Capacity of a C-Mn Steel", Central Electricity Generating Board, North Western Region Scientific Services Department Report NWR/SSD/84/0012/N, 1984.

31. Chell, G. G., "The Effects of Sub-critical Crack Growth on the Fracture Behaviour of Cracked Ferritic Steels After Warm Prestressing", *Fatigue Engng. Mater. Struct.*, Vol. 9, 1986, pp. 259-274.

32. Lemaitre, J., "Local Approach to Fracture," *Eng. Fract. Mechs.*, Vol. 25, 1986, pp. 523-537.

33. Dawicke, D. S., Poe, Jr., C. C., Newman, Jr., J. C., and Harris, C. E., "An Evaluation of the Pressure Proof Test Concept for Thin Sheet 2024-T3," *Theoretical and Applied Fracture Mechanics*, Vol. 14, 1990, pp. 101-116.

34. Matejczyk, D. E., "Retardation Analytical Model to Extend Service Life," Rocketdyne Division, Rockwell International Final Report RI/RD86-217, 1986.

35. Chell, G. G., "Fatigue Crack Growth Laws for Ductile and Brittle Materials Including the Effects of Static Modes and Elastic-Plastic Deformation", *Fatigue Engng. Mater. Struct.*, Vol. 7, 1984, pp. 237-250.

36. Heald, P. T., Lindley, T. C., and Richards, C. E., "The Influence of Stress Intensity and Microstructure on Fatigue Crack Propagation in a 1% Carbon Steel," *Mat. Sci. Engng.*, Vol. 10, 1972, pp. 235-240.

37. Nix, K. J., Lindley, T. C., Knee, N., and Chell, G. G., "An Investigation of Fatigue Crack Growth in a Ductile Material at High Growth Rates," *Fat. Engng. Mater. and Struct.*, Vol. 11, 1988, pp. 205-220.

38. "ABAQUS: User's Manual," HPS Inc., 1992.

39. "ANSYS: Engineering Analysis System User's Guide," Swanson Analysis Systems Inc., 1992.

40. Miller, A. G., "Review of Limit Loads of Structures Containing Defects," *Int. J. Press. Ves. and Piping*, Vol. 32, 1988, pp. 197-327.

41. Kanninen, M. F., and Popelar, C. H., *Advanced Fracture Mechanics*, Oxford University Press, 1985.

42. Anderson, T. L., *Fracture Mechanics: Fundamentals and Applications*, 2nd Edition, CRC Press, 1995.

43. Zahoor, A., "Ductile Fracture Handbook," EPRI Report NP-6301-D, Three Volumes, 1989.

44. Wang, W.-Q. Li, A.-J., and Ding, P.-F., "The Influence of Biaxial Stresses on the Failure Assessment Curve," ASME PVP Vol. 304, Fatigue and Fracture Mechanics in Pressure Vessels and Piping, 1995 pp. 531-537.

45. PD6494:1991, "Guidance on Methods for Assessing the Acceptability of Flaws in Fusion Welded Structures," British Standards Institute, London, 1991.

46. R6, 1991, "Assessment of the Integrity of Structures Containing Defects," Milne, I., Ainsworth, R. A., Dowling, A. R., and Stewart, A. T., Central Electricity Generating Board Report Number R/H/R6-Revision 3, and Int. J. Press. Ves. and Piping, Vol. 32, 1988, pp. 1-196.

47. Bloom J. M., "Evaluation of Flaws in Ferritic Piping," ASME Code Appendix J: Deformation Plasticity Failure Assessment Diagram (DPFAD), EPRI Report NP-7492, August, 1991.

48. Buchheim, G. M., Osage, D. A., Prager, M., and Warke, W. R., "An Overview of Risk-Based Inspection Methods and User Needs for the Petrochemical Industry," ASME PVP-Vol. 261, pp. 245-256, 1993.

49. API, Draft 1 of API 579, "Recommended Practice for Fitness-For-Service," 1995.

50. Chell, G. G., "A J Estimation Scheme for Cracks at Notches," work performed as part of "Elastic-Plastic and Fully Plastic Fatigue Crack Growth," Contract NAS8-37828, NASA George C. Marshall Space Flight Center, Southwest Research Institute Project 06-5013, 1992-present.

51. Sherry, A. H., Sharples, J. K., Sanderson, D. J., Gardner, L., and Ainsworth, R. A., "Constraint Effects Within the R6 Framework: Validation by Small and Large Scale Fracture Test Results for A533B-1 Steel," ASME PVP-Vol. 304, 1995, pp. 511-529.

52. Ingham, T., and Morland, E., "Influence of Time-dependent Plasticity on Elastic-plastic Fracture Toughness," *Elastic-Plastic Fracture, 2nd Symposium*, ASTM STP 803, Vol. 1, 1983, pp. I-712-I-746.

53. ASTM E399, "Test Method for Plane Strain Fracture Toughness Testing of Metallic Materials," ASTM Standards, Section 3, *Metals Test Methods and Analytical Procedures*, 1996.

54. ASTM E740, "Practice for Fracture Testing for Surface-Crack Tension Specimens," ASTM Standards, Section 3, *Metals Test Methods and Analytical Procedures*, 1996.

55. ASTM E813, "Test Method for J_{Ic} : A Measure of Fracture Toughness," ASTM Standards, Section 3, *Metals Test Methods and Analytical Procedures*, 1996.

56. ASTM E561, "Practice for R-Curve Determination," ASTM Standards, Section 3, *Metals Test Methods and Analytical Procedures*, 1996.

57. ASTM E1152, "Test Method for Determining J-R Curves," ASTM Standards, Section 3, *Metals Test Methods and Analytical Procedures*, 1996.

58. ASTM B645, "Practice for Plane Strain Fracture Toughness Testing of Aluminum Alloys," ASTM Standards, Section 3, *Metals Test Methods and Analytical Procedures*, 1996.

59. ASTM B646, "Practice for Fracture Toughness Testing of Aluminum Alloys," ASTM Standards, Section 3, *Metals Test Methods and Analytical Procedures*, 1996.

60. NASGRO, "Fatigue Crack Growth Computer Program," Version 2.0, NASA Lyndon B. Johnson Space Center, 1994. (Version 3.0 is due for release.)

61. Dawes, M. G., Pisarski, H. G., and Squirrell, H. G., "Fracture Toughness Tests on Welded Joints," ASTM STP 995, ASTM Philadelphia, 1989, pp. II-191–II-213.

62. Orange, T. W., "Method and Models for R-Curve Instability calculations," NASA TM 100935, 1988.

63. O'Dowd, N. P., and Shih, C. F., "Family or Crack Tip Fields Characterized by a Triaxiality Parameter—I. Structure of Fields," *J. Mechs. Phys.*, Vol. 39, 1991, pp. 989-1015.

64. Dodds, R. H., Shih, C. F., and Anderson, T. L., "Continuum and Micromechanics Treatment of Constraint in Fracture," University of Illinois, Urbana, Report UILU-ENG-92-2014, 1992.

65. Ainsworth, R. A., "The Assessment of Defects in Structures of Strain Hardening Material," Engng. Fract. Mech., Vol. 19, 1984, pp. 633-642.

66. Bloom, J. M., "Deformation Plasticity Failure Assessment Diagram (DFFAD) for Materials with Non-Ramberg-Osgood Stress-Strain Curves," Presented at 1994 ASME-PVP Conference, Minneapolis, Minnesota, June, 1994.

67. Chell, G. G., McClung, R. C., and Russell, D. A., "Application of Failure Assessment Diagrams to Proof Test Analysis," ASME PVP-Vol. 304, 1995, pp.475-485.

68. Kumar, V., German, M. D., and Shih, C. F., "An Engineering Approach for Elastic- Plastic Fracture Analysis," EPRI Report NP-1931, July, 1981.

69. Orient, G., work performed as part of "Elastic-Plastic Fatigue Crack Growth," Contract NAS8-37828, NASA George C. Marshall Space Flight Center, Southwest Research Institute Project 06-5013, 1992-present.

70. Kumar, V., German, M. D., Wilkening, W. W., Andrews, W. R., deLorenzi, H. G., and Mowbray, D. F., "Advances in Elastic-Plastic Fracture Analysis," EPRI Report NP-3607, August 1984.

71. Bloom, J. M., and Lee, D. R., "Fully Plastic J-Integral Solutions for Pressurized Cylindrical Vessels Having Semi-Elliptical Surface Flaws," *Proc. Joint IAEA/CSNI Specialist Meeting on Fracture Mechanics and Verification by Large Scale Testing*, Oak Ridge, TN, October 1993, NUREG Report NUREG/CP-0131, Oak Ridge Report ORNL/TM-12413.

72. Yagawa, G., Kitajima, Y., and Ueda, H., "Three Dimensional Fully Plastic Solutions for Semi-Elliptical Surface Cracks," *Int. J. Press. Ves. and Piping*, Vol. 53, 1993, pp. 457-510.

73. Wang, Y.-Y., "Analysis of Fracture Initiation in Surface Cracked Plates," M.S. Thesis, 1988, MIT. See also Parks, D. M., and Wang, Y.-Y., "*Analytical, Numerical, and Experimental Aspects of Three Dimensional Fracture Processes,*" *AMD-Vol. 91*, 1988, ASME, pp. 19-32.

74. Miller, A. G., and Ainsworth, R. A., "Consistency of Numerical Results for Power Law Hardening Materials and the Accuracy of the Reference Stress Approximation for J," *Engineering Fracture Mechanics*, Vol. 32, 1989, pp. 233-247.

75. Wirsching, P. H., and Carlson, J. R., "Model Identification for Engineering Variables," *Journal of Engineering Mechanics*, Vol. 103, No. EM1, February 1977.

76. Joch, J., Ainsworth, R. A., Hyde, T. H., and Neale, B. K., "Fracture Parameters and Fracture Assessment for Welded Structures," presented at the International Symposium on Mis-Matching of Welds, KKSS-Research Centre Geeshacht, Germany, May 26-28, 1993.

77. Turner, C. E., "The Ubiquitous η-Factor," *Fracture Mechanics Twelfth Conference, ASTM STP 700, ASTM STP 700*, 1980, pp. 314-337.

78. Paris, P. C., Ernst, H., and Turner, C. E., "A J-Integral Approach to Development of η-Factors," *Fracture Mechanics: Twelfth Conference, ASTM STP 700*, 1980, pp. 338-351.

79. Wu, X.-R., and Carlsson, A. J., *Weight Functions and Stress Intensity Factor Solutions*, Pergamon Press, 1991.

80. Tada, H., Paris, P., and Irwin, G., *The Stress Analysis of Cracks Handbook*, 2nd Edition, Del Research Corporation, 1985.

81. Ewing, D. J. F., "Stress Intensity Factors for Plates and Shells with Long Part-Through Cracks, As Calculated by a Line Spring Model," U. K. Central Electricity Generating Board Report TPRD/L/3163/R87, August, 1987.

82. Kiefner, J. F., Maxey, W. A., Eiber, R. J., and Duffey, A. R., 1973, "Failure Stress Levels of Flaws in Pressurized Cylinders," ASTM STP 536, pp. 461-481.

83. Milne, I., and Knee, N., "Report on EGF Task Group 1 Exercise in Predicting Ductile Instability; Phase II: Experimental Cracked Pressure Vessel," Central Electricity Generating Board, Report Number TPRD/L/2771/N84, 1984.

84. Krenk, S., *Int. J. Fracture*, Vol 14., 1973, p. 123.

85. Panontin, T. L., and Hill, M. R., "The Applicability of Proof-Test Based Life Prediction to High Toughness Metal Structures," ASME PVP-Vol. 260, 1993, pp. 181-190.

86. Knee N., "Report on Phase IV on the European Fracture Group Round Robin exercise on the Prediction of Ductile Instability, CEGB Report Number TPRD/L/3043/R86 (1986).

87. Nix, K. J., Chell, G. G., Knee, N., and Lindley, T. C., "An Investigation of the Interaction Between Ductile Tearing and Fatigue in a Low Alloy Steel," *Advances in Fracture and Fatigue for the 1990's, Vol. 1: Load History Effects of Fracture Resistance*, PVP-Vol. 166, ASME, 1989, pp. 33-39.

88. Becher, P. E., and Pedersen, A., "Application of Statistical Linear Elastic Fracture Mechanics to Pressure Vessel Reliability Analysis," *Nuclear Engineering and Design*, Vol. 27, 1974, pp. 413-425.

89. Lidiard, A. B., and Williams, M., "The Sensitivity of Pressure Vessel Reliability to Material and Other Factors," *Reliability Problems of Reactor Pressure Components*, Proc. Symp. Application of Reliability Technology to Nuclear Power Plants, Vienna, Austria, October 1977, pp. 233-249.

90. Barnett, R. L., and Hermann, P. C., "Proof Testing in Design with Brittle Materials," *Journal of Spacecraft*, Vol. 2, No. 6, 1965, pp. 956-961.

91. Wu, Y.-T., Millwater, H. R., and Cruse, T. A., "An Advanced Probabilistic Structural Analysis Method for Implicit Performance Functions," *AIAA Journal*, Vol. 28, No. 9, September 1990, pp. 1663-1669.

92. Wu, Y.-T., "An Adaptive Importance Sampling Method for Structural System Reliability Analysis," *Reliability Technology*, AD - Vol. 28, T. A. Cruse, Ed., ASME, December 1992, pp. 217-231.

93. Cruse, T. A., Chamis, C. C., and Millwater, H. R., "An Overview of the NASA (LeRC)-SwRI Probabilistic Structural Analysis Program," Proc. 5th Int. Conf. Structural Safety and Reliability, (ICOSSAR), August 1989, Vol. 3, pp. 2267-2274.

94. Millwater, H. R., Wu, Y.-T., Dias, J. B., McClung, R. C., Raveendra, S. T., and Thacker, B. H., "The NESSUS Software System for Probabilistic Structural Analysis," Proc. 5th Conf. Structural Safety and Reliability (ICOSSAR), August 1989, Vol. 3, pp. 2283-2290.

95. Chell, G. G., and McClung, R. C., "Algorithms for Crack Instability," Draft Topical Report, NASA Contract NAS8-37828, Marshall Space Flight Center, SwRI Project No. 06-5013, July 1996.

96. Gates, R. S.,"The Relationship Between Load Factors and Failure Probabilities Determined from a Full Elastic-Plastic Probabilistic Fracture Mechanics Analysis," *International Journal of Pressure Vessels and Piping*, Vol. 13, 1983, pp. 155-167.

97. S. Kaiser, "On the Relation Between Stable Crack Growth and Fatigue," *Fatigue Engng. Mater. Struct.*, Vol. 6, 1983, pp. 33-55.

98. Joyce, J. A., and Culafic, V., "Characterization of Interaction Effects Between Ductile Tearing and Intense Fatigue Cycling," *Int. J. Fracture*, Vol. 36, 1988, pp. 89-100.

APPENDIX A: STATE-OF-THE-ART FRACTURE MECHANICS FOR PROOF TEST ANALYSIS

A1. STRESS ANALYSIS

Understanding the characteristics and mechanical responses of hardware during proof loading is crucial for development of successful proof testing procedures. Fracture mechanics based proof assessments depend on accurate component modeling, material characterization, and analysis to provide realistic component stresses.

Stress analyses provide the magnitudes and distributions of stresses and strains in component critical sections. These quantities are required for fracture mechanics analyses. The accuracy of the stress analyses is determined by how accurately service and proof test loading conditions are known. Structural modeling is an important consideration in the analysis of complicated structural geometries, flaws, and other features, such as welds. Unless the crack tip driving force is being evaluated from stress analysis results, the stress analysis should be performed on the flaw-free structure and be capable of defining the principal stress magnitudes and directions.

Welded sections are particularly important as sites for pre-existing or initiating flaws: there is an increased likelihood of generating processing and fabrication flaws in the weldment compared to the parent metal. Complications arise in the stress analyses of welds due to inhomogeneous material properties resulting from uneven heating and cooling, geometrical discontinuities caused by weld misfit and unflushed weld beads, remaining residual cool down stresses when no stress relief operation is performed, and strength variations that may exist between welds and the adjacent parent metal (under- and over-matching welds). These all contribute to difficulties in accurately determining both primary load, as well as residual stress, distributions at weldments.

Finite element methods provide the most versatile approach for performing numerical stress analyses, and are generally the preferred method in the analyses of complicated three-dimensional structures. Computer codes such as ABAQUS [38] and ANSYS [39] are widely available and used.

A1.1 Structural and Constitutive Modeling

Constitutive models that accurately describe material deformation responses are essential for stress analyses and the determination of fracture assessment parameters during proof and operation. Ideally, the models should have the capabilities of simulating monotonic, cyclic and time-dependent material behavior, particularly if service history effects are considered important. Changes in material deformation due to service conditions (from cyclic hardening and softening, strain aging embrittlement, etc.) may be important in the analyses of proof tests performed to support re-certification of hardware.

In practice, detailed finite element stress analyses may prove to be untenable due to time constraints and cost. In these cases a simplified stress analysis may be justified, allowing a reduction in geometrical complexity and boundary conditions to facilitate the use of coarse and/or two- dimensional finite element models, or analytical solutions. Approximate techniques should result in a conservative proof test analysis compared with the use of more sophisticated methods.

It is important to simulate the level of plastic constraint and geometric restraints that exist in the structure, as these affect deformation in the vicinity of a flaw. This is particularly the case when numerical methods are being used to evaluate fracture mechanics parameters. Factors which may significantly influence plastic constraint include local geometry (e.g. thickness, geometric discontinuities); far field state of stress (plane stress versus plane strain); far field applied loading type (tensile forces or bending moments); degree of crack tip plasticity (small scale or large scale yielding); whether the defect is submerged in a plastic enclave (crack tip yielding to free surface, potential load shedding or stress redistribution); and boundary conditions (restraints against rotation, imposed displacements).

A1.2 Categorization of Loads and Stresses

The applied loads have to be categorized as either primary (mechanical) or secondary (thermal, residual) if approximate estimation schemes are to be used to evaluate EPFM parameters. This is because primary and secondary stresses have different effects on the crack tip driving force when significant crack tip plasticity develops. (These aspects are discussed more fully in Sections A4.4 and A5.5.) Separate stress analyses should be performed to determine the different stress distributions resulting from primary and secondary loads.

A primary load (stress) is one that influences the plastic collapse load of the hardware. Plastic collapse occurs when the ductility of the material is exhausted. (Failure of a uniaxial tensile specimen by necking is an example.) Plastic collapse occurs at, or after, net section yield when a global mechanism for slip deformation has been established that enables, in principle, unlimited deformation to occur (see Section A3). (The plastic collapse load and the net section yield load are synonymous in materials with no strain hardening.) Primary stresses are produced by applied loads, such as tensile forces and moments, rotational loading, and internal pressure, and must satisfy static equilibrium (i.e., the resulting through-wall stress distributions should integrate to produce internal forces and moments that balance the applied forces and moments).

A secondary load (stress) is one that does not contribute to plastic collapse. Secondary stresses are self-equilibrated and are associated with strain and displacement controlled loading. Self-equilibrated stresses integrate to produce zero net forces and moments on the structure. Thermal and residual stresses are examples of secondary stresses. Residual stresses are the main secondary stresses likely to be present in proof tested hardware.

Displacement induced stresses and thermal stresses arising from the effects of constrained thermal expansion can give rise to net forces and moments on the cracked section which may simulate the effects of primary loads. In addition, stresses which are self-equilibrated within the structure may not be self-equilibrated within the part containing a flaw. Unfortunately, there are no easy rules for determining the stress category of borderline cases, and in many instances the categorization of the applied loads into either primary or secondary will have to be a matter of judgement by the analyst, based on taking into account that the categorization should always err on the conservative side with regard to a fracture mechanics proof test analysis.

A1.3 Residual Stresses

Residual and preload stresses are developed during fabrication, installation, surface treatment processes, and usage (local yielding). The residual/preload stresses of a component are oftentimes difficult to estimate but can have a significant effect on the calculated defect tolerance. In estimating

residual stresses, the analyst should take into consideration the limitations of mechanical stress relief (shakedown) imposed by triaxial states of stress.

Residual stresses are persistent, in the sense that they exist in the absence of primary loading, and add to static stresses during service, as well as during the proof test. Therefore, they should be accounted for in both proof test and service analyses in a consistent manner.

A1.4 Stress Redistribution

There is a potential during the proof loading for redistribution of stresses to occur in those regions of the component where the local stress is at or near yield point magnitude. These regions are normally associated with geometric discontinuities, such as sharp corners and holes, and residual welding stresses. If the component is being re-certified after being subjected to service loadings, then consideration should be given to residual stresses formed by local plasticity during operation, from severe thermal loading or local geometric discontinuities. Allowances should be made in proof test analyses for redistribution that lowers the stress in fracture critical regions as failure to do so may result in underprediction of maximum proof test survival flaws. Further considerations should include the impact of load amplitude and load type changes between proof test and operation.

A1.5 Conservative Stress Analyses

A proof test analysis will be conservative if, all else being equal, assumptions are made in the stress analysis that result in an underprediction of the stresses in fracture critical regions and/or overprediction of section size. This implies, for example, modeling of the hardware using upper bound wall thickness tolerances, possibly ignoring tensile residual stresses, and in the case of a proof test analysis performed on hardware for recertification, making adequate allowance for shakedown during service if this could have resulted in compressive stresses under proof test conditions.

In practice, the degree of conservatism that can be introduced into stress analysis is limited by the need to avoid unnecessary proof test failures, and to avoid unduly eroding the efficacy of the proof test. As such, proof test requirements should not be based upon low stressed, non-critical regions of the hardware.

A2. LINEAR ELASTIC FRACTURE MECHANICS

Since the application of linear elastic fracture mechanics (LEFM) principles to structural and proof test analyses have been addressed in other NASA documents [7-9], they are not covered in detail here.

A2.1 Stress Intensity Factors

LEFM is based on the stress intensity factor, K, which characterizes the stress and strain fields at a loaded crack tip, and also determines the elastic strain energy release rate (crack tip driving force), G, that governs the potential energy change in the loaded system due to an incremental crack advance, where

$$G = \frac{K^2}{E'} \tag{A2.1}$$

In this equation, $E'=E$ for plane stress conditions and $E'=E/(1-\nu^2)$ for plane strain conditions, where E is Young's modulus, and ν is Poisson's ratio.

K has proven a highly successful fracture mechanics parameter for predicting crack instability and sub-critical crack growth rates in situations where small scale yielding (SSY) prevails at the crack tip. However, it is now well known that LEFM fails to predict fracture behavior in situations where large scale yielding (LSY) develops. The reason is that K under-predicts the value of crack tip driving force when significant crack tip plasticity develops. However, the stress intensity factor (SIF) still plays an important role in the formulation of EPFM fracture parameters (see Section A4).

The SIF is dependent on the crack shape and size, the structural geometry, and the type of loading (specifically, K depends on the distribution of stress determined in the flaw free structure at the crack location). In general, K can be expressed in the form

$$K(a,c,\sigma(x),t,L,\theta) = \sigma\sqrt{\pi a}\ F\left(\frac{a}{t},\frac{a}{c},\frac{\sigma(x)}{\sigma},\frac{L}{t},\theta\right) \qquad \text{(A2.2)}$$

where a is the flaw depth and $2c$ its length, $\sigma(x)$ is the local variation in stress in the defect free structure as a function of position, x, σ is a convenient normalizing stress, t is the thickness of the section containing the flaw, L is a structural dimension (e.g. the radius of a cylindrical pressure vessel or a notch root), θ is an angle that locates a position on the crack front, and F is a dimensionless function, the so-called influence function. Values of F have been derived for many cracked structures and may be found in stress intensity factor handbooks. Table A2.1 provides references to sources which may prove useful for deriving SIF solutions.

A2.2 Combined Primary and Secondary Loads

The value of K is determined by only that part of the stress in the uncracked structure that acts over the area occupied by the flaw. Different loading types that result in identical stress distributions over the flaw area will produce identical K values, all other things being the same. Hence, for a given structural geometry and prescribed displacement boundary conditions, K is independent of the source of the stress: whether it originates from mechanical loading (such as pressure), body forces (such as rotation), thermal loading or residual stresses. Since K is a linear elastic parameter, the principle of linear superposition can be used to add the K contributions from different sources of loading. For example, if P represents a primary load and S a secondary load that result in local stress distributions, $\sigma(x,P)$ and $\sigma(x,S)$, respectively, then

$$K(\sigma(x,P) + \sigma(x,S)) = K(\sigma(x,P)) + K(\sigma(x,S)) \qquad \text{(A2.3)}$$

Under linear elastic conditions, fracture is determined by the value of K corresponding to all the applied loads, and it is not necessary to separate out the contributions arising from primary and secondary load sources, as is the case in elastic-plastic fracture mechanics.

Table A2.1 Available technology for determining stress intensity factors

Reference	Description
Fatigue Crack Growth Computer Program: "NASA/FLAGRO" Version 2.0, NASA, Lyndon B. Johnson Space Flight Center, Houston, Texas, May, 1994	A computer program based on fracture mechanics principles that can be used to calculate SIFs, and to run complete safe-life analyses
Stress Intensity Factors Handbook, Y. Murakami, Volumes 1, 2, and 3, Committee on Fracture Mechanics, The Society of Materials Science, Japan, 1987, published by Pergamon Press	A compendium of SIF solutions
Handbook of Stress Intensity Factors, G. C. Sih, Institute of Fracture and Solid Mechanics, Lehigh University, 1973.	A compendium of SIF solutions
The Stress Analysis of Cracks Handbook, H. Tada, P. C. Paris and G. R. Irwin, 2nd Edition, Del Research Corporation, 1985	A compendium of SIF solutions
Weight Functions and Stress Intensity Factor Solutions, X.-R. Wu and A. J. Carlsson, Pergamon Press, 1991	A compendium of weight and influence function solutions.

A3. NET SECTION YIELD LOADS

A3.1 Introduction

The value of the net section yield load for the flawed hardware is required to evaluate J using the reference stress estimation schemes described in Section A4.

The maximum safe load that a structure can support is determined by its plastic collapse, or limit load. The plastic collapse load and the net section yield load are equal for materials that behave in an elastic-perfectly plastic manner and display no strain hardening capability. The plastic collapse load can be calculated using limit analysis, which makes a number of assumptions about material behavior. These are not meant to restrict the applications of the results to real materials, but are simply there for the purpose of calculation. The assumptions are:

a) The material deforms in an elastic-perfectly plastic manner, i.e., it has no capacity to strain harden, and the ductility is infinite.

b) If the structure contains a defect then it is also assumed that it has infinite toughness so that failure from the crack tip cannot occur before the limit load is reached.

The review paper by Miller [40] also illustrates another problem related to determining the collapse loads for complex structures, namely, that these structures often require mechanisms (e.g. plastic hinges) to develop at more than one location before the structure can undergo the deformations needed to cause plastic collapse.

A3.2 Fundamental Considerations

Two theorems are generally employed to determine the plastic collapse (net section yield) load of a structure. The first gives lower bound solutions and states that a structure will not collapse if the applied forces can be balanced by a redistribution of the induced stress so that the stress nowhere exceeds the yield stress. To apply this theorem it is not necessary to invoke a collapse mechanism; i.e., a postulated system of planes on which plastic sliding occurs. This theorem has an important corollary: self-equilibrated thermal and residual stresses cannot result in plastic collapse or change the limit load since they do not produce any net forces or moments on the structure. A redistribution of stress can, therefore, always be found where the stresses are less than yield. This does not mean that local yielding cannot occur, which may have a deleterious effect on the defect tolerance of a structure if the defect is located in the locally yielded region. Furthermore, materials do not have an infinite toughness and so they are susceptible to failures in highly stressed areas before the plastic collapse load can be attained. Self-limiting stresses resulting from imposed displacements on the structure cannot lead to plastic collapse.

The second theorem gives upper bound results and states that the structure will collapse if any mechanism can be found in which the rate of internal work is less than or equal to the rate of external work done by the applied forces. This theorem ensures that the displacements at all points in the structure will be geometrically compatible with one another. Clearly, when the two theorems predict the same result, then that result is the exact solution. The first theorem is usually the easiest to apply, and it will generally produce the more accurate results if the deformation occurs in plane stress (as is the case, for example, with very thin sections). The second theorem is more accurate if the deformation takes place under plane strain conditions (e.g. as may occur in thick section components). It is conservative for service assessment purposes to assume, if in doubt, that the structure deforms in plane stress. However, for proof test applications, a conservative analysis will require the use of the upper bound theorem and the assumption of plane strain when determining net section yield loads. This is because plane strain conditions give rise to multi-axial stressing conditions which tend to suppress yielding.

A3.3 Available Solutions

The problems associated with determining plastic limit loads for complex structures may inevitably lead to the use of solutions which correspond to simplified models of the actual structure. To avoid this problem, it is possible to perform scaled-down geometrically similar model tests of the defected structure using very ductile materials to reduce unacceptable pessimism which may occur in theoretically estimating plastic collapse loads. The use of scaled-down models is possible because the limit load linearly scales with the yield stress σ_y and the dimensions of the flaw and structure. Hence, the net section yield load for the structure, P_y^*, is related to the net section yield load measured on a scaled-down geometrically similar model, P_y^{model}, by $P_y^* = P_y^{model}(wt/w_{model}t_{model})$, where w and t are the width and thickness of the structure, and w_{model} and t_{model} are the width and thickness of the scaled-down model. In order to avoid uncertainties regarding the effects of strain hardening, it is preferable to perform the model tests using materials which do not appreciably strain harden.

It is possible to estimate the limit load from the results of an elastic-plastic finite element stress analysis of the defected structure. If this approach is adopted, then a finite element computer program which has been validated for large strains should be used. To date, this method has not been widely used for determining plastic collapse loads. Both the results of model testing, and of finite element programs, will still need careful interpretation, especially if they relate to complicated three-dimensional structures.

The most useful source of net section yield loads is the review of Miller [40]. This contains solutions for a range of practical cracked structures, such as pressurized cylinders and spheres, as well as plate-like geometries, such as center and edge cracked plates. Miller's solutions are complemented by the solutions for the characteristic net section yield loads given in the Electric Power Research Institute (EPRI) elastic-plastic handbooks. References to EPRI sources of net section yield load solutions are given in Table A4.1 of Section A4.2.

The proof test analyst should be warned that many theoretically estimated net section yield loads provide lower bound solutions to the actual ones. This is because they are intended for use in assessing fracture under service conditions. A conservative proof test analysis requires a solution which is an upper bound or a good estimate of the actual net section yield load. These kinds of solutions are difficult to derive from plastic limit load theory without making assumptions that result in an unduly pessimistic solution. The hardware validation tests and supporting analysis presented in Section B4 of Appendix B demonstrates the need for net section yield loads for ductile materials that are verified by experimental test results.

A4. ELASTIC-PLASTIC FRACTURE MECHANICS: CRACK TIP DRIVING FORCE, *J*

The EPFM parameter, *J*, provides a natural extension of the concepts underpinning LEFM to situations where crack tip plasticity is important [41,42]. Under conditions of plane strain and plane stress, *J* characterizes the stress and strain fields at a yielded crack tip, and the potential energy release rate due to crack extension. Its value reduces to the value of *G* under SSY conditions, and LEFM is recovered in this fracture regime. Hence, if *J* is determined from a linear elastic analysis its value, J_e, will be related to *K* by $J_e=G=K^2/E'$.

The crack tip field characterizations of *K* and *J* provide the vital link between engineering quantities that can be evaluated using continuum mechanics, and the mechanisms which control fracture on the microstructural level. Hence, the assumption is made that the critical conditions at a loaded crack tip that initiate crack propagation correspond to critical values of *K* (in the SSY regime) and *J* (in the SSY and LSY regimes). This assumption has been verified by experimental fracture data under conditions where *K* and *J* are predicted to provide one parameter characterizations of crack tip fields. Situations where the one parameter characterization is not a valid assumption are discussed in Section A7.2 under the sub-heading "Plastic Constraint and Section Thickness."

In this section, failure criteria for brittle and ductile materials expressed in terms of *J* are defined, and relatively simple methods of determining *J* are presented. More precise numerical techniques, such as finite element analysis, can be used to obtain accurate values of *J*, but implementation of these alternatives is demanding in terms of time and cost, especially if sensitivity analyses are performed to assess the effects of uncertainties in the values of assessment data.

Table A4.1 Summary of EPRI *J* estimation scheme solutions

Crack Geometry	Load Type	Reference
Compact tension specimen	Pin loading	A
Center cracked panel	Uniform stress	A
Single edge cracked plate	Uniform stress	A
	Three-point bending	A
	Pure bending	B
	Combined tension and bending	C
Double edge cracked plate	Uniform stress	A
Cylinder with internal axial crack	Internal pressure	A
Cylinder with external axial crack		B
Cylinder with internal circumferential crack		A
Cylinder with external circumferential crack		B
Cylinder with through-wall circumferential crack	Uniform stress	C
Cylinder with through-wall circumferential crack	Pure bending	C
Single radial crack from round hole	Uniform biaxial stressing	C

A – "An Engineering Approach for Elastic-Plastic Fracture Analysis," by V. Kumar, M. D. German, C. F. Sih, EPRI Topical Report No. EPRI NP-1931, July, 1981.

B – "Estimation Technique for the Prediction of Elastic-Plastic Fracture Analysis," V. Kumar, W. W. Wilkening, W. R. Andrews, M. D. German, H. G. deLorenzi, and D. F. Mowbray, 5th and 6th Semiannual Report to EPRI, February, 1981 to January, 1982.

C – "Advances in Elastic-Plastic Fracture Analysis," V. Kumar, M. D. German, W. W. Wilkening, W. R. Andrews, H. G. deLorenzi, and D. F. Mowbray, EPRI Report NP-3607, August, 1984.

EPFM based on J is closely related to Failure Assessment Diagrams described in Section A5. These diagrams are derived from a J analysis and provide a pictorial representation of EPFM analyses that offers a number of advantages over representations that are expressed directly in terms of J. One of these is that a single diagram can be used to represent the behavior of J for arbitrary crack sizes and shapes and different loading types. Hence, diagrammatic representations of various kinds of J behaviors are often deferred until Section A5 in order to take advantage of the beneficial characteristics of Failure Assessment Diagrams.

A4.1 Failure Criteria

Brittle Materials

The onset of fracture in brittle materials occurs when the applied crack tip driving force equals the fracture toughness of the material. This failure criterion is mathematically expressed as

$$J = J_{mat} \tag{A4.1}$$

where the fracture toughness, signified as J_{mat}, is expressed in the same units as the driving force, J. The relationship of J_{mat} to various measures of fracture toughness, such as J_{IC}, is discussed in Section A7.2.

Ductile Materials

The failure criterion governing the fracture (instability) of ductile materials is more complicated than that for brittle materials because the fracture toughness does not have a unique value in the former case, but is dependent on the amount of ductile tearing that has occurred (see Figure A4.1). Hence, as the crack tip driving force (J) increases, the crack will extend by an amount such that its toughness increases to balance the increase in the driving force. This situation will not, however, continue indefinitely, and eventually the increase in driving force with further crack extension will exceed the corresponding increase in the toughness. This defines the ductile failure criterion, that is expressed mathematically as

$$J(c) = J_R(\Delta c_t) \tag{A4.2}$$

while, simultaneously, satisfying the equation

$$dJ(c)/dc = dJ_R(\Delta c_t)/d(\Delta c_t) \tag{A4.3}$$

where c is the instantaneous through crack length and J_R is the toughness corresponding to an amount of ductile tearing, Δc_t (see Section A7.2). The failure criterion expressed by equations (A4.2) and (A4.3) is shown schematically in Figure A4.1.

A4.2 J Estimation Scheme for Primary Loads

The Electric Power Research Institute (EPRI) has sponsored the development of handbooks of solutions for the elastic-plastic fracture mechanics parameter, J. These handbooks are intended to provide a compendium of J solutions similar to the many compendia that now exist for K solutions. The

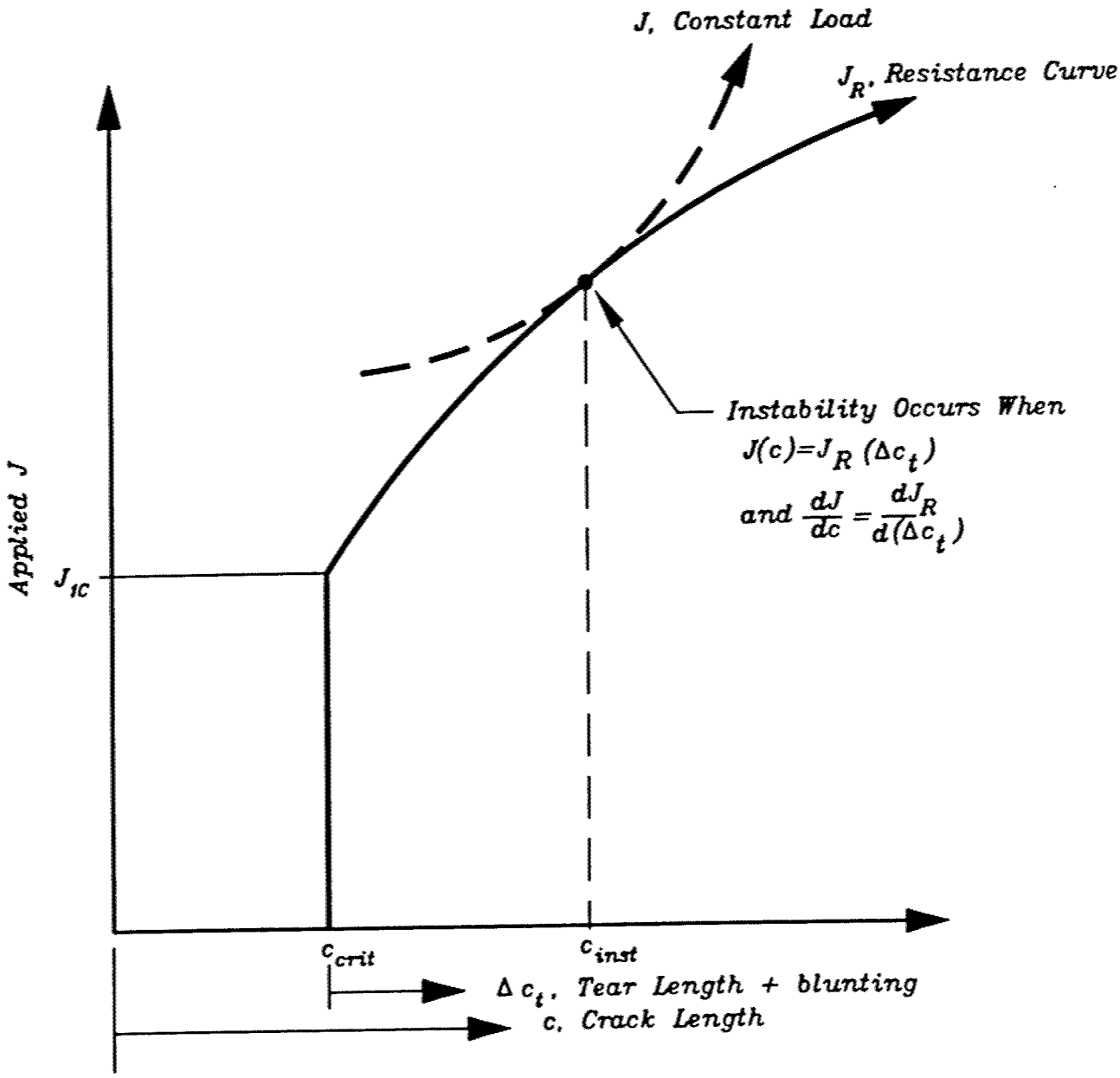

Figure A4.1 The toughness of ductile materials has no unique value but depends on the tear length, Δc_t. Instability is defined when the applied J curve as a function of crack length, c, becomes tangential to the J-R curve.

EPRI handbook scheme provides relatively simple analytical expressions for J that are applicable to defected structures subjected to primary loads and materials whose stress-strain behavior can be represented by the Ramberg-Osgood relationship. The available EPRI handbook solutions are summarized in Table A4.1. Besides these, Zahoor [43] has summarized and extended some of the EPRI solutions, but the methods used in his extrapolation and interpolation procedures are not explained, and no validation is presented to support them. Given this situation, some of his solutions should be treated with caution, and the analyst is recommended to refer back to the original EPRI handbook source solutions whenever possible.

The Ramberg-Osgood equation provides a convenient parametric form for representing the monotonic uniaxial stress-strain behavior of metallic materials and is given by

$$\frac{\epsilon}{\epsilon_o} = \frac{\sigma}{\sigma_o} + \alpha \left(\frac{\sigma}{\sigma_o} \right)^n \tag{A4.4}$$

where ϵ is the total strain (elastic plus plastic) due to the stress, σ; α, and n are material constants, and ϵ_o is a "yield" strain corresponding to the "yield" stress σ_o, where $\epsilon_o = \sigma_o/E$. The second term on the right hand side of this equation represents the component of plastic strain, ϵ^p.

In the EPRI scheme, J is resolved into elastic and plastic components, J_e and J_p, respectively, where

$$J(c,P) = J_e(c_e,P) + J_p(c,P) \tag{A4.5}$$

and J_e is a first order plastic corrected value of the linear elastic solution for J that interpolates between linear elastic and fully plastic behavior (Figure A4.2). It is given by

$$J_e(c_e,P) = J_e(c + \phi r_y,P) = \frac{K^2(c_e,P)}{E'} \tag{A4.6}$$

The effective crack depth, c_e, is defined as

$$c_e = c + \phi r_y \tag{A4.7}$$

and includes a plastic zone correction determined by the terms ϕ and r_y that are defined as

$$\phi = \frac{1}{1 + \left(\frac{P}{P_o(c)} \right)^2} \tag{A4.8}$$

$$r_y = \frac{1}{\beta \pi} \left[\frac{n-1}{n+1} \right] \left(\frac{K(c,P)}{\sigma_o} \right)^2 \tag{A4.9}$$

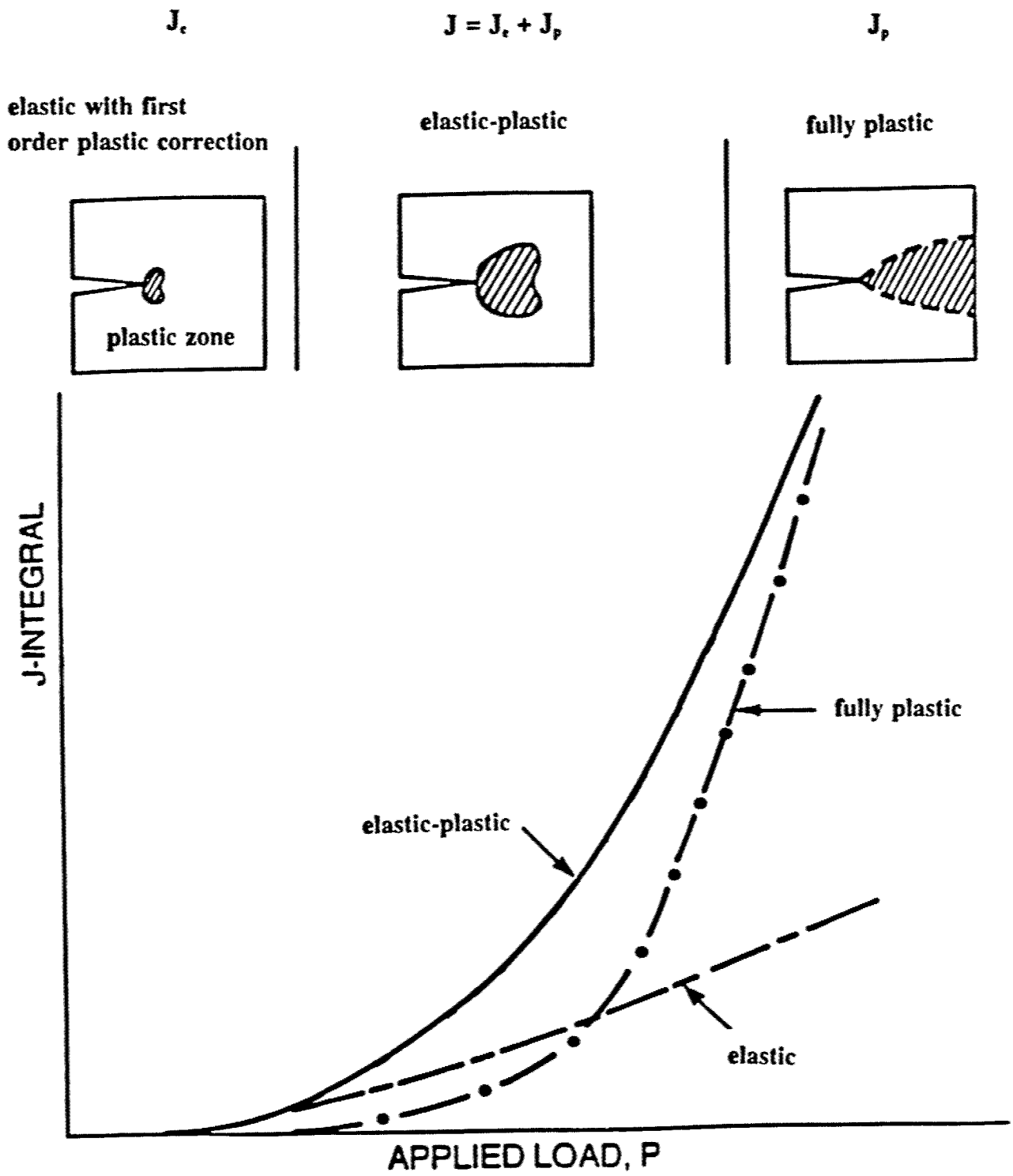

Figure A4.2 In the EPRI J estimation scheme, the expression for J is resolved into elastic, J_e, and plastic, J_p, components.

respectively, β equals 2 for plane stress, and 6 for plane strain, P is the applied load, and P_o a characteristic normalizing net section yield load. The EPRI handbooks give equations for evaluating the yield loads, P_o. This parameter depends on crack size, c, Ramberg-Osgood yield, stress, σ_o, and structural dimensions (for example, wall thickness and radius in the case of cylindrical pressure vessels). For a center crack panel of width $2w$ and thickness t containing a through crack of total length, $2c$ deforming in plane stress, $P_o=2wt(1-c/w)\,\sigma_o$.

Although the analytical forms of the plastic component, J_p, used in the EPRI scheme differ slightly depending on the cracked structure, it is convenient for illustrative purposes to adopt the following single expression for all geometries

$$J_p(c,P) = \alpha\ \epsilon_o\ \sigma_o\ (w-c)\left[\frac{c}{w}\right] h_1\left(\frac{c}{w},\frac{L}{w},n\right)\left(\frac{P}{P_o(c)}\right)^{n+1} \tag{A4.10}$$

where w is the section width and the values of the function h_1 are tabulated in the EPRI handbooks for various structures, and values of c/w and n (see Table A4.1). The parameter L represents a characteristic structural dimension, such as the mean radius of a cylinder.

By using so-called reference stress methods (see Section B1 in Appendix B) it is possible to express J in the following approximate but more general form

$$J(c,P) = J_e(c_e,P) + V^*\alpha\ J_e(c,P)\left[\frac{P}{P_o^*(c)}\right]^{n-1} \tag{A4.11}$$

where P_o^* is the load at net section yield evaluated using the Ramberg-Osgood yield stress, σ_o. In general, P_o^* will not equal the EPRI normalizing yield load, P_o, although it may have a form very similar to it. $V^*=\mu V$, where V is a dimensionless "structural" parameter that, in general, has a value of around 1, and $\mu=1$ for plane stress, and $\mu=(1-\nu_p^2)/(1-\nu_e^2)$ for plane strain, where ν_e and ν_p are elastic and plastic values of Poisson's ratio, ν, respectively. For metals, ν_e has a value usually in the range 0.28-0.30, and $\nu_p=0.5$.

In the absence of more precise solutions, equation (A4.11) is recommended for calculating J in fracture mechanics analyses of Ramberg-Osgood materials subjected to primary loading. If the material stress-strain curve cannot be adequately represented by a Ramberg-Osgood equation, but instead, is represented in graphical or tabular form, then the following form for J is recommended

$$J(c,P) = J_e(c_e,P) + V^*\ J_e(c,P)\left[\frac{E\,\epsilon^p_{ref}}{\sigma_{ref}}\right] \tag{A4.12}$$

where the reference stress, σ_{ref}, is defined as

$$\sigma_{ref} = \left[\frac{P}{P_o^*}\right]\sigma_o \tag{A4.13}$$

and the reference plastic strain, ϵ_{ref}^p, is the uniaxial plastic strain corresponding to a uniaxial stress equal to σ_{ref}.

In an arbitrary stress-strain relationship, the strain hardening exponent, n, appearing in the evaluation of c_t is no longer explicitly defined as it is in the Ramberg-Osgood equation. In this case, the exponent n should be determined from fitting a power law stress-strain curve of the form:

$$\frac{\epsilon}{\epsilon_o} = \frac{\sigma}{\sigma_o}, \ \sigma \le \sigma_o, \ \frac{\epsilon}{\epsilon_o} = \frac{\sigma}{\sigma_o} + \alpha\left(\frac{\sigma - \sigma_o}{\sigma_o}\right)^n, \ \sigma > \sigma_o \tag{A4.14}$$

to the plastic strains in the range $0.0 \le \epsilon^p \le 0.004$, which is twice the plastic strain corresponding to a stress equal to the 0.2% yield stress. Since the expression for c_t is based on small scale yielding theory, this strain range should be representative of the strains likely to be generated at the crack tip plastic zone under conditions of contained plasticity.

Values of the dimensionless parameter V are given in Table A4.2 and were derived from a statistical analysis of finite element J_p solutions for a large number of cracked geometries (see Section B1.2 of Appendix B). The lower and upper bound values in the table correspond to minus and plus two standard deviations from the mean, respectively.

Table A4.2 Recommended value of V for use in fracture mechanics applications
$V^* = \mu V$, where $\mu = 1$ for plane stress and $\mu = (1 - \nu_p^2)/(1 - \nu_e^2)$ for plane strain

Statistical Relevance	V
Median Value	1.169
Lower bound (Proof Test Applications)	0.741
Upper bound (Service Applications)	1.873

Methods of estimating K, and hence J_e, and the net section yield load, P_o^*, are discussed in Sections A2 and A3, respectively.

A4.3 Treatment of Stress Concentrators (Geometrical Discontinuities)

Equations (A4.11) and (A4.12) are also applicable to cracks emanating from stress concentrators, such as notches and other geometrical discontinuities. In these cases, the effect of the stress gradient at

the concentrator is incorporated into the evaluation of J_e, but the net section yield load, P_o^*, should be evaluated for an extended through crack length, c_{ext}, equal to the depth of the discontinuity plus the length of the crack (Figure A4.3). For example, if a through edge crack emanates from an edge notch of depth, D_n, then

$$c_{ext} = D_n + c \tag{A4.15}$$

and equation (A4.11) becomes

$$J(c,P) = J_e\left(c_e,P\right) + V^* \alpha\, J_e(c,P) \left[\frac{P}{P_o^*(c_{ext})}\right]^{n-1} \tag{A4.16}$$

where c_e is defined in equation (A4.7).

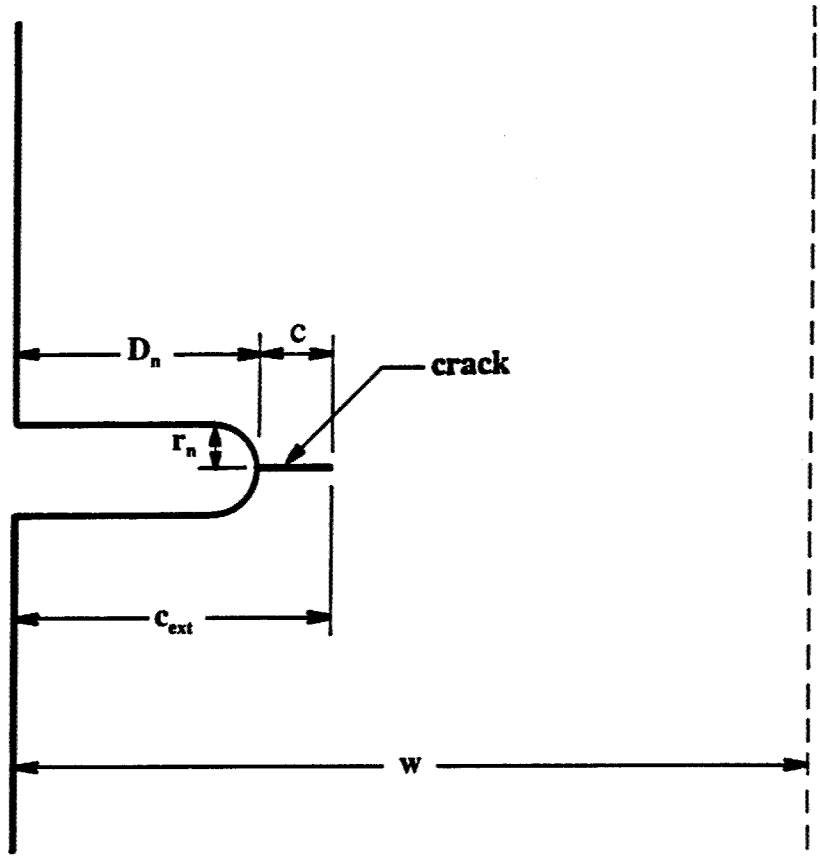

Figure A4.3 Schematic showing the nomenclature used to describe the dimensions associated with a flaw at a stress concentrator.

The value of J_e should be evaluated from a linear elastic stress analysis, as equation (A4.16) automatically incorporates the effects of plastic deformation that can occur at a stress concentrator in the absence of a flaw. The behavior of J for cracks at geometrical discontinuities is discussed further in terms of Failure Assessment Diagrams in Section (A5.4).

A4.4 Treatment of Combined Primary and Secondary Loads

In LEFM, the stress intensity factor, $K(P+S)$, for combined primary and secondary loading is simply the linear sum of the stress intensities evaluated separately. Hence,

$$J_e(c,P+S) = \frac{K^2(c,P+S)}{E'} = \frac{[K(c,P)+K(c,S)]^2}{E'} \tag{A4.17}$$

where P and S signify primary and secondary loads, respectively. However, the effect of combined loading on J is more complicated in EPFM. Although secondary loads contribute fully to J in the linear elastic regime, as shown by equation (A2.3), and they can have a significant effect on the value of J in the elastic-plastic fracture regime below net section yield ($P<P_o^*$), their influence on fracture diminishes in the plastic regime after net section yield ($P>P_o^*$). This is because self-equilibrated secondary stresses are normally induced by prescribed strains and displacements that are effectively wiped out by the development of large scale yielding, resulting in a reduction and possibly elimination of the corresponding secondary stresses.

The EPRI scheme addresses this problem by including the secondary loading only in the first order plastic term, $J_e(c_e)$, and not in J_p, which is determined only by the primary load. This scheme is recommended for use in proof test analysis because it is relatively easy to implement, and because it captures the main aspects of crack tip plasticity for combined primary and secondary loading. The combined loading expression for J is

$$J(c,P+S) = J_e\left(c_e,P+S\right) + V^* \alpha\, J_e(c,P)\left[\frac{P}{P_o^*(c)}\right]^{n-1} \tag{A4.18}$$

where

$$J_e\left(c_e,P+S\right) = \frac{K^2(c_e,P+S)}{E'} \tag{A4.19}$$

and $c_e = c + \phi r_y$, where ϕ is given by equation (A4.8) and r_y by equation (A4.9) with $K(c, P+S)$ replacing $K(c, P)$. Validation substantiating this approach is presented in Section B1.4.

Note that J_e is evaluated using a linear elastic analysis and plastic relaxation and re-distribution of the secondary stress is not explicitly accounted for in the scheme. This has two ramifications that the proof test analyst should be aware of. First, under some circumstances, the proposed scheme could result in an overestimation of J if the combined values of the linear elastic primary and secondary stresses significantly exceeds the yield stress, resulting in underprediction of the largest flaw capable of surviving

the proof test. Absent an accurate elastic-plastic solution for J, the rules illustrated in Table A4.3 are suggested for deriving an approximate combined stress distribution, $\sigma(x, P+S)$, for use in evaluating J_e in the J estimation scheme. The proposed simple method makes no allowance for multiaxial stressing.

Table A4.3 Approximate combined elastic-plastic stress for evaluating $J_e(c_e, P+S)$

Linear Elastically Derived Stresses		**Combined Stress, $\sigma(x, P+S)$**
Total Stress	**Primary Stress**	
$\sigma(x, S)+\sigma(x, P)\leq\sigma_y$	$\sigma(x, P)$=any value	$\sigma(x, S)+\sigma(x, P)$
$\sigma(x, S)+\sigma(x, P)>\sigma_y$	$\sigma(x, P)\leq\sigma_y$	σ_y
$\sigma(x, S)+\sigma(x, P)>\sigma_y$	$\sigma(x, P)>\sigma_y$	$\sigma(x, P)$

Second, the use of linear elastic stress analysis means that the calculated value of J is a function of the instantaneous values of P and S and is not dependent on the load path taken to attain these values. A load history dependence will be apparent in the instantaneous value of J if J_e is evaluated using a combined stress distribution derived from elastic-plastic stress analysis, as this distribution will depend on load path.

The effects of combined loading on elastic-plastic fracture behavior are illustrated in terms of Failure Assessment Diagrams in Section (A5.5).

A4.5 Treatment of Combined Primary Loads

The extension of the J estimation scheme to combined primary loading is relatively straightforward. If the two loads are P_1 and P_2, and $\lambda = P_2/P_1$ then J can be evaluated from the expression

$$J(c,P_1,\lambda) = J_e(c_e,P_1,\lambda) + V^* \alpha\ J_e(c,P_1,\lambda) \left[\frac{P_1}{P_o^*(c,P_1,\lambda)}\right]^{n-1} \qquad \text{(A4.20)}$$

where $P_o^*(c,P_1,\lambda)$ is the net section yield load for the combined loading expressed in terms of the value of P_1 at net section yield.

As for the case of combined primary and secondary loads, the value of J calculated from equation (A4.20) is a function only of the instantaneous values of P_1 and λ and not on the load path.

A4.6 Treatment of Multiaxial Applied Stresses

In many fracture mechanics analyses the effects of multiaxial stressing are not considered. Combined tensile, shear and torsional loading gives rise to mixed Mode I, Mode II and Mode III loading, as discussed in Section (A6.4). In this section, the problem of multiaxial stressing due to tensile principal stresses that load the crack under linear elastic conditions only in Mode I is addressed. An example of this is an axial crack in a pressurized cylinder. The three principal stress components in this case are the hoop stress (which provides the Mode I loading), the axial stress, and the radial through wall stress.

There are two aspects which need to be considered in the formulation of a J estimation scheme for multiaxial stresses: the effect of the linear elastic component of J, and the effect on the net section yield load. Considering the former, the principal stress normal to the plane of the crack produces Mode I loading, and the other two components of the principal stresses act parallel to the crack plane and do not influence the stress intensity factor and hence J_e. However, care should be taken that the effects of multiaxial stressing are adequately taken into account in determining the Mode I stress component. For example, the stress distribution at a hole is significantly different under nominal uniaxial stressing than the distribution under biaxial stressing.

Multiaxial loading can have a significant effect on the net section yield load, P_o^* and this should be adequately taken into account. For example, for a center cracked panel of width $2w$ and thickness t containing a crack of total length $2c$ subjected to biaxial stressing (where the stress component σ_2 is an in-plane stress) and deforming in plane stress

$$P_o^*(c,\sigma_1,\lambda) = \frac{P_o^*(c,\sigma_1,\lambda=0)}{\left[1+\lambda^2(b/w)^2-\lambda(b/w)\right]^{\frac{1}{2}}} \tag{A4.21}$$

where $b=w-c$ and $P_o^*(c,\sigma_1,\lambda=0)=2bt\sigma_o$ and $\lambda=\sigma_2/\sigma_1$ [44].

The following is an example J estimation scheme for biaxial tensile loading where the principal stress normal to the crack plane is σ_1, the component parallel to the plane is σ_2, and $\lambda=\sigma_2/\sigma_1$

$$J(c,\sigma_1,\lambda) = J_e(c_e,\sigma_1,\lambda) + V^*\alpha\, J_e(c,\sigma_1)\left[\frac{P_1}{P_o^*(c,\sigma_1,\lambda)}\right]^{n-1} \tag{A4.22}$$

where P_1 is the applied load corresponding to the stress, σ_1. The dependence of J_e on λ is through the dependence of c_e on P_o^*. Validation of equation (A4.22) is presented in Section B1.5 in terms of Failure Assessment Diagrams.

A4.7 Treatment of Flaws with Multiple Degrees of Freedom (DOF)

Flaws that have one degree of freedom (DOF) can be characterized for analysis purposes by a single value for the crack tip driving force. An example of a one DOF flaw is a through crack subjected to uniform tension. The crack tip driving force for two DOF cracks (such as surface flaws) varies with position around the crack front. In these cases it is usual to use two crack tip driving force values to characterize directionally dependent flaw growth rates and shape changes during crack extension, and for use in failure criteria. Crack driving forces are normally evaluated at the deepest point on the surface crack, and at a location on the crack front at or near the surface.

The recommended J formulation for these cases is not significantly different from the estimation scheme for one DOF flaws. The differences relate to the use of the appropriate J_e for each crack tip position, and the manner in which the first order plastic correction is applied. In general, P_o^* appears to

be reasonably independent of crack front position. The values of V^* given in Table (A4.2) are still applicable, as their derivation included results for multiple DOF flaws. Hence, as an example, the recommended J for a surface crack subjected to primary loading is of the form

$$J(a,c,P,\theta) = J_e(a_e,c_e,P,\theta) + V^*(\theta)\,\alpha\, J_e(a,c,P,\theta)\left[\frac{P}{P_o^*(a,c)}\right]^{n-1} \tag{A4.23}$$

where a is the depth of the flaw, c is half the surface length, the angle θ is 90° at the deepest point and 0° at the surface point on the crack, and the effective flaw size to be used in the first order plastic correction is defined as a semi-elliptical defect with dimensions

$$a_e = a + \phi r_y^a \;,\; c_e = c + \phi r_y^c \tag{A4.24}$$

where superscripts a and c refer to positions on the surface flaw corresponding to the deepest point ($\theta = 90°$) and surface point ($\theta = 0°$), respectively.

$$\phi = \frac{1}{1 + \left(\dfrac{P}{P_o^*(a,c)}\right)^2} \tag{A4.25}$$

and

$$r_y^a = \frac{1}{\beta^a \pi}\left[\frac{n-1}{n+1}\right]\left(\frac{K(a,c,P,\theta = 90°)}{\sigma_o}\right)^2 \tag{A4.26}$$

$$r_y^c = \frac{1}{\beta^c \pi}\left[\frac{n-1}{n+1}\right]\left(\frac{K(a,c,P,\theta = 0°)}{\sigma_o}\right)^2 \tag{A4.27}$$

where $\beta^a = 6$, and $\beta^c = 2$, in recognition that the deepest point will be in near plane strain deformation under small scale yielding (SSY) conditions, and the surface point will be in plane stress. Similarly, $V^*(\theta=90°)$ is the appropriate plane strain value of V^*, and $V^*(\theta=0°)$ is the appropriate plane stress value, where the constraint effect is included in the value of μ (see Table A4.2).

A4.8 Treatment of Welds

The analysis of flaws in welds presents a number of difficulties associated with material inhomogeneity and uncertainties in the value of residual stresses. If the residual stress distribution is known, then the effect of these secondary stresses can be accounted for in a proof test analysis by following the procedures described in Section A4.4. The effect of material inhomogeneity on J is more difficult to assess, and will be dependent on whether the weld is over-matched (has a higher yield stress than the base metal) or under-matched (is softer than the base metal). The problem of dealing with welds is aggravated by the potential for crack tip plasticity to spread from the weld metal into the base metal (and vice versa). This will depend not only on the relative tensile properties of the weld and base metals, but also on the thickness and shape of the weld, and the location of the crack within or adjacent to it. Most welds are over-matched, so this situation will be addressed first.

For a given applied load and crack size, the value of J decreases as the yield stress increases since a high yield stress will suppress crack tip yielding. Conversely, the value of J will increase as the yield stress decreases. A conservative proof test analysis for a flaw in an over-matched weld can be performed by assuming that the crack tip plastic zone remains totally within the weld and the value of J is determined by the tensile properties of the weld. Conversely, a conservative service analysis can be performed by assuming that the first order plastic correction to J_e is determined by the weld properties (because the plastic zone size will be relatively small and remain in the weld), but the fully plastic component, J_p, is determined by the softer base metal (because this is controlled by the large scale spread of plasticity into the base metal where the lower yield stress will promote yielding over a greater area). This situation is reversed if the weld is under-matched. In this case, a proof test analysis should be performed assuming that the first order plastic correction J_e is determined by weld tensile properties, and the base properties determine the fully plastic component, J_p. In a service analysis of an under-matched weld, it should be assumed that the plastic zone always remains in the weld and the value of J_e and J_p are both determined by the weld metal yield stress.

These recommendations are summarized by the equation below

$$J(c,P) = J_e(c_e[M_1],P) + V^* \alpha^{M_2} J_e(c,P) \left[\frac{P}{P_e^* \left(\sigma_e^{M_2} \right)} \right]^{\left(n^{M_2} - 1 \right)} \qquad \text{(A4.28)}$$

where M_1 and M_2 signify the material tensile properties (either weld or base metal) that are to be used in the evaluation of the first order plastic correction, J_e, or the fully plastic component, J_p, respectively. The materials signified by M_1 and M_2 for proof test and service analyses of over-matched and under-matched welds are specified in Table A4.4.

It is emphasized that only limited validation is available to substantiate these recommendations (see Section B1.6) and they are predominantly based on engineering judgement. They should only be used when circumstances prevent a more detailed elastic-plastic fracture mechanics analysis from being performed.

Table A4.4 Recommended tensile properties to be used in the evaluation of J for cracks in over-matched and under-matched welds

Analysis Type	Over-matched		Under-matched	
	First Order Plastic Correction Material M_1	Fully Plastic Solution Material M_2	First Order Plastic Correction Material M_1	Fully Plastic Solution Material M_2
Cracks in the Weld				
Proof Test	weld	weld	weld	base
Service	weld	base	weld	weld
Cracks at the Weld/Base Metal Interface				
Proof Test	weld	weld	base	base
Service	base	base	weld	weld

As an example of the application of these recommendations, the following equation represents an approximate expression for J for a flaw in the under-matched weld of a proof tested component subjected to a primary load

$$J(c,P) = J_e\left(c_e\left[\sigma_o^{weld}, n^{weld}, P_o^*\left(\sigma_o^{weld}\right)\right], P\right) + V^* \alpha^{base} J_e(c,P)\left[\frac{P}{P_o^*\left(\sigma_o^{base}\right)}\right]^{(n^{base}-1)} \quad \text{(A4.29)}$$

Cracks that are on or very near the boundary between the weld and base metals are special cases that require a different treatment. This region can be microstructurally complex due to the influence of the heat affected zone. In these cases the following conservative approach can be adopted. If the weld is over-matched then evaluate J for proof test analysis using the weld metal tensile properties, and use the base metal properties for service assessments. Conversely, if the weld is under-matched then use the base metal properties for proof test analysis and weld metal properties for service assessments. This approach is summarized in Table A4.4. It is emphasized that this conservative recommendation for the treatment of cracks at weld and base metal interfaces is based solely on engineering judgement.

A4.9 A Simplified Approach: Material Specific *J* Estimation Scheme

Under some circumstances it may be possible to formulate the J estimation scheme in such a way that the dependence on structural features, crack size and shape, and load type is minimized. The advantages of this are a failure curve that is a function predominantly of material stress-strain behavior that can be applied to any structural, crack and loading configuration (see Section A5.10).

The J estimation scheme for primary loads given by equation (A4.11) is

$$J(c,P) = J_e(c,P)\left[\frac{J_e(c_e,P)}{J_e(c,P)} + V^* \alpha \left(\frac{P}{P_o^*}\right)^{n-1}\right] \tag{A4.30}$$

For the same load ratio P/P_o^*, equation (A4.30) relates $J_p(c,P)$ to $J_e(c,P)$ and a term that contains structural, crack, and load dependencies only through the ratio $J_e(c_e,P)/J_e(c,P)$. To remove these dependencies, structural integrity procedures such as the widely used document PD6493:1991 [45] and its precursor, R6 [46], assume that the ratio can be represented by the approximate form

$$\frac{J_e(c_e,P)}{J_e(c,P)} = \left(1 + \frac{\frac{1}{2}\left(\frac{P}{P_o^*}\right)^2}{1 + \alpha\left(\frac{P}{P_o^*}\right)^{n-1}}\right)$$

Substituting this into equation (A4.30) results in the following J estimation scheme for Ramberg-Osgood materials

$$J(c,P) = J_e(c,P)\left[1 + \frac{\frac{1}{2}\left(\frac{P}{P_o^*}\right)^2}{1 + \alpha\left(\frac{P}{P_o^*}\right)^{n-1}} + V^* \alpha \left(\frac{P}{P_o^*}\right)^{n-1}\right] \tag{A4.31}$$

and the equivalent equation for arbitrary stress-strain behavior is

$$J(c,P) = J_e(c,P)\left[1 + \frac{\frac{1}{2}\left(\frac{P}{P_o^*}\right)^2}{E\epsilon_{ref}/\sigma_{ref}} + V^* \left(E\epsilon^p_{ref}/\sigma_{ref}\right)\right] \tag{A4.32}$$

These equations are referred to here as the material specific J estimation scheme because for cracked geometries subjected to the same load ratios, P/P_o^*, they relate $J(c,P)$ to $J_e(c,P)$ and a term that is a function of material tensile properties since, for a conservative proof test or service analysis the value of V^* is independent of the structure being assessed (see Table A4.2). As will be seen in Section A5.10, equations (A4.31) and (A4.32) result in Failure Assessment Diagrams which are functions only of a material's stress-strain behavior.

The material specific J estimation scheme is mainly applicable to cracks emanating from smooth surfaces that are subjected to primary loading. However, it can also be applied to estimating J values at stress concentration features, provided that the crack depth is comparable to or greater than the root radius of the notch. The laboratory and hardware verification analyses presented in Sections B2, B3, B4, and B5 are all based on equation (A4.31).

A4.10 Effects of Plastic Constraint on *J*

The influence of plastic constraint on J is difficult to quantify not only because the degree of constraint can vary from structure to structure, and from load type to load type, but also because it can vary with the level of the applied load and whether the crack tip is undergoing SSY or LSY. The influence of constraint and the way it is characterized will also change according to whether the material fails by a brittle or ductile mechanism. In addition, the current state of EPFM technology is not at the stage where explicitly incorporating plastic constraint effects into a J estimation scheme is routine. Given this situation, it is presently recommended that the proof test analyst take advantage of existing J solutions and estimation schemes, and include the effect of plastic constraint in EPFM analyses through its effect on fracture toughness values derived from testing specimens that simulate, or under-estimate, the plastic constraint likely to be found in the hardware. (For conservative service assessment, test specimens should over-estimate the plastic constraint in the structure. See Sections A7.2 and A7.4.)

A4.11 Summary of Recommended *J* Estimation Schemes

A summary of J estimation formulae is given in Table A4.5. The following data are needed to implement the J estimation schemes:

- the applied proof load(s) (e.g. pressure, tensile force)
- the through-wall stress distribution normal to the plane containing the assessed crack corresponding to the proof load(s)
- the through-wall stress distribution normal to the plane containing the assessed crack corresponding to any secondary load (such as residual stresses)
- postulated or observed flaw shapes and sizes
- stress intensity factor solutions corresponding to the proof and secondary loads
- net section yield loads corresponding to the proof load(s)
- uniaxial stress-strain data for base metal and/or weld metal
- the through-wall stress distribution parallel to the plane containing the assessed crack corresponding to the proof load(s) (only necessary for biaxial loading)

Table A4.5 J estimation formulae

Stress-strain Curve: Ramberg-Osgood Equation: $\frac{\varepsilon}{\varepsilon_o} = \frac{\sigma}{\sigma_o} + \alpha\left(\frac{\sigma}{\sigma_o}\right)^n$

Primary Load, P

$$J(c,P) = J_e(c_e,P) + V^* \alpha\, J_e(c,P)\left[\frac{P}{P_o^*(c)}\right]^{n-1} \qquad (1)$$

Values of V^* are given in Table A4.2.

Primary Load, P and Stress Concentrator

$$J(c,P) = J_e(c_e,P) + V^* \alpha\, J_e(c,P)\left[\frac{P}{P_o^*(c_{eff})}\right]^{n-1} \qquad (2)$$

$c_{eff}=D_n+c$

Combined Primary Load, P, and Secondary Load, S

$$J(c,P+S) = J_e(c_e,P+S) + V^* \alpha\, J_e(c,P)\left[\frac{P}{P_o^*(c)}\right]^{n'-1} \qquad (3)$$

Combined Primary Loads, P_1 and P_2

$$J(c,P_1,\lambda) = J_e(c_e,P_1,\lambda) + V^* \alpha\, J_e(c,P_1,\lambda)\left[\frac{P_1}{P_o^*(c,P_1,\lambda)}\right]^{n-1}, \quad \lambda = \frac{P_2}{P_1} \qquad (4)$$

Table A4.5 (continued) J estimation formulae

Biaxial Stresses, σ_1 and σ_2

$$J(c,\sigma_1,\lambda) = J_e(c_e,\sigma_1,\lambda) + V^* \alpha J_e(c,\sigma_1)\left[\frac{P_1}{P_o^*(c,\sigma_1,\lambda)}\right]^{n-1}, \quad \lambda = \frac{\sigma_2}{\sigma_1} \tag{5}$$

Flaws with Two Degrees of Freedom

$$J(a,c,P,\theta) = J_e(a_e,c_e,P,\theta) + V^*(\theta)\,\alpha\, J_e(a,c,P,\theta)\left[\frac{P}{P_o^*(a,c)}\right]^{n-1} \tag{6}$$

Flaws in Welds

$$J(c,P) = J_e(c_e[M_1],P) + V^*\,\alpha^{M_2} J_e(c,P)\left[\frac{P}{P_o^*\left(\sigma_o^{M_2}\right)}\right]^{\left(n^{M_2}-1\right)} \tag{7}$$

M_1 and M_2 are defined in Table A4.4.

Material Specific

$$J(c,P) = J_e(c,P)\left[1+\frac{\frac{1}{2}\left(\frac{P}{P_o^*}\right)^2}{1+\alpha\left(\frac{P}{P_o^*}\right)^{n-1}} + V^*\,\alpha\left(\frac{P}{P_o^*}\right)^{n-1}\right] \tag{8}$$

Table A4.5 (continued) J estimation formulae

Stress-strain Curve: Arbitrary Relationship

Primary Load, P

$$J(c,P) = J_e(c_e,P) + V^* J_e(c,P) \left[\frac{E\epsilon^p_{ref}}{\sigma_{ref}}\right] \tag{9}$$

Values of V^* are given in Table A4.2 and $\sigma_{ref} = \frac{P}{P_e^*}\sigma_e$.

The strain hardening exponent, n, appearing in the evaluation of c_e is determined from fitting a power law stress-strain curve of the form:

$$\frac{\epsilon}{\epsilon_e} = \frac{\sigma}{\sigma_e}, \ \sigma \le \sigma_e, \ \frac{\epsilon}{\epsilon_e} = \frac{\sigma}{\sigma_e} + \alpha\left(\frac{\sigma - \sigma_e}{\sigma_e}\right)n, \ \sigma > \sigma_e$$

in the plastic strain range $0.0 \le \epsilon^p \le 0.004$.

Primary Load, P and Stress Concentrator

$$J(c,P) = J_e(c_e,P) + V^* J_e(c,P) \left[\frac{E\epsilon^p_{ref}}{\sigma_{ref}(c_{ext})}\right] \tag{10}$$

$c_{ext}=D_n+c$

Combined Primary Load, P, and Secondary Load, S

$$J(c,P+S) = J_e(c_e,P+S) + V^* J_e(c,P) \left[\frac{E\epsilon^p_{ref}}{\sigma_{ref}}\right] \tag{11}$$

Combined Primary Loads, P_1 and P_2

$$J(c,P_1,\lambda) = J_e(c_e,P_1,\lambda) + V^* J_e(c,P_1,\lambda) \left[\frac{E\epsilon^p_{ref}}{\sigma_{ref}(P_1,\lambda)}\right], \ \lambda = \frac{P_2}{P_1} \tag{12}$$

Biaxial Stresses, σ_1 and σ_2

$$J(c,\sigma_1,\lambda) = J_e(c_e,\sigma_1,\lambda) + V^* J_e(c,\sigma_1) \left[\frac{E\epsilon^p_{ref}}{\sigma_{ref}(\sigma_1,\lambda)}\right], \ \lambda = \frac{\sigma_2}{\sigma_1} \tag{13}$$

Table A4.5 (continued) J estimation formulae

Flaws with Two Degrees of Freedom

$$J(a,c,P,\theta) = J_e(a_e,c_e,P,\theta) + V^*(\theta)\,J_e(a,c,P,\theta)\left[\frac{E\,\epsilon^p_{ref}}{\sigma_{ref}(a,c)}\right] \tag{14}$$

Flaws in Welds

$$J(c,P) = J_e(c_e[M_1],P) + V^*\,J_e(c,P)\left[\frac{E\,\epsilon^p_{ref}}{\sigma_{ref}}\right]^{M_2} \tag{15}$$

M_1 and M_2 are defined in Table A4.4.

Material Specific

$$J(c,P) = J_e(c,P)\left[1 + \frac{\frac{1}{2}\left(\frac{P}{P_o^*}\right)^2}{\left[\frac{E\,\epsilon_{ref}}{\sigma_{ref}}\right]} + V^*\left[\frac{E\,\epsilon^p_{ref}}{\sigma_{ref}}\right]\right] \tag{16}$$

A5. ELASTIC-PLASTIC FRACTURE MECHANICS: FAILURE ASSESSMENT DIAGRAMS (FADs)

A5.1 Background

The Failure Assessment Diagram (FAD) approach is now a well established EPFM technology in Europe and also in a number of industries in the United States. The pragmatic basis of the approach has helped promote its adoption for use in assessing the structural integrity of flawed components. In the United States the approach has been included in ASME Section XI as Code Case N494 [47], and in the fitness-for-service methodology developed by the petrochemical industry [48,49]. FADs form the basis of the assessment of fracture behavior in the document PD6493:1991, "Guidance on Methods for Assessing the Acceptability of Flaws in Fusion Welded Structures" [45], that is widely used in the States and abroad.

A FAD consists of two axes and a failure curve (Figure A5.1). The abscissa, labelled L_r, measures the nearness of a defected structure to failure by plastic collapse under the specified loads. Plastic collapse is a mode of fracture usually associated with ductile structural fracture. The ordinate, labelled K_r, measures the nearness of the defected structure to failure under linear elastic fracture conditions. These conditions are usually associated with brittle structural fractures. The failure curve represents a

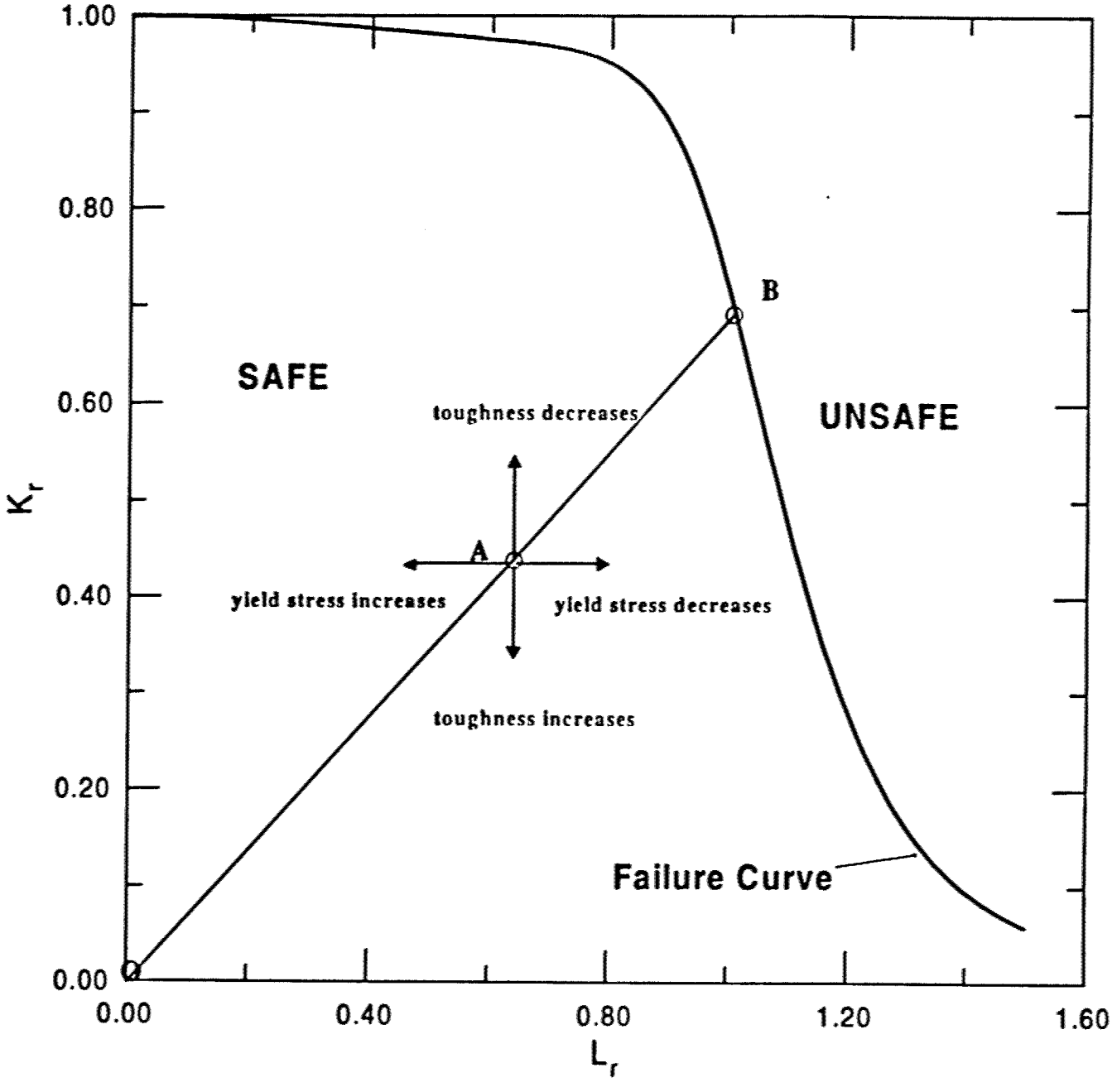

Figure A5.1 A Failure Assessment Diagram (FAD) showing a failure curve, the safe and unsafe regions, assessment points (A and B), and the result of varying toughness and yield stress on the position of an assessment point. The critical value of the load, *P*, corresponding to the assessment point A is readily obtained as (OB/OA)P.

failure criterion, and separates the FAD into "safe" and "unsafe" regions. In essence, the failure curve interpolates between linear elastic and fully plastic fracture criteria. An assessment point consisting of calculated values of L_r and K_r is plotted on the FAD (point A in Figure A5.1) and the integrity of the structure is judged by the location of the point with respect to the failure curve.

The FAD approach that is recommended for use in this proof test guidelines document differs from the approach adopted elsewhere. One of the reasons for this departure is that in a proof test analysis the meaning of conservative assessment data is different from the meaning in a service analysis. The FAD approach was, and is continuing to be, developed as a failure avoidance method for use in service analyses. Another reason is that the results of recent finite element elastic-plastic analyses of cracks at stress concentrators performed in another NASA sponsored program [50] indicate that the current FAD technology needs to be modified to allow for the influence of localized yielding in the structure, such as can occur at notches and other geometrical discontinuities where cracks may be present.

FADs provide a convenient graphical way of representing the results of a fracture mechanics analysis based on J. Although they can be used to graphically perform either a brittle or ductile fracture analysis, it is often more convenient to do the computational aspects of the analyses in terms of J and to use FADs to present the results and the implications of the assessment in a clear and easily understood form.

A5.2 Relationship to J and Construction of Failure Assessment Diagrams for Primary Loads

Failure curves can be readily derived from the results of an elastic-plastic fracture analysis based on J, or the J estimation schemes described in Section A4, by introducing the two parameters, K_r^* and L_r^* defined as

$$L_r^* = \frac{P}{P_y^*(c)} \ , \ K_r^* = \sqrt{\frac{J_e(c,P)}{J(c,P)}} \qquad \text{(A5.1)}$$

where P_y^* is the applied load at net section yielding evaluated using the actual 0.2% offset yield stress, σ_y, rather than the Ramberg-Osgood yield stress, σ_o. Essentially, the value of L_r^* determines whether the cracked structure has undergone net section yielding (corresponding to $L_r^*=1$) under the given load P, and K_r^* determines whether the crack can be treated using LEFM (corresponding to $K_r^*=1$).

As the applied load increases, L_r^* increases, crack tip plasticity increases, and the value of K_r^* decreases. If the locus of points (L_r^*,K_r^*) are plotted on the FAD as a function of applied load, P, then the result is a curve similar to that shown in Figure A5.1 that will, in general, be dependent on the structural geometry, crack size and shape, applied load type, and material tensile properties.

A5.3 Failure Curves and Failure Criteria

Brittle Materials and Properties of the FAD

The curve generated by the points L_r^* and K_r^* is a failure curve, as can be seen by using the failure criterion for brittle materials as an example. At fracture $J=J_{mat}$, and $P=P_{crit}$, and the corresponding values of L_r^* and K_r^* evaluated for $P=P_{crit}$ are failure values that fall on the locus defined by equation (A5.1). Hence, the failure criterion for brittle materials is attained when an assessment point for a defected structure defined by the coordinates L_r and K_r calculated from the expressions

$$L_r = \frac{P}{P_y^*(c)} \ , \ K_r = \sqrt{\frac{J_e(c,P)}{J_{mat}}} = \frac{K(c,P)}{K_{mat}} \tag{A5.2}$$

falls on the failure curve generated using equation (A5.1). The proximity of a calculated assessment point to the failure curve gives an indication of the integrity of the structure: if the assessment point falls below the failure curve this implies that the structure is safe for the specified load; if it falls on or outside the failure curve this implies the structure is unsafe.

It is worth noting here several useful properties of the FAD. First, L_r and K_r vary linearly with the load, P, with the result that the distance of an assessment point from the origin is linearly proportional to the applied load. Hence, the calculation of critical proof loads can be performed graphically, as shown in Figure A5.1. Second, because L_r is inversely related to yield stress ($P_y^*(c)$ is directly proportional to yield stress), and K_r is independent of yield stress, a sensitivity analysis with respect to uncertainties in the value of the yield stress can be readily performed since changes in this quantity move the assessment point parallel to the L_r axis, either decreasing the value of L_r (if the yield stress increases), or increasing it (if the yield stress decreases). Similar sensitivity analyses can be performed with respect to fracture toughness, as changes in this quantity only affect the value of K_r (see Figure A5.1).

The critical crack size for a specified applied load can be determined from the FAD by plotting assessment points, L_r and K_r, as a function of crack size. The crack size that produces an assessment point that falls on the failure curve is the critical crack size (Figure A5.2).

The FAD clearly displays the likely fracture mode of the structure depending on the position of an assessment point on the diagram. Figure A5.3 shows the FAD partitioned into three approximate regions: if an assessment point falls into Region 1 (corresponding approximately to $L_r \leq 0.6$) then failure will probably result in a brittle structural fracture (i.e., fracture can be predicted by LEFM); if the point falls into Region 3 (corresponding approximately to $L_r > 1$) then ductile structural fracture is likely (i.e., fracture can be predicted by fully plastic behavior); if the point falls into Region 2 (defined approximately by $0.6 < L_r \leq 1$) then the fracture mode will be intermediate (i.e., EPFM is needed to predict fracture).

Although the failure curve for primary loading is dependent on the structural geometry, crack shape and size, and loading type, in practice this dependence is relatively small unless the crack is situated at or near a geometrical discontinuity. If this is not the case, then the major dependence of the curve is related directly to the material stress-strain behavior. In effect, the structural dependence of the failure curve is largely removed by normalizing J by its elastic value, J_e, and normalizing the applied load by the net section yield load. This can be seen mathematically by substituting the reference stress estimation for J into equation (A5.1). The resulting failure curve for Ramberg-Osgood materials has the form

$$K_r^* = \left[\frac{J_e(c_e,P)}{J_e(c,P)} + V^* \alpha \left(L_r^* \frac{\sigma_y}{\sigma_e} \right)^{n-1} \right]^{-\frac{1}{2}} \tag{A5.3}$$

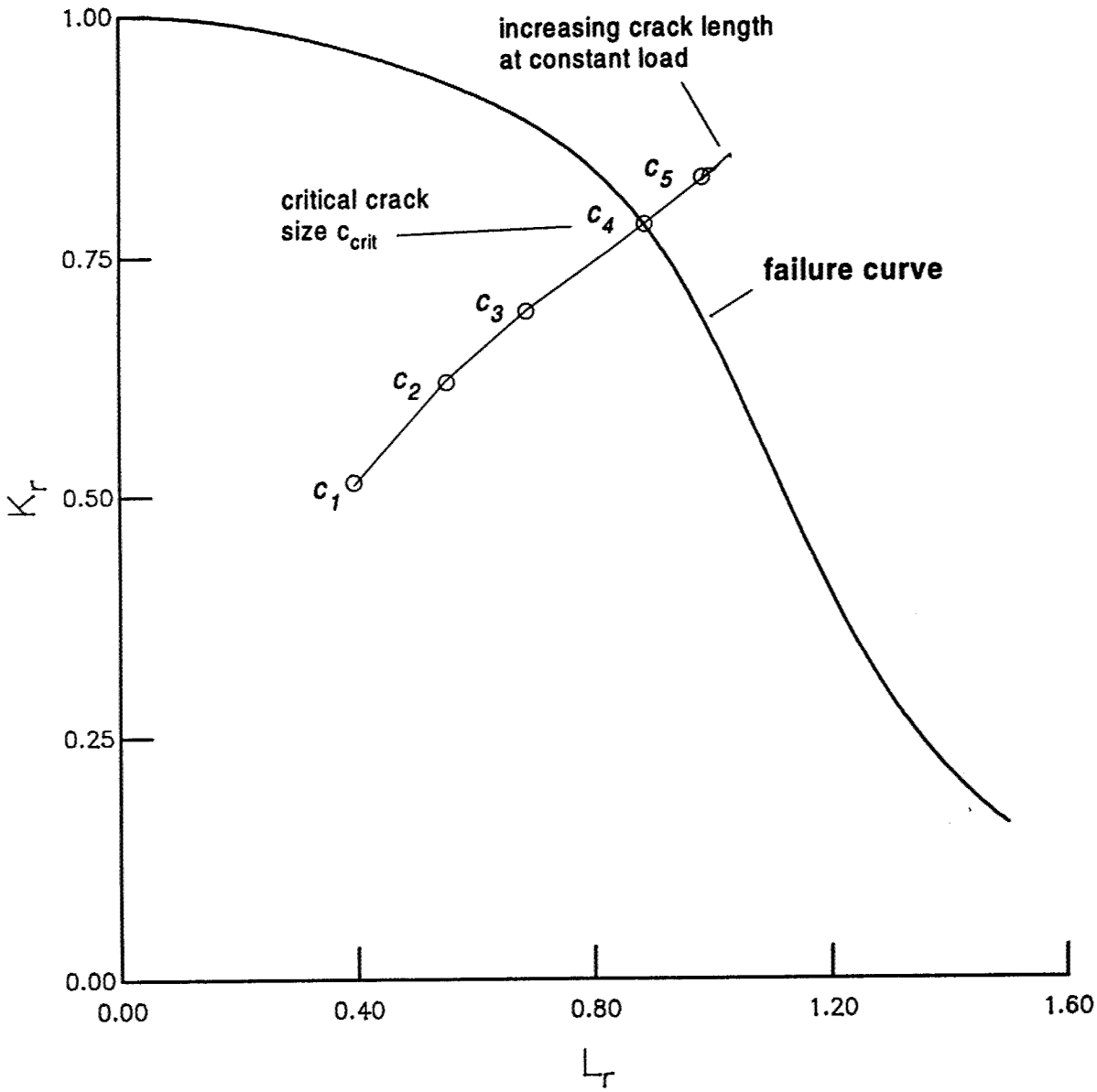

Figure A5.2 Determining the critical crack size for a brittle material using the FAD approach.

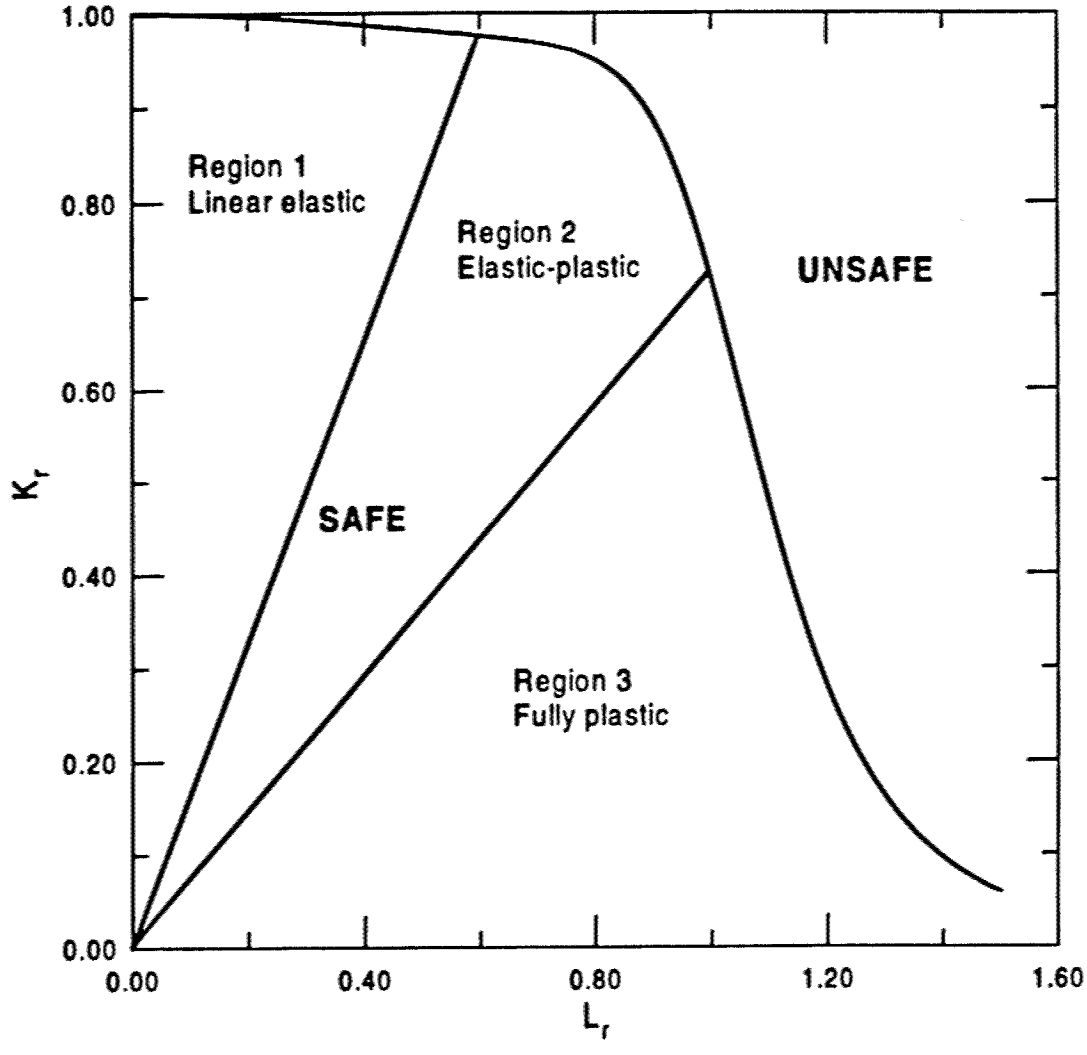

Figure A5.3 The FAD can be partitioned into three regions. The location of an assessment point with respect to the three regions identifies the failure mode as likely to be linear elastic (Region 1), elastic-plastic (Region 2) or fully plastic (Region 3).

where the ratio σ_y/σ_o appears because L_r^* is calculated using σ_y in the FAD approach, while J for Ramberg-Osgood materials is expressed in terms of P/P_o^*.

For general stress-strain behavior, the failure curve has the form

$$K_r^* = \left[\frac{J_e(c_e,P)}{J_e(c,P)} + V^* \ (E\epsilon_{ref}^p/\sigma_{ref})\right]^{-\frac{1}{2}} \tag{A5.4}$$

where the equations

$$\sigma_{ref} = \left[\frac{P}{P_y^*}\right]\sigma_y = L_r\sigma_y \ , \ \epsilon_{ref}^p = \epsilon_{ref}^p(\sigma_{ref}) = \epsilon_{ref}^p(L_r\sigma_y) \tag{A5.5}$$

display the dependence of the plastic component of the strain on L_r. Recognizing that $J_e(c_e,P)/J(c,P)$ ~1 and V^*~1, then the dominance of the material tensile quantities (such as the Ramberg-Osgood plastic strain parameters, α and n) in determining the form of the failure curve is apparent. These aspects are addressed further in Section A5.10.

Ductile Materials

The FAD can be used to predict ductile crack instability by a suitable change in the definition of L_r and K_r to take into account the increase in toughness with ductile crack growth. The new definitions are

$$L_r = \frac{P}{P_y^*(c+\Delta c_t)} \ , \ K_r = \sqrt{\frac{J_e(c+\Delta c_t,P)}{J_R(\Delta c_t)}} = \frac{K(c+\Delta c_t,P)}{K_R(\Delta c_t)} \tag{A5.6}$$

where c is the through crack length before tearing commences. During stable ductile tearing under an increasing applied load, $J(c+\Delta c_t,P)=J_R(\Delta c_t)$, and the assessment points corresponding to tearing, Δc_t, will fall on the failure curve for the instantaneous crack depth $c+\Delta c_t$. After the ductile failure criterion is satisfied [equations (A4.2) and (A4.3)] the assessment point will move off the failure curve into the unsafe region as the applied load is further increased (Figure A5.4).

The instability conditions can be more readily represented on the FAD by generating a locus of assessment points using equation (A5.6) but with the load, P, held constant as the tear length, Δc_t, increases. In Figure A5.4 the assessment point 1 corresponds to the applied load, P_1, at the initiation of ductile tearing. Increasing the load to P_2 moves the assessment point 1 to 2, which falls outside the failure curve. This load will cause the crack to advance by tearing, but the increase in $K_R(\Delta c_t)$ is usually much greater than the increase in K due to tearing Δc_t and the constant load locus corresponding to the increase

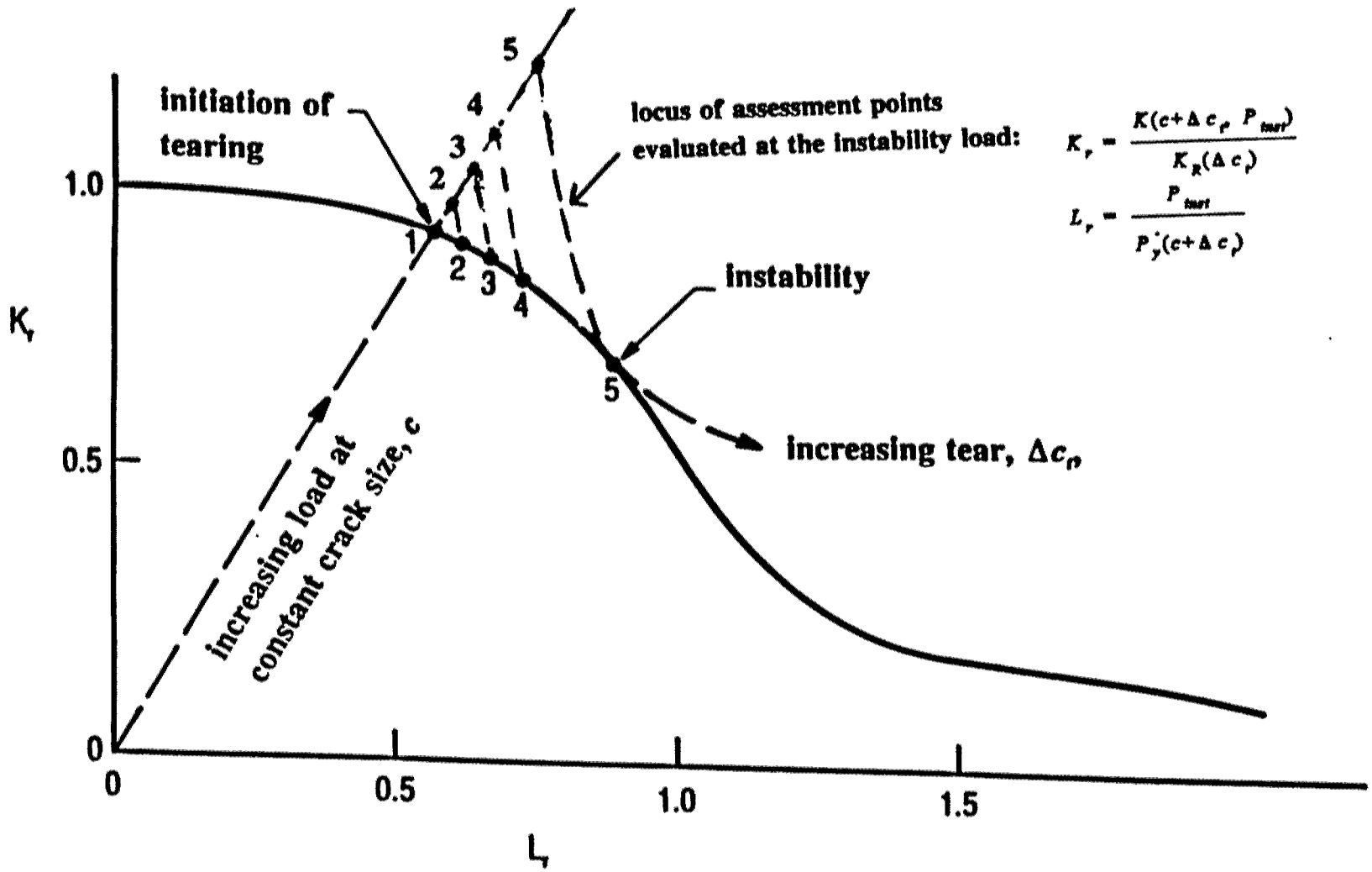

Figure A5.4 The critical load for a ductile material can be obtained using the FAD approach by determining the applied load that results in a constant load locus that forms a tangent to the failure curve (load P_s in the figure).

in Δc_t intersects the failure curve at point 2, where the crack is predicted to arrest. Similar behaviors occur as the load is further increased to P_3 and P_4. Eventually, at a load P_5 in Figure A5.4, the constant load locus forms a tangent to the failure curve. Loads greater than P_5 will result in load loci that always remain outside of the failure curve. The load P_5 is the critical load to cause ductile crack instability, and defines the failure criterion for ductile materials within the FAD concept. The tangency point between the constant load locus and the failure curve is equivalent to the tangency point between J and the J-R curve (Figure A4.1).

The procedure for determining the critical crack size from a FAD analysis is illustrated in Figure A5.5. Assessment points are plotted on the diagram as a function of crack length, c, for the specified applied load. These assessment points are evaluated from K_r values determined using K_{mar} Typical points corresponding to crack lengths $c_1+\Delta c_b$, $c_2+\Delta c_b$, etc. are shown in Figure A5.5 where Δc_b is the amount of blunting/tearing corresponding to J_{mat}. Constant load loci are constructed as a function of Δc_t for selected crack lengths, c_1, c_2, c_3 etc. from K_r and L_r values determined for crack lengths $c_1+\Delta c_t$, $c_2+\Delta c_t$, etc. and toughness values, $K_R(\Delta c_t)$ where Δc_t is the total crack extension due to blunting and tearing. The locus that forms a tangent to the failure curve identifies the critical crack length, c_{crit}, the crack length at instability, c_{inst}, and the amount of tearing up to instability. This crack length is labelled c_5 in Figure A5.5.

A5.4 Treatment of Stress Concentrators (Geometrical Discontinuities)

The failure curve shown in Figure A5.1 is typical of the kinds of curves that are derived from J analyses of structures without stress concentrating features. A stress concentrator can result in local plasticity at its root. This plastic zone can sometimes completely engulf small flaws that develop at the root. Under these circumstances, if the flaw is much smaller than the plastic enclave of the concentrator, then the crack experiences loading conditions of high stress and strain typical of nominal stress levels of above yield point magnitude. This can have a pronounced effect on the elastic-plastic crack tip driving force relative to the linear elastic value calculated by ignoring plasticity. The effect manifests itself as a local "dip" in the failure curve at loads that are relatively small (low L_r values), but still large enough to result in a yielding at the root of the concentrator ($K_t\sigma_{nom} > \sigma_y$, where K_t is the stress concentration factor, and σ_{nom} the nominal stress). An example of this local yielding phenomenon is shown in Figure A5.6. At high loads (above net section yield, L_r>1) the local effects are wiped out by large scale yielding and the value of J, and the failure curve, become insensitive to the local conditions at the root of the geometrical discontinuity and take on values similar to those of a crack of length $c_{ext}=D_n+c$ subjected to the nominal stress (see Figure A5.6). Similarly, if the crack length $c > 0.5r_n$, where r_n is the notch root radius, the crack does not fully experience the effects of the local yielding, and at all stress levels (L_r values) the failure curve for the crack at the concentrator, and a crack of length c_{ext} are similar (Figure A5.6).

These forms of behavior are all reflected in the recommended J expression for cracks at stress concentrators given in Section A4.3 and Table A4.4.

Small cracks at concentrators provide a good illustration of how the shape of the failure curve for a specific material can be significantly dependent on the structural geometry.

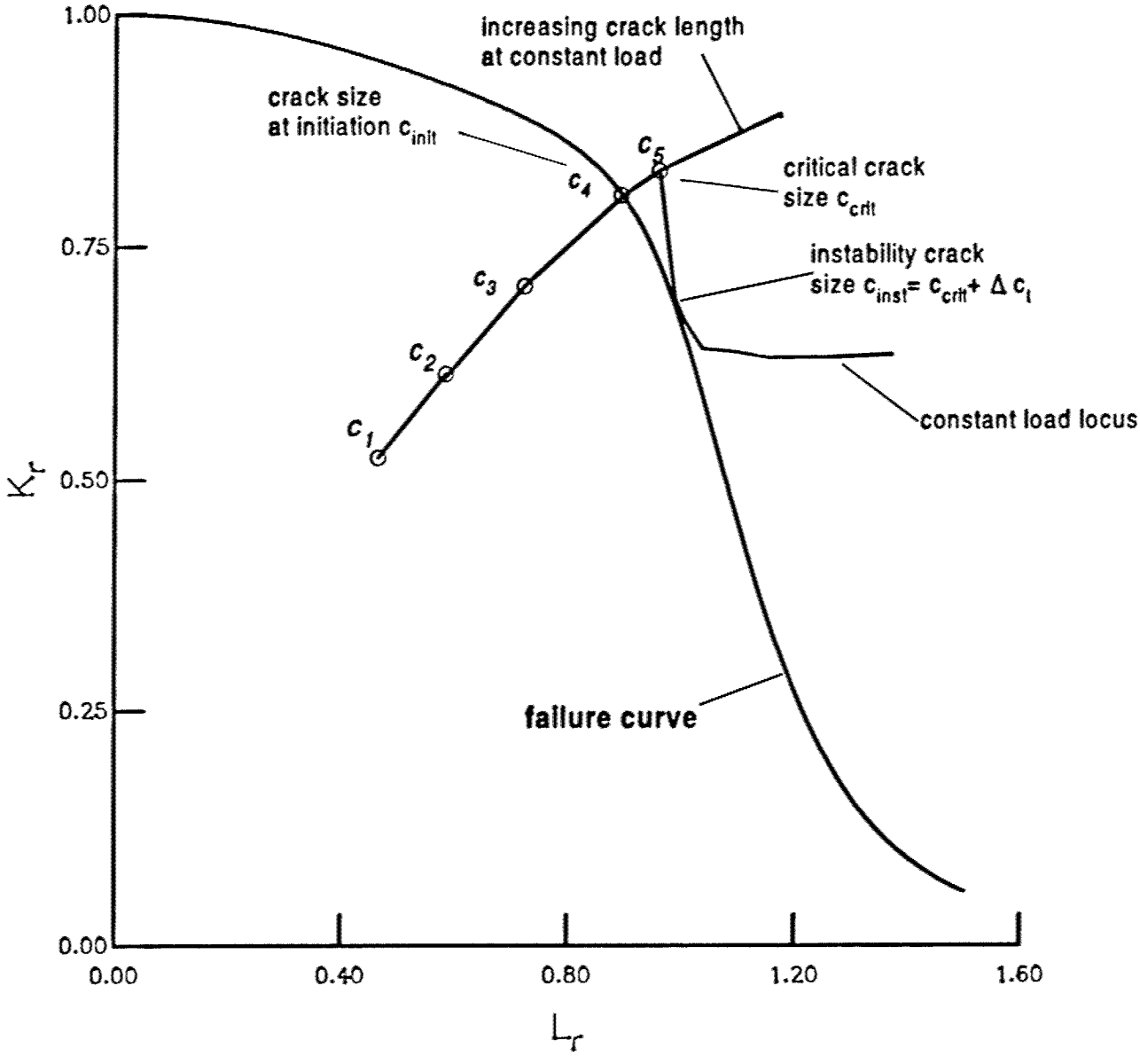

Figure A5.5 The critical crack size for a ductile material can be obtained using the FAD approach by determining the crack length that has a constant load locus that forms a tangent to the failure curve (crack size, c_5, in the figure).

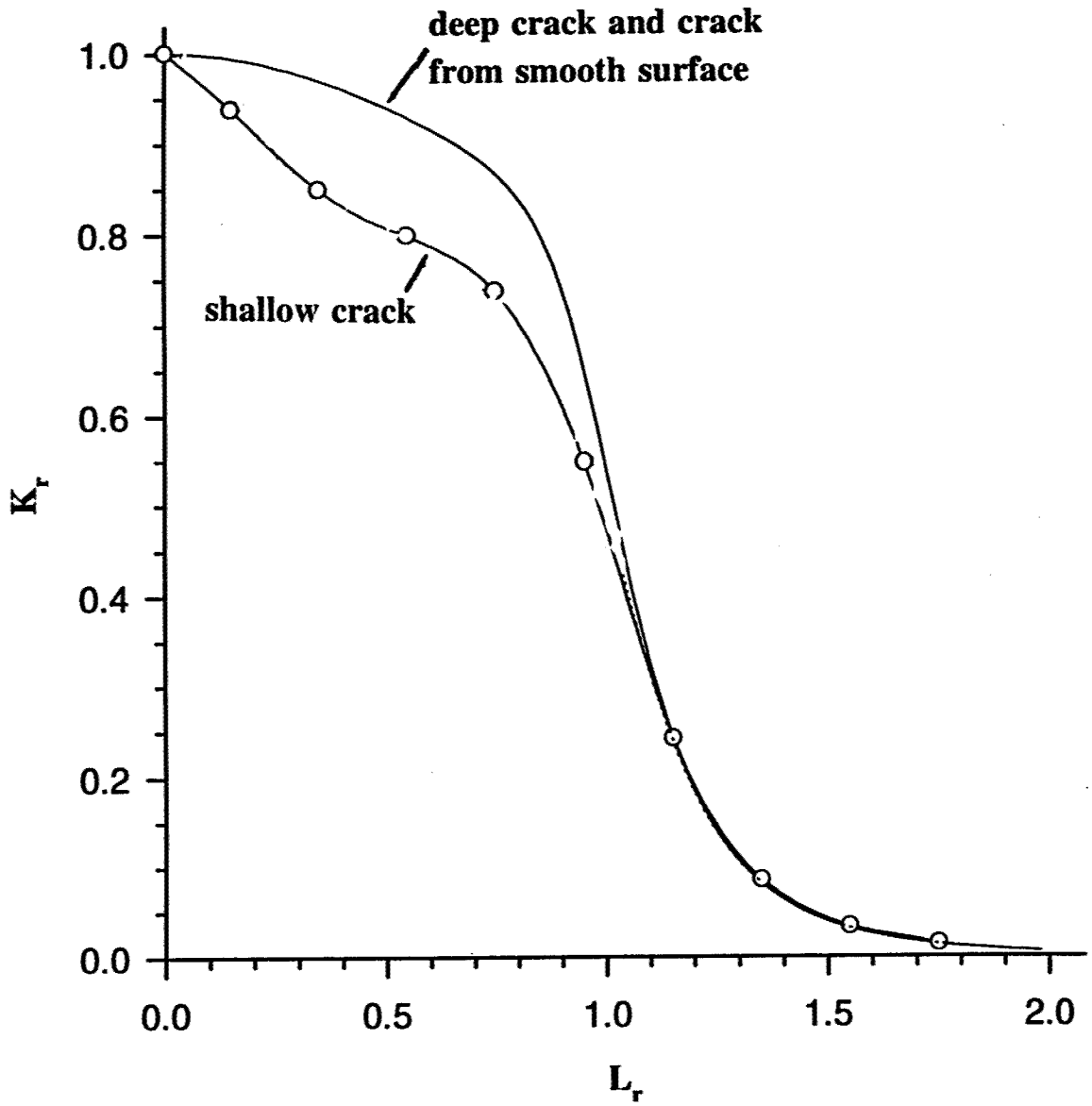

Figure A5.6 Shallow cracks at geometrical discontinuities can have failure curves that are significantly different from deeper cracks, or cracks that emanate from smooth surfaces. The shallow crack failure curve corresponds to a flaw whose length is only 0.155 times the root radius of a notch with a stress concentration factor of 8.4.

A5.5 Treatment of Combined Primary and Secondary Loads

The failure curve for combined primary and secondary loading is constructed from the locus of assessment points, L_r^*, K_r^* derived from a J analysis

$$L_r^* = \frac{P}{P_y^*(c)} \ , \ K_r^* = \sqrt{\frac{J_e(c,P+S)}{J(c,P+S)}} \tag{A5.7}$$

The secondary load alone can produce a crack tip plastic zone that results in a first order plastic correction such that $J_e(c_e,S)/J_e(c,S)>1$ and $K_r^*<1$ when $P=0$. Hence, the form of the failure curve for combined primary and secondary loads may look like Curve 1 in Figure A5.7. However, relatively deep cracks in steeply falling secondary stress fields can have a first order plastic corrected value that results in $J_e(c_e,S)/J_e(c,S)<1$. A failure curve displaying the effects of this kind of behavior is shown schematically as Curve 2 in Figure A5.7.

At primary load levels significantly above net section yield the effects of the secondary loading on the failure curve become insignificant as large scale yielding effectively wipes out their influence. The fully plastic component, J_p, dominates the contribution to J in this loading regime.

A5.6 Treatment of Combined Primary Loads

The failure curve for combined primary loads P_1 and P_2 is constructed assuming proportional loading. If $P_2 = \lambda P_1$ then

$$L_r^* = \frac{P_1}{P_y^*(c,P_1,\lambda)} \ , \ K_r^* = \sqrt{\frac{J_e(c,P_1,\lambda)}{J(c,P_1,\lambda)}} \tag{A5.8}$$

The failure curve for combined primary loads is similar to the one for a single primary load, P_1, because of the assumption of proportional loading.

A5.7 Treatment of Multiaxial Applied Stresses

The influence of multiaxial tensile stresses on the failure curve is through their effects on the stress intensity factor, and the net section yield load, P_y^*, as discussed in Section A4.6. An example FAD for biaxial stressing is discussed in Section B1.5.

A5.8 Treatment of Flaws with Multiple Degrees of Freedom

Failure curves and FADs that are specific to each DOF should be constructed and the critical condition for each DOF assessed against the specific failure curve taking into account possible interactions between each DOF as the crack size and shape changes. More detailed examples of the application of FADs to flaws with multiple degrees of freedom are given in Sections A9 and A10.

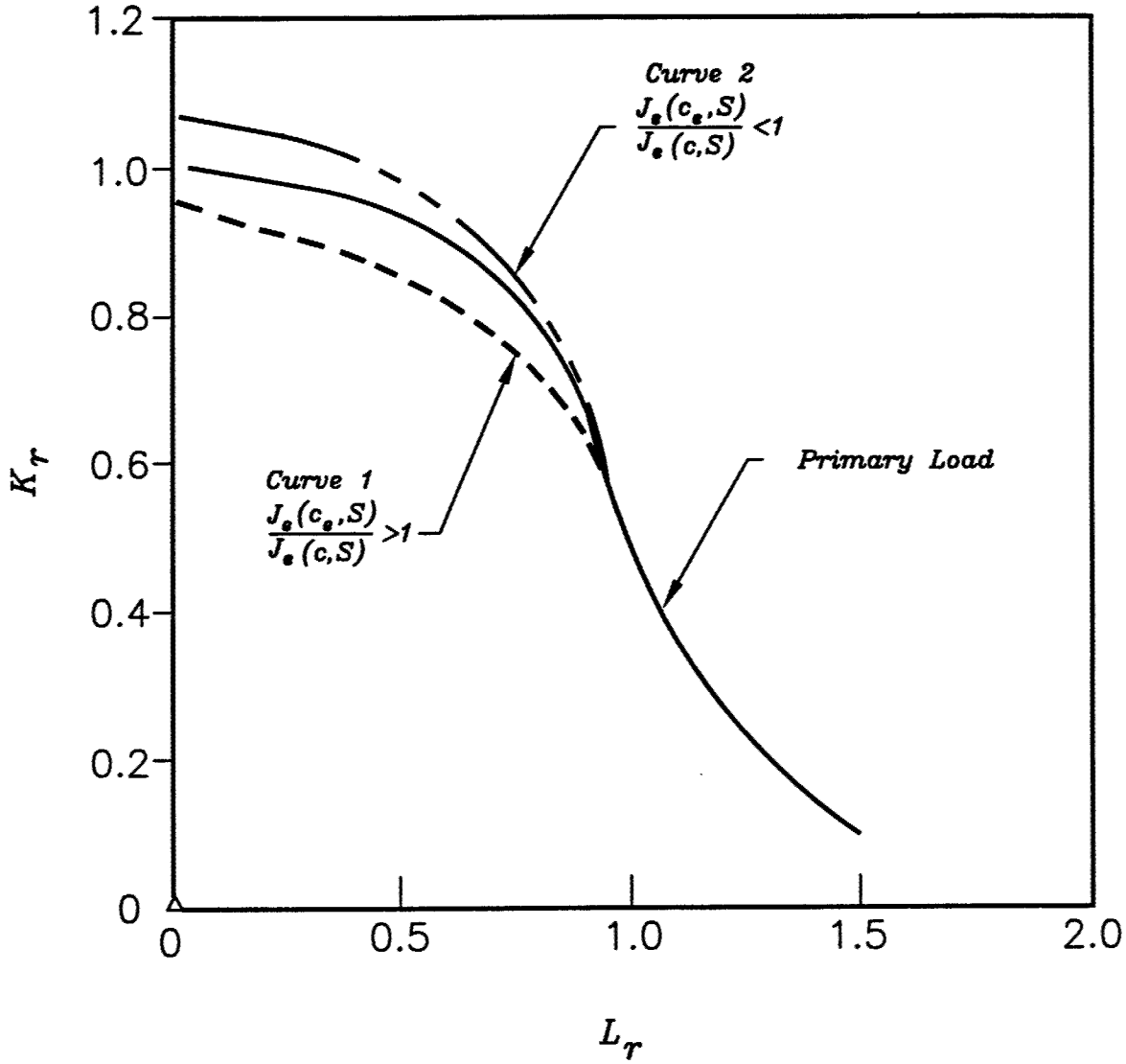

Figure A5.7 Failure curves for flaws subjected to combined primary and secondary loads can be significantly different from the failure curves for the same flaws subjected to primary loading, as shown in this figure.

A5.9 Treatment of Welds

Following the J estimation scheme for cracks in welds described in Section A4.8, the corresponding failure curve can be derived by plotting a locus of assessment points defined as

$$L_r^* = \frac{P}{P_y^*(c, M_{weld})}, \quad K_r^* = \left[\frac{J_e(c,P)}{J_e(c_e[M_1],P) + J_p(c,P,M_2)}\right]^{\frac{1}{2}} \tag{A5.9}$$

where M_1 and M_2 signify the material tensile properties (either weld or base metal) to be used in the evaluation of the first order plastic correction, and the fully plastic component J_p, respectively. The appropriate material properties to use are identified in Table A4.3. The symbol M_{weld} signifies weld material properties should always be used as this will depend on the yield properties of both the base and weld metals. Note that the net section yield load, P_y^*, is defined in terms of the yield load for weld material. In general, this will not be the yield load for the cracked mismatched weld.

In Section B1.6 failure curves derived from equation (A5.9) are compared to failure curves generated from the results of a finite element J calculation as part of the validation performed to substantiate the use of this equation.

A5.10 A Simplified Approach: Material Dependent FADs

Under some circumstances it may be possible to formulate the J estimation scheme in such a way that the dependence on crack size and shape is minimized. The advantage of this is a failure curve that is predominantly a function only of material stress-strain behavior over a range of crack sizes.

There are three situations of major practical importance for proof test analysis where this simplified approach to generating failure curves may be useful. These are cases where there is a single applied primary load and a structure in which the fracture critical regions do not coincide with significant geometrical discontinuities, cases where flaws are presumed to exist at geometrical discontinuities, and cases involving combined primary and secondary loading.

Case 1: Primary Loading With No Significant Structural Discontinuities

As mentioned in Section A5.3, equation (A5.4) represents the equation for a failure curve that is predominantly dependent on material tensile properties as signified by the constants α and n that appear in the Ramberg-Osgood stress-strain equation. The structural, crack, and load dependencies appear in equation (A5.4) only through the ratio $J_e(c_e,P)/J_e(c,P)$. To remove these dependencies, structural integrity procedures such as the widely used document PD6493:1991 [45] and its precursor, R6 (Revision 3) [46], assume that the ratio can be represented by the approximate form

$$\frac{J_e(c_e,P)}{J_e(c,P)} = \left(1 + \frac{L_r^2/2}{E\epsilon_{ref}/\sigma_{ref}}\right) \tag{A5.10}$$

The corresponding failure curve is described by the relationship

$$K_r^* = \left[1 + \frac{L_r^{*2}/2}{E\epsilon_{ref}/\sigma_{ref}} + V^* \left(E\epsilon_{ref}^p/\sigma_{ref}\right) \right]^{-\frac{1}{2}} \tag{A5.11}$$

In PD6493:1991 and R6 the final structural dependence, signified by V^*, is removed by setting it to 1 and the failure curve is only a function of material tensile properties. Here, V^* is retained in equation (A5.11) but its value is defined by Table A4.2, so that, for a given application (proof test or service analysis), equation (A5.11) is still material specific. This means that a generic failure curve can be constructed from stress-strain data that can be applied to all structures, cracks, and load types. This simplification greatly enhances the appeal of the FAD approach, since it means that assessment data for different crack sizes and shapes can all be represented on the same FAD and the integrity of the defected hardware judged against the same failure curve.

Examples of failure curves generated from equation (A5.11) for different hypothetical materials are shown in Figure A5.8. These curves were derived for different n values from a Ramberg-Osgood law with α=1. The exponent n=25 characterizes a material with little strain hardening capacity (such as is the case for some aluminum alloys). As the value of n decreases the strain hardening capacity will typically increase. Hence, the nickel-based superalloy IN-718 has a value of n of around 15, and n=10 is representative of some ferritic steels, while n=5 may typically be found to fit the stress strain behavior of austenitic steels.

Case 2: Stress Concentrators

As demonstrated in Section A5.4, the failure curves for small cracks at geometrical discontinuities can differ significantly from the failure curves for cracks at smoother features. However, the change in the failure curve for small changes in crack size will be small. It can be argued that this fact allows a single failure curve to be used in some circumstances to approximately describe the failure behavior of flaws that are being assessed against ductile fracture.

An example of the way failure curves change with small changes in relative crack size is illustrated in Figure A5.9. This figure shows failure curves for cracks in a stress field that simulates the kind of stress gradient that can occur at a severe geometrical discontinuity and the failure curve for a flaw at a smooth surface subjected to the nominal loading. These failure curves were generated using the J estimation scheme outlined in Section A4.3 for a 5% through the thickness flaw (c/w=0.05), and for flaws that differ from this size by ±10% (c/w=0.055 and 0.045, respectively) and ±25% (c/w=0.0625 and 0.0375, respectively). It can be seen that these changes in crack size do not produce a significant change in the failure curve compared to the curve for c/w=0.05, although each of the curves shows a large "dip" compared to the failure curve for a crack at a smooth surface.

Case 3: Combined Primary and Secondary Loading

The situation for combined loading is similar to that for a crack at a geometrical discontinuity in that the secondary load can result in a failure curve for the combined loading that is significantly dependent on crack size and shape compared to the failure curve for primary loading. However, as in the case for

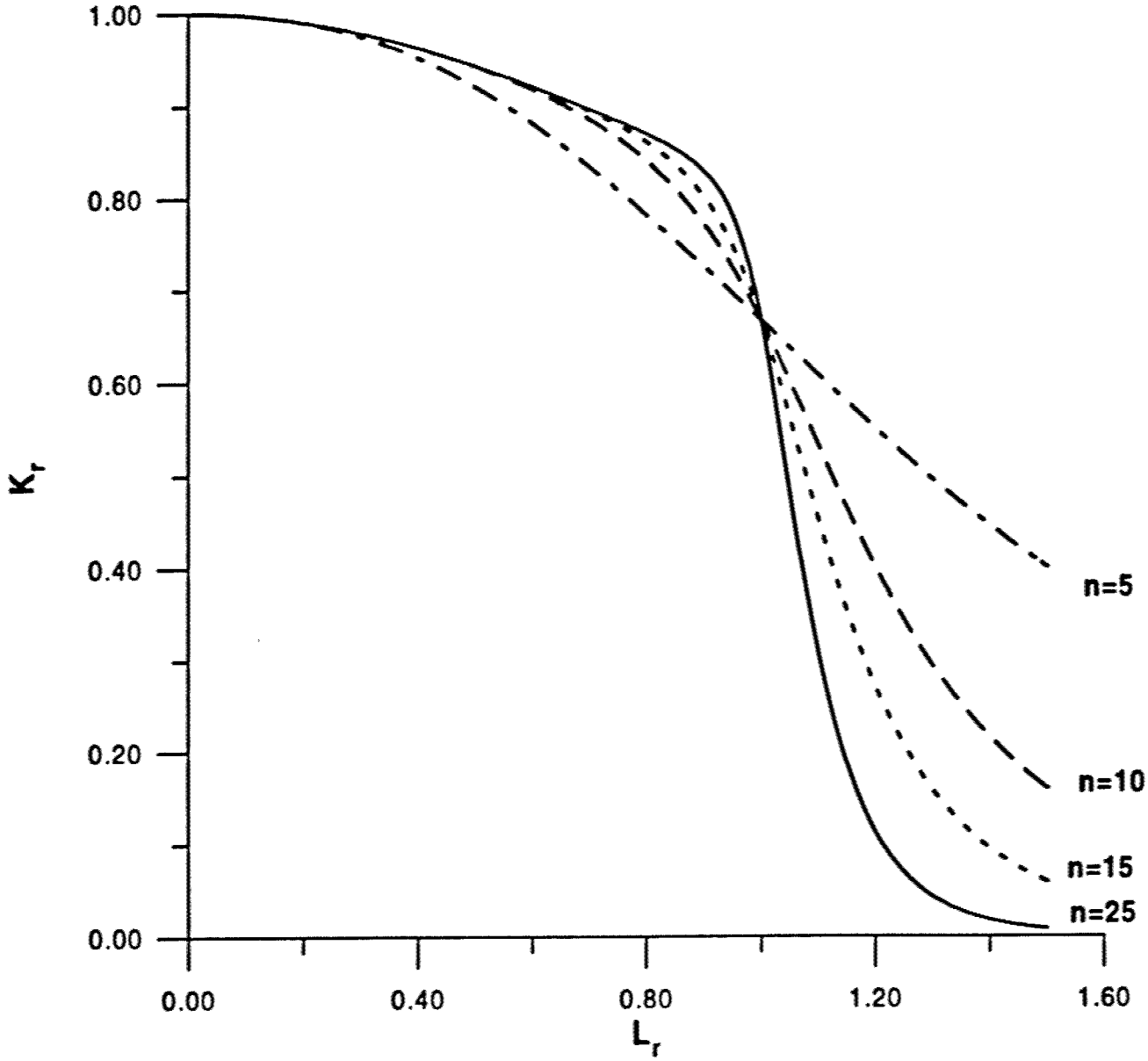

Figure A5.8 Failure curves for four hypothetical materials with strain hardening exponents similar to those that may be measured for an aluminum alloy (n=25), a nickel-based superalloy (n=15), a ferritic pressure vessel steel (n=10), and an austenitic steel (n=5).

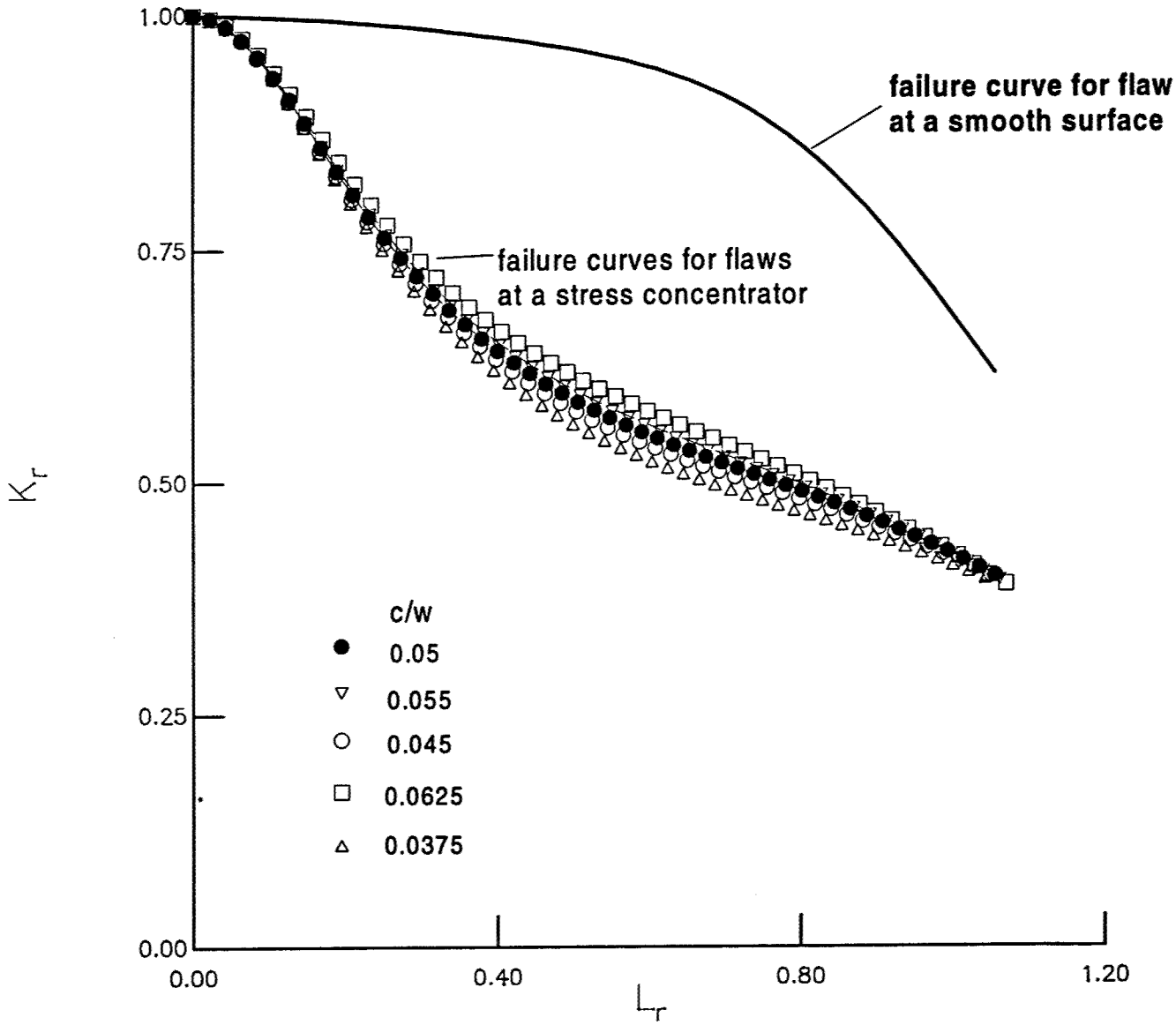

Figure A5.9 The failure curves for shallow flaws at stress concentrators may be significantly different from the failure curve for a flaw at a smooth surface. Even so, as shown, the shallow flaw failure curves may change very little for small changes in crack size.

stress concentrators, changes in the curve for small changes in crack size are likely to be insignificant. Typical changes that may be expected in failure curves with small changes in crack size are illustrated in Figure A5.10. The failure curves in this figure were derived using a residual stress with a peak value equal to the yield stress. These failure curves were generated using the J estimation scheme outlined in Section A4.4 for a 20% through-the-thickness flaw (c/w=0.20), and for flaws that differ from this size by ±10% (c/w=0.22 and 0.18, respectively) and ±25% (c/w=0.25 and 0.15, respectively).

Recommended Conditions for Use of the Simplified FAD Approach

A single material dependent failure curve derived from equation (A5.11) may be used to assess critical loads and crack sizes for brittle and ductile materials in structures containing flaws that emanate from relatively smooth surfaces (Case 1), or deep flaws at geometrical discontinuities (Case 2). The same material dependent curve may also be used to represent the results of a fracture analysis.

Single structural dependent failure curves may be used to assess critical loads for flaws at stress concentrators (Case 2) and for combined primary and secondary loading (Case 3). The curves will be applicable to brittle and ductile materials if they are derived for an initial flaw size in the absence of tearing. These structural dependent curves should be derived for stress concentrators and combined primary and secondary loading using equations (A4.16) and (A4.18), respectively.

A single structural dependent failure curve may be used to represent the results of a critical crack size calculation on the FAD if the failure curve is derived for the critical flaw size, where the critical flaw size is calculated using an appropriate J estimation scheme.

A5.11 Effects of Plastic Constraint

It is recommended that the effects of plastic constraint be included within the FAD approach through the change it produces in the measured fracture toughness. This is consistent with the approach described in Section A4.10. Although proposals have been made on how to explicitly incorporate plastic constraint effects through their influence on the failure curve, as well as the toughness [51], at this time the technology is not developed sufficiently for these to be generally applied with confidence to flawed structures.

A.6 FAILURE MECHANISMS AND FAILURE CRITERIA

A6.1 Brittle Materials

The fracture of brittle materials is controlled by failure mechanisms that operate local to a loaded crack tip and control the events on the microstructural scale that lead to rapid crack extension. Ferritic steels at temperatures below their ductile-brittle toughness transition temperatures are examples of brittle materials. Other metallic alloys, such as austenitic steels and aluminum alloys, which normally display ductile failure behavior, can also undergo brittle failure if their microstructure contains brittle particles, composed predominantly of ferrite in the case of austenitic steels, and silicates in the case of aluminum alloys. These brittle particles can act as initiation sites for micro-sized cracks that fracture under the influence of the high stress field generated at a loaded crack tip. This mechanism is similar to that which causes brittle failure in ferritic steels, but in that case, the brittle particles may be carbides or some other brittle precipitate.

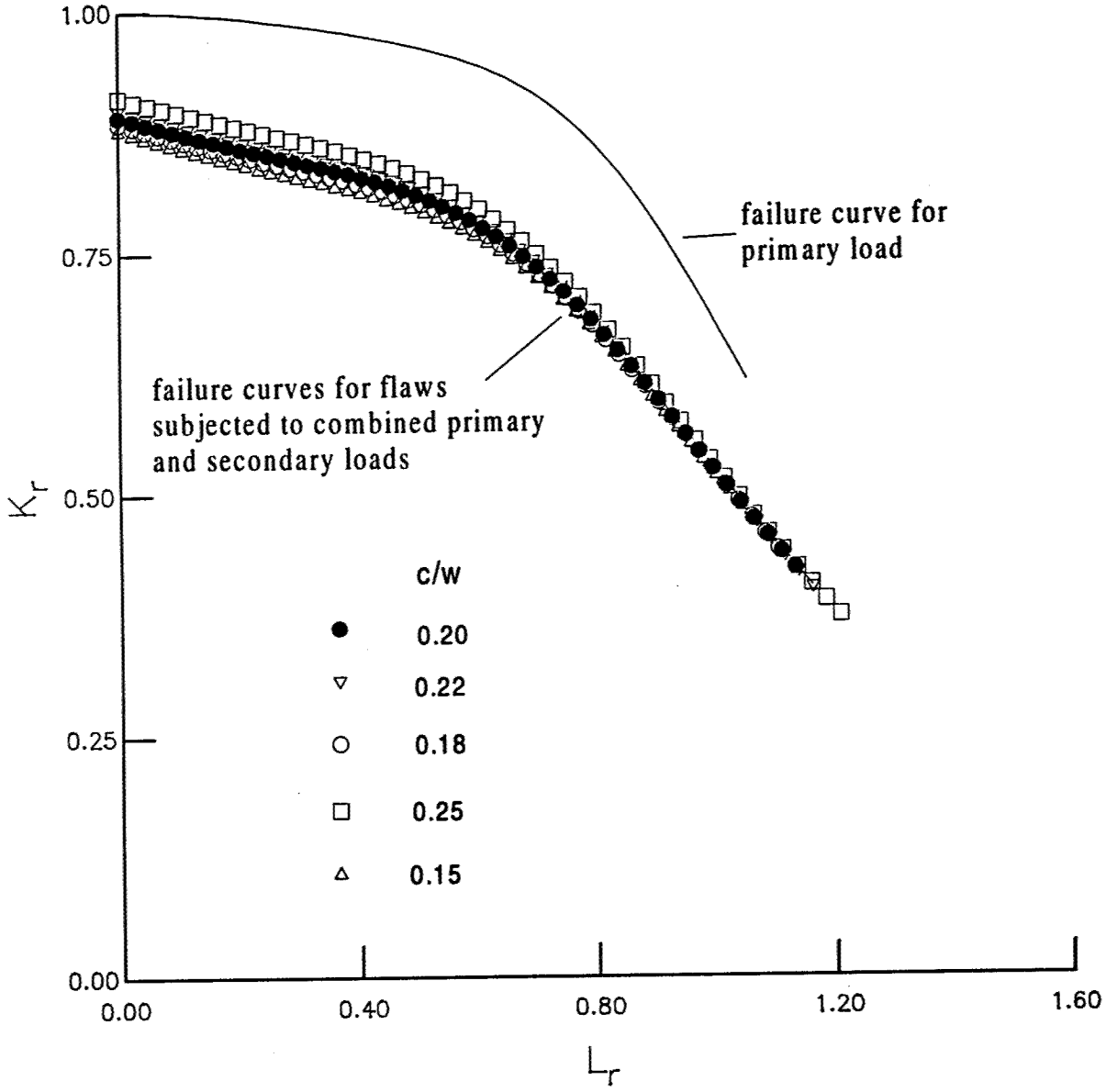

Figure A5.10 The failure curves for flaws subjected to combined primary and secondary loads may be significantly different from the failure curve for a primary load. Even so, as shown, the failure curves for the combined loading may change very little for small changes in crack size.

Brittle mechanisms are usually controlled by the local crack tip stress state and are promoted by elevated principal stresses resulting from high yield and high triaxial (hydrostatic) stresses. (Triaxial stressing in the crack tip region produces high plastic constraint because yielding is suppressed by hydrostatic stresses.) Fracture is usually transgranular and has a crystalline appearance, typical of cleaved grains (although intergranular brittle fractures can also occur in embrittled materials). The fracture surface is normally flat and failure occurs at average stress levels below those of general yielding. Although failure by brittle mechanisms is usually synonymous with brittle structural fracture, this is not always the case, and combinations of structural thickness, crack size, high fracture toughness and low yield stress can occur which result in the development of large scale plasticity in the crack tip region prior to fracture, and consequently, local deformations at failure similar to those normally associated with ductile structural fracture.

The fracture toughness of brittle materials can be characterized by a single value, although this value may be dependent on temperature, strain rate, section thickness and plastic constraint (the latter two are related, but constraint can also be changed by changing the type of loading, for example, from tension to bending). Figure A6.1 schematically illustrates the influence these parameters have on the toughness of ferritic steels below the ductile-brittle transition temperature: the toughness transition temperature is shifted by changes in loading rate, section thickness and plastic constraint. Increasing loading rates, section thickness and plastic constraint cause a relative reduction in toughness at a given temperature (an increase in the transition temperature, see Figure A6.1).

The increase in toughness with increase in temperature is typical of ferritic steels and embrittled austenitic steels. The increase can be attributed to the reduction in yield stress as temperature increases. This causes a reduction in the crack tip stress field which drives the brittle failure mechanisms. The toughness does not continue to increase forever, and eventually crack tip conditions become more favorable for ductile failure mechanisms to operate, and this mechanism takes over control of crack advance, giving rise to a transition to ductile failure behavior. This transition is characterized by a change in toughness from lower shelf (brittle) to upper shelf (ductile) failure. However, the onset of crack advance by stable ductile tearing does not totally eliminate the possibility of fracture occurring by brittle failure mechanisms, especially just on the upper shelf (see Figure A6.1). After some stable tearing, crack tip conditions can again become favorable for brittle failure mechanisms to operate, leading to an abrupt interrupt of stable tearing by brittle failure.

A6.2 Ductile Materials

The fracture of ductile materials is controlled by failure mechanisms that operate adjacent to a loaded crack tip and initiate crack extension by ductile tearing on the microstructural level. Ductile mechanisms are usually controlled by local crack tip strains that require relatively large amounts of energy to deform the material. They are promoted by low yield stresses and low plastic constraint (low hydrostatic stresses allow plastic strain to develop). The fracture surface usually has a dimpled appearance, characteristic of the growth and coalescence of voids. The fracture surface can be flat, inclined to the direction of the applied stress (slanted), or be a combination of the two (flat changing to slant as the crack extends).

The fracture toughness of ductile materials is not usually characterized by a single value, as they display an increase in toughness with crack extension under a rising load. For a given amount of ductile crack extension, the toughness tends to increase as plastic constraint decreases, or as the proportion of shear lip (slant fracture) increases (Figure A6.2). In general, the toughness is not a sensitive function of

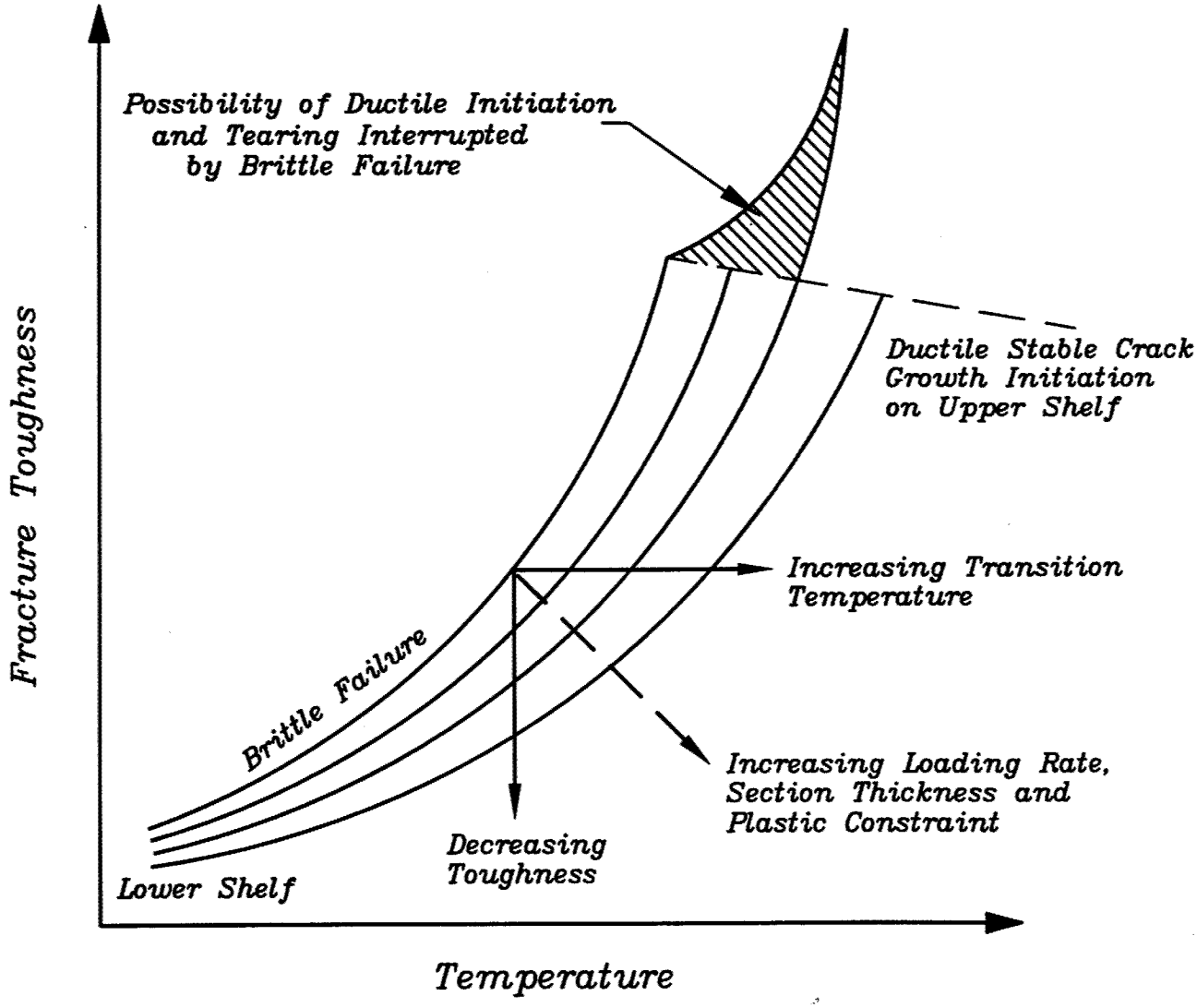

Figure A6.1 Schematic showing how the toughness of brittle materials depends on temperature, loading rate, section thickness, and plastic constraint in the ductile-brittle toughness transition region.

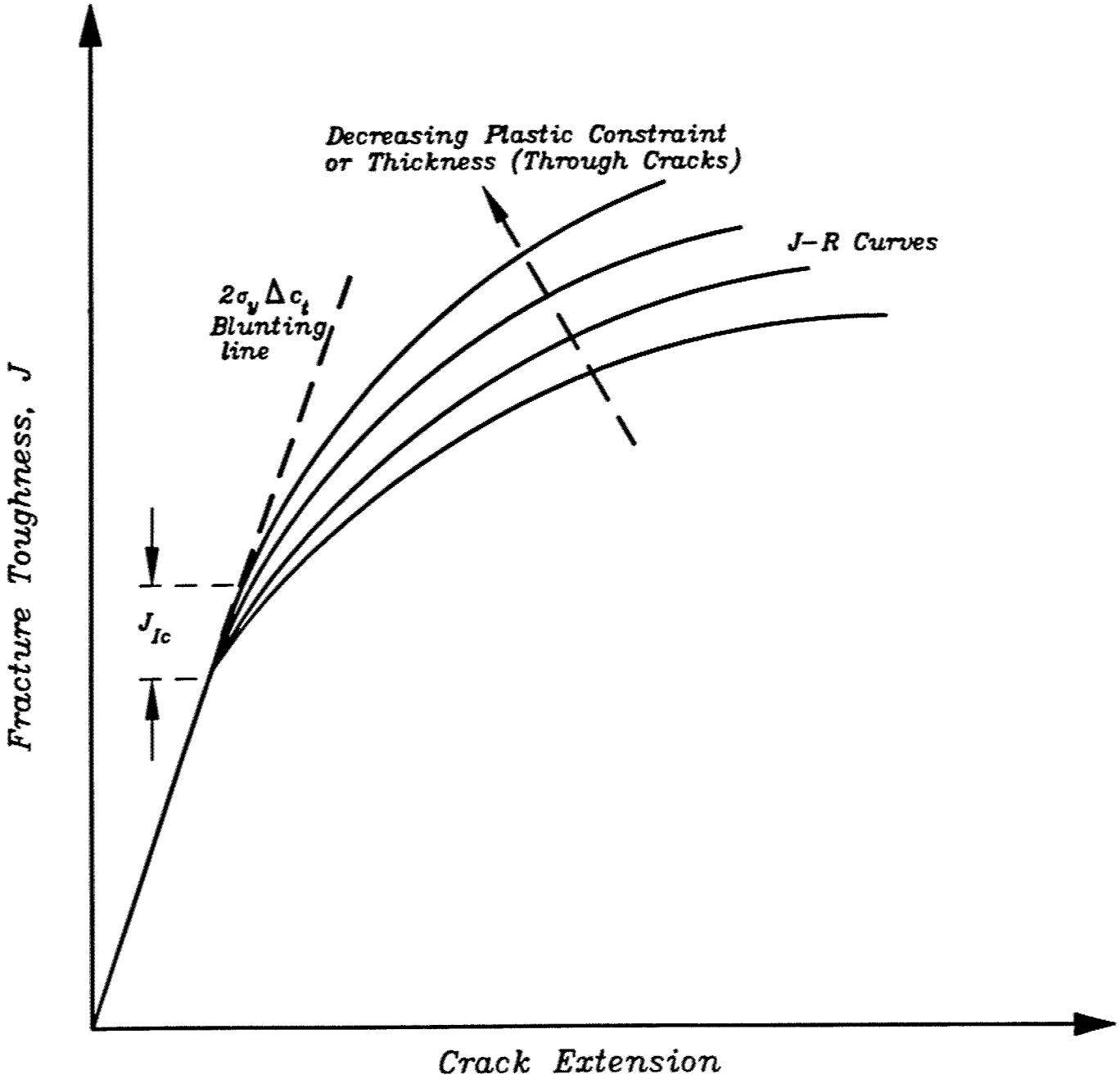

Figure A6.2 Schematic showing how *J-R* curves change with plastic constraint and section thickness.

temperature, with the value measured at the initiation of ductile tearing tending to decrease as the temperature increases. Fracture generally occurs at high average stress levels and is normally (but not always) preceded by significant amounts of plastic deformation characteristic of ductile structural fracture. Under some circumstances (for example, ferritic steels at temperatures in the ductile-brittle transition region), brittle failure can intervene to cause fracture after stable crack extension has been initiated by ductile mechanisms (compare Figure A6.1).

A6.3 Sub-Critical Crack Growth

Sub-critical crack growth can occur by several mechanisms during the course of proof testing: stress corrosion cracking is possible in defected hardware exposed to aggressive environments under sustained loading conditions; so-called cold creep or time-dependent ductile tearing can occur in ductile materials statically loaded above the point at which ductile tearing has commenced; creep crack extension is possible at high temperatures; and fatigue crack growth can occur in hardware subjected to cyclic loading, especially in the presence of aggressive environments.

As pointed out by Tiffany [7], stress corrosion cracking can be particularly onerous because crack extension can occur not only during loading and hold at the proof load, but also during unloading, and even during later storage of the hardware if the load is not reduced to zero, or tensile residual stresses are present. Examples of aggressive environments are water, saline solutions, methanol, and gaseous hydrogen, among many others. Stress corrosion cracking is initiated when the crack tip driving force exceeds a critical value, called the threshold value. Above this value the rate of crack propagation can be high and lead to failure in relatively short times. Hence, the attainment of a threshold crack tip driving force is frequently used to define failure under these conditions.

It is known that cracked materials can fail by time-dependent deformation (so-called low temperature creep) when subjected to a constant sustained load, the time to failure depending on the level of crack tip plastic deformation and whether ductile tearing resulted from the initial loading [52]. The time to failure is shorter the greater the crack tip plasticity, and can become particularly small after net section yield has occurred. Since tearing of ductile materials has to be postulated to occur in order to perform a conservative proof test analysis, the potential for time dependent deformation during the hold period should be conceded and properly allowed for if it is judged to be of significance. It is unlikely in the aerospace industry that proof test temperatures will be high enough to result in creep crack growth during the time taken for the test.

Fatigue crack growth due to cyclic loading should only occur during multiple cycle proof testing. In practice, the amounts of crack extension that can occur from multiple cycling are likely to be very small unless defected hardware is exposed simultaneously to an aggressive environment. However, in proof test analyses it is necessary to concede that large flaws may be present in the hardware and that at the maximum applied proof load the flaws will be on the point of incipient instability. Under these circumstances, the rate of cyclic crack advance can be significantly increased by a synergistic mechanical interaction between the crack extensions resulting from monotonic (static) and cyclic failure mechanisms. The static mechanisms are controlled by the monotonic value of the crack tip driving force, cyclic crack growth rates are controlled by the cyclic change in the crack tip driving force. The static mechanisms may consist of local cleavage of grains in brittle materials, and coalescence of adjacent voids in ductile materials. The synergy between static and fatigue crack growth mechanisms is greatly enhanced as failure is approached. These aspects are addressed further in Section D2 of Appendix D.

A6.4 Mixed Mode Failure

The most onerous loading experienced by defects is usually that due to the component of stress which acts perpendicularly to the plane containing the crack. This form of loading, called Mode I, is the most common. However, situations can arise where cracks can experience shearing (Mode II, in plane-shear) and/or torsional (Mode III, out-of-plane shear) forces. These forms of crack loading are illustrated in Figure A6.3.

Shear and torsional loading tend to reduce the hydrostatic stresses at a crack tip compared to Mode I loading. However, there is little mechanistic understanding of how fracture toughness is influenced by the presence of Mode II and III loads. Hence, the failure criteria which govern combinations of Mode I, Mode II, and Mode III loading modes are only poorly understood. Given these difficulties, it is not possible at the present time to recommend either a mixed mode EPFM parameter or failure criteria for use in a proof test analysis.

A.7 MATERIAL PROPERTIES

A7.1 Mechanical Properties

Mechanical properties are required for stress analysis and to determine the value of the applied elastic-plastic fracture mechanics (EPFM) crack tip driving force parameter, J. The elastic constants, such as Young's modulus, E, are needed for linear elastic stress analysis, and the 0.2% offset yield stress, σ_y, the ultimate strength, σ_u, and detailed engineering stress-strain data are needed for elastic-plastic stress analysis and EPFM.

The Ramberg-Osgood equation provides a convenient parametric form for representing the monotonic uniaxial stress-strain behavior. This is given by equation (A4.4). In general, the Ramberg-Osgood yield stress, σ_o, will not equal the 0.2% offset yield stress. Although equation (A4.4) may appear to require three material constants, in fact only two are necessary, as can be seen by re-writing the equation in the following form

$$\epsilon = \frac{\sigma}{E} + \alpha^{*}\sigma^{n} \qquad \text{(A7.1)}$$

where $\alpha^{*}=\alpha\,\sigma_o^{n-1}/E$.

Most metallic materials have values of $\alpha \approx 1$ and $\sigma_o \approx \sigma_y$. If this is not found to be the case for the material under consideration, then the appropriateness of using a Ramberg-Osgood equation to represent the stress-strain behavior should be investigated. For example, the tensile properties of IN-718 at ambient temperature can be represented to a good appropriateness by a Ramberg-Osgood equation with $\alpha=1$ and $\sigma_o=1240$ MPa (compared with $\sigma_y=1112$ MPa). In contrast, it is not possible to represent a material that displays a yield discontinuity, or yield drop, by the Ramberg-Osgood law. In these cases, either tabular data of stress and strain, or an alternative constitutive equation, can be used.

The engineering stress-strain and true stress-true strain parameters are related (up to the point of necking) by the equations

$$\sigma_t = (1 + \epsilon_{eng})\,\sigma_{eng} \qquad \text{(A7.2)}$$

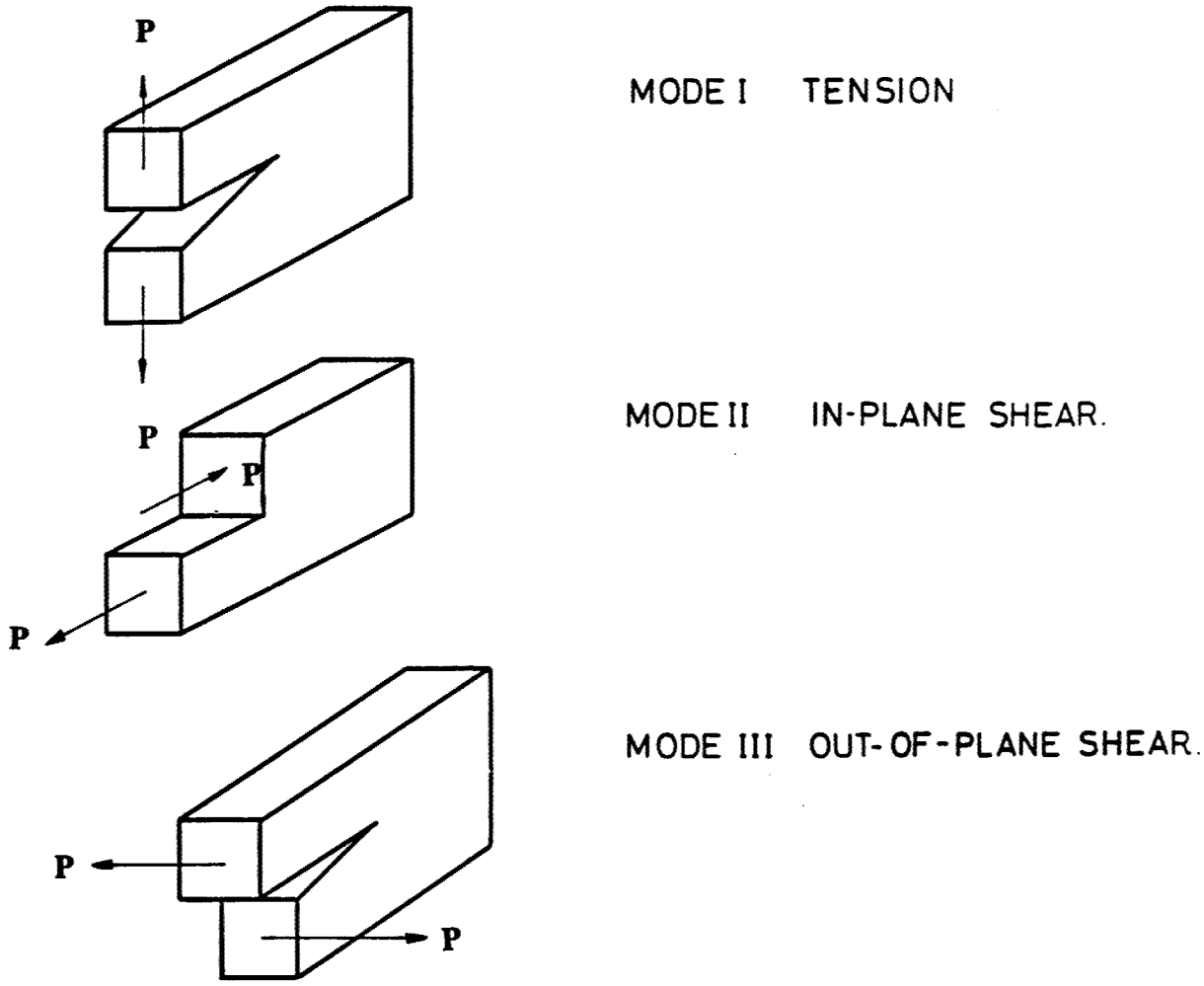

Figure A6.3 Illustration of the Mode I, II, and III loads and the resulting deformations.

$$\epsilon_t = \ln(1 + \epsilon_{eng}) \tag{A7.3}$$

where subscripts *t* and *eng* signify true and engineering, respectively. The engineering stress- strain curve should be used in the evaluation of EPFM parameters and in deriving failure curves for FAD applications.

A7.2 Fracture Toughness

As discussed in Sections A6.1 and A6.2 the measured value of fracture toughness depends on the failure mechanism (brittle or ductile), temperature, strain rate, section thickness, and plastic constraint (crack tip stress triaxiality). The fracture toughness of brittle materials can be extremely sensitive to these parameters at temperatures in the ductile-brittle region (see Figure A6.1).

Measuring Fracture Toughness

ASTM Standards address a number of ways of measuring fracture toughness, depending on the likely fracture response of the material. Plane strain fracture toughness (K_{Ic}) testing procedures are addressed in standard ASTM E399 [53]. In principle, it is possible to obtain valid plane strain fracture toughness values for metals failing by either brittle or ductile mechanisms by following these procedures. Note that, in the case of ductile materials, the measured K_{Ic} value could include a certain amount of stable crack growth and still be valid. Standard ASTM E740 [54] details the steps and requirements for measuring the residual strength of surface-cracks, and how this can be converted into a nominal fracture toughness value, K_{Ic}. Standard ASTM E813 [55] describes the procedures for determining J_{Ic}, a measure of fracture toughness based on the EPFM parameter, *J*. This method can only be applied to materials that fail by ductile mechanisms as the derivation of J_{Ic} is dependent on measuring the toughness as a function of ductile crack extension. The method incorporates the effects of crack tip plasticity on the measured crack tip driving force, *J*, from which J_{Ic} is derived. Explicit recognition of stable crack extension is recognized in standards ASTM E561 [56] and ASTM E1152 [57] that can be used to measure *R*-curves and *J-R* curves, respectively. An *R*-curve is based on the use of the linear elastic fracture mechanics (LEFM) parameter, *K*, possibly modified to include the effects of small amounts of crack tip plasticity, while a *J-R* curve takes full account of all levels of crack tip plasticity through the use of *J* as a fracture parameter. Special consideration is given in the ASTM procedures to the practices to be followed in determining the fracture toughness of aluminum alloys (standards ASTM B645 [58] and ASTM B646 [59]).

The user manual for the NASGRO [60] computer program provides equations that relate the plane strain fracture toughness, K_{Ic}, determined according to the ASTM E399 [53], to the toughness, K_c, under mixed flat and slant (plane stress) fracture conditions, and the surface crack toughness, K_{Ie}. According to the NASGRO manual, K_c is a thickness-dependent material toughness that can be derived from K_{Ic} for some materials using the relationship

$$K_c = K_{Ic}\left\{1 + B_k \exp - \left[A_k \frac{t}{t_o}\right]^2\right\} \tag{A7.4}$$

where

$$t_o = 2.5\left(\frac{K_{Ic}}{\sigma_y}\right)^2 \tag{A7.5}$$

and A_k and B_k are empirical constants, t the wall thickness, and σ_y the yield stress. NASGRO also gives an equation to estimate the toughness of part-through surface cracks from K_{Ic} according to

$$K_{Ie} = K_{Ic} \left(1 + C_k \, K_{Ic} / \sigma_y\right) \tag{A7.6}$$

where C_k is an empirical constant with units of length$^{-1/2}$.

Although the foregoing relationships could be useful for deriving toughness estimates appropriate to actual structural thicknesses, it is emphasized that these equations are empirically derived and should only be used with great caution outside of their region of empirical validity.

There appear to be no ASTM standards for measuring the fracture toughness of metallic materials that fail by brittle mechanisms based on the EPFM parameter, J. There are no recognized test standard procedures for measuring fracture toughness for cracks subjected to mixed mode loading. There are no standards for the fracture toughness testing of cracks in welds, although various institutions have produced or are producing recommendations as to how this should be done (for example, Dawes, Pisarski, and Squirrell, [61]). Weldments present particular problems for testing because of the heterogeneous microstructures, and distortions that can occur due to residual stresses.

Although the toughness values of ductile materials are characterized by resistance curves, there are no established procedures for fitting equations to these curves. Orange [62] has proposed several convenient empirical equations that have been demonstrated to provide satisfactory fits to experimental data. The simplest is a power law equation of the form

$$J_R = A_1 \Delta c_t^{A_2} \tag{A7.7}$$

where A_1 and A_2 are empirical constants determined from a best fit to the whole of the resistance data (including the blunting line), Δc_t, is the total amount of blunting and crack extension, and J_R is the corresponding toughness value expressed in terms of J.

The use in proof test analysis of equations that do not differentiate crack tip blunting from ductile tearing is recommended, especially in aerospace hardware where wall thicknesses can be extremely thin or very small uncracked through-thickness ligaments can exist. For example, wall thicknesses of around 0.25 mm (0.01 in.) may be encountered in the space shuttle main engine (SSME) nozzle tubes. This thickness is comparable with the amount of blunting and crack extension corresponding to the value of J_{Ic} on the J-R curve for IN-718, one of the materials used in the manufacture of SSME components. The ASTM test standard E1152 [57] recognizes the general utility of a power law regression as an aid to some analyses as it is most easily mathematically inverted to obtain Δc_t as a function of J, which simplifies ductile tearing computations.

In these Guidelines, the symbol J_{mat} will be used as a measure of fracture toughness corresponding to the onset of crack instability in brittle materials, and the approximate initiation of stable tearing in ductile materials. The value of J_{mat} can be determined from a measured value of toughness expressed in terms of the linear elastic stress intensity factor, K (e.g. K_{Ic} or K_{Ie}), using the equation that relates J to K under linear elastic conditions, namely

$$J = \frac{K^2}{E'} \tag{A7.8}$$

In ductile materials J_{mat} may be identified with J_{Ic}, as measured according to ASTM Test Standard E813 [55] and designated in the test procedures as "a measure of fracture toughness" to reflect the fact that J_{Ic} does not define the onset of ductile tearing.

Plastic Constraint and Section Thickness

The dependence of measured brittle and ductile toughness values on geometry and load type is well documented (for example, Anderson [42]) and is commonly attributed to the effects of crack-tip plastic constraint. This constraint is generally lower for through cracks in thin sections compared to thick sections, high stresses compared to low stresses, and surface cracks subjected to tension or internal pressure compared to applied bending. Many of the conditions that result in low plastic constraint are characteristic of aerospace applications. Plastic constraint is important because, if the constraint in the hardware under either proof test or service conditions does not match the constraint in the test specimen used to determine the fracture toughness, then this measured toughness value may not be directly transferrable to the hardware. This may not present a serious problem when performing service analyses because the standard test methods for measuring fracture toughness have validity requirements to ensure that the plastic constraint in the test specimen is equal to, or greater than, that likely to be encountered in hardware. However, problems can arise when using standard test fracture toughness data in a proof test analysis (see Section A7.4).

Current thinking in the international fracture community is that the change in the measured fracture toughness with specimen geometry (plastic constraint) is due to the breakdown of J as a single parameter characterization of the elastic-plastic crack-tip fields (similar to the way K fails to properly characterize elastic-plastic crack-tip stress fields). This theoretical characterization provides the vital link between the crack tip driving force expressed in terms of a calculable engineering parameter, J, and the physical mechanism (brittle or ductile) that governs crack extension. Current attention on this so-called loss of J-dominance is focused on using J in conjunction with a stress based parameter, Q, as a two-parameter characterization of crack-tip stress fields that includes the effects of loss of constraint (for example, O'Dowd and Shih [63]; Dodds, Shih, and Anderson [64]). This approach implies that the fracture toughness can be determined using a highly constrained specimen geometry, and the effects of changes in plastic constraint can be accounted for solely in the evaluation of a modified crack tip driving force, J, that will be a function of the value of Q appropriate to the cracked structure.

The effects of plastic constraint on brittle materials is schematically illustrated in Figure A6.1, the effects on J-R curve behavior are shown in Figure A6.2. In the latter case, the effects of plastic constraint tend to be more pronounced after ductile tearing has commenced, the fracture toughness parameter, J_{Ic}, appearing to be less sensitive to loss of constraint.

To date, the practical applications of J-Q theory have been primarily focused on elastic-plastic fracture behavior dominated by brittle fracture (cleavage). This is a stress driven failure mechanism that is controlled by the maximum principle stress at a crack tip. The potential applications of J-Q and other theories to ductile tearing are only now beginning to be explored in detail. In general, ductile failure mechanisms are controlled by both crack tip strains and hydrostatic stresses that

promote void growth and coalescence. It is possible that further advances on this topic will emerge in the next few years.

The fracture toughness of through cracks tends to increase as the section thickness decreases, due to the development of slant fracture as the crack propagates. Although this is a consequence of a reduction of plastic constraint in the thin section compared to a thicker section (plane stress deformation as opposed to plane strain), the change in crack morphology from flat to slant also makes a significant contribution to the enhancement in toughness. The ductile failure mechanism associated with slant fracture differs from the mechanism controlling flat fracture. The former is governed by shear strains and is less dependent on hydrostatic stressing.

A7.3 Sub-Critical Crack Growth

The major forms of sub-critical crack growth that could occur during a single cycle proof test are stress corrosion cracking (SCC) and low temperature creep (time-dependent deformation). Cyclic crack extension occurring in a multiple cycle proof test, will be enhanced by an aggressive environment (corrosion-fatigue).

The rate of flaw propagation from SCC is usually rapid once the linear elastic crack tip driving force, K, exceeds the threshold value, K_{ISCC}. Once K_{ISCC} is exceeded, the rate appears to be relatively insensitive to the applied K until a critical value is attained that heralds the onset of fracture. The important parameters necessary to assess the amount of crack extension are K_{ISCC}, the propagation rate above threshold, $(dc/dt)_{SCC}$, and the amount of time, t_{th}, during the proof test that K exceeds K_{ISCC}. It is not clear what effect crack tip plasticity has on SCC, but it is suggested, absent more detailed information, that K be replaced by $(E'J)^{1/2}$ for the purposes of determining whether SCC will be initiated and over what time period.

A proof test should be designed to avoid SCC if at all possible. The effects of SCC on fracture toughness are not properly understood, and SCC will increase the applied crack tip driving force by physically extending the crack. Both of these phenomena are difficult to quantify at the present time, which will lead to uncertainties in the estimated flaw screening capability of the proof test, and could result in hardware that contains an unacceptable level of damage entering service.

Similarly, the effects of low temperature creep are not readily quantifiable. It is not known whether a threshold J value exists below which no time-dependent effects will be observed. Given these facts, it is recommended that the hold time at maximum load in the proof test be kept to the shortest possible time in order to avoid unnecessary, and unquantifiable, damage. This approach will also help to minimize the potential for SCC.

The amount of fatigue crack extension per cycle, $(dc/dN)_f$, that occurs from cyclic loading during a multiple cycle proof test can be calculated from the cyclic change, ΔK, in K and a Paris Law of the form

$$\left(\frac{dc}{dN}\right)_f = A\,(\Delta K)^m \qquad \text{(A7.9)}$$

where c is the instantaneous crack length, and A and m are material constants. This equation can be used even though there may be extensive crack tip plasticity at the maximum load in the proof test. The

reason is that the cyclic yield stress is approximately twice the monotonic yield stress, which limits the size of the cyclic crack tip plastic zone that can develop under proof test conditions, where, in general, the minimum load in the cycling will always be positive or zero.

The values of the materials constants A and m will depend on temperature and test fluid. Aggressive environments, including water, can significantly increase measured cyclic growth rates with respect to inert conditions.

The fatigue crack growth rate is known to increase as the conditions for crack instability are approached and static failure modes contribute additional crack extension at the maximum load in the cycle. This effect is addressed in Section D7.2.

A7.4 Conservative Data For Use in a Proof Test Analysis

Special consideration should be given to selecting the material data to be used in a proof test analysis as these may be different from the data chosen for use in a conservative service analysis. For example, in a conservative service analysis, data are used which will under-predict critical flaw sizes under operating conditions, while in a conservative proof test analysis, data are used which result in an over-prediction of the largest flaw size that could just survive the proof test load. As a consequence, upper bound fracture toughness values are needed for a conservative proof test analysis, and lower bound values for a service analysis, where "upper" and "lower" are statistically meaningful values. However, by following this recommendation and implementing proof test logic, the efficacy of the proof test analysis could be seriously eroded. To avoid this possibility, it may sometimes be desirable to use consistent data for both analyses. For example, conservative (lower bound) toughness data in a safe-life analysis to specify CIFS's that are being screened by the proof test, and similar data (lower bound toughness) in the proof test analysis. Alternatively, if the intent is to use the proof test to define the maximum flaw sizes entering service for the purposes of a safe-life calculation, then it may be desirable to use similar data (e.g. mean fracture toughness values) in both the proof test and safe-life analyses.

Although the approach of using consistent assessment data in the proof test and safe-life analysis is desirable in principle, to implement this approach without technical justification could, in some circumstances, result in post proof tested hardware entering service containing defects which do not assure a safe-life. For example, if the proof test temperature is different from the service temperature, then the failure mechanism could also be different. This possibility could arise for ferritic pressure vessel steels where the proof test and service temperatures spanned the ductile to brittle toughness transition temperature. As a general rule, upper shelf (ductile) toughness increases with increasing yield stress, while lower shelf (brittle) toughness decreases with increasing yield stress. Hence, microstructural conditions that result in good toughness on the upper shelf could possibly result in low toughness on the lower shelf. In these cases, use of upper bound toughness for both proof test and safe-life analysis would not be justifiable on physical grounds.

The existence of special cases (such as the foregoing) which demonstrate the dangers of unquestionably assuming consistent upper or lower bound assessment data for both proof test and safe-life analysis should not prevent the proof test analyst from seeking to justify the use of consistent data. Indeed, the analyst is encouraged to do this in order to minimize what may be unnecessary conservatisms in a proof test analysis. Justification for the use of consistent proof test and service analyses data could be based, for example, on the fact that proof test and service environments are the same; that the microstructure of the material is known to be very homogeneous; and that little crack growth is predicted

during the service lifetime. It is prudent to perform a sensitivity analysis (see Section 6.3) in cases where consistent data are employed.

Fracture Toughness

In the case of fracture toughness, there are three possible contributions to upper and lower bound values. The first is a statistical one that represents the uncertainties in material variables (e.g. microstructure) as measured by the standard deviation relative to a mean value. The second represents the effects of structural and mechanical variables (e.g. plastic constraint) on the mean value. The third relates to measurement and data reduction uncertainty, as in laboratory-to-laboratory variability. Hence, an upper bound value of toughness is herein defined as a statistically meaningful quantity derived from the upper statistical values of the toughness scatter band obtained from test specimens that simulate the plastic constraint conditions in the hardware, or that simulate conditions of lower plastic constraint. It follows, that a lower bound value of toughness is a statistically meaningful quantity derived from the lower statistical values of the toughness scatter band obtained from test specimens that simulate the plastic constraint conditions in the hardware, or that simulate conditions of greater plastic constraint. Upper and lower bound values can be expressed in the form of factors to be applied to mean toughness values, or as values corresponding to defined cumulative probabilities and confidence levels.

The ASTM test method standards described in the Section A7.2 are directed at generating valid toughness data that are measured relative to cracks in specimens with high plastic constraint. These data should result in conservative service analyses when applied to structures where plastic constraint and section thicknesses differ appreciably from the test configuration on which the data were measured. However, there are presently no test standards for measuring fracture toughness data that can be used to define upper bound toughness values for use in a conservative proof test analysis.

There are three possible ways to overcome this problem for proof test analysis. The first way is to quantify through experiment, analysis and modeling the effect of plastic constraint on toughness, and to use the developed model to predict the mean toughness that is appropriate for the proof tested hardware. This approach will not always be practical due to the cost and time needed to implement it. The second way is to take advantage of existing ASTM valid toughness data and try to modify it for use in a proof test analysis using simple empirically based rules. This approach can be applied to brittle materials where existing data provide information on how plastic constraint influences the ductile-brittle toughness transition temperature. It is also appropriate for ductile materials. Note that for the latter materials it is possible to derive conservative *J-R* curves for use in analysis from a knowledge of the yield stress, σ_y. This can be done by recognizing that the extension of the blunting line on the *J-R* curve to larger values of crack extension provides an overestimate of measured toughness values (see Figure A6.2). The blunting line can be approximately described by an equation of the form (compare the gradient of the exclusion line in Figure 3 of ASTM Standard E813 [55])

$$J_{blunting} = 2\,\sigma_y \Delta c_t = J_R^{conservative}(\Delta c_t) \qquad \text{(A7.10)}$$

This provides a conservative estimate for a *J-R* curve that can be used in a proof test analysis.

The third approach is to measure toughness values on test specimens that simulate, or underestimate, the plastic constraint in the proof tested hardware. This empirical approach is recommended as it avoids complicated and expensive three-dimensional stress analysis and material behavior modeling. However, it is important that the toughness measurement be made on specimens that have cracks of the correct orientation even though the material may be highly homogeneous. For example, a surface flaw in a pressure vessel will experience a different plastic constraint to a through crack, especially if the vessel wall is very thin. Among other differences, a through crack in a thin section will likely generate significantly more slant fracture than a surface flaw. There are practical limitations in performing tests on surface cracks in thin specimens as the depths of the cracks have to be very accurately controlled so that variations along the crack front are small compared with the remaining uncracked ligament. In the case of ductile materials, the *J-R* curve should be measured up to the maximum possible amount of ductile tearing.

The specification of an upper bound fracture toughness for weldments presents additional difficulties because of the microstructural variations associated with these. In these cases, judgment has to be made as to the likely location of the crack tip with respect to the weld-base metal boundary. Alternatively, toughness data should be obtained for the weld and base metals, and the heat affected zones, and the highest values used in the proof test analysis.

Tensile Properties

Uniaxial engineering stress-strain data are needed for the evaluation of J. A conservative proof test analysis requires that upper bound yield properties be used in order to produce an underestimate of J. Under small scale yielding conditions the value of J is approximately given by K^2/E' and is insensitive to the choice of tensile data, aside from the first order adjustment for crack tip plasticity.

The choice of tensile properties for use in J estimation schemes for cracks in welds is not straightforward and will depend on whether the weld is under-matched (has a lower yield stress than the base metal) or over-matched (has a higher yield stress than the base metal). The crack tip plastic zone will tend to remain in the weld metal if the weld is under-matched, while it will more readily spread into the base metal if the weld is over-matched. Further discussion on a J estimation scheme for cracks at welds is provided in Sections A4.8 and A5.9. It is noted here, that if the weld is over-matched, then only the detailed stress-strain curve for the weld metal are required to obtain a conservative under-estimate for J for proof test analyses, while if the weld is under-matched, then stress-strain curves for both the weld and base metals are necessary.

The values of the parameters, α, σ_o, and n in Table A7.1 may be used to construct a Ramberg-Osgood stress-strain curve for use in a proof test analysis if only the yield, σ_y, and ultimate, σ_u, stresses of the material are known, and a lower bound estimate of the uniform elongation, ϵ_f, is available (either measured as the engineering strain at maximum load in a uniaxial tensile test, or based on best engineering judgement). The expression for the exponent n in Table A7.1 is simply derived from the Ramberg-Osgood equation by assuming that the strain ϵ_f is attained at a stress of σ_u. It is emphasized, that every effort should be made to obtain material and measure the stress-strain curve before using the values in Table A7.1.

Table A7.1 Approximate Ramberg-Osgood parameters

α	σ_o	n
1	σ_y	$log(E\epsilon_f/\sigma_y)/log(\sigma_u/\sigma_y)$

A8. FRACTURE AND FAILURE MODES

It is useful to ascertain prior to proof testing whether fracture of the hardware will be by a brittle or ductile structural fracture mode. This information is particularly useful if displacement and/or strain measurements are being made on the hardware. Similarly, although the terms functional and structural fracture are generally applied to the modes of failure that can occur in service, they can profitably be employed to describe the failure mode of hardware being proof tested. Knowing the fracture and failure mode will enable appropriate precautions to be taken to minimize the effects of fracture, should it occur during the test.

A8.1 Brittle Structural Fracture

Brittle structural fracture is a type of catastrophic failure in structural materials that usually occurs at relatively low loads, without significant prior plastic deformation, and at extremely high speed. The fracture is usually characterized by a flat fracture surface with little or no shear lips (slant fracture surface) and at average stress levels below those of general yielding. Although generally associated with a brittle failure, under some circumstances brittle structural fracture can occur due to crack extension initiated by a ductile failure mechanism.

The condition for a brittle structural failure is that the displacements in the hardware vary linearly with the applied load. This implies that plastic deformation, if it occurs, will be highly localized. Hence, conditions of SSY will prevail at a crack that propagates to cause structural failure.

In SSY the crack tip plastic zone size, r_p, is related to the stress intensity factor, K, through an equation of the form

$$r_p = 2r_y = \frac{2}{\beta\pi}\,\frac{n-1}{n+1}\left(\frac{K}{\sigma_y}\right)^2 \qquad \text{(A8.1)}$$

where β=2 for plane stress, and β=6 for plane strain, and n is the exponent in the Ramberg-Osgood stress-strain relationship. The condition for brittle structural failure can be expressed in terms of a dimensionless parameter, Γ, as

$$\Gamma = \frac{r_p}{D} = \frac{2}{\beta\pi D}\,\frac{n-1}{n+1}\left(\frac{K_{mat}}{\sigma_y}\right)^2 \le \frac{1}{10} \qquad \text{(A8.2)}$$

where D is a typical dimension given by the minimum of the crack size and the remaining uncracked ligament. The parameter, K_{mat}, is equal to the appropriate toughness value (e.g. K_{Ic}, K_{Ic}, or K_c). In ductile materials, K_{mat} can be equated to the toughness corresponding to ductile crack instability.

From equation (A8.2), it can be seen that brittle structural failure is promoted by plane strain conditions, large cracks in thick structures (large D), high yield stresses, and low fracture toughness. Brittle structural failure can also be identified by the position of a failure assessment point plotted on a Failure Assessment Diagram, as discussed in Section A5.3.

A8.2 Ductile Structural Fracture

Ductile structural fracture is a type of failure in structural materials that occurs at relatively large loads and is generally preceded by significant amounts of plastic deformation. The fracture surface can be either predominantly flat (surface cracks) or inclined to the direction of the applied stress (through wall, fully penetrating cracks). The percentage of shear lip (inclined fracture) observed in through-wall crack failures is strongly dependent on the wall thickness, and increases as the wall thickness decreases. Although generally associated with a ductile failure mechanism, under some circumstances ductile structural fracture can occur due to crack extension initiated by a brittle failure mechanism.

Ductile structural failure is synonymous with large deformations local to the crack region, and local displacements that vary non-linearly with the applied load. This implies large scale yielding (LSY) with the crack tip plastic zone extended across the uncracked ligament (net section yield).

Ductile structural failure is signified by values of $\Gamma \geq 1$. From equation (A8.2), it can be seen that it is promoted by plane stress conditions, small cracks in thin structures (small D), low yield stresses, and high fracture toughness. Ductile structural failure can also be identified by the position of a failure assessment point plotted on a Failure Assessment Diagram, as discussed in Section A5.3.

A8.3 Functional Failure

Functional failure prevents a part from performing its design function, but does not result in catastrophic failure of the part. An example of functional failure is non-hazardous leak-before-burst (LBB) in a pressure vessel.

It is a necessary, but not a sufficient condition, that the failure mechanism be ductile in order to ensure a functional failure. Brittle materials will generally fail in a catastrophic mode, with a high probability of high energy projectiles causing severe secondary damage. However, the potential for ductile materials to fail catastrophically should not be overlooked. This can occur because brittle failure interrupts stable ductile crack growth due to environmental embrittlement or due to a proof test temperature that is in the ductile-brittle transition region, or because of ductile crack instability. (Good examples of the latter are provided by the hardware verification tests discussed in Section B4 and Appendix B.)

A8.4 Structural Failure

Structural failure is synonymous with catastrophic fracture. It is the expected failure mode for brittle materials, but can also occur as a consequence of burst in ductile materials. Burst occurs when a surface crack propagates through the wall to become a through crack whose length is sufficient to cause ductile crack instability. The possibility of structural failure can be ascertained as part of a leak-before-burst

(LBB) analysis (see Section A11). Structural failure of proof tested hardware is also possible if a leak should occur under simulated service conditions that results in the release of volatile substances.

Burst is promoted by proof test loading systems (such as pneumatic pressurization) that can store large amounts of energy, and materials which display relatively flat *J-R* curves. To avoid these situations, it is recommended that internal pressurization be accomplished using hydraulic fluids whenever possible.

A fracture mechanics based LBB analysis should be performed for ductile materials prior to proof testing to establish whether the hardware failure mode will be a functional failure, or a structural failure, so that appropriate safety and other precautions can be taken. This type of analysis is described in more detail in Section A11.

A9. DETERMINING CRITICAL APPLIED LOADS

This section describes how to evaluate critical loads for one and two DOF flaws in brittle and ductile materials using *J*-based and FAD-based analyses. The assumptions made in the calculations for two DOF flaws can be readily extended to three DOF flaws, such as embedded elliptical defects. The procedures outlined are based on combined primary and secondary loading, with the critical load being determined with respect to the primary load. The recommended *J* estimation scheme for combined primary and secondary loading is presented in Section A4.4. The construction of FADs for combined primary and secondary loading is treated in Sections A5.5 and A5.10.

A9.1 Brittle Materials: *J*-Based Analysis

The steps to be followed in determining the critical loads for one and two DOF flaws using the *J* approach are outlined in this section.

Flaws with One Degree-of-Freedom

The load, P_{crit}, required to cause fracture in a brittle material containing an initial one DOF flaw of length c_i can be calculated from the brittle failure criterion (Section A4.1) by solving the following equation for P_{crit}

$$J(c_i + \Delta c_b, P_{crit} + S) = J_{mat} \tag{A9.1}$$

where Δc_b is the crack extension resulting from blunting of the crack tip, and is given approximately by

$$\Delta c_b = \frac{J_{mat}}{2\sigma_y} \tag{A9.2}$$

In most proof test applications $\Delta c_b << c_i$ and may be ignored, but this may not be the case for surface flaws in very thin components.

Flaws with Two Degrees-of-Freedom

The critical load, P_{crit}, for a two DOF surface flaw of depth a_i and half surface length c_i is the minimum of P_{crit}^{a} and P_{crit}^{c} where these loads are the solutions to the equations

$$J(a_i + \Delta a_b, c_i + \Delta c_b, P_{crit}^{a} + S, \theta = 90°) = J'_{mat} \tag{A9.3}$$

$$J(a_i + \Delta a_b, c_i + \Delta c_b, P_{crit}^{c} + S, \theta = 0°) = J''_{mat} \tag{A9.4}$$

where, in general, the toughness values J'_{mat} and J''_{mat} (and the corresponding blunting lengths, Δa_b and Δc_b) will be different due to different constraint conditions at the deepest and surface points on a flaw.

A9.2 Brittle Materials: FAD-Based Analysis

The steps to be followed in determining the critical loads for one and two DOF flaws using the FAD approach are outlined in this section.

Flaws with One Degree-of-Freedom

(i) Construct a structural dependent failure curve for a crack of depth $c_i + \Delta c_b$ using the engineering stress-strain curve for the material.

(ii) Plot an assessment origin O' with coordinates $(L_r^o = 0, K_r^o)$ on the FAD corresponding to the secondary load and a zero value for the primary load, $P=0$ (Figure A9.1).

(iii) Plot an assessment point, A, with coordinates (L_r, K_r) on the FAD corresponding to the secondary load and an arbitrary, non-zero value of the primary load, P.

(iv) The critical load is given by

$$P_{crit} = \frac{O'B}{O'A} P \tag{A9.5}$$

where O'A is the distance of the point A from O', and O'B is the length of a line from O' through A that cuts the failure curve at B (Figure A9.1).

Flaws with Two Degrees-of-Freedom

(i) Construct structural dependent failure curves for the deepest and surface points corresponding to a crack of depth $a_i + \Delta a_b$ and half surface length $c_i + \Delta a_b$.

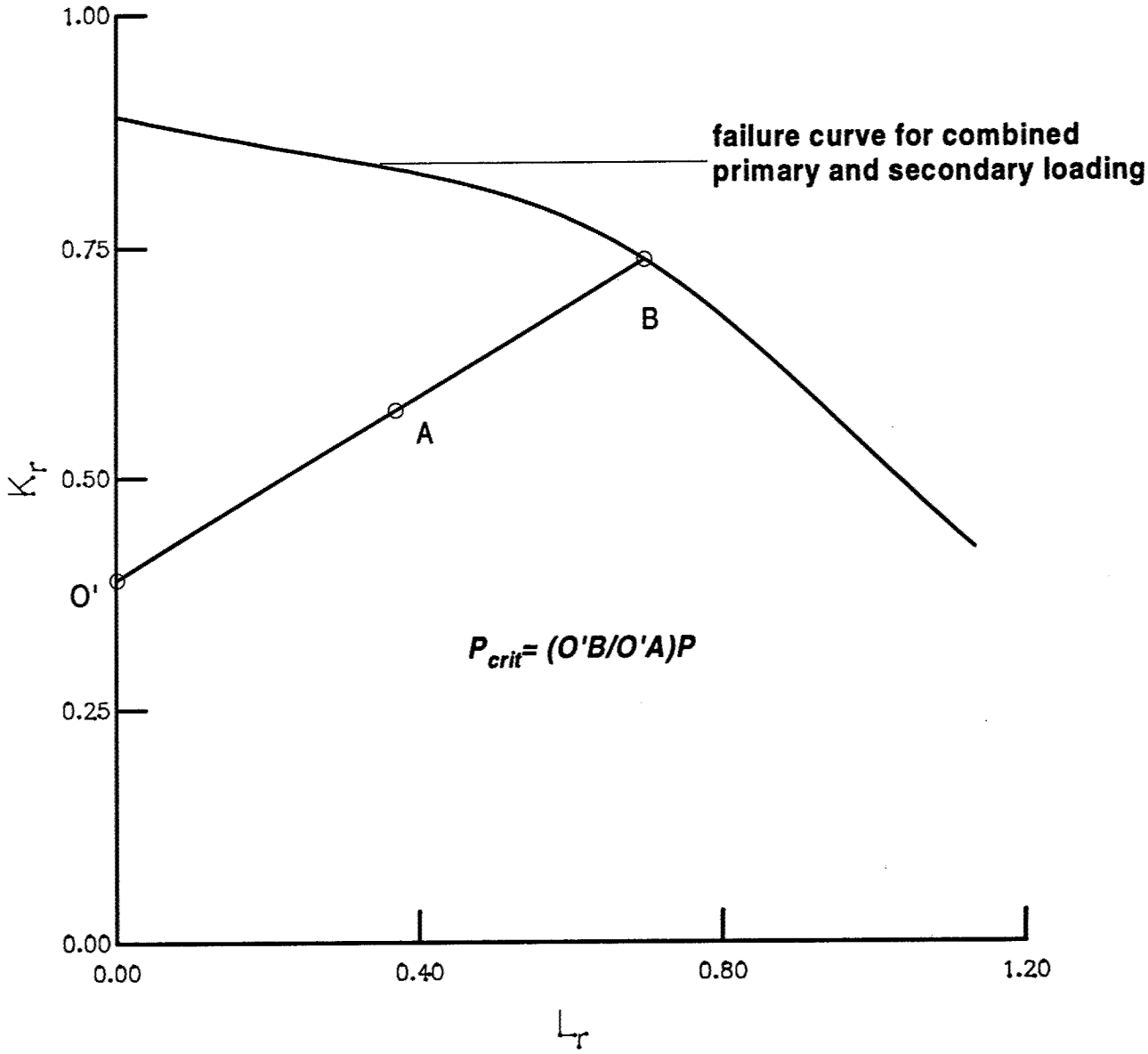

Figure A9.1 Determining the critical load of a flawed brittle material for combined primary and secondary loadings using the FAD.

Perform steps (ii) to (iii) for the deepest and surface points on the flaw:

(ii) Plot an assessment origin O' with coordinates ($L_r^o=0, K_r^o$) on the FAD corresponding to the secondary load with the primary load, $P=0$ (compare Figure A9.1).

(iii) Plot an assessment point, A, with coordinates (L_r, K_r) on the FAD corresponding to the secondary load and an arbitrary, non-zero value of the primary load, P.

(iv) Evaluate the critical loads for the deepest and surface points on the flaw, P_{crit}^a and P_{crit}^c, respectively, using the FAD and assessment points appropriate to each location, where

$$P_{crit}^{a,c} = \frac{O'B}{O'A} P^{a,c} \tag{A9.6}$$

and O'A is the distance of the point A from O', and O'B is the length of a line from O' through A to the failure curve (compare Figure A9.1).

(v) The critical load for the flaw, P_{crit} is given by

$$P_{crit} = min(P_{crit}^a, P_{crit}^c) \tag{A9.7}$$

A9.3 Ductile Materials: J-Based Analysis

The evaluation of the critical loads for defected ductile materials is more complicated than for brittle materials. It is often informative to determine the value of the applied load to initiate ductile tearing, P_{init} as well as the load to cause ductile crack instability, P_{crit}. The value of P_{init} is evaluated in a similar manner to P_{crit} for brittle materials with J_{mat} identified as J_{Ic} or some other suitable measure of ductile fracture toughness.

Flaws with One Degree-of-Freedom

The critical load for a one DOF flaw is the solution to the equation

$$J(c, P_{crit} + S) = J_R(\Delta c_t) \tag{A9.8}$$

that simultaneously satisfies the equation

$$dJ(c, P_{crit} + S) / dc = dJ_R(\Delta c_t) / d(\Delta c_t) \tag{A9.9}$$

where $c=c_i+\Delta c_t$ and Δc_t is the total crack extension due to blunting and tearing. The instability criterion represented by these equations is shown schematically in Figure A4.1.

Flaws with Two Degrees-of-Freedom

The determination of the critical load at instability for two DOF flaws is more complicated, and, in practice, simplifying assumptions concerning crack shape changes due to ductile tearing may have to be made to reduce the two DOF problem to a one DOF case. Surface flaws tend to tear more at the deepest point than at the surface point because the lower plane stress plastic constraint at the free surface results in an elevation in the local toughness with respect to the more highly constrained deepest point. In fact, slant fracture is frequently observed on fractured surfaces adjacent to the free surface positions on surface flaws. Therefore, it is reasonable to assume, unless specific circumstances indicate otherwise, that the surface length of a surface flaw will remain constant, and ductile crack extension will only occur at the deepest point, reducing the problem to a one DOF flaw. Alternatively, it could be assumed that the aspect ratio (a/c) of the flaw remains constant during tearing, but ductile growth is controlled by the conditions at the deepest point on the flaw. It is not clear, a priori, which of these assumptions concerning crack shape development is the more conservative, and it is recommended that calculations be made assuming both possibilities.

The critical load for a two DOF flaw where the surface length is held fixed at c_i, is the solution to the equation

$$J(a, c_i, P^a_{crit} + S, \theta = 90°) = J_R(\Delta a_t) \tag{A9.10}$$

that simultaneously satisfies the equation

$$dJ(a, c_i, P_{crit} + S, \theta = 90°) / da = dJ_R(\Delta a_t) / d(\Delta a_t) \tag{A9.11}$$

where $a = a_i + \Delta a_t$.

The critical load for a two DOF flaw where the aspect ratio, $e = a_i / c_i$, is held fixed is the solution to the equation

$$J(a, c = \frac{a}{e}, P^a_{crit} + S, \theta = 90°) = J_R(\Delta a_t) \tag{A9.12}$$

that simultaneously satisfies the equation

$$dJ(a, c = \frac{a}{e}, P^a_{crit} + S, \theta` = 90°) / da = dJ_R(\Delta a_t) / d(\Delta a_t) \tag{A9.13}$$

A9.4 Ductile Materials: FAD-Based Analysis

The determination of the critical loads for ductile materials based on a FAD analysis entails a series of calculations that essentially follow the same procedures as detailed in Section A9.2. The additional steps are related to the generation of loci consisting of assessment points evaluated at a constant applied load as a function of tear length, Δc_t.

Flaws with One Degree-of-Freedom

(i) Construct a structural dependent failure curve for a crack of depth $c_i+\Delta c_k$ using the engineering stress-strain curve for the material. This curve is assumed to be appropriate for crack changes, Δc, that are small compared to c_i.

Repeat steps (ii) to (iv) for successively increasing increments of ductile tear, Δc_1, Δc_2... starting with the value $\Delta c_1=\Delta c_k$:

(ii) Plot an assessment origin O_i with coordinates $(L_r^o=0, K_r^o(c_i+\Delta c_i))$ on the FAD corresponding to the secondary load and a zero value for the primary load, $P=0$.

(iii) Plot an assessment point, A_i, with coordinates $(L_r(c_i+\Delta c_i), K_r(c_i+\Delta c_i))$ on the FAD corresponding to the secondary load and an arbitrary, non-zero value of the primary load, P.

(iv) The load to cause ductile crack extension Δc_i is given by

$$P_i = \frac{O_i B_i}{O_i A_i} P \qquad \text{(A9.14)}$$

where O_i is the distance of the point A_i from O_i and O_iB_i is the length of a line from O_i through A_i that cuts the failure curve at B_i (Figure A9.2(a)).

(v) Plot P_i against Δc_i (see Figure A9.2(b)).

(vi) The critical load, P_{crit} is equal to the maximum value of P_i and the tear length at which this maximum occurs is the amount of tearing at instability, Δc_{inst} [see Figure A9.2(b)].

If the assessment points, A_1, A_2, etc. are displaced along the lines $O_iA_iB_i$ by the factor P_{crit}/P, they will form a curve that is similar to the constant load locus shown in Figure A5.4 where the load P_5 equals P_{crit}.

Flaws with Two Degrees-of-Freedom

In practical applications it may be necessary to reduce the assessment of a two DOF flaw to an equivalent one DOF case by either assuming that no tearing occurs at the surface point on the defect, or that tearing occurs so as to maintain a constant aspect ratio (see Section A9.3). In either case, an assessment is usually made with respect to the deepest point on the flaw.

After a decision has been made concerning the method to be used to reduce the problem to one DOF, the determination of the critical load proceeds as for the one DOF case using the values of L_r and K_r evaluated at the deepest point and taking due account of the dependence of these quantities on a_i, c_i, and Δa_i.

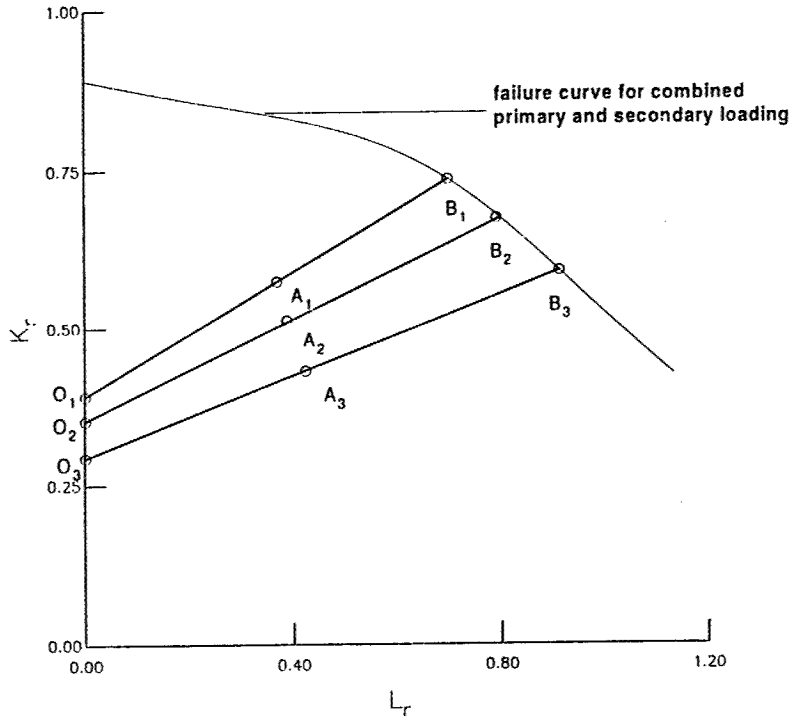

(a)

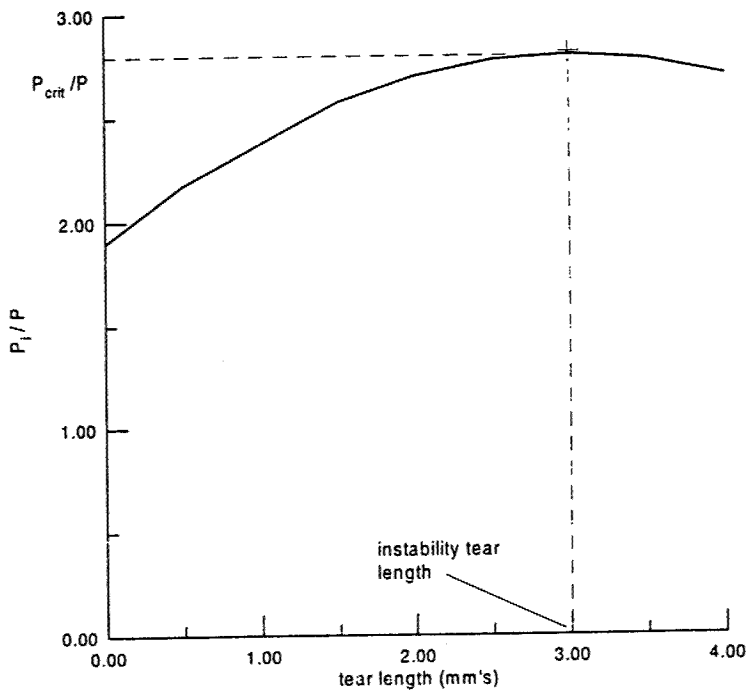

(b)

Figure A9.2 Determining the critical load of a flawed ductile material. (a) Evaluating the load factors $P_i/P=OB_i/OA_i$ for different tear lengths, (b) P_{crit}/P corresponds to the maximum load factor.

A10. DETERMINING CRITICAL CRACK SIZES

This section describes how to evaluate critical crack sizes for one and two DOF flaws in brittle and ductile materials. The assumptions made in the calculations for two DOF flaws can be readily extended to three DOF flaws, such as embedded elliptical defects. The procedures outlined are based on combined primary and secondary loading. The FAD procedures in Section A10.2 are applicable to the case where a material dependent failure curve can be used and are appropriate for primary loading, defects emanating from smooth surfaces, and deep flaws at geometrical discontinuities that behave like through flaws of length c_{crit} subjected to the nominal stress on the cracked section (see Sections A4.3 and A5.4).

A10.1 Brittle Materials: *J*-Based Analysis

Flaws with One Degree-of-Freedom

The critical crack length for a one DOF flaw subjected to a constant applied load, P, is calculated by solving the following equation for c_{crit},

$$J(c_{crit} + \Delta c_b, P + S) = J_{mat} \tag{A10.1}$$

where Δc_b, the crack extension resulting from blunting of the crack tip, is not included in the value of c_{crit} since the critical crack size is the flaw length that will blunt and result in fracture under a constant load and blunting occurs after the load is applied. However, in most proof test applications $\Delta c_b << c_i$ and may be ignored, but this may not be the case for surface flaws in very thin components.

Flaws with Two Degrees-of-Freedom

To determine the critical crack size for two DOF surface flaws necessitates reducing this type of flaw to a one DOF defect. As in the calculation of critical loads described in Section A9.2, this can be done in two possible ways: either assuming the surface length of the flaw remains constant during crack shape development and determining the corresponding crack depth at fracture, or assuming that the aspect ratio remains constant. In the former case, the critical crack depth size, a_{crit}, is determined when either

$$J(a_{crit} + \Delta a_b, c_{crit} + \Delta c_b, P + S, \theta = 90°) = J'_{mat} \tag{A10.2}$$

or

$$J(a_{crit} + \Delta a_b, c_{crit} + \Delta c_b, P + S, \theta = 0°) = J''_{mat} \tag{A10.3}$$

where $2c_{crit}$ is the prescribed initial surface length of the flaw.

In the latter case, where the aspect ratio, $e=a/c$, is held constant, the critical crack size is determined when either

$$J\left(a_{crit} + \Delta a_b, \frac{a_{crit} + \Delta a_b}{e}, P + S, \theta = 90°\right) = J'_{mat} \tag{A10.4}$$

or

$$J\left(a_{crit}+\Delta a_b, \frac{a_{crit}+\Delta a_b}{e}, P+S, \theta = 0° \right) = J''_{mat} \tag{A10.5}$$

where $c_{crit} = a_{crit}/e$.

A10.2 Brittle Materials: Material Dependent FAD-Based Analysis

In this section, the steps to be followed in determining the critical crack sizes for one and two DOF flaws in brittle materials using the FAD approach are outlined. The procedures are applicable only to primary loading, defects emanating from smooth surfaces, and deep flaws at stress concentrators.

Flaws with One Degree-of-Freedom

(i) Construct a material dependent failure curve using the engineering stress-strain curve for the material.

Repeat step (ii) for the specified primary load while incrementally increasing the initial crack length, c_1, c_2, c_3... until assessment points are obtained that fall on either side of the failure curve:

(ii) Plot an assessment point, A_i, with coordinates $(L_r(c_i+\Delta c_b), K_r(c_i+\Delta c_b))$ on the FAD.

(iii) The critical crack length, c_{crit}, is the value of the initial crack that results in an assessment point that falls on the failure curve (crack length c_4 in Figure A10.1).

Flaws with Two Degrees-of-Freedom

The two DOF crack should first be reduced to a one DOF problem by either fixing the half-surface length of the flaw or the aspect ratio. The steps to be followed are then similar to those for the one DOF flaw except that assessment points are plotted on the FAD for both the deepest and surface points on the defect.

A10.3 Ductile Materials: *J*-Based Analysis

The evaluation of the critical crack sizes for ductile materials is more involved than for brittle materials. It is often useful to determine the crack size that would just initiate ductile tearing, c_{init}, as well as the critical size to cause ductile crack instability, c_{crit}. The value of c_{init} is evaluated in a similar manner to c_{crit} for brittle materials with J_{mat} identified as J_{Ic} or some other suitable measure of ductile fracture toughness.

Flaws with One Degree-of-Freedom

The instability crack depth, c_{inst}, for a one DOF flaw is the root of the equation

$$J(c_{inst}, P + S) = J_R(\Delta c_t) \tag{A10.6}$$

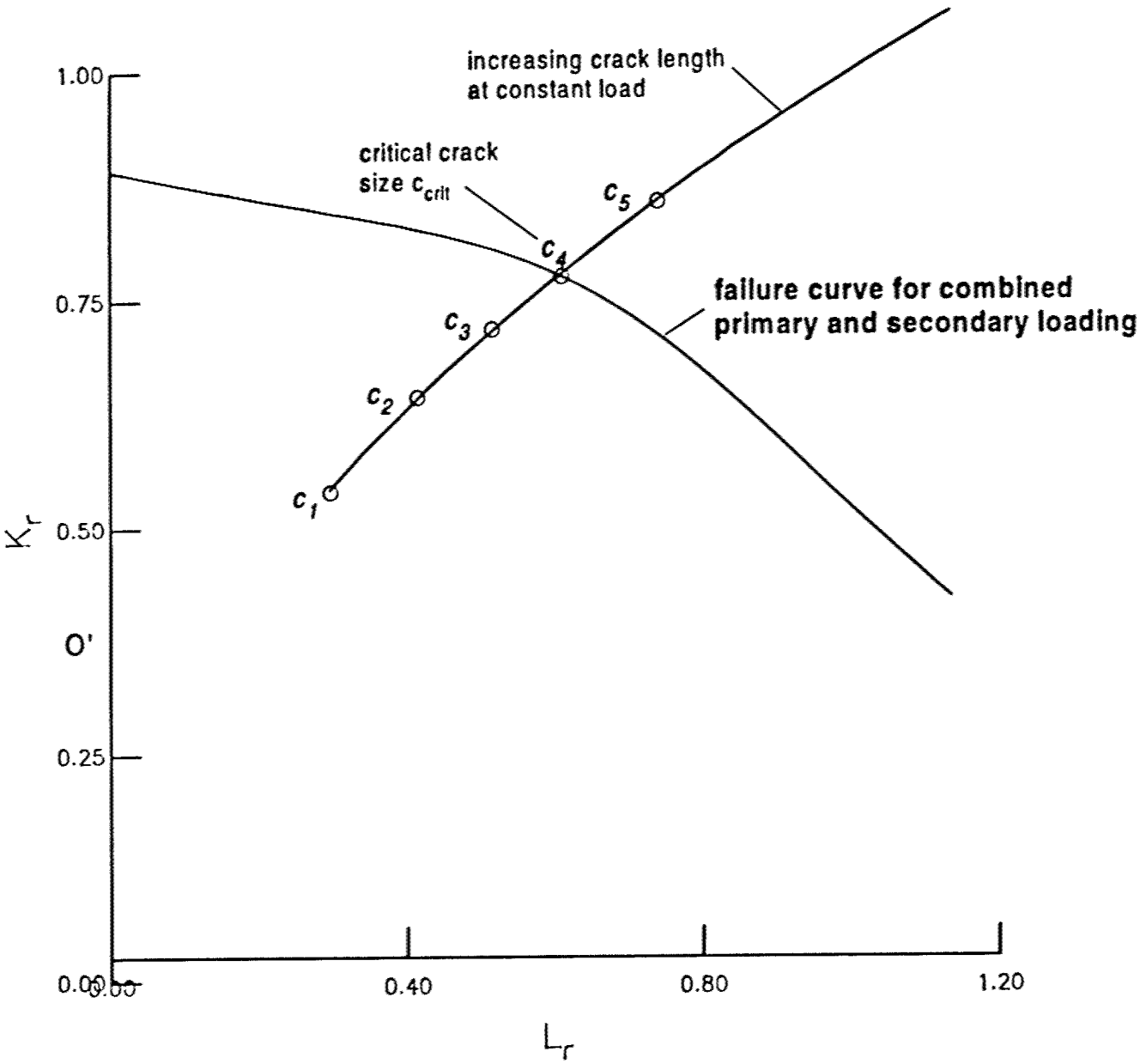

Figure A10.1 Determining the critical crack size (c_4) for a brittle material.

that simultaneously satisfies the equation

$$dJ(c_{inst}, P+S)/dc = dJ_R(\Delta c_t)/d(\Delta c_t) \tag{A10.7}$$

where $c_{inst}=c_{crit}+\Delta c_t$ and Δc_t is the total crack extension due to blunting and tearing. The instability criterion represented by these equations is shown schematically in Figure A4.1. Note that the critical through crack length, c_{crit}, is not equal to the instability crack length. The former is equal to the flaw length that will initiate ductile tearing and grow under a constant applied load to instability.

Flaws with Two Degrees-of-Freedom

The determination of the critical sizes of two DOF flaws requires some simplifying assumptions concerning crack shape changes due to ductile tearing. It is often convenient, as in the evaluation of critical loads for ductile materials, to reduce the two DOF problem to a one DOF problem. This can be done, for example, by fixing the surface length and determining the crack depth that would cause ductile instability. Alternatively, the flaw shape can be assumed to maintain a constant aspect ratio, with tearing controlled by the value of J at the deepest point.

The critical crack depth for a two DOF flaw where the surface length is held fixed at $2c_i$ and instability is assumed controlled by the deepest point on the flaw is the root of the equation

$$J(a_{inst}, c_i, P+S, \theta = 90°) = J_R(\Delta a_t) \tag{A10.8}$$

that simultaneously satisfies the equation

$$dJ(a_{inst}, c_i, P+S, \theta = 90°)/da = dJ_R(\Delta a_t)/d(\Delta a_t) \tag{A10.9}$$

where $a_{inst}=a_{crit}+\Delta a_t$.

The critical crack depth for a two DOF flaw where the aspect ration, $e=c/a$, is held fixed is the root of the equation

$$J\left(a_{inst}, c_{inst} = \frac{a_{inst}}{e}, P+S, \theta = 90°\right) = J_R\left(\Delta a_t\right) \tag{A10.10}$$

that simultaneously satisfies the equation

$$dJ\left(a_{inst}, c_{inst} = \frac{a_{inst}}{e}, P+S, \theta = 90°\right)/da = dJ_R\left(\Delta a_t\right)/d\left(\Delta a_t\right) \tag{A10.11}$$

A10.4 Ductile Materials: Material Dependent FAD-Based Analysis

In this section, the procedures to be followed in determining the critical crack sizes for one and two DOF flaws in ductile materials using the FAD approach are described. The procedures are applicable only to primary loading, defects emanating from smooth surfaces, and deep flaws at geometrical discontinuities.

Flaws with One Degree-of-Freedom

(i) Construct the material dependent failure curve using engineering stress-strain tensile data.

Repeat step (ii) for the specified primary load while incrementally increasing the initial crack length, c_1, c_2, c_3... until assessment points are obtained that fall on either side of the failure curve:

(ii) Plot an assessment point, A_j, with coordinates $(L_r(c_j+\Delta c_b), K_r(c_j+\Delta c_b))$ on the FAD.

(iii) The crack length at the initiation of ductile tearing, $c_{init}=c_j$, where c_j is the crack length that results in an assessment point that falls on the failure curve (point c_4 of Figure A10.2).

Repeat step (iv) for values of $c_j>c_{init}$ until a constant load locus is obtained that forms a tangent to the failure curve:

(iv) Plot a constant load locus as a function of tear length, Δc_t, for the initial crack length, c_j, where the locus consists of assessment points with coordinates defined as

$$L_r = \frac{P}{P_y(c_j + \Delta c_t)} \ , \ K_r = \frac{K(c_j + \Delta c_t, P + S)}{K_R(\Delta c_t)} \qquad \text{(A10.12)}$$

(v) The critical crack size, c_{crit}, is the value of c_j that results in the constant load locus that forms a tangent to the failure curve (Figure A10.2). The crack length at instability, c_{inst}, is equal to $c_{crit}+\Delta c_t$, where Δc_t is the tear length plus blunting at the tangency point.

Flaws with Two Degrees-of-Freedom

The two DOF crack should first be reduced to a one DOF problem by either fixing the half-surface length of the flaw or the aspect ratio. The steps to be followed are then similar to those for the one DOF flaw with the assessment point being plotted on the FAD for the deepest point on the defect, which is assumed to initiate ductile instability.

A10.5 Special Aspects of Critical Crack Size Calculations

Flaws with Two or More Degrees-of-Freedom

There are no unique critical crack sizes for flaws with multiple DOF. For example, in the case of a surface flaw there is a critical flaw depth corresponding to every possible surface length. In these cases it is informative to determine a locus of critical flaw sizes for the specified applied load(s). An example

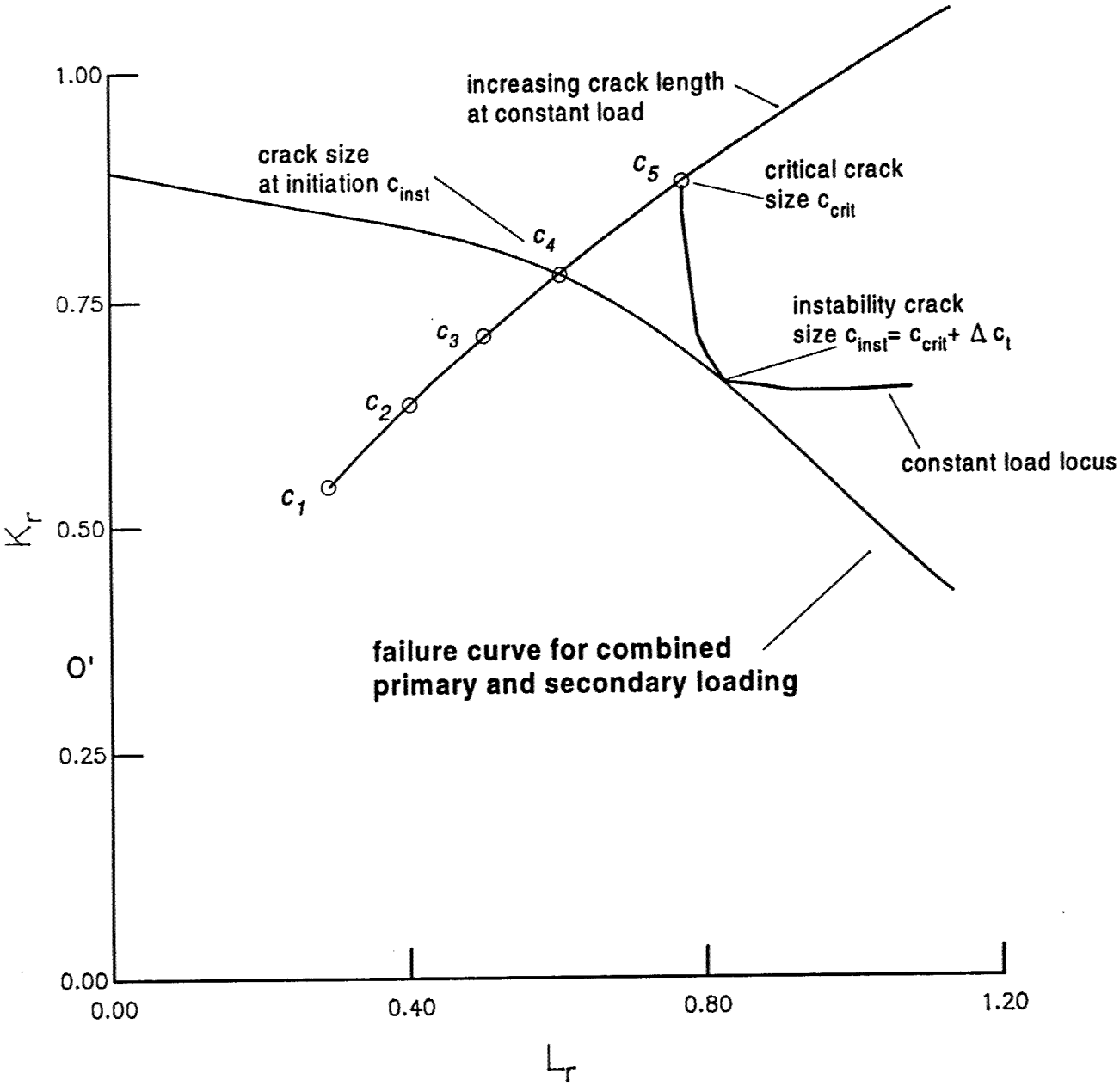

Figure A10.2 Determining the critical crack size (c_5) for a ductile material.

of such a locus is shown schematically in Figure 3.2 of Section 3.1 for a surface flaw and labelled initial flaw sizes based on proof test analysis. These kinds of calculations are also an essential step in a leak-before-burst (LBB) analysis (see Section A11).

Combined Primary and Secondary Loading

Care should be taken when evaluating critical flaw sizes under combined primary and secondary loading that J is a monotonically increasing function of crack size. It is possible, especially in situations where the primary load is relatively small compared with the secondary load, and the secondary load produces steep stress gradients, that the value of J does not monotonically increase with crack size, but instead goes through a maximum followed by a minimum before again increasing at deep crack depths. This behavior is illustrated in Figure A10.3 for the evaluation of a one DOF flaw in a brittle material and it could result in two different critical crack sizes being calculated for the hardware. In these situations, and unless justification is available to conclude otherwise (for example, from supplemental NDE inspections), it should be assumed that the deepest of the two flaw sizes is present at the end of a proof test.

It is recommended that the values of J as a function of crack size be calculated and graphically displayed in order to reveal behavior that could result in complications in the calculation of the critical flaw sizes, and in the interpretation of the results.

A11. LEAK-BEFORE-BURST (LBB) (APPLICABLE ONLY TO DUCTILE MATERIALS)

A11.1 LBB Logic

It is useful to perform leak-before-break (LBB) analyses to ascertain the possible consequences of failure for pressurized components during the proof test. It is desirable to design the proof test to avoid burst, especially if the hardware is pneumatically pressurized.

It is emphasized that LBB cannot be established for materials that fracture by brittle failure mechanisms, even if they display some ductile tearing prior to brittle failure.

The LBB logic is very simple: a flaw will result in LBB if it penetrates the vessel wall to cause a detectable leak before it attains a size sufficient to cause a burst. This definition of LBB identifies one of the requirements for making an LBB case, namely, reliable leak detection equipment has to be used in conjunction with the proof test. Since a proof test occurs under controlled conditions, the task of detecting leaks is made considerably easier than it would under service conditions. However, there could still be problems, particularly with sub-assemblies where access may be difficult.

Another requirement for making an LBB case is that the surface flaw length at which the leak occurs due to a surface flaw should be calculable, and in order to establish a conservative LBB case, the resulting through-wall flaw length at leak should be conservatively estimated. This can be achieved by using upper bound values for the fracture toughness and yield properties in calculating the surface flaw length at leak in a similar fashion to which they are employed in the proof test logic, and using lower bound toughness and tensile properties when calculating the critical through-wall flaw length, as is done in a service analysis. Appendix C of the Johnson Space Center fracture control document, JSC 25863 [3], provides toughness values for use in LBB analyses for a variety of metallic materials.

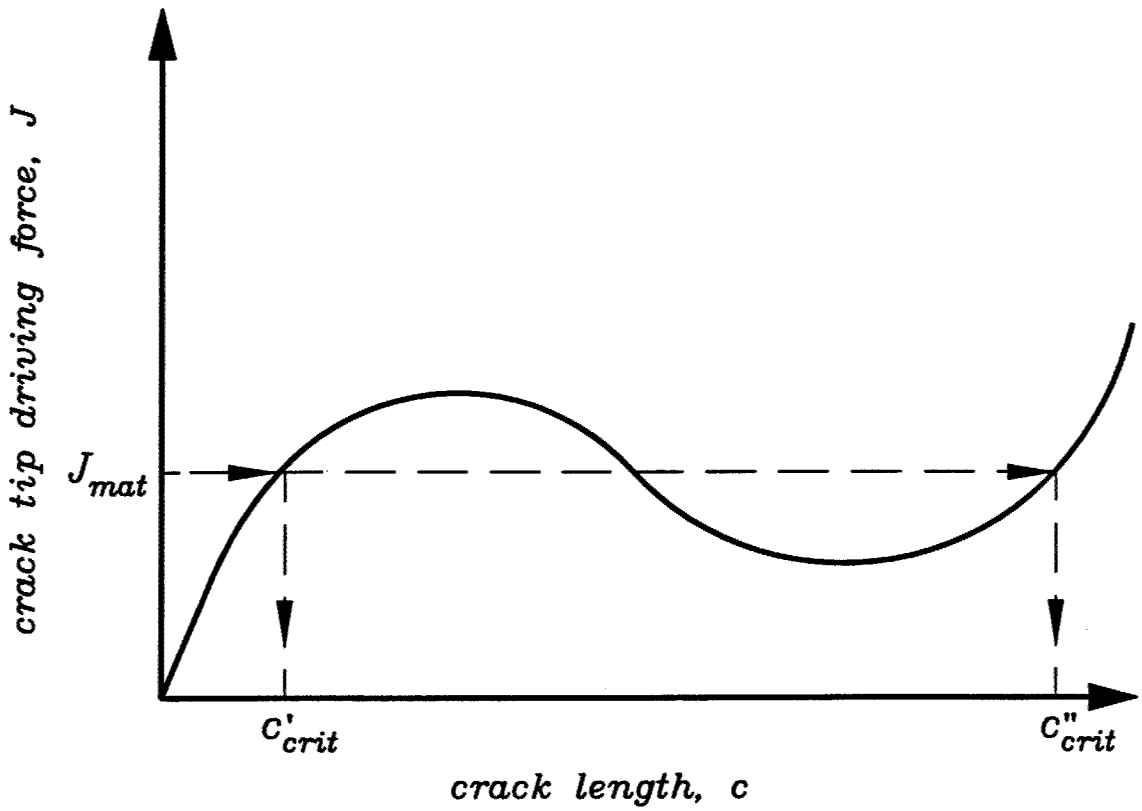

Figure A10.3 Schematic showing how, under some circumstances (such as combined primary and secondary loads), two critical crack sizes, c'_{crit} and c''_{crit}, may be predicted.

In practice, it is almost impossible to predict the changes in crack shape that accompany penetration and leak from a surface flaw. Plastic constraint effects can give rise to so-called "canoeing" or "tunnelling" where the crack extends in its own plane, but preferentially, in a direction normal to growth at the deepest point, while growth at the surface points (which would be in the same direction as the tunnelling) is inhibited by plane stress effects. An additional length, usually equal to the wall thickness, is added to the calculated surface length of the flaw at penetration and leak to allow for these effects. Clearly an LBB case cannot be made for through-wall penetration of very long surface flaws.

A11.2 LBB Diagram

NASA FCR document NASA-STD-5003 [11] states that an acceptable approach to LBB is to show that a through crack of a length 10 times the wall thickness will not result in unstable fracture. However, this criterion pertains to service conditions and may be relaxed in the case of a proof test analysis.

In the case of surface flaws, an LBB diagram can be constructed that identifies those flaws that will produce a burst, and those flaws that will produce a leak, if the hardware should fail during proof testing. This diagram is derived using a locus of instability crack sizes, calculated following similar procedures to those outlined in Sections A10.3 and A10.4 for flaws with two degrees of freedom. The total instability surface lengths of the flaws are increased by the wall thickness to allow for dynamic effects and tunnelling, and the results plotted on an LBB diagram, as schematically shown in Figure A11.1. The outstanding parameter needed to make the LBB case is the critical length of the through-wall crack, l_{crit}. If the penetrated flaw exceeds this length then the vessel will burst rather than leak. The hatched region in Figure A11.1 highlights the initial size of surface flaws that will grow by ductile tearing under the specified proof load to result in leak-before-burst.

The critical crack length, l_{crit}, can be calculated following the procedures outlined in Sections A10.3 and A10.4 for flaws with one degree of freedom. For example, from Section A10.3, the critical crack length, l_{crit}, is the root of the equation

$$J(l_{inst}/2, P) = J_R(\Delta c_t) \qquad \text{(A10.13)}$$

that simultaneously satisfies the equation

$$dJ(l_{inst}/2, P)/d(l/2) = dJ_R(\Delta c_t)/d(\Delta c_t) \qquad \text{(A10.14)}$$

where $l_{inst} = l_{crit} + 2\Delta c_t$.

In order to perform a conservative LBB analysis, the evaluation of l_{crit} should be carried out using lower bound toughness and yield values.

A11.3 Critical LBB Load

In the case of surface flaws, a critical load, P_{LBB}, can be calculated using the procedures described in Sections A9.3 and A9.4 for flaws with one degree of freedom and a postulated or measured initial flaw size distribution. In order to perform a conservative LBB analysis, the evaluation of P_{LBB} should be carried out using lower bound values for the fracture toughness and yield properties, in a similar fashion

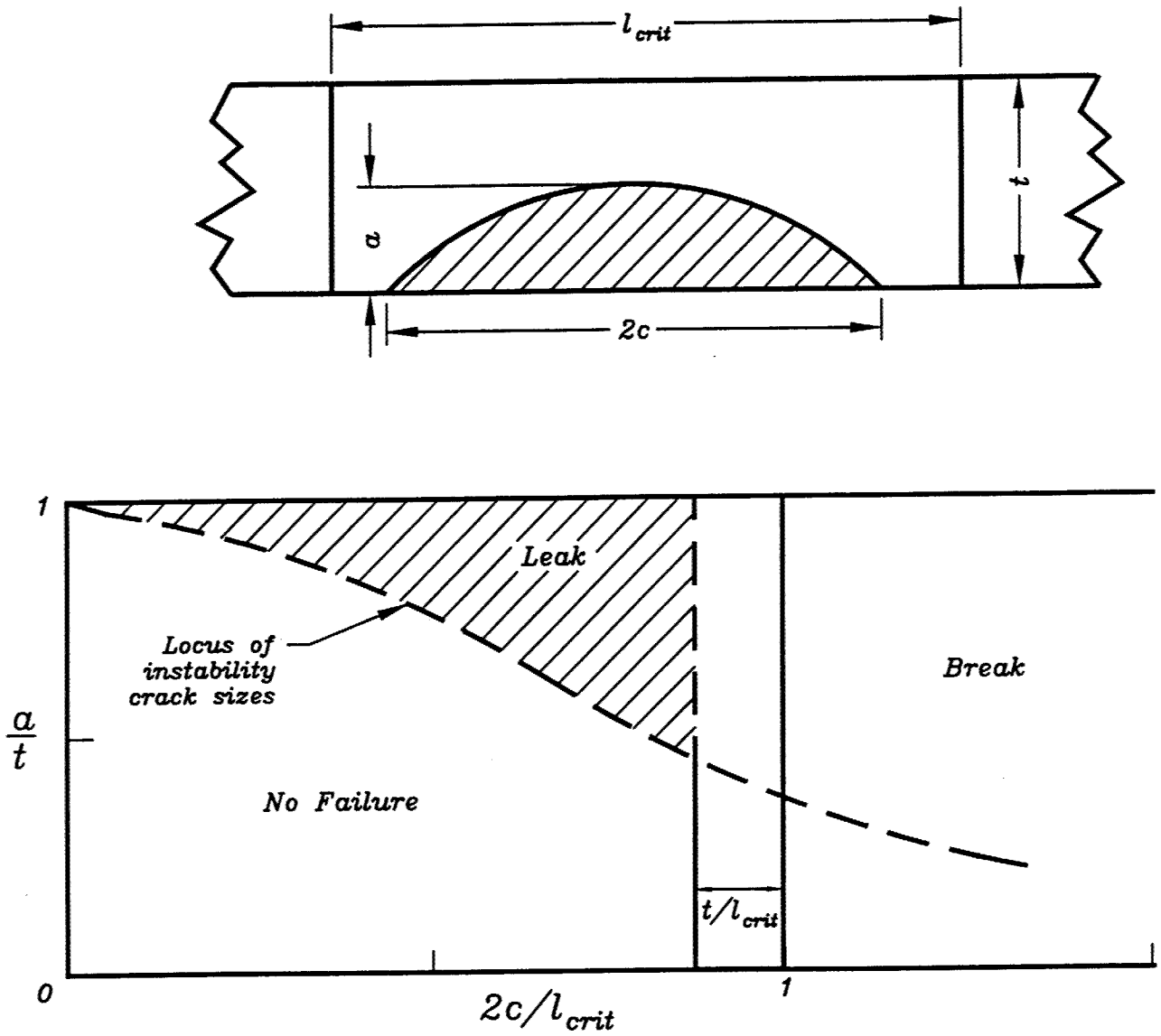

Figure A11.1 Leak-before-burst diagram.

to which lower bounds are employed in a conservative service analysis. The load P_{LBB} identifies those proof loads that will produce a burst, and those loads that will produce a leak, should the hardware fail during proof testing.

The calculation of P_{LBB} is performed for an assumed through crack whose length, l_{LBB}, is calculated as follows. From the postulated initial surface flaw size distribution determine those flaws that are predicted to become unstable under the specified proof load. Identify the flaw from this group that has the longest surface length. The through crack length, l_{LBB}, should be taken as this longest surface length plus the wall thickness (this allows for so-called crack tunnelling). The load, P_{LBB}, is then calculated, for example, as the root of the equation

$$J(l/2, P_{LBB}) = J_R(\Delta c_r) \tag{A10.15}$$

which simultaneously satisfies the equation

$$dJ(l/2, P_{LBB}) / d(l/2) = dJ_R(\Delta c_r) / d(\Delta c_r) \tag{A10.16}$$

where $l = l_{LBB} + 2\Delta c_r$. Proof loads that exceed or equal P_{LBB} will result in burst (structural failure), while those that are less than P_{LBB} will result in a leak (functional failure for non-hazardous situations).

APPENDIX B: VALIDATION

B1. THEORETICAL VALIDATION: *J* ESTIMATION SCHEMES/FAILURE ASSESSMENT DIAGRAMS

B1.1 Introduction

This section presents validation using elastic-plastic finite element *J* results for the following reference stress based *J* estimation schemes and Failure Assessment Diagram (FAD) constructions that are recommended for use in Appendix A when performing proof test analyses:

- primary loads
- cracks emanating from stress concentrators
- cracks subjected to combined primary and secondary loads
- cracks subjected to biaxial stressing
- cracks in welds

B1.2 Primary Loads

In the EPRI *J* estimation scheme, *J* is represented as the linear addition of elastic, J_e, and plastic, J_p, components. It is sufficient to demonstrate only the accuracy of J_p estimated using the reference stress approach in order to validate the *J* estimation scheme recommended in Appendix A for cracks at smooth surfaces subjected to primary loading. This is because the EPRI elastic-plastic handbooks (see Table A4.1) have already verified the use of the EPRI scheme, and the reference stress approach to generalizing this scheme only differs from the EPRI approach in the way that J_p is calculated.

B1.2.1 Reference Stress Approach

The reference stress approach developed by Ainsworth [65] is closely related to the EPRI scheme for estimating J_p and provides a powerful analytical tool for deriving solutions for J_p in cases where alternative computational solutions are not available. It is for this reason that the approach is recommended for use in proof test analyses as a relatively simple means of estimating J_p

A widely used representation of J_p within the EPRI estimation scheme is

$$J_p = \alpha\, \sigma_o \epsilon_o [w-c] \left[\frac{c}{w}\right] h_1\left(\frac{c}{w}, n, \frac{L}{w}\right) \left[\frac{P}{P_o}\right]^{n+1} \qquad \text{(B1.1)}$$

where c is the crack depth, w is the section width, and w-c is the uncracked ligament. Values for the functions h_1 are tabulated in the EPRI handbooks for various structural geometries and depend on c/w, n, and, in general, a normalized structural geometry parameter, L/w, where L represents, for example, the radius of a cylinder or a notch root radius. P is the applied load, and P_o a characteristic net section yield load defined for each structural geometry and load type in the EPRI handbooks.

One of the aims of the reference stress approach developed by Ainsworth [65] is to choose a net section yield load, P_o^*, so that the function $h_1(c/w,n,L/w)$ which appears in the EPRI scheme for J_p can be replaced by an alternative function, $h_1^*(c/w,L/w)$, which no longer depends on n (see also Bloom [66]; Chell, McClung, Russell [67]). In terms of the reference stress parameters P_o^* and h_1^*, J_p is written as

$$J_p = \alpha \sigma_o \epsilon_o [w - c] \left[\frac{c}{w}\right] h_1^* \left(\frac{c}{w}, \frac{L}{w}\right) \left[\frac{P}{P_o^*}\right]^{n+1} \tag{B1.2}$$

The reference stress, σ_{ref}, is defined through the equation

$$\sigma_{ref} = \left[\frac{P}{P_o^*}\right] \sigma_o \tag{B1.3}$$

Ainsworth [65] made the simplifying approximation that $h_1^*=h_1(n=1)$. This approximation enables h_1^* to be expressed in terms of the linear elastic solution for J_e since $J_p(n=1)=\mu J_e$ where $\mu=(1-\nu_p^2)/(1-\nu_e^2)$ for plane strain, and $\mu=1$ for plane stress, and ν_e and ν_p are the elastic and plastic values of Poisson's ratio respectively. The result is

$$h_1^* = \frac{E \mu J_e}{\left[[w - c] \frac{c}{w}\right] \sigma_{ref}^2} \tag{B1.4}$$

which, when substituted into equation (B1.2) yields Ainsworth's reference stress approximation for J_p

$$J_p = \mu E J_e \frac{\epsilon_{ref}^p}{\sigma_{ref}} \tag{B1.5}$$

This result provides a simple and powerful approximate expression for evaluating J_p over a much greater range of structural and engineering parameters than is presently possible using the existing EPRI handbook solutions. The expression implies that the dependence of J_p on engineering parameters is fully accounted for by the dependence of J_e and σ_{ref} on these parameters, and that the dependence on stress-strain behavior is simply derived from the constitutive relationship between strain and stress.

B1.2.2 Derivation of an Optimum Reference Stress Solution

In this section, an "optimized" reference stress solution to J_p is constructed such that h_1^* is independent of strain hardening exponent n. The expression for the reference stress solution for J_p

involves a yield load, P_o^*, a function h_1^*, and a function $V(c/w,L/w)$. The values of these functions are derived using a simple scheme which optimizes the accuracy of the reference stress solution to reproduce known computed values of $h_1(c/w,n)$ for a range of exponents n. Hence, the derived values of P_o^* and h_1^* are sometimes prefixed by the adjective "optimum" to differentiate them from values obtained using alternative methods.

Since, $J_p(n=1)=\mu J_e$, it cannot depend explicitly on either the yield loads, P_o or P_o^*. Hence the solutions for $n=1$ are not used directly in the proposed optimization scheme.

An expression for h_1^* is obtained by comparing equations (B1.1) and (B1.2)

$$h_1^*\left(\frac{c}{w},\frac{L}{w}\right) = h_1\left(\frac{c}{w},n,\frac{L}{w}\right)\left[\frac{P_o^*}{P_o}\right]^{n+1} \quad , \; n \geq 2 \tag{B1.6}$$

Although n appears in the terms on the right hand side of this equation, the purpose of the optimization scheme is to make the product of these terms independent of n. Re-arranging equation (B1.6) yields

$$P_o^*(n) = P_o\left[\frac{h_1^*\left(\frac{c}{w}\right)}{h_1\left(\frac{c}{w},n\right)}\right]^{\frac{1}{n+1}} \quad , \; n \geq 2 \tag{B1.7}$$

where $P_o^*(n)$ are yield loads whose values are to be determined. The dependence of $P_o^*(n)$ on n is introduced intentionally to reflect numerical inaccuracies that occur in the computation of $h_1(c/w,n)$. If these errors were absent, then according to the reference stress approach the optimum yield load, P_o^*, would be independent of n. The aim of the optimization scheme is to reduce the dependence of the calculated $P_o^*(n)$ values on n by judicious choice of h_1^* while at the same time reproducing the computed values of $h_1(c/w, L/w, n)$ as closely as possible.

Equation (B1.7) cannot be solved directly for $P_o^*(n)$ as the value of h_1^* is not known a priori. Instead, h_1^* is treated as a variational parameter whose value is chosen so as to minimize the dependence of $P_o^*(n)$ on n. Hence, the value of h_1^* is varied until a "sample variance" parameter, ρ, attains a minimum value, where

$$\rho = \sum_{n \geq 2}\left(P_o^*(n) - P_o^*\right)^2 \tag{B1.8}$$

and the required optimum yield load, P_o^*, is given by

$$P_o^* = \frac{1}{N}\sum_{n \geq 2} P_o^*(n) \tag{B1.9}$$

where N is the number of n values for which computed J_p solutions are available. Bloom [66] has used a similar scheme to derive yield loads from computed solutions for J_p, but he, like Ainsworth [65], assumed $h_1^*=h_1(n=1)$, which does not necessarily optimize the accuracy of reference stress solution to reproduce the J_p solutions.

Once P_o^* and h_1^* have been determined, the value of $h_1(c/w,n)$ can be estimated for any value of n through the equation

$$h_1\left(\frac{c}{w},n\right) = h_1^*\left(\frac{c}{w}\right)\left[\frac{P_o}{P_o^*}\right]^{n+1}, \quad n \geq 2 \tag{B1.10}$$

Since $h_1(c/w,n=1)$ is not used in the optimization scheme it is not related to h_1^* through P_o^*, but through another parameter, $P_o^*(1)$ where

$$P_o^*(1) = P_o\left[\frac{h_1^*(c/w)}{h_1(c/w,n=1)}\right]^{1/2} \tag{B1.11}$$

Hence, from equation (B1.6)

$$h_1\left(\frac{c}{w},n\right) = h_1\left(\frac{c}{w},n=1\right) V(c/w,L/w)\left[\frac{P_o}{P_o^*}\right]^{n-1} \tag{B1.12}$$

where the parameter, V, is given by

$$V(c/w,L/w) = \left[\frac{P_o^*(1)}{P_o^*}\right]^2 = \frac{h_1^*(c/w,L/w)}{h_1(c/w,n=1,L/w)} \tag{B1.13}$$

Using the parameter, V, and equations (B1.2) and (B1.12), J_p can be written for $n>1$ as

$$J_p = J_e \mu V(c/w,L/w) \alpha \left[\frac{P}{P_o^*}\right]^{n-1} \tag{B1.14}$$

Equation (B1.14) establishes the relationship between the plastic and elastic components of J. Furthermore, using the Ramberg-Osgood law and the reference stress, σ_{ref}, given in equation (B1.3), equation (B1.14) can be re-written as

$$J_p = J_e \mu V(c/w, L/w) \left[\frac{E \epsilon_{ref}^p}{\sigma_{ref}} \right] \tag{B1.15}$$

where ϵ_{ref}^p is the reference plastic strain corresponding to the value of σ_{ref} on the uniaxial stress-strain curve. Note that in equation (B1.15) J_p has been expressed in a form which is applicable to materials with arbitrary stress-strain behavior. This is an important benefit of the reference stress.

Equations (B1.14) and (B1.15) are the expressions recommended for evaluating J_p in Section A4.2.

B1.2.3 Validation of the Reference Stress J Estimation Scheme

Examples of the ability of the optimization scheme to accurately represent the finite element solutions for $h_1(c/w,n)$ in terms of $h_1^*(c/w)$ and optimum net section yield loads are shown in Figures B1.1 and B1.2. These figures show the computed values of $h_1(c/w,n)$ obtained from Kumar et al. [68] and Orient [69] for an edge cracked plate in plane strain subjected to tensile loading (Figure B1.1), and for a surface semi-elliptical flaw in a plate subjected to a tensile force (Figure B1.2), respectively, plotted against the values predicted using equation (B1.12). The nearness of the points to the one-to-one line indicates the accuracy of the optimum yield approach: predictions that fall on the line are exact. The results in Figure B1.1 cover six crack depths in the range $0.125 \le c/w \le 0.75$, and seven strain hardening exponents in the range $2 \le n \le 16$. The results in Figure B1.2 include three crack depths in the range $0.2 \le c/w \le 0.8$, three aspect ratios in the range $0.2 \le a/c \le 1$ where a is the crack depth, c is half the surface length, and three n values in the range $5 \le n \le 15$, and are presented for the deepest point [Figure B1.2(a)] and the surface points [Figure B1.2(b)] on the flaws.

It can be seen that the reference stress method predicts $h_1(c/w,n)$ values which are in very good agreement with the computed results. The accuracies indicated in Figures B1.1 and B1.2 are typical of the accuracies with which the method reproduces the values of $h_1(c/w,n)$ for other cracked geometries and loading systems.

B1.2.4 Statistical Analysis of Calculated Values of V

To determine the dependence of V on engineering parameters, values of V and P_o^* have been derived for an extensive assortment of structural geometries, crack shapes and sizes, and applied load types from published finite element results for the function $h_1(c/w,n,L/w)$. The determination of the values of V and P_o^* that produce the best agreement between the reference stress approximation to J_p and the computed solutions requires that values of $h_1(c/w,n,L/w)$ be available for a range of strain hardening exponents, n. From these solutions for different n, single values for V and P_o^* can be derived for a specific set of engineering features.

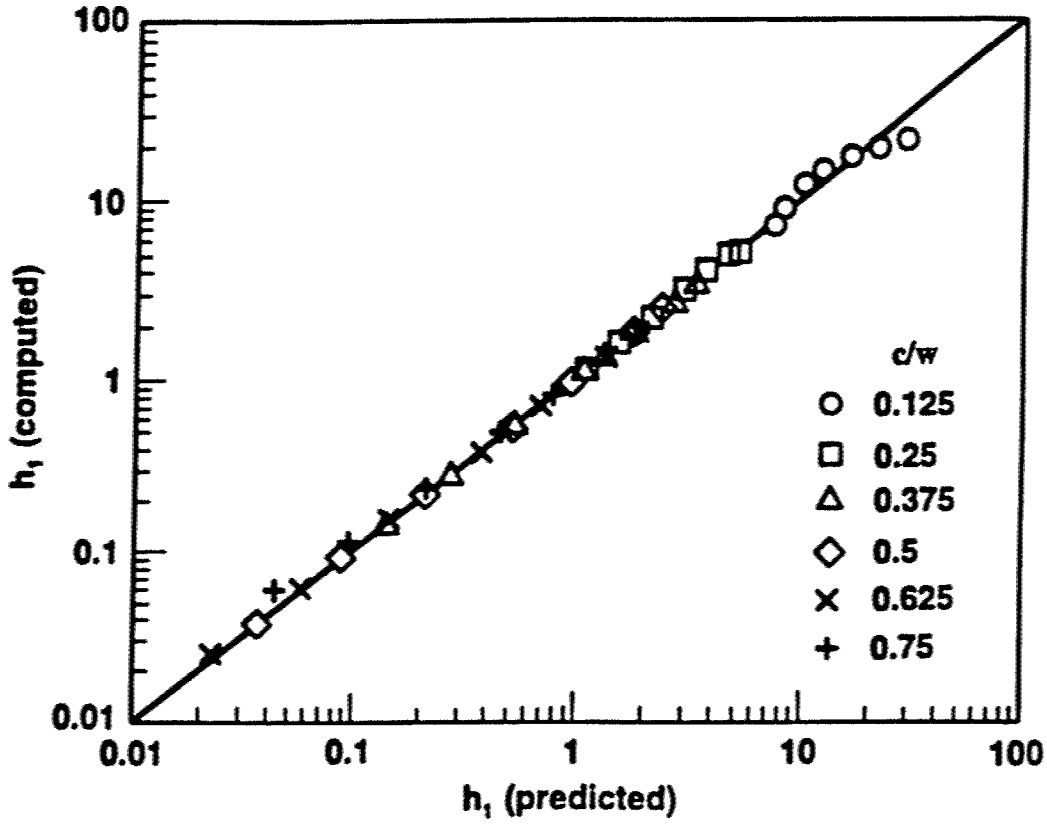

Figure B1.1 Comparison of computed plane strain values of the h_j functions for a single edge cracked plate in tension for $n = 2, 3, 5, 7, 10, 13$, and 16 with the predictions of the reference stress approach derived using the optimization scheme.

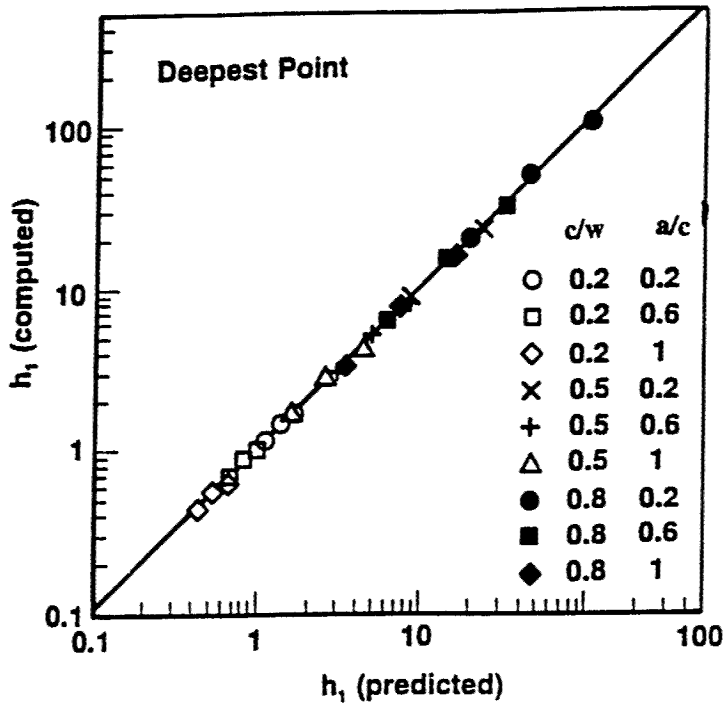

(a)

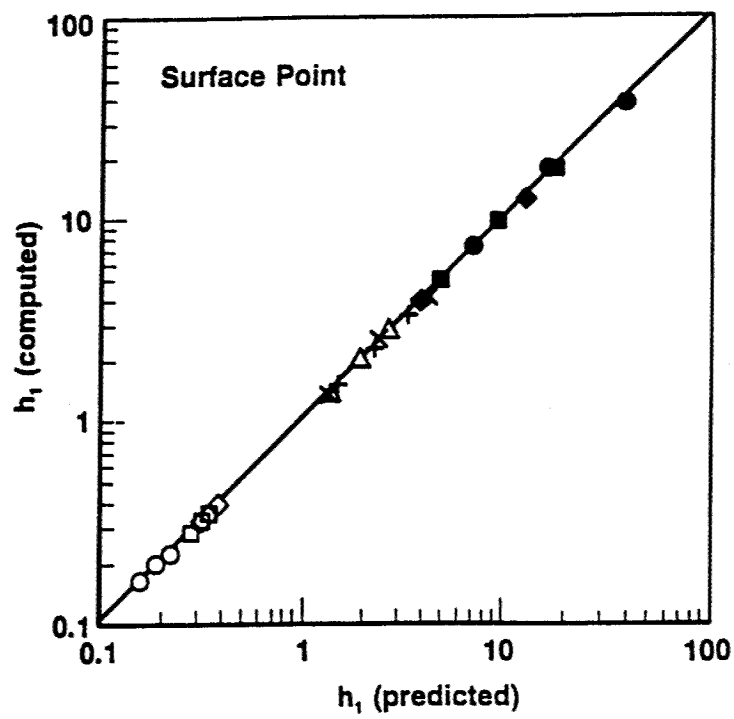

(b)

Figure B1.2 Comparison of computed values of the h_1 functions for a surface flaw in a plate subjected to tension for n=5, 10, and 15 with the predictions of the reference stress approach derived using the optimization scheme. (a) Results for the deepest point on the flaw. (b) Results for the surface point.

In all, 189 values of $V(c/w,L/w)$ were derived from computed $h_1(c/w,n,L/w)$ values for the following flawed structural geometries and engineering parameters:

* two-dimensional geometries:
  - single edge cracks in plates subjected to tensile loads (plane stress and plane strain) [68]
  - double edge cracks in plates subjected to tensile loads (plane stress and plane strain) [68]
  - single edge cracks in plates subjected to bending (plane stress and plane strain) [68]
  - center cracked plates (plane stress and plane strain) [68]
  - cracks emanating from an embedded round hole subjected to biaxial stressing [68]
  - part-through axially cracked cylinders subjected to internal pressure [68]
  - part-through circumferential cracks in cylinders subjected to tensile forces [68]
* three-dimensional geometries:
  - circumferential through-wall cracks in cylinders subjected to tensile forces [70]
  - circumferential through-wall cracks in cylinders subjected to applied moments [70]
  - semi-elliptical flaws (deepest point) on the internal surface of a cylinder subjected to internal pressure [71]
  - semi-elliptical flaws (deepest, surface and near-surface points) in plates subjected to tensile forces [69,72,64,73]
  - semi-elliptical flaws (deepest, surface and near-surface points) in plates subjected to bending [73]

The minimum calculated value for V was 0.6, and the maximum was 2.3. It is emphasized that the variation in the values of the derived V values for different structural and engineering parameters reflects not only real explicit dependencies of V on these parameters, but also apparent dependencies due to uncertainties in the computed numerical values of h_1 and inaccuracies introduced by the method employed for deriving the fully plastic J_p solutions from the actual computed values of J, which included both linear elastic and first order plastic components. Thus, significant differences in V values were sometimes observed in J_p values obtained by different workers for the same geometry, crack size and load type. For example, this was the case for some of the results reported by Orient [69] and Yagawa [72] for surface semi-elliptical flaws in plates. Other workers, such as Bloom and Lee [71], have also commented on the need for care when deducing the fully plastic component of J from its elastic-plastic value. Criteria for assessing the accuracy of computed fully plastic J_p solutions have been discussed by Miller and Ainsworth [74] which also discusses the accuracy of the reference stress approach in terms of load factors required to make the results of this method equal to computed solutions for J_p.

It is of interest to note that although there are differences between the values of J_p computed by different workers for nominally the same cracked structure, within any particular set of results the values of h_1 still appear to scale as the ratio $h_1^*(P/P_o^*)^{n+1}$, even though the derived values of P_o^* may differ between sets.

The 189 derived V values were statistically analyzed by separating the data into three groups corresponding to:

(i) All the data (189 samples)

(ii) The values for the deepest points on both the two dimensional (108 samples) and three dimensional (24 samples) flaws (a total of 132 samples).

(iii) The values for the surface (24 samples) and near surface (33 samples) points for the three-dimensional semi-elliptical flaws (a total of 57 samples). The near surface points corresponded to positions on the flaws at angles of 9°, 10°, and 18° from the free surface.

The samples in Groups (i)-(iii) were statistically examined using normal, exponential, Weibull, Extreme Value, and Lognormal distributions. From the results of this analysis, the following conclusions were drawn:

(1) Based on statistical tests [75], the cumulative distribution function that best described the data in Groups (i)-(iii) is the Type 1 Extreme Value Distribution (EVD). The cumulative distribution function for the Type 1 EVD is

$$F_X(x) = exp\left[-\exp\left(-\alpha'\left[x - \beta'\right]\right)\right] \tag{B1.16}$$

where α' and β' are related to the mean, μ_x, and standard deviation, σ_x, by the equations

$$\mu_x = \beta' + \frac{0.577}{\alpha'}, \quad \sigma_x = \frac{1.283}{\alpha'} \tag{B1.17}$$

The values of α', β', μ_x, and σ_x for each of the data samples in the three groups are shown in Table B1.1. The form of the empirical and derived distributions for the Group (i) data are shown in Figure B1.3. The empirical distribution function was determined by the formula

$F_i(v) = \dfrac{(i - ½)}{n}$, for $v_i \le v < v_{(i+1)}$, in which v_i is the i'th smallest value of V [75].

Table B1.1 Type 1 EVD parameter values derived from the sample V values in groups (i)-(iii)

Group	α'	β'	μ_x	σ_x
(i)	4.4018	1.0380	1.1691	0.2915
(ii)	4.1776	1.0363	1.1744	0.3071
(iii)	4.9563	1.0428	1.1592	0.2426

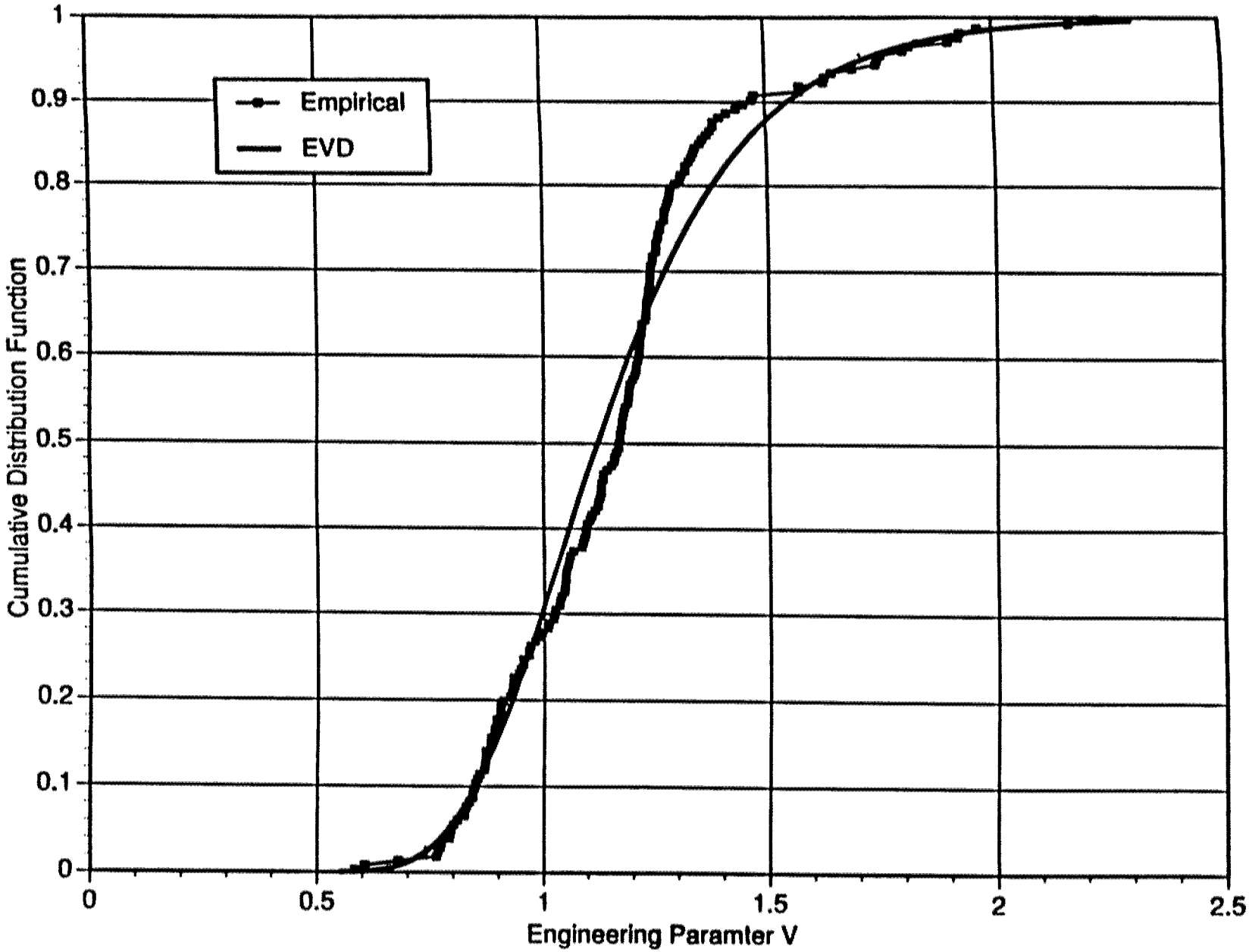

Figure B1.3 Cumulative distribution function for the engineering parameter, *V*, for Group (i) data. The Type 1 Extreme Value distribution best fits the empirical distribution of the derived values of *V*.

(2) A linear regression analysis of the V values in Groups (ii) and (iii) corresponding to the deepest and surface points on three-dimensional semi-elliptical flaws indicated that the values at these two positions were not correlated (the correlation coefficient was approximately 0.01).

The accuracy of the reference stress approach for calculating J_p is dependent on knowing an accurate value for the applied stress intensity factor, K, the reference stress, σ_{ref}, and the structural dependent parameter, V. It is difficult to generalize the uncertainties associated with calculating K and σ_{ref}, and it is usual to assume V=1. However, the present analysis shows that the uncertainty in the value of V arising from crack size and shape, structural geometry, and loading system can be quantified in terms of a Type 1 Extreme Value distribution function. This function can be used to incorporate uncertainties in the reference stress approximation for J_p into a probabilistic based methodology, and to define statistically meaningful upper and lower bound values of V for service and proof test analyses, respectively. These values have been calculated for the Group (i) data (all 189 samples) and the results are displayed in Table A4.2.

B1.2.5 Material Dependent FADs for Primary Loading

It is convenient to represent the optimized reference stress J results in terms of FADs to more clearly see the effects of different V values on J_p. The relationship between FAD failure curves and J is derived in Section A5.2. The simplifying approximations that lead to material specific J estimation schemes and failure curves are described in Sections A4.9 and A5.10, respectively. Material specific failures curves are incorporated into the defect assessment procedures, PD6493 [45] and R6 [46]. In Level 3 of PD6493 and Option 2 of R6, the equation for generating these curves is

$$K_r^* = \left(\left[\frac{E\,\epsilon_{ref}}{\sigma_{ref}} \right] + \frac{0.5\,L_r^{*2}}{\left[\frac{E\,\epsilon_{ref}}{\sigma_{ref}} \right]} \right)^{-\frac{1}{2}} \tag{B1.18}$$

where now ϵ_{ref} is the total reference strain corresponding to σ_{ref}, and $\sigma_{ref}=L_r^*\sigma_o$ where $L_r^*=P/P_o^*$. The second term on the right hand side of this equation represents a first order plastic correction that helps smooth the transition from elastic to fully plastic conditions.

Equation (B1.18) can be modified to include the structurally dependent term $V(c/w, L/w)$

$$K_r^* = \left(1 + \mu\, V(c/w, L/w) \left[\frac{E\,\epsilon_{ref}}{\sigma_{ref}} - 1 \right] + \frac{0.5\,L_r^{*2}}{\left[\frac{E\,\epsilon_{ref}}{\sigma_{ref}} \right]} \right)^{-\frac{1}{2}} \tag{B1.19}$$

(see Section A5.10). The material specific curve of equation (B1.18) is recovered from this equation when V=1 and plane stress deformation is assumed (μ=1). Hence, a value of V=1 signifies that the failure curve will not depend on structural features. As reported in Section B1.2.4, the minimum calculated value for V was 0.6, and the maximum was 2.3 with a mean value of 1.169, which is

similar to the value of V=1 assumed in the material specific failure curves defined in PD6493 [45] and R6 [46]. Failure curves derived using various values of V between the minimum and maximum values and μ=1, are shown in Figure B1.4, where they illustrate the effect of changing V values. The curves were based on the material properties of the nickel-based superalloy IN-718, where the stress-strain curve at room temperature can be described by a Ramberg-Osgood law with α=1 and n=15.8. The results illustrate the relative insensitivity of the failure curves to V when L_r^* is defined in terms of the optimum yield load as P/P_o^*.

The greatly reduced sensitivity of failure curves to structural features when the optimum net section yield load is used as a normalizing load is further illustrated in Figure B1.5. Figure B1.5(a) shows the upper and lower bounding curves obtained from the reference stress approach using optimum net section yield loads and the published J solutions for α=3, n=5. In contrast, Figure B1.5(b) shows the same data plotted using the normalizing net section yield loads employed in the EPRI J estimation scheme. In Figure B1.5, the curves signified as "Reference Stress" correspond to the case where V=1 and μ=1.

The results in Figure B1.5(b) illustrate that inaccurate choices for net section yield loads can produce apparent structural sensitivities in failure curves, whereas the results in Figure B1.5(a) show that elastic-plastic fracture behavior can be represented to a good approximation by a failure curve that is a function only of stress-strain behavior, provided accurate net section yield loads are used.

B1.2.6 Conclusions

The purpose of this section is to describe the theoretical basis for the J estimation/FAD procedure for primary loads which are employed in Section A4.2. This has been partly accomplished by demonstrating that failure curves are relatively insensitive to structural features, and are predominantly determined by uniaxial stress-strain behavior. In addition, the current work has shown that the reference stress method provides accurate upper and lower bound estimates for J_p for use in service and proof test analyses, respectively, provided accurate net section yield loads are used.

It should be noted that the structural dependence of the failure curve (i.e., the value of V) will significantly influence the outcome of an assessment only if failure is predicted to occur under elastic-plastic conditions. Predicted failure conditions in the linear elastic and fully plastic regimes will not be sensitive to the value of the structural parameter, V, as these conditions are governed by the stress intensity factor and the net section yield load, respectively. Hence, for a given set of material property values, the accuracy of the results of an assessment based on a FAD will be mainly determined by the accuracy of the net section yield load.

B1.3 Cracks at Stress Concentrators

B1.3.1 Introduction

In this section, the J estimation scheme proposed for cracks at notches in Section A4.3 is validated against finite element elastic-plastic J results obtained by Orient [69] for symmetrical cracks emanating from parallel sided double edge notches in plates subjected to tensile forces and undergoing plane stress deformation. The solutions were obtained for material stress-strain behavior governed by the Ramberg-Osgood law.

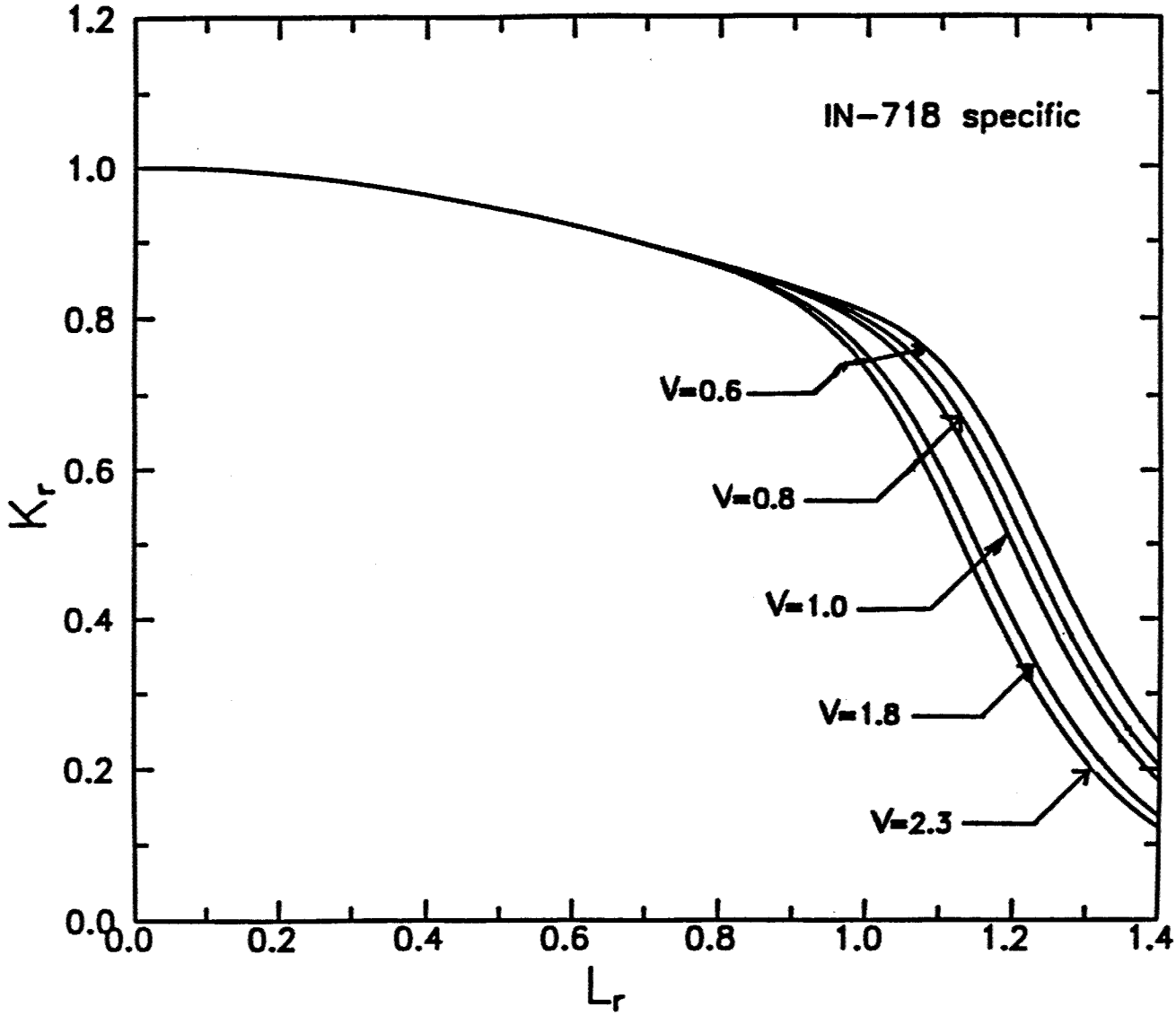

Figure B1.4 Effect of uncertainty in the value of *V* on the material specific failure curve for IN-718.

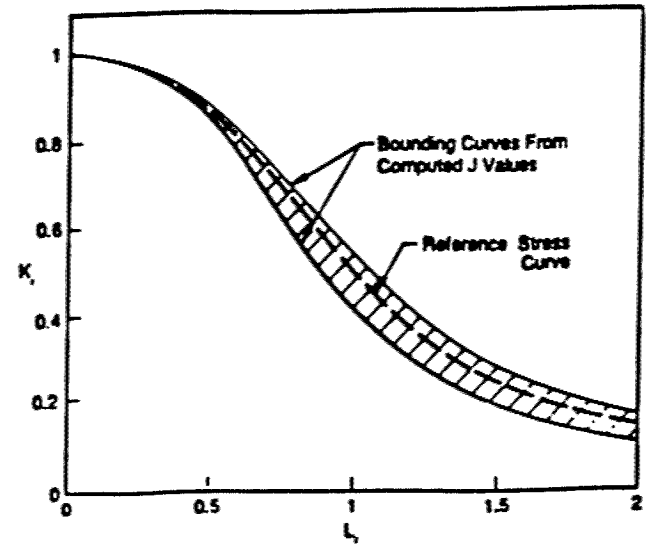

(a)

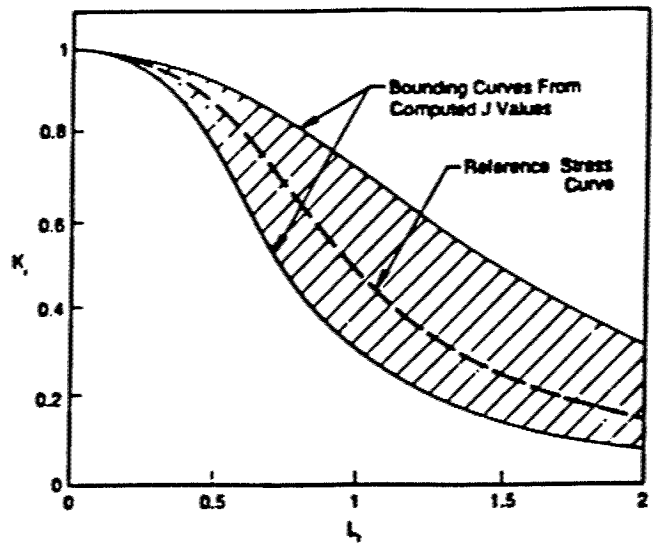

(b)

Figure B1.5 Failure curves derived from finite element J solutions using optimized (a) and conventional (b) net section yield loads, P_o, to calculate L_r

Orient computed 88 values of J for various c_{ext}/w and n values and for D_n/r_n=2.41, 6.2, and 11.6, which correspond to stress concentration factors, K_t, of 4.2, 6.3, and 8.4, where

$$K_t = \frac{stress\ at\ notch}{gross\ section\ stress} \tag{B1.20}$$

Here, $c_{ext}=D_n+c$, where D_n is the depth of the notch, c is the depth of the crack measured from the root of the notch, w is half the width of the plate, and r_n is the radius of the semi-circular notch tip. The relationships between c, c_{ext}, r_n, D_n, and w, are shown schematically in Figure A4.3 of Appendix A.

B1.3.2 J Estimation Scheme

Chell [50] has analyzed the results of Orient [69] and expressed them in terms of the EPRI J estimation scheme

$$J = J_e + J_p \tag{B1.21}$$

where J_e is a first order plastically corrected value of the linear elastic solution for J given by

$$J_e(c_e,P) = J_e(c + \phi r_y,P) \tag{B1.22}$$

where the effective depth, $c_e=c+\phi r_y$, includes a plastic zone correction determined by the terms ϕ and r_y which are defined as

$$\phi = \frac{1}{1 + \left(\frac{P}{P_o(c_{ext})}\right)^2} \tag{B1.23}$$

$$r_y = \frac{1}{2\pi}\left[\frac{n-1}{n+1}\right]\left(\frac{K_I(c,P)}{\sigma_o}\right)^2 \tag{B1.24}$$

The plastic component, J_p, is expressed as

$$J_p = \alpha\ \epsilon_o\ \sigma_o(w - c_{ext})\ h_1(c_{ext}/w,n,D_n/r_n)\left(\frac{P}{P_o(c_{ext})}\right)^{n+1} \tag{B1.25}$$

The characteristic yield load, P_o, is defined for the double edge cracked plate in plane stress as

$$P_o = \frac{4}{\sqrt{3}} (w - c_{ext}) t \sigma_o \tag{B1.26}$$

where t is the section thickness.

Chell [50] applied the optimized reference stress method (RSM) to the results of Orient [69] using the expression for J given by equation (A4.16)

$$J = J_e(c + \phi^* r_y, P) + \alpha J_e(c, P) V^* (c_{ext}/w, D_n/r_n) \left[\frac{P}{P_o^*(c_{ext})} \right]^{n-1} \tag{B1.27}$$

Orient derived a total of 88 J solutions for Ramberg-Osgood constants given by α=1, σ_o=60 ksi, and n=3, 5, 10, and 15, and various crack depths. The detailed results and analysis are reported by Chell [50]. Here only a representative set of the results will be discussed in detail.

Orient's results were analyzed using the optimized RSM described in Section B1.2. The derived values of V^* were found to vary between about 1.2 and 1.4, well within the range of V^* values obtained for the 189 geometries analyzed in Section B1.2. These values support the use of the recommended conservative values provided in Table A4.2 of Appendix A. The optimized net section yield loads, P_o^*, for the notched geometries were found to be nearly equal to the optimized net section yield loads for unnotched double edge cracked plates containing symmetrical flaws of depths equal to c_{ext}. This result supports the assumption that the net section yield load is not sensitive to the notch details.

B1.3.3 Validation Using Failure Assessment Diagrams

It is convenient to transfer the J results obtained from the finite element computations and the optimized RSM into failure curves which can be plotted on a Failure Assessment Diagram (FAD) to facilitate a comparison of the two sets of solutions, and to identify trends in behavior as the value of K_t changes. The FAD provides a simple diagrammatic representation of J solutions which makes apparent the effect of increasing crack tip plasticity as the applied load is increased. The failure curves can be generated by evaluating the parameters L_r^* and K_r^* as a function of the load P using the equations

$$L_r^* = \frac{P}{P_o(c_{ext}/w)} \ , \ K_r^* = \sqrt{\frac{J_e(c,P)}{J(c,P)}} \tag{B1.28}$$

The value of L_r^* measures the nearness of the flawed structure to net section yielding (by definition, L_r^*=1 corresponds to net section yielding), and the value of K_r^* determines the effects of crack tip plasticity with respect to linear elastic behavior. (By definition, K_r^*=1 corresponds to J=J_e and linear elastic fracture mechanics may be applied, whereas a value of K_r^*<1 indicates that fully plastic

behavior is appropriate and $J \approx J_p$) The RSM estimate of J will be conservative compared to the finite element results when the RSM failure curve falls inside the finite element failure curve, but will underestimate the finite element J value when the reverse situation occurs. For a given applied load (L_r^* value) the ratio of J solutions is given by

$$\frac{J(RSM)}{J(finite\ element)} = \left[\frac{K_r(finite\ element)}{K_r(RSM)} \right]^2 \qquad \text{(B1.29)}$$

Figures B1.6 through B1.11 show FADs constructed using equations (B1.27) and (B1.28) based on the derived V^* values (dashed lines) and, for comparison purposes, with $V^*=1$ (solid lines), and FADs derived from the finite element J analyses performed by Orient for $n=10$ (open circles). The figures cover FADs for shallow and deep cracks emanating from notches with K_t values of 4.2, 6.3, and 8.4. The RSM approximations to J were evaluated using optimized yield loads, P_o^*.

The agreement between FADs derived using the RSM and the finite element FADs is good, indicating that the accuracy of the RSM approach to estimating J will be sufficient for engineering applications. The good agreements between the RSM and finite element solutions displayed in Figures B1.6 to B1.11 are typical of the agreements obtained for all of the 88 analyses performed using Orient's solutions. It can be seen that the sensitivity of the RSM failure curves to the value of V^*, as represented by the solid and dashed curves, is small, even in the fully plastic regime ($L_r>1$) where the value of V^* is expected to have the greatest impact on the value of J_p

B1.3.4 Conclusions

The elastic-plastic value of J for cracks at notches can be estimated by combining the EPRI and RSM estimation schemes as recommended in Section A4.3 of Appendix A. The EPRI scheme provides a means of evaluating J in the linear elastic and small scale crack tip yielding regimes which incorporates local notch stress concentration effects. The RSM approach provides a way of estimating the effects of widespread plasticity (net section yielding) on J. The recommended values of V^* given in Table A4.2 of Appendix A are conservative with respect to proof test and service analyses when applied to cracks at notches. Although the notch details influence the net section yield loads derived from finite element J analyses, the effect is small, and yield loads based on the nominal load and the extended crack depth, c_{ext} can be used in the RSM J estimation procedure.

B1.4 Combined Primary and Secondary Loads

B1.4.1 Introduction

The recommended approach in Section A4.4 of Appendix A for combined primary and secondary loads is to use a combination of the EPRI J Estimation scheme [70] and the reference stress approach. In the EPRI scheme the secondary loads contribute only to the elastic component, J_e of J. The plastic component, J_p, is determined only by the primary load. This engineering approach is consistent with the fact that secondary loads cannot influence fully plastic behavior, as the net section

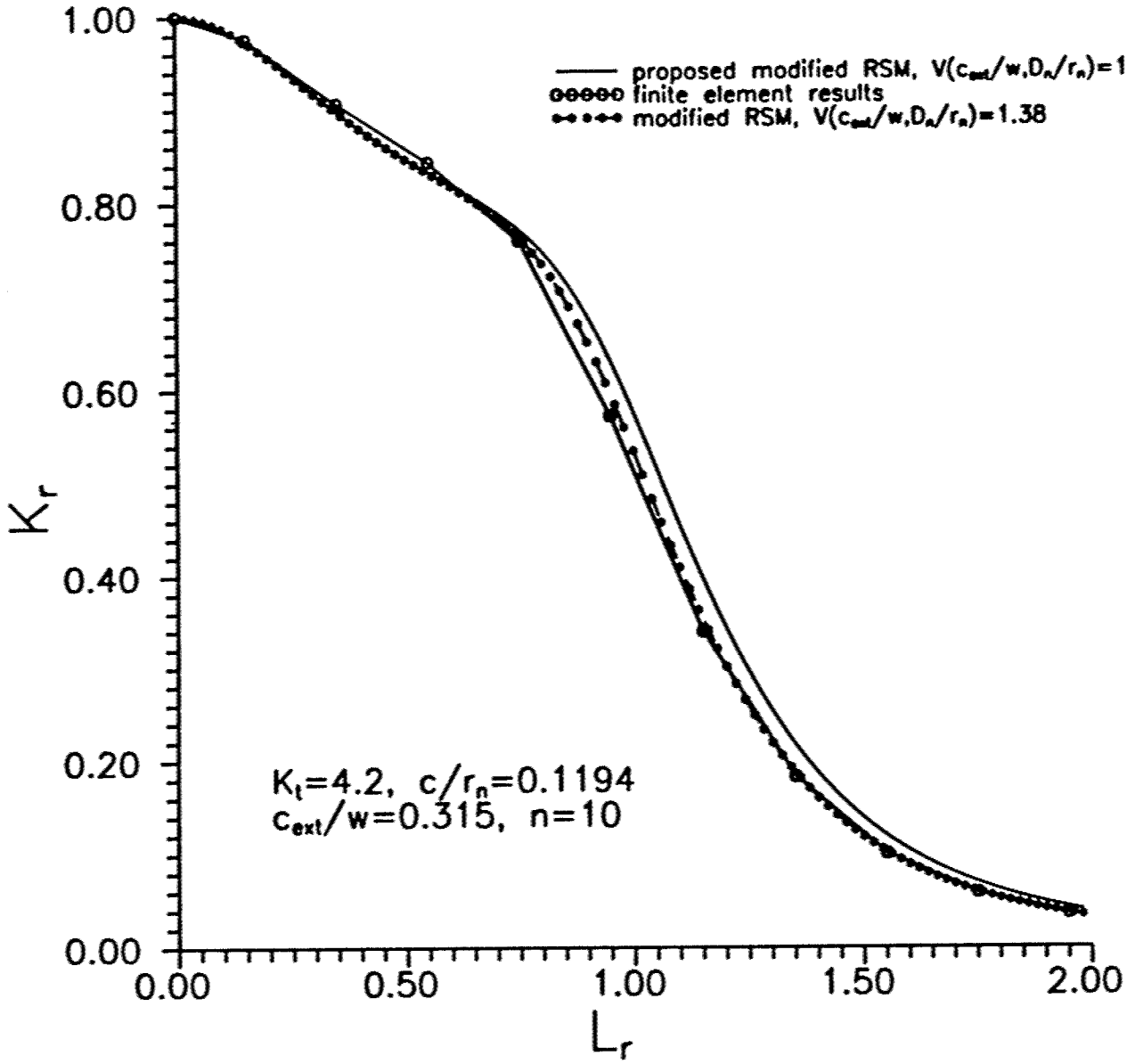

Figure B1.6 Comparison of failure curves derived from finite element computations with optimized RSM solutions for cracks emanating from double edge notched plates subjected to uniform stressing for K_t=4.2, c/r_n=0.1194, c_{ext}/w=0.315, and n=10.

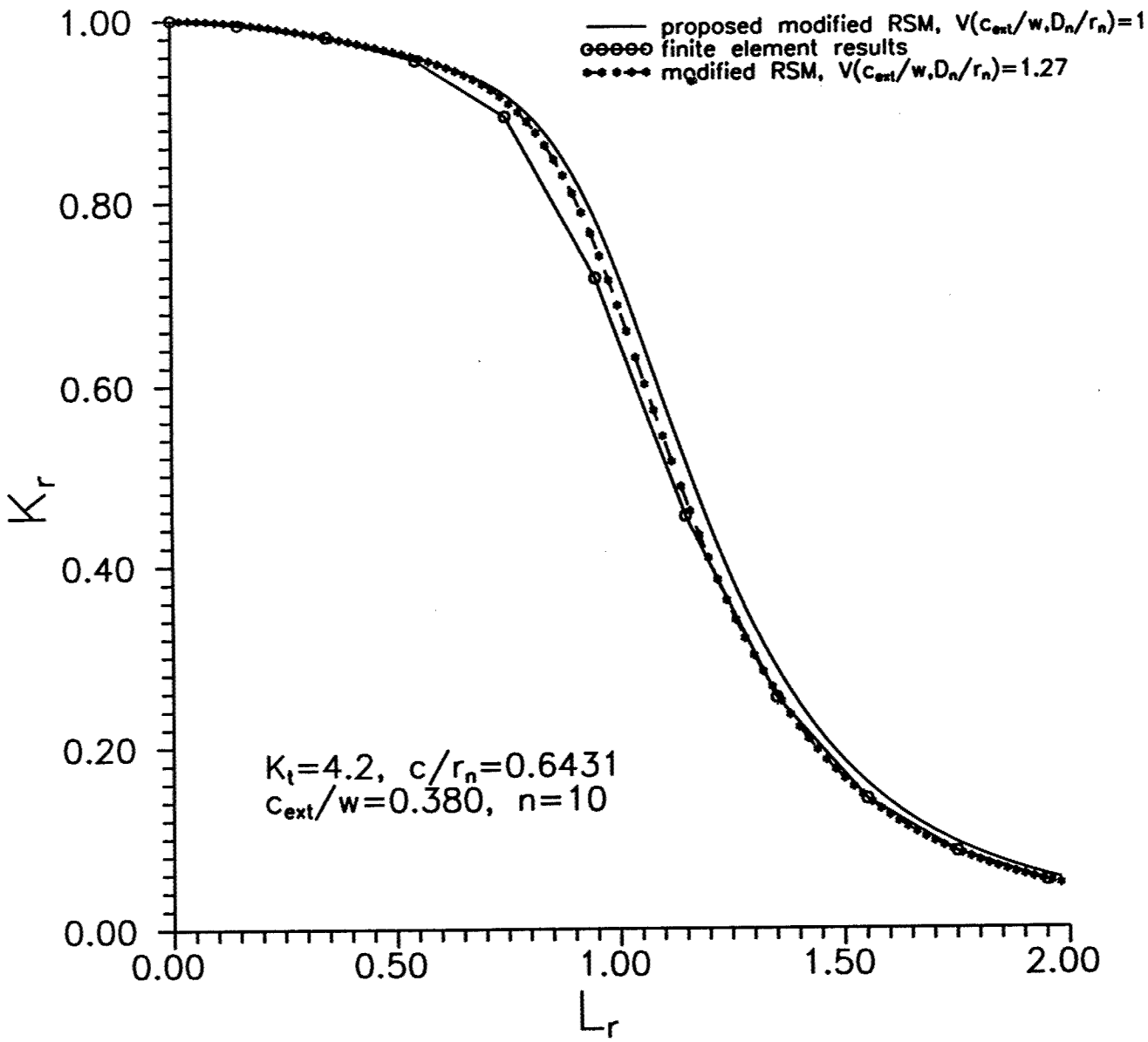

Figure B1.7 Comparison of failure curves derived from finite element computations with optimized RSM solutions for cracks emanating from double edge notched plates subjected to uniform stressing for $K_t=4.2$, $c/r_n=0.6431$, $c_{ext}/w=0.380$, and $n=10$.

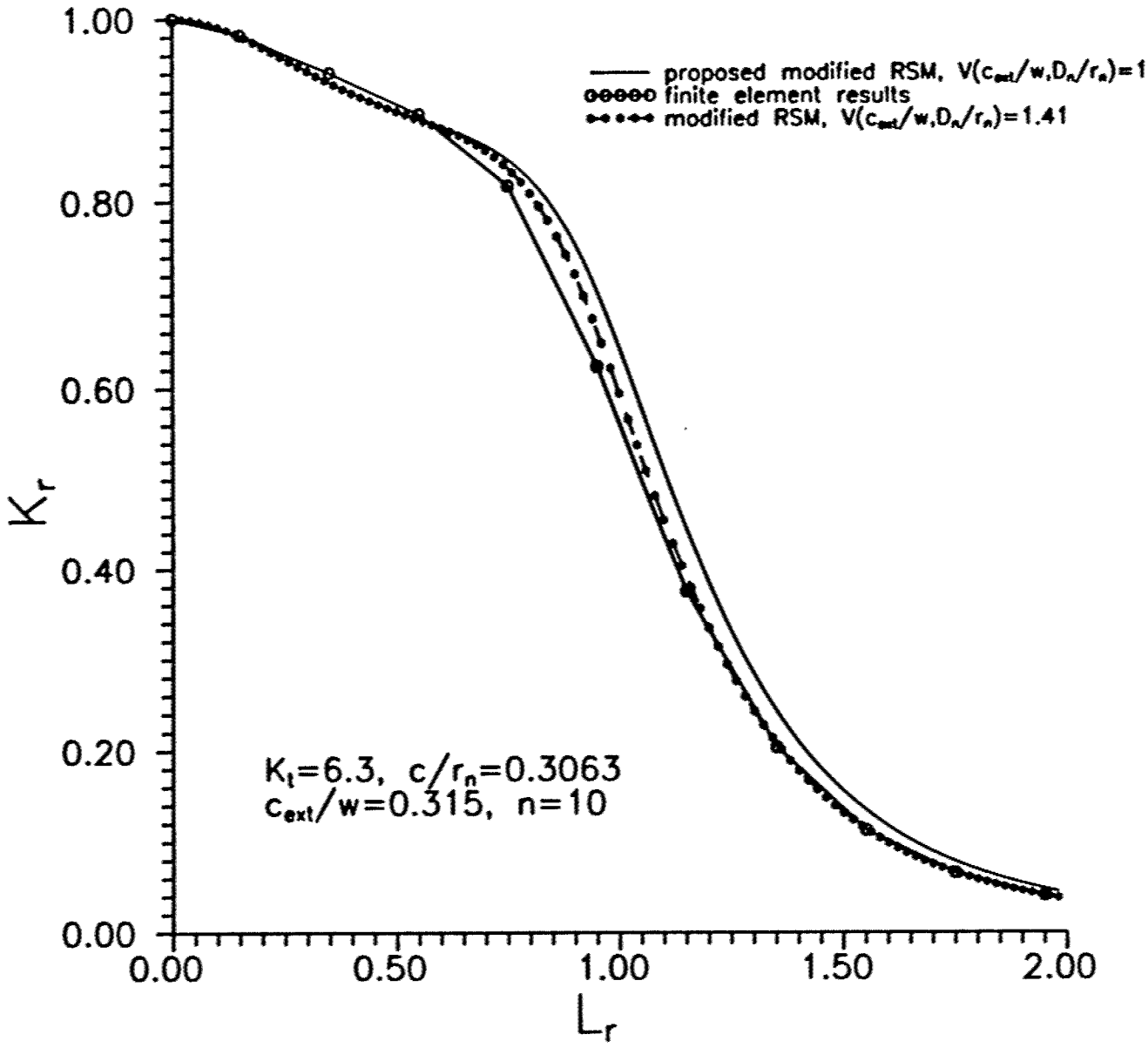

Figure B1.8 Comparison of failure curves derived from finite element computations with optimized RSM solutions for cracks emanating from double edge notched plates subjected to uniform stressing for $K_t=6.3$, $c/r_n=0.3063$, $c_{ext}/w=0.315$, and $n=10$.

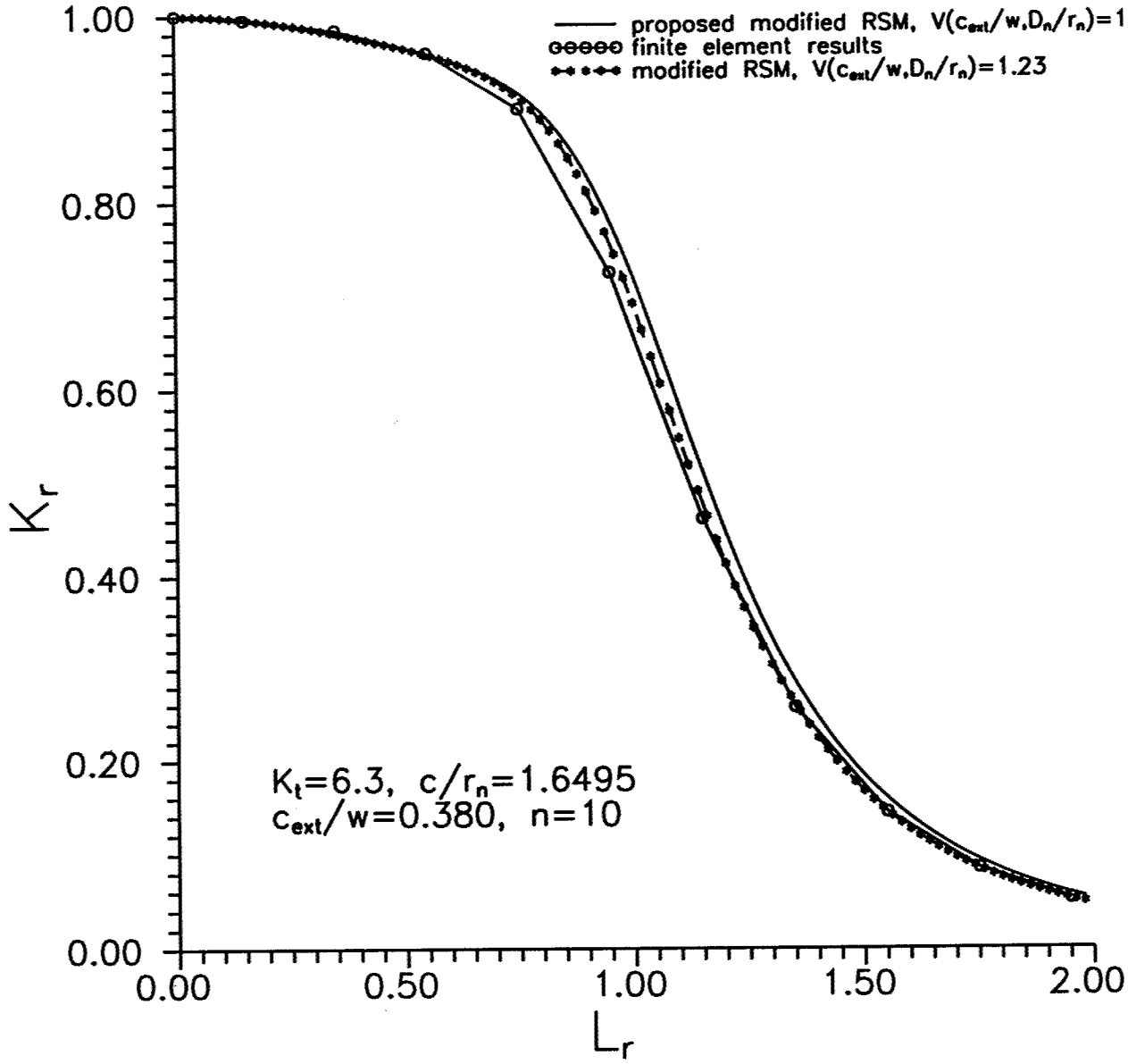

Figure B1.9 Comparison of failure curves derived from finite element computations with optimized RSM solutions for cracks emanating from double edge notched plates subjected to uniform stressing for $K_t=6.3$, $c/r_n=1.6495$, $c_{ext}/w=0.380$, and $n=10$.

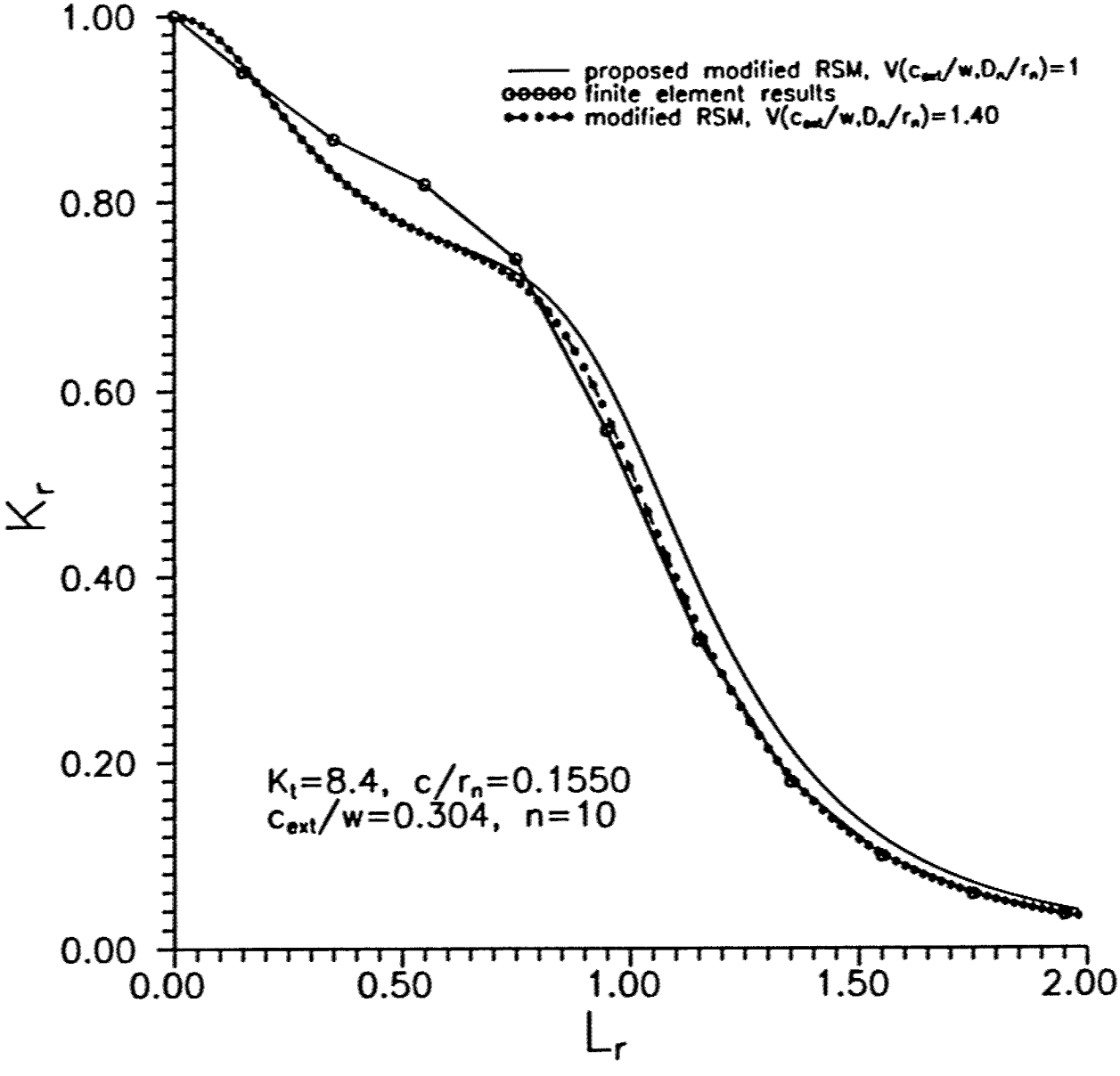

Figure B1.10 Comparison of failure curves derived from finite element computations with optimized RSM solutions for cracks emanating from double edge notched plates subjected to uniform stressing for $K_t=8.4$, $c/r_n=0.1550$, $c_{ext}/w=0.304$, and $n=10$.

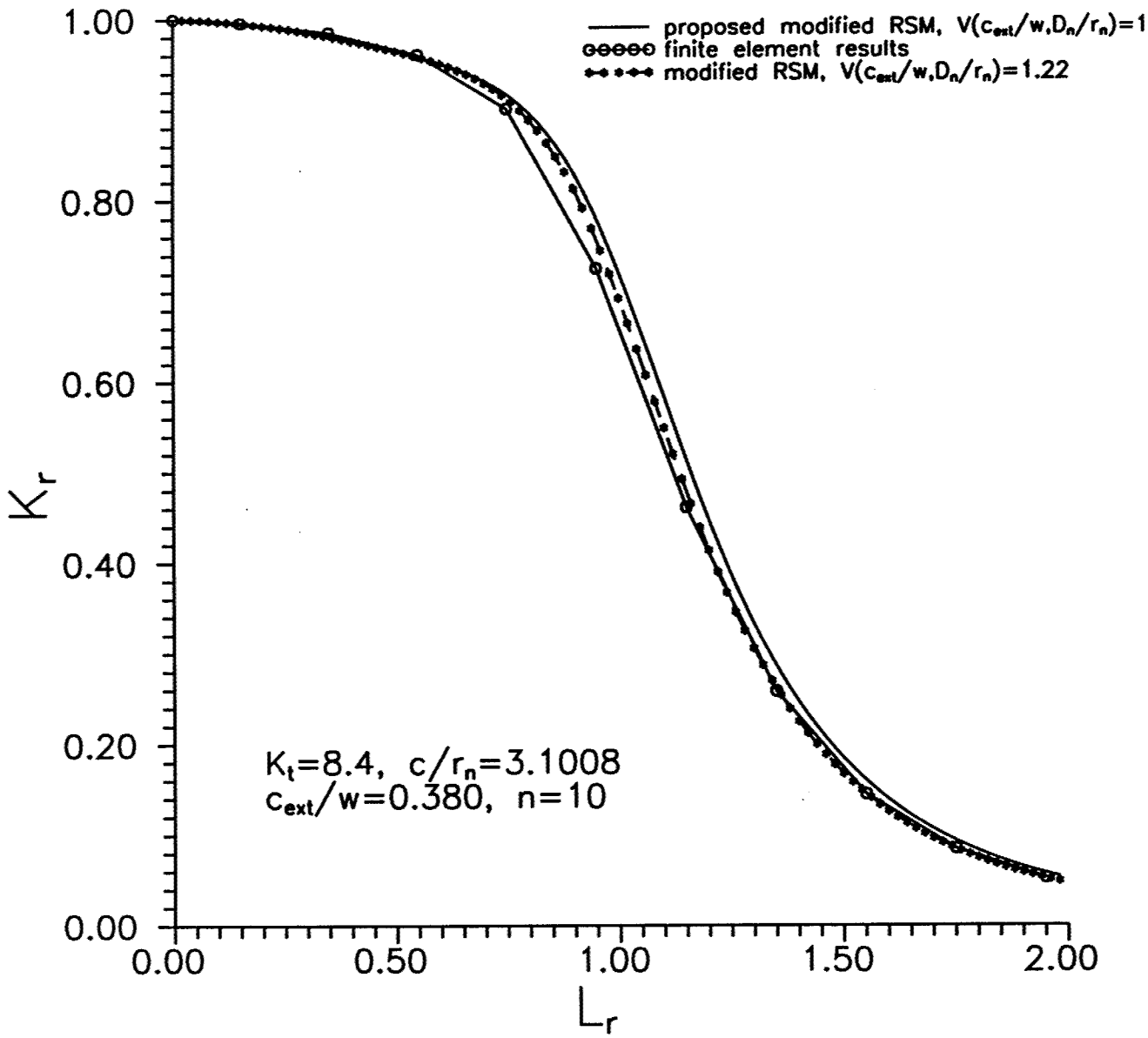

Figure B1.11 Comparison of failure curves derived from finite element computations with optimized RSM solutions for cracks emanating from double edge notched plates subjected to uniform stressing for $K_t=8.4$, $c/r_n=3.1008$, $c_{ext}/w=0.380$, and $n=10$.

yield load is determined only by primary loads. The validation presented in this section to substantiate the use of the EPRI scheme is based on the work performed by General Electric in Schenectady under EPRI sponsorship to verify EPRI's approach. However, following the recommendation in Section A4.4, it is emphasized that reductions in tensile stresses from plastic yielding should be adequately allowed for when performing a proof test analysis in order to avoid possible non-conservatisms in estimating flaw screening capability. It is suggested in Section A4.4 that this can be accomplished following a simple procedure for estimating the relaxed stresses (see Table A4.3) and evaluating J_e using these relaxed stresses.

B1.4.2 Validation: EPRI Elastic-Plastic Handbook Solutions

In the proposed EPRI estimation scheme J is expressed in the form

$$J(c,P+S) = J_e(c_e,P+S) + J_p(c,P) \tag{B1.30}$$

where the effective crack length, c_e, is evaluated using r_y determined from equation (A4.9) with $K(c,P+S)$ replacing $K(c,P)$. J_p is the EPRI solution for the primary load expressed in terms of the appropriate $h_1(c/w,L/w,n)$ function. The J estimation scheme proposed in Section A.4.4 replaces the EPRI expression for J_p by the reference stress approximation (see equation A4.18) which will reproduce the EPRI solutions to good accuracy if evaluated using optimized values of V^* and P_o^* (see Section B1.2). Hence, validation of the EPRI scheme also validates the RSM of Section A4.4 within the accuracy that V^* and P_o^* can be estimated.

The EPRI scheme has been validated for a number of cracked structures subjected to combined primary and secondary (thermal) loading. The validation is described in detail in Kumar et al. [70], and is not reproduced here. The cases analyzed and used in the verification were:

- A single edge cracked plate subjected to remote uniform tension and two quadratic through-wall temperature gradients which produced elastically calculated peak tensile stresses of 36.5% and 73% of the yield stress.
- A center cracked plate subjected to remote uniform tension and a quadratic through-wall temperature gradient that produced an elastically calculated peak tensile stress of 104.3% of the yield stress.
- An internally pressurized axially cracked cylinder subjected to two quadratic through-wall temperature gradients which produced elastically calculated peak tensile stresses of 53.5% and 107% of the yield stress.
- A circumferentially cracked cylinder subjected to remote tension and a quadratic through-wall temperature gradient that produced an elastically calculated peak tensile of 274% of the yield stress.

B1.5 Multiaxial Stresses

B1.5.1 Introduction

The recommended expression for evaluating J for cracks subjected to multiaxial applied stressing is given by equation (A4.22) in Appendix A. In this expression, which is applicable to biaxial tressing, it is assumed that the elastic component, J_e, is only influenced by the stress component that

acts normal to the crack plane, although determination of the effective crack length, c_e, involves the net section yield load, $P_o^*(c,\sigma_1,\lambda)$, which depends on the multiaxial stress state through the ratio $\lambda=\sigma_2/\sigma_1$. Similarly, the plastic component, J_p, also depends on $P_o^*(c,\sigma_1,\lambda)$.

The validation of equation (A4.22) is provided by the computational results of Wang, Li, and Ding [44], who presented their J results in the form of a FAD. The validation is inferred from the fact that the failure curves corresponding to different biaxial stress conditions are relatively insensitive to the biaxial stress ratio, λ, as implied by equation (A4.22).

B1.5.2 Validation Based on Failure Assessment Diagrams

Wang, Li, and Ding [44] have computed finite element solutions for J for a center cracked panel subjected to uniform biaxial stressing characterized by λ values of 0 (uniaxial), 0.5, 1 (equi-biaxial), 1.5, 1.8, 2, and 2.2. The results were expressed in the form of failure curves plotted on a FAD, see Figure B1.12. The failure curves were generated using the equation

$$L_r^* = \frac{P_1}{P_y^*(c,P_1,\lambda)}, \quad K_r^* = \sqrt{\frac{J_e(c,P_1)}{J(c,P_1,\lambda)}} \tag{B1.31}$$

where P_y^* was evaluated using equation (A4.21), and P_1 is the load corresponding to the stress σ_1. The stress-strain curve of the material had a yield discontinuity, which is apparent in the sharp drop in the failure curves at L_r=1.

From Figure B1.12 it is clear that the failure curves are similar for all λ values, as predicted by equations (A4.22) and (B1.31). The failure curves include the curve for uniaxial stressing, which, from the results analyzed in Section B1.2, is known to be well represented by equation (A4.22) with λ=0. Hence, the work of Wang, Li, and Ding [44] verifies the recommended J estimation scheme.

B1.6 Cracks at Welds

B1.6.1 Introduction

In this section, the J estimation scheme recommended in Section A4.8 of Appendix A for cracks at welds is validated for proof test and service analyses using FAD based failure curves derived from finite element computations for circumferential cracks in a girth weld reported by Joch et al. [76]. These authors generated J solutions for both over-matched and under-matched welds. In order to get a "best estimate" comparison, the finite element results are compared with the predictions of equations (A4.29) and (A5.9) with V^*=1, which is near the mean value. The material tensile properties used for M_1 and M_2 are those specified in Table A4.4 of Section A4.8. The geometry analyzed is shown in Figure B1.13.

B1.6.2 Validation for Over-Matched Welds

Joch et al. [76] generated failure curves for two crack depths (c/w=0.68 and 0.25) and various combinations of weld and base metal stress-strain properties. The stress-strain curves used by Joch et al. were fitted by Ramberg-Osgood laws for the purposes of this validation. Table B1.2 summarizes the three cases analyzed. The results are displayed in Figures B1.14, B1.15, and B1.16 for cases 1, 2, and 3, respectively, and include predicted failure curves derived using equations (A4.29) and (A5.9) for both proof test and service applications. In these figures, there is either good agreement between the recommended procedure for evaluating the failure curves (particularly for proof test applications), or the recommended procedure produces mainly conservative results for a proof test analysis with respect to the finite element results.

Table B1.2 Summary of the over-matched cases used in the validation

Case 1			
c/w=0.68	α	n	σ_o (MPa)
weld	0.6364	22.2	660
base	1.2	6.69	350
Case 2			
c/w=0.25	α	n	σ_o (MPa)
weld	1.05	5.9	500
base	1.05	5.9	400
Case 3			
c/w=0.25	α	n	σ_o (MPa)
weld	1.05	5.9	600
base	1.05	5.9	400

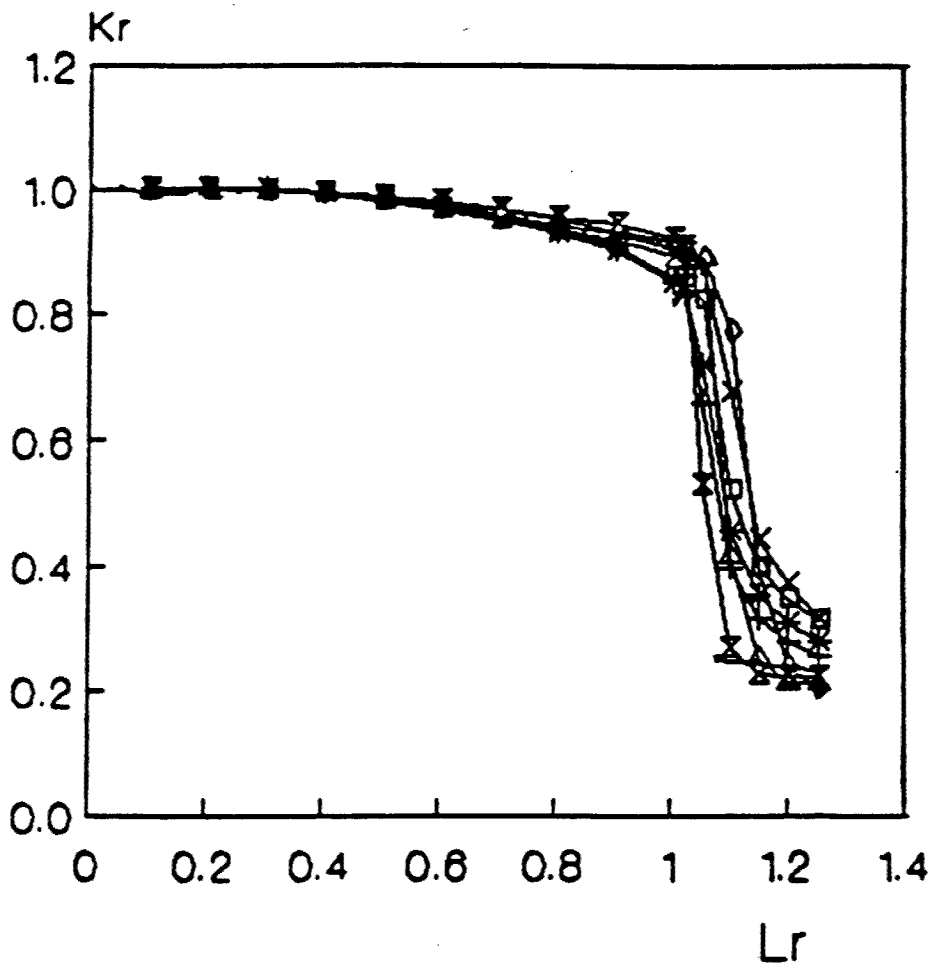

Figure B1.12 Failure curves for a center cracked plate subjected to uniform biaxial stressing based on the results of Wang, Li, and Ding [44]. | λ=0 (uniaxial), ✳ λ=0.5, □ λ=1 (equi-biaxial), × λ=1.5, ◊ λ=1.8, △ λ=2, ⧗ λ=2.2.

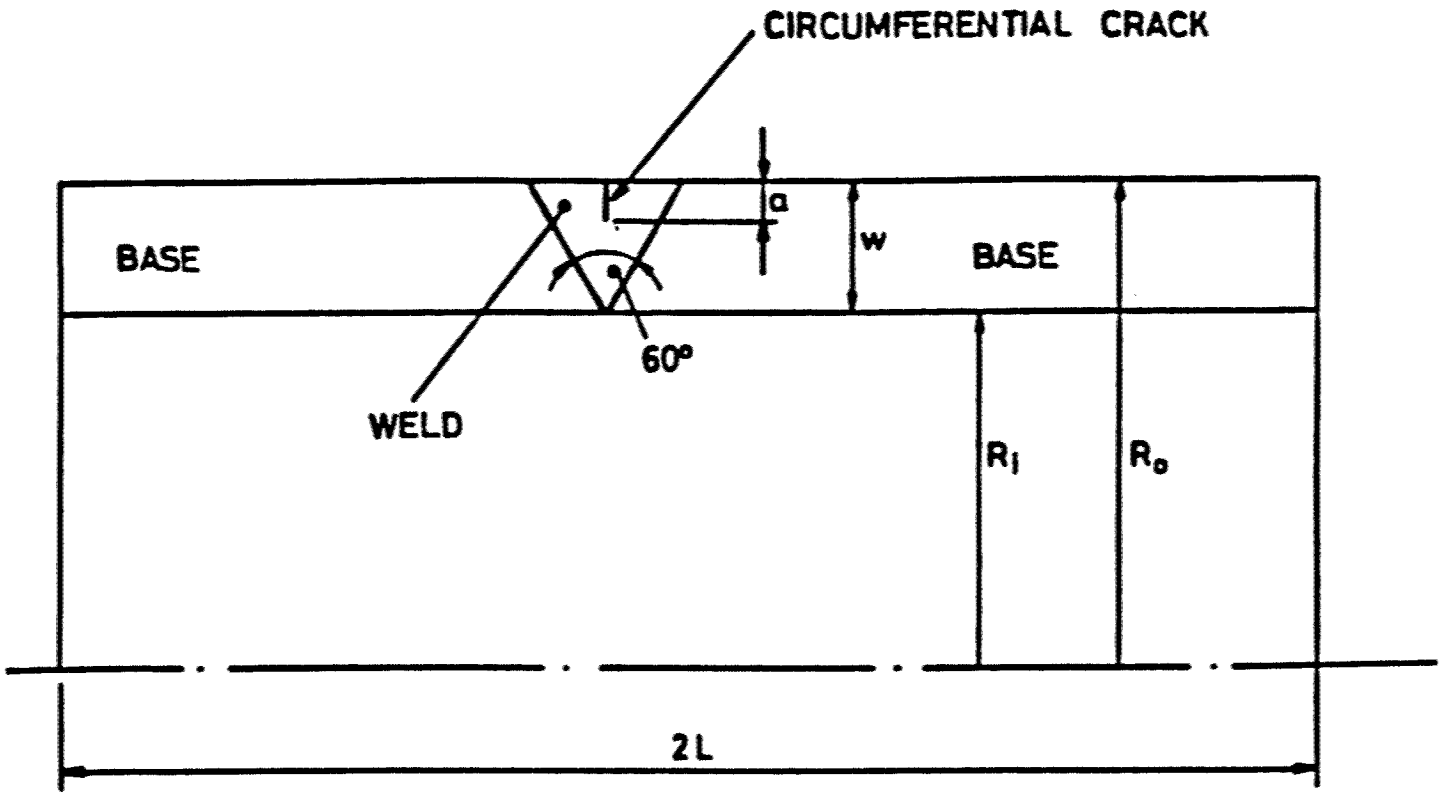

Figure B1.13 Schematic representation of the circumferential cracked weld analyzed by Joch et al. [76].

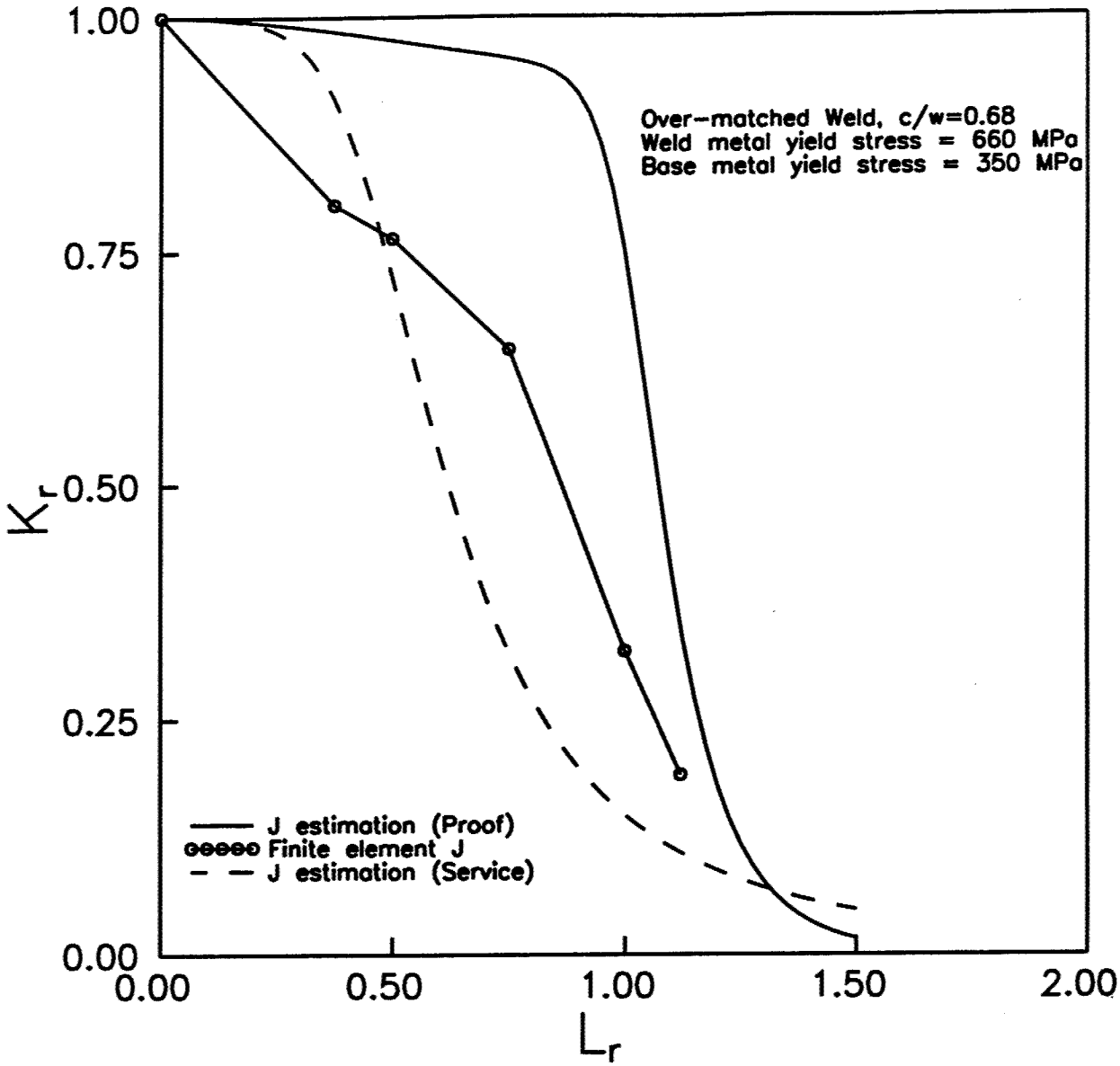

Figure B1.14 Comparison of failure curves for an over-matched weld (Case 1) for proof test and service applications generated using the recommended procedures and the finite element results of Joch et al. [76].

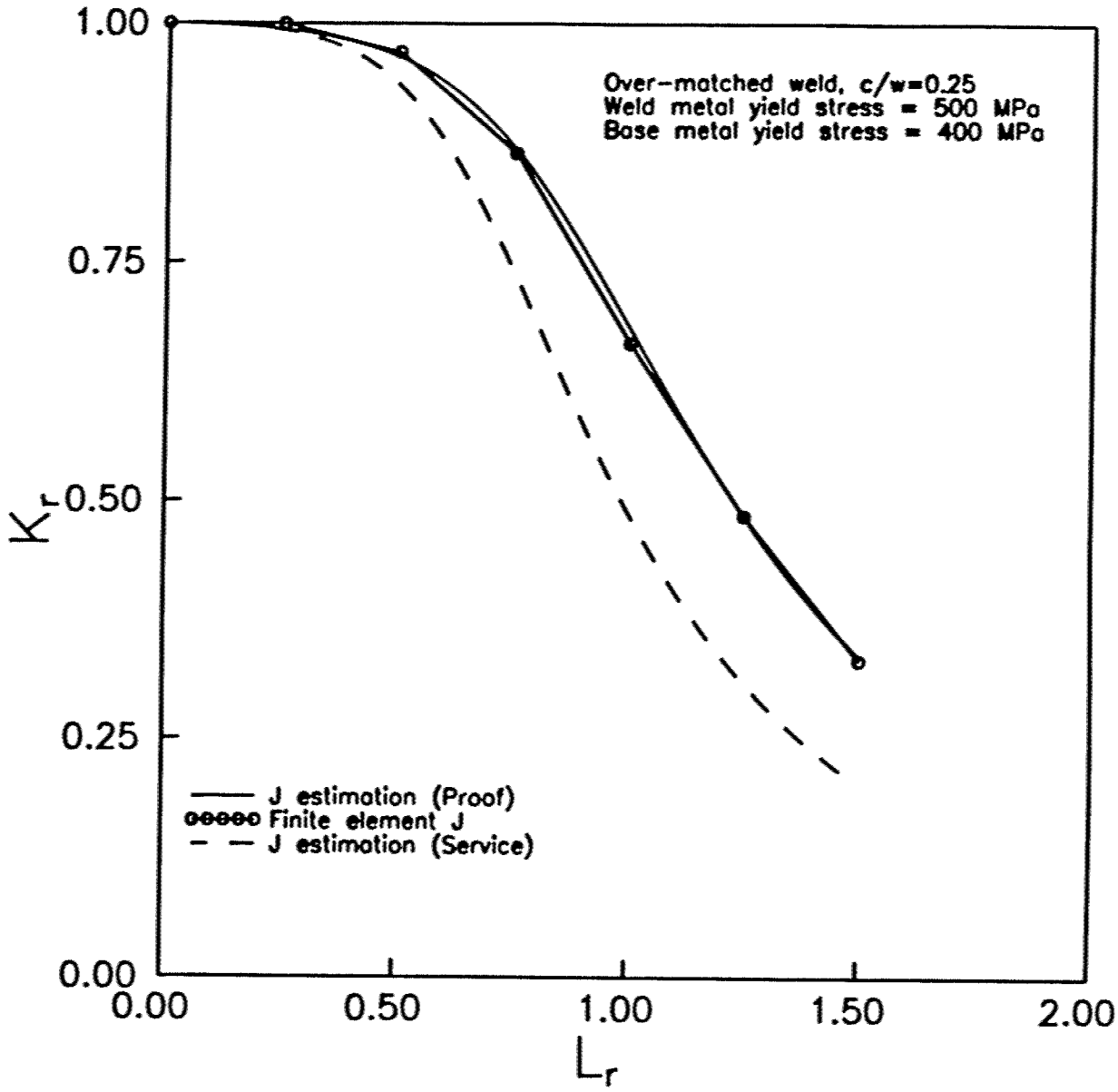

Figure B1.15 Comparison of failure curves for an over-matched weld (Case 2) for proof test and service applications generated using the recommended procedures and the finite element results of Joch et al. [76].

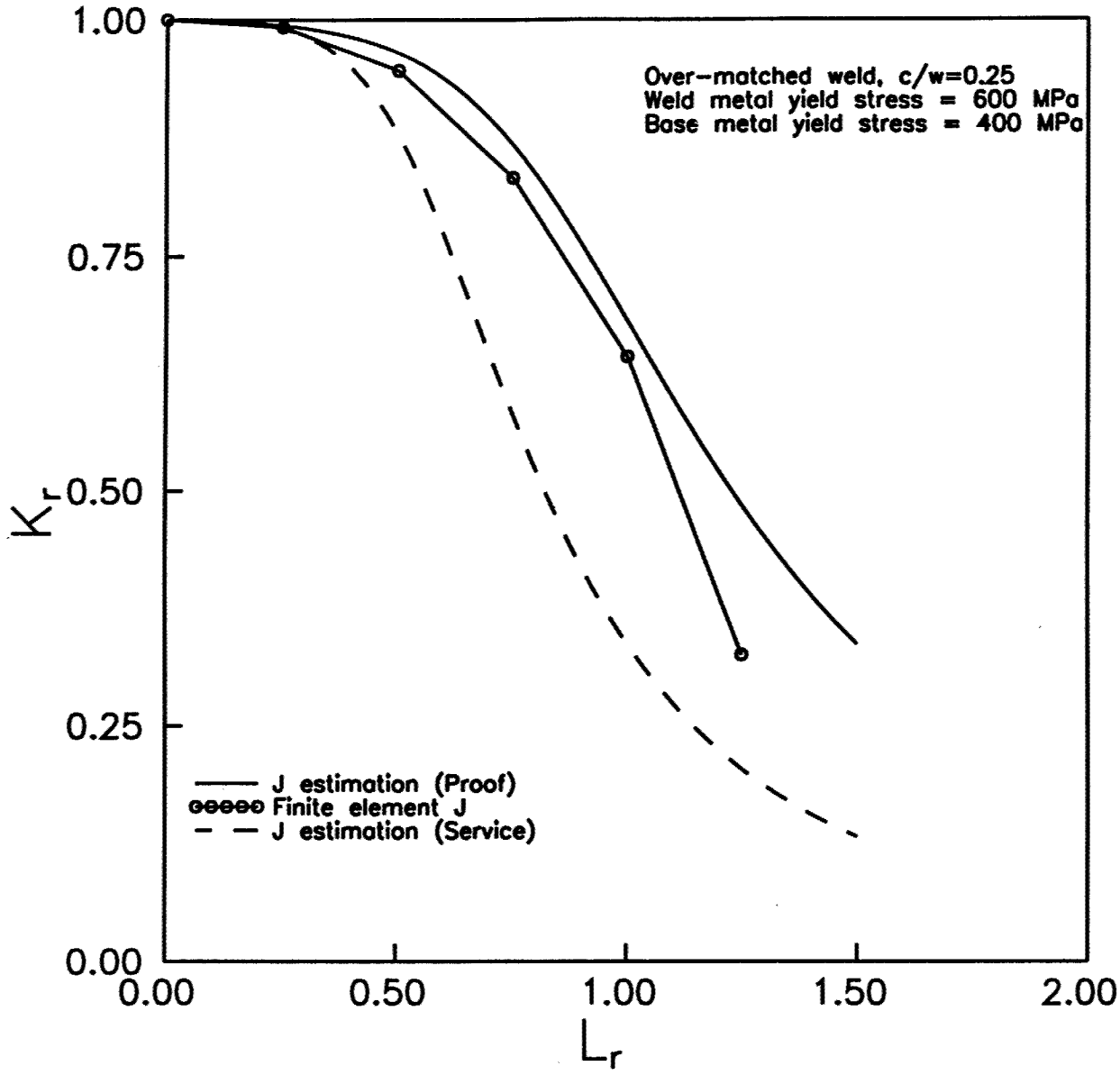

Figure B1.16 Comparison of failure curves for an over-matched weld (Case 3) for proof test and service applications generated using the recommended procedures and the finite element results of Joch et al. [76].

B1.6.3 Validation for Under-Matched Weld

The results of Joch et al. [76] are analyzed for one crack depth (c/w=0.68) and a single combination of weld and base metal stress-strain properties. As before, the stress-strain curves used by Joch et al. were fitted by Ramberg-Osgood laws for the purposes of this validation. Table B1.3 summarizes the under-matched weld analyzed (case 4). The results are displayed in Figure B1.17, and include predicted failure curves derived using equations (A4.29) and (A5.9) for both proof test and service applications. There is good agreement between the recommended procedure for evaluating the failure curves for proof test applications and the finite element results, and the recommended procedure for service applications produces mainly a conservative result with respect to the finite element failure curve.

Table B1.3 Summary of the under-matched case used in the validation

Case 4			
c/w=0.68	α	n	σ_o (MPa)
weld	1.2	6.69	350
base	0.6364	22.2	660

B1.6.4 Conclusions

The J estimation schemes recommended in Section A.4.8 for proof test applications have been validated against finite element results for cracked over-matched and under-matched welds. The validation for the over-matched welds included a case where the ratio of weld to base metal yield stresses was 1.88 and, for the under-matched weld, the ratio was 0.53.

B2. LABORATORY VALIDATION: J ESTIMATION SCHEMES/FAILURE ASSESSMENT DIAGRAM

B2.1 Introduction

The laboratory validation was performed at SwRI using restrained single edge cracked plate (RSECP) specimens. Tension specimens are less frequently used in elastic-plastic fracture toughness testing then compact tension and bend specimens. Therefore, a recognized standard method of deriving experimentally measured J values is not available for these geometries. In addition, the J_R curve measured on the specimen sizes used in the laboratory verification testing will not be valid according to ASTM E1152 Standard [57]. This does not present a problem in the present case, since one of the purposes of the testing was to obtain "structurally" relevant toughness values that can be used to analyze cracks in thin-walled hardware (see Section B4).

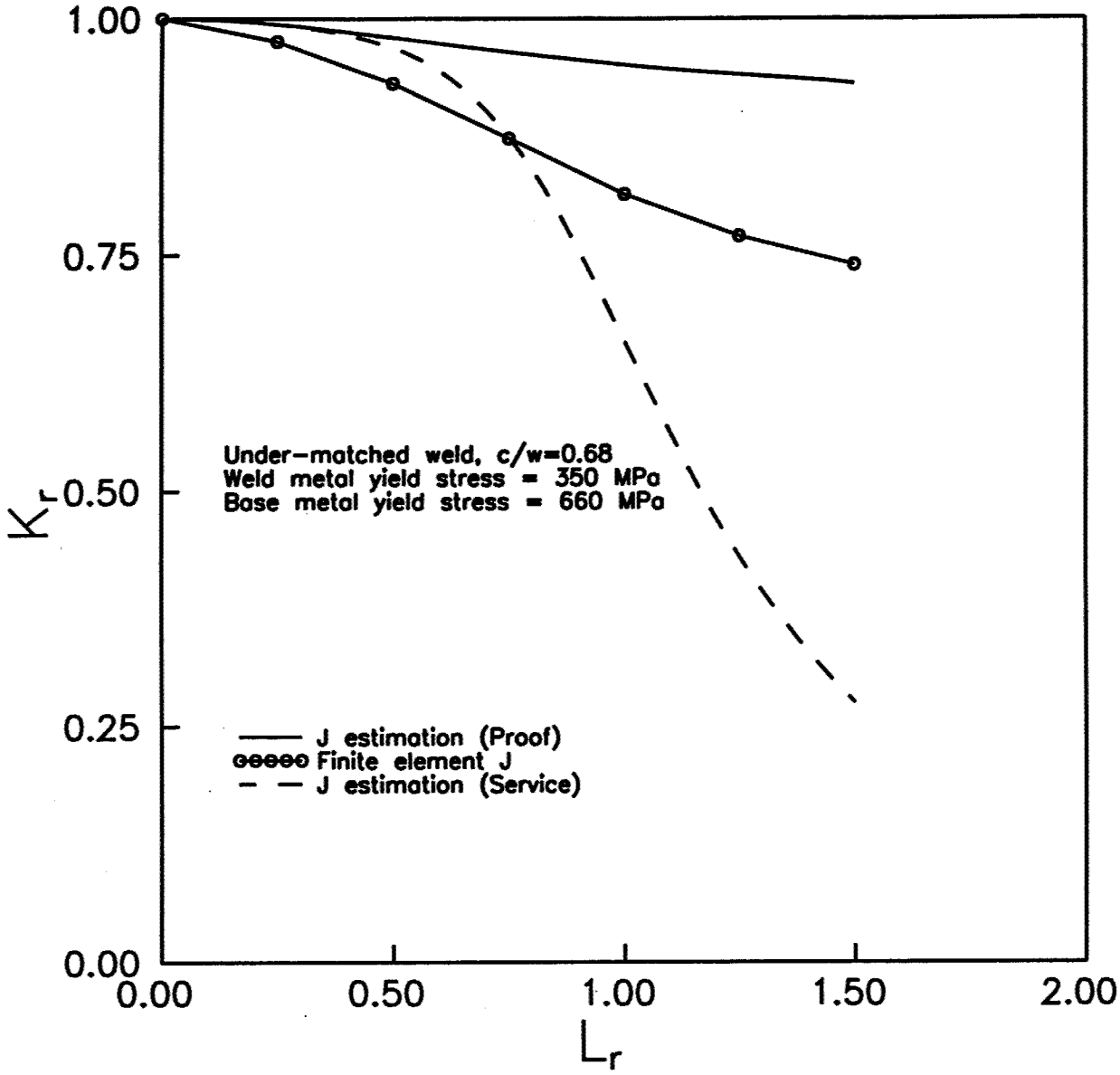

Figure B1.17 Comparison of failure curves for an under-matched weld (Case 4) for proof test and service applications generated using the recommended procedures and the finite element results of Joch et al. [76].

A method is required to analyze the data measured on the RSECP specimens that is both relatively easy to apply, and which will result in measured J values of an acceptable accuracy. After some review and consideration, the so-called η-factor approach was chosen. The η-factor relates the J-Integral to the area under the load/load pin displacement curve. In non-strain hardening materials, the plastic η-factor, η_p, can be derived from the net section yield load, P_o, using the expression

$$\eta_p = -\frac{(w-c)}{P_o}\frac{dP_o}{dc} \tag{B2.1}$$

where c is the crack depth, and w the section size. Unfortunately, the accuracy of this simple way of determining η_p is limited by the accuracy with which the load, P_o, is known. Expressions for P_o are available in the EPRI elastic-plastic handbooks, but these loads are not necessarily the correct ones, as they are used primarily as normalizing reference loads in the EPRI expressions for J, not explicitly as yield loads.

An alternative approach to the foregoing was adopted. The alternative approach, which is described in the following section, takes advantage of the EPRI elastic-plastic handbook solutions for the plastic components of J, the load pin displacement, and the mouth opening displacement, in order to derive η-factors which will enable J to be determined from the plastic component of the area under the appropriate load-displacement curve. The J-Integral is then simply given as the sum of the calculated elastic component of J (which is readily derived from the applied stress intensity factor) and the measured plastic component of J. The ability to determine J from the mouth opening displacement has the advantage that this displacement is more sensitive to small changes in crack tip plasticity than is the load pin displacement, as it is physically nearer the crack tip.

B2.2 Test Analysis Methods

The measured data in the SwRI tests consisted of load-line and mouth opening displacements as a function of applied load, with periodic unloading for determining the instantaneous stiffness to infer crack extension in keeping with ASTM E1152 [57]. It is necessary to estimate J and the instantaneous crack depth from these data in order to determine the J_R-curve. In the method, J was evaluated as the sum of elastic and plastic components

$$J = J_e + J_p \tag{B2.2}$$

B2.2.1 Estimating J

The experimentally measured value of J is derived from load-displacement data analyzed using plastic η_p-factors which relate the plastic area under the load/load-line displacement curve, W_p to J_p [77,78].

$$J_p = \frac{\eta_p W_p}{t(w-c)} \tag{B2.3}$$

Since W_p includes all plastic work, including first order plasticity, the elastic component, J_e, is evaluated from K^2/E' at the instantaneous load and crack depth but without applying a first order plastic correction, as is done in the EPRI J estimation scheme.

A similar equation applies to the load/mouth opening displacement curve

$$J_p = \frac{\eta_p^* W_p^*}{t(w - c)} \tag{B2.4}$$

where the * superscript refers to quantities related to the mouth opening.

The η-factors that appear in equations (B2.3) and (B2.4) were derived from finite element J solutions for a center cracked panel, as described in Section B2.2.2. The yield mechanism in center cracked panels is expected to be very similar to that occurring in the RSECP specimens because in both cases yielding occurs on 45° slip planes.

If crack extension due to tearing occurs during the test, then equation (B2.3) needs to be modified to subtract from the total area under the curve the contribution arising from the explicit change in crack depth. This correction is necessary because J is evaluated assuming the material is non-linear elastic and hence J is a function of the instantaneous crack depth, load, and displacement (for example, see ASTM E1152 [57]). Thus, if $c(n+1)$ is the instantaneous crack depth estimated from the compliance measured during the $(n+1)$'th, and $c(n)$ is the depth inferred from the previous unloading compliance measurement, then it can be shown

$$J_p(n+1) = \frac{J_p(n)\left[\dfrac{b(n)}{\eta_p(n)} - \dfrac{c(n+1) - c(n)}{2}\right] + \dfrac{\Delta W_p}{t}}{\left[\dfrac{b(n+1)}{\eta_p(n+1)} + \dfrac{c(n+1) - c(n)}{2}\right]} \tag{B2.5}$$

where

$$\Delta W_p = \frac{P(n+1) + P(n)}{2} \Delta \delta_p \tag{B2.6}$$

and

$$\Delta \delta_p = \delta(n+1) - \delta(n) \tag{B2.7}$$

where δ is the total residual plastic displacement measured at zero load $(P=0)$, and $b(n)=w-c(n)$. It is implicitly assumed that $c(n+1)/c(n)\approx 1$.

Although equation (B2.4) can be used directly to determine J_p before ductile tearing, it is necessary to convert the area under the mouth opening displacement curve into the equivalent area under the load-line displacement curve in order to calculate the J_R-curve. This can be done using the equation

$$\frac{\Delta W_p}{\Delta c} = W_p \left[\frac{1}{W_p^{\bullet}} \frac{\Delta W_p^{\bullet}}{\Delta c} + \frac{1}{\eta_p^{\bullet}} \frac{\Delta \eta_p^{\bullet}}{\Delta c} - \frac{1}{\eta_p} \frac{\Delta \eta_p}{\eta_p} \right] \tag{B2.8}$$

Equation (B2.8) allows the incremental change ΔW_p to be determined for an incremental change in crack depth, $\Delta c=c(n+1)-c(n)$.

B2.2.2 Evaluating η-factors

The proof test conditions relevant to the SSME high pressure oxidizer ducts used in the hardware validation (Section B.4) is characterized as internal pressure loading of a thin section cylinder. The pressure loading will result in relatively uniform membrane stresses which are associated with low plastic constraint, similar to those conditions found in center (CCP) and shallow single edge (SECP) cracked plates subjected to tensile loads. Steep stress gradients resulting from stress concentration features will tend to produce a higher level of constraint, at least until near general yielding, after which large scale plasticity will reduce the constraint local to the crack tip. Deeper cracked SECPs in tension produce both tensile forces and bending moments on the uncracked ligament, and thus give an intermediate constraint between pure tension (low constraint) and pure moment (high constraint). Thus, CCP and SECP specimens would seem to be appropriate for simulating the crack tip plastic constraint typically found in internally pressurized proof tested components.

The plastic η-factor, η_P, relates the plastic component of J, J_P, to the plastic work, W_P, done by the applied load, P. The total work done is equal to the total area under the load/load pin displacement curve, which consists of an elastic component, W_e, as well as W_P.

In the EPRI elastic-plastic handbook [68], J_P, and the corresponding plastic pin displacement, Δ_P, for single edge (SECP) and center (CCP) cracked plates are expressed in the form

$$J_P = \alpha\, \sigma_o \epsilon_o c \frac{(w - c)}{w}\, h_1\left(\frac{c}{w}, n\right)\left(\frac{P}{P_o}\right)^{n+1} \tag{B2.9}$$

$$\Delta_P = \alpha\, \epsilon_o c\, h_3\left(\frac{c}{w}, n\right)\left(\frac{P}{P_o}\right)^{n} \tag{B2.10}$$

where α, σ_o, and n are the coefficients in the Ramberg-Osgood power law relating strain to stress. The values of the functions, h_1 and h_3, are tabulated in reference [68] for a range of a/b and n values. Expression for the reference load, P_o, are also given.

The plastic work, W_p, can be derived by substituting equation (B2.10) in the expression

$$W_P = P\Delta_p - \int_o^P \Delta_p\, dP \tag{B2.11}$$

and integrating, to yield

$$W_p = \left(\frac{n}{n+1}\right) P\Delta_p \tag{B2.12}$$

Substituting this into equation (B2.3) finally gives

$$\eta_P = \left(\frac{n+1}{n}\right) \frac{\sigma_o (w - c)^2 t}{w} P_o \frac{h_1\left(\frac{c}{w}, n\right)}{h_3\left(\frac{c}{w}, n\right)} \tag{B2.13}$$

Experimentally, it is often more convenient to measure the crack mouth opening displacement, δ, rather than the load pin displacement. Furthermore, this displacement is a more sensitive indication of crack tip plasticity than the pin displacement because it is nearer to the tip. The EPRI handbook provides expression for the plastic component of δ, δ_P, in the form [68].

$$\delta_p = \alpha \epsilon_o c h_2\left(\frac{c}{w}, n\right)\left(\frac{P}{P_o}\right)^n \tag{B2.14}$$

where values of h_2 $(c/w,\ n)$ are tabulated in the handbook. This equation is very similar to equation (B2.10) for Δ_p, with the function h_2 replacing h_3.

Tables B2.1 and B2.2 display η-factors derived from the pin displacements of CCPs and SECPs in tension for plane stress and plane strain plastic constraint, and strain hardening materials with power law exponents of 10 and 16. (The value of 16 is appropriate to IN-718.) Tables B2.3 and B2.4 show similar results based on mouth opening displacements. The irregular trends in some of the values is probably attributable to inaccuracies in the elastic-plastic finite element results given in the EPRI handbook.

Three important conclusions can be drawn from the results presented in Tables B2.1 to B2.4. First, the value of the η-factor appears to be relatively insensitive to the state of stress (plane stress versus plane strain) except for shallow cracks in SECPs. This fact will help remove most of the inaccuracies in measuring J due to uncertainties in plastic constraint. Second, the η-factors for the CCP and SECP derived from the mouth opening have similar values over the whole range of crack depths for which results are available. This would prove to be very convenient. Third, for most crack depths, the η-factors appear to be relatively insensitive to the value of the strain hardening exponent. This property will help reduce uncertainties in J due to uncertainties in the stress-strain behavior.

The restrained edge cracked plates (RSECPs) used in the laboratory verification test program are intended to simulate unconstrained conditions by inhibiting bending on the uncracked ligament and promoting yielding on 45° planes. Since EPRI J solutions are not available for the RSECP specimens, the η-factors for the CCP specimens were used in the experimental determination of J and the J_R-curves of the IN-718 material.

B2.2.3 Elastic Displacements and Stress Intensity Factors

The stress intensity factor (SIF) and the crack displacements can be determined from a knowledge of the weight function (WF), which depends on the specimen boundary conditions (end restraints and fixed grip configuration). It is assumed that the restraints in the RSECP test specimen configuration oppose the moment normally induced by a pin-loaded configuration. This assumption was confirmed by measured net section yield loads, which varied linearly as the load bearing area, as opposed to the non-linear dependence expected for pin-loaded specimens.

Table B2.1 η_p values corresponding to n=10 for use in experimentally measuring J_P from the plastic work under the load/load pin displacement curve

c/w	Center Cracked Plate		Single Edge Cracked Plate (Tension)	
	Plane Stress	Plane Strain	Plane Stress	Plane Strain
0.125	1.74	1.72	0.72	0.53
0.25	1.08	1.13	1.63	1.14
0.375	0.94	0.95	2.34	1.87
0.5	0.91	0.91	2.29	2.29
0.625	0.87	0.85	2.35	2.34
0.75	0.91	0.91	2.10	2.17
0.875	0.93	0.91	2.14	2.20

Table B2.2 η_p values corresponding to n=16 for use in experimentally measuring J_P from the plastic work under the load/load pin displacement curve

c/w	Center Cracked Plate		Single Edge Cracked Plate (Tension)	
	Plane Stress	Plane Strain	Plane Stress	Plane Strain
0.125	1.30	1.26	0.96	0.62
0.25	0.98	0.98	1.84	1.29
0.375	0.95	0.95	2.38	1.80
0.5	0.93	0.94	2.26	2.31
0.625	0.89	0.89	2.31	2.34
0.75	0.94	0.95	3.10	2.13

Table B2.3 η_p^* values corresponding to n=10 for use in experimentally measuring J_P from the plastic work under the load/mouth opening displacement curve

c/w	Center Cracked Plate		Single Edge Cracked Plate (Tension)	
	Plane Stress	Plane Strain	Plane Stress	Plane Strain
0.125	0.96	0.95	0.97	0.95
0.25	0.92	0.91	0.98	0.94
0.375	0.91	0.91	1.01	0.98
0.5	0.91	0.91	0.93	0.95
0.625	0.88	0.86	0.97	0.94
0.75	0.91	0.92	0.90	0.92
0.875	0.93	0.92	0.99	1.01

Table B2.4 η_p^* values corresponding to n=16 for use in experimentally measuring J_P from the plastic work under the load/mouth opening displacement curve

c/w	Center Cracked Plate		Single Edge Cracked Plate (Tension)	
	Plane Stress	Plane Strain	Plane Stress	Plane Strain
0.125	0.96	0.89	0.90	0.93
0.25	0.92	0.94	0.98	0.96
0.375	0.95	0.95	1.00	0.93
0.5	0.93	0.94	0.92	0.95
0.625	0.90	0.89	0.95	0.93
0.75	0.94	0.95	0.89	0.90

Line spring model solutions were used as reference SIF solutions for the RSECP specimens. These solutions depend on the gage length, S, over which the restraints are applied. The WF can be estimated from these reference solutions by guessing its form to within an unknown term, and determining the unknown term by forcing compatibility between the WF and the reference SIF (for example, see Wu and Carlsson [79].

The weight function form chosen in the present case was similar to that used for center and double edge cracks (see Tada, Paris, and Irwin [80])

$$W(c,x) = \frac{\left[2\tan\left(\frac{\pi c}{2w}\right)/w\right]^{1/2}\left[M(c/w) - (M(c/w)-1)\frac{x}{c}\right]\cos\left(\frac{\pi x}{2w}\right)}{\left[\sin^2\left(\frac{\pi c}{2w}\right) - \sin^2\left(\frac{\pi x}{2w}\right)\right]^{1/2}} \tag{B2.15}$$

where $M(c/w)$ is the unknown. In terms of the WF, the SIF, K, is given by

$$K = \int_0^c W(c,x)\,\sigma(x)\,dx \tag{B2.16}$$

This equation can be used to determine $M(c/w)$ if K and the corresponding stress, $\sigma(x)$, are known.

The crack displacements (surface to surface) are given by (Wu and Carlsson [79])

$$\phi(x) = \frac{2}{E'}\int_x^c W(x',x)K(x')\,dx' \tag{B2.17}$$

where x is the position on the crack face measured from the free surface. Hence, the crack mouth opening displacement (CMOD) is given by

$$\phi(0) = \frac{2}{E'}\int_0^c W(x',0)K(x')\,dx' \tag{B2.18}$$

where

$$W(x',0) = \frac{\left[2\tan\left(\frac{\pi x'}{2w}\right)/w\right]^{1/2} M(x'/w)}{\sin\left(\frac{\pi x'}{2w}\right)} \tag{B2.19}$$

and

$$M(c/w) = \frac{\left[\frac{\left(\frac{\pi c}{2w}\right)}{\tan\left(\frac{\pi c}{2w}\right)}\right]^{1/2} Y(c/w) - I_2}{I_2 - I_1} \tag{B2.20}$$

where

$$Y(c/w) = \frac{K}{\sigma(\pi c)^{1/2}} \tag{B2.21}$$

and

$$I_1 = \int_0^{\frac{\pi}{2}} d\theta = \frac{\pi}{2} \tag{B2.22}$$

and

$$I_2 = \int_0^{\frac{\pi}{2}} \frac{x_\theta}{c}\, d\theta \tag{B2.23}$$

where

$$x_\theta = \frac{2w}{\pi} \sin^{-1}\left(\sin\left(\frac{\pi c}{2w}\right)\sin(x)\right) \tag{B2.24}$$

Equation (B2.20) was obtained by substituting equation (B2.15) into equation (B2.16) and solving for *M(c/w)*.

The *K* solution for the RSECP specimens was obtained from Ewing's [81] line spring model solution. For a span, *S*, the solution is given by

$$K(c,P,S/w) = \frac{P}{wt}\sqrt{\pi c}\ Y(c/w, S/w) \tag{B2.25}$$

where

$$Y(c/w,S/w) = \left[Y_1^M(c/w) - \frac{Y_1^{MB}(c/w)Y_1^B(c/w)}{Y_1^{BB}(c/w) + S/(6\pi w)}\right] / \sqrt{(1 - c/w)} \quad c/w \le 0.5 \tag{B2.26}$$

$$Y(c/w,S/w) = \left[Y_2^M(c/w) - \frac{Y_2^{MB}(1 - c/w)Y_2^B(c/w)}{Y_2^{BB}(1 - c/w) + S/(6\pi w)}\right] / \sqrt{(1 - c/w)} \quad c/w > 0.5 \tag{B2.27}$$

and

$$Y_1^M(x) = 1.12(1 + 5.474x^2 - 2.448x^4 + 20.0x^6)\sqrt{(1 - x)} \tag{B2.28}$$

$$Y_2^M(x) = \frac{1.12\ (0.264 + 0.736x)}{(1 - x)\sqrt{x}} \tag{B2.29}$$

$$Y_1^B(x) = 0.3733\ (3 - 3.6x + 13.5x^2 - 20x^4 + 43.2x^6)\sqrt{1 - x} \tag{B2.30}$$

$$Y_2^B(x) = \frac{0.3733}{(1 - x)\sqrt{x}} \tag{B2.31}$$

$$Y_1^{MB}(x) = 0.20907\ x^2(3 - 2.4x + 9.487x^2 + 43.4x^3 - 142.07x^4 + 173.65x^5 - 27.89x^6) \tag{B2.32}$$

$$Y_2^{MB}(x) = \frac{0.20907(1 - 1.472x + 0.37064x^2)}{x^2} \tag{B2.33}$$

$$Y_1^{BB}(x) = 0.069689\ x^2(9 - 14.4x + 46.98x^2 - 46x^3 + 89.02x^4 - 184x^5 + 193.9x^6) \tag{B2.34}$$

$$Y_2^{BB}(x) = \frac{0.069689(1 - 1.3404x^2)}{x^2} \tag{B2.35}$$

The dependence of CMOD, $\phi(0)$, on the gage length, S, over which the end restraints are applied is through the dependence of K, on S. Since the derived WF was approximate, the value of S used to evaluate K [and hence $M(c/w)$ and $W(x',x)$] was chosen to reproduce the measured stiffness, P/CMOD, corresponding to the crack depth at the start of the test, in preference to using a measured gage length, which would have been ill-defined because of the complexity of the gripping arrangements.

The load line displacement due to the crack is given by applying Castigliano's theorem as

$$\delta_c = \frac{2B}{PE'}\int_0^c K^2(c')dc' \tag{B2.36}$$

B2.2.4 Specimen Stiffness for Unloading Compliance

Let c_i and c_f be the initial and final crack depths measured in a specimen after the test is completed, and S_e and S_t be the experimentally measured and theoretically calculated elastic stiffnesses, equal to the reciprocal of the gradient of the unloading line on a load-displacement plot. In general, $S_e \neq S_t$, and the following procedure is followed to re-scale the theoretical stiffness values to interpolate the stiffness values for crack depths between c_i and c_f Define

$$R_1 = \frac{S_t(c_i)}{S_e(c_i)},\ R_2 = \frac{S_t(c_f)}{S_e(c_f)} \tag{B2.37}$$

Then for crack depth c, where $c_i \le c \le c_f$, the interpolated value of $S(c)$ to be used to determine the instantaneous depth c can be obtained by solving the equation

$$S_t(c) = S_e(c)\left[\frac{c_f - c}{c_f - c_i} R_1 + \frac{c - c_i}{c_f - c_i} R_2\right] \tag{B2.38}$$

where $S_e(c)$ is the instantaneous measured stiffness.

B2.3 Test Results

B2.3.1 J_R-Curves for Nickel-Based Superalloy IN-718

J_R-curves for IN-718 have been measured at SwRI on nominally 0.5 inch (12.7 mm) and 0.25 inch (6.35 mm) wide, 1 inch (25.4 mm) thick restrained single edge cracked plates (RSECP) of IN-718. The specimen designs are illustrated in Figure B2.1. The specimens were restrained from rotation at the ends by the threaded circular end sections which screwed into massive threaded grips. The resulting test geometry is non-standard and requires sophisticated testing techniques and analysis (see Section B2.2).

Initially, electric discharge machining (EDM) notches were introduced into one of the flat sides of the 0.5 inch (12.7 mm) wide specimen blanks. These notches were then fatigue pre-cracked to produce sharp flaws from the notch tips. After this activity, the 0.25 inch specimens were produced by machining 0.125 inch from each of the flat sides of the 0.5 inch specimens. The final cracked RSECP specimens had nominal crack depth to width *(c/w)* ratios of 0.25, 0.5, and 0.7. After the fracture testing was performed, the cracked specimens were broken into two pieces and the actual fatigue pre-cracked lengths measured using an optical microscope and a nine point averaging technique, as recommended in ASTM Standard E1152 [57]. These results, and the specimen designations, are shown in Table B2.5. The first number in the designation indicates the type of test performed: 1 indicates a fracture toughness test, 2 indicates a fatigue test performed without a simulated proof test overload (see Section B6.3 for more details), 3 indicates a toughness test performed during an overload simulating proof loading (see Section B6.2 for more details). The second number in the designation indicates the nominal specimen width: 1 indicates w=0.5 inch, 2 indicates w=0.25 inch. The letter in the designation indicates the intended nominal initial crack depth to specimen width ratio: A indicates c/w=0.25, B indicates c/w=0.5, and C indicates c/w=0.7.

The tests were monitored for crack mouth opening displacement and effective load line displacement as a function of applied load. The load-line displacements were measured on the sides of the specimens at positions mid-way through the thickness and over a gage lengths of 2 inch (50.8 mm). The mouth openings were measured using clip gages mounted on knife edges attached in the middle of the specimen thicknesses and placed approximately 0.09 inch (2.29 mm) either side of the cracks. The gage length between the two knife edges was approximately 0.326 inch (8.28 mm), and the heights of the edges above the specimens varied between 0.07 inch (1.78 mm) and 0.1 inch (2.54 mm). During the testing, the loading was periodically stopped, and the specimens partially unloaded, in order to generate unloading compliance data for inferring the amount of ductile crack extension from post-test analyses.

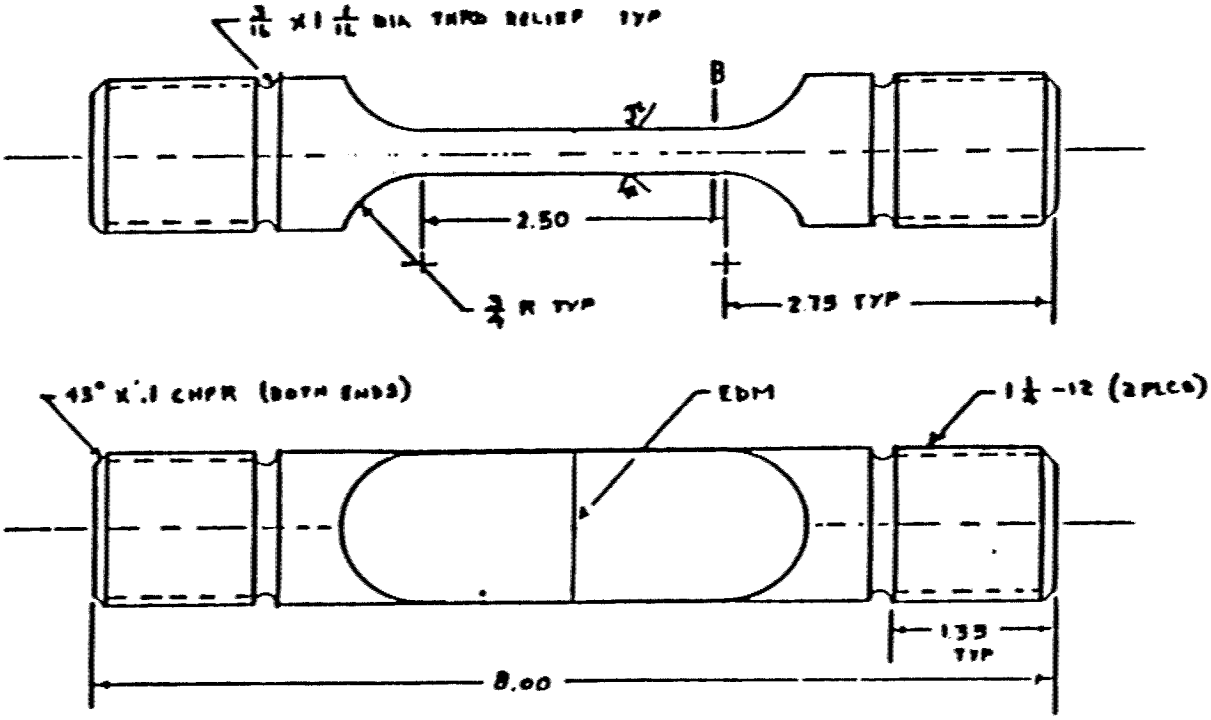

Figure B2.1 Restrained edge cracked plate (RSECP) test specimen design.

Table B2.5 Specimen and crack dimensions for the RSECP specimens

* Specimens used in simulated proof test overload tests followed by fatigue crack growth tests to simulate service cyclic loading

** Specimens used in fatigue crack growth tests to simulate service cyclic loading

Specimen number	Specimen width, w inch (mm)	Specimen thickness, t inch (mm)	Initial crack depth, c_i inch (mm)	Final crack depth, c_f inch (mm)	Ductile tear length, Δc_f inch (mm)	c_i/w	c_f/w	Initiation load kips (kN)	Maximum load kips (kN)
1.1.A	0.4964 (12.61)	0.979 (24.87)	0.1453 (3.691)	0.1715 (4.356)	0.0262 (0.655)	0.2927	0.3455	56.8 (252.6)	61.9 (275.3)
1.1.B	0.4954 (12.58)	0.976 (24.79)	0.2721 (6.911)	0.3049 (7.744)	0.0328 (0.833)	0.5493	0.6155	30.1 (133.9)	36.3 (161.5)
1.1.C	0.4967 (12.62)	0.976 (24.79)	0.3702 (9.403)	0.3893 (9.888)	0.0191 (0.485)	0.7453	0.7838	19.7 (87.6)	22.5 (100.1)
1.2.A	0.2496 (6.340)	1.001 (25.43)	0.0871 (2.213)	0.1767 (4.488)	0.0896 (2.276)	0.3490	0.7079	29.1 (129.4)	30.1 (133.9)
1.2.B	0.2495 (6.337)	0.999 (25.37)	0.1527 (3.879)	0.1849 (4.696)	0.0322 (0.818)	0.6120	0.7411	16.3 (72.5)	17.1 (76.1)
1.2.C	0.2503 (6.358)	0.999 (25.37)	0.1978 (5.024)	0.2328 (5.913)	0.0350 (0.889)	0.7903	0.9301	9.9 (44.0)	10.1 (44.9)
2.1.B **	0.4890 (12.42)	1.001 (25.43)	0.3478 (8.834)	n/a	n/a	0.7112	n/a	n/a	n/a
2.2.A **	0.2504 (6.360)	1.001 (25.43)	0.1674 (4.252)	n/a	n/a	0.6685	n/a	n/a	n/a
3.1.B *	0.4980 (12.649)	1.003 (25.48)	0.2735 (6.947)	0.3674 (9.332)	0.0939 (2.385)	0.5492	0.7378	31.2 (138.8)	36.6 (162.8)
3.2.B *	0.2466 (6.264)	0.998 (25.35)	0.1530 (3.886)	0.1686 (4.282)	0.0156 (0.3962)	0.6204	0.6837	15.2 (67.6)	16.3 (72.5)

The J_R-curve measurements were performed under displacement control to avoid the possibility of unstable crack propagation. The tests were stopped soon after the attainment of a maximum load, when the applied load was falling due to changes in the cracked specimen stiffness arising from crack extension and ligament plasticity. The measured maximum load would be the instability load under load control conditions. These loads are shown in Table B2.5 and are consistent with the expected net section yield loads for restrained specimens (i.e., the loads decreased approximately linearly with increasing c/w). A typical load-line displacement curve is shown in Figure B2.2 for specimen 3.1.B.

Analyses of the measured load-displacement data were performed as described in Section B.2.2 to obtain applied J values (J_R) as a function of crack extension. A computer program was written to perform the needed calculations off-line after the tests had been completed. This program read the electronically recorded digitalized load and displacement data from diskettes. Effective specimen spans were inferred from the elastic components of the load-line and crack mouth opening displacements. For a given applied load, the program calculated the instantaneous specimen stiffness and crack extension, and then evaluated the plastic area under the load-displacement curve to derive J_p.

The calculated effective spans derived from measured elastic load-line and crack mouth opening displacements (CMODs) are shown in Table B2.6. These spans, S, are the distances over which rotations of the ends of the specimens were predicted to be restrained in the RSECPs. The effective spans were chosen so that the elastic equations for the displacements given in Section B2.2.3 coincided with the measured values. The spans estimated from the load-line and CMOD are similar for deep cracks (specimens ending in the letter C), but differ significantly for shallower cracks. The reasons for this are three-fold. The first reason can be seen from Figure B2.3, which shows the function $Y(c/w, S/w)$ as a function of c/w for different S/w that cover the range of interest in the present work, where $Y(c/w, S/w)=K/[\sigma(\pi c)^{1/2}]$. This function, which appears in the expressions for the load-line and CMOD displacements, is not very sensitive to S/w at small c/w. The second reason is that whereas the load-line displacement can be directly evaluated from $Y(c/w, S/w)$, the determination of the CMOD involves knowledge of the weight function which was derived from $Y(c/w, S/w)$ and not directly measured quantities. The third reason is that the measured load-line displacements include contributions from the uncracked parts of the specimens as well as from the crack. Since the contribution from the crack is small compared to the uncracked contribution at small crack lengths, this implies that the load-line displacement will be relatively insensitive to the presence of small cracks, which will increase measurement errors for these.

The unloading compliance method used to assess the instantaneous crack depth indicated negative crack growth during the initial part of the loading. This so-called crack backup effect is not uncommon, and has been observed by others when testing compact tension specimens and single edge cracked plates. The reason for the crack backup has been attributed to rotation of the specimen due to the asymmetry introduced by the crack, although the actual cause has not been rigorously established. The rotation in compact tension specimens can be accounted for by correcting the measured mouth opening displacements using simple geometric constructions based on a point of rotation mid-way between the crack tip and the back face of the specimen. A similar approach has been used for pin-loaded edge cracked plate specimens. However, the rotation is limited in the RSECP specimens which were tested at SwRI because of the fixed grip nature of the loading. Hence it was considered that the usually used rotation point was not appropriate for RSECP specimens. An

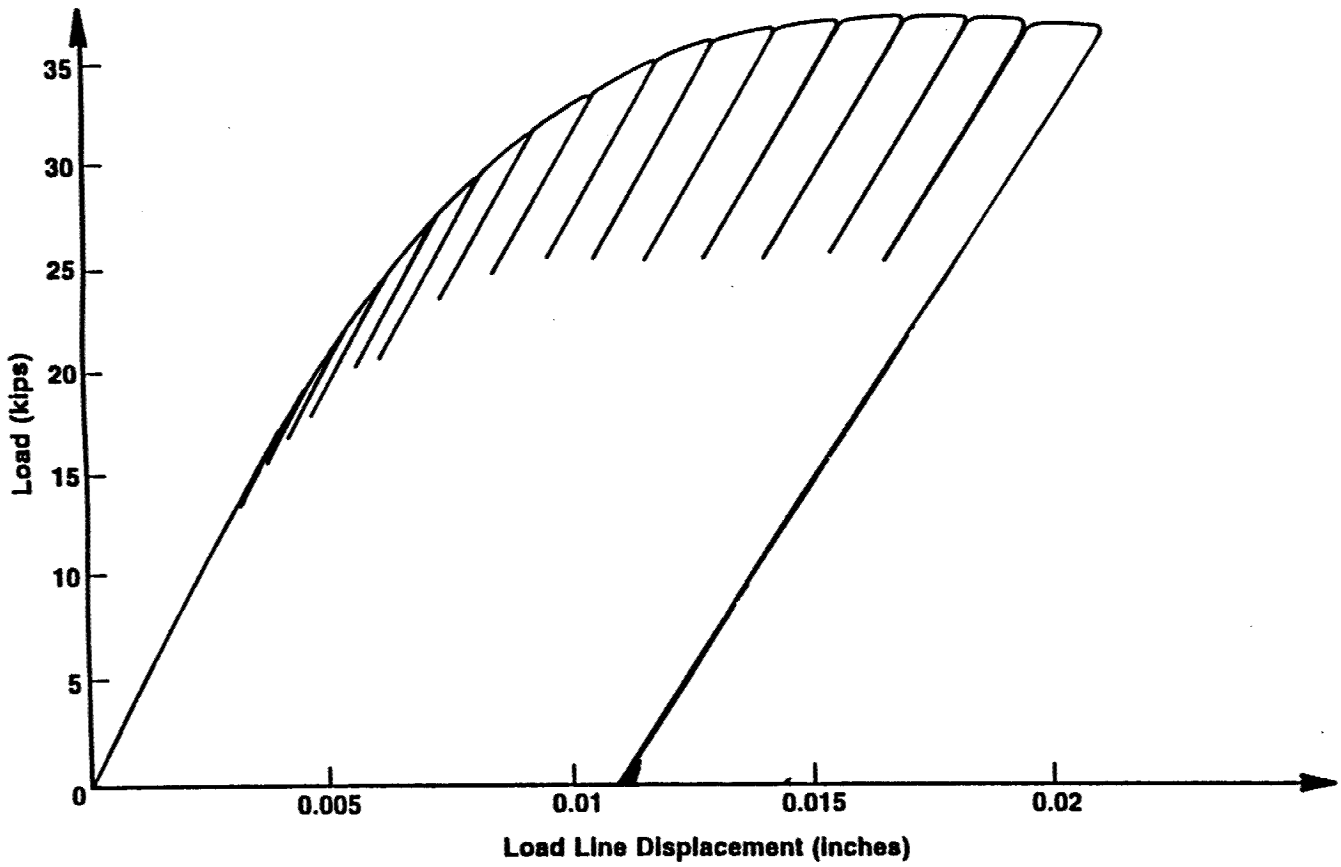

Figure B2.2 Typical load-displacement trace for specimen 3.1.B showing unloading steps used in unloading compliance crack depth measurements.

Table B2.6 Calculated effective spans over which ends of RSECP specimens were restrained

Specimen No.	Effective span for load line displacement, inch (mm)	Effective span for mouth opening displacement, inch (mm)
1.1.A	1.0 (25.4)	3.0 (76.2)
1.1.B	2.0 (50.8)	3.5 (88.9)
1.1.C	4.0 (101.6)	3.75 (95.3)
1.2.A	1.65 (41.2)	2.5 (63.5)
1.2.B	1.7 (43.2)	2.5 (63.5)
1.2.C	2.5 (63.5)	3.4 (86.4)
3.1.B	3.2 (81.3)	3.2 (81.3)
3.2.B	1.4 (35.6)	2.7 (68.6)

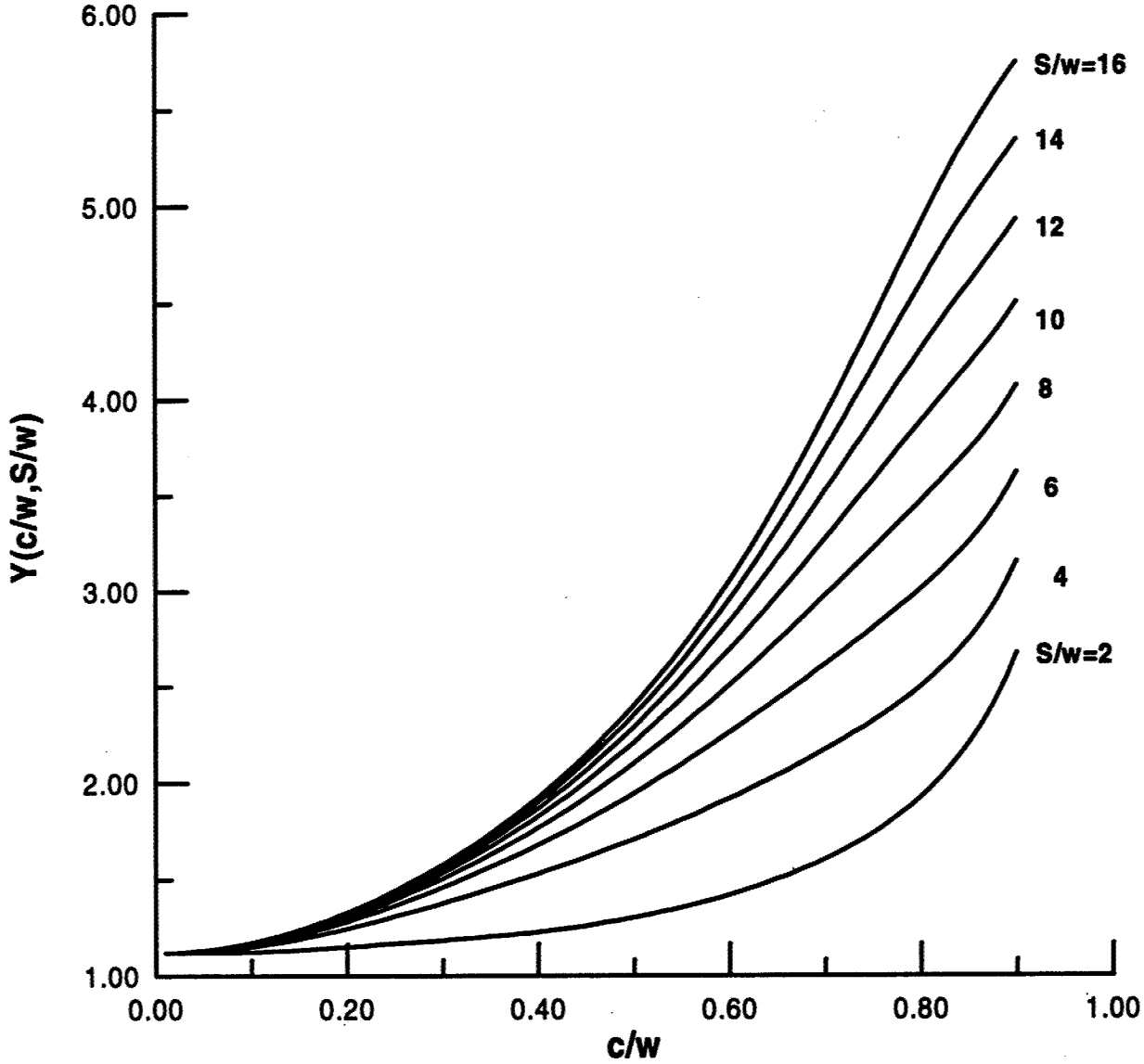

Figure B2.3 Calculated values of $Y(c/w, S/w)$ as a function of c/w for various S/w for the RSECP specimens.

analysis was performed using weight function theory to derive rotation points for the RSECP specimens. The results were incorporated into the computer software developed to analyze the test results. The rotation correction was found to have negligible effect on the results, as anticipated because of the end restraints. However, this analysis had to be performed to discount the possibility of rotation being a cause of the crack backup.

In the light of these results, the method used to process the unloading compliance data was modified. In the modification, the data were searched to locate the unloading cycle in which the specimen stiffness was a maximum. Beyond this maximum in the stiffness, the unloading compliance method indicates a positive change in the crack depth, even though the derived absolute value of the crack length is less than its initial value. At the J value corresponding to the maximum, the amount of actual physical crack extension was assumed to fall on the blunting line with a gradient of twice the yield stress, and any further extension was measured with respect to this point on the blunting line.

Substantiation of this procedure is provided in the results shown in Figures B2.4 to B2.6. It can be seen from these figures that the J_R-curve undergoes an apparent discontinuous change in gradient as the tear length approaches very small values, and that the gradient of the curve at small tear lengths is consistent with the gradient of the blunting line (shown as the full line in the figures).

After the tests were completed, the specimen fracture surfaces were heat tinted and the final crack depths and tear lengths at the end of the tests measured using a nine point averaging procedure and an optical microscope. The results are shown in Table B2.5.

The measured J_R-curves for specimens 1.1A, 1.1.B, 1.1.C, 1.2.A, 1.2.B, 1.2.C, 3.1.B, and 3.2.B are shown in Figure B2.7. Also shown is a representative J_R-curve measured by Rocketdyne on a standard compact tension specimen. As expected, because of lower constraint, the J_R-curves for the RSECP specimens display higher toughness values than the compact tension curve. These data re-enforce the need to obtain representative J_R-curve data for hardware that is being proof tested.

B2.3.2 Failure Assessment Diagrams for Nickel-Based Superalloy IN-718

Failure curves which define the Failure Assessment Diagram (FAD) for IN-718 can be determined experimentally by plotting the points K_r^*, L_r^* on the FAD where

$$K_r^* = \left(\frac{J_e(c,P)}{J(c,P)} \right)^{\frac{1}{2}}, \; L_r^* = \frac{P}{P_y^*(c)} \tag{B2.39}$$

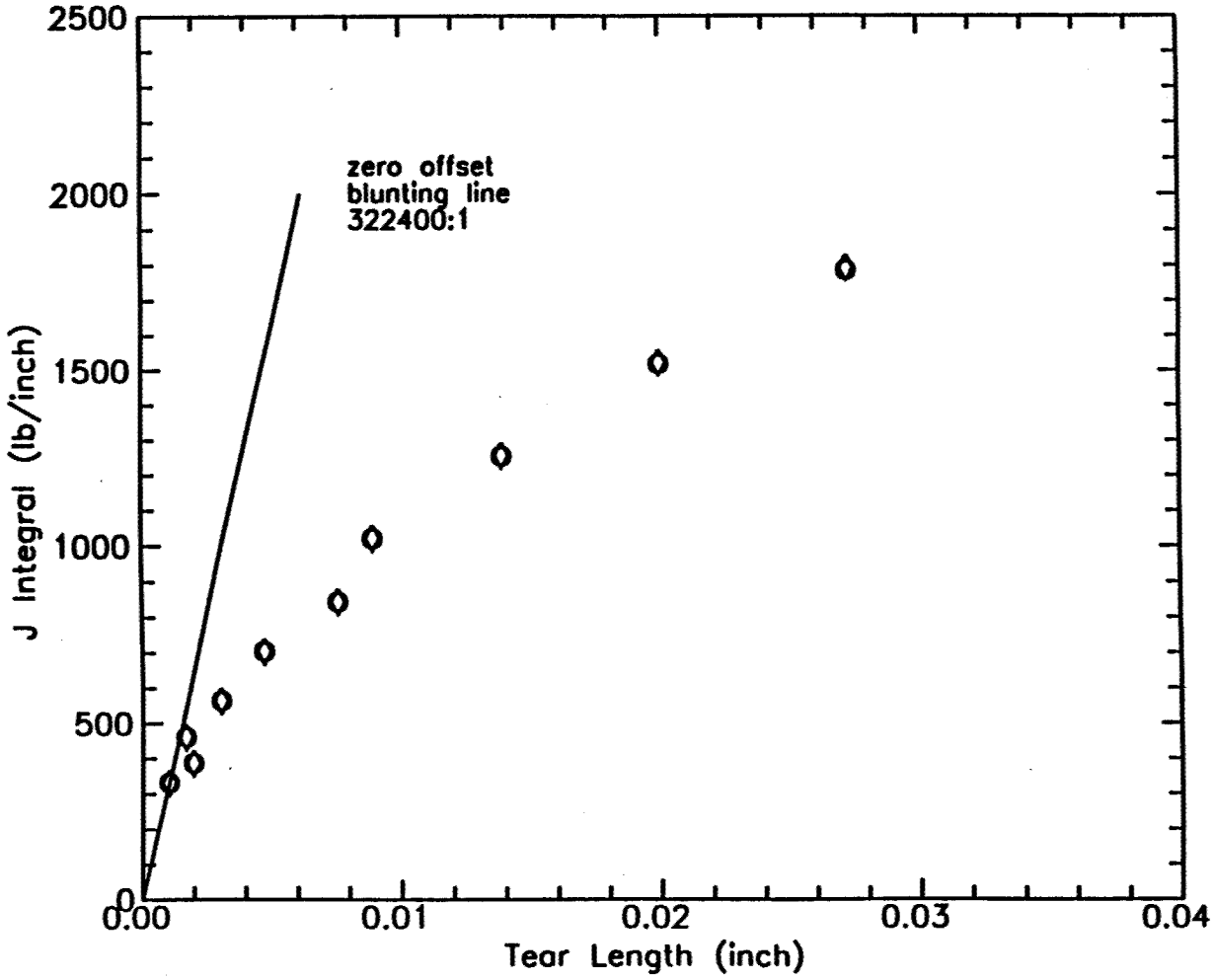

Figure B2.4 Substantiation of procedure followed to compensate for crack backup effects for specimen 1.1.A.

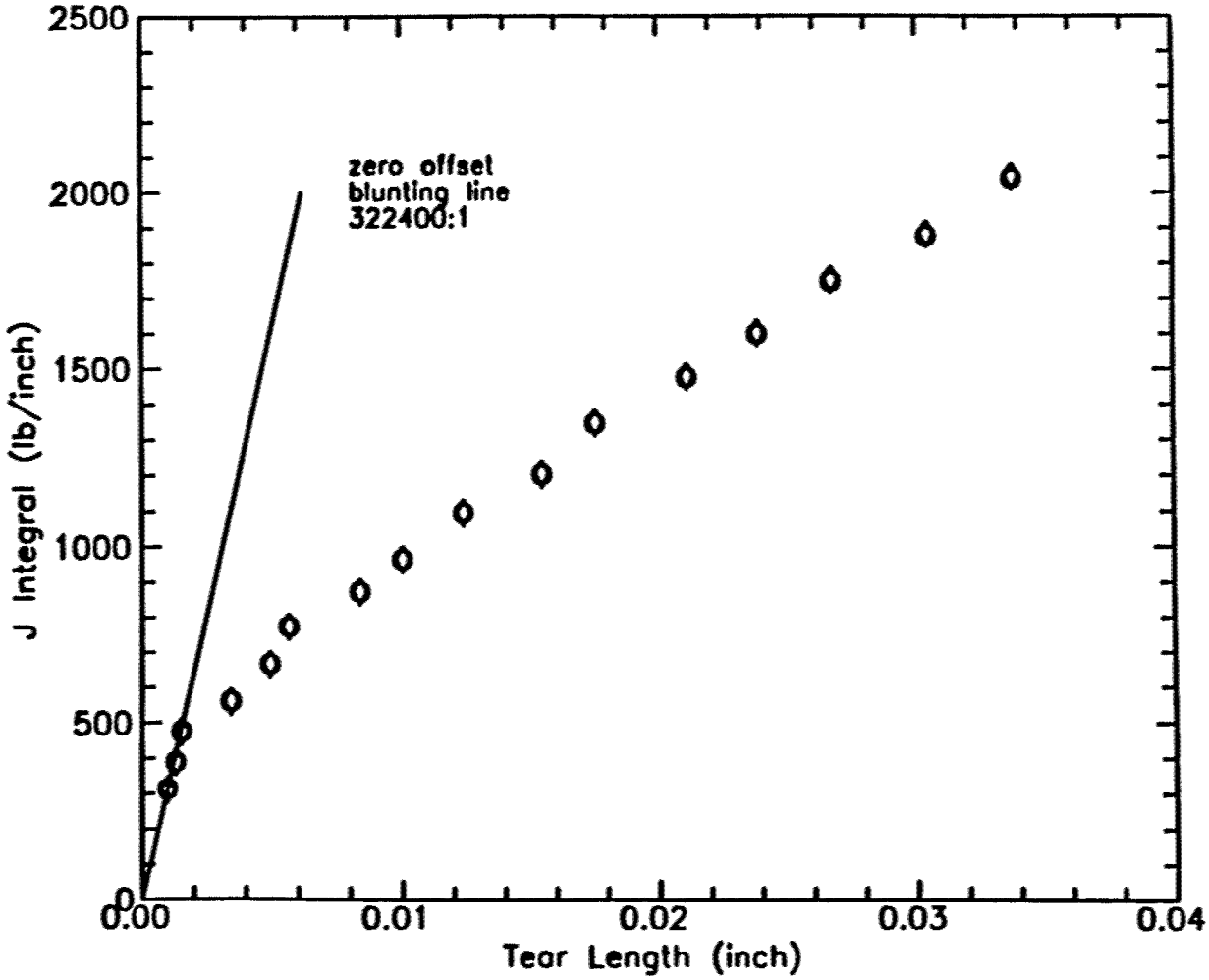

Figure B2.5 Substantiation of procedure followed to compensate for crack backup effects for specimen 1.1.B.

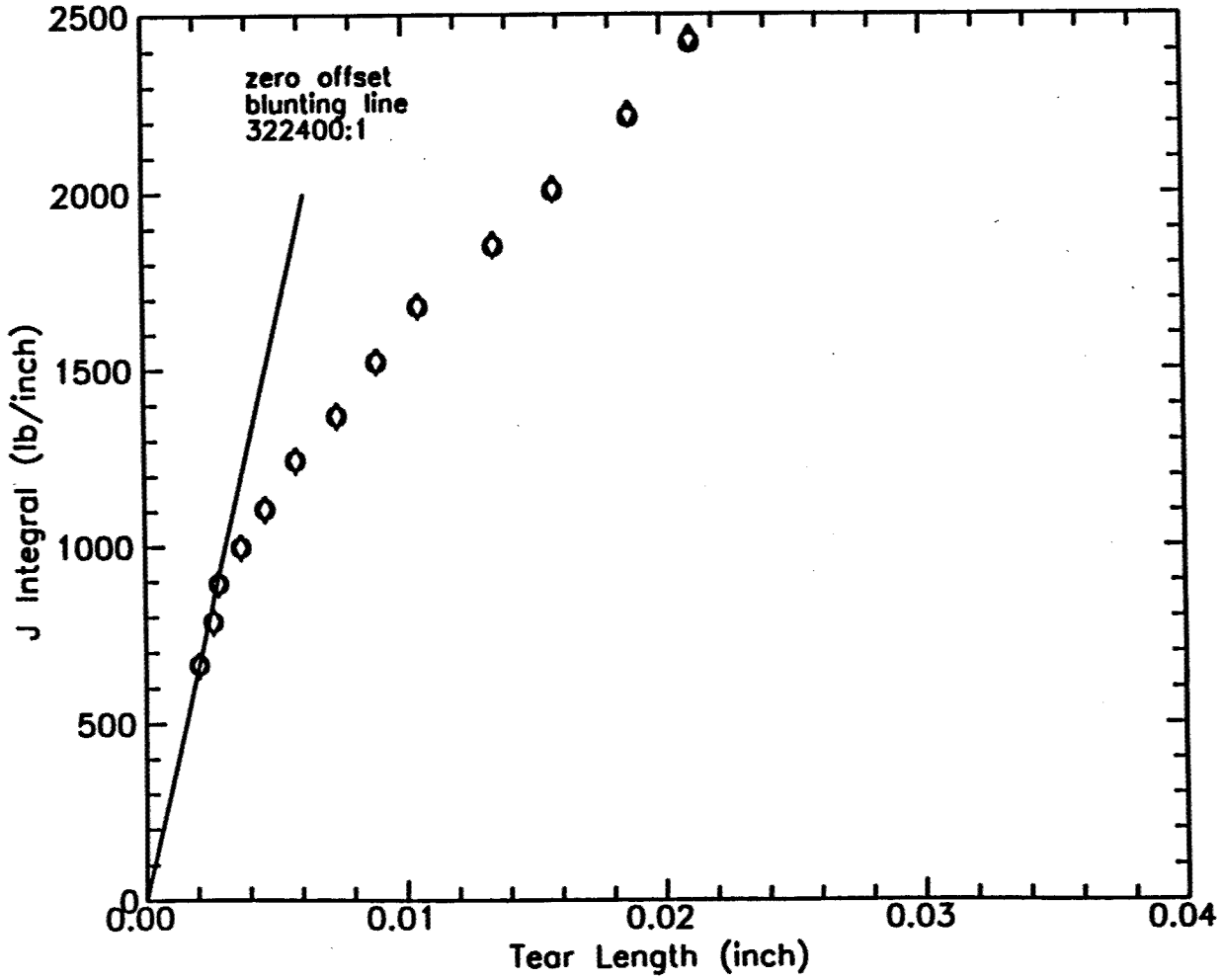

Figure B2.6 Substantiation of procedure followed to compensate for crack backup effects for specimen 1.1.C.

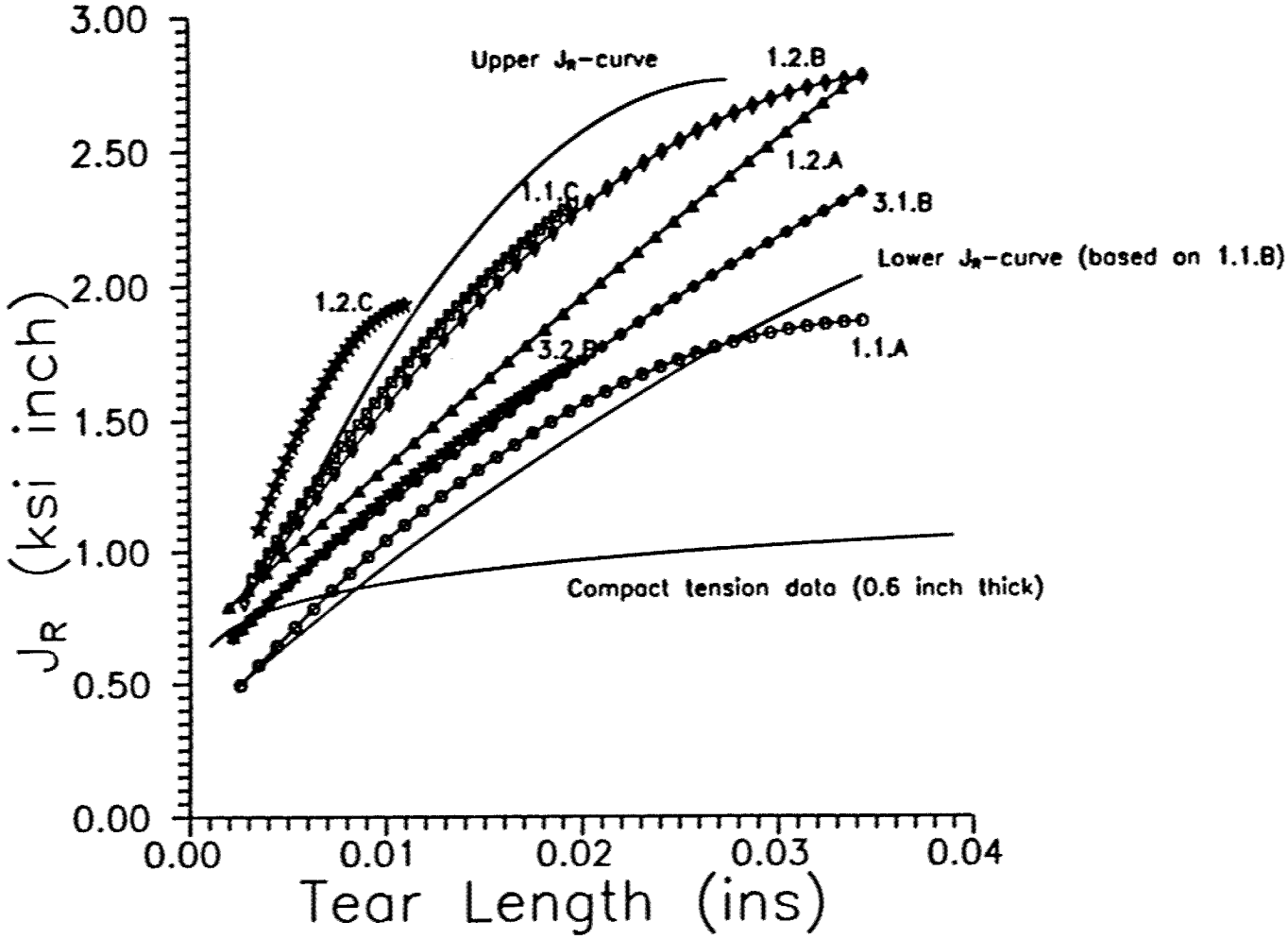

Figure B2.7 J_R-curves measured on the RSECP specimens showing effects of low constraint compared to compact tension data. The upper and lower bound curves were used in the hardware verification analyses described in Section B.4.

and c and P are the instantaneous crack depth and applied load. J is the measured elastic-plastic value in the fracture test and is equal to the value of J_R corresponding to the instantaneous crack blunting and ductile tearing. Hence,

$$K_r^* = \left(\frac{J_e(c_i + \Delta c_t, P)}{J_R(\Delta c_t)} \right)^{\frac{1}{2}} , \quad L_r^* = \frac{P}{P_y^* (c_i + \Delta c_t)} \tag{B2.40}$$

A value of P_y^* is required in order to plot the experimental curve. In the present case, the following net section yield load was used

$$P_y^* = \sigma_y w t \left[1 - c/w\right] \tag{B2.41}$$

The experimental curve predicted from equation (B2.40) can be compared with the theoretical, material specific curve derived from equation (A5.11) for a Ramberg-Osgood material

$$K_r^* = \left[1 + \frac{0.5 \left[L_r^* \left(\frac{\sigma_y}{\sigma_o} \right) \right]^2}{1 + \alpha \left[L_r^* \left(\frac{\sigma_y}{\sigma_o} \right) \right]^{n-1}} + V^* \alpha \left[L_r^* \left(\frac{\sigma_y}{\sigma_o} \right) \right]^{n-1} \right]^{-\frac{1}{2}} \tag{B2.42}$$

where α, n, and σ_o are constants appearing in the Ramberg-Osgood equation. The values of these constants for IN-718 at ambient temperature have been determined by Rocketdyne to be: α=1, n=15.8, and σ_o=179.8 ksi (1240 MPa). The ratio (σ_y/σ_o) appears because L_r^* is evaluated using the yield stress

$$L_r^* = \frac{P}{P_y} = \left(\frac{P}{P_o} \right) \left(\frac{\sigma_o}{\sigma_y} \right) \tag{B2.43}$$

where σ_y=161.2 ksi (1111 MPa). The range of possible values for the structural parameter, V^*, are given in Table A4.2. In order to calculate a best estimate failure curve, V^* was set equal to 1, which is near the mean value.

The failure curve predicted by equation (B2.42) is shown as a solid line in Figure B2.8 together with the experimentally derived failure curves for the RSECP specimens 1.1.A, 1.1.B, 1.1.C, 1.2.A,

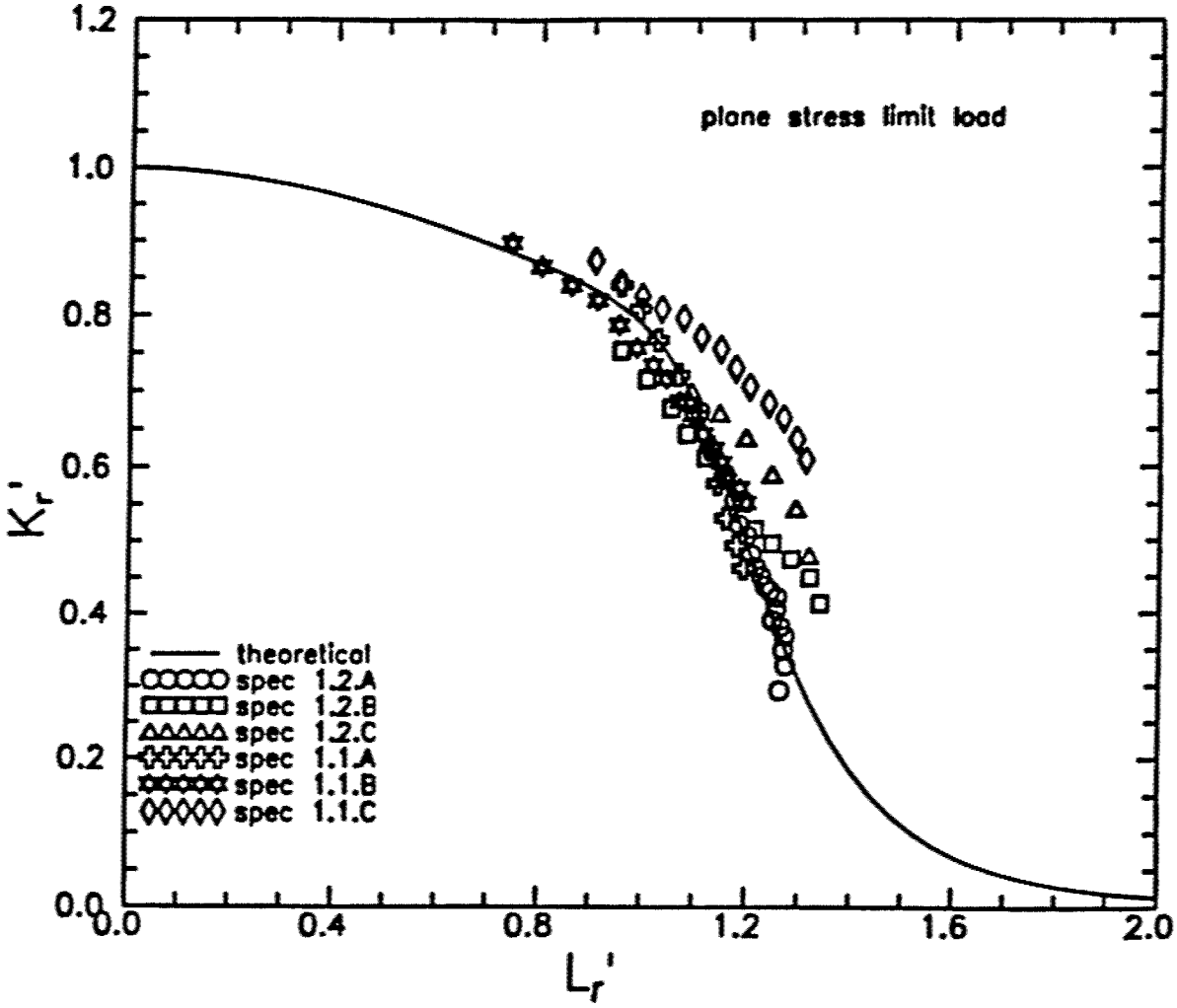

Figure B2.8 Comparison of IN-718 material specific failure curve (full line) with experimentally measured curves derived from the RSECP test results.

1.2.B, 1.2.C generated using equation (B2.40). The agreement between the theoretical failure curves and the experimental curves is good for all crack depths and both specimen widths. This agreement substantiates the use of a material specific failure curve for IN-718 subjected to primary loading.

B2.3.3 Failure Assessment Diagrams for Aluminum Alloy 2024-T3511

Two sets of tests were performed at SwRI on 2024-T3511 aluminum alloy extrusion, one involving center cracked panels (CCPs) and the other single edge cracked panels (SECPs). The CCP specimens had a section width, $2w$, of 0.5" (12.7 mm), and a thickness, t, of 0.25" (6.35 mm), and the SECP specimens had a width, w, of 0.25" (6.35 mm) and a thickness, t, of 0.5" (12.7 mm). In each specimen, a blunt notch was machined of nominal crack depth to thickness (c/w) ratio given by one of the following: 0.3, 0.4, 0.5, 0.6, 0.7, and 0.8. The sizes of the specimens together with the use of blunt notches were designed to enhance the level of crack tip plasticity that developed prior to fracture. The radii of the notches were small enough (0.01 inch, 0.254 mm) so that the J values measured in the tests would be similar to the J values for an equivalent sharp flaw. The intent of using notches with finite root radii, was that ductile tearing would be suppressed and a greater part of the FAD would be generated before instability than would be the case with a sharp crack. This design appears to have been successful, and significant notch tip plasticity was generated at the maximum loads attained in the tests in spite of the low toughness of the aluminum alloy (32 ksi inch$^{1/2}$, 35.2 MPa m$^{1/2}$).

A preliminary FAD analysis was performed to theoretically estimate the material specific failure curve for the aluminum alloy using stress-strain data derived from uniaxial tensile load and displacement data. The explicit stress-strain curve was used to construct an aluminum 2024-T3511 failure curve by employing the equation [compare equation (A5.11)]

$$K_r^* = \left(1 + \frac{0.5 L_r^{*\,2}}{\left[\dfrac{E\,\epsilon_{ref}}{\sigma_{ref}} \right]} + V^*(c/w, L/w) \left[\frac{E\,\epsilon_{ref}}{\sigma_{ref}} - 1 \right] \right)^{-\frac{1}{2}} \tag{B2.44}$$

where

$$L_r^* = \frac{P}{P_y^*}\ , \quad \sigma_{ref} = L_r^*\,\sigma_y \tag{B2.45}$$

and ϵ_{ref} is the uniaxial strain obtained from the stress-strain curve corresponding to the stress σ_{ref}. The aluminum alloy showed little strain hardening capacity, and behaved like a non-hardening (elastic-perfectly plastic) material, with the result that the failure curve fell steeply after general yielding of the cracked section (see solid line in Figure B2.9). The yield stress, σ_y, was 55 ksi (379 MPa), the ultimate stress 67 ksi (462 MPa), and the alloy showed an elongation measured over a 1 inch (25.4 mm) gage length of 20%.

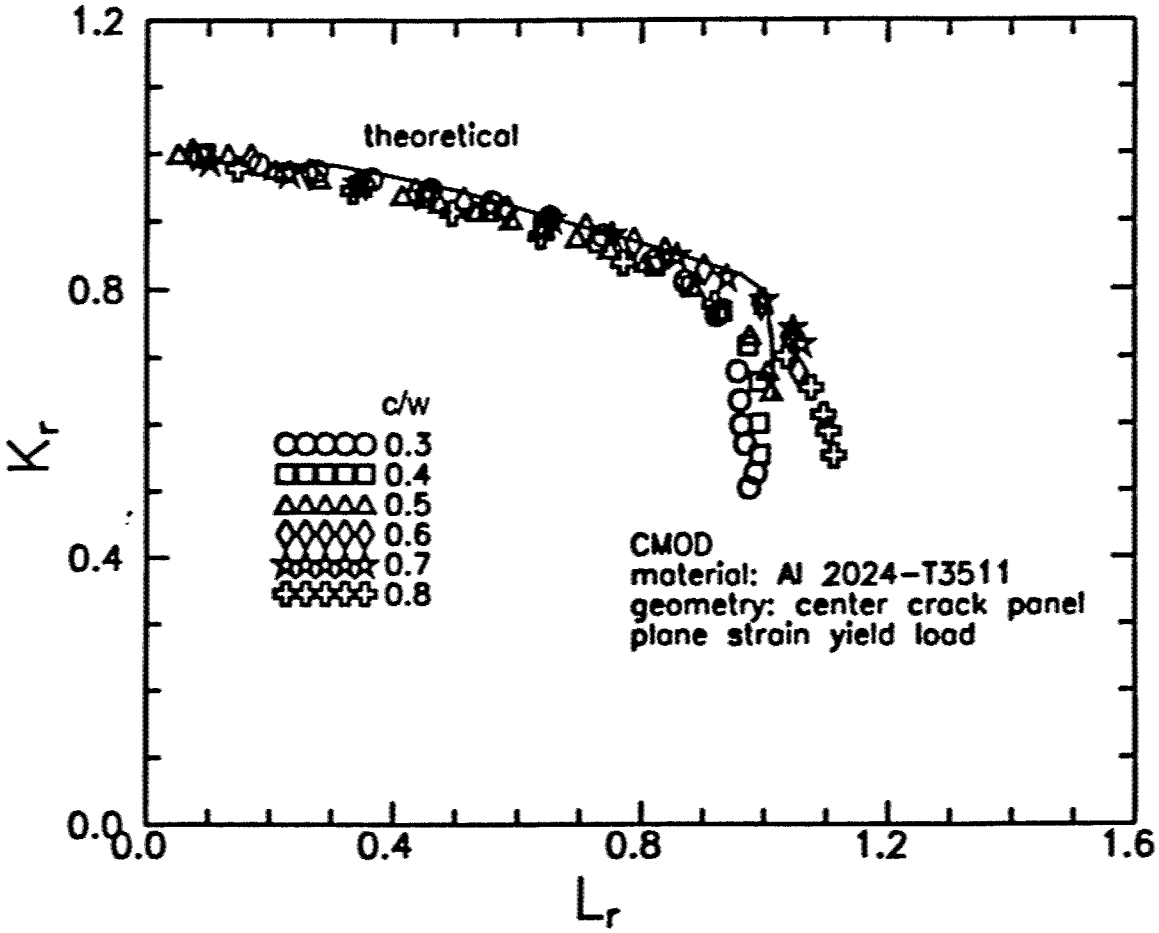

Figure B2.9 Comparison of the material specific failure curve (solid line) for the aluminum alloy with the experimentally determined failure curves obtained from tests on center cracked panels (CCPs) containing crack depths varying between 30% and 80% of the thickness. The value of L_r^* was determined using a plane strain plastic limit load.

In the tests, the specimens were loaded in tension and the load line displacements and the crack mouth opening displacements (CMODs) were recorded against the applied load under displacement control until a maximum load was reached, when the specimens were unloaded. As previously stated, the tests were intended to measure J without producing ductile tearing. The plastic component of the areas under the CMOD versus load curves were used to derive values for the plastic component of J, J_p, as a function of applied load using the appropriate η_p^* factors detailed in Tables B2.3 and B2.4 of Section B2.2.2. The total J was calculated as the sum of J_p and the elastic component, $J_e=K^2/E'$, where K is the stress intensity factor. The failure curve coordinates corresponding to the instantaneous load, P, were evaluated using the equations

$$K_r^* = \left[\frac{J_e(c,P)}{J_e(c,P)+J_p(c,P)}\right]^{\frac{1}{2}}, L_r^* = \frac{P}{P_y^*(c)} \tag{B2.46}$$

The FAD containing the failure curves obtained by applying these procedures to the CCP specimens is shown in Figure B2.9. Initially, the plane stress net section yield load given by

$$P_y^* = 2tw\,\sigma_y(1 - c/w) \tag{B2.47}$$

was used to estimate L_r^*, but it was clear that this under-estimated the measured maximum loads recorded in the tests. Hence, a plane strain net section yield load given by

$$P_y^* = (2tw)\,1.15\,\sigma_y(1 - c/w) \tag{B2.48}$$

was used instead.

The fact that the plane strain limit load appeared to be more appropriate than the plane stress limit load was surprising, as plane stress deformation was anticipated for the size of specimens tested. However, the results presented in Figure B2.9 show excellent agreement between the theoretical material specific FAD based on the measured stress-strain curve (solid curve) and the measured FADs (open symbols) for all of the crack depths tested.

The analysis of the SECP results was not as straightforward as for the CCP specimens, and difficulties were encountered associated with the gripping arrangement used to hold the SECP specimens in the testing machine. Each end of the plates was gripped between two friction pads which were intended to inhibit rotation of the ends, providing a fixed grip loading. However, the linear response on the measured CMOD curves agreed with the standard linear elastic solutions for unrestrained SECPs, indicating that the friction grips were not restraining bending, at least in the linear elastic region. However, the gripping arrangement influenced, in some indeterminate way, the net section yield load of the specimens, so that the measured maximum loads were not consistent with

either an unrestrained SECP or a RSECP. This can be seen from Figure B2.10 which shows the experimentally measured maximum loads (signified as P_{max}) normalized by the load to cause yielding in the flaw free specimen (P_y) plotted against c/w. Also shown in the figure are the normalized net section yield loads for a restrained edge cracked plate in plane stress, and the optimized plane strain solution for a un-restrained SECP (see Section B1.2). Neither of these two theoretical solutions provide an accurate description of the experimentally determined maximum loads. Because of this, the values of L_r^* for the experimental failure curves were calculated by equating P_y^* to the experimentally measured maximum loads. The results are displayed in Figure B2.11, and the experimental FADs now show very good agreement with the theoretical material specific failure curve.

B3. LABORATORY VALIDATION: PREDICTING CRITICAL CRACK SIZES AND CRITICAL LOADS FOR IN-718

B3.1 Critical Loads

The measured applied loads as a function of tear length, Δc_t, for the RSECP specimen tests reported in Section B2.3.1 are shown in Figures B3.1 to B3.4. The loads go through a maximum because the J_R-curve tests were performed under displacement control. The maximum loads correspond to the instability loads under load control. The unloading after the maximum (instability point) occurs in a specimen because the change in specimen stiffness due to rapid crack propagation produces load-line displacement rates which exceed the imposed machine displacement rates, and this forces the cracks to remain stable.

The data displayed in Figures B3.1 to B3.4 can be predicted by solving the following equation for the applied load, P

$$J(c_i + \Delta c_t, P) = J_R(\Delta c_t) \qquad \text{(B3.1)}$$

as the tear length, Δc_t, is increased. The load at the initiation of tearing, P_{init}, is attained when Δc_t equals Δc_b, the crack extension due to blunting corresponding to $J_R(\Delta c_t)=J_{max}$. The initiation load would equal the instability load if the IN-718 material had exhibited brittle fracture with no crack growth resistance. Since IN-718 is ductile, the instability load, P_{inst}, is equal to the predicted maximum load and the ductile tear length at instability, Δc_{inst}, is the tear length, Δc_t, at the maximum load. The J_R-curves measured on the RSECP specimens are shown in Figure B2.7.

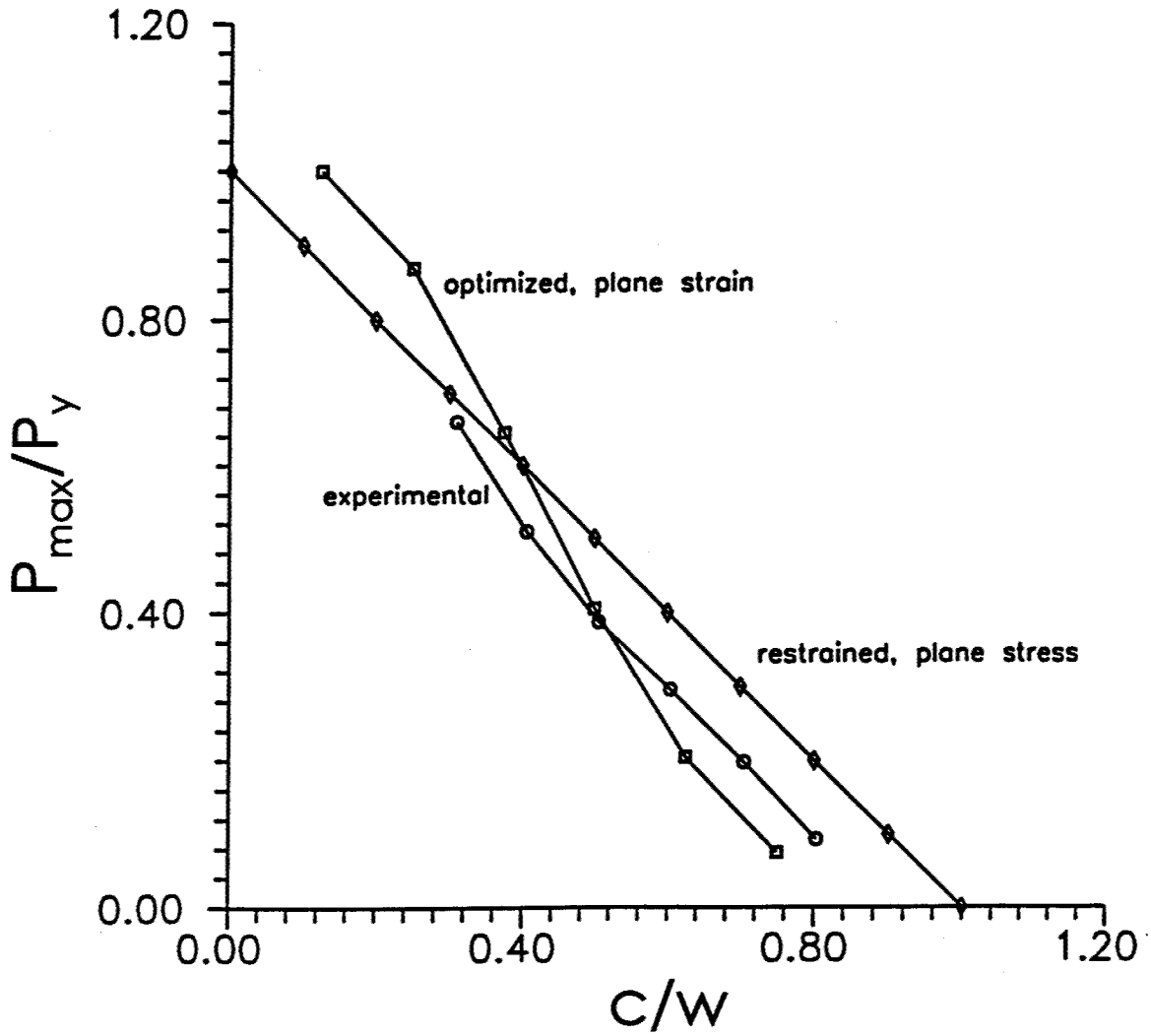

Figure B2.10 Comparison of normalized maximum limit loads, P_{max}/P_y, for SECPs as a function of normalized crack depth, *c/w*, where P_y is the load to yield the flaw-free specimen. The experimental data are based on the maximum loads recorded in the tests.

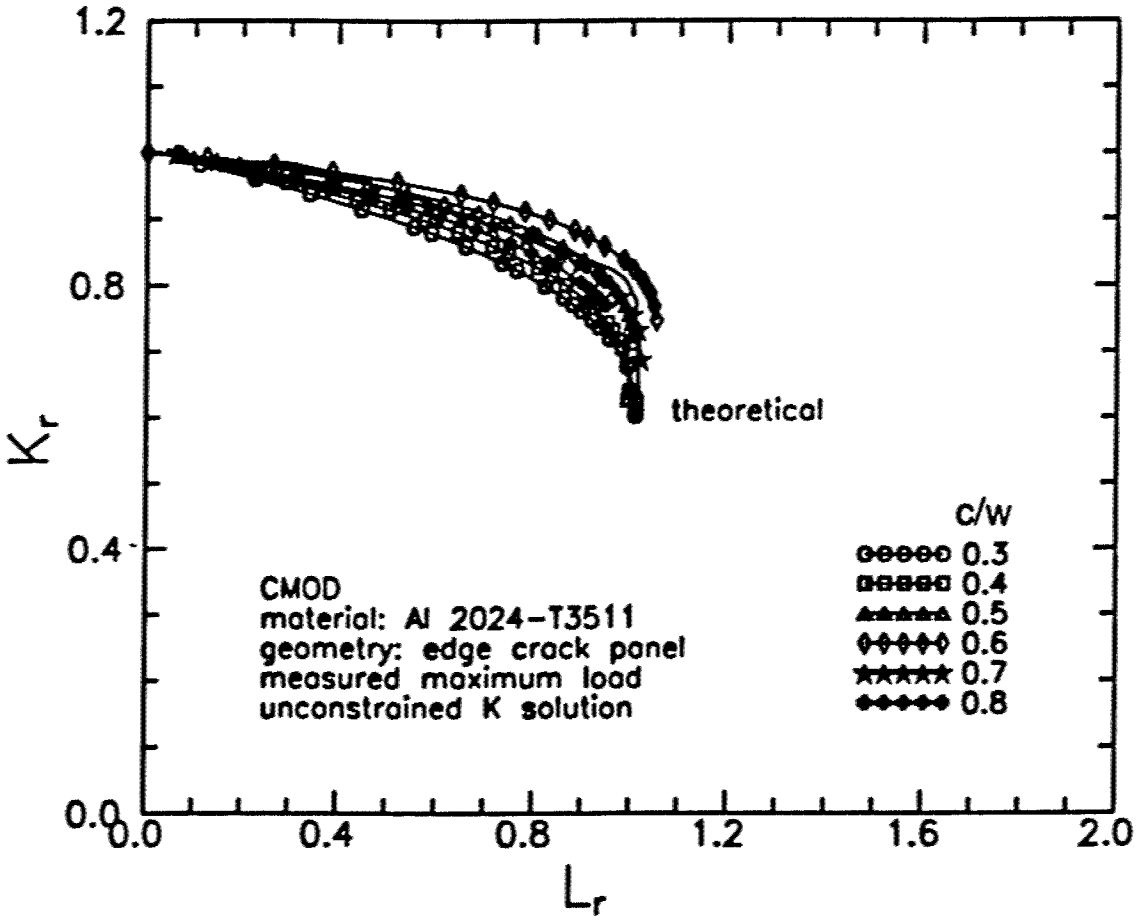

Figure B2.11 Comparison of the material specific failure curve (solid line) for the aluminum alloy with the experimentally determined failure curves obtained from tests on single edge cracked panels (SECPs) containing crack depths varying between 30% and 80% of the thickness. The value of L_r^* was determined using the measured maximum loads recorded in the tests.

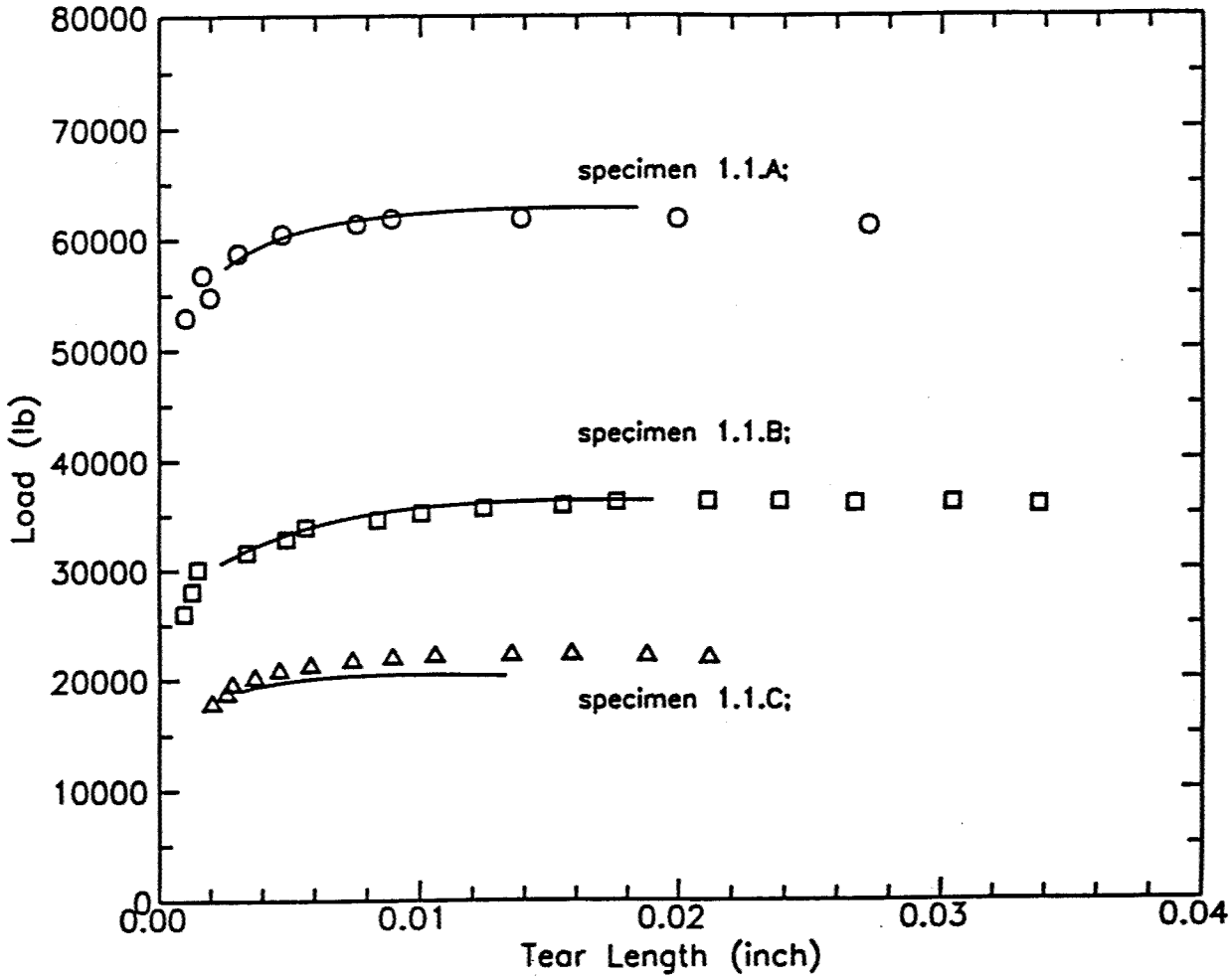

Figure B3.1 Comparison of predicted (solid line) and experimental (open symbols) loads versus tear length behaviors of RSECP specimens 1.1.A, 1.1.B, and 1.1.C. (1000 lb = 4.448 kN, 1 inch = 25.4 mm)

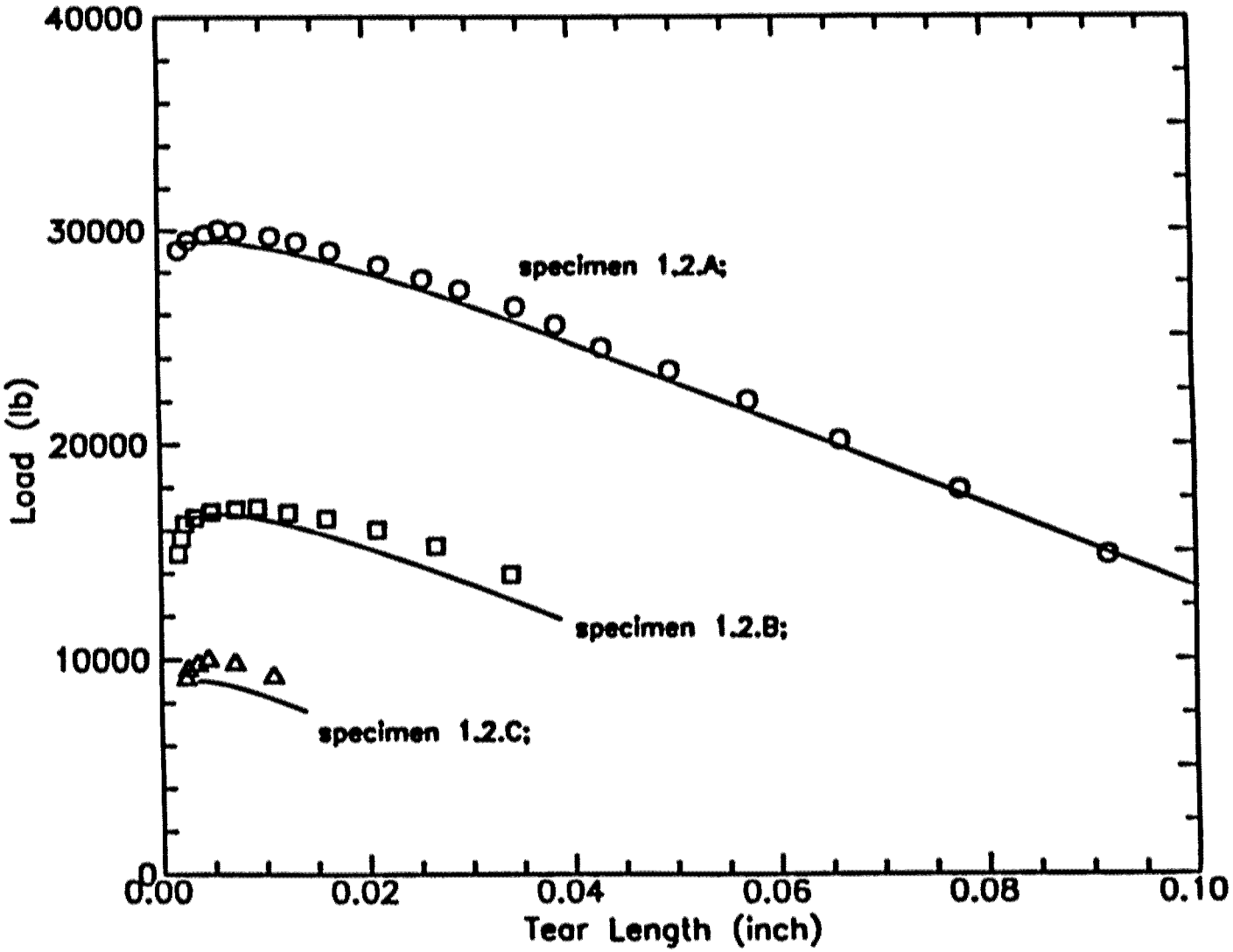

Figure B3.2 Comparison of predicted (solid lines) and experimental (open symbols) loads versus tear length behaviors of RSECP specimens 1.2.A, 1.2.B, and 1.2.C.

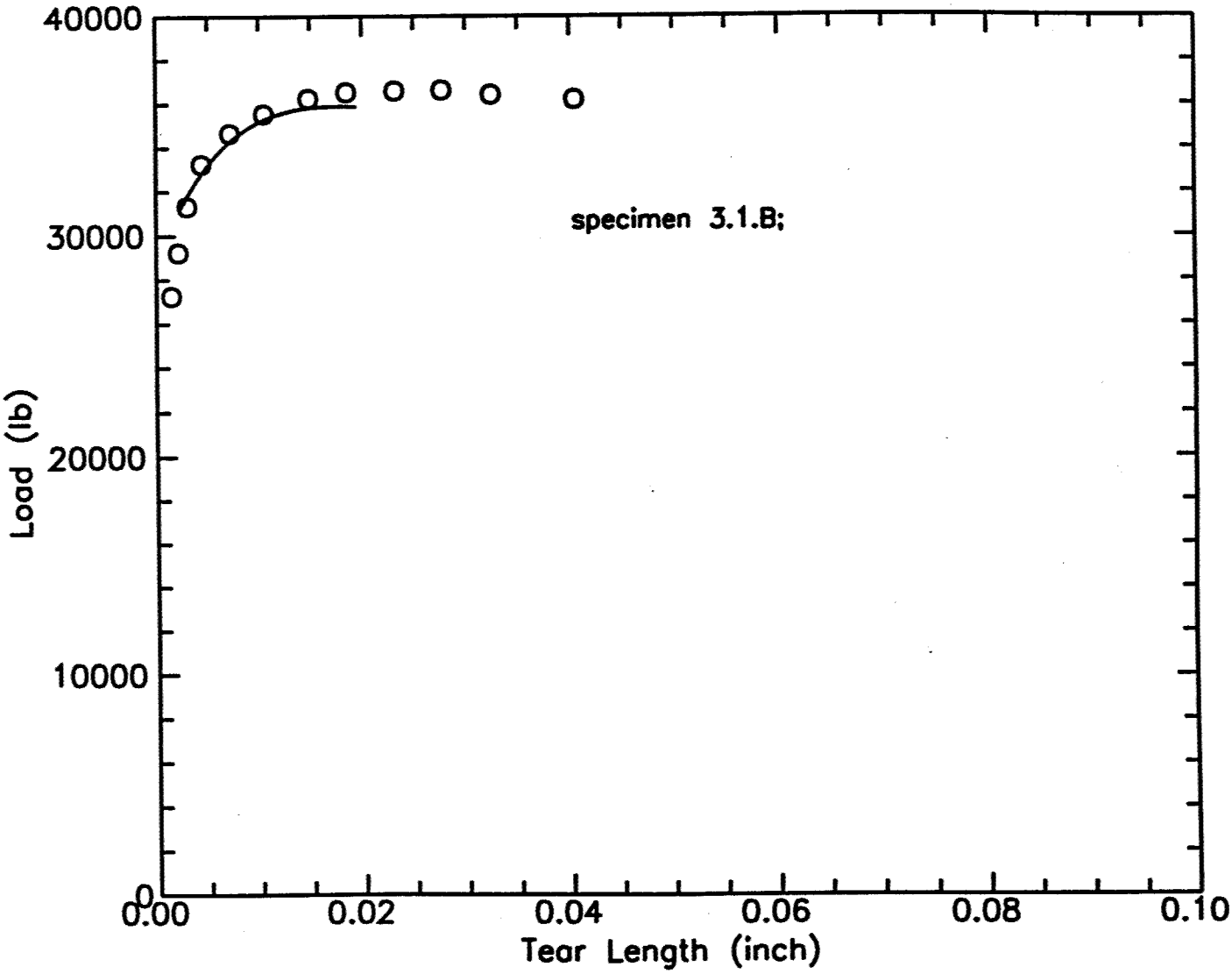

Figure B3.3 Comparison of predicted (solid lines) and experimental (open symbols) loads versus tear length behavior of specimen 3.1.B. (1000 lb = 4.448 kN, 1 inch = 25.4 mm)

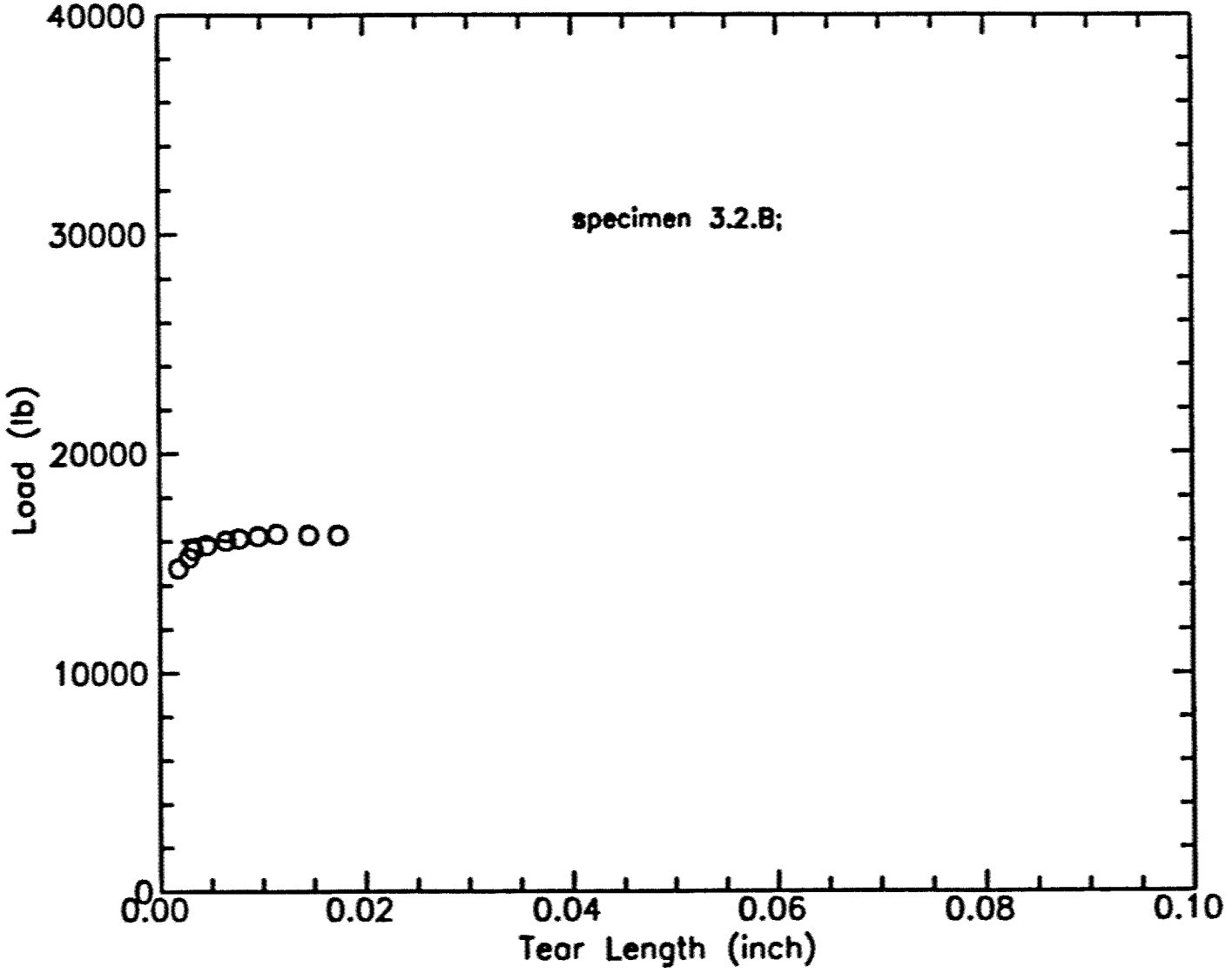

Figure B3.4 Comparison of predicted (solid lines) and experimental (open symbols) loads versus tear length behavior of specimen 3.2.B. (1000 lb = 4.448 kN, 1 inch = 25.4 mm)

The load-tear length behaviors for the RSECP specimens were predicted using equation (B3.1) and the measured J_R-curve corresponding to the specimen being analyzed. Thus the J_R-curve in Figure B2.7 corresponding to specimen 1.1.C was used to predict the fracture behavior of that specimen. The reason for doing this was to avoid uncertainties in the predictions due to material variability between specimens. In the calculations the values of J were determined employing the material specific J estimation scheme for a Ramberg-Osgood material [see equation (A4.31)]

$$J(c+\Delta c_t,P) = J_e(c+\Delta c_t,P)\left[1 + \frac{0.5\left[\dfrac{P}{P_o(c+\Delta_t)}\right]^2}{1+\alpha\left[\dfrac{P}{P_o(c+\Delta c_t)}\right]^{n-1}} + V^*\alpha\left[\frac{P}{P_o(c+\Delta c_t)}\right]^{n-1}\right] \tag{B3.2}$$

where the net section yield load, P_o, was defined as the plane stress net section yield load

$$P_o(c) = \sigma_o wt(1 - c/w) \tag{B3.3}$$

Equation (B3.2) was used to derive the experimental failure curves shown in Figure B2.8.

In order to obtain a "best estimate" critical load prediction, V^* was set equal to 1. The value of $J_e=K^2/E'$ was determined using the line spring model and the effective span length over which bending was restrained. This length was calculated for each specimen as discussed in Section B2.2.3.

For computational convenience, the J_R-curves shown in Figure B2.7 were fitted by quadratic polynomials of the form

$$J_R(\Delta c_t) = J_o + J_1\Delta c_t + J_2(\Delta c_t)^2 \tag{B3.4}$$

The coefficients and the validity range of the polynomials are displayed in Table B3.1. The lower range, Δc_{min}, is equal to Δc_b, the amount of blunting at the initiation of tearing, and was determined by solving the equation

$$2\sigma_y\Delta c_b = J_R(\Delta c_b) \tag{B3.5}$$

The upper range, Δc_{max}, was given by the maximum tear length that was measured in the J_R-curve tests.

Table B3.1 Toughness parameters related to the quadratic fit to the measured J_R-curves of the IN-718 RSECP specimens

Specimen No.	J_{mat}, ksi inch (MPa m)	J_0, ksi inch (MPa m)	J_1, ksi (MPa m/mm)	J_2, ksi inch^{-1} (MPa m/mm^2)	Δc_{min} (= Δc_b), inch (mm)	Δc_{max}, inch (mm)
1.1.A	0.495 (0.0868)	0.276 (0.0484)	88.83 (0.614)	-1239.4 (-0.337)	0.00245 (0.0622)	0.04 (1.016)
1.1.B	0.492 (0.0863)	0.338 (0.0593)	65.73 (0.454)	-478.2 (-0.130)	0.00234 (0.0594)	0.04 (1.016)
1.1.C	0.890 (0.156)	0.499 (0.0875)	131.6 (0.909)	-2011.0 (-0.547)	0.00297 (0.0754)	0.02 (0.508)
1.2.A	0.793 (0.139)	0.657 (0.1152)	68.5 (0.473)	-193.0 (-0.0525)	0.00199 (0.0505)	0.10 (0.254)
1.2.B	0.812 (0.142)	0.485 (0.0851)	122.4 (0.845)	-1623.1 (-0.441)	0.00267 (0.0678)	0.04 (1.016)
1.2.C	1.088 (0.191)	0.201 (0.0353)	294.8 (2.036)	-12466.7 (-3.388)	0.00301 (0.0765)	0.015 (0.381)
3.1.B	0.693 (0.122)	0.549 (0.0963)	66.88 (0.462)	-423.9 (-0.115)	0.00215 (0.0546)	0.04 (1.106)
3.2.B	0.674 (0.118)	0.503 (0.0882)	79.94 (0.552)	-932.1 (-0.253)	0.00214 (0.0544)	0.02 (0.508)

The predicted load versus tear length behaviors for the RSECP specimens are shown as the full lines in Figures B3.1 to B3.4. There is excellent agreement between the predicted behaviors and the measured ones. The predicted loads at the initiation of ductile tearing and instability (maximum load), and the tear length at instability, can be compared to the experimental values in Table B3.2. There is very good agreement between the two sets of results. This is confirmed in Figure B3.5 which shows the measured loads at initiation and instability plotted against the predicted loads. Exact agreement between predicted and measured values occurs when the plotted points fall on the full line shown in the figure.

Table B3.2 Predicted and measured critical and instability crack depths corresponding to the maximum load (ductile failure)

Specimen Number	Critical depth, inch (mm)		Instability depth, inch (mm)	
	Predicted	Measured	Predicted	Measured
1.1.A	0.147 (3.73)	0.145 (3.68)	0.160 (4.06)	0.153 (3.89)
1.1.B	0.274 (6.96)	0.272 (6.91)	0.289 (7.34)	0.292 (7.42)
1.1.C	0.359 (9.12)	0.370 (9.40)	0.367 (9.32)	0.384 (9.75)
1.2.A	0.087 (2.21)	0.087 (2.21)	0.092 (2.34)	0.091 (2.31)
1.2.B	0.154 (3.91)	0.153 (3.89)	0.157 (3.99)	0.160 (4.06)
1.2.C	0.195 (4.95)	0.198 (5.03)	0.196 (4.98)	0.200 (5.08)
3.1.B	0.275 (6.99)	0.277 (7.04)	0.291 (7.89)	0.304 (7.72)
3.2.B	0.154 (3.91)	0.153 (3.89)	0.156 (3.96)	0.165 (4.19)

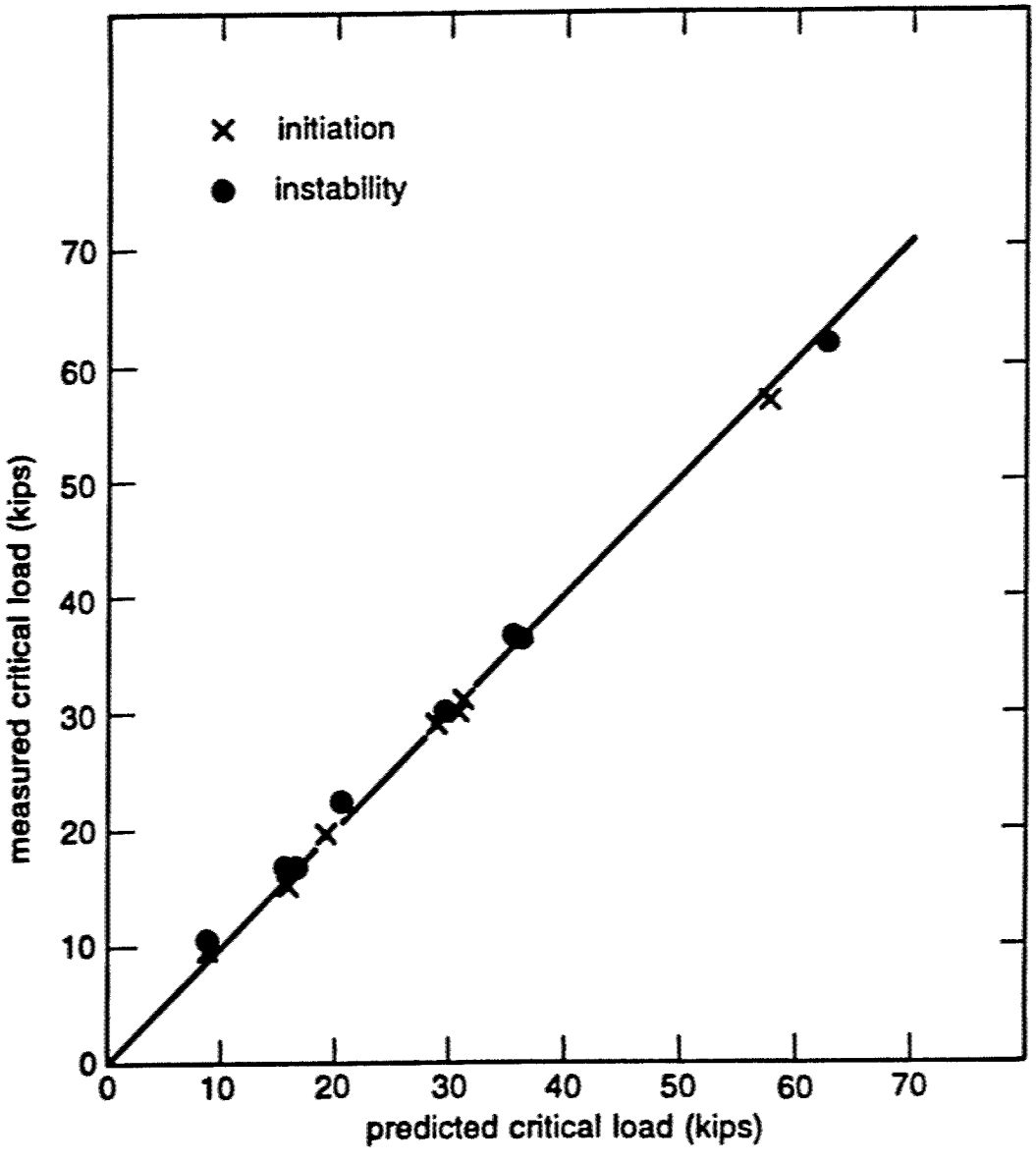

Figure B3.5 Comparison of measured and predicted critical loads for IN-718 RSECP specimens. (1 kip = 4.448 kN)

B3.2 Critical Crack Sizes

The critical crack sizes in the RSECP specimens corresponding to the measured loads at initiation and instability have been calculated using the IN-718 material specific J estimation scheme [equation (B3.2)] by solving the following equation for c_{init}

$$J(c_{init} + \Delta c_b, P_{init}) = J_{mat} = J_R(\Delta c_b) \tag{B3.6}$$

and the following simultaneous equations for c_{inst} and Δc_{inst}

$$J(c_{inst}, P_{inst}) = J_R(\Delta c_{inst}) \tag{B3.7}$$

$$\frac{dJ(c = c_{inst}, P_{inst})}{dc} = \frac{J_R(\Delta c_t = \Delta c_{inst})}{d(\Delta c_t)} \tag{B3.8}$$

where $c_{inst}=c_{crit}+\Delta c_{inst}$. In the calculations the J_R-curves specific to each specimen were used.

The predicted crack depths corresponding to initiation (which would be the critical crack sizes if the IN-718 material had behaved in a brittle manner and had not displayed J_R-curve behavior) are displayed in Table B3.3 together with the measured values (equal to the crack depths at the start of the J_R tests). There is excellent agreement between predicted and measured values. The predicted critical and instability crack depths can be compared with the experimentally measured values in Table B3.4. Again, there is very good agreement between predicted and measured values. This agreement is confirmed in Figure B3.6, which shows the experimentally measured crack depths at initiation and instability plotted against the predicted values. All the points fall very close to the full line which indicates exact agreement.

B3.3 Analysis Using FADs

The assessment point corresponding to the measured initiation of ductile tearing was plotted on the IN-718 material specific FAD given by equation (B2.42) for each tested RSECP specimen using the equations

$$L_r = \frac{P_{init}}{P_y(c_{init} + \Delta c_b)}, \quad K_r = \frac{K(c_{init} + \Delta c_b, P_{init})}{K_{mat}} \tag{B3.9}$$

Table B3.3 Predicted and measured critical crack depths corresponding to the load at initiation (or brittle failure)

Specimen Number	Critical Depth, inch (mm)	
	Predicted	Measured
1.1.A	0.151 (3.84)	0.145 (3.68)
1.1.B	0.279 (7.09)	0.272 (6.91)
1.1.C	0.368 (9.35)	0.370 (9.40)
1.2.A	0.087 (2.21)	0.087 (2.21)
1.2.B	0.157 (3.99)	0.153 (3.89)
1.2.C	0.196 (4.98)	0.198 (5.03)
3.1.B	0.279 (7.09)	0.277 (7.04)
3.2.B	0.153 (3.89)	0.153 (3.89)

Table B3.4 Predicted and measured loads at initiation (or brittle failure) and ductile instability (maximum load)

Specimen Number	Initiation Load, kips (kN)		Instability Load, kips (kN)		Tear Length, ins, (mm)	
	Predicted	Measured	Predicted	Measured	Predicted	Measured
1.1.A	57.5 (255.8)	56.8 (252.7)	62.8 (279.4)	61.9 (275.4)	0.016 (0.406)	0.008 (0.203)
1.1.B	30.6 (136.1)	30.1 (133.9)	36.4 (161.9)	36.3 (161.5)	0.017 (0.432)	0.020 (0.508)
1.1.C	19.0 (84.52)	19.7 (87.63)	20.4 (90.75)	22.5 (100.1)	0.010 (0.254)	0.014 (0.356)
1.2.A	28.7 (127.7)	29.1 (129.4)	29.6 (131.7)	30.1 (133.9)	0.007 (0.178)	0.004 (0.102)
1.2.B	16.6 (73.84)	16.3 (72.51)	16.8 (74.73)	17.1 (76.07)	0.006 (0.152)	0.008 (0.203)
1.2.C	9.0 (40.04)	9.9 (44.04)	9.0 (40.04)	10.1 (44.93)	0.004 (0.102)	0.002 (0.051)
3.1.B	31.1 (138.3)	31.2 (138.8)	35.9 (159.7)	36.6 (162.8)	0.017 (0.432)	0.027 (0.686)
3.2.B	15.9 (70.73)	15.2 (67.62)	16.1 (71.62)	16.3 (72.51)	0.005 (0.127)	0.012 (0.305)

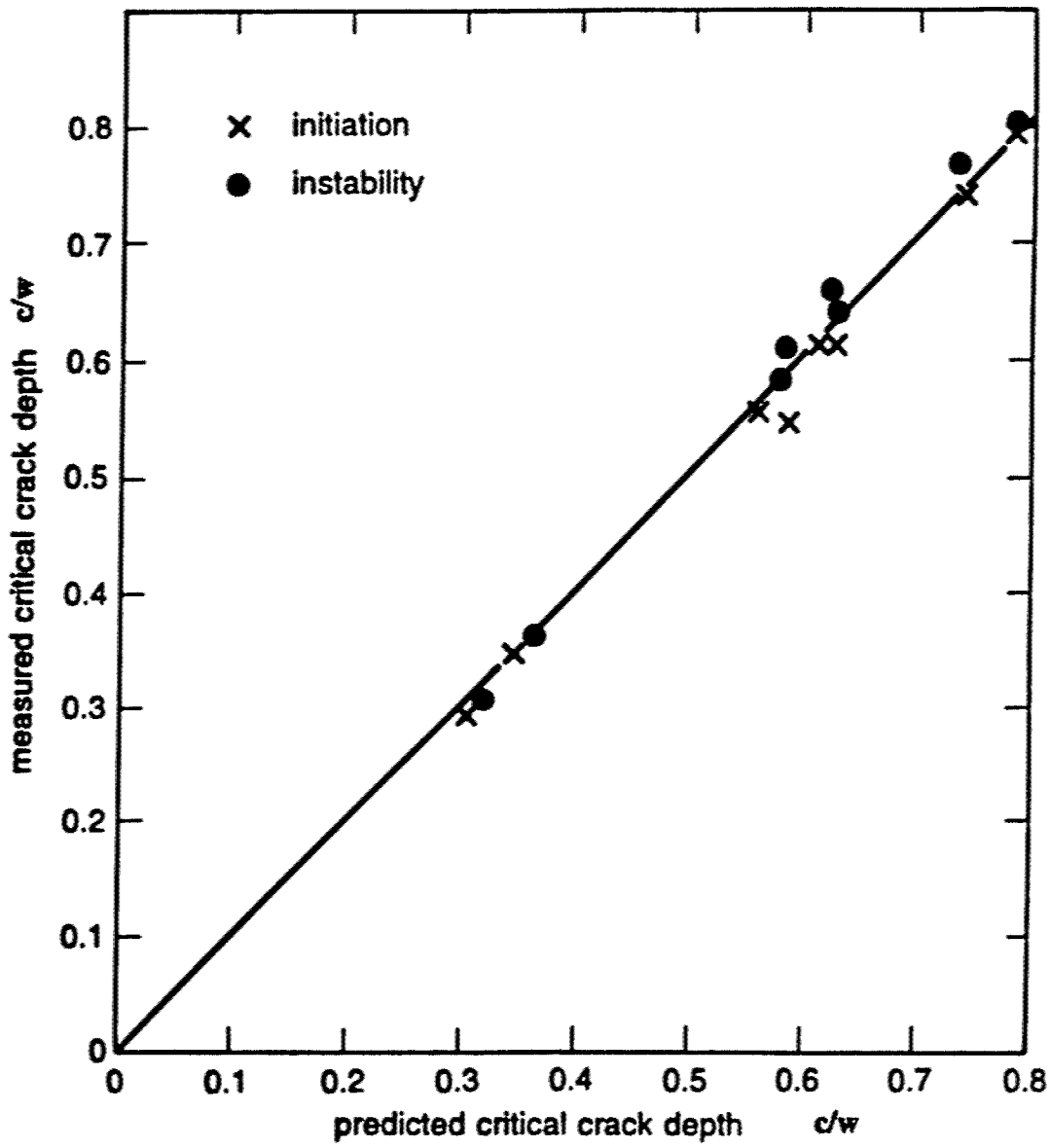

Figure B3.6 Comparison of measured and predicted normalized critical crack depths for IN-718 RSECP specimens.

Similarly, the constant load locus for each specimen evaluated at the measured instability (maximum) load was plotted using the equations

$$L_r = \frac{P_{inst}}{P_y(c_{crit}+\Delta_t)} \quad , \quad K_r = \frac{K(c_{crit}+\Delta c_t, P_{inst})}{\sqrt{E' J_R(\Delta c_t)}} \tag{B3.10}$$

The results are shown in Figures B3.7 to B3.14, where the open circles represent the constant load locus, and the assessment points at initiation and instability are indicated by full circles. If the FAD approach was exact, the experimental assessment points at initiation and instability should fall on the failure curve, and the constant load locus would be tangential to the curve. As can be seen from Figures B3.7 to B3.14, this requirement is nearly met for all the specimens tested. This is not surprising because the FAD is a pictorial representation of the J analyses described in Sections B3.1 and B3.2 and will produce predicted fracture results of equal accuracy.

Validation of the FAD approach is summarized in Figure B3.15 which shows all the experimental assessment points corresponding to initiation and instability plotted on a single FAD. The FAD approach would be exact if the points fell on the failure curve. This figure clearly displays the great advantage of the material specific FAD as a means of clearly representing the results of fracture analyses performed for the same material but for different cracked geometries.

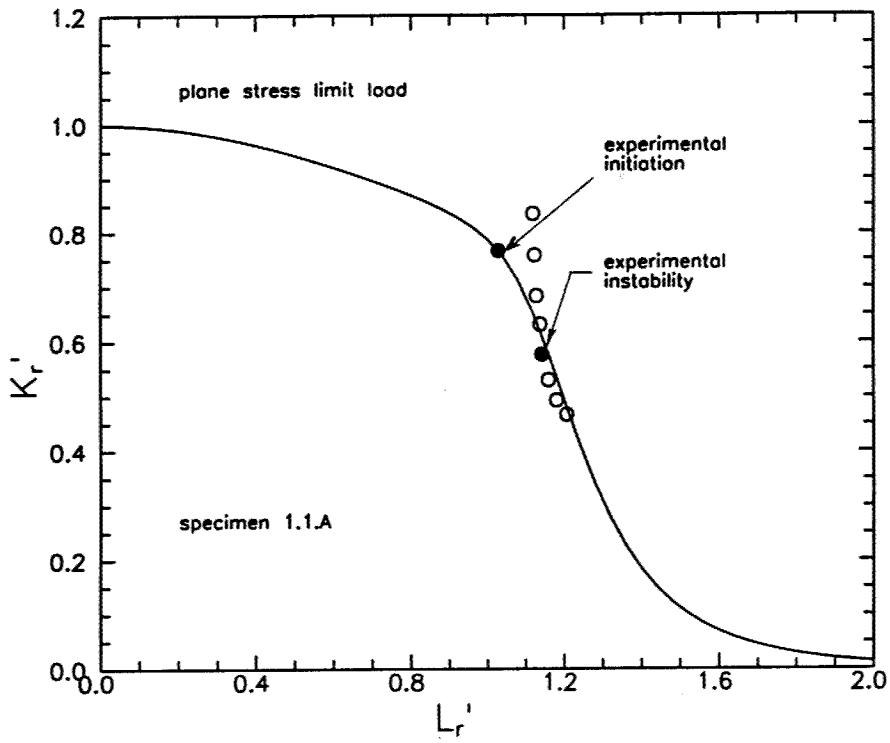

Figure B3.7 Comparison of derived experimental assessment points at initiation and ductile instability (full symbols) with the theoretical failure curve for specimen 1.1.A. The open symbols represent the experimental constant load locus evaluated at the maximum (instability) load.

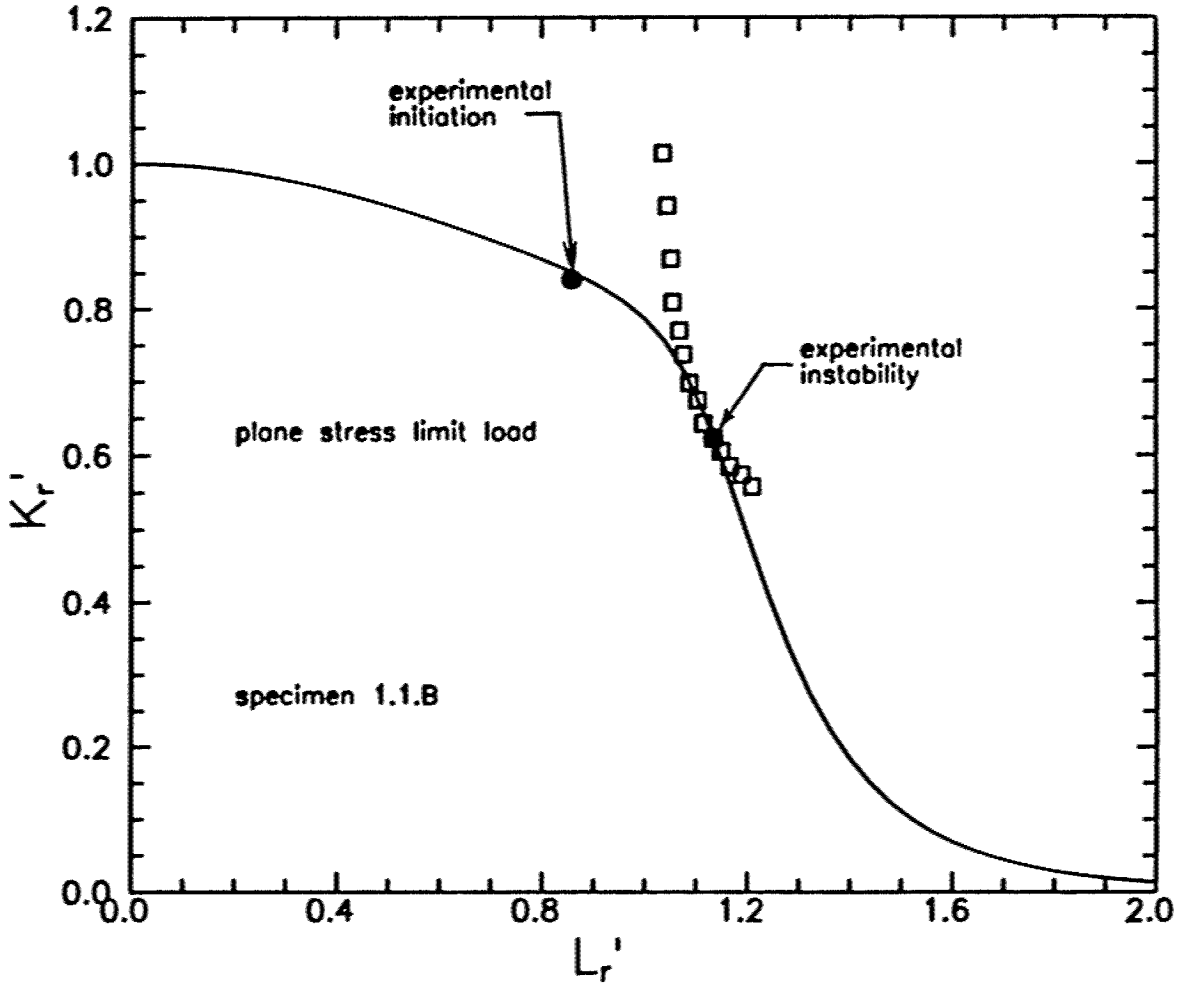

Figure B3.8 Comparison of derived experimental assessment points at initiation and ductile instability (full symbols) with the theoretical failure curve for specimen 1.1.B. The open symbols represent the experimental constant load locus evaluated at the maximum (instability) load.

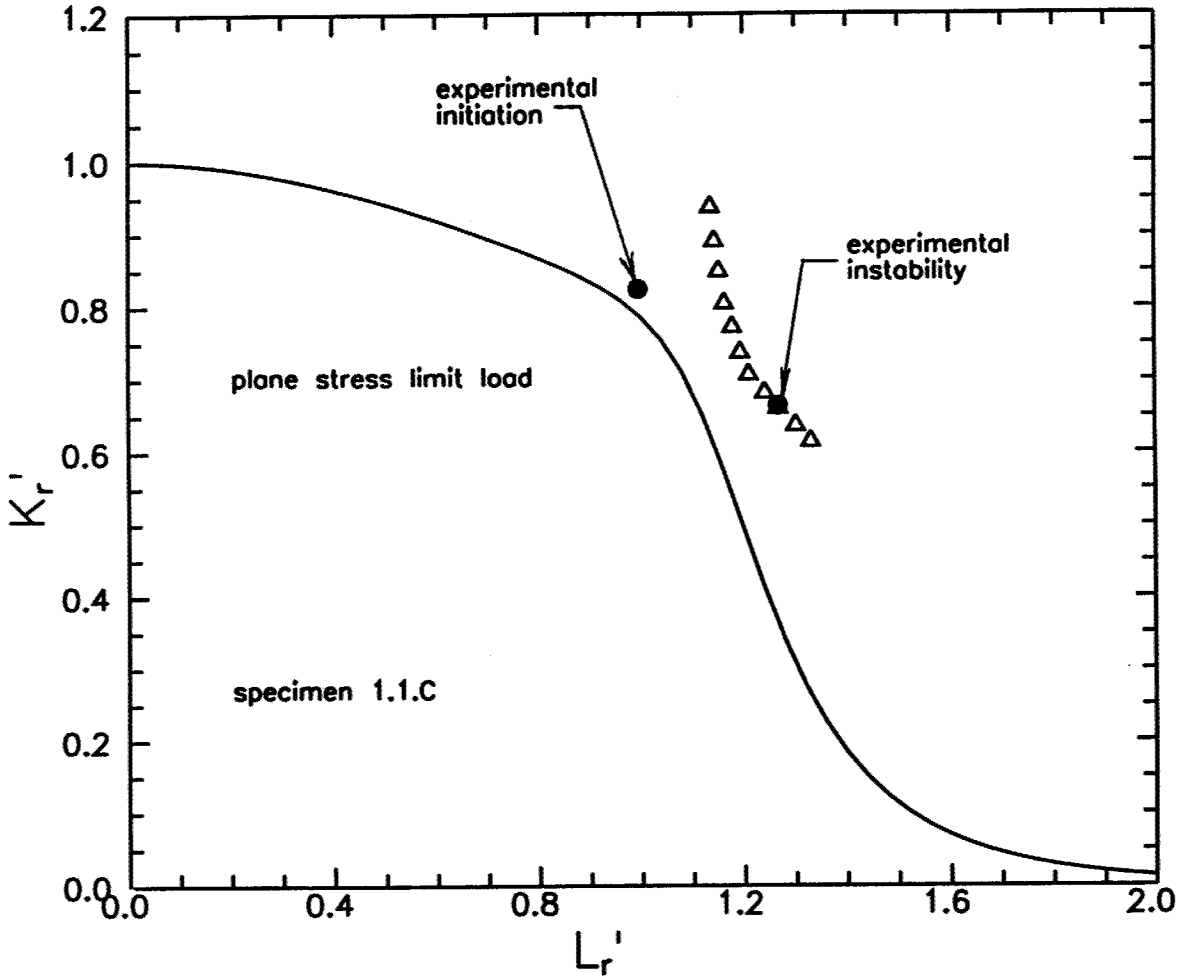

Figure B3.9 Comparison of derived experimental assessment points at initiation and ductile instability (full symbols) with the theoretical failure curve for specimen 1.1.C. The open symbols represent the experimental constant load locus evaluated at the maximum (instability) load.

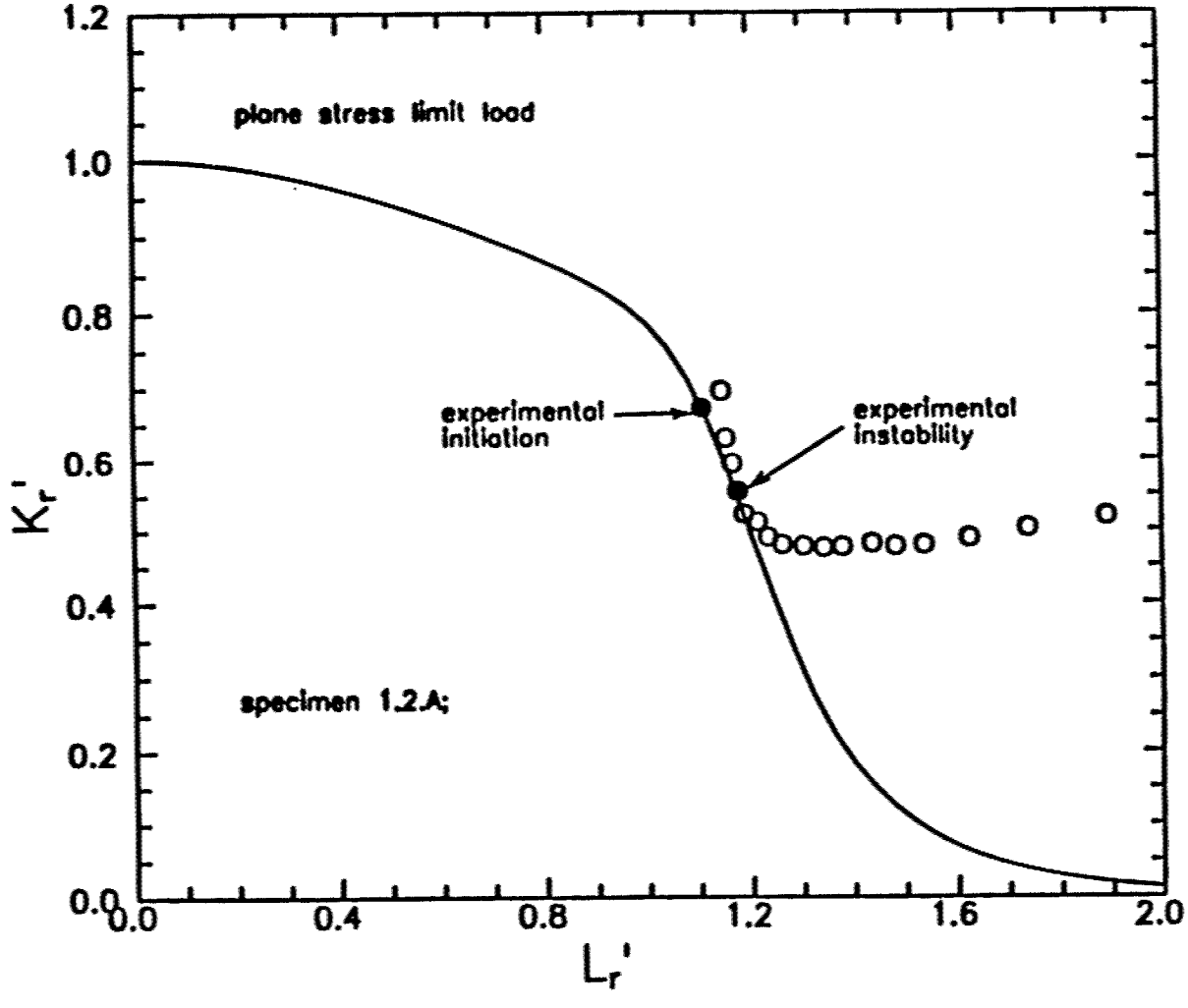

Figure B3.10 Comparison of derived experimental assessment points at initiation and ductile instability (full symbols) with the theoretical failure curve for specimen 1.2.A. The open symbols represent the experimental constant load locus evaluated at the maximum (instability) load.

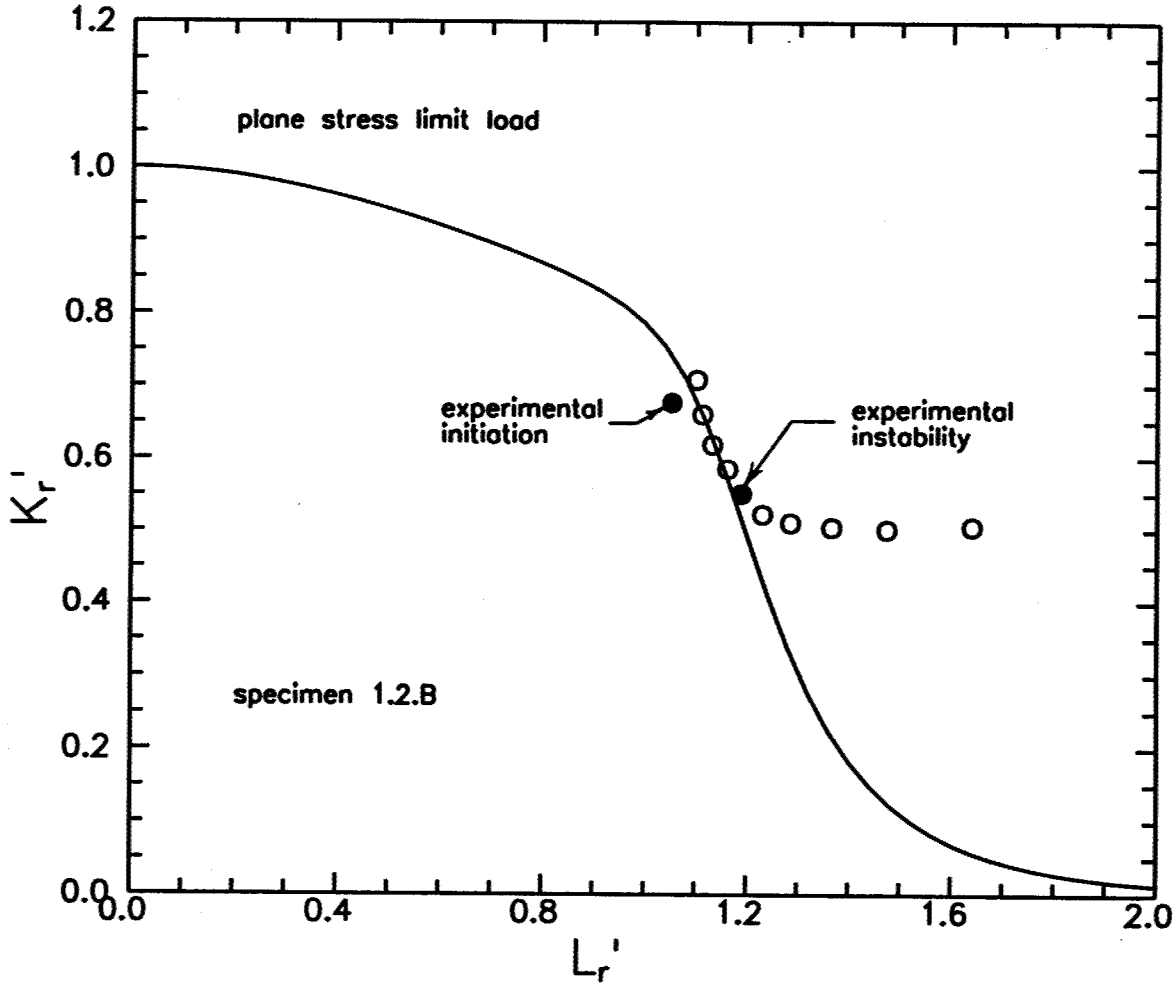

Figure B3.11 Comparison of derived experimental assessment points at initiation and ductile instability (full symbols) with the theoretical failure curve for specimen 1.2.B. The open symbols represent the experimental constant load locus evaluated at the maximum (instability) load.

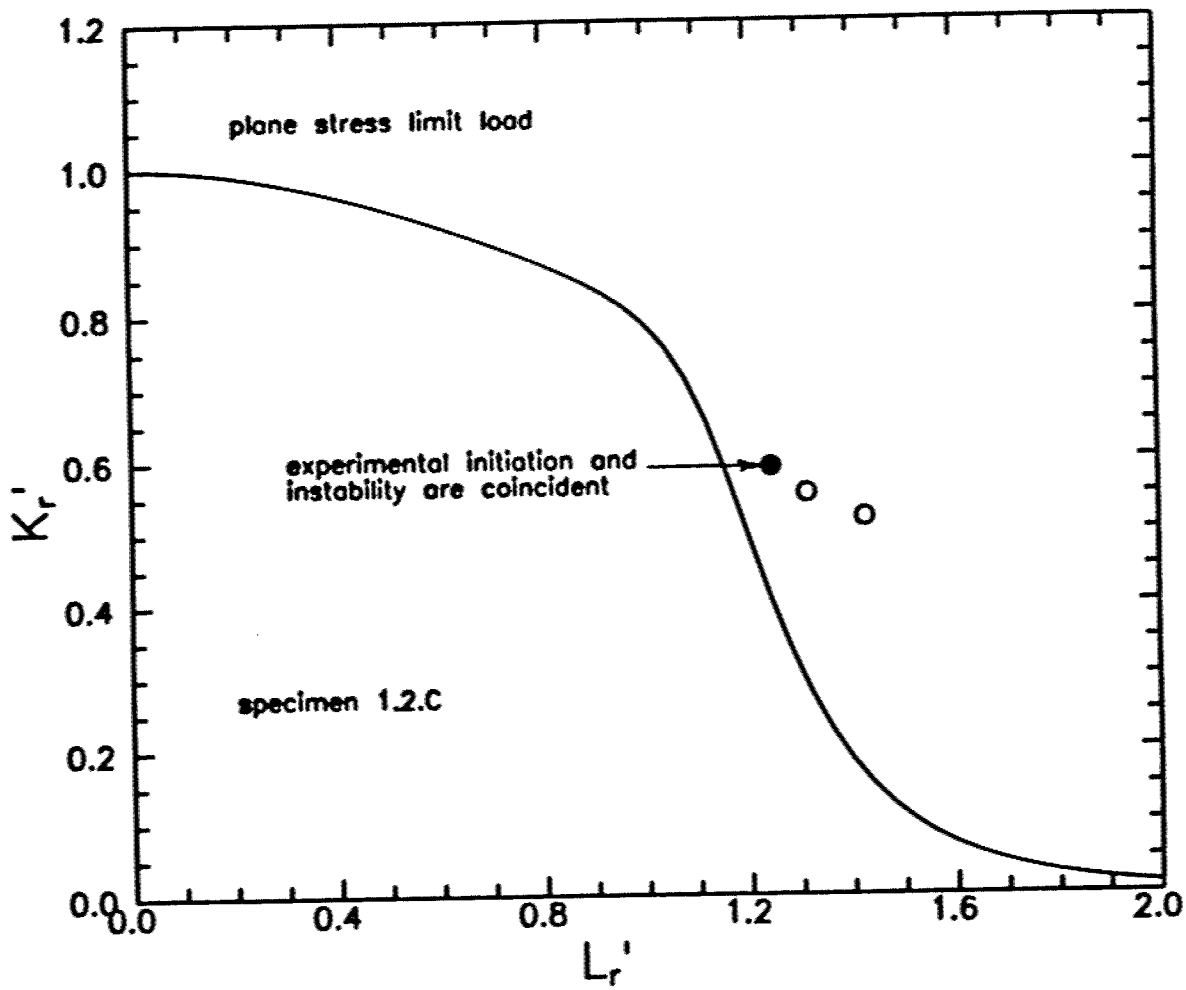

Figure B3.12 Comparison of derived experimental assessment points at initiation and ductile instability (full symbols) with the theoretical failure curve for specimen 1.2.C. The open symbols represent the experimental constant load locus evaluated at the maximum (instability) load.

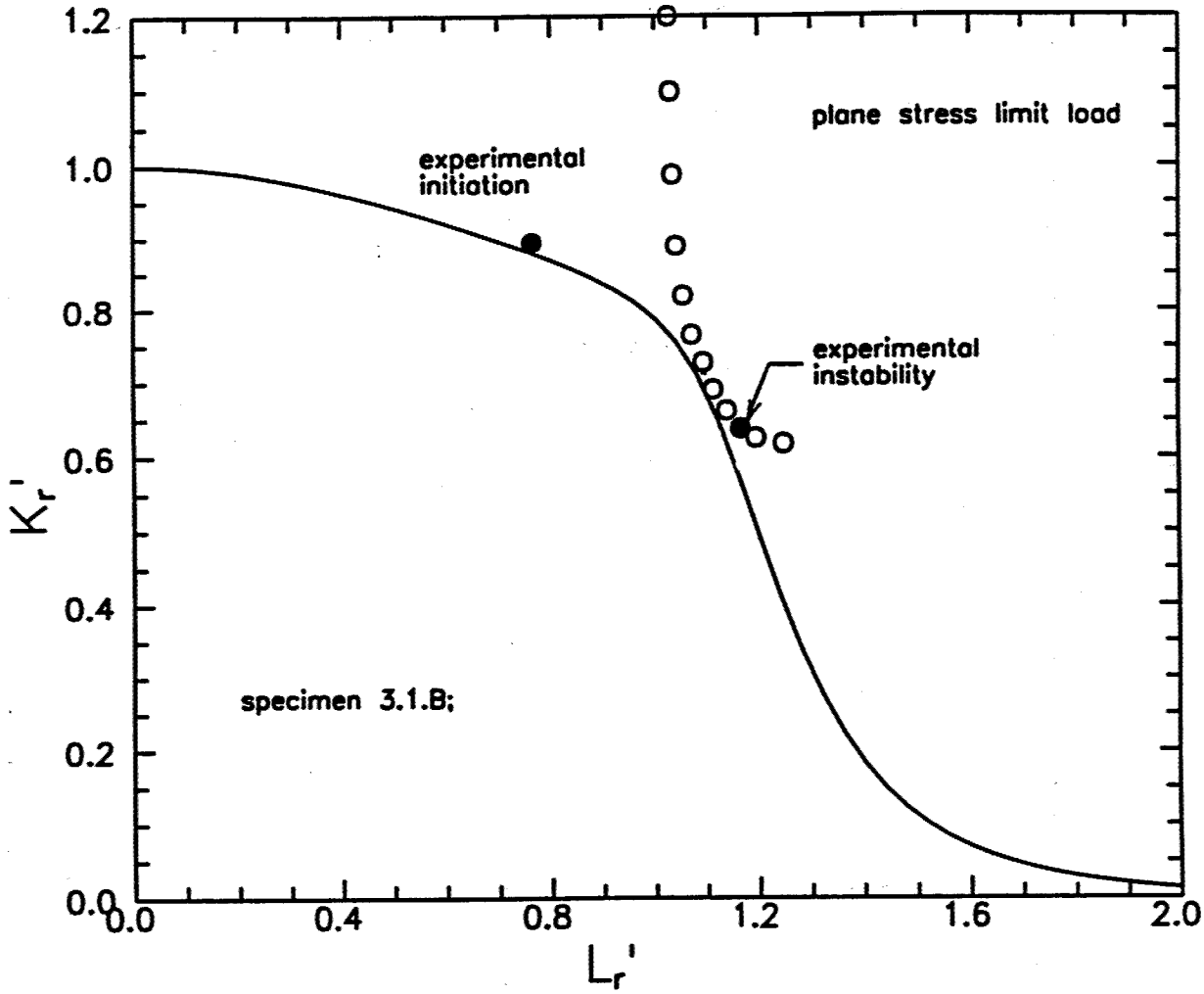

Figure B3.13 Comparison of derived experimental assessment points at initiation and ductile instability (full symbols) with the theoretical failure curve for specimen 3.1.B. The open symbols represent the experimental constant load locus evaluated at the maximum (instability) load.

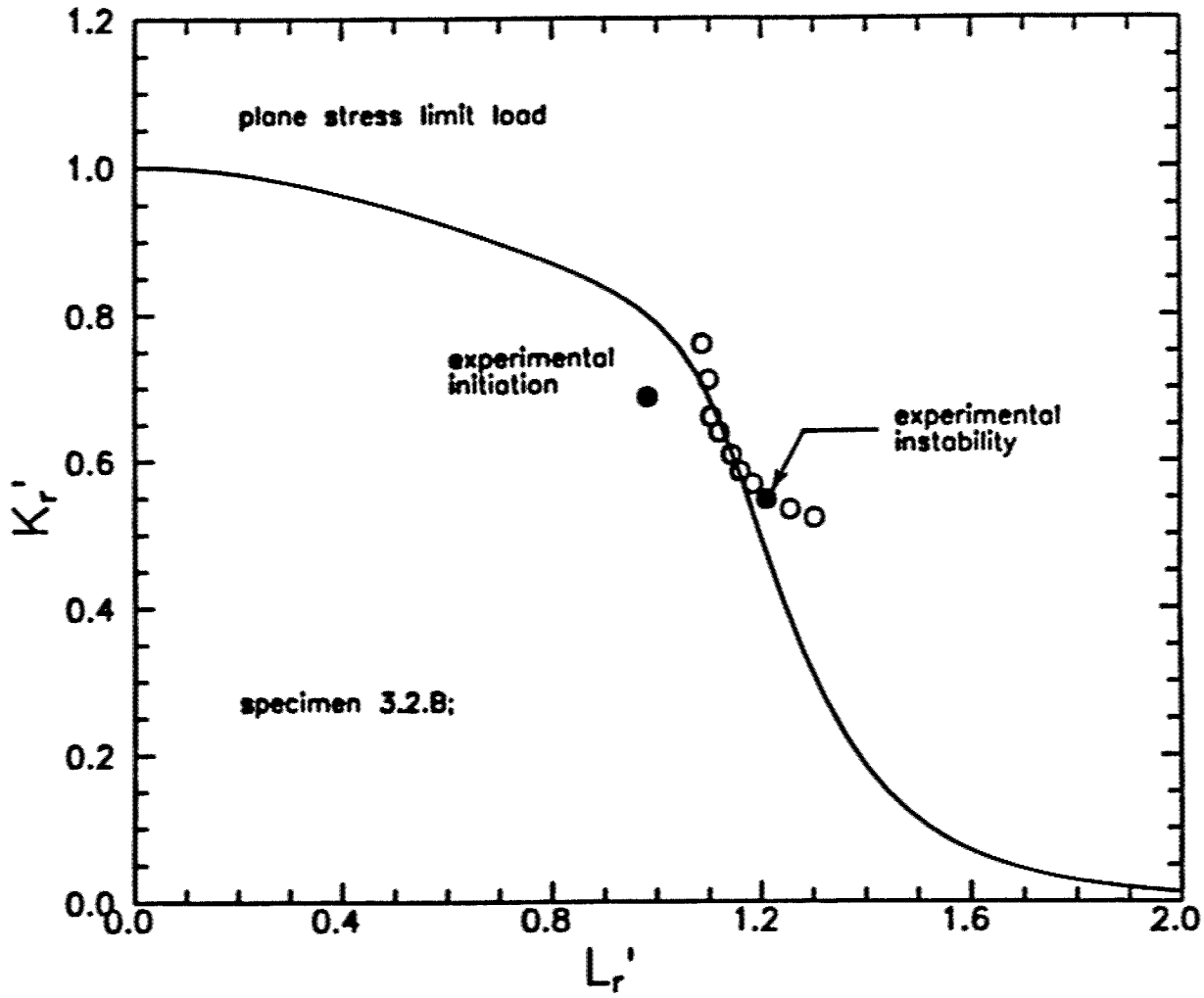

Figure B3.14 Comparison of derived experimental assessment points at initiation and ductile instability (full symbols) with the theoretical failure curve for specimen 3.2.B. The open symbols represent the experimental constant load locus evaluated at the maximum (instability) load.

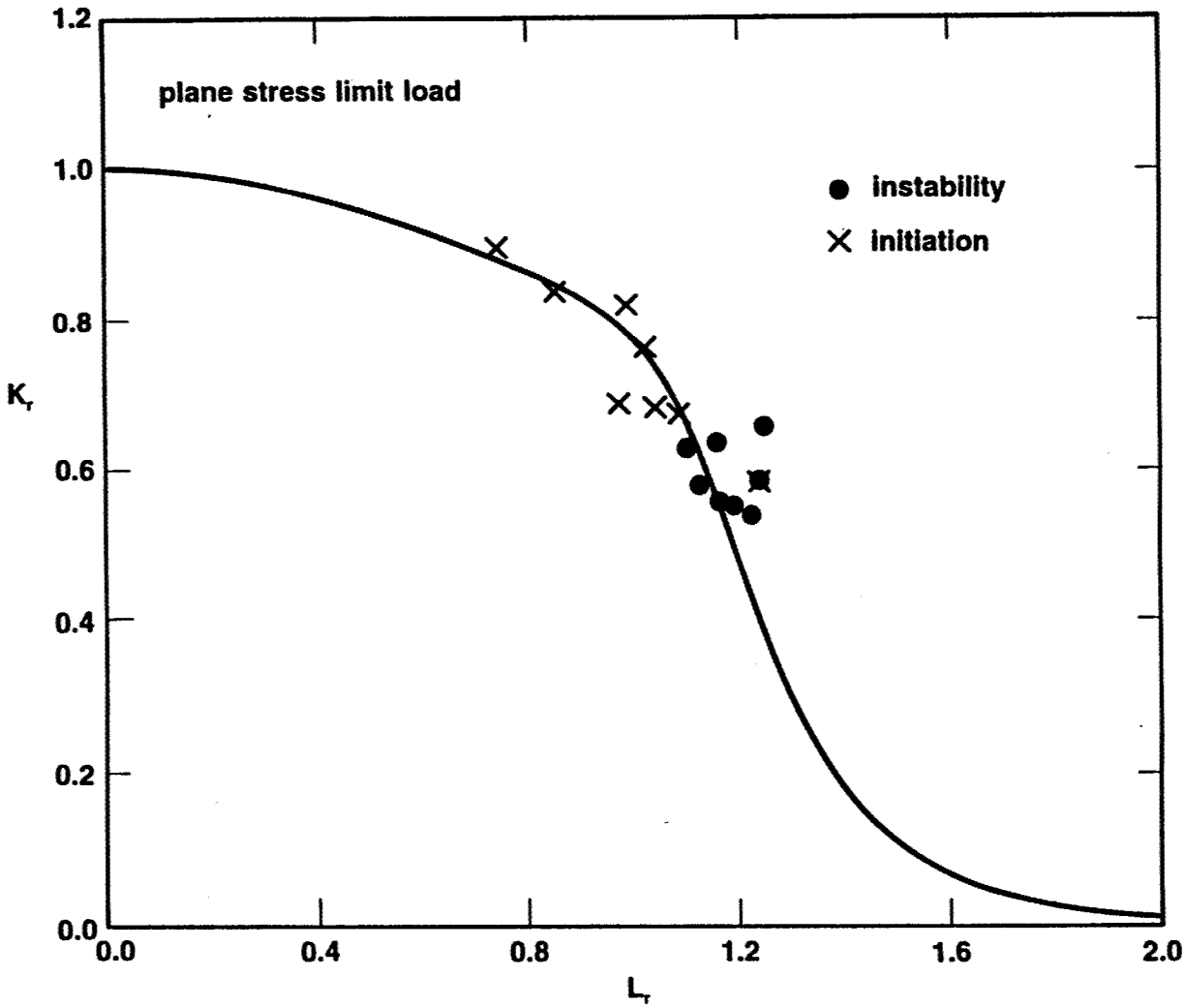

Figure B3.15 Summary of predicted values of assessment points for all the tested IN-718 RSECP specimens at ductile crack initiation and instability compared to the theoretical material specific failure curve for IN-718.

B4. HARDWARE VALIDATION: PREDICTING CRITICAL CRACK SIZES AND CRITICAL LOADS FOR IN-718

B4.1 Overview of Hardware Tests

To validate the proof test analysis methodology, hardware tests were performed at Rocketdyne's proof test facilities in Canoga Park, California, on three pre-flawed retired SSME high pressure oxidizer ducts made from the nickel-based superalloy IN-718 that were pressurized to failure. The results of these tests were later analyzed at SwRI. The ducts were chosen for testing because of their availability, and because they were made of a ductile material and had thin walls typical of many pressurized aerospace engine components. A photograph of one of the ducts prior to testing is shown in Figure B4.1. The ducts were approximately 30 inches (762 mm) in length and contained curved and straight sections of various wall thicknesses. Conveniently, a straight section of the duct that was approximately 2 inches (50.8 mm) in length also coincided with the minimum wall thickness which, according to design drawings, was 0.114 inch (2.90 mm) thick with an internal diameter of 4 inches (101.6 mm) (see Figure B4.2). It was prudent to introduce flaws in a section of the pipe that had a minimum thickness in order to avoid possible failure of the duct at an unflawed location during testing.

Four axial flaws were machined and then sharpened by fatigue precracking on the outside surface of the straight section of each of the ducts. The fatigue loading was accomplished by cycling the internal pressure. Figure B4.3 shows one of the EDM flaws. The four externally machined axially oriented surface flaws had different depths and surface lengths and were spaced at 90° intervals around the circumference of the ducts to reduce interaction effects, the location of the cracks being signified as T (top), R (right), B (bottom) and L (left). The three ducts (labelled Duct 1, 2 and 3) were pressurized to failure at ambient temperature and the failure pressures recorded. In all cases, the failures exhibited burst rather than leak-before-burst behavior and the fracture originated from the flaw at the R location. The failures were sufficiently violent to have propagated the R cracks several inches along the axis of the duct before arrest occurred due to de-pressurization and/or the crack running into thicker section material or a bend (Figure B4.4).

After the tests were completed, the sections containing the cracks were cut-up and the parts containing the non-propagating cracks fractured so that crack sizes could be measured and fracture surfaces inspected. The local thicknesses of the duct walls in the regions of each flaw were also measured, as pre-test ultrasonic and other NDT methods had indicated a circumferential and longitudinal variation in the wall thickness. The observed dimensions of the wall thicknesses and crack sizes at each flaw location are shown in Table B4.1. The wall thicknesses differed significantly from the minimum specified values given in the design drawings (Figure B4.2).

Fractographic investigations of the cracks at Rocketdyne using optical and SEM techniques showed that fatigue crack extension had occurred at the EDM notches at the deepest points during fatigue precracking (Figure B4.5), and there was no discernible extension at the surface locations. The fracture appearance of the R cracks beyond the fatigue precracking zones showed ductile dimpled zones of varying depth, characteristic of stretch zones (crack tip blunting). Beyond this, the fracture surfaces showed no visible features to delineate stable tearing from the onset of ductile instability (Figure B4.6).

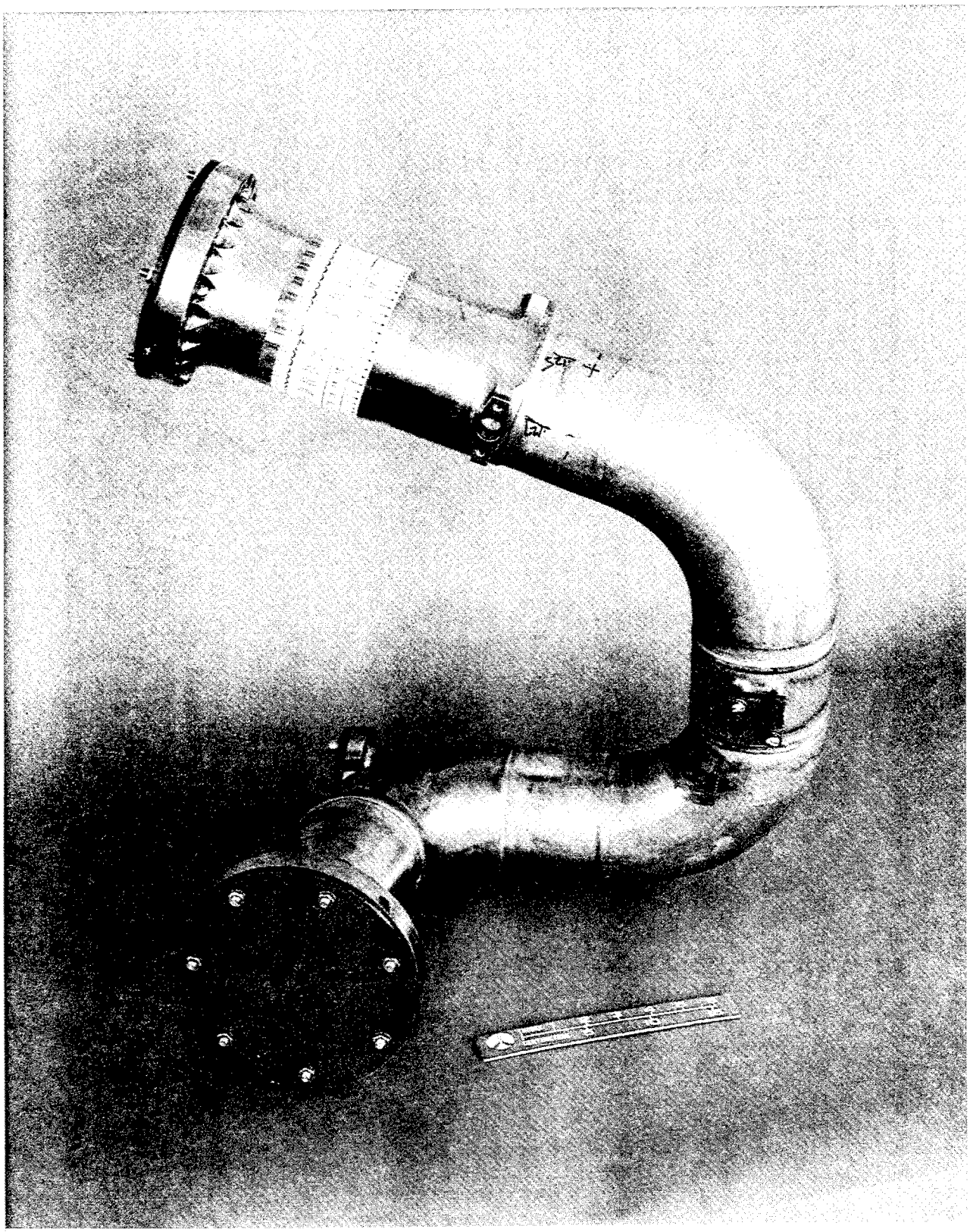

Figure B4.1 Photograph of one of the tested ducts.

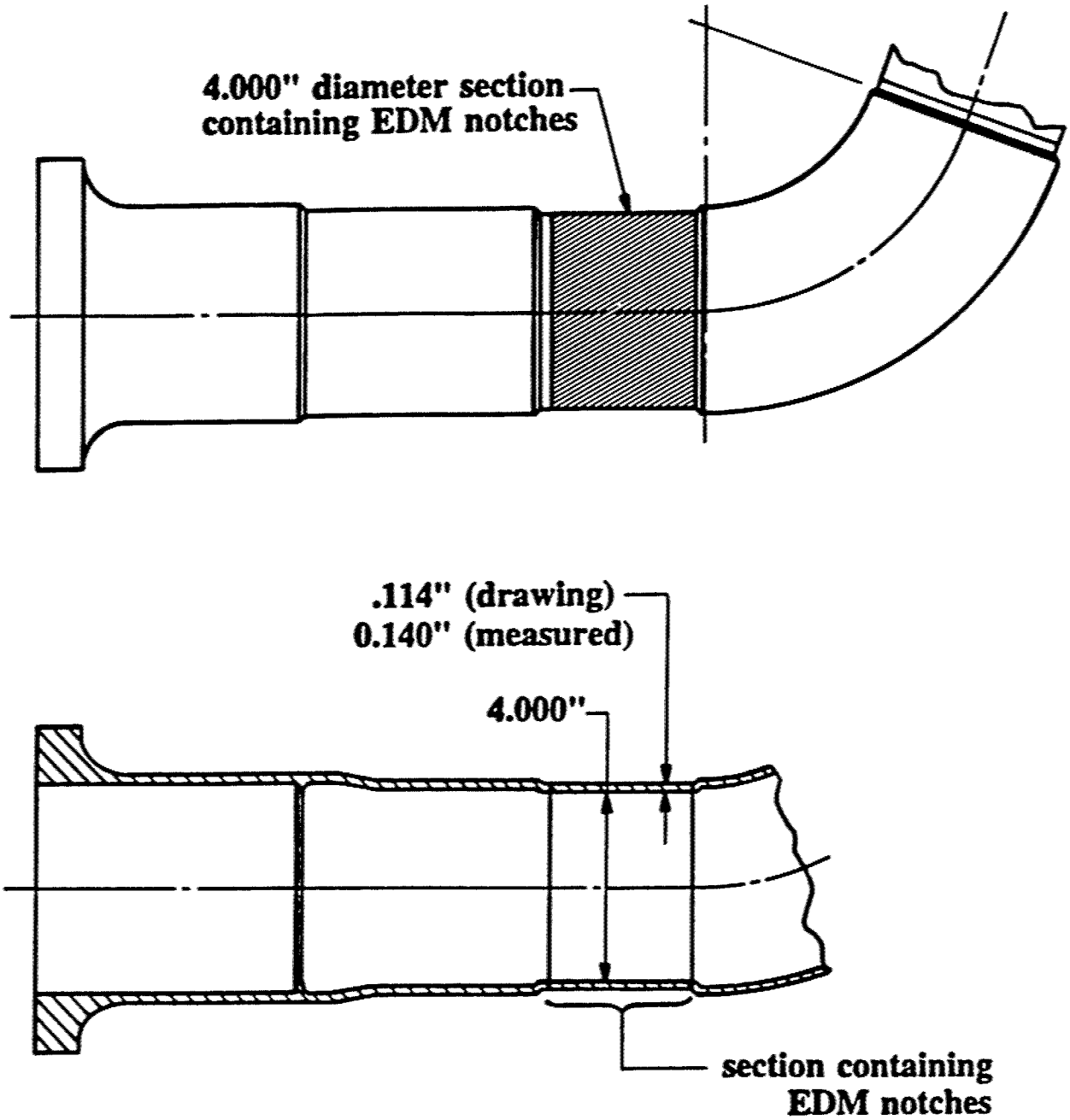

Figure B4.2 Schematic of part of the first SSME duct tested at Rocketdyne showing the straight section where the EDM notches were machined. Four axial notches were introduced in the middle of the section at 90° intervals around the circumference.

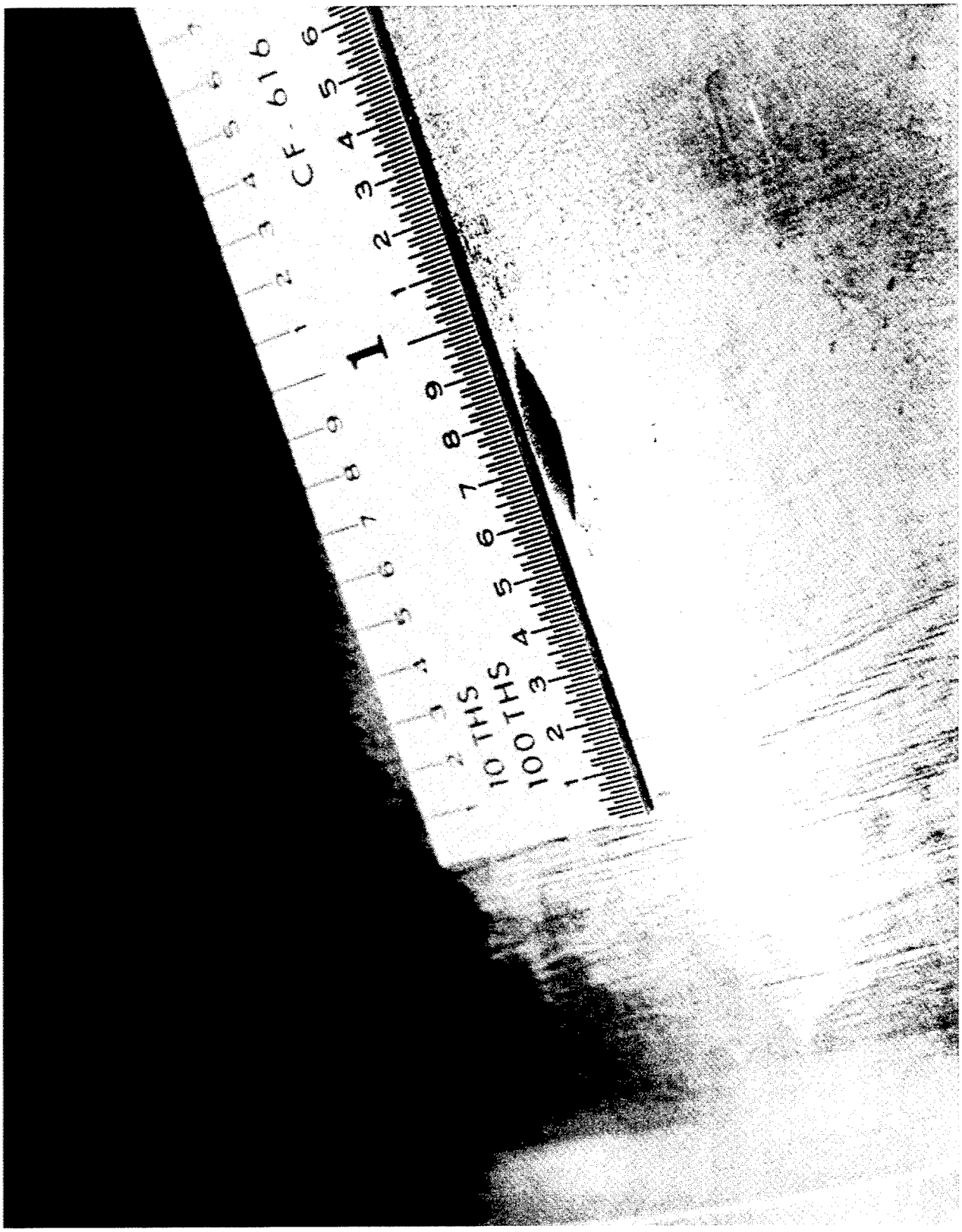

Figure B4.3 Photograph of one of the EDM notches.

Figure B4.4 All three ducts failed in a burst mode similar to the example shown here.

Table B4.1 Local wall thicknesses and dimensions of cracks after pre-fatigue cracking

Duct 1			
Flaw Position	**Local Wall Thickness, inch (mm)**	**Crack depth, *a* inch (mm)**	**Crack Surface Length, 2c inch (mm)**
Top (T)	0.139 (3.53)	0.1000 (2.54)	0.356 (9.04)
Right (R)	0.140 (3.56)	0.0965 (2.45)	0.658 (16.71)
Bottom (B)	0.141 (3.58)	0.1015 (2.58)	0.446 (11.33)
Left (L)	0.147 (3.73)	0.0740 (1.88)	0.517 (13.13)
Duct 2			
Flaw Position	**Local Wall Thickness, inch (mm)**	**Crack depth, *a* inch (mm)**	**Crack Surface Length, 2c inch (mm)**
Top (T)	0.139 (3.53)	0.0948 (2.41)	0.802 (20.37)
Right (R)	0.140 (3.56)	0.0928 (2.36)	1.053 (26.75)
Bottom (B)	0.140 (3.56)	0.0892 (2.27)	0.919 (23.34)
Left (L)	0.1476 (3.75)	0.0845 (2.15)	1.191 (30.25)
Duct 3			
Flaw Position	**Local Wall Thickness, inch (mm)**	**Crack depth, *a* inch (mm)**	**Crack Surface Length, 2c inch (mm)**
Top (T)	0.136 (3.45)	0.0743 (1.89)	1.623 (41.22)
Right (R)	0.133 (3.38)	0.0852 (2.16)	1.231 (31.27)
Bottom (B)	0.131 (3.33)	0.0767 (1.95)	1.000 (25.4)
Left (L)	0.140 (3.56)	0.0793 (2.01)	1.406 (35.7)

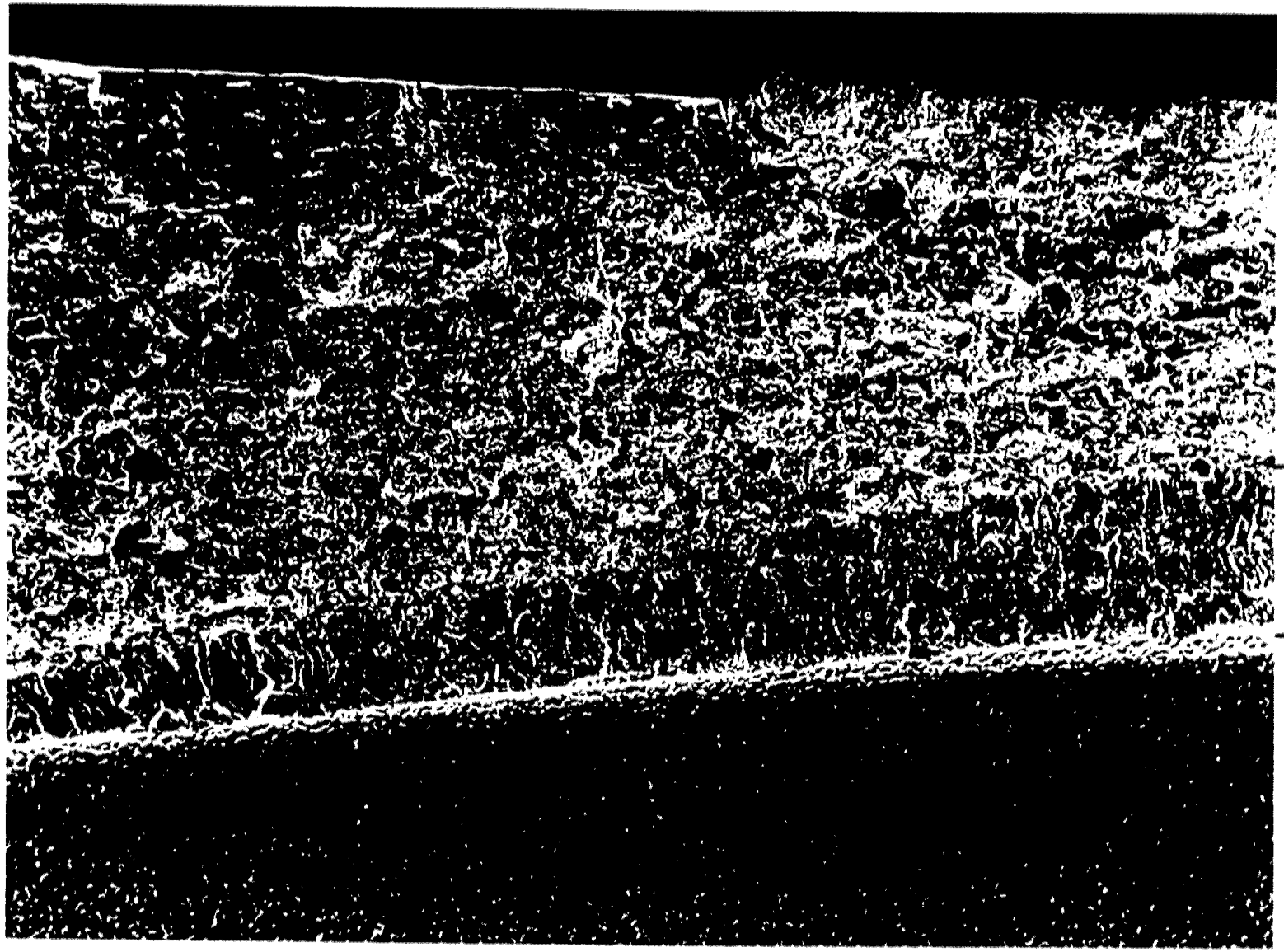

Figure B4.5 Photograph of one of the fractured halves of the crack at location R which resulted in failure showing the EDM notch, the fatigue crack, and the region of fast ductile failure.

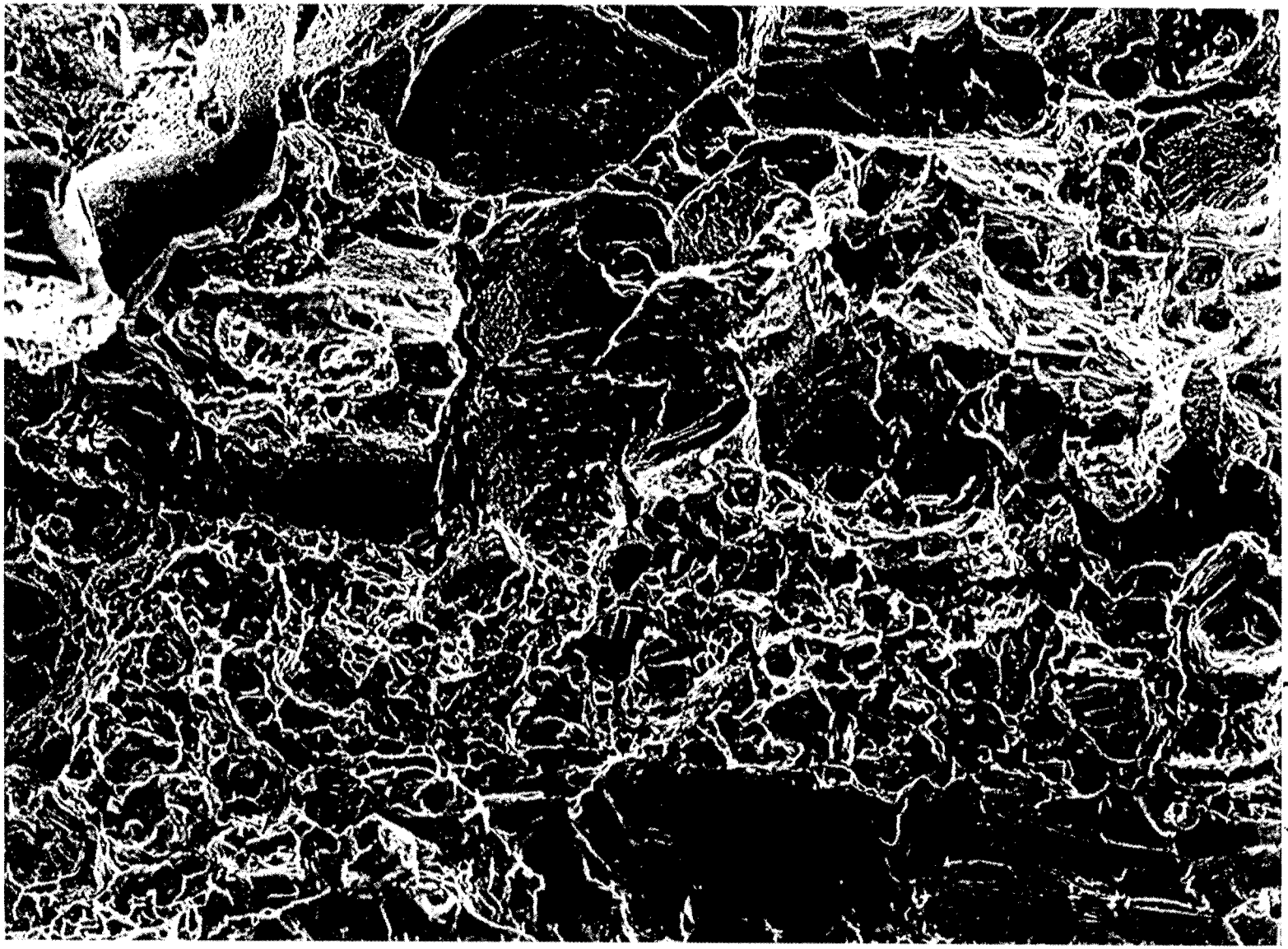

Figure B4.6 Micrograph of the crack at location R showing the stretch zone beyond the fatigue crack, and the ductile failure region beyond the stretch zone.

B4.2 Assessment Data for *J* Estimation and Material Specific Failure Assessment Diagram

The flaws introduced into the ducts were surface flaws with two DOF. As mentioned, the surface flaws showed no indication of fatigue crack propagation at the surface and hence the two DOF cracks were reduced to one DOF cracks for analysis purposes by assuming that tearing occurred only at the deepest points on the flaws and performing the assessment with respect to these. Since the tests involved internal pressurization, the appropriate expression for J is given by equation (6) of Table A.4.5. In the present case, because the flaws originated from smooth surfaces and were subjected only to a primary load, J and the FAD failure curve were evaluated using the material specific approximation for a Ramberg-Osgood material [equation (8)] in Table A4.5. The expression for J at the deepest point on a surface flaw is

$$J\left(a+\Delta a_t, c, P, \theta=90^\circ\right)=J_e\left(a+\Delta a_t, c, P, \theta=90^\circ\right)\left[1+\frac{0.5\left[\dfrac{P}{P_e(a+\Delta a_t, c)}\right]^2}{1+\alpha\left[\dfrac{P}{P_e(a+\Delta a_t, c)}\right]^{n-1}}+V^*\alpha\left[\frac{P}{P_e(a+\Delta a_t, c)}\right]^{n-1}\right] \quad \text{(B4.1)}$$

where Δa_t is the amount of ductile tearing at the instantaneous load, P. The failure curve corresponding to equation (B4.1) is given by

$$K_r^* = \left[1+\frac{0.5\left[L_r^*\left(\dfrac{\sigma_y}{\sigma_e}\right)\right]^2}{1+\alpha\left[L_r^*\left(\dfrac{\sigma_y}{\sigma_e}\right)\right]^{n-1}}+V^*\alpha\left[L_r^*\left(\frac{\sigma_y}{\sigma_e}\right)\right]^{n-1}\right]^{-\frac{1}{2}} \quad \text{(B4.2)}$$

where

$$L_r^* = \frac{P}{P_y^*\,(a+\Delta a_t, c)} \quad \text{(B4.3)}$$

and P_y^* is the net section yield pressure evaluated using the yield stress.

The assessment data needed to perform fracture predictions for the tested flawed ducts are uniaxial stress-strain curves, *J-R* curves, stress intensity factor solutions and net section yield pressures for each of the flaws.

B4.2.1 Tensile Data

Tensile data are needed in the J estimation scheme and the FAD approach to determine the assessment parameter, L_r, and to generate a material dependent failure curve, where

$$L_r = \frac{P}{P_y^*(a,c)} \tag{B4.4}$$

and P is the internal pressure, and P_y the value of the pressure at net section yield.

In the analysis the parameter V^* was set to 1, which is approximately the mean value for wide variety of cracked structures. A more conservative, smaller value of V^* should be used in actual proof test analyses (see Table A4.2), but, for validation purposes, the mean value was considered appropriate. Ambient temperature tensile data for IN-718 were available in the form of a Ramberg-Osgood law derived from tests performed at Rocketdyne

$$\frac{\epsilon}{\epsilon_o} = \frac{\sigma}{\sigma_o} + \alpha \left[\frac{\sigma}{\sigma_o}\right]^n \tag{B4.5}$$

where ϵ is the strain corresponding to the stress, σ, σ_o is a characteristic yield stress, $\epsilon_o = \sigma_o/E$, α is a constant, and E is Young's modulus. For IN-718, σ_o=179.8 ksi (1240 MPa), α=1, n=15.8, and E=30,000 ksi (207,000 MPa). The yield stress is 161.2 ksi (1111 MPa), and the ultimate strength is 205.5 ksi (1417 MPa).

B4.2.2 J-R Curves

Toughness data in the form of J-R curves are necessary in order to calculate ductile crack growth behavior and to evaluate the FAD parameter, K_r, where

$$K_r = \frac{K}{\sqrt{(E' J_R(\Delta a_t))}} \tag{B4.6}$$

and K is the applied stress intensity factor (SIF) and $J_R(\Delta a_t)$ is the toughness for tear length Δa_t

Plastic constraint is known to influence measured ductile toughness values, with cracked geometries of low constraint displaying higher toughness values than geometries with high constraint. A conservative proof test analysis necessitates the use of toughness data that have a constraint either equal to or less than the constraint likely to be experienced in the tested hardware. To overcome this, J-R curves were measured at SwRI on specimens designed to simulate the constraint likely to be experienced in the flawed ducts. Tests were performed on restrained edge cracked plate specimens of widths equal to 0.5 inch (12.7 mm) and 0.25 inch (6.35 mm) and nominal thicknesses equal to 1 inch (25.4 mm), subjected to tensile loading, following similar procedures to those described in ASTM Test Standard E1152 for more conventional testing configurations. Details of the tests and

analysis employed are given in Sections B2.2 and B2.3. The restraint used eliminated the bending on the uncracked ligament, resulting in a plastic yielding mechanism typical of a low constrained center cracked panel. A similar low constraint is expected for an axial crack in a pressurized cylinder.

J-R curves were measured on each RSECP specimen size for cracks with nominal depths of 30%, 50%, and 70% of the section. Although the measured J-R curves are not valid according to E1152, they represent structurally relevant data that can be used to predict the fracture behavior of the flawed ducts. The resulting curves are shown in Figure B4.7 along with the appropriate specimen numbers. (For comparison, a parametric fit to J-R curves for IN-718 previously measured by Rocketdyne on standard compact tension specimens of thicknesses 0.6 inch is also shown in Figure B4.7.) The letters A, B, and C of the specimen number signify nominal crack depths of 30%, 50%, and 70% of the section, respectively. The first numeral indicates the type of test performed (1 indicates J_R-curve testing, and 3 indicates a simulated proof test overload which was also analyzed to produce a J_R curve). The second numeral signifies the specimen width, 1 indicating 0.5 inch and 2 indicating 0.25 inch (see Section B2.3.1 for more details).

The toughness data were characterized by "upper" and "lower" J_R-curve behaviors for assessment purposes, shown as the solid curves in Figure B4.7, that were fitted by quadratic polynomials of the form

$$J_R(\Delta a_t) = J_0 + J_1 \Delta a_t + J_2 (\Delta a_t)^2 \qquad \text{(B4.7)}$$

where J_0, J_1 and J_2 are coefficients whose values are given in Table B4.2. The quadratic fit is valid for the tear range $\Delta a_{min} \leq \Delta a_t \leq \Delta a_{max}$, where the minimum and maximum tear lengths, Δa_{min} and Δa_{max}, respectively, are also defined in Table B4.2, as are the inferred lower and upper bound J_{max} values corresponding to J_R evaluated at Δa_{min} ($=\Delta a_b$, the estimated blunting at initiation of tearing).

Table B4.2 Characterization of the structurally relevant toughness of IN-718

J-R Curve Type	J_{max} ksi inch (MPa m)	J_0 ksi inch (MPa m)	J_1 ksi (MPa m/mm)	J_2 ksi/inch (MPa m/mm^2)	Δa_{min} inch (mm)	Δa_{max} inch (mm)
lower	0.492 (0.0864)	0.338 (0.0594)	65.73 (0.454)	-478.2 (-0.130)	0.0024 (0.061)	0.04 (1.016)
upper	1.088 (0.191)	0.255 (0.0448	180.5 (1.247)	-3250 (-0.884)	0.0051 (0.130)	0.03 (0.762)

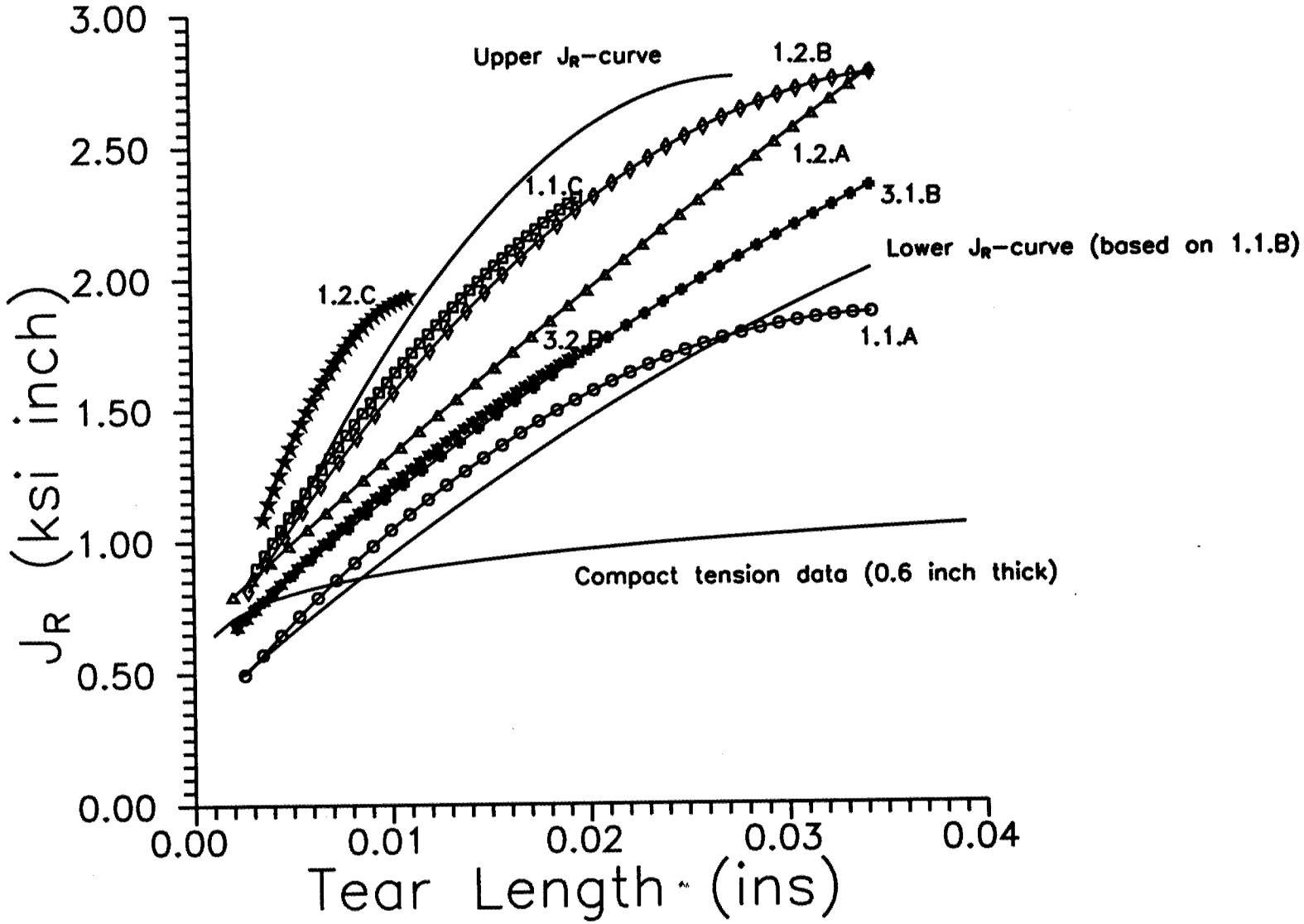

Figure B4.7 Measured J_R-curves for IN-718 showing the lower and upper J_R-curves used in the fracture analyses.

B4.2.3 Stress Intensity Factor Solutions

The stress intensity factor (SIF) is required to determine J_e and the parameter K_r. Solutions for the SIF for an axial surface flaw on the outside of a pressurized duct with a mean radius, R_m, to wall ratio, t, of 14.8 (2.07 inch/0.14 inch) was obtained using the software module, KCALC, developed and copyrighted by SwRI. (NASGRO also has K solutions for longitudinal surface flaws in hollow cylinders, geometry SC04.) The KCALC module utilizes influence functions to express the SIF in the form

$$K(a,c,\sigma(x),t,R_m,\theta) = \sigma\sqrt{\pi a}\,F\left(\frac{a}{t},\frac{a}{c},\frac{\sigma(x)}{\sigma},\frac{R_m}{t},\theta\right) \tag{B4.8}$$

where a is the flaw depth and $2c$ its surface length, $\sigma(x)$ is the local variation in stress as a function of position, x, σ is a convenient normalizing stress (e.g. $R_m P/t$, where P is the pressure), θ is an angle that locates a position on the crack front, and F is a dimensionless function, the so-called influence function.

B4.2.4 Net Section Yield Pressures

The net section yield pressure is needed to evaluate J and the parameter L_r Expressions for the pressure at net section yield are contained in the review by Miller [40]. However, these expressions turned out to significantly underestimate the pressures that were attained during the testing of the ducts. Although the use of lower net section yield pressures are conservative with respect to a service analysis, this is not the case if these values are used in a proof test analysis as they will result in an underestimate of the flaw screening capability of the proof test. This could result in hardware entering service that contains initial flaw sizes larger than those assumed to be present from the proof test analysis. Therefore, it was necessary to investigate alternative expressions for the yield pressure to try and find a more accurate value. Eventually, after reviewing the results of FAD analyses of Ducts 1 and 2, the following modified version of the formula given by Kiefner, Maxey, Eiber, and Duffey [82] was selected for use in the detailed analyses of all three ducts

$$P_y^*(a,c) = \frac{\sigma_y t}{R_m}\,\frac{\left[1-\frac{a}{t}\right]}{\left[1-\frac{a}{t}/M(\rho,a/t)\right]} \tag{B4.9}$$

where

$$M(\rho,a/t) = \left(1+1.05\frac{a}{t}\rho^2\right)^{\frac{1}{2}},\quad \rho = \frac{c}{\sqrt{R_m t}} \tag{B4.10}$$

and $2c$ is the surface length of the flaw. The term a/t appearing in the expression for $M(\rho,a/t)$ was introduced as a result of the present investigations, and suppresses the influence of crack bulging on the net section yield pressure of a surface crack compared with that for a through crack of the same

length. This equation was independently verified by using it to predict the failure pressure measured for the CEGB Pressure Vessel Test 1 reported by Milne and Knee [83] as part of validation in support of the R6 FAD procedures. This ferritic steel pressure vessel (R_m/t=6.54, t=84 mm) contained an external surface flaw (a=61 mm, c=100mm) and was pressurized to a failure (maximum) pressure of 80.45 MPa, compared to a predicted instability pressure of 79.7 MPa obtained using equation (B4.9) in a FAD analysis (see Section B5.1 for more details).

B4.3 Determination of Critical Pressures and Crack Depths

Ductile instability analyses were performed to predict the fracture behavior of the three tested ducts in order to validate the material dependent J estimation scheme and the corresponding FAD approach for use in proof test analyses of thin section ductile materials. Two sets of predictions were made for each of the four flaws in the three ducts using the locally measured wall thicknesses given in Table B4.1. (Local instead of average wall thicknesses were used because it was found that the results of the calculations were sensitive to the value of the thickness). In the first set, the initiation and critical pressures for all the flaws in the ducts were predicted using the lower and upper J-R curves shown in Figure B4.7 and Table B4.2. The initiation pressure is that required to initiate ductile tearing while the critical pressure will result in an initial flaw extending by ductile tearing and becoming unstable. The pressure at initiation, P_{init}, was calculated from the equation

$$J(a_i + \Delta a_b, c_i, P_{init}, \theta = 90°) = J_{mat} \tag{B4.11}$$

where a_i and c_i are the initial flaw depth and half surface length. The instability pressure, P_{inst}, was determined as the maximum value of the pressure obtained by solving the equation

$$J(a_i + \Delta a_t, c_i, P, \theta = 90°) = J_R(\Delta a_t) \tag{B4.12}$$

as the tear length, Δa_t, increased. The results of these calculations are displayed in Tables B4.3 to B4.5 for Ducts 1, 2, and 3, respectively.

In the second set of calculations, the critical and instability crack depths for the initial surface flaw lengths were evaluated at the measured instability pressures for each of the ducts using the lower and upper J-R curves. The critical flaw depth corresponds to the crack that will grow by ductile tearing under constant load to result in ductile instability. The instability flaw depth is equal to the critical depth plus the amount of ductile tearing at instability. This is the flaw size that will just survive a proof test. The critical crack depths, a_{crit}, were evaluated for each initial surface flaw length, $2c_i$, by solving the following simultaneous equations for a_{inst} and Δa_{inst}, where $a_{inst}=a_{crit}+\Delta a_{inst}$

$$J(a_{inst}, c_i, P_{inst}, \theta = 90°) = J_R(\Delta a_{inst}) \tag{B4.13}$$

$$\frac{dJ(a = a_{inst}, c_i, P_{inst}, \theta = 90°)}{da} = \frac{dJ_R(\Delta a_t = \Delta a_{inst})}{d(\Delta a_t)} \tag{B4.14}$$

The results of these calculations are shown in Tables B4.6 to B4.8 for Ducts 1, 2, and 3, respectively. In all three ducts, the flaw situated at the Right (R) location was found to result in the lowest instability pressures and the smallest critical flaw depths.

It can be seen from Tables B4.3 to B4.8 that use of structurally relevant *J-R* curves together with the proposed new net section yield pressures results in predicted critical pressures and crack depths that are in good agreement with the measured values, making due allowance for the uncertainties in the predictions due to uncertainties in the *J-R* curves for each of the ducts. The results from Tables B4.3 to B4.8 for the flaws at the R locations are shown in Figures B4.8 and B4.9 in the form of plots of predicted pressures and crack depths against the measured values. Points that fall on the one-to-one line indicate precise predictions of the critical pressure and crack depths. Points that fall above the line indicate that the analysis is resulting in underpredictions, while points below the line indicate overpredictions. These figures clearly demonstrate the excellent predictive power of the simplified material specific J estimation scheme and the corresponding failure curve.

The results of the calculations are displayed in terms of FADs in Figures B4.10 to B4.15 in the form of constant load loci. The loci were generated for each flaw using the measured instability pressures for each duct and lower and upper J_R-curve behaviors. The loci consist of assessment points that are determined as a function of tear length using the equations

$$L_r = \frac{P_{inst}}{P_y(a_i + \Delta a_t, c_i)} \ , \ K_r = \frac{K(a_i + \Delta a_t, c_i, P_{inst})}{\sqrt{E' J_R(\Delta a_t)}} \qquad \text{(B4.15)}$$

Those flaws that are unstable under the instability pressure will produce a load locus that falls outside of the material specific failure curve. If a locus falls inside, then no tearing is predicted for that flaw. If the locus initially falls outside of the failure curve and then cuts through it, then ductile tearing followed by arrest is predicted. The instability conditions correspond to the flaw that produces a locus that makes a tangent to the failure curve (compare Figure A5.5). Since the constant load locus for the flaw at the R location always falls outside of the loci compared to the other flaws, these flaws are predicted to control the fracture behaviors of the three ducts, as was found to be the case. The FADs present a convenient way of presenting the results of a *J* analysis for each duct on a single diagram that allows the most onerous flaw (the one at the R location) to be easily identified.

B4.4 Leak-Before-Burst Analyses

When the R location cracks in the three ducts became unstable they failed in a burst mode, propagating through the duct walls then axially as through cracks (Figure B4.4). These kinds of behavior can be predicted by showing that the axial length of the cracks at leak exceeded the critical axial through cracks needed to cause instability (see Section A11).

Table B4.3 Predicted initiation and instability pressures for Duct 1
Failure was predicted to occur from the flaw at location R.
These results are shown in a bold font.

Duct 1
Measured pressure at instability = 10,200 psi (70.3 MPa)
Observed failure location = Right (R)
Measured initial flaw sizes:
Top (T): a = 0.1000 inch (2.54 mm), 2c = 0.356 inch (9.04 mm)
Right (R): a = 0.0965 inch (2.45 mm), 2c = 0.658 inch (16.71 mm)
Bottom (B): a = 0.1015 inch (2.58 mm), 2c = 0.446 inch (11.33 mm)
Left (L): a = 0.0740 inch (1.88 mm), 2c = 0.517 inch (13.13 mm)

Predicted Pressures

Flaw Position	Upper J-R curve		Lower J-R curve	
	Initiation psi (MPa)	Instability psi (MPa)	Initiation psi (MPa)	Instability psi (MPa)
Top (T)	11,900 (82.05)	12,135 (83.67)	10,947 (75.48)	11,571 (79.78)
Right (R)	**10,390 (71.64)**	**10,478 (72.24)**	**9,268 (63.90)**	**9,870 (68.05)**
Bottom (B)	11,289 (77.84)	11,450 (78.95)	10,269 (70.80)	10,873 (74.97)
Left (L)	12,762 (87.99)	13,245 (91.32)	11,499 (79.29)	12,634 (94.00)

Table B4.4 Predicted initiation and instability pressures for Duct 2
Failure was predicted to occur from the flaw at location R.
These results are shown in a bold font.

Duct 2 **Measured pressure at instability = 9,200 psi (63.4 MPa)** Observed failure location = Right (R) Measured initial flaw sizes: Top (T): a = 0.0948 inch (2.41 mm), 2c = 0.802 inch (20.37 mm) Right (R): a = 0.0928 inch (2.36 mm), 2c = 1.053 inch (26.75 mm) Bottom (B): a = 0.0892 inch (2.27 mm), 2c = 0.919 inch (23.34 mm) Left (L): a = 0.0845 inch (2.15 mm), 2c = 1.191 inch (30.25 mm)				
Predicted Pressures				
Flaw Position	Upper J-R curve		Lower J-R curve	
	Initiation psi (MPa)	Instability psi (MPa)	Initiation psi (MPa)	Instability psi (MPa)
Top (T)	9,637 (66.45)	9,684 (66.77)	8,606 (59.33)	9,095 (62.71)
Right (R)	**9,018 (62.18)**	**9,038 (62.32)**	**8,065 (55.61)**	**8,470 (58.40)**
Bottom (B)	9,747 (67.20)	9,807 (67.62)	8,635 (59.54)	9,201 (63.44)
Left (L)	10,102 (69.65)	10,187 (70.24)	8,827 (60.86)	9,538 (65.76)

Table B4.5 Predicted initiation and instability pressures for Duct 3
Failure was predicted to occur from the flaw at location R.
These results are shown in a bold font.

Duct 3
Measured pressure at instability = 7,500 psi (51.7 MPa)
Observed failure location = Right (R)
Measured initial flaw sizes:
Top (T): a = 0.0743 inch (1.89 mm), 2c = 1.623 inch (41.22 mm)
Right (R): a = 0.0852 inch (2.16 mm), 2c = 1.231 inch (31.26 mm)
Bottom (B): a = 0.0767 inch (1.95 mm), 2c = 1.000 inch (25.40 mm)
Left (L): a = 0.0793 inch (2.01 mm), 2c = 1.406 inch (35.71 mm)

Predicted Pressures

Flaw Position	Upper J-R curve		Lower J-R curve	
	Initiation psi (MPa)	Instability psi (MPa)	Initiation psi (MPa)	Instability psi (MPa)
Top (T)	8,767 (60.45)	8,793 (60.63)	7,833 (54.01)	8,221 (56.68)
Right (R)	**8,159 (56.26)**	**8,165 (56.30)**	**7,352 (50.69)**	**7,647 (52.73)**
Bottom (B)	9,375 (64.64)	9,438 (65.08)	8,337 (57.48)	8,850 (61.02)
Left (L)	9,214 (63.53)	9,255 (63.81)	8,181 (56.41)	8,661 (59.72)

Table B4.6 Predicted critical and instability crack sizes for the Duct 1
Failure was predicted to occur from the flaw at location R.
This result is shown in a bold font.

Duct 1 Measured pressure at instability = 10,200 psi (70.33 MPa) Observed failure location = Right (R) Measured initial flaw depths: Top (T): a = 0.1000 inch (2.54 mm) **Right (R): a = 0.0965 inch (2.45 mm) (Critical Depth)** Bottom (B): a = 0.1015 inch (2.58 mm) Left (L): a = 0.0740 inch (1.88 mm)				
Predicted Crack Depths				
Flaw Position	Upper *J-R* curve		Lower *J-R* curve	
	Critical Depth, inch (mm)	Instability Depth, inch (mm)	Critical Depth, inch (mm)	Instability Depth, inch (mm)
Top (T)	0.1205 (3.06)	0.1256 (3.19)	0.1175 (2.98)	0.1218 (3.09)
Right (R)	**0.0998 (2.53)**	**0.1069 (2.72)**	**0.0921 (2.34)**	**0.1020 (2.59)**
Bottom (B)	0.1171 (2.97)	0.1222 (3.10)	0.1124 (2.85)	0.1187 (3.01)
Left (L)	0.1208 (3.07)	0.1259 (3.20)	0.1161 (2.95)	0.1224 (3.11)

Table B4.7 Predicted critical and instability crack sizes for the Duct 2
Failure was predicted to occur from the flaw at location R.
This result is shown in a bold font.

Duct 2 Measured pressure at instability = 9,200 psi (63.4 MPa) Observed failure location = Right (R) Measured initial flaw depths: Top (T): a = 0.0948 inch (2.41 mm) **Right (R): a = 0.0928 inch (2.36 mm) (Critical Depth)** Bottom (B): a = 0.0892 inch (2.27 mm) Left (L): a = 0.0845 inch (2.15 mm)				
Predicted Crack Depths				
Flaw Position	Upper *J-R* curve		Lower *J-R* curve	
	Critical Depth, inch (mm)	Instability Depth, inch (mm)	Critical Depth, inch (mm)	Instability Depth, inch (mm)
Top (T)	0.0998 (2.53)	0.1057 (2.68)	0.0936 (2.38)	0.1018 (2.59)
Right (R)	**0.0912 (2.32)**	**0.0977 (2.48)**	**0.0845 (2.15)**	**0.0932 (2.37)**
Bottom (B)	0.0958 (2.43)	0.1020 (2.59)	0.0893 (2.27)	0.0977 (2.48)
Left (L)	0.0952 (2.42)	0.1015 (2.58)	0.0886 (2.25)	0.0972 (2.47)

Table B4.8 Predicted critical and instability crack sizes for the Duct 3
Failure was predicted to occur from the flaw at location R.
This result is shown in a bold font.

Duct 3 Measured pressure at instability = 7,500 psi (51.7 MPa) Observed failure location = Right (R) Served failure location = Right (R) Measured initial flaw depths: Top (T): a = 0.0743 inch (1.89 mm) **Right (R): a = 0.0852 inch (2.16 mm) (Critical Depth)** Bottom (B): a = 0.0767 inch (1.95 mm) Left (L): a = 0.0793 inch (2.01 mm)				
Predicted Crack Depths				
Flaw Position	Upper *J-R* curve		Lower *J-R* curve	
	Critical Depth, inch (mm)	Instability Depth, inch (mm)	Critical Depth, inch (mm)	Instability Depth, inch (mm)
Top (T)	0.0872 (2.21)	0.0923 (2.34 mm)	0.0822 (2.09 mm)	0.0886 (2.25 mm)
Right (R)	**0.0915 (2.32)**	**0.0965 (2.45 mm)**	**0.0868 (2.20 mm)**	**0.0929 (2.36 mm)**
Bottom (B)	0.0963 (2.45 mm)	0.1014 (2.58 mm)	0.0922 (2.34 mm)	0.0978 (2.48 mm)
Left (L)	0.0965 (2.45 mm)	0.1016 (2.58 mm)	0.0920 (2.34 mm)	0.0980 (2.49 mm)

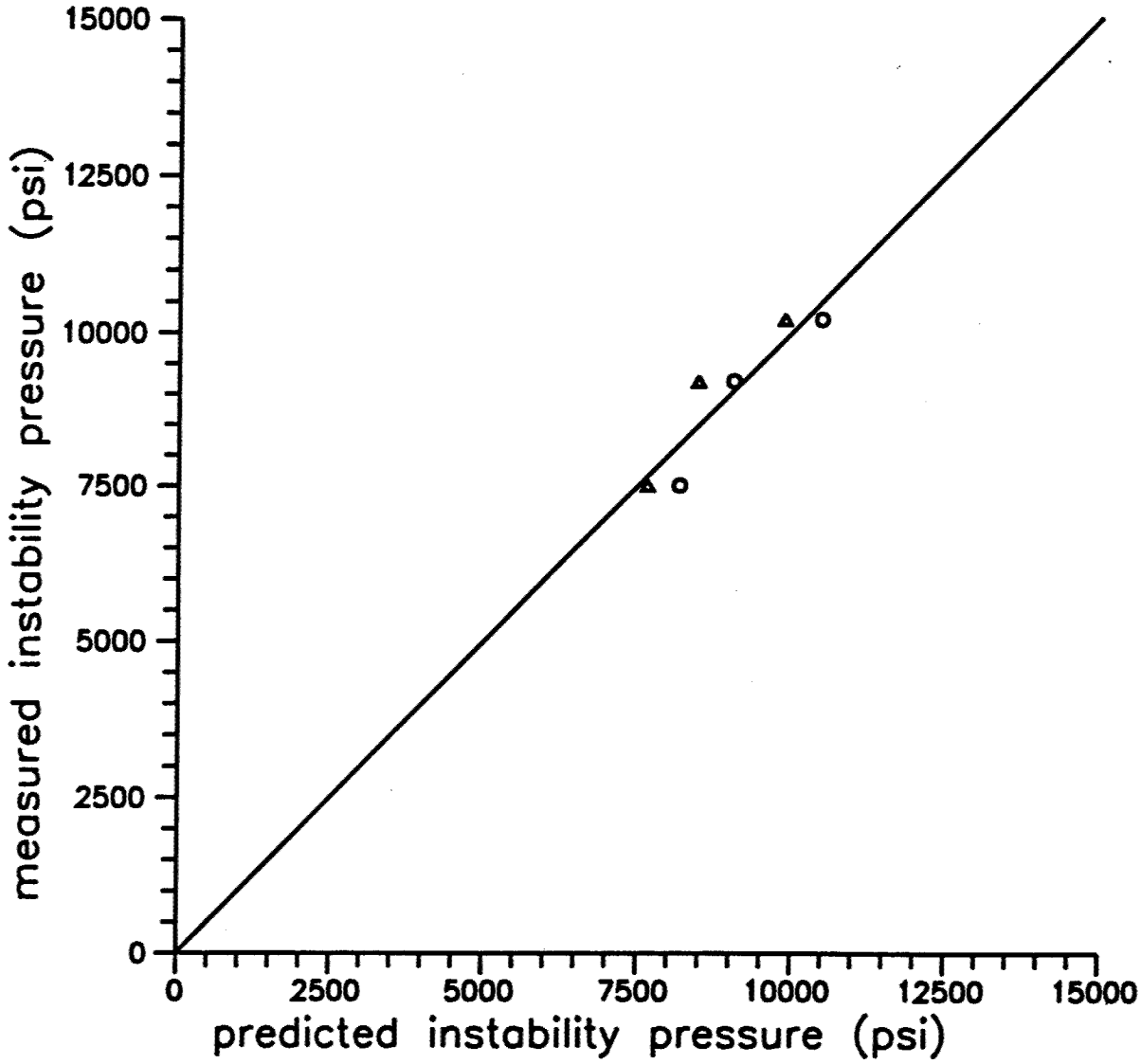

Figure B4.8 The measured internal pressures at instability plotted against the predicted values for the three flawed SSME HP oxidizer ducts. The predicted values were calculated assuming "upper" and "lower" toughness behaviors (signified by the open circles and the open triangles, respectively). (1000 psi = 6.895 MPa)

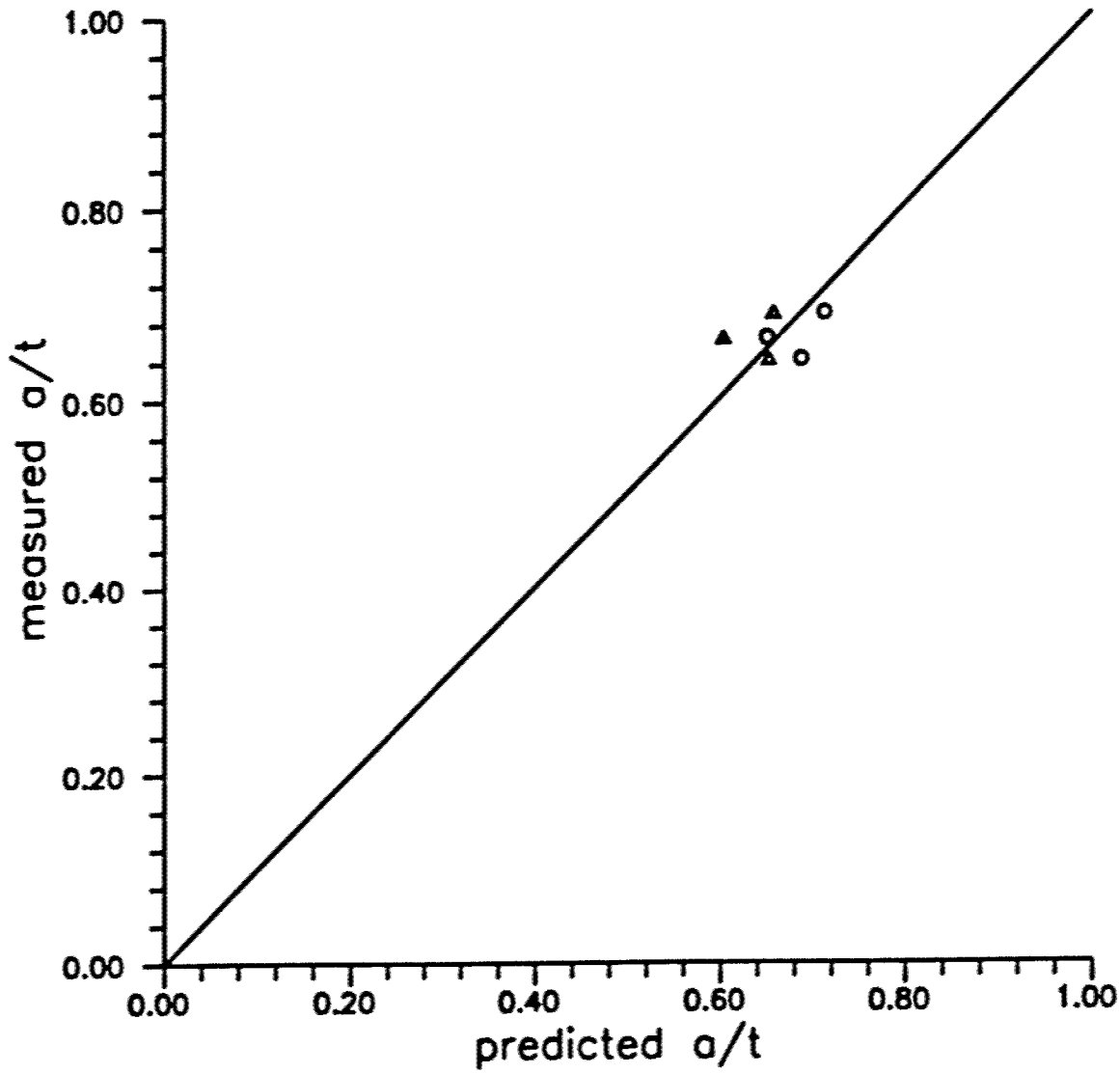

Figure B4.9 The normalized measured critical crack depths plotted against the predicted values for the three flawed SSME HP oxidizer ducts. The predicted values were calculated assuming "upper" and "lower" toughness behaviors (signified by the open circles and the open triangles, respectively).

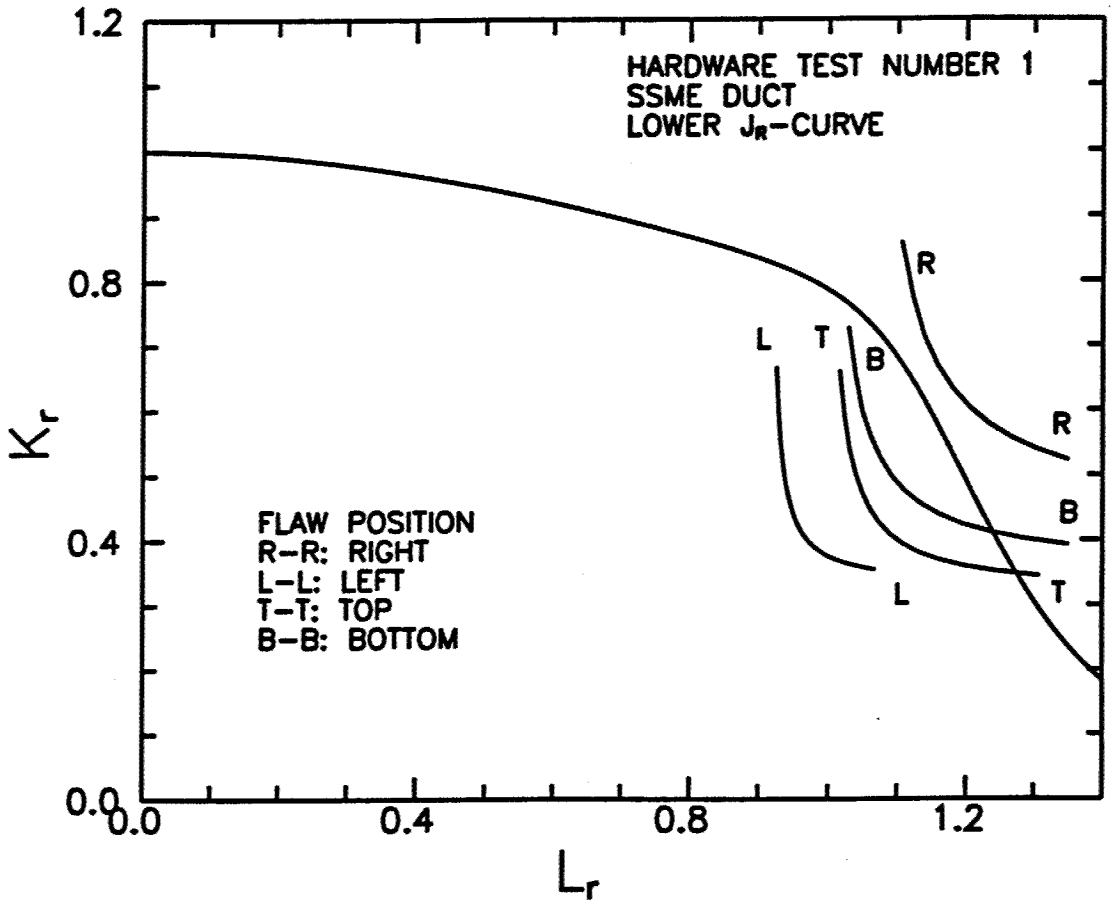

Figure B4.10 Failure assessment diagram showing the failure loci for the four flaws in Duct 1 calculated assuming lower toughness behavior.

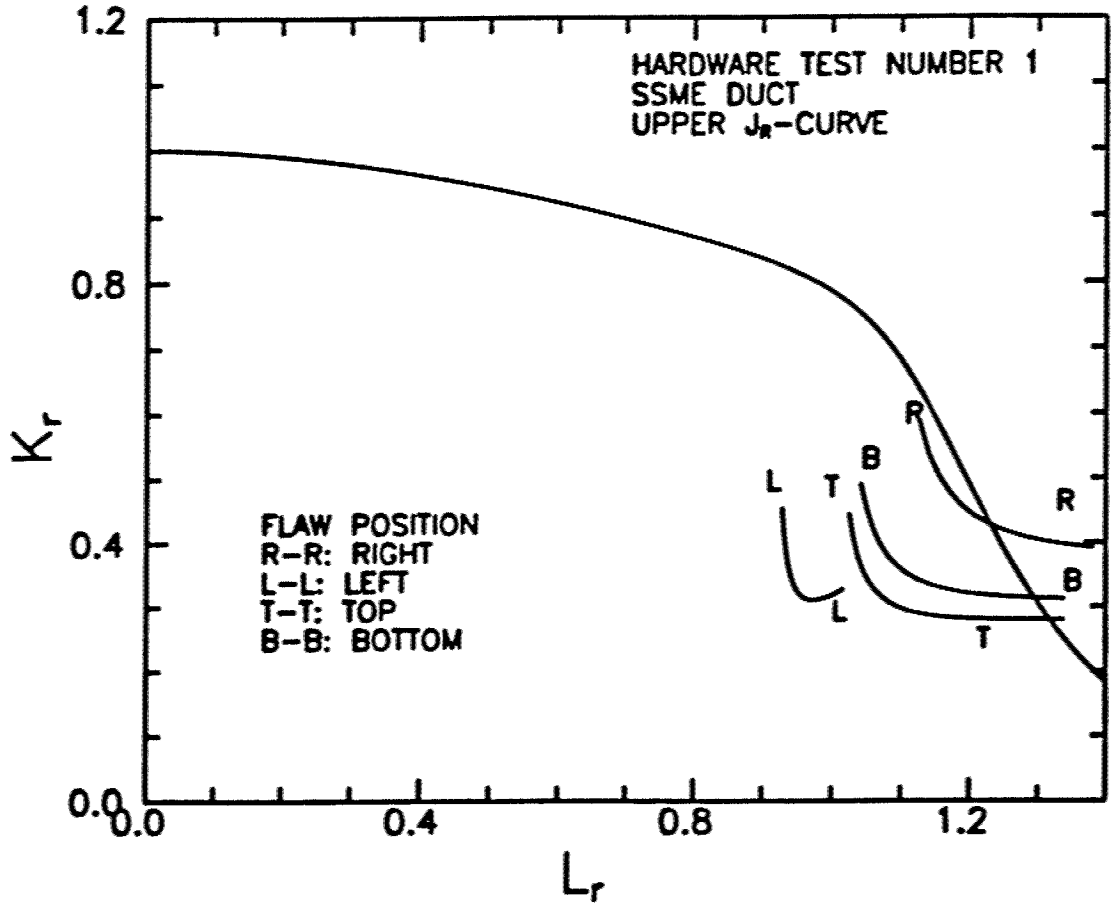

Figure B4.11 Failure assessment diagram showing the failure loci for the four flaws in Duct 1 calculated assuming upper toughness behavior.

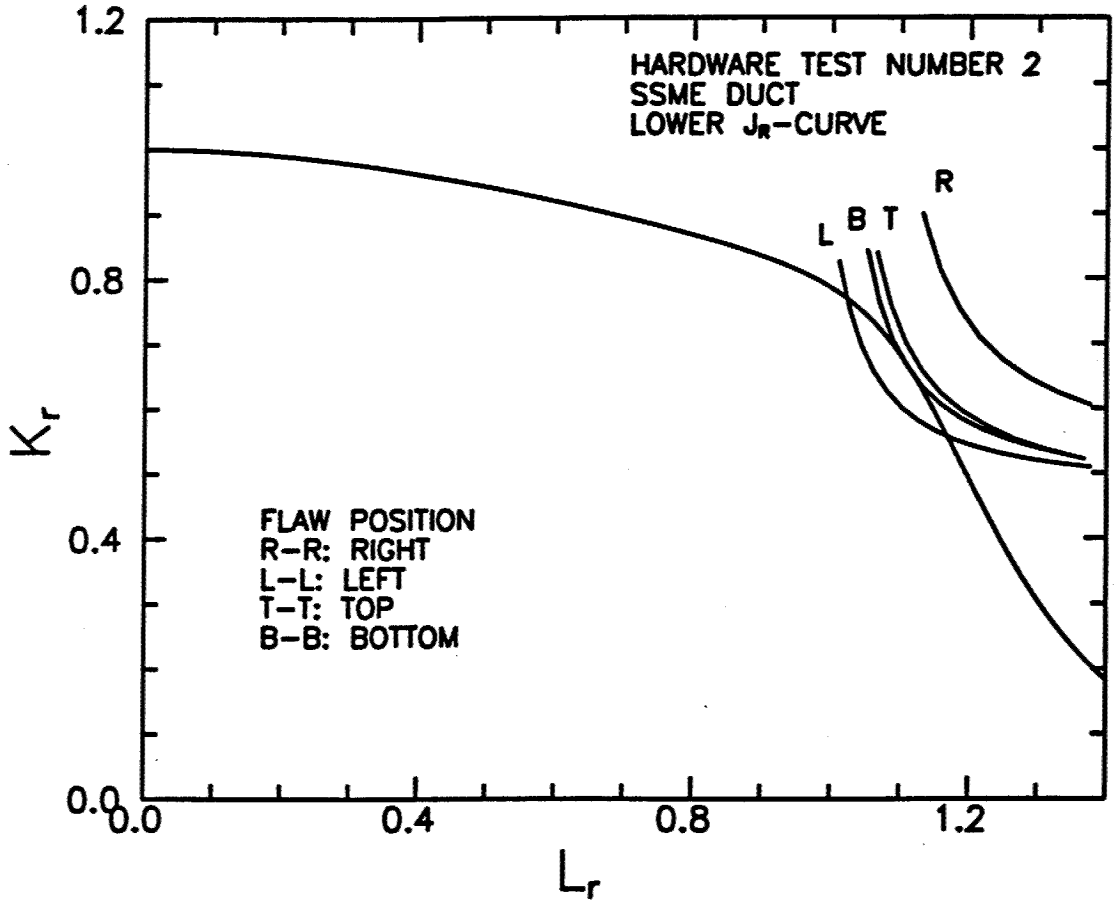

Figure B4.12 Failure assessment diagram showing the failure loci for the four flaws in Duct 2 calculated assuming lower toughness behavior.

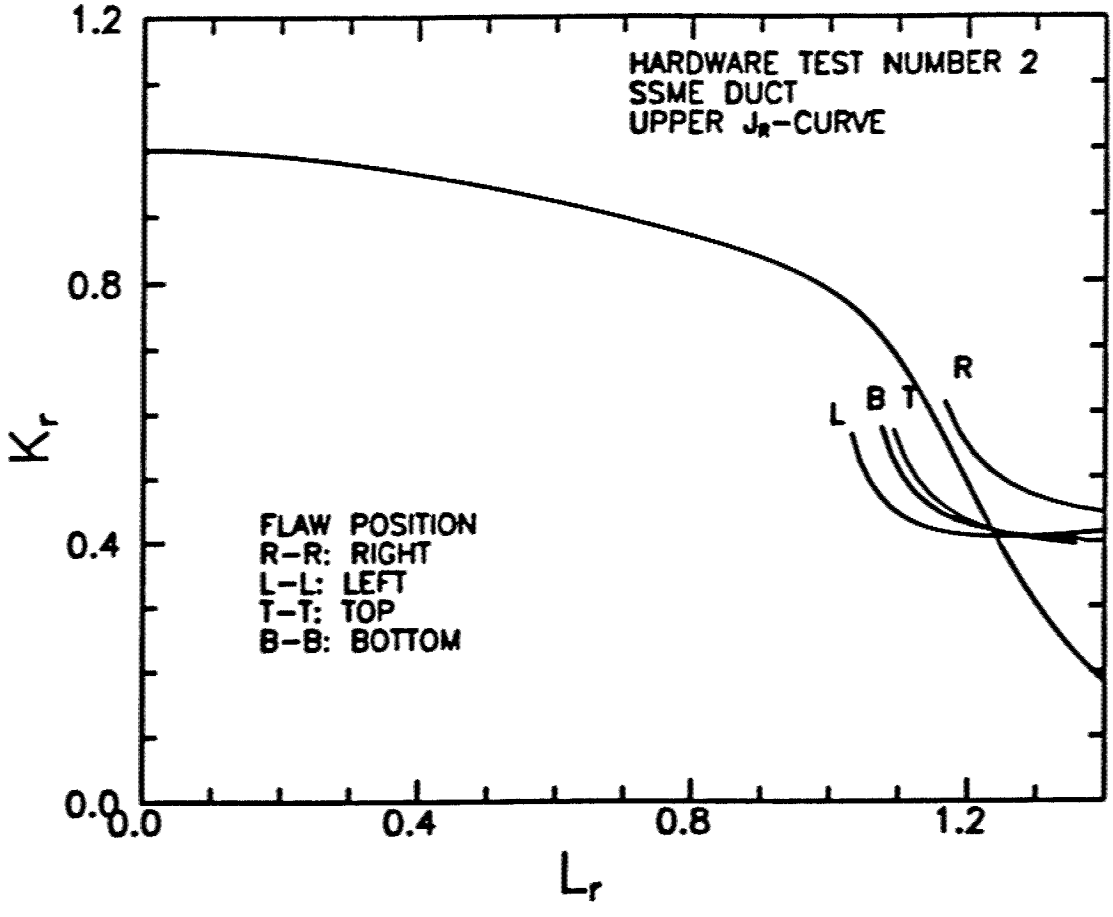

Figure B4.13 Failure assessment diagram showing the failure loci for the four flaws in Duct 2 calculated assuming upper toughness behavior.

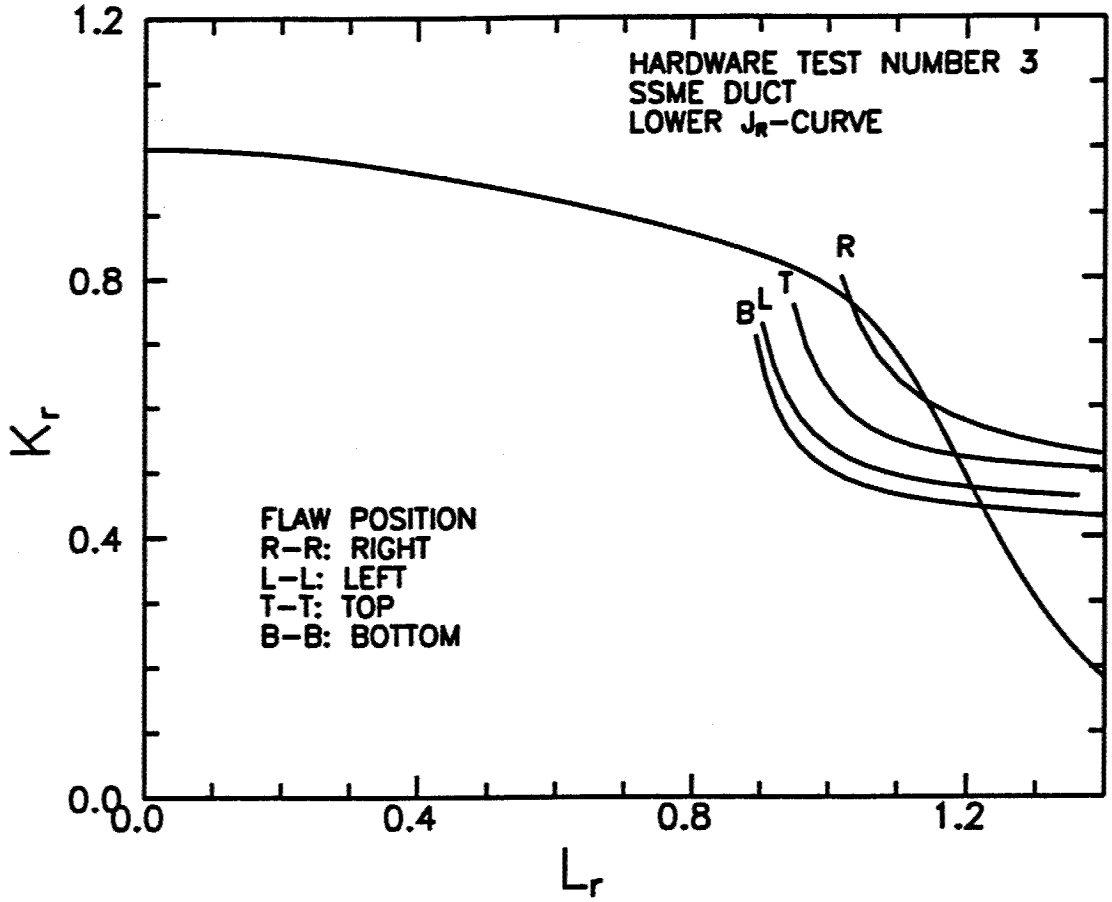

Figure B4.14 Failure assessment diagram showing the failure loci for the four flaws in Duct 3 calculated assuming lower toughness behavior.

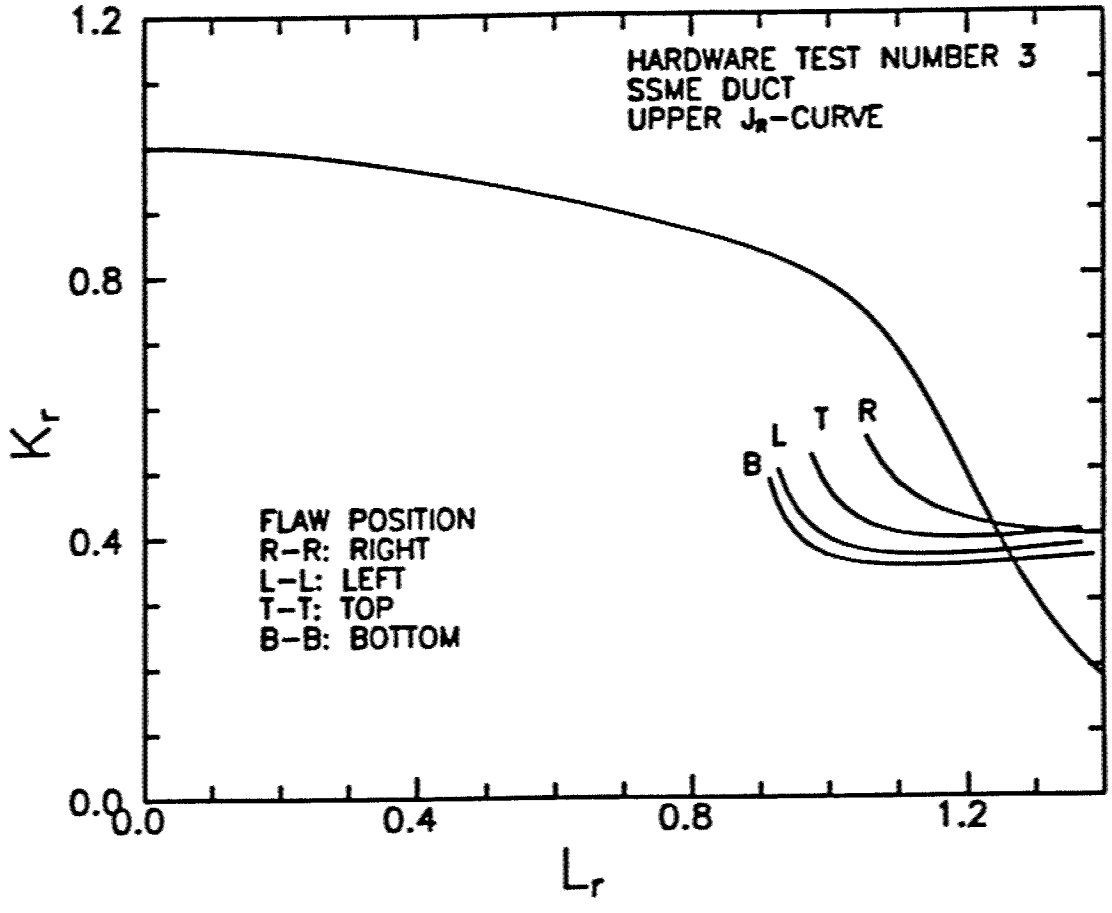

Figure B4.15 Failure assessment diagram showing the failure loci for the four flaws in Duct 3 calculated assuming upper toughness behavior.

Figures B4.16-B4.18 show calculated assessment loci for through cracks in the three ducts based on the lower and upper J-R curves. The loci were evaluated using the measured failure pressures for the ducts and axial through cracks equal to the measured initial surface lengths, $2c_i$, of the cracks at location R (see Table B4.1). (When performing a conservative LBB analysis, it is recommended in Section A11 that a through crack length of $2c_i+t$ be used, but in this validation, a best estimate LBB analysis was performed based on the initial surface flaw length.) The SIF for the through crack was derived from the results given by Krenk [84] expressed in the form

$$K = \frac{R_m}{t} P \sqrt{\pi c} \, (1 + 0.7044\,\rho + 0.8378\,\rho^2)^{\frac{1}{2}} \;,\; 0 \le \rho \le 4.4 \tag{B4.16}$$

and the net section yield pressure was taken as [40].

$$P_y = \frac{\sigma_y t}{R_m} \frac{1}{M(\rho, a/t = 1)} \tag{B4.17}$$

Since for all three ducts the constant load loci fall well outside the failure curves, the figures clearly demonstrate that when the flaws have penetrated the duct walls they will propagate unstably in a direction parallel to the axes of the ducts. Hence the FAD approach correctly predicted the observed leak and burst behaviors for all three ducts.

B4.5 Discussion and Conclusions

The fracture tests on flawed SSME high pressure oxidizer ducts were performed to provide validation for the material specific J estimation scheme and FAD approach being proposed for use in proof test analysis of aerospace hardware. The approaches were found to be successful in predicting the fracture behavior of the three tested ducts.

The successful analyses of the simulated proof tests were facilitated by the following observations based on the experience gained from the fracture analyses. These observations highlight some important aspects of proof test analyses that the analyst should be aware of.

(1) The accuracy of the analyses in predicting the critical conditions for the flawed IN-718 ducts was sensitive to the values of the net section yield pressures used in the calculations. In the present study, a frequently used expression for the net section yield pressure was modified based on the results of an early analysis of the test data. The modified expression [equation (B4.9)] was verified by using it in a successful analysis of the CEGB Pressure Vessel Test 1 which was performed to provide hardware validation for the R6 FAD procedures [83]. Without this modification the critical pressures and crack sizes measured in the duct tests would have been significantly underestimated. This would have resulted in a non-conservative assessment of the flaw screening capability of a proof test performed on the ducts.

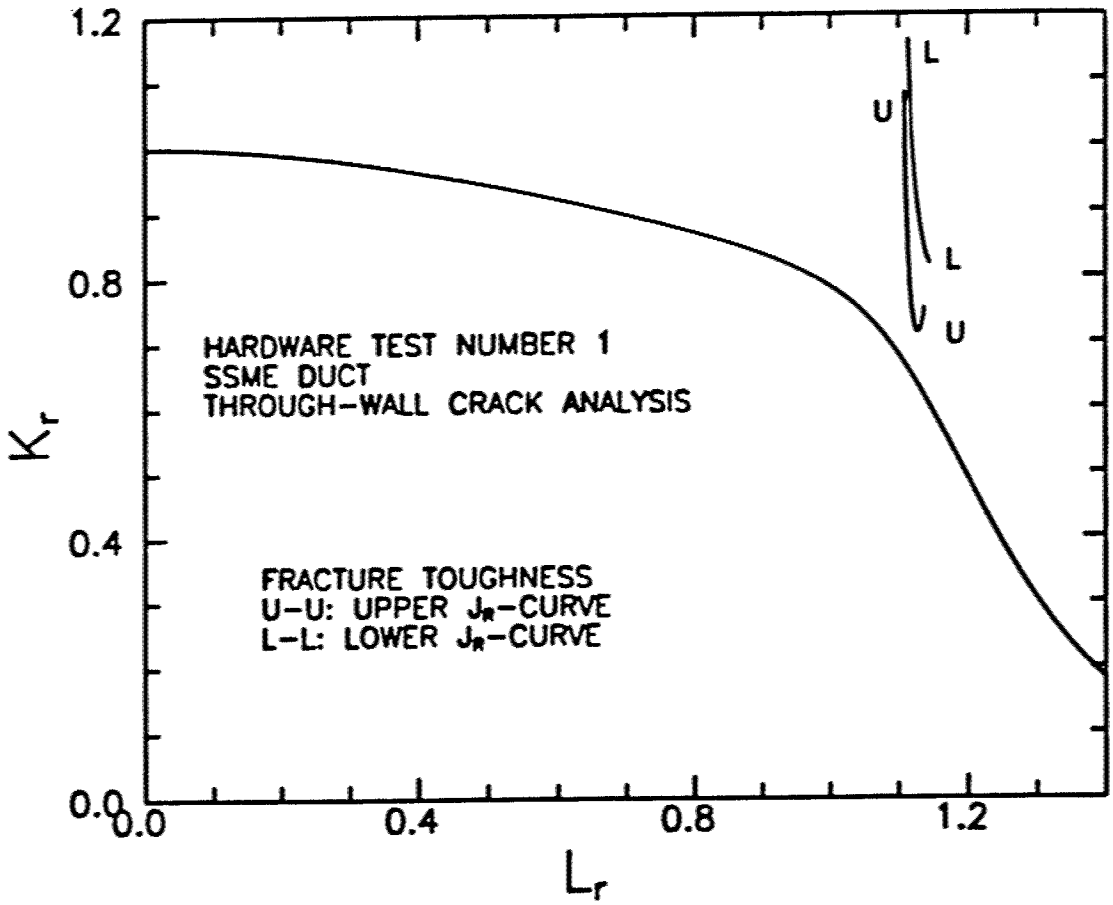

Figure B4.16 Failure assessment diagram showing failure loci for an axial through-wall flaw located at position R in Duct 1 calculated assuming upper and lower toughness behavior.

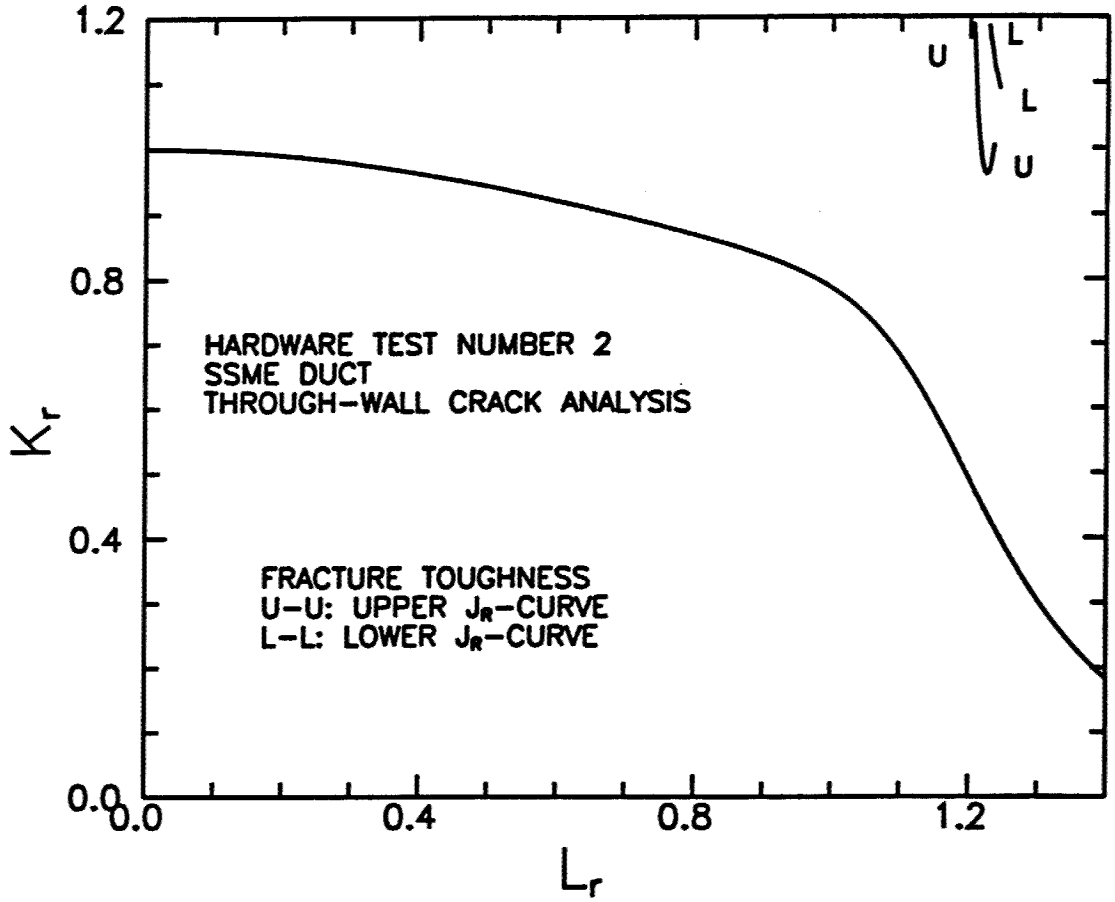

Figure B4.17 Failure assessment diagram showing failure loci for an axial through-wall flaw located at position R in Duct 2 calculated assuming upper and lower toughness behaviors.

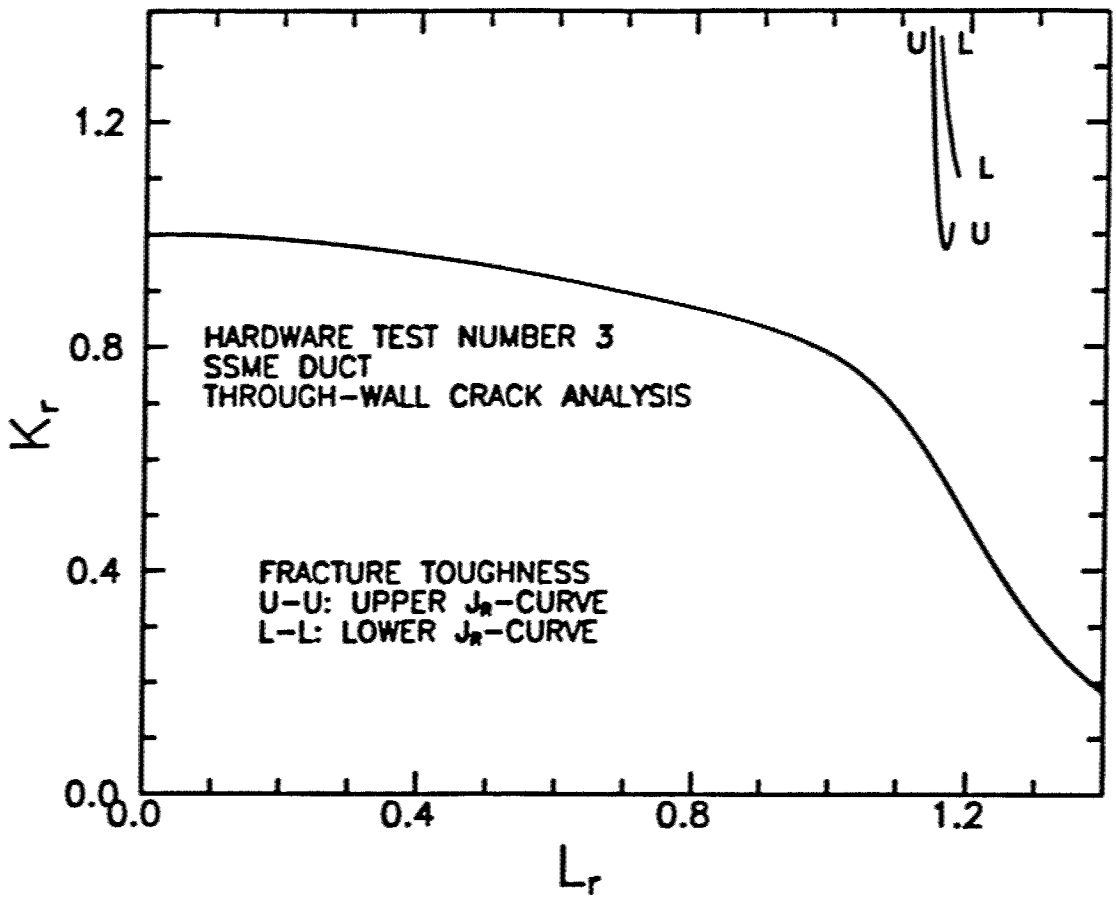

Figure B4.18 Failure assessment diagram showing failure loci for an axial through-wall flaw located at position R in Duct 3 calculated assuming upper and lower toughness behaviors.

(2) The thickness of the ducts varied around the circumference and was different at each of the flawed locations on the ducts. Although the absolute differences were small, the ducts were thin walled (like many SSME components) and the variations in thickness were sufficient to result in significant differences in the predicted fracture behavior. The minimum wall thickness specified on design drawings for the ducts was 0.114 inch, compared to an average measured value of around 0.140 inch. The use of the design thickness values in a FAD analysis would have resulted in an underprediction of the critical pressures and crack sizes for the ducts (the hoop stress would have been over-predicted for a given internal pressure), and a non-conservative proof test analysis result.

(3) An assumption was made that ductile tearing during the pressurization only occurred at the deepest points on the flaws in order to facilitate the FAD calculations. This reduced a two degrees of freedom crack to a one degree of freedom crack. Additional calculations were made assuming that the crack maintained a constant aspect ratio during ductile tearing, with growth being determined by the conditions at the deepest points on the flaws. These calculations were performed to check the sensitivity of the FAD results to the original assumption concerning ductile tearing. The results of this exercise indicated that FAD analysis was insensitive to the assumption made concerning ductile crack growth development.

(4) Some of the fracture analyses were repeated using the J estimation scheme described in Section A4.7 which is based on a modification to the EPRI estimation scheme where, for a Ramberg-Osgood material, J is written in the form

$$J(a,c,P,\theta) = J_e(a_e,c_e,P,\theta) + V^*(\theta)\,\alpha\, J_e(a,c,P,\theta)\left[\frac{P}{P_o(a,c)}\right]^{n-1} \qquad \text{(B4.18)}$$

The results of these calculations were very similar to those obtained using the material specific J estimation scheme. This demonstrates that either scheme may be used to assess surface flaws emanating from smooth surfaces without stress concentration features.

(5) J-R curves used in the present analyses were measured on restrained edge cracked plate specimens designed to simulate the low plastic constraint likely to be present in thin walled pressurized components. These measured J-R curves differed significantly from a J-R curve derived from tests performed on more highly constrained compact tension specimens (compare Figure B4.7). It is important for proof test analyses based on the FAD approach that the J-R curves used are relevant to the constraint conditions of the proof tested hardware in order to avoid a non-conservative proof test analysis.

(6) The FAD approach correctly predicted the burst behaviors of the three flawed ducts. This is important, as it is prudent to perform a leak-before-burst analysis prior to proof testing because of the possible safety and other implications of structural fracture of the tested hardware. In contrast to the fracture predictions made to estimate the flaw screening capability of the proof test, which utilizes upper bound toughness data in order to be conservative, the calculation of the critical through crack length for a leak-before-burst analysis should be based on lower bound toughness values.

B5. HARDWARE VALIDATION: PREDICTING CRITICAL CRACK SIZES AND CRITICAL LOADS FOR FERRITIC STEELS

B5.1 Ferritic Steel Pressure Vessel: CEGB Test 1

B5.1.1 Overview of Testing

The Central Electricity Generating Board (CEGB) in the United Kingdom performed hardware tests on flawed pressure vessels as part of its validation program in support of the FAD based R6 structural integrity assessment procedures [45,46]. The pressure vessel was hydraulically pressurized to failure and the instability (maximum) pressure recorded. One of these tests, signified as CEGB Test 1, is analyzed here. This test had been previously analyzed by Milne and Knee [83] using the R6 FAD approach. A schematic of the ferritic steel pressure vessel geometry showing the location of the machined axial surface flaw introduced into the pressure vessel prior to testing, is shown in Figure B5.1. The A533B steel plate pressure vessel had an internal diameter of 1015 mm (40 inch) and a wall thickness in the region of the flaw of 84 mm (3.31 inch) and was tested at 46°C. The depth of the flaw was 61 mm (2.4 inch) and its surface length was 200 mm (7.87 inch). A leak-before-burst failure was observed.

B5.1.2 Assessment Data for J Estimation and Material Specific Failure Assessment Diagram

The flaws introduced into the ducts were surface flaws with two DOF. Since the tests involved internal pressurization, a similar J estimation scheme and material specific FAD approach can be used as was described in Section B4. Hence, the assessment data needed to perform fracture predictions for the tested flawed pressure vessel are an uniaxial stress-strain curve, a J-R curve, stress intensity factor solutions, and net section yield pressures for the flaw.

Tensile Data

Tensile data for the A533B steel are available graphically in Milne and Knee [83] in the form of a stress-strain curve. To facilitate the present analysis, this curve was fitted by Ramberg-Osgood law with σ_o=556 MPa, α=1.677, n=17.7, and E=210,000 MPa. The yield stress is 556 MPa, and the ultimate strength is 686 MPa.

J-R Curve

Milne and Knee [83] provide a J-R curve for the ferritic steel measured on a compact tension specimen following procedures similar to those detailed in ASTM Standard E1152 [57]. It is judged that the thickness of the pressure vessel is sufficient for these test data to be regarded as structurally relevant toughness data for proof test analysis purposes.

The toughness data presented by Milne and Knee [83] were fitted by a quadratic polynomial [compare equation (B4.7)] where the values of the coefficients, J_o, J_1, and J_2, are defined in Table B5.1, where the J_{mat} values correspond to J_R evaluated at Δa_{min}, and Δa_{max} defines the tear length validity range for the fit.

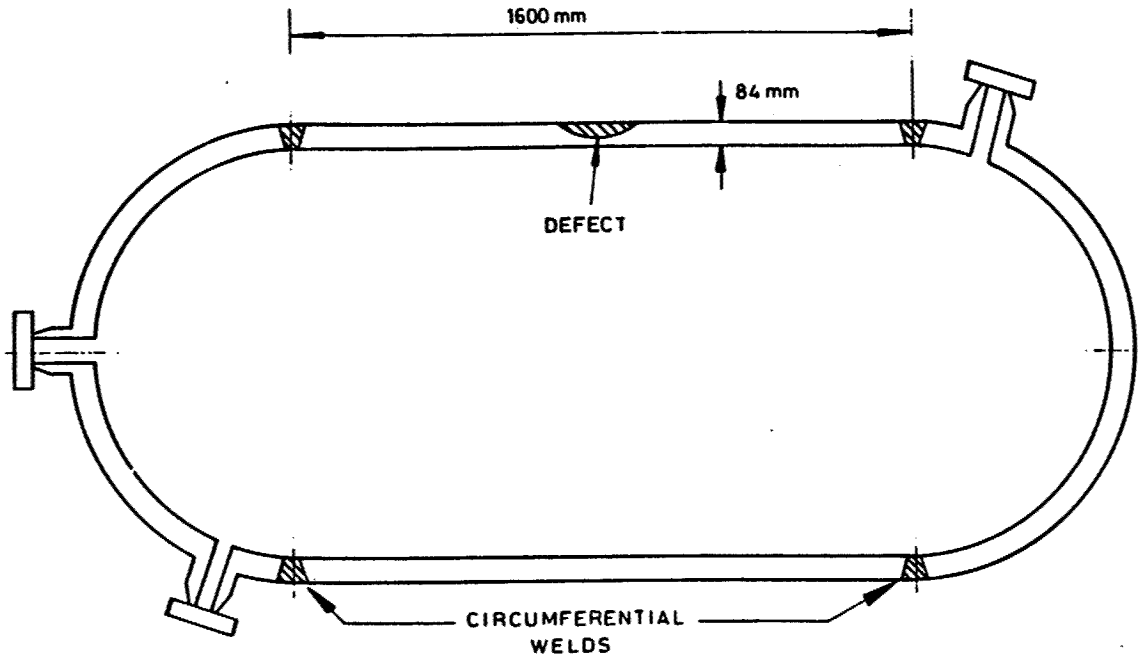

Figure B5.1 Geometry of CEGB test vessel.

Table B5.1 Characterization of the structurally relevant toughness of A533B steel

J_{max} MPa m (ksi inch)	J_0 MPa m (ksi inch)	J_1 MPa m/mm (ksi)	J_2 MPa m/mm^2 (ksi inch^{-1})	Δa_{min} mm (inch)	Δa_{max} mm (inch)
0.433 (2.467)	0.361 (2.057)	0.5033 (72.9)	-0.023253 (-85.53)	0.145 (0.0057)	5.0 (0.197)

Stress Intensity Factor Solutions

As in Section B4.2.3, the KCALC software module developed by SwRI was used to determine the stress intensity factors for the flaw. In the present case, R_m/t=6.54 (549.5/84).

Net Section Yield Pressures

The same net section yield pressure was used as defined by equation (B4.9).

B5.1.3 Determination of Critical Pressures and Crack Depths

Ductile instability analyses were performed to predict the fracture behavior of the flawed pressure vessel. Two sets of predictions were made. In the first set, the critical pressures were predicted while in the second set the critical crack depth was determined. In both sets of calculations, the assessments were made against the deepest point on the flaw and tearing was assumed to occur only at this point, the surface length of the flaw being held constant. This procedure reduced the two degree of freedom flaw to one degree of freedom flaw that facilitated the needed computations.

The results of the calculations are displayed in Figure B5.2 in the form of a constant load locus generated for the measured instability pressure. It can be seen that this locus is very nearly tangential to the material specific failure curve, showing that the predicted instability pressure is very nearly equal to the measured maximum pressure. The measured and predicted critical pressure and crack depth are shown in Table B5.2. The predicted critical pressure and crack depth are in excellent agreement with the measured values, as was indicated by Figure B5.2. The predicted instability flaw depth is equal to the critical depth plus the amount of tearing up to instability.

Table B5.2 Comparison of the measured and predicted critical pressure and flaw depth for CEGB Test 1

Measured (critical) pressure at instability = 80.45 MPa (11.67 ksi)		**Measured (critical) flaw depth a = 61 mm (2.40 inch)**	
Predicted initiation pressure MPa (ksi)	Predicted instability pressure MPa (ksi)	Predicted critical flaw depth mm (inch)	Predicted instability flaw depth mm (inch)
74.0 (10.73)	79.9 (11.56)	60.2 (2.37)	65.2 (2.57)

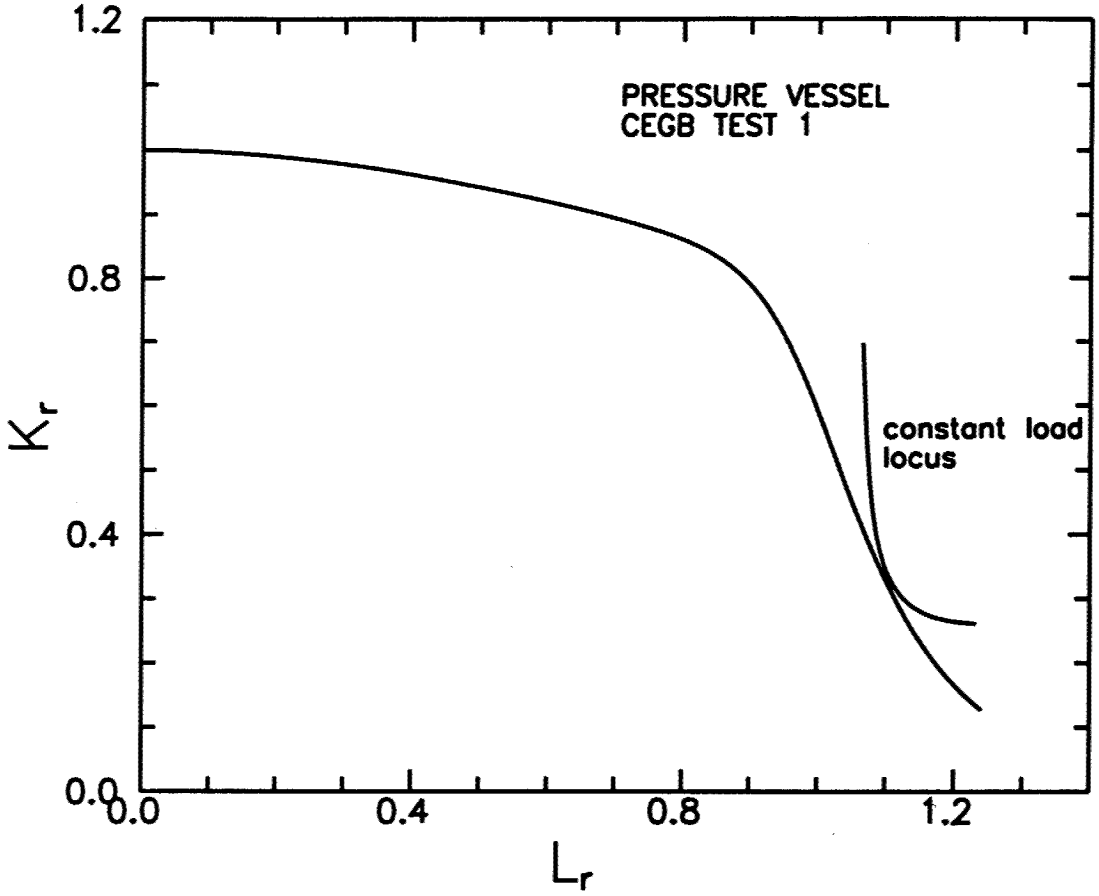

Figure B5.2 Constant load locus evaluated for the measured instability pressure in CEGB Test 1 compared to the material specific failure curve for the ferritic pressure vessel steel.

B5.1.4 Leak-Before-Burst

The CEGB Test 1 pressure vessel leaked but did not burst because the ferritic pressure vessel was hydraulically pressurized specifically to avoid burst. However, it is informative to analytically assess the likelihood of leak-before-burst (see Section 4.7.3). This has been done, following similar procedures to those described in Section B4.4. The calculated assessment locus for a through crack equal to the surface length of the flaw and subjected to the maximum pressure is shown in Figure B5.3. Since the locus falls just outside of the failure curve, this indicates the FAD approach would have predicted failure by burst if the pressure vessel had been pneumatically pressurized.

B5.2 High Toughness Steel Pressure Vessel with Circumferential Through Crack: NASA Ames Test

B5.2.1 Overview of Testing

A hydrostatic test was performed on a thin walled pipe containing a circumferential through crack as part of investigations at NASA Ames Research Center into problems associated with proof-test based life prediction of pressure vessels made of high-toughness (ductile) materials [85]. The pipe, which was made of A106B steel with a 16 inch (406.4 mm) diameter and a wall thickness of 0.281 inch (7.14 mm), contained a 16 inch (406.4 mm) long circumferential through crack that resulted in failure during the hydrostatic test.

B5.2.2 Assessment Data for J Estimation and Material Specific Failure Assessment Diagram

Due to symmetry about the center of the flaw, the through crack has one DOF for analysis purposes. The tests involved internal pressurization, so a similar J estimation scheme and material specific FAD approach can be used as described in Section B4.2. Hence, the assessment data needed to perform fracture predictions for the tested flawed pressure vessel are an uniaxial stress-strain curve, J-R curve, stress intensity factor solutions and net section yield pressures for the circumferential through flaw.

Tensile Data

The Ramberg-Osgood law parameters for the A106B steel are given by Panontin and Hill [85] as σ_o=54.5 ksi, α=1.25, n=5.5, and E=33000 ksi. The yield stress is 54.5 ksi, and the ultimate strength is 84 ksi.

J-R Curves

Panontin and Hill [85] provided *J-R* curve data in graphical form based on tests performed on 1.25 inch (31.8 mm) compact tension specimens according to ASTM Standard E813 [55]. These *J-R* curves are not formally valid, as E813 is intended for J_{Ic} testing, and although a *J*-resistance curve is measured as part of the procedures involved, the analysis used to derive this curve from the measured area under the load-displacement curve is not corrected for the contribution from explicit tearing. Hence the J-R data presented will produce an overestimate of J_R for a given tear length compared with data derived following ASTM Standard E1152 [57]. This overestimate will partly compensate for the fact that the pipe wall is only 0.281 inch thick, and hence constraint effects would tend to elevate a measured structurally relevant toughness above that measured in a valid J-R test.

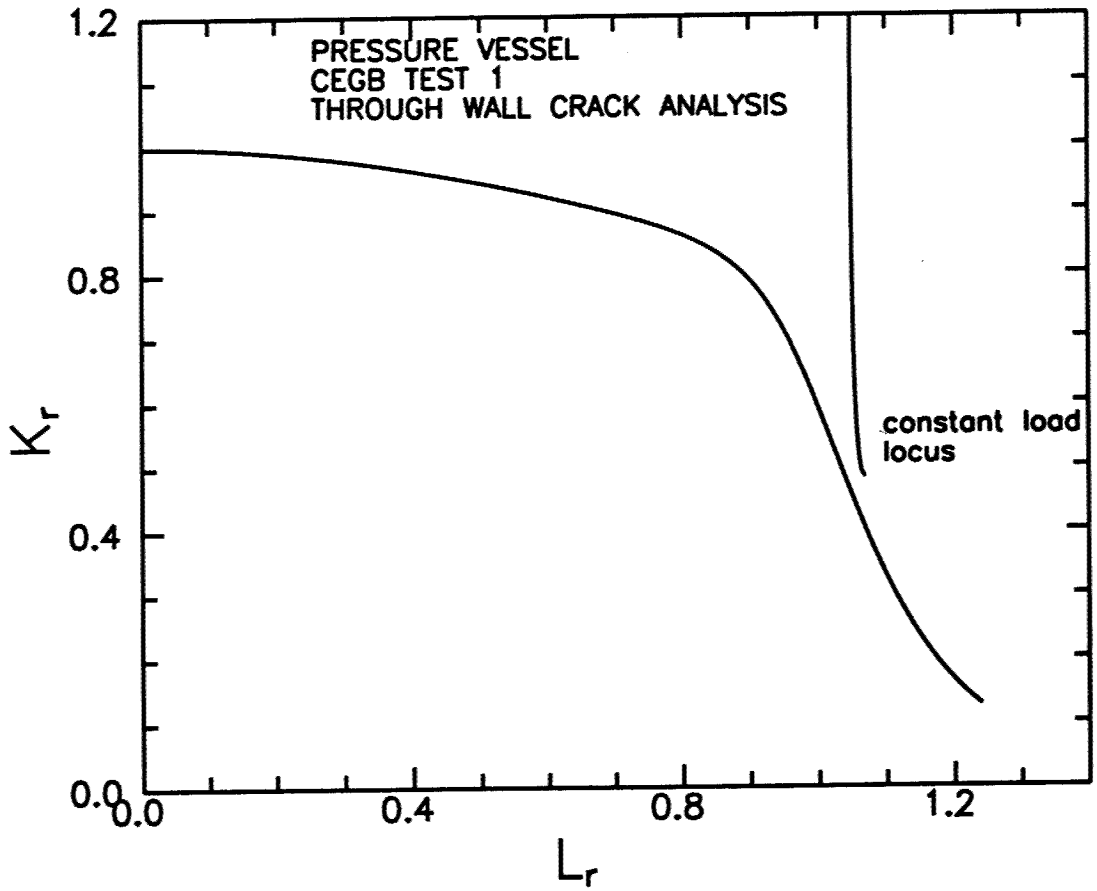

Figure B5.3 Constant load locus evaluated at the measured instability pressure in CEGB Test 1 for a through crack compared to the material specific failure curve for the pressure vessel steel.

The toughness data presented by Panontin and Hill [85] were fitted by a quadratic polynomial [compare equation (B4.7)] where the values of the coefficients, J_0, J_1, and J_2, are defined in Table B5.3, where the J_{mat} values correspond to J_R evaluated at Δc_{min}. The quadratic equation does not provide a good fit to the measured *J-R* data at small tear lengths, but this was judged not to be significant because instability was predicted to occur after a relatively large amount of tearing.

Table B5.3 Characterization of the structurally relevant toughness of A106B pipe steel

J_{mat} ksi inch (MPa m)	J_0 ksi inch (MPa m)	J_1 ksi (MPa m/mm)	J_2 ksi inch^{-1} (MPa m/mm^2)	Δc_{min} inch (mm)	Δc_{max} inch (mm)
3.260 (0.572)	3.260 (0.572)	19.57 (0.135)	-14.29 (-0.00388)	0.0 (0.0)	0.65 (16.5)

Stress Intensity Factor Solutions

The SIF for a circumferential through crack in a pipe with R_m/t=28.5 (8/0.281) was obtained using a computer program, THICKCYL, developed at SwRI for assessing circumferential through cracks in cylinders subjected to internal pressure and external bending. This program includes the effects of internal pressure on the SIF solution. The SIF solutions in THICKCYL are in good agreement with those contained in the computer program ADISC (Assessment of Defects in Spheres and Cylinders) which was developed by the CEGB and accepted by the Nuclear Installation Inspectorate in the U.K. for use in assessing nuclear components.

Net Section Yield Pressures

The net section yield pressure for cylinders containing circumferential through cracks was taken as (for example, see Miller [40])

$$P_y^* = \frac{t\sigma_y}{R_m}\left[1 - \frac{\beta + 2\sin^{-1}\left(\sin\frac{\beta}{2}\right)}{\pi}\right] \tag{B5.1}$$

where $\beta = c/R_m$, and c is half the mean circumferential crack length.

B5.2.3 Determination of Critical Pressures and Crack Depths

Ductile instability analyses were performed to predict the critical pressure and crack length at instability for the cracked pipe. The results of the calculations are displayed in Figure B5.4 in the form of a constant load locus generated for the measured instability pressure of 1475 psi (10.17 MPa). It can be seen that this locus is very nearly tangential to the material specific failure curve for A106B steel, showing that the predicted instability pressure is very nearly equal to the measured maximum

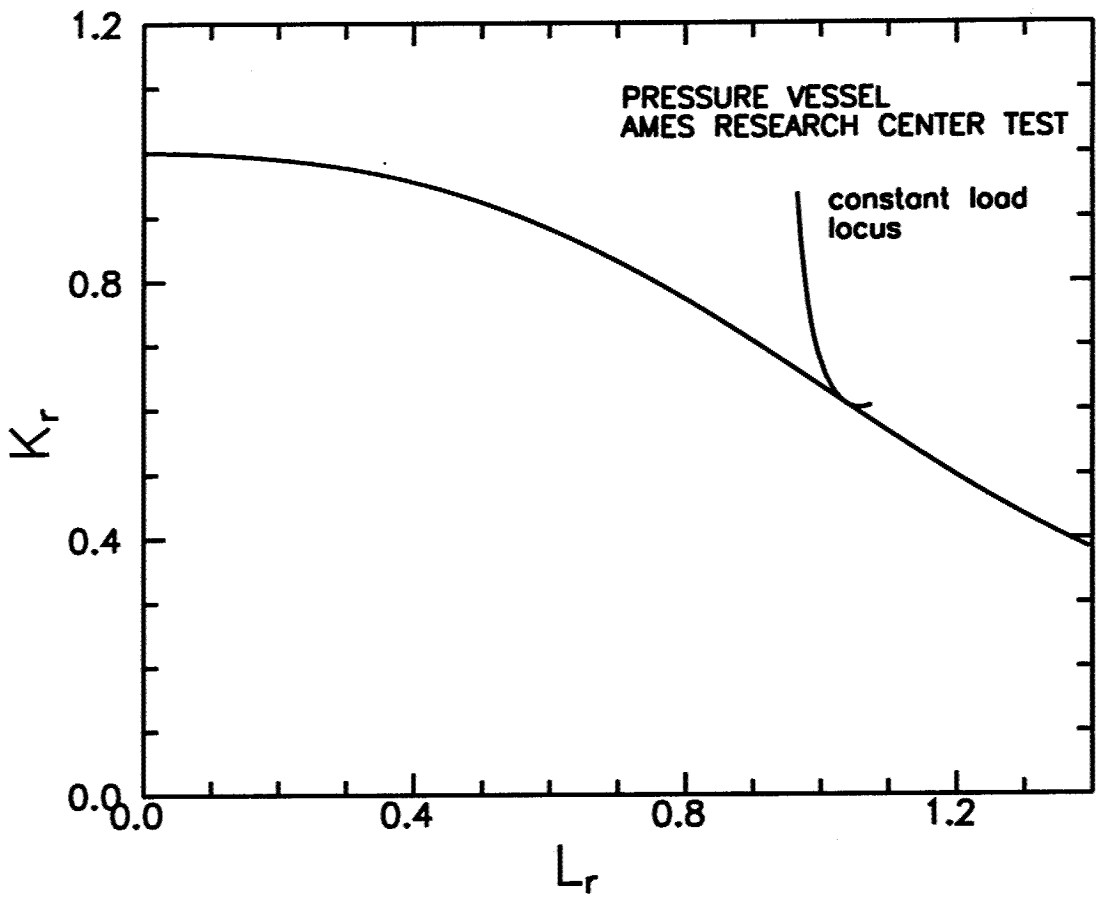

Figure B5.4 Constant load locus evaluated at the measured instability pressure for the NASA Ames pressure vessel compared to the material specific failure curve for the ferritic steel.

pressure. The measured and predicted critical pressures and crack lengths are shown in Table B5.4. It can be seen that the predicted critical pressure and crack length are in excellent agreement with the measured values.

Table B5.4 Comparison of the measured and predicted critical pressures for the NASA Ames hydrostatic test

Predicted initiation pressure psi (MPa)	Measured instability pressure psi (MPa)	Predicted instability pressure psi (MPa)	Measured critical crack length inch (mm)	Predicted critical crack length inch (mm)	Predicted instability crack length inch (mm)
1227 (8.46)	1475 (10.17)	1485 (10.24)	16.0 (406.4)	16.08 (408.4)	16.93 (430.0 mm)

B5.3 Ferritic Steel Pressure Vessel with Flawed Weld: CEGB Test 3

B5.3.1 Overview of Testing

As part of the R6 validation program, the CEGB also performed a test on a pressure vessel containing a flaw in a longitudinal seam sub-merged arc weld, signified as CEGB Test 3. The geometry of the pressure vessel was the same as in the CEGB Test 1 (see Figure B5.1), but the axial flaw was located in the stress relieved seam weld adjacent to a repair weld that induced a residual stress in the region of the flaw (see Figure B5.5). The vessel was hydraulically pressurized at 66°C until a maximum pressure was attained. The test is reported by Knee [86]. The measured average residual stress profile normal to the axial flaw is show in Figure B5.6.

B5.3.2 Assessment Data for J Estimation and Material Specific Failure Assessment Diagram

Although the flaw introduced into the weld had two DOF, it was assessed against the deepest point only. A full analysis is not performed here, the intent is to show that the recommended method for treating cracks at welds would produce a conservative result with respect to either a proof test or service analysis by comparing the constant load locus calculated at the measured instability (maximum) pressure with the failure curves generated following the recommended treatment of welds in Sections A4.8 and A5.9. Although the test involved combined loading primary and secondary (internal pressurization plus a residual stress), the failure curve generated assuming primary loading provides a good representation of the combined primary and secondary failure curve. This allows a *J* estimation scheme and material specific FAD approach to be used. The assessment data needed to perform fracture predictions for the tested flawed pressure vessel are uniaxial stress-strain curves for the weld and base metals, a *J-R* curve, stress intensity factor solutions (including the effects of the residual stress) and net section yield pressures for the surface flaw.

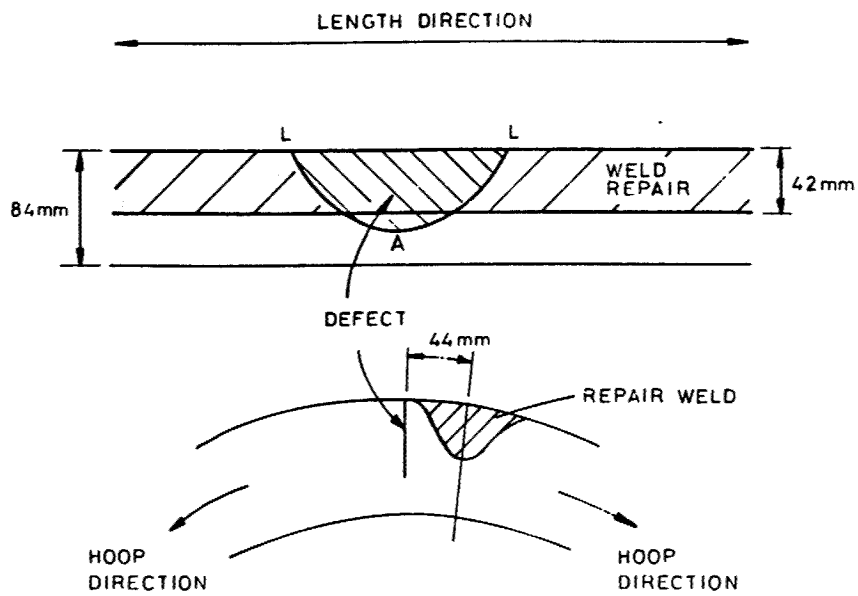

Figure B5.5 Location of the flaw in the CEGB Test 3 pressure vessel with respect to the weld repair. The flaw was in a stress relieved seam weld.

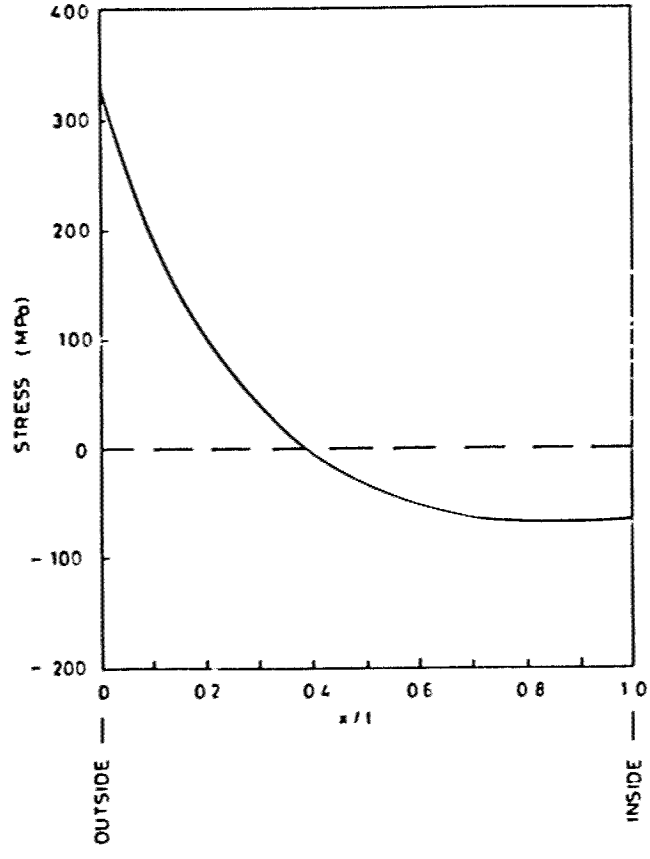

Figure B5.6 Typical profile of residual stress across crack plane in CEGB pressure vessel Test 3.

Tensile Data

Tensile data for the A533B steel and the weld metal were available from Knee [86] in the form of a stress-strain curve. To facilitate the present analysis, these curves were fitted by Ramberg-Osgood laws. The results for the base metal are: σ_o^{base}=556 MPa, α^{base}=1.677, n^{base}=17.7, σ_y^{base}= 556 MPa, with an ultimate strength of 686 MPa. The results for the weld metal are: σ_o^{weld}=357 MPa, α^{weld}=2.166, n^{weld}=10.3, σ_y^{weld}=357 MPa, with an ultimate strength 544 MPa. Young's modulus for both metals is taken as E=210,000 MPa. It can be seen that the weld is under-matched and, from Table A4.4, the failure curve for use in proof test analysis involves both weld and base metal properties, while the failure curve for use under service conditions involves only weld metal properties.

J-R Curves

Knee [86] also provides a *J-R* curve for the weld metal measured using a compact tension specimen following procedures similar to those detailed in ASTM Standard E1152. It is judged that the thickness of the pressure vessel is sufficient for these test data to be regarded as structurally relevant toughness data for proof test analysis purposes.

The toughness data presented by Knee [86] were fitted by a quadratic polynomial [compare equation (B4.7)] where the values of the coefficients, J_0, J_1, and J_2, are defined in Table B5.5, where the J_{mat}, values correspond to J_R evaluated at Δa_{min}.

Table B5.5 Characterization of the structurally relevant toughness of A533B steel

J_{mat}, MPa m (ksi inch)	J_0 MPa m (ksi inch)	J_1 MPa m/mm (ksi)	J_2 MPa m/mm^2 (ksi inch^{-1}	Δa_{min} mm (inch)	Δa_{max} mm (inch)
0.3177 (1.810)	0.276 (1.573)	0.2087 (30.21)	-0.004507 (-16.58)	0.20 (0.00787)	10.45 (0.411)

Stress Intensity Factor Solutions

As in Section B4.2.3, the KCALC software module developed by SwRI was used to determine the stress intensity factors for the flaw. In the present case, R_m/t=6.54 (549.5/84).

Net Section Yield Pressures

The same net section yield pressure is used as defined by equation (B4.9).

B5.3.3 Determination of Constant Load Locus

The results of the calculations are displayed in Figure B5.7 in the form of a constant load locus generated for the measured instability pressure. It can be seen that this locus falls just inside the proof test failure curve and outside the service failure curve, as required for conservative proof test and service analyses, respectively.

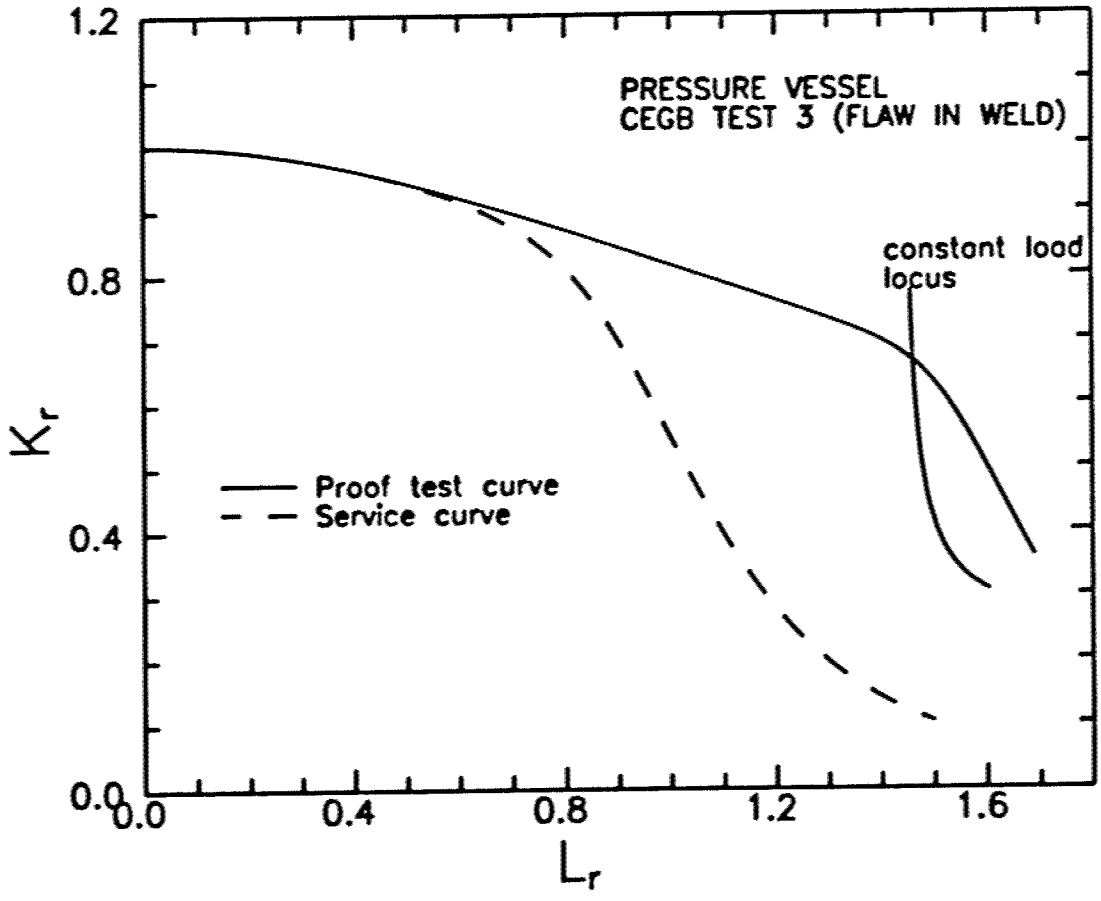

Figure B5.7 Constant load locus evaluated at the measured instability pressure for CEGB Test 3 compared to material specific failure curves for use in proof test and service analyses.

B6. LABORATORY VALIDATION: EFFECT OF PROOF TEST OVERLOAD ON SUBSEQUENT SERVICE FATIGUE AND FRACTURE BEHAVIOR

B6.1 Introduction

Laboratory tests have been performed at SwRI to verify some of the recommendations made in Sections 8.2 and 8.3 regarding the ramifications of proof test overloading on subsequent service assessments. The tests were performed on similar restrained single edge cracked plate (RSECP) specimens of IN-718 to those described in the validation testing reported in Sections B2 and B3. Some of the results of the simulated proof test loading have already been discussed in these sections as unloading compliance measurements were made during the overloading and the monitored load-displacement behavior used to derive the J_R-curves shown in Figure B2.7.

The present validation tests involved two types of loading scenarios with two specimens subjected to each scenario. In the first scenario two specimens (designated 3.1.B and 3.2.B) were subjected to a simulated proof test overload followed by simulated service cycling until failure by fatigue crack propagation occurred (Figure B6.1). The service cycling was performed at a maximum cyclic load of approximately 85% of the overload, and at an R ratio (minimum load/maximum load) of nearly zero. In the second scenario, two specimens (designated 2.1.B and 2.2.A) were cycled to failure at 85% of the proof overload used in the first scenario, but without the overload being applied (Figure B6.2). This scenario simulated service cycling in the absence of a proof test overload. The four tests performed in the two scenarios were intended to demonstrate the effects of the proof overload on subsequent service fatigue and fracture behavior by enabling measured fatigue lives with and without the simulated proof overload to be compared.

B6.2 Scenario 1: Simulated Proof Overload Followed by Service Cycling to Failure

The load level chosen for the proof overloads was designed to induce ductile tearing. The overloading was performed under displacement control to avoid fracturing the specimens. The overload tests were stopped and the specimens unloaded as soon as possible following the attainment of a maximum load (see Figure B6.1). Under load control, the maximum load would coincide with the critical load needed to produce ductile instability. Hence, after the overloading the specimens contained cracks that had been on the point of incipient instability under the maximum proof load conditions. This is the assumed state of hardware used in a safe-life analysis based upon hypothetical initial flaws whose sizes have been calculated to just survive the proof test using a fracture mechanics based analysis. After the overload, the specimens were cycled to failure under load control.

The dimensions of the two specimens, 3.1.B and 3.2.B, are shown in Table B6.1. Also shown in the table are the initial crack depths, c_i, in the specimens at the start of the proof loading, the final crack depths, c_f, immediately after the proof overload had been applied, the proof load, P_{proof}, and the maximum cyclic load, $P_{service}$, applied during the subsequent simulated service cycling. The initial and final crack depths were measured on the fractured surfaces of the specimens with the aid of an optical microscope after the tests had been completed. These measurements were facilitated by clear demarcations on the fractured surfaces showing where tearing that occurred during the proof overload changed to fatigue crack growth at the start of the service cycling. The difference between c_i and c_f is due to crack extension by ductile tearing during the proof loading. These tear lengths are shown in Table B6.1.

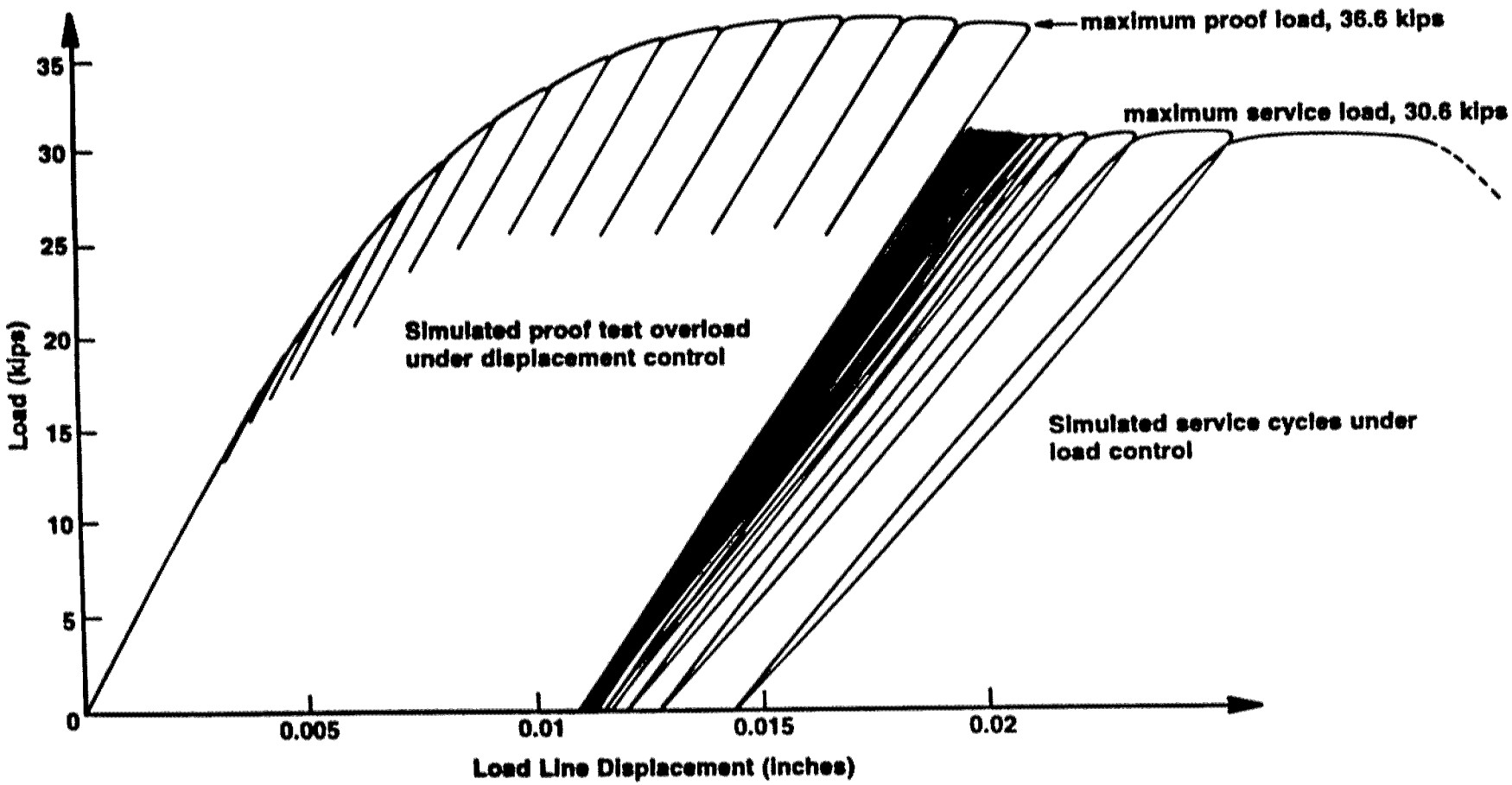

Figure B6.1 Load displacement trace for specimen 3.1.B illustrating a simulated proof test overload followed by continuous simulated service cycling to failure.

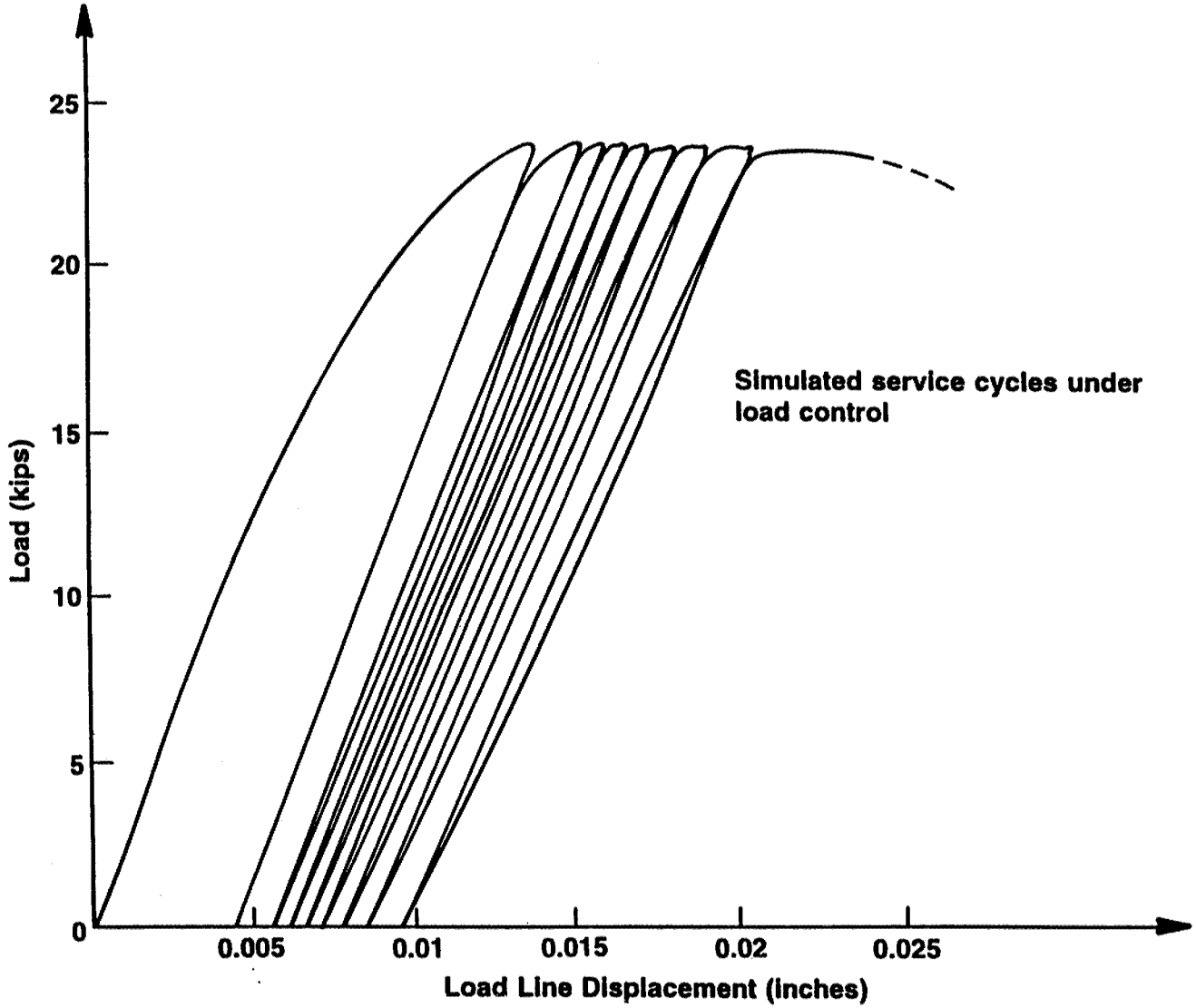

Figure B6.2 Load displacement trace for specimen 2.1.B subjected to simulated service cycles under load control.

Table B6.1 Data measured in the tests to investigate the effect of simulated proof test overload on subsequent service lifetime

Spec. No.	Spec. width inch (mm)	Spec. thickness inch (mm)	Initial crack depth, c_i inch (mm)	Final crack depth, c_f inch (mm)	Tear length inch (mm)	Proof load, P_{proof} kips (kN)	Service load, $P_{service}$ kips (kN)	$\sigma_{net}^{service}$ ksi (MPa)	Initiation load, P_{init} kips (kN)	σ_{net}^{init} ksi (MPa)	J_{mat} ksi inch (MPa m)	J_{proof} ksi inch (MPa m)
3.1.B	0.4980 (12.65)	1.003 (25.48)	0.2735 (6.947)	0.3159 (8.024)	0.0424 (1.077)	36.6 (162.8)	30.2 (134.3)	165.4 (1140)	31.2 (138.8)	138.6 (956)	0.673 (0.118)	2.550 (0.448)
3.2.B	0.2466 (6.26)	0.998 (25.35)	0.1530 (3.886)	0.1686 (4.282)	0.0156 (0.3962)	16.3 (72.5)	14.0 (62.3)	179.8 (1240)	15.2 (67.6)	162.7 (1122)	0.674 (0.118)	1.620 (0.284)
2.1.B	0.4890 (12.42)	1.001 (25.43)	0.3478 (8.834)	n/a	n/a	n/a	24.0 (106.8)	n/a	n/a	n/a	n/a	n/a
2.2.A	0.2504 (6.360)	1.001 (25.43)	0.1674 (4.252)	n/a	n/a	n/a	13.7 (60.9)	n/a	n/a	n/a	n/a	n/a

As previously mentioned, the overload part of the scenario was used to derive J_R-curves for each of the specimens. The values of J at the initiation of ductile tearing, J_{mat}, and at the maximum proof load, J_{proof}, derived from the J_R measurements are also shown in Table B6.1, as are the measured loads at the initiation of tearing, P_{init}.

The observed number of simulated service cycles to failure following the proof overload for specimens 3.1.B and 3.2.B are shown in Table B6.2. It is clear in Figure B6.1 that the initial cyclic displacement response of the specimens immediately following the overload was linear, even though the net section stresses, $\sigma_{net}^{service}$, at the maximum service loads, $P_{service}$, exceeded the net section stresses, σ_{net}^{init}, at the loads, P_{init}, at which tearing commenced during the overload, where

$$\sigma_{net}^{service} = \frac{P_{service}}{t(w - c_f)} \ , \ \sigma_{net}^{init} = \frac{P_{init}}{t(w - c_i)} \qquad \text{(B6.1)}$$

(see Table B6.1). This indicates that tearing was suppressed during the initial service cycling since an increase in crack depth would produce a change in specimen stiffness and non-linear displacement behavior. It is only after a number of cycles have been applied that non-linear deformation begins to appear in the load-displacement traces indicating the re-initiation of tearing. This behavior had been anticipated based on load history effects observed in tear-fatigue tests performed on steels. These tests had indicated that tearing is suppressed during cyclic loading if J_{max} was reduced, even though the new value of J_{max} exceeded J_{mat}.

Table B6.2 Measured and predicted cycles to failure

Spec. No.	Measured cycles to failure	Predicted tear-fatigue cycles to failure		Predicted fatigue cycles to failure	
		Lower J_R-curve	Upper J_R-curve	Equation (B6.4)	Equation (B6.4) ×4
3.1.B	27	n/a	n/a	n/a	n/a
3.2.B	36	n/a	n/a	n/a	n/a
2.1.B	9	1	7	256	64
2.2.A	17	1	44	332	83

B6.3 Scenario 2: Simulated Service Cycling to Failure Without a Proof Load

The maximum cyclic load levels in specimens 2.1.B and 2.2.A were designed to initiate tearing on the first load cycle and the cyclic hystereitic behavior observed immediately following the first loading to maximum load substantiates that this intent was achieved (Figure B6.2). The load-displacement behavior shown in Figure B6.2 contrasts with the cyclic behavior seen after the overload (Figure B6.1). The number of measured cycles to failure in the service cycle tests are presented in Table B6.2.

B6.4 Comparison of Scenario 1 and Scenario 2 Fatigue and Fracture Behaviors

It can be seen from the results shown in Table B6.2 that the effect of the proof overload is to increase the number of cycles to failure compared with the specimens where the proof loading was not applied. This is because the effect of the proof overload is to suppress tearing in the early part of the service cycles, whereas ductile tearing and fatigue crack extension are occurring simultaneously in the tests where the overload was omitted.

In the work by Nix et al. [87], a change in the test conditions was made from load control to control by maintaining a constant level of cyclic plastic work. This produced a corresponding change in the applied J_{max} values at the end of each cycle from values that increased with each cycle (dJ_{max}/dN increasing) before the change, to values that remained nominally constant ($dJ_{max}/dN=0$) after the change. The suppression of tearing produced by this change in test conditions is consistent with the predictions of simple tear-fatigue models which assume that crack extension per cycle due to cyclic load changes and ductile tearing are linearly additive. In these models, the enhanced fatigue crack growth rate due to ductile tearing, dc/dN, can be described through the equation

$$\left(\frac{dc}{dN}\right) = \left(\frac{dc}{dN}\right)_f + \frac{\left(\frac{dJ_{max}}{dN}\right)}{\left(\frac{dJ_{max}(\Delta c_t)}{d(\Delta c_t)}\right)} \tag{B6.2}$$

where $(dc/dN)_f$ is the fatigue crack growth rate in the absence of tearing, and $J(\Delta c)$ is the toughness value measured in terms of J at the tear length Δc_t (see Section D2.2).

The models assume that during crack extension the material at the crack tip retains a history of the deformation that has occurred within the fracture process zone. In other words, the ductile fracture process zone at the crack tip advances with the crack and is not re-generated as the tip extends by fatigue. While dJ_{max}/dN is increasing, crack stability considerations dictate that J_R must equal J_{max}, and hence

$$J_R(\Delta c_t) = J_{max}(c_i + \Delta c_f + \Delta c_t) \tag{B6.3}$$

where c_i is the initial crack depth, and Δc_f is the total amount of fatigue crack growth up to the present time. Further tearing will not occur at maximum load during the current cycle if J_{max} does not exceed its value in the previous cycle because, from equation (B6.3), the instantaneous toughness is given by the value of J_{max} that occurred during the previous cycle.

The tear-fatigue model described above immediately explains why tearing was initially suppressed in tests 3.1.B and 3.2.B during load cycling following the simulated proof overload: the reduction in maximum load after the overload produced a corresponding reduction in J_{max} to a level well below the value of J_R at the end of the proof loading. However, it is clear from the load-load line displacement traces in Figure B6.1 that tearing was re-initiated after some number of cycles following the beginning of simulated service cycling. Since J_{max} increases during crack extension resulting from

the service cycling, this re-initiation event is not unexpected as the crack tip advances by fatigue crack growth through the fracture process zone formed during the proof overload.

Calculations were performed to predict tear-fatigue in RSECP specimens based on equation (B6.2). In these the applied value of J at the maximum load, J_{max}, was estimated using the IN-718 material specific J estimation scheme. The fatigue crack growth law used to predict $(dc/dN)_f$ was

$$\left(\frac{dc}{dN}\right)_f = 0.5 \times 10^{-10}(\Delta K)^{3.15} \; inch/cycle \qquad \text{(B6.4)}$$

where ΔK is the cyclic change in the stress intensity factor between minimum and maximum load. Growth rates predicted from equation (B6.4) are approximately 0.5 times slower than the average growth rates for IN-718 reported in NASA Contractor Report 4318 [14]. However, equation (B6.4) is consistent with estimates of fatigue crack growth rates made during pre-cracking of two of the RSECP specimens tested in the current program.

In tests 2.1.B and 2.2.A, concurrent ductile tearing and fatigue crack extension occurred during the first cyclic load changes. The J_R-curves for these two specimens can be estimated from the J_R-curves that have been measured on other specimens tested as part of the laboratory proof test verification program (see Figure B2.7). Upper and lower bounding J_R-curves derived from these data were used in the prediction of the tear-fatigue behavior of specimens 2.1.B and 2.2.A. The predicted number of cycles to failure based on tear-fatigue and fatigue are shown in Table B6.2 where they can be compared with the experimentally measured values. The designation lower and upper for the tear-fatigue predictions refers to use of the lower and upper bound J_R-curves in equation (B6.2). In both cases, the fatigue component of growth was evaluated according to equation (B6.4). The designation upper in the fatigue predictions refers to the use of growth rate equal to 4 times that predicted by equation (B6.4). The rate predicted by equation (B6.4) and the upper rate approximately bound the fatigue rates reported in NASA Contract Report 4318.

The predicted results presented in Table B6.2 substantiate the observation based on the measured load displacement traces that tear-fatigue occurred in both specimens during the service cycle simulations. Whereas the measured cycles to failure fall within, or only just outside, the predicted range of cycles based on lower and upper J_R-curves, the fatigue predictions considerably overestimate the measured cycles to failure. Comparing the measured cycles to failure in Table B6.2, it is clear that the proof overload has beneficially increased the number of service cycles required to cause failure with respect to the cycles applied without the proof overload.

It is not possible to make precise predictions on the number of cycles to failure in the two specimens that were subjected to a simulated proof test overload prior to service cycles without making assumptions concerning the effect of the overload on the subsequent toughness and fatigue crack growth rate behaviors. However, as previously observed, the overload appeared to suppress tearing during the service cycles applied immediately following the overload, which would indicate that the effective toughness at the start of service exceeded the initiation value, J_{mat}

To demonstrate this point, and to emphasize the beneficial effect conferred on subsequent fracture behavior by application of the proof test overload, a set of calculations was made to determine the critical crack size, and critical load, which would result in failure at the start of the service cycling in specimens 3.1.B and 3.2.B. The results of these calculations are shown in Table B6.3, together with the measured values extracted from Table B6.1. The predicted values were calculated using the IN-718 specific J estimation scheme and the J_R-curves for each specimen which were measured during the proof test overload.

It can be seen from Table B6.3 that the predicted load at ductile instability in the absence of the proof test overload is less than the applied (measured) maximum service load calculated for the crack depth at the start of the service cycles. Furthermore, the predicted critical crack depth for the applied (measured) service load is less than the crack depth at the start of the service cycles. These results predict that the specimens 3.1.B and 3.2.B should have failed on first application of the service cycle maximum load following the proof overload. The fact that they did not, and that a significant number of cycles were necessary before failure did occur, is a demonstration of the beneficial effect of the proof test overload on IN-718 when this load results in ductile crack extension. This is a very significant conclusion because it implies that for IN-718 (and, by inference, other ductile materials) the proof test overload does not impair subsequent fracture performance, but may actually enhance the material's resistance to ductile crack extension under service loading immediately following a proof test.

Table B6.3 Calculated critical conditions at the start of service cycling in the absence of the proof test overload

Spec. No.	Initial crack depth, c_i inch (mm)	Predicted critical crack depth inch (mm)	Service load, $P_{service}$ kips (kN)	Predicted instability load kips (kN)
3.1.B	0.3159 (8.024)	0.3126 (7.94)	30.2 (134.3)	29.3 (130.3)
3.2.B	0.1686 (4.28)	0.1677 (4.26)	14.0 (62.3)	13.5 (60.0)

B6.5 Conclusions

1. The fracture resistance (J_R-curves) of flaws that enter service after tearing during the proof test is at least equal to the fracture resistance of the same sized flaws that enter service without undergoing the proof test overload. Hence, it is conservative for service analyses to ignore the effect of the proof test on ductile fracture behavior.

2. Similarly, it is conservative to ignore the effects of the proof overload on subsequent fatigue crack growth rates during service as the overload suppresses tear-fatigue under service loading immediately following the overload.

APPENDIX C: EXAMPLE PROOF TEST ANALYSES

The Road Map detailed in Section 6.1 of the main text is illustrated by two example proof test analyses. Both of the examples are hypothetical, and illustrate how the Road Map can provide guidance to the analyst by highlighting the important stages that should be addressed in typical proof test analyses. In the first example, a brittle failure analysis of a cracked longitudinal seam-weld in a ferritic steel pressure vessel is performed. In this example, the proof test load is specified and the flaw screening capability of the test is determined. In the second example, a ductile failure analysis of an axial flaw in a space shuttle main engine (SSME) high pressure oxidizer duct is performed. In this case, a flaw of a specified depth is assumed to be present in the hardware and the minimum proof load needed to screen for this flaw is calculated. The minimum proof load analysis is supported by a leak-before-burst analysis in order to assess the possible consequences of failure during the proof loading.

Sections C1 and C2 take the reader stage by stage through brittle and ductile analyses, respectively, according to the Road Map presented in Figure 6.1.

C1. EXAMPLE 1: SEAM-WELDED PRESSURE VESSEL: FLAW SCREENING

Stage 1: Hardware Definition: The hardware is a ferritic steel pressure vessel that contains a 600 mm long stress-relieved longitudinal seam-weld. The pressure vessel has an outer diameter of 533.4 mm (21 inch) and a wall thickness of 25.4 mm (1 inch). The operating temperature of the vessel could be below 0°C, which is below the ductile-brittle toughness temperature of the steel.

Stage 2: Safe-Life Analysis (Fracture Critical Regions): The seam-weld is considered to be a fracture critical region.

Stage 3: Proof Test Conditions: The proof test will take place at 0°C under internal pressure in order to simulate service conditions. The vessel will be hydraulically pressurized up to the proof pressure over a period of 5-10 minutes. The hold time at the maximum pressure will be two minutes. Time-dependent effects are not expected to be significant at 0°C. The vessel is cooled prior to the start of the test by ice on the outside.

Stage 4: Material Properties (Mechanical): At the proof test temperature of 0°C, the base and weld materials have the tensile properties displayed in Table C1.1. The stress-strain behaviors of weld and base metals have been represented by Ramberg-Osgood laws. In both cases, the yield stress and the Ramberg-Osgood characteristic yield stress, σ_o, are equal. The weld is over-matched.

Stage 5: Stress Analysis: The seam-weld is subjected to the hoop stress due to the internal pressure. This stress can be simply estimated as $R_m P/t$, where R_m is the mean radius. The weld is stress relieved after fabrication. Although there are expected to be residual stresses still remaining, these are likely to be small compared to the pressure stresses. It is conservative to ignore the residual stresses in the proof test analysis because in the present example they are assumed to be tensile in the region of the screened flaws. Hence, only the pressure stresses are needed.

Stage 6: Material Properties (Sub-critical Crack Growth): The proof test environment is considered non-aggressive so that sub-critical crack growth constants will not be required.

Table C1.1 Base and weld metal tensile properties

Property Value	Base Metal	Weld Metal
Young's Modulus	210,000 MPa (30,000 ksi)	210,000 MPa (30,000 ksi)
Poisson's Ratio	0.3	0.3
Yield Stress	490 MPa (70 ksi)	560 MPa (80 ksi)
Ultimate Strength	586 MPa (85 ksi)	620 MPa (90 ksi)
α	0.95	1.0
n	9.5	10.0
σ_o	490 MPa (70 ksi)	560 MPa (80 ksi)

Stage 7: Sub-critical Crack Growth: No sub-critical crack growth is anticipated during the proof test and up to the time the pressure vessel enters service.

Stage 8: Safe-Life Analysis (Critical Initial Flaw Sizes): A preliminary safe-life analysis indicates that all surface flaws that are longer than 50.8 mm (2 inch) and deeper than 12.5 mm (0.5 inch) could present a threat to the integrity of the pressure vessel over a lifetime equal to four times the service life. Hence the proof test analysis should encompass this range of surface flaws.

Stage 9: NDE: In this example it is assumed that no NDE will be performed on the pressure vessel prior to proof testing.

Stage 16: Primary Role: In the absence of NDE, the proof test will be the primary means of flaw screening.

Stage 18: Additional Analysis Input: A proof test analysis will be performed to determine the flaw screening capability, necessitating additional input.

Stage 19: Proof Load Requirements: Since the proof test is the primary flaw inspection technique, a proof load factor of 1.5 will be employed. This exceeds the minimum requirement of 1.2.

Stage 20: Proof Load: The operating pressure is 18.4 MPa (2.67 ksi). Therefore, the proof pressure will be 27.6 MPa (4 ksi).

Stage 21: Safe-Life Testing: The preliminary safe-life analysis reported in Stage 8 defines the types of flaws to be screened.

Stage 23: J Estimation/FAD: The flaws to be analyzed are axial surface defects in an over-matched longitudinal seam-weld. The loading is primary, and there are no geometrical discontinuities to be considered. In this case, J can be determined using a material specific estimation scheme where J has the form (compare equation (A4.31)

$$J(a,c,P) = J_e(a,c,P)\left[1 + \frac{0.5\left[\frac{P}{P_o^{weld}}\right]^2}{1 + \alpha^{weld}\left[\frac{P}{P_o^{weld}}\right]^{n_{weld}-1}} + 0.6107\,\alpha^{weld}\left[\frac{P}{P_o^{weld}}\right]^{n_{weld}-1}\right] \qquad \text{(C1.1)}$$

where, from Table A4.2, $V^* = 0.824V = 0.6107$ for a proof test analysis in plane strain. $J_e(a, c, P)$ can be evaluated from K^2/E'. Although the K values can be obtained from NASGRO geometry SC04, longitudinal surface flaws in hollow cylinders, they were determined using the SwRI computer program, KCALC. P_o^{weld} is given by [see equation (B4.9) of Appendix B]

$$P_o^{weld} = \frac{\sigma_o^{weld}\,t}{R_m}\,\frac{\left[1 - \frac{a}{t}\right]}{\left[1 - \frac{a}{t}/M(\rho, a/t)\right]} \qquad \text{(C1.2)}$$

where a is the crack depth, $2c$ is the surface length of the flaw and

$$M(\rho, a/t) = \left(1 + 1.05\,\frac{a}{t}\,\rho^2\right)^{\frac{1}{2}}, \quad \rho = \frac{c}{\sqrt{R_m t}} \qquad \text{(C1.3)}$$

The corresponding equation for the material specific failure curve is [compare equation (A5.11)]

$$K_r^* = \left[1 + \frac{0.5\left[L_r^*\right]^2}{1 + \alpha^{weld}\left[L_r^*\right]^{n_{weld}-1}} + 0.6107\,\alpha^{weld}\left[L_r^*\right]^{n_{weld}-1}\right]^{-\frac{1}{2}} \qquad \text{(C1.4)}$$

<u>Stage 24: Failure Mechanism</u>: Under proof test conditions, the ferritic steel will fail by a brittle mechanism.

<u>Stage 25: Material Properties (J_{mat})</u>; An upper bound estimate of the fracture toughness at 0°C is 66 MPa $m^{1/2}$ (60 ksi $inch^{1/2}$). Plane strain conditions are considered appropriate for the pressure vessel and hence J_{mat} = 0.0191 MPA m (0.109 ksi inch).

<u>Stage 26: Analysis Type</u>: A flaw screening analysis is required.

Stage 27: Instability Crack Size: The critical crack depths for specified surface flaw lengths can be determined from a J analysis as described in Section A10.1. The deepest point on the defect has the highest J value. The results of a typical J calculation are shown in Figure C1.1 for a fixed surface flaw length of 101.6 mm (4 inch) and varying crack depths. The critical crack depth is obtained when $J = J_{mat}$ = 0.0191 MPa m which, in this case, gives a critical crack depth of 9.46 mm (0.372 inch).

The critical crack depths can also be obtained from a FAD based analysis (see Section A10.2). The failure curve for the weld metal defined by equation (C1.4) is shown in Figure C1.2. Also shown are failure assessment points evaluated for a range of crack depths at the proof pressure. The assessment points are evaluated from the equations

$$L_r = \frac{P}{P_y(a,c)} \ , \ K_r = \frac{K(a,c,P)}{K_{mat}} \qquad \text{(C1.5)}$$

The critical crack depth is the one that produces an assessment point that falls on the failure curve. This crack depth is also 9.46 mm, consistent with the J analysis result.

Stage 28: Flaw Screening Diagram: The results of performing the critical crack depth analyses described in Stage 27 as a function of various flaw surface lengths, $2c$, are shown in Figure C1.3. This figure is the flaw screening diagram for the example analysis. As stated in Stage 8, the safe-life analysis requires that all flaws that are longer than 50.8 mm ($2c/t$=2) and deeper than 12.5 mm (a/t=0.5) be screened by the proof test. It can be seen from Figure C1.3 that this requirement is not quite attained for the specified proof factor of 1.5 as flaws which have depths greater than 12.5 mm and surface lengths less than 63.5 mm ($2c/t$=2.5) are predicted to survive the proof test. Hence, the proof factor will have to be increased above 1.5 to ensure the required safe-life for the pressure vessel. The results of increasing the factor to 1.65 are also shown in Figure C1.3 and this increase can be seen to increase the flaw screening capability so that the required safe-life can be met.

C2. EXAMPLE 2: HIGH PRESSURE OXIDIZER DUCT: MINIMUM PROOF PRESSURE

Stage 1: Hardware Definition: The hardware is a nickel-based superalloy (IN-718) high pressure oxidizer duct used in the SSME. This duct is similar to the one used in the hardware validation tests described in Section B4. It is assumed that the section of the duct most at risk is a straight section which has the thinnest wall and hence experiences the highest stresses arising from internal pressurization. According to design drawings, the duct has an outer diameter of 107.4 mm (4.228 inch) and a minimum wall thickness of 2.896 mm (0.114 inch). However, non-destructive measurements of the wall indicate that the actual thickness is 3.556 mm (0.140 inch), significantly greater than the minimum. The measured dimensions have to be used in a proof test analysis as the design minimum value would result in an over-estimate of the pressure stresses and result in a non-conservative (low) estimate of the minimum proof pressure needed to screen flaws of specified sizes.

Stage 2: Safe-Life Analysis (Fracture Critical Regions): The straight section of the duct is considered to be a fracture critical region.

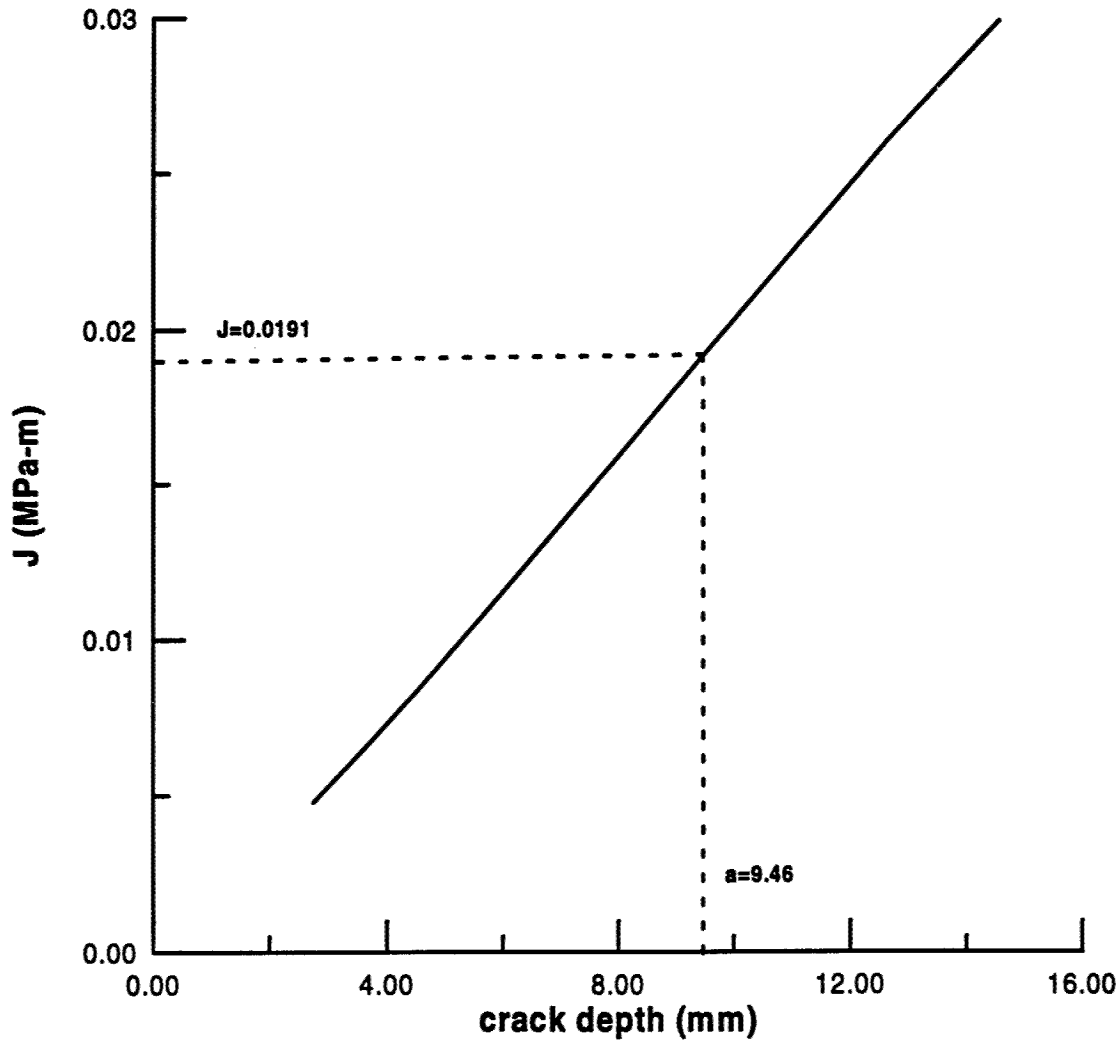

Figure C1.1 Example 1: Applied J as a function of crack depth.

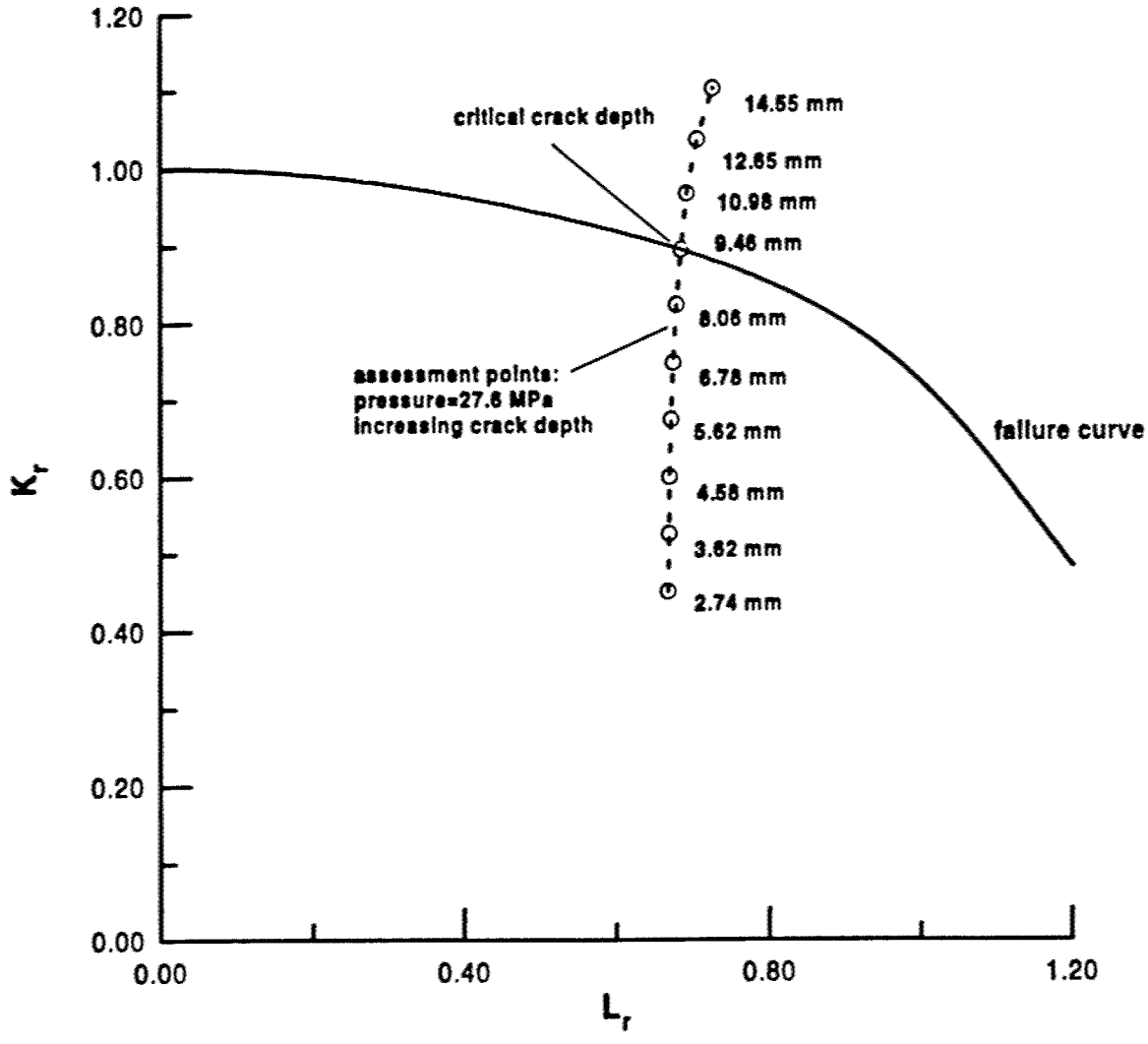

Figure C1.2 Example 1: Critical crack depth determined from the FAD.

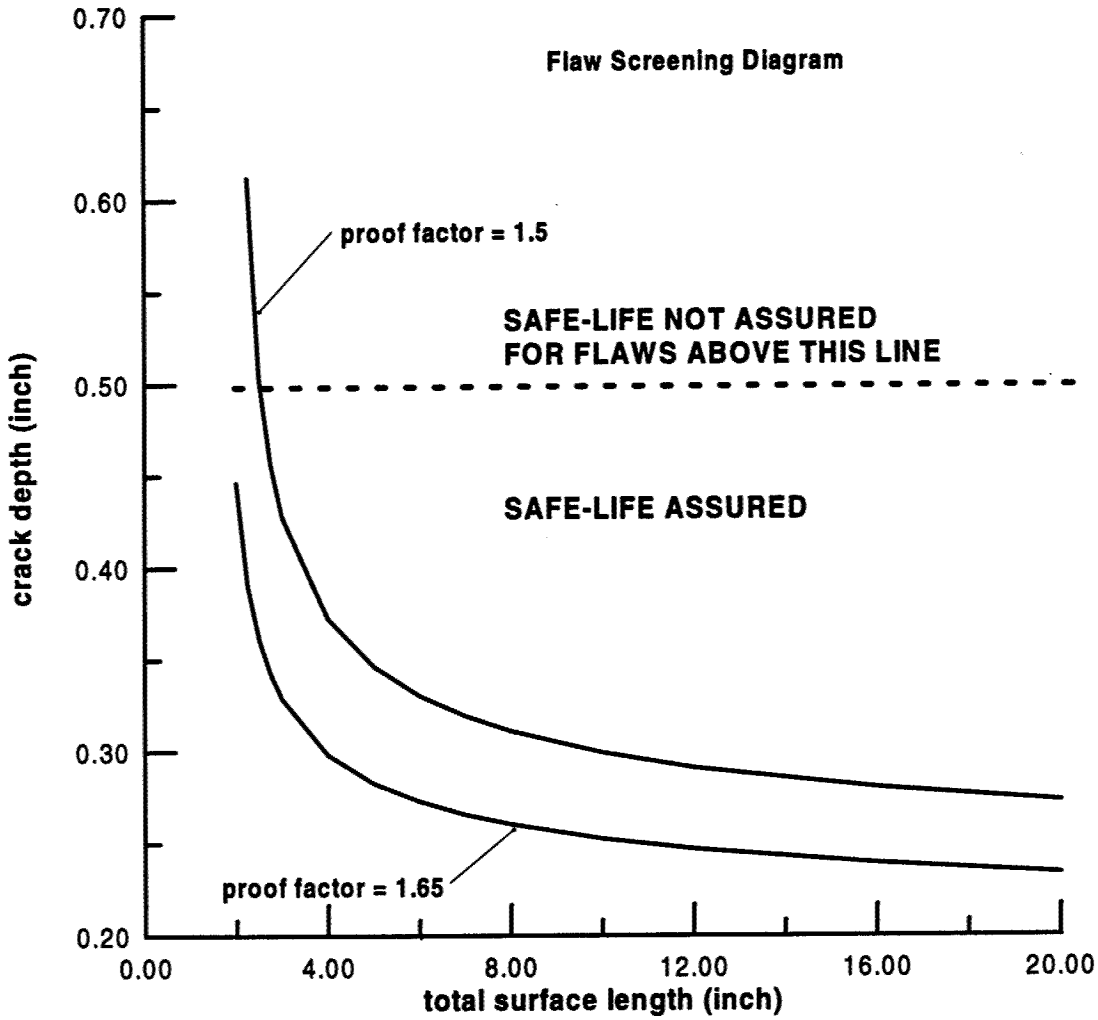

Figure C1.3 Example 1: Flaw screening diagram.

Stage 3: Proof Test Conditions: The proof test will take place at ambient temperature under internal pressure. The vessel will be hydraulically pressurized up to the proof pressure over a period of 5-10 minutes. The hold time at the maximum pressure will be 30 seconds, which is considered sufficient to stabilize the pressure while avoiding time-dependent effects.

Stage 4: Material Properties (Mechanical): The measured tensile properties of IN-718 at the proof test temperature are displayed in Table C2.1. The engineering stress-strain data are represented by a Ramberg-Osgood law. In this material, the measured yield stress is not equal to the Ramberg-Osgood parameter, σ_o.

Table C2.1 Tensile properties for IN-718

Property	Value
Young's Modulus	210,000 MPa (30,000 ksi)
Poisson's Ratio	0.3
Yield Stress	1112 MPa (161.2 ksi)
Ultimate Strength	1417 MPa (205.5 ksi)
α	1.0
n	15.8
σ_o	1240 MPa (179.8 ksi)

Stage 5: Stress Analysis: The duct is subjected to the hoop stress due to internal pressure. This stress can be simply estimated as $R_m P/t$.

Stage 6: Material Properties (Sub-critical Crack Growth): The proof test environment is considered non-aggressive so that sub-critical crack growth laws will not be required.

Stage 7: Sub-critical Crack Growth: No sub-critical crack growth is anticipated during the proof test and up to the time the duct enters service.

Stage 8: Safe-Life Analysis (Critical Initial Flaw Sizes): A preliminary safe-life analysis indicates that surface flaws that are deeper than 1.778 mm (0.07 inch) could present a threat to the integrity of the duct over a lifetime equal to four times the service life. Hence, the proof test analysis should assume a flaw of this depth is present.

Stage 9: NDE: A visual inspection of the duct has been performed, but no NDE instrumentation has been used.

Stage 10: NDE (Detected Flaw Sizes): NDE indicated a hair-line crack on the outside of the straight section of the duct that is 38.1 mm (1.5 inch) long. The inspection could not reveal the depth of this flaw.

Stage 11: Proof Role (Detected Flaws): Since the depth of the flaw could not be estimated, it is assumed that its depth could exceed the CIFS.

Stage 12: Primary Role: The proof test will likely be the primary means of flaw screening.

Stage 14: NDE Detection Capability: The visual inspection technique cannot provide any guidance on the flaw depth. No prior hardware sectioning had been performed, so defect sizes based on process control cannot be estimated or bounded.

Stage 15: Proof Roles (Undetected Flaws): Since the depth of the flaw is unknown, it has to be assumed to be larger than the CIFS.

Stage 16: Primary Role: The proof test will be the primary means of flaw screening for both the known defect and any undetected flaws that may be present.

Stage 18: Additional Analysis Input: A proof test analysis will be performed to determine the minimum proof pressure to ensure the required safe-life.

Stage 22: Initial Crack Sizes: It is assumed that a flaw which is 38.1 mm (1.5 inch) long and 1.778 mm (0.07 inch) deep is present in the duct. The needed safe-life cannot be guaranteed for flaws deeper than this.

Stage 23: J Estimation/FAD: The flaws to be analyzed are axial surface defects in a straight section of the duct where there are no geometrical discontinuities. In this case J can be determined using a material specific estimation scheme where J has the form:

$$J = J_e(a,c,P)\left[1 + \frac{0.5\left[\frac{P}{P_o}\right]^2}{1 + \alpha\left[\frac{P}{P_o}\right]^{n-1}} + 0.6107\,\alpha\left[\frac{P}{P_o}\right]^{n-1}\right] \qquad \text{(C2.1)}$$

where, from Table A4.2, $V^* = 0.824V = 0.6107$ for a proof test analysis in plane strain. $J_e(a,c,P)$ can be evaluated from K^2/E'. Although K values can be obtained from NASGRO geometry SC04, longitudinal surface flaws in hollow cylinders, it was determined using the SwRI computer program KCALC. P_o is given by [compare equation (C1.2)]

$$P_0 = \frac{\sigma_0 t}{R_m}\frac{\left[1 - \frac{a}{t}\right]}{\left[1 - \frac{a}{t}/M(\rho, a/t)\right]} \qquad \text{(C2.2)}$$

The corresponding material specific failure curve is

$$K_r^* = \left[1 + \frac{0.5\left[L_r^*\left(\frac{\sigma_y}{\sigma_o}\right)\right]^2}{1 + \alpha\left[L_r^*\left(\frac{\sigma_y}{\sigma_o}\right)\right]^{n-1}} + 0.6107\,\alpha\left[L_r^*\left(\frac{\sigma_y}{\sigma_o}\right)\right]^{n-1} \right]^{-\frac{1}{2}} \tag{C2.3}$$

where the ratio (σ_y/σ_o) appears because L_r^* is evaluated using the yield stress

$$L_r^* = \frac{P}{P_y} = \left(\frac{P}{P_o}\right)\left(\frac{\sigma_o}{\sigma_y}\right) \tag{C2.4}$$

Stage 24: Failure Mechanism: Under proof test conditions, the IN-718 duct will fail by a ductile mechanism.

Stage 31: Material Properties (J_R-Curve): An upper bound estimate of the J_R-curve at ambient temperature is needed. This upper bound curve has to be structurally relevant and reflect the low plastic constraint in the duct due to the very thin wall and the pressure loading. Suitable J_R-curve data are available based on fracture tests performed on relatively thin (6.35 mm) restrained edge cracked plate specimens. These data, expressed in the form of a quadratic polynomial in tear length

$$J_R(\Delta a_t) = J_0 + J_1 \Delta a_t + J_2[\Delta a_t]^2 \tag{C2.5}$$

are shown in Table C2.2. The lower and upper validity limits for this quadratic fit are shown as Δa_{min} and Δa_{max} in the table. Also shown is J_{max}, the value of J_R corresponding to a tear/blunting length of Δa_{min}.

Table C2.2 J_R-curve parameters

J_{max} MPA m (ksi inch)	J_o MPa m (ksi inch)	J_1 MPa m/mm (ksi)	J_2 MPa m/mm^2 (ksi inch^{-1})	Δa_{min} mm (inch)	Δa_{max} mm (inch)
0.191	0.0448	1.247	-0.884	0.1295	0.762
(1.088)	(0.255)	(180.5)	(-3250)	(0.0051)	(0.03)

Stage 32: Analysis Type: A minimum proof load analysis is required.

Stage 35: Critical Load: The determination of the critical pressure for the specified flaw size (a = 1.778 mm, $2c$ = 38.1 mm) from a J analysis is described in Section A9.3. The deepest point on the defect has the highest J value. A number of calculations have to be performed in order to determine the pressure which will result in the applied J curve becoming tangential to the J_R-curve, taking into account ductile tearing as the pressure increases. The calculated pressure to cause tearing will initially increase as the amount of tearing increases until the critical pressure is attained. To obtain stable tearing beyond this point, it is necessary to decrease the pressure. Hence, if increments of tearing are allowed and the corresponding pressure to produce these is calculated, these pressures will go through a maximum (the critical pressure) at the instability point, and then decrease with further tearing. An example of these kinds of calculations is shown in Figure C2.1. In this figure, applied J values evaluated using equation (C2.1) are shown as a function of increasing pressure for various crack depths equal to the initial depth, 1.778 mm, plus three increments of tear. The J_R values corresponding to each tear increment were obtained using equation (C2.5) and the coefficients in Table C2.2. The J_R value corresponding to the first increment of tear (0.152 mm) is 0.214 MPa m, and the pressure at which this J_R value is attained is 70.0 MPa. The J_R value for the second increment of tear (0.203 mm) is 0.261 MPa m and corresponds to a pressure of 70.1 MPa. The value of J_R for the third increment of tear (0.254 mm) is 0.304 MPa m and corresponds to a pressure of 69.6 MPa, which is below the previous two. In fact the maximum (critical) pressure is 70.1 MPa (see Figure C2.2 which shows the calculated pressures plotted against tear length).

The critical pressure can also be obtained from a FAD based analysis (see Section A9.4). The IN-718 material specific failure curve defined by equation (C2.3) is shown in Figure C2.3. Also shown are failure assessment points which form an assessment locus (A-B) for an arbitrarily chosen pressure of 34.5 MPa, where the assessment points are evaluated for increasing tear lengths using the equations

$$L_r(\Delta a_t) = \frac{P}{P_y(a + \Delta a_t, c)} \ , \ K_r(\Delta a_t) = \frac{K(a + \Delta a_t, c, P)}{K_R(\Delta a_t)} \qquad \text{(C2.6)}$$

where Δa_t is the tear length and a and $2c$ are the initial flaw size. The pressure needed to make each point on the assessment locus fall on the failure curve can be calculated as shown in Figure A9.1. The pressures obtained from this procedure are the same as those shown in Figure C2.2. The assessment locus, A'-B', shown in Figure C2.3 is calculated using the maximum (critical) pressure by ratioing each assessment point on A-B by OA'/OA=OB'/OB=70.1/34.5=2.03. As required, the locus is tangential to the failure curve showing that the pressure of 70.1 MPa is the critical pressure.

Stage 36: Proof Load Diagram: The minimum proof load is equal to the critical pressure of 70.1 MPa for the postulated flaw. Since only a single flaw was evaluated, it is not necessary to construct a proof load diagram.

The combined tearing and blunting at ductile instability due to the critical pressure is 0.203 mm from Figure C2.1, and this is the maximum extension that an existing flaw is predicted to undergo in order to be on the point of incipient fracture at the end of the proof test. Hence, an initial flaw

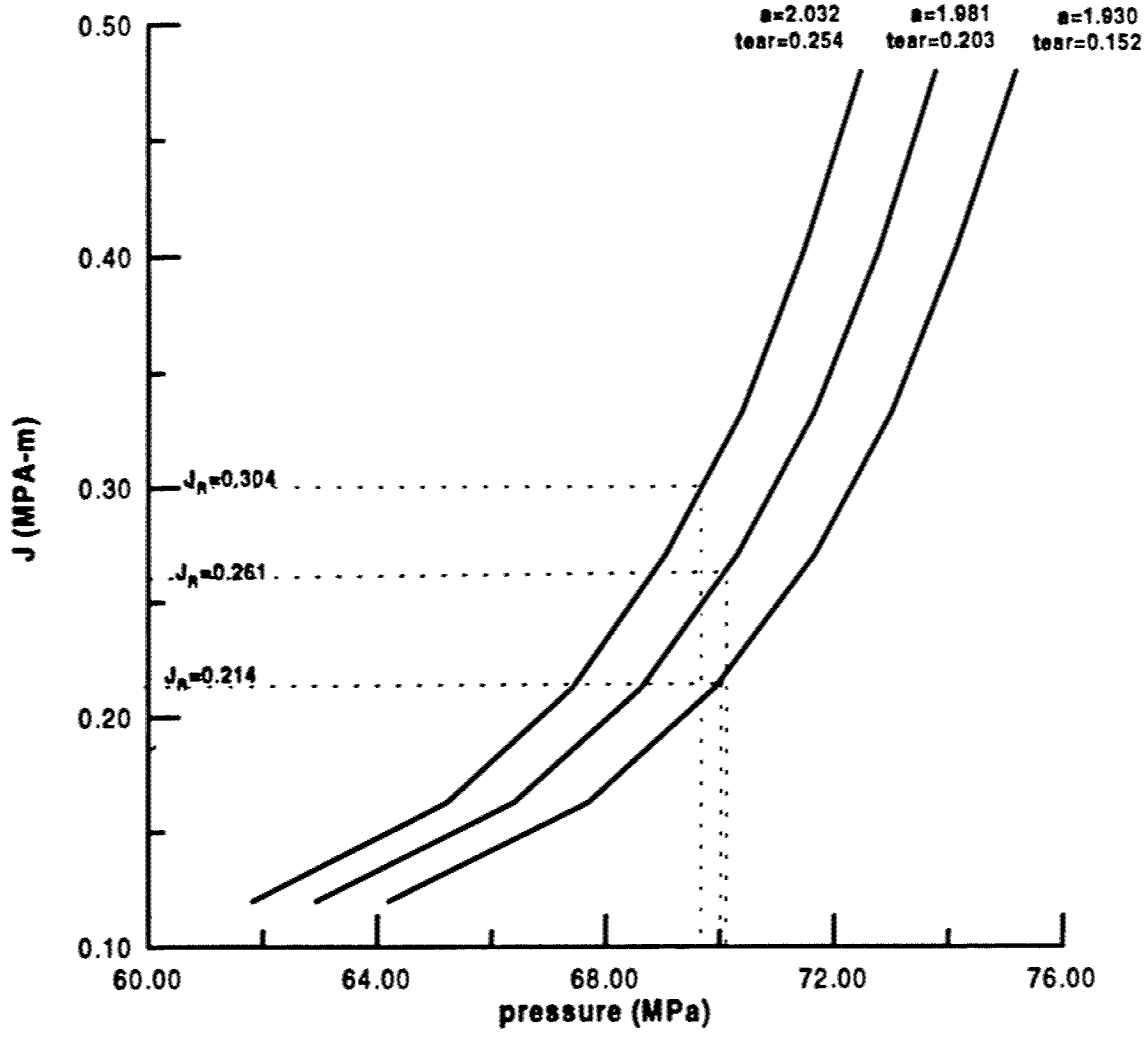

Figure C2.1 Example 2: Applied J values as a function of pressure for various tear lengths.

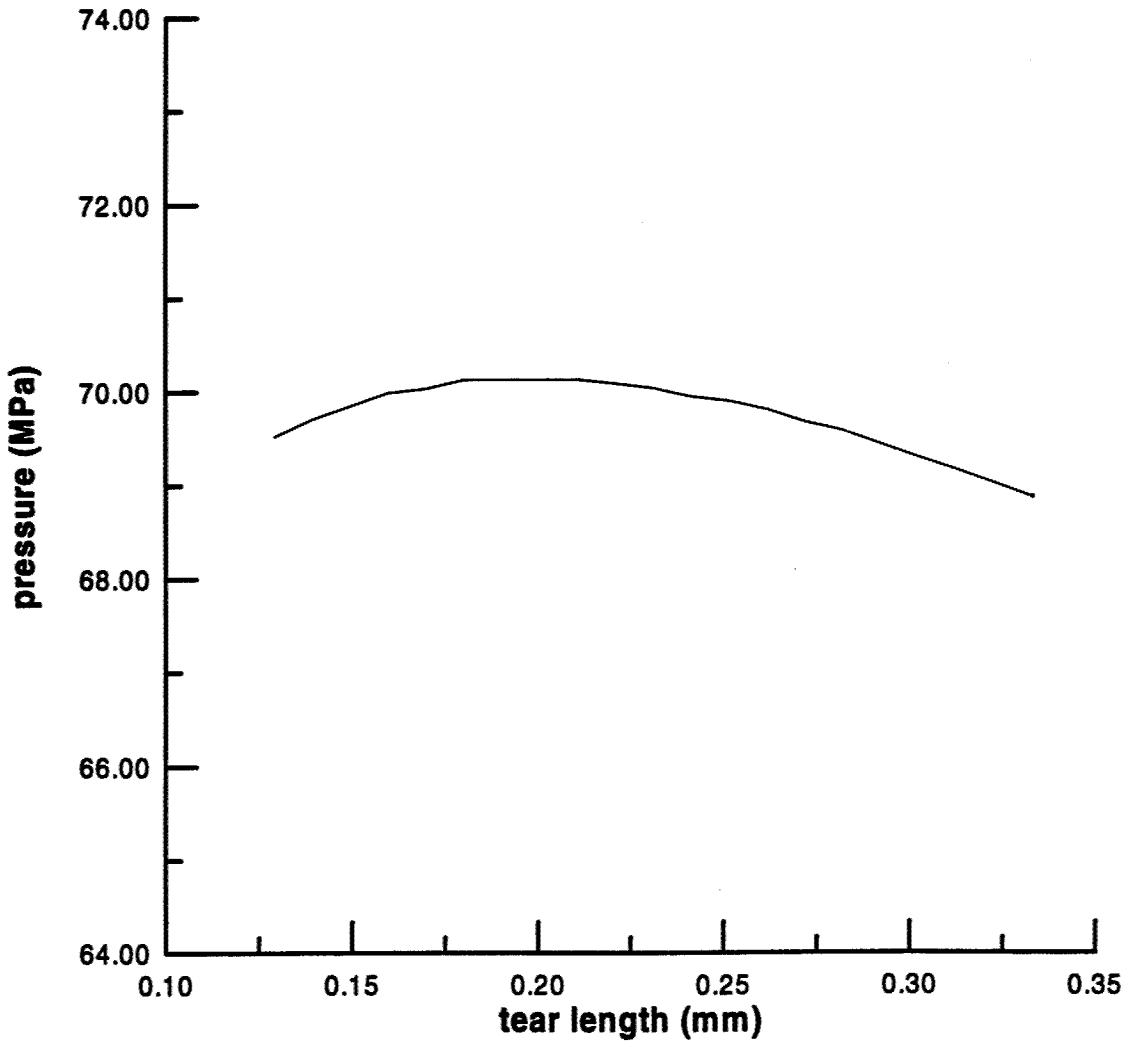

Figure C2.2 Example 2: Pressure as a function of tear length.

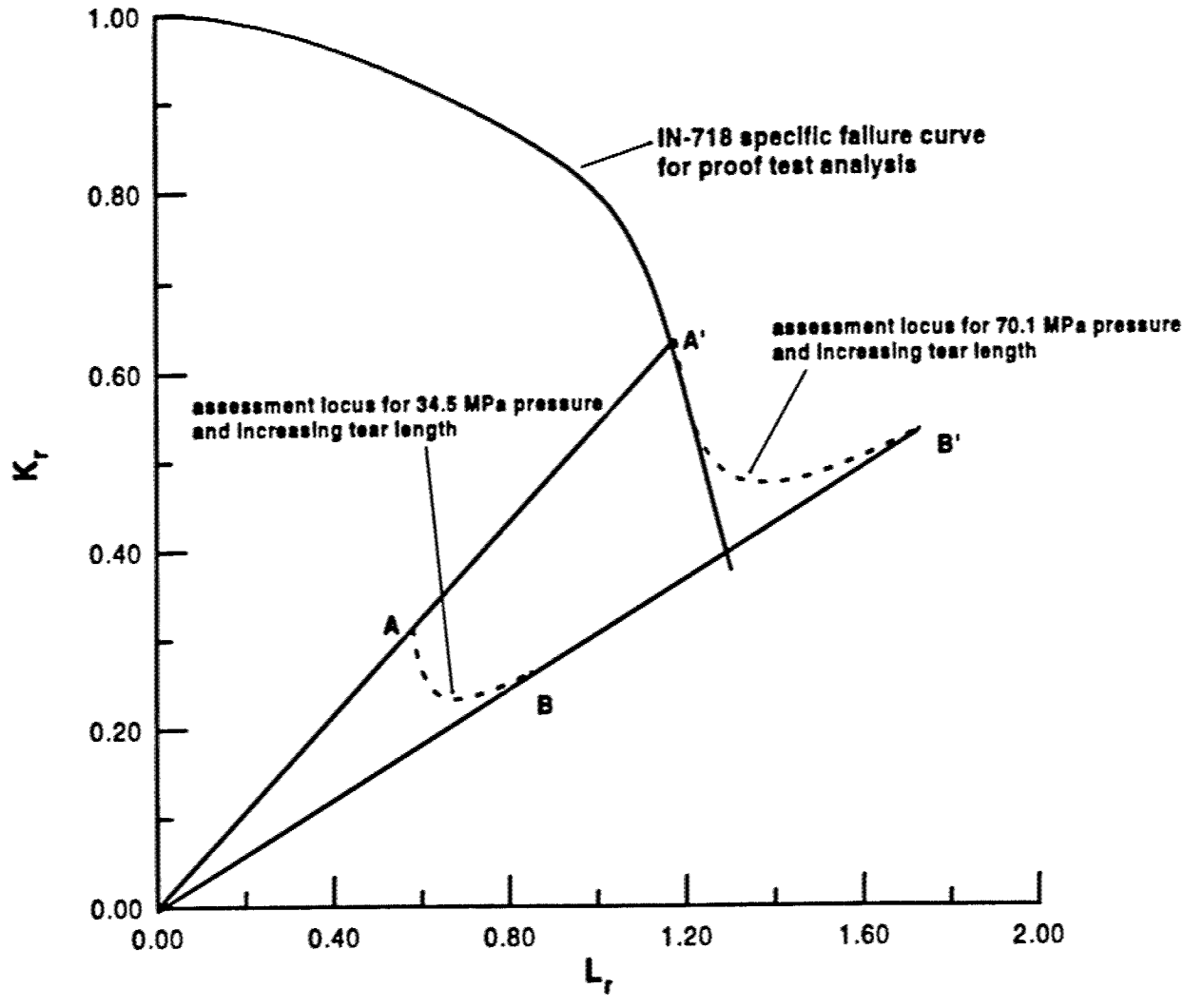

Figure C2.3 Example 2: Determining the minimum proof pressure using the FAD.

of depth 1.778 mm could grow to a depth of 1.981 mm by the end of the proof test. This new depth exceeds the maximum depth of 1.778 mm needed to ensure a safe-life (see Stage 8). Hence, it is necessary to determine a new minimum proof pressure based on an assumed initial flaw depth which is less than 1.778 mm. The critical pressure calculations were repeated assuming a flaw depth of 1.55 mm (0.061 inch). The critical (minimum proof) pressure for this flaw was determined to be 75.4 MPa (10.94 ksi) and the final crack depth after blunting and tearing was predicted to be 1.769 mm (0.0696 inch), which would ensure the required safe-life.

Stage 37: Failure Mode and Leak-Before-Burst: Since the failure mechanism is ductile and there are no hazardous materials involved in the proof test, the failure mode is classified as non-hazardous and a leak-before-burst analysis is recommended.

Stage 38: J Estimation/FAD (Through Crack): The flaws to be analyzed for the LBB are through-wall axial defects. J can be determined using a material specific estimation scheme where J has the form

$$J = J_e(2c + t, P)\left[1 + \frac{0.5\left[\frac{P}{P_o}\right]^2}{1 + \alpha\left[\frac{P}{P_o}\right]^{n-1}} + 1.873\,\alpha\left[\frac{P}{P_o}\right]^{n-1}\right] \tag{C2.7}$$

where, from Table A4.2, $V^*=V=1.873$ for a lower bound (service) analysis in plane stress (thin section). $J_e(2c + t, P)$ can be evaluated from K^2/E', where K values were obtained from Krenk (1978) expressed in the form

$$K = \frac{R_m}{t} P\sqrt{\pi c}\,(1 + 0.7044\,\rho + 0.8378\,\rho^2)^{\frac{1}{2}}\ ,\ 0 \le \rho \le 4.4 \tag{C2.8}$$

and P_o was taken to be [40]

$$P_0 = \frac{\sigma_0 t}{R_m}\frac{1}{M(\rho, a/t = 1)} \tag{C2.9}$$

The corresponding material specific failure curve is

$$K_r^* = \left[1 + \frac{0.5\left[L_r^*\left(\frac{\sigma_y}{\sigma_o}\right)\right]^2}{1 + \alpha\left[L_r^*\left(\frac{\sigma_y}{\sigma_o}\right)\right]^{n-1}} + 1.873\,\alpha\left[L_r^*\left(\frac{\sigma_y}{\sigma_o}\right)\right]^{n-1}\right]^{-\frac{1}{2}} \tag{C2.10}$$

where the ratio (σ_y/σ_o) appears because L_r^* is evaluated using the yield stress. In this example, the tensile properties of IN-718 are assumed to be independent of the orientation and so are the same as the values in Table C2.1.

Stage 39: Material Properties (J_R-Curve, through-wall orientation): A lower bound estimate of the J_R-curve at ambient temperature in the through-wall orientation is needed. This lower bound curve should be conservative with respect to the J_R-curve that reflects the plastic constraint in the duct due to the very thin wall and the pressure loading. Suitable J_R-curve data expressed in the form of a quadratic polynomial in tear length

$$J_R(\Delta c_t) = J_0 + J_1 \Delta c_t + J_2 \left[\Delta c_t\right]^2 \tag{C2.11}$$

are shown in Table C2.3. The lower and upper validity limits for this quadratic fit are shown as Δc_{min} and Δc_{max} in the table. Also shown is J_{max}, the value of J_R corresponding to a tear/blunting length of Δc_{min}. The value of J_R is conservatively assumed to be independent of tear length at tear lengths greater than Δc_{max}, and equal to the value evaluated at Δc_{max}.

Table C2.3 J_R-curve parameters for through-wall cracks

J_{max} MPA m (ksi inch)	J_0 MPa m (ksi inch)	J_1 MPa m/mm (ksi)	J_2 MPa m/mm^2 (ksi inch^{-1})	Δc_{min} mm (inch)	Δc_{max} mm (inch)
0.0863	0.0593	0.454	-0.130	0.0610	1.016
(0.492)	(0.338)	(65.73)	(-478.2)	(0.0024)	(0.04)

Stage 40: Analysis Type: The critical pressure corresponding to the assumed through crack is to be calculated.

Stage 43: Critical Load (LBB): The determination of the critical pressure for burst for the specified crack of length 41.66 mm (=2c+t) from a J analysis is described in Section A9.3 for a one degree of freedom crack. The calculations proceed in a similar fashion to the steps detailed in Stage 35. The resulting critical pressure is 31.92 MPa (4.63 ksi) which is attained after 1.016 mm of tearing when the J_R-curve has reached a saturation value of $J_R(\Delta c_t = \Delta c_{max})$. Since the minimum proof test pressure was calculated to be in excess of 80 MPa, it is clear that burst rather than leak is the predicted failure mode for the duct.

APPENDIX D: ASPECTS OF ADVANCED PROOF TEST ANALYSES

D1. PROBABILITY ANALYSIS

D1.1 Limit States and Distribution Functions

In a probability analysis the uncertainty in an input variable, x say, is characterized by a distribution function, $f_X(x)$. The variable is allowed to have any random value within the range defined by the distribution function, and $f_X(x)dx$ determines the likelihood of the variable having a value between x and $x+dx$. In reliability analyses it is customary to define failure in terms of a limit state, signified as g, where failure is predicted when $g \leq 0$. For example, in terms of brittle fracture the limit state can be specified as

$$g = J_{mat} - J \tag{D1.1}$$

In this equation there are uncertainties in the value of the toughness, J_{mat}, and uncertainties associated with the evaluation of J through its dependence on crack size, shape, applied load, structural modeling, and material stress-strain behavior.

In a service life calculation, g may be specified as

$$g = 4\, t_{mission} - t_{service} \tag{D1.2}$$

where $t_{mission}$ is the mission life and $t_{service}$ the calculated service life. The value of the latter will depend on a material properties (such as crack growth rate law constants, fracture toughness), assumed initial flaw sizes, cyclic changes in the applied stress and other factors.

In general, because there may be many random variables (as illustrated by the foregoing examples) the probability of failure, P_f, involves the evaluation of a multi-dimensional integral

$$P_f = \int_{\Omega} f_X(x)\, dx \tag{D1.3}$$

where x will be a vector of random variables, $f_X(x)$, is the joint probability density function of the random variables, X is the variable name, and Ω is the failure domain in random variable space defined by $g \leq 0$. If all the variables are independent, then $f_X(x)$ is simply given as the product of the probability density functions for each of the variables.

Distribution functions can typically be represented by standard functional forms such as Weibull, lognormal, normal, or exponential distributions. Most of these distribution functions can be characterized by mathematical forms which describe both the central tendency of the data (for example, the average or mean value, X_{mean}) and the likely scatter of the data around this central tendency (often described in terms of the standard deviation, σ_X). A typical distribution function is

usually completely described by two (sometimes three) scalar parameters such as X_{mean} and σ_X. For example, the exponential has the form

$$f_X(x) = \lambda^* \, exp[-\lambda^* x] \ , \ x > 0 \tag{D1.4}$$

and the mean and standard deviation are equal and given by

$$X_{mean} = \frac{1}{\lambda^*} \ , \ \sigma_X = \frac{1}{\lambda^*} \tag{D1.5}$$

respectively.

D1.2 Data Requirements

One of the most significant issues limiting the use of probabilistic methods to proof test analysis is the lack of comprehensive probabilistic data bases that contain specific information about the appropriate distribution functions for crack size, fracture toughness, etc. These data are central to realizing the full potential of probabilistic methods for quantifying uncertainties. Current material data bases for aerospace propulsion component design or fracture control are typically deterministic. They provide little, if any, information about the statistical nature of the data, although some anecdotal information for a very limited number of materials is scattered throughout the literature [88,89]. In the future, the advent of general probabilistic design and analysis methods for aerospace propulsion systems is likely to lead to some increases in the amount of probabilistic information available.

Statistical distributions for initial flaw shapes and sizes are particularly important for evaluating the minimum proof load needed to ensure a specified service life at a required reliability level. These data for SSME hardware and fabrication processes have been collected by Rocketdyne and reported in Hudak et al. [14]. They provide an example of the kind of data that are required to build up a distribution function in order to formulate a probabilistic analysis. From data on material test coupons, selected SSME hardware, and available MCPT failure information, SwRI constructed histograms representing the frequency of occurrence against initial crack depths (a), as shown in Figure D1.1 McClung et al. [15] found that a statistical description of the crack depth data was provided by an exponential distribution function with a mean value, X_{mean}=0.0212 inch. This distribution is shown as the dashed curve in Figure D1.1.

D1.3 Application to Proof Test Analysis

Formal proof test optimization requires the simultaneous evaluation of a joint reliability problem: the probability of component failure during the proof test, and then during the subsequent service exposure. These issues are illustrated schematically in Figure D1.2. As the ratio of proof load to design load increases, the probability of failure during the proof test increases. On the other hand, the probability of failure in service for a component which has previously survived this proof test is likely to decrease with increasing proof factor. Optimum design of a proof test must mathematically optimize these two reliability functions, weighing the consequences of proof failure versus service failure.

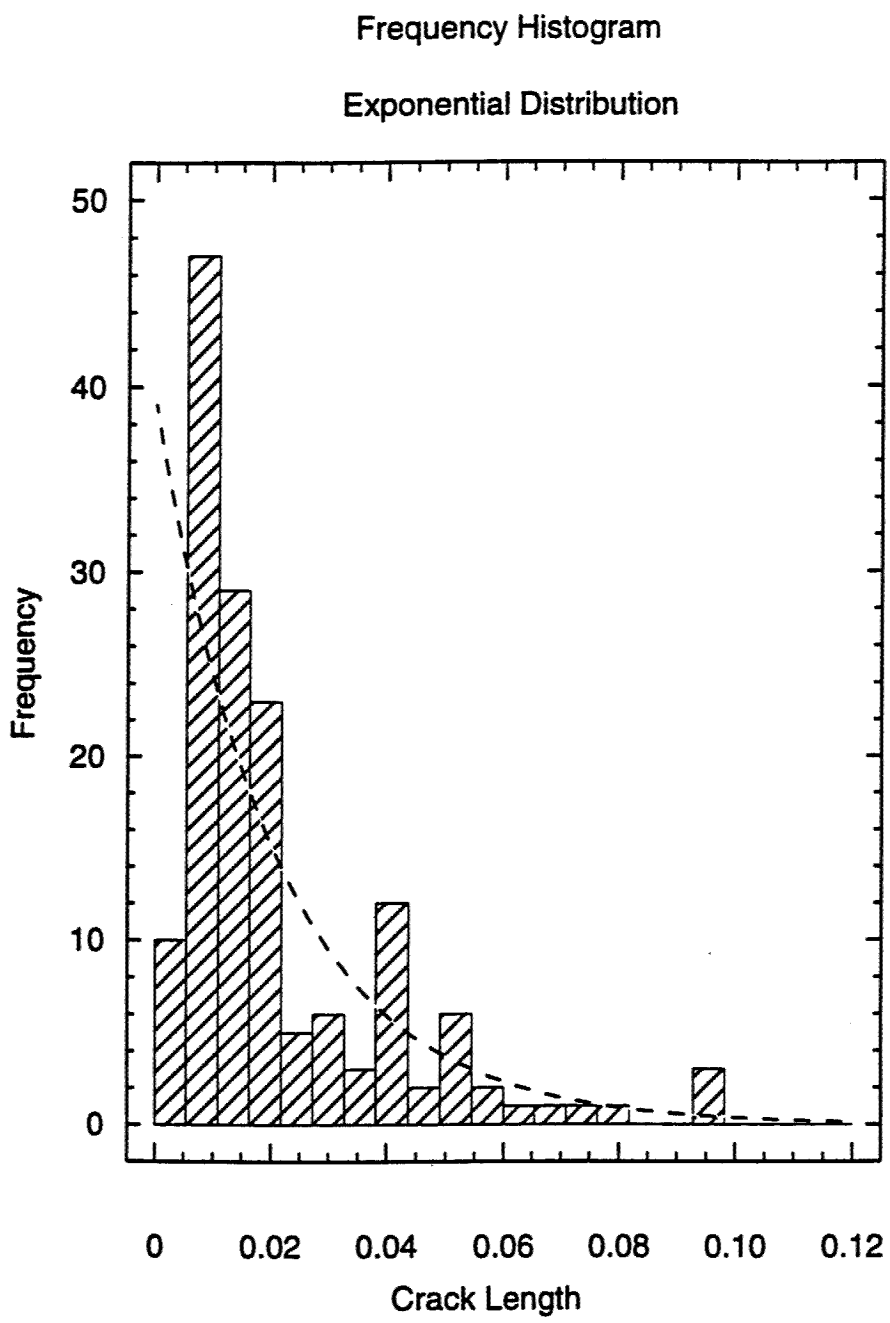

Figure D1.1 Distribution of crack depths and corresponding exponential distribution.

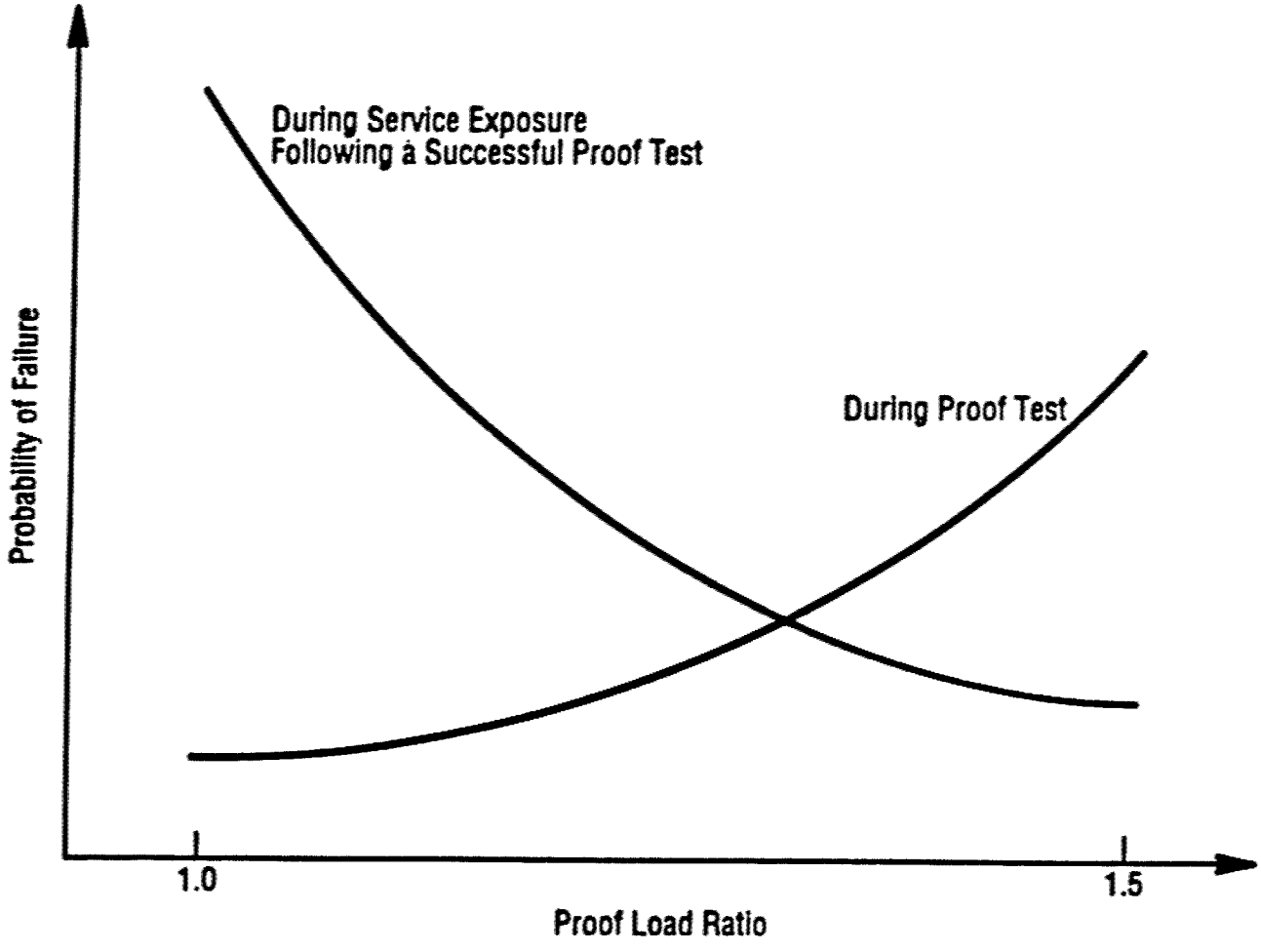

Figure D1.2 Schematic representation of interacting reliability issues associated with proof testing and subsequent service.

Selection of a specific computational method to solve a probabilistic problem depends on both the questions posed and the complexity of the analysis involved. A simple brittle fracture formulation will permit a relatively straightforward solution technique. There are many examples of brittle fracture problems being solved probabilistically in the literature [90,88,89]. Very few examples are available of probabilistic elastic-plastic fracture solutions, but the work of Gates [96] provides an example of one of these. A proof test analysis presents additional difficulties such as allowing for ductile tearing and multiple cycles (see McClung et al. [15]).

Although a comprehensive and rigorous treatment of the probabilistic analysis of proof testing is not feasible at this time, simplifying assumptions can be made to facilitate the computations while still providing meaningful reliability information concerning the efficacy of the proof loading.

The design or evaluation of a proof test on a probabilistic basis may require the identification of a target reliability level; i.e., a quantitative standard to determine whether the demonstrated or estimated component reliability is "good enough." The definition of this standard will likely need to originate outside the framework of the proof test methodology, perhaps in some overall reliability assessment of the entire engine or subsystem.

A probabilistic investigation of the effect of multiple cycle proof testing (MCPT) compared to single cycle proof testing (SCPT) has recently been completed by SwRI in another NASA sponsored program of work. The SCPT is, of course, a special case of MCPT, and the proof test analyst is referred to Section D2 for a summary of the SwRI findings. More details can be obtained from the final report on this work, titled "Comparison of Single Versus Multiple Cycle Proof Testing," for an example of the application of probability analysis to proof testing (McClung et al. [15]).

D1.4 Enabling Technology

The most general technique for determining the probability of failure is based on Monte Carlo simulation. Monte Carlo is a well-known and well-established technique which has often been applied to fracture problems. Approximate techniques based on the Fast Probability Integration (FPI) concept [91], offer similar accuracy to Monte Carlo but much greater speed and some additional output information. These methods can be applied to well-behaved failure functions. Some of the more complicated computations, such as those involving conditional probabilities and NDE inspection, require more advanced system reliability analysis methods that combine an efficient importance sampling method with the FPI method [92].

The advent of probabilistic methodologies is proving an important new development for NASA applications in structural integrity and life analysis. The current centerpiece of NASA technology in probabilistic structural analysis for propulsion systems is the NESSUS (Numerical Evaluation of Stochastic Structures Under Stress) software system developed by Southwest Research Institute under contract to NASA [93,94]. This computer code, developed to support the larger project on "Probabilistic Structural Analysis Methods (PSAM) for Select Space Propulsion System Components" is already being used at NASA Centers, by aerospace contractors, and in other industries as well. Although it does not presently address proof test analyses, it should be possible to develop a NESSUS application module that supports the design and analysis of proof tests.

D2. MULTIPLE CYCLE PROOF TEST ANALYSIS: CRACK GROWTH DUE TO STATIC AND CYCLIC LOADING

In the deterministic proof test analyses which are addressed in these guidelines, MCPT will adversely change the flaw distribution in the hardware by causing additional crack growth compared to SCPT and will, therefore, apparently provide no additional benefit. However, there are circumstances where MCPT is performed on components because it is unavoidable (for example, if the component is part of an assembly process where proof testing is performed at different stages). It should also be remembered that MCPT may have been selected because of the perceived benefits it will confer on the subsequent service reliability. As discussed in Section 7.2, this reasoning will be based on historical data and/or the results of theoretical modeling using probability analysis. In either case, once the decision has been made to use MCPT because of the increase in service reliability it confers, then it will be necessary to include the predicted amount of crack extension due to ductile tearing at the maximum loads in the cycles (the contributions from static loading), and due to fatigue crack extension (the contributions from cyclic loading) in a proof test analysis. Crack growth from these mechanisms will impact the calculation of proof loads and the inferred flaw size distribution at the end of the proof test.

In the absence of ductile tearing, the amount of fatigue crack growth that can occur during MCPT is very limited. However, if the maximum proof load in a cycle is high enough, this can induce ductile tearing which enhances the fatigue extension and can result in significant crack extension. The interaction between static and cyclic crack growth appears to be predominantly mechanical, with fatigue crack propagation providing the means for increasing the crack tip driving force (J) which is necessary for tearing to occur on the next cycle. The effect of ductile tearing on the fatigue crack propagation rate is illustrated in Figure D2.1, which shows that the fatigue rate per cycle can be enhanced by one or two orders of magnitude due to tearing [37,87].

The estimated amount of combined tearing-fatigue crack extension can be bounded by assuming two different models for the fracture resistance behavior during MCPT. In the first, the ductile fracture process zone at the crack tip is assumed to retain all information about previous tear events as it is incrementally advanced by fatigue crack growth into newly deforming material. This is called "Memory Model." In the second, the ductile fracture zone is assumed to loose all information about previous tearing events as it is advanced by fatigue crack extension. This is called "Loss of Memory Model."

The following descriptions of the "Memory Model" and "Loss of Memory Model" for evaluating combined tearing and fatigue crack growth rates are closely based on work performed at SwRI under a NASA MSFC sponsored program on elastic-plastic fatigue crack growth. This work is reported in more detail by Chell and McClung [95]. The Memory Model is recommended for analysis of MCPT as it is likely to be the more appropriate under proof test conditions, but the Loss of Memory Model will predict greater amounts of crack extension during MCPT than will the Memory Model, and hence will be more conservative relative to flaw growth during proof testing, but may or may not be relative to service reliability.

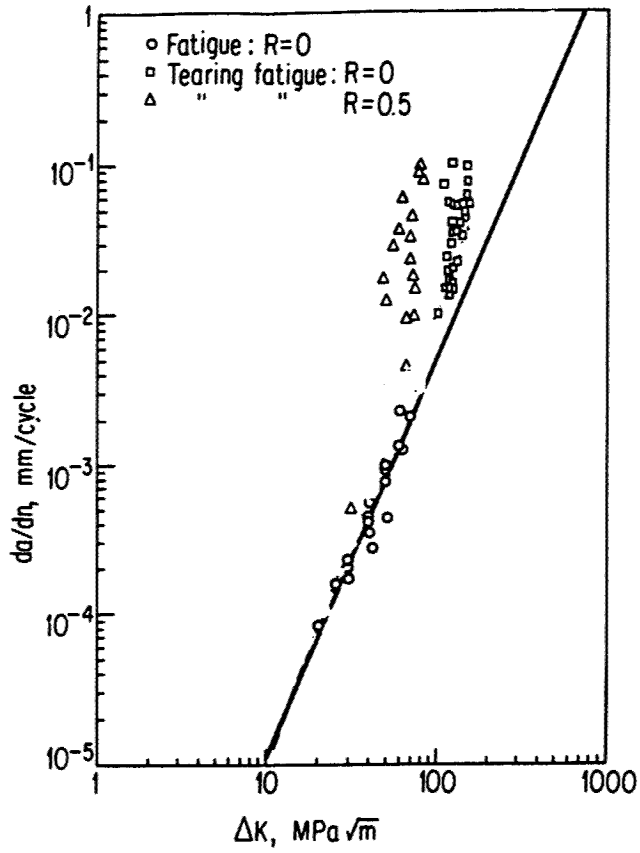

Figure D2.1 Example of the enhanced crack growth rate due to tear-fatigue compared to fatigue crack growth rates.

D2.1 Memory Model

A simple model for including the effects of monotonic ductile fracture modes on fatigue crack growth rates has been proposed by Kaiser [97] and Chell [35] for cyclic loading typical of proof test conditions where only tensile loads are applied and the R ratio (= minimum load/maximum load) is zero or positive. In this model, there is no mechanistic interaction between fracture and fatigue mechanisms, but a synergistic interaction occurs due to the increase in crack-tip driving forces from physical crack extensions resulting from each mechanism. In the model, the instantaneous crack extension per cycle, *da/dN*, is assumed equal to the linear addition of the crack growth rates from each of the mechanisms

$$\frac{da}{dN} = \left(\frac{da}{dN}\right)_f + \left(\frac{da}{dN}\right)_t \tag{D2.1}$$

where a is the instantaneous crack depth during the proof test and $(da/dN)_t$ is the contribution from tearing given by

$$\left(\frac{da}{dN}\right)_t = 0, \ if \ J_{max} \le J_{mat} \tag{D2.2}$$

$$\left(\frac{da}{dN}\right)_t = \frac{dJ_{max}}{dN} / \frac{dJ_R}{d(\Delta a_t)}, \ if \ J_{max} > J_{mat}, \ \frac{dJ_{max}}{dN} > 0 \tag{D2.3}$$

$$\left(\frac{da}{dN}\right)_t = 0, \ if \ \frac{dJ_{max}}{dN} \le 0 \tag{D2.4}$$

Using equation (D2.3) and replacing dJ_{mat}/dN by $(dJ_{mat}/da)(da/dN)$, then equation (D2.1) can be re-arranged into the form [35]

$$\frac{da}{dN} = \frac{\left(\frac{da}{dN}\right)_f}{1 - \frac{dJ_{max}}{da} / \frac{dJ_R}{d(\Delta a_t)}} \tag{D2.5}$$

which predicts an infinite growth rate when the ductile instability criterion, equation (A4.3), is satisfied.

During stable crack growth the applied J must be balanced by the material's resistance to crack extension, J_R, and hence after n cycles

$$J_{max,n}(a_o + \Delta a_{f,n} + \Delta a_{t,n}) = J_R(\Delta a_{t,n}) \tag{D2.6}$$

where a_o is the crack depth at the start of the proof test and $\Delta a_{t,n}$ is the total ductile tearing after n cycles given by

$$\Delta a_{t,n} = \sum_{i=1}^{n} \delta \Delta a_{t,i} = \sum_{i=1}^{n} (\Delta a_{t,i} - \Delta a_{t,i-1}) \tag{D2.7}$$

where $\delta \Delta a_{t,i}$ is the change in tear length per cycle. The total crack extension due to fatigue after n cycles, $\Delta a_{f,n}$ is given by

$$\Delta a_{f,n} = \sum_{i=1}^{n} \left(\frac{da}{dN} \right)_{f,i} \tag{D2.8}$$

where $(da/dN)_{f,i}$ is the growth rate on the i'th cycle. The crack depth after n cycles, a_n is given by $a_o + \Delta a_{f,n} + \Delta a_{t,n}$.

If at the end of n cycles the Memory Model becomes inappropriate due to a "Loss of Memory" event, then the "memory" of how the total tear length, $\Delta a_{t,n}$, was accumulated is permanently lost (see Section D2.2.2).

The evaluation of $\Delta a_{f,n} + \Delta a_{t,n}$ using Equations (D2.6) and (D2.7) is a computationally easier task than integrating Equation (D2.5) over n cycles.

In the proposed tear-fatigue Memory Model:

(a) fatigue crack extension and ductile tearing are assumed to occur on the load-up part of the cycle and to be independent mechanisms that do not interact except through the mechanical interaction from physical crack extensions associated with each mechanism.

(b) consistent with (a), $(da/dN)_{f,n}$ for the n'th cycle, is evaluated for the crack length, $a_o + \Delta a_{f,n-1} + \Delta a_{t,n-1}$.

(c) provided $(dJ_{max}/dN)_n$ is positive, $\Delta a_{t,n}$ is evaluated from Equation (D2.6) as if $J_{max,n}$ had been applied at the beginning of the n'th cycle to a crack of initial depth $a_o + \Delta a_{f,n}$, and no tearing had occurred during previous cycling.

(d) if $(dJ_{max}/dN)_n$ is zero or negative (i.e., J_{max} remains constant or decreases between the $(n-1)$'th and n'th cycles), then no tearing will occur on the n'th cycle even though $J_{max} > J_{mat}$. (This situation could occur if, for example, the applied loading is displacement controlled, or if the crack is subjected to thermal stressing which results in steep stress gradients.)

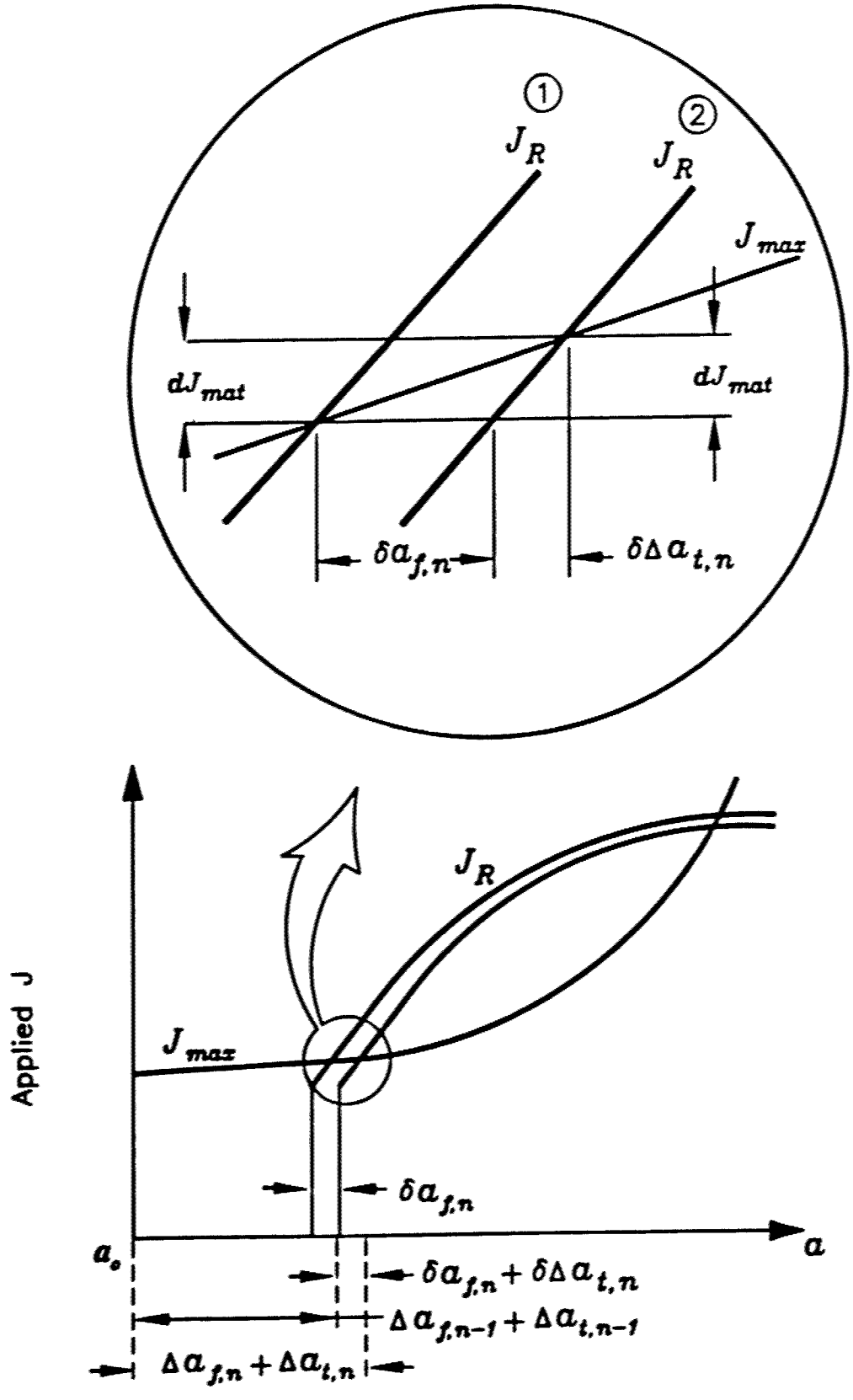

Figure D2.2 Schematic representation of tear-fatigue Memory Model. The insert shows the changes in each quantity per cycle.

Items (c) and (d) imply that the crack-tip ductile process zone retains information about previous tearing events and tearing will not commence until $J_{max,n}$ exceeds $J_{max,n-1}$ on the load-up part of the *n'th* cycle. Hence, the proposed model is herein called the Memory Model for tear-fatigue (see Figure D2.2). In contrast, if a memory of previous cyclic events was not retained within the ductile process zone, then ductile tearing would be expected to begin as soon as J_{max} exceeded J_{mat} on every load-up part of a cycle (see Figure D2.3). This is herein called the Loss of Memory Model and is described in the next section. Limited experimental data support the assumption underpinning items (c) and (d) and the application of the Memory Model. This evidence is discussed in Section D2.3.

The derivation of Equation (D2.6) presupposes that the Memory Model is appropriate for the *n* proof test cycles. Situations where this is not the case are discussed in the next section.

D2.2 Loss of Memory Model

In situations where the Memory Model is not applicable, then a conservative approach to tear-fatigue crack growth should be adopted based on the Loss of Memory Model (see Figure D2.3). This situation can arise, for example, when:

(i) $J_{max,n+1} < J_{max,n}$ and $J_{max,n+1} > J_{mat}$. An example of this possibility is the reduction in the maximum proof test load after a number of cycles.

(ii) There is a significant change in the toughness of the material at the crack tip as it propagates by tear-fatigue. For example, this could occur at a weld where a flaw propagates through weld to base metal, or vice versa.

The recommended procedure for evaluating tear-fatigue in the Loss of Memory Model is to use equation (D2.1) but with $(da/dN)_t$ defined as

$$\left(\frac{da}{dN}\right)_{t,n} = 0, \ if \ J_{max,n} \le J_{mat} \tag{D2.9}$$

$$\left(\frac{da}{dN}\right)_{t,n} = \delta \, \Delta \, \dot{a}_{t,n} \ , \ if \ J_{max,n} > J_{mat} \tag{D2.10}$$

where $\delta \Delta a_{t,n}^{*}$, the change in tear length per cycle and for the *n'th* cycle, is obtained by solving the equation

$$J_{max,n}\left(a_o + \Delta \, a_{f,n} + \Delta \, \dot{a}_{t,n-1} + \delta \, \Delta \, \dot{a}_{t,n}\right) = J_R\left(\delta \, \Delta \, \dot{a}_{t,n}\right) \tag{D2.11}$$

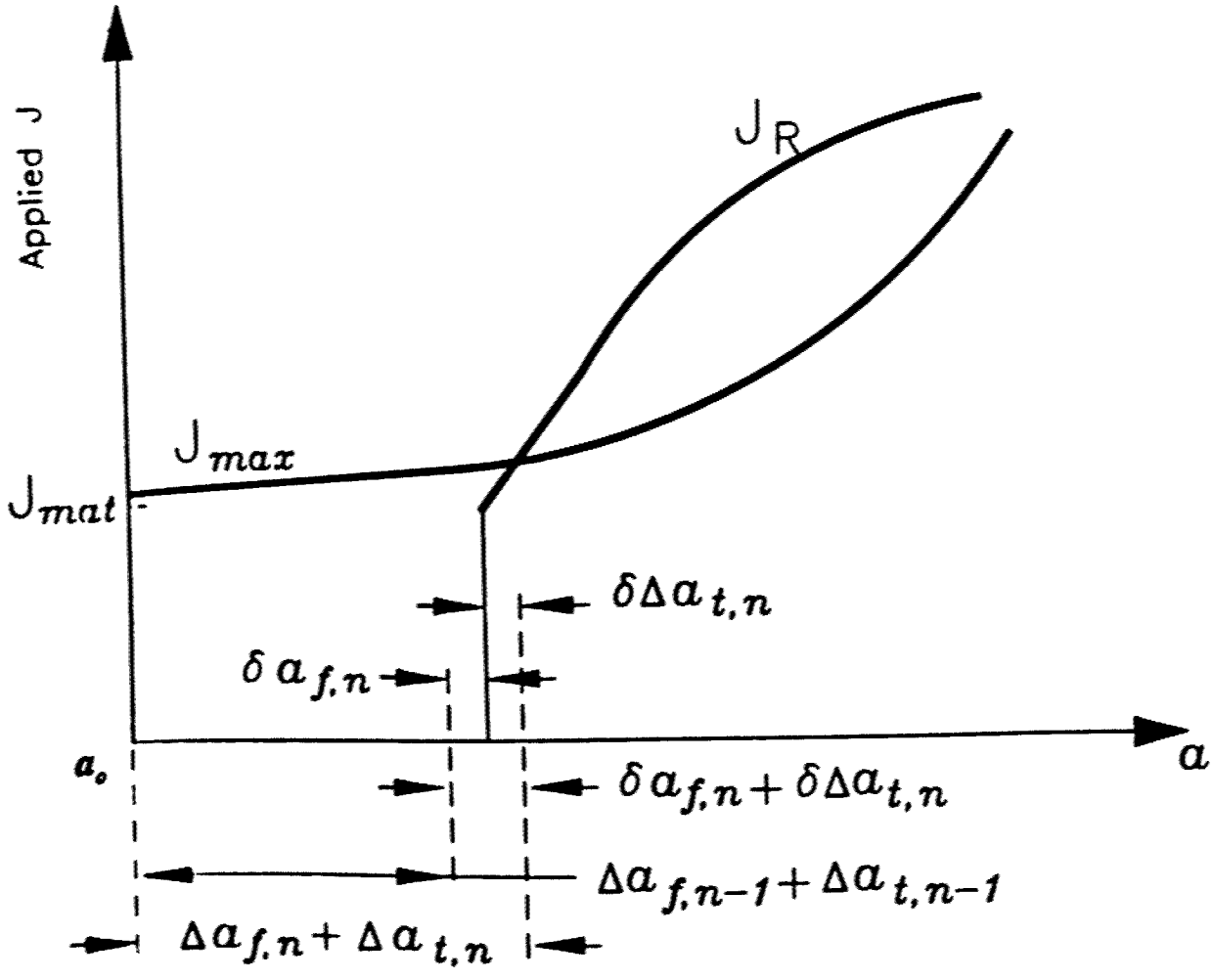

Figure D2.3 Schematic representation of tear-fatigue Loss of Memory model.

and J_R is the toughness pertaining to the proof test environment. The superscript * signifies that ductile tearing has occurred during MCPT under Loss of Memory conditions. The total accumulated tear after n-1 Loss of Memory cycles is given by

$$\Delta a^*_{t,n-1} = \sum_{i=1}^{n-1} \delta \Delta a^*_{t,i} \tag{D2.12}$$

The derivation of equation (D2.11) presupposes that the Loss of Memory Model is appropriate for all the n proof test cycles.

D3. SUBSTANTIATION OF THE TEAR-FATIGUE MODELS

The limited experimental evidence to date where the test conditions satisfied the requirements of Section D2.2.1 show a good correlation between the measured crack growth rates and the predictions of equations (D2.1) to (D2.3). This evidence encompasses the results of Kaiser [97], Nix, et al. [37], and Nix, et al. [87] on steels. Figure D2.4, taken from Nix, et al. [37] shows typical results when the predicted growth rates are plotted against the measured rates.

Recent tear-fatigue behavior observed in fracture tests on IN-718 (a material used in the SSME) as part of the proof test verification tests analyzed in Section B6 found good agreement with the predictions of the tear-fatigue model.

The prediction of the Memory Model that tearing will cease during tear-fatigue if $dJ_{max}/dN \leq 0$, even though $J_{max} > J_{mat}$, has been substantiated in test results reported by Nix et al. [37], and Joyce and Culafic [98]. Nix et al. [37] reported a dramatic reduction in measured growth rates when a change in test conditions was made from a constant plastic load line displacement increment per cycle (where the measured dJ_{max}/dN increased each cycle), to a constant energy input per cycle (where dJ_{max}/dN was nominally zero) (see Figure D2.5). Before the mode change, the measured and tear-fatigue predicted growth rates were 103 μm/cycle and 107 μm/cycle, respectively. After the mode change, the measured and predicted rates were 16 μm/cycle and 11.5 μm/cycle, respectively, and consistent with propagation occurring by fatigue only. This result is even more remarkable when it is realized that the measured value of J_{max} after the mode change was about 1500 kN/m, and ductile tearing was suppressed even though the measured value of J_{mat} was only 141 kN/m.

Joyce and Culafic [98] investigated load history effects in a HSLA steel. In their tests, they periodically imposed large tear steps at high load levels on specimens after they had undergone about 1 mm crack extension due to continuous cycling at lower load levels. They showed that the tearing steps had little measurable effect on the fatigue crack growth rate. In other words, tearing was suppressed after the load (J_{max}) was reduced.

Similar qualitative behavior was observed in the two "Scenario 1" tests on IN-718 reported in Section B6. These tests involved subjecting cracked specimens to a simulated proof test overload up to incipient instability, unloading, followed by simulated service load cycling to failure. Although J_{max} at the maximum load in the service cycle exceeded J_{mat}, there was clear evidence from recorded load-line displacements that tearing did not occur under simulated service conditions until significant crack extension due to fatigue cycling had occurred.

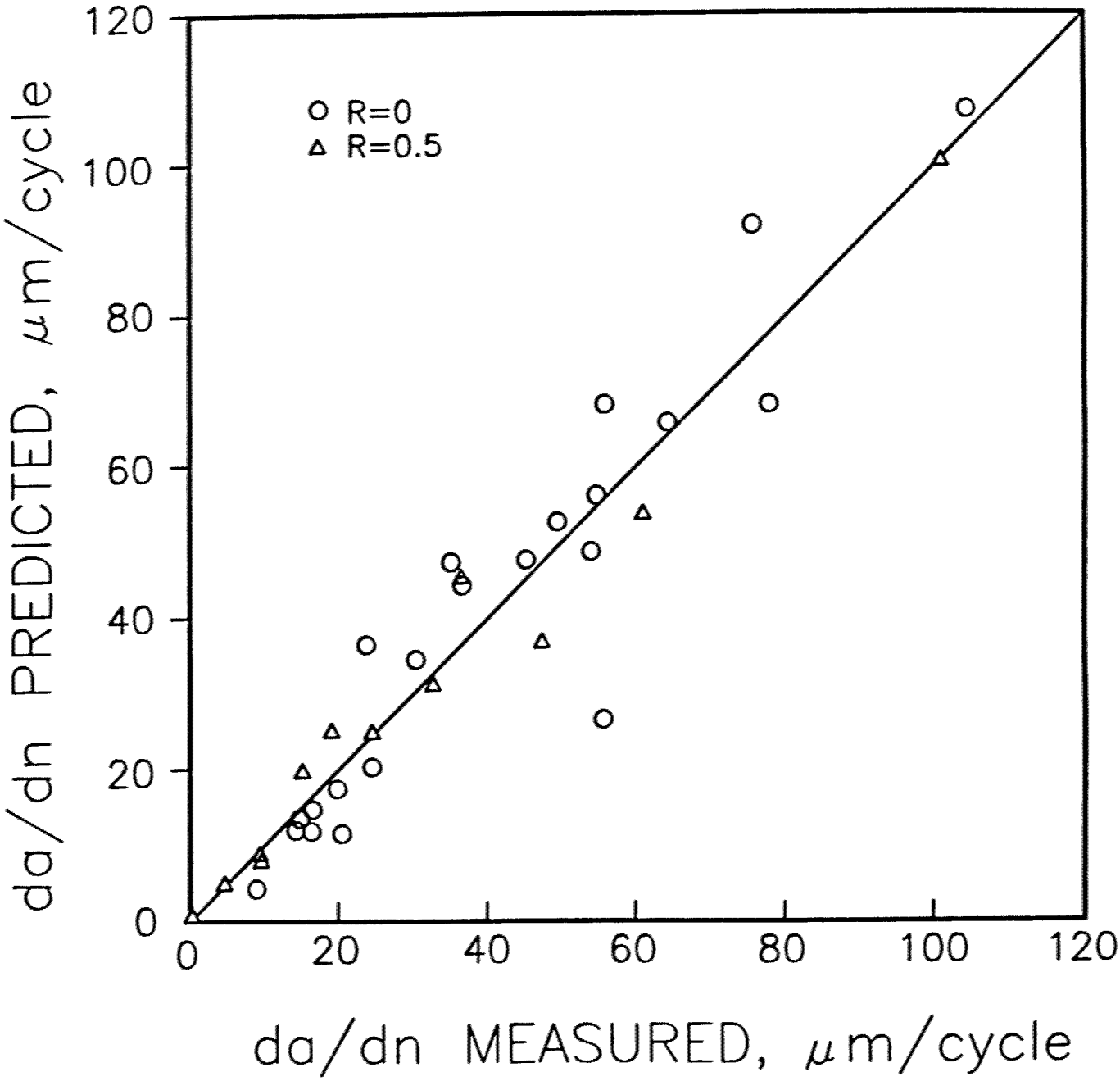

Figure D2.4 Predicted tear-fatigue crack growth rates versus measured values for a mild steel. (After Nix et al. [37]).

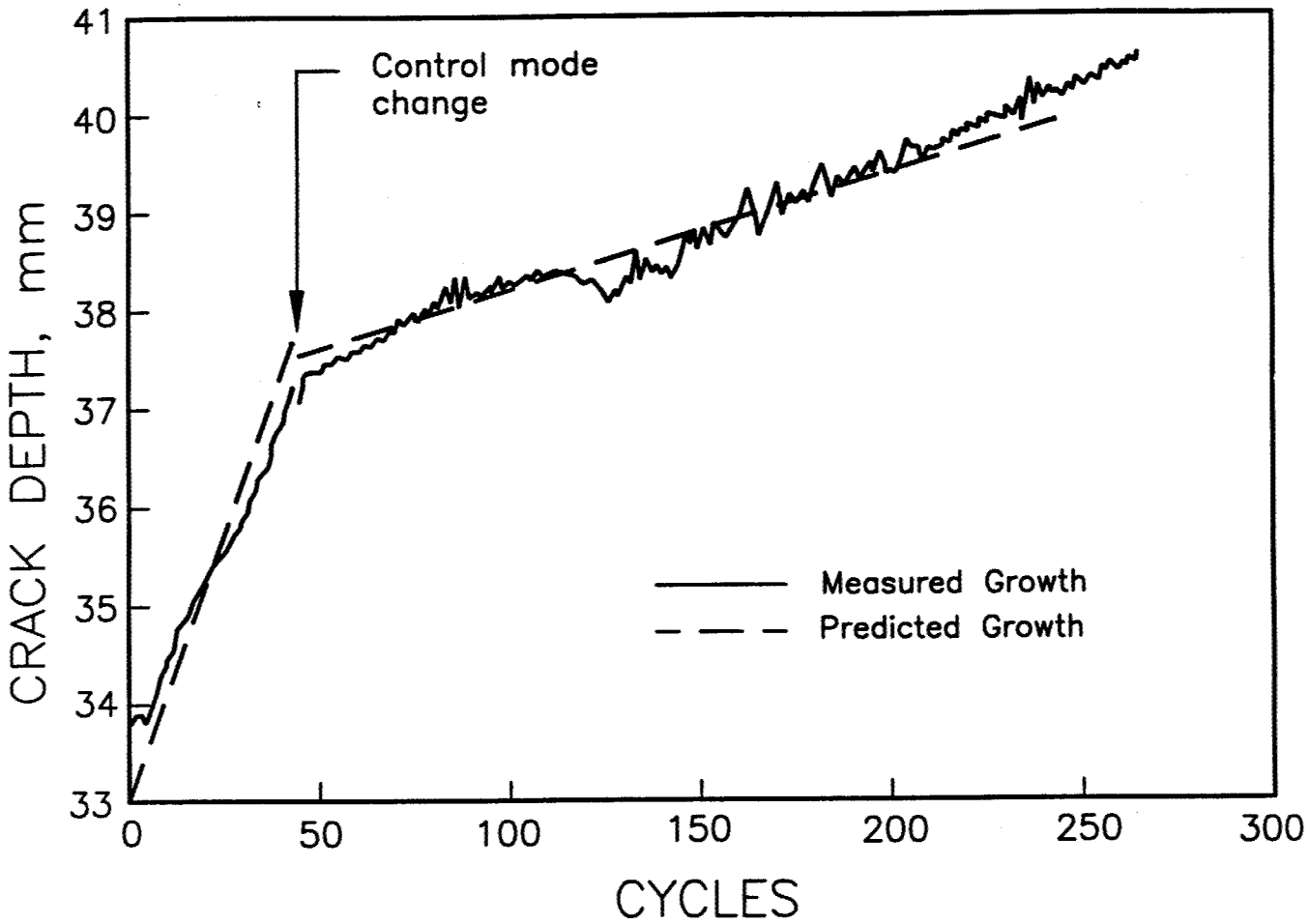

Figure D2.5 Example of the suppression of tearing during a tear-fatigue test when a control mode change reduced dJ_{max}/dN from 22.6 kN/m to 0 kN/m. (After Nix et al. [37]).

REPORT DOCUMENTATION PAGE

Form Approved
OMB No. 0704-0188

Public reporting burden for this collection of information is estimated to average 1 hour per response, including the time for reviewing instructions, searching existing data sources, gathering and maintaining the data needed, and completing and reviewing the collection of information. Send comments regarding this burden estimate or any other aspect of this collection of information, including suggestions for reducing this burden, to Washington Headquarters Services, Directorate for Information Operation and Reports, 1215 Jefferson Davis Highway, Suite 1204, Arlington, VA 22202-4302, and to the Office of Management and Budget, Paperwork Reduction Project (0704-0188), Washington, DC 20503.

1. AGENCY USE ONLY *(Leave Blank)*	2. REPORT DATE	3. REPORT TYPE AND DATES COVERED
	July 1999	Contractor Report (Final)

4. TITLE AND SUBTITLE
Guidelines for Proof Test Analysis

5. FUNDING NUMBERS
NAS8–39380

6. AUTHORS
G.G. Chell, R.C. McClung, C.J. Kuhlman, D.A. Russell,* K. Garr,* and B. Donnelly*

7. PERFORMING ORGANIZATION NAMES(S) AND ADDRESS(ES)
Southwest Research Institute
P.O. Drawer 28510
San Antonio, TX 78228–0510

8. PERFORMING ORGANIZATION REPORT NUMBER
M–932

9. SPONSORING/MONITORING AGENCY NAME(S) AND ADDRESS(ES)
George C. Marshall Space Flight Center
Marshall Space Flight Center, Alabama 35812

10. SPONSORING/MONITORING AGENCY REPORT NUMBER
NASA/CR—1999–209427

11. SUPPLEMENTARY NOTES
Prepared for Structures and Dynamics Laboratory, Science and Engineering Directorate.
Technical Monitor: Charles L. Denniston
*Subcontract Support from Rocketdyne Division, Boeing North American, 6633 Canoga Ave., Canoga Park, CA 91303

12a. DISTRIBUTION/AVAILABILITY STATEMENT
Unclassified-Unlimited
Subject Category 39
Standard Distribution

12b. DISTRIBUTION CODE

13. ABSTRACT *(Maximum 200 words)*

These guidelines integrate state-of-the-art elastic-plastic fracture mechanics (EPFM) and proof test implementation issues into a comprehensive proof test analysis procedure in the form of a road map which identifies the types of data, fracture mechanics based parameters, and calculations needed to perform flaw screening and minimum proof load analyses of fracture critical components. Worked examples are presented to illustrate the application of the road map to proof test analysis. The state-of-the art fracture technology employed in these guidelines is based on the EPFM parameter, *J*, and a pictorial representation of a *J* fracture analysis, called the failure assessment diagram (FAD) approach. The recommended fracture technology is validated using finite element *J* results, and laboratory and hardware fracture test results on the nickel-based superalloy Inconel 718, the aluminum alloy 2024–T3511, and ferritic pressure vessel steels. In all cases the laboratory specimens and hardware failed by ductile mechanisms. Advanced proof test analyses involving probability analysis and multiple-cycle proof testing (MCPT) are addressed. Finally, recommendations are provided on how to account for the effects of the proof test overload on subsequent service fatigue and fracture behaviors.

14. SUBJECT TERMS
proof test analysis, elastic-plastic fracture mechanics, *J*-integral, failure assessment diagrams, reference stress approach, cracks at stress concentrators, defected welds, residual stresses, resistance curves, ductile crack growth, tear-fatigue, multiple-cycle proof testing, probability analysis, proof test overload effects, nondestructive examination, Inconel 718, aluminum 2024–T3511, ferritic pressure vessel steels, hardware testing, laboratory fracture tests

15. NUMBER OF PAGES
360

16. PRICE CODE
A16

17. SECURITY CLASSIFICATION OF REPORT	18. SECURITY CLASSIFICATION OF THIS PAGE	19. SECURITY CLASSIFICATION OF ABSTRACT	20. LIMITATION OF ABSTRACT
Unclassified	Unclassified	Unclassified	Unlimited

National Aeronautics and
Space Administration
AD33
George C. Marshall Space Flight Center
Marshall Space Flight Center, Alabama
35812